NASA Contractor Report 3664

TECH LIBRARY KAFB, NM

00b24b7

Development of Aerodynamic Prediction Methods for Irregular Planform Wings

David B. Benepe, Sr.

NASA

NASA Contractor Report 3664

Development of Aerodynamic Prediction Methods for Irregular Planform Wings

David B. Benepe, Sr.
General Dynamics
Fort Worth, Texas

NASA

National Aeronautics
and Space Administration

Scientific and Technical
Information Branch

1983

TABLE OF CONTENTS

TABLE OF CONTENTS (Cont'd.)

TABLE OF CONTENTS (Cont'd.)

LIST OF TABLES

LIST OF TABLES (Cont'd.)

LIST OF FIGURES

LIST OF FIGURES (Cont'd.)

LIST OF FIGURES (Cont'd.)

LIST OF FIGURES (Cont'd.)

LIST OF FIGURES (Cont'd.)

LIST OF FIGURES (Cont'd.)

LIST OF FIGURES (Cont'd.)

LIST OF FIGURES (Cont'd.)

LIST OF FIGURES (Cont'd.)

LIST OF FIGURES (Cont'd.)

LIST OF FIGURES (Cont'd.)

LIST OF FIGURES (Cont'd.)

LIST OF FIGURES (Cont'd.)

LIST OF FIGURES (Cont'd.)

LIST OF FIGURES (Cont'd.)

LIST OF FIGURES (Cont'd.)

LIST OF FIGURES (Cont'd.)

LIST OF FIGURES (Cont'd.)

LIST OF FIGURES (Cont'd.)

LIST OF FIGURES (Cont'd.)

LIST OF FIGURES (Cont'd.)

LIST OF FIGURES (Cont'd.)

LIST OF FIGURES (Cont'd.)

LIST OF FIGURES (Cont'd.)

LIST OF FIGURES (Concluded)

INTRODUCTION

In the early 1970's, the Langley Research Center of The National Aeronautics and Space Administration initiated a combined experimental and analytical investigation to study the aerodynamic characteristics of irregular planform wings (also sometimes referred to as cranked wings (ref. 1) or double-delta wings (ref. 2). For this study, the planforms were referred to as wing-fillet combinations with the inboard more highly swept portion of the planform being defined as a fillet.

The early phase of the study was directed toward improving the aerodynamics of the space shuttle orbiter (e.g., ref. 3), although the general long-range goals are applicable toward improved design of aircraft as well as certain advanced aerospace vehicles. The benefits to be derived from the use of fillets with selected planforms include linearization of the subsonic lift-curve slope to high angles of attack. With regard to the space shuttle orbiter design, the improved lift at the angle of attack specified for landing allowed for either reduced landing speed or reduced wing planform area for specified mission return weight. In addition, proper tailoring of the wing-fillet combination allows linearization of the curve of pitching moment against angle of attack to angles for high lift; thus, trim penalties on both lift and performance are reduced. Although these subsonic benefits might be favorable, the question arose as to what effect a near-optimum design would have on the desired hypersonic trim angle and stability requirements (dictated by cross-range or heating constraints). Since both subsonic and hypersonic conditions were the two prime areas of concern in the application of wing-fillet combinations, the overall study was designated the Subsonic-Hypersonic Irregular Planform Study (SHIPS).

With regard to the overall SHIPS program, the objectives of the study are to generate an experimental data base from low subsonic to hypersonic speeds accounting for secondary effects of Reynolds number, airfoil section, leading-edge radius and sweep as well as planform geometry; to provide an aerodynamic prediction technique for irregular planform wings based on these extensive wind-tunnel results; and to provide empirically determined

boundaries to serve as design guides regarding linearized lift, pitch, and realistic longitudinal center-of-pressure locations as functions of Mach number.

The present report is an element of the overall SHIPS program and presents the results of an investigation to develop a prediction technique for the low-speed static aerodynamic characteristics in pitch of a class of low-aspect ratio irregular planform wings for application in preliminary design studies of advanced aerospace vehicles.

The presentation is organized in the following manner.

- The scope of the investigation is discussed first to provide a basis for understanding the goals and the technical approaches used.

- The experimental data base is described in enough detail to support certain judgments that were made during the course of the investigation.

- A presentation of the many geometric parameters used in the investigation and the equations used to generate them is provided.

- The results of an evaluation of previously existing prediction methods are presented and discussed.

- Efforts made to develop additional correlations of test data to help formulate new prediction methods are described and results presented.

- The development of the basic set of prediction methods for lift, drag, and pitching moment of irregular planforms having NACA 0008 airfoils is described.

- The analyses accomplished to account for the secondary effects of Reynolds number, airfoil thickness, airfoil thickness distribution and airfoil camber are illustrated and modifications made to the prediction methods are presented.

2

● Comparisons between predicted lift, drag and pitch-
ing moments and test data are presented.

● Concluding remarks are presented.

● The effects of Reynolds number on the lift-correla-
tion parameter are described in an Appendix.

LIST OF SYMBOLS AND NOMENCLATURE

$A = Æ$ — Aspect ratio

$A_{BASIC} = A_W$ — Aspect ratio of basic wing

A_{TRUE} — Aspect ratio of irregular planform wing

A_1 — Aspect ratio of inboard wing panel

A_2 — Aspect ratio of outboard wing panel

a.c. — Aerodynamic center

$a.c._{\%c_1}$ — Aerodynamic-center location, in percent of root chord of irregular planform

$a.c._{\%\bar{c}}$ — Aerodynamic center location, in percent of mean geometric chord of irregular planform

b — Wing span, meters (ft)

c — Wing chord, meters (ft)

C_R — Root chord of basic wing, meters (ft)

C_T — Tip chord of basic wing, meters (ft)

C_1 — Root Chord of inboard wing panel, meters (ft)

C_2 — Root Chord of outboard wing panel, meters (ft)

C_D — Drag coefficient

4

$C_{D_{BASE}}$ -   Base-drag coefficient

C_{D_C} -   Cross-flow drag coefficient

$C_{D_{FRICT}}$ -   Friction-drag coefficient

$C_{D_{FORM}}$ -   Form-drag coefficient

$C_{D_{INTER}}$ -   Interference-drag coefficient

C_{D_L} -   Drag due to lift

$C_{D_{min}}$ -   Minimum-drag coefficient

$C_{D_{MISC}}$ -   Miscellaneous-drag coefficient

C_F -   Friction-drag coefficient

C_f -   Flat-plate skin-friction coefficient

C_{f_i} -   Incompressible flat-plate skin-friction coefficient

$C_{f_{TURB}}$ -   Turbulent skin-friction coefficient

LIST OF SYMBOLS AND NOMENCLATURE (Cont'd.)

C_L — Lift Coefficient

$C_{L_{\alpha = 0}}$ — Lift coefficient at $\alpha = 0$

$C_{L_{BREAK}}$ — Lift coefficient at upper limit of primary slope region of pitching moment

$C_{L_{max}}$ — Maximum-lift coefficient

C_{L_p} — Potential flow lift coefficient from nonlinear potential flow (lifting surface) theory

$C_{L_{SPENCER}}$ — Lift coefficient produced by Spencer's empirical method for irregular planforms

$C_{L_{WINSTAN_{SLE}}}$ — Lift coefficient produced by WINSTAN empirical method for sharp leading edge double delta planforms

C_{L_α} — Lift-curve slope evaluated near zero lift, 1/radians or 1/degrees

$\left(C_{L_\alpha}\right)_0$ — Lift-curve slope in low-lift region

C_{ℓ_d} — Design lift coefficient for two-dimensional airfoil

C_m — Pitching-moment coefficient

$C_{m_{\alpha = 0}}$ — Pitching-moment coefficient at zero angle of attack

6

$C_{m.25\bar{c}} =$
CM-.25CBAR
- Pitching-moment referenced to quarter chord location of mean geometric chord

$C_{m\alpha}$
- Slope of pitching-moment variation with angle of attack evaluated near zero angle of attack

$C_{m\alpha\,0,1,2,3,\\4,5,6,7}$
- Slopes of linear segment in pitching-moment prediction method

$\bar{c} = MGC = CBAR$
- Mean geometric chord, meters (ft)

$\bar{c}_{eff} = \bar{c}_{WF}$
- Mean geometric chord of irregular planform, meters (ft)

$\bar{c}_{ref}$
- Value of mean geometric chord used as reference length for pitching-moment coefficient

F_1, F_2
- Functions in White-Christoph skin-friction analysis

FF
- Form factor in minimum-drag prediction

FR
- Body fineness ratio for arbitrary crossection body

$F.S._{a.c.}$
- Fuselage station location of aerodynamic center, inches

f
- Function in skin-friction analysis

f_1
- Stall progression factor used in lift prediction

H_B
- Height of rectangular part of body cross section, meters (ft)

7

H_f -   Control surface hinge factor used in minimum-drag analysis and prediction

IF   -   Interference factor used in minimum-drag analysis

K   -   Admissible surface roughness (equivalent sand-grain roughness) diameter, cm (inches)

K_1 -   Function in admissible roughness prediction

L   -   Characteristic length for calculation of Reynolds number in skin-friction analysis, m (ft)

L_B -   Overall body length, meters (ft)

$LER_{\bar{c}_w}$ -   Leading-edge radius at mean geometric chord of basic-wing planform, meters (ft)

LER_{c_T} -   Leading-edge radius of tip chord, meters (ft)

L_N -   Forebody length, meters (ft)

L_{REF} -   Reference length for pitching-moment coefficient

l -   Overall length of irregular planform, meters (ft)

M   -   Mach number

$MGC = MAC = \bar{c} = CBAR$ -   Mean geometric (aerodynamic) chord length, meters (ft)

R_B -   Radius of semicircular portion of body cross-section, meters (ft)

$\left(R_{e_{LER}}\right)_n$ -   Reynolds number based on leading edge radius and velocity evaluated normal to leading edge

$R_{L.S.}$ -   Lifting surface interference factor used in minimum-drag prediction

R_N -   Reynolds number

R_{N_L} -   Reynolds number based on characteristic length of aircraft component

$R_{N/L}$ -   Unit Reynolds number, 1/meter   (1/ft)

$R_{N_{LER_{\bar{c}_w}}}$ -   Reynolds number based on leading-edge radius of mean geometric chord of basic wing

$R_{N_{LER_T}}$ -   Reynolds number based on leading-edge radius at tip

$R_{N_{min}}$ -   minimum Reynolds number   ⎫   defined in text

$R_{N_{max}}$ -   Maximum Reynolds number   ⎬   for use in pre-

$R_{N_{std}}$ -   Standard Reynolds number   ⎭   diction method

$R_{|W-B|}$ -   Wing-body-interference factor used in minimum-drag calculation

"R"   -   Leading-edge-suction ratio

$"R"_{BW}$ -   Plateau value of leading-edge-suction ratio from correlation of basic wing data

$"R_1"$ -   Plateau value of leading-edge-suction ratio for irregular planforms

$"R_{(\alpha)}"$ -   Leading-edge-suction ratio as function of angle of attack

LIST OF SYMBOLS AND NOMENCLATURE (Cont'd.)

$"R_{(\alpha)}"_{1,2,3,4,5,6,7}$ — Value of leading-edge-suction ratio in various regions of linear segmented representation

r — Leading-edge radius of airfoil, meters (ft)

r/c — Leading-edge radius as decimal fraction of airfoil chord

r — Recovery factor used in skin friction analysis only

S_{BASE} — Base area contributing to base drag in minimum drag prediction, Sq. meters (Sq. ft)

S_{REF} — Reference area for aerodynamic coefficients (prediction methods use $S_{REF} = S_{TRUE}$, Sq. meters (Sq. ft))

S_{TRUE} — Total planform area of irregular planforms, Sq meters (Sq ft)

S_W — Wing area of basic wings, Sq. meters (Sq. ft)

S_{WET_B} — Wetted area of body, Sq. meters (Sq. ft)

$S_{WET_{W_1}}$ — Wetted area of inboard wing panels, Sq. meters (Sq. ft)

$S_{WET_{W_2}}$ — Wetted area of outboard wing panels, Sq meters (Sq. ft)

s — Wing semispan, meters (ft)

$\mathcal{A}$ — Slenderness ratio = $s/\mathcal{l}$

Taw	-	Adiabatic wall temperature
T	-	Free-stream temperature
t	-	Function in skin-friction equation
t	-	Airfoil thickness - meters (ft)
t/c	-	Airfoil thickness as fraction of chord
W	-	Basic-wing planform
W_1	-	Inboard wing panel of irregular planform
W_2	-	Outboard wing panel of irregular planform
W_B	-	Body width, meters (ft)
X	-	Longitudinal distance from apex of planform, meters (ft)
$X_{c.g.}$	-	X location of pitching-moment reference point, meters (ft)
X_i	-	X distance from apex to break in leading-edge sweep
X_r	-	Longitudinal distance from body nose or wing leading edge to point of transition to turbulent flow, meters (ft)
$(x/c)_{a.c.}$	-	Chordwise location of aerodynamic center as decimal fraction of wing chord

LIST OF SYMBOLS AND NOMENCLATURE (Cont'd.)

$(x/c)_{t/c_{max}}$ — Chordwise location of airfoil maximum thickness as fraction of chord

$\bar{x}$ — X distance from apex of planform or panel to leading edge of mean geometric chord

$\bar{y}$ — Spanwise distance from root chord of planform or wing panel to mean geometric chord

α — Angle of attack, degrees or radians

α_{BREAK} — Angle of attack for upper limit of primary slope region of pitching moment, degrees

α_s — Angle of attack for initial flow separation used in Chappel's wing flow separation analysis, degrees

α_{STALL} — Limit of linear lift in WINSTAN cranked wing analysis, degrees

$\alpha_{1,2,3,4,5,6,7}$ — Angle-of-attack boundaries in suction ratio and pitching-moment predictions, degrees

$\alpha_{2_{ref}, 3_{ref}, 4_{ref}, 5_{ref}}$ — Angle-of-attack boundaries for reference Reynolds number condition in suction-ratio prediction, degrees

β — Prandtl Glauert factor: $\beta = \sqrt{1-M^2}$

$\delta\alpha_{(1),2,3,4,5}$ — Incremental value of angle-of-attack boundary due to a change in Reynolds number, degrees

$\delta C_{L_{VOR_{SLE}}}$ — Incremental value of lift coefficient caused by vortex flow from sharp wing leading edge

$\Delta a.c._{BREAK}$ — Change in aerodynamic center location at angle of attack for upper limit of primary slope region of pitching moment

Δc_L — Increment of lift coefficient above linear theory

$\Delta c_{L_{RLE}}$ — Increment of lift coefficient for round leading edge

$\Delta c_{L_{SLE}}$ — Increment of lift coefficient for sharp leading edge

Δx — Fictitious distance ahead of transition in mixed laminar-turbulent flow prediction for skin friction, meters (ft)

$\Delta\left(\delta\alpha_{( )}{}^{Cos\Lambda_W}\right)$ — Incremental value of change in angle-of-attack boundary function due to a change in Reynolds number, degrees

$\Delta\left(\dfrac{c_L}{c_{L\alpha}}\dfrac{A_i}{\eta_\beta}\right)$ — Incremental value of lift correlation parameter (note three different types of increments are discussed in the text)

$\Delta\alpha_{(3-2)}$ — Incremental value of angle of attack between boundaries α_3 and α_2, degrees

$\Delta\alpha_{(4-3)}$ — Incremental value of angle of attack between boundaries α_4 and α_3, degrees

$\Delta\alpha_{(5-4)}$ — Incremental value of angle of attack between boundaries α_5 and α_4, degrees

η_B = ETAB   –   Nondimensional spanwise location of break in leading-edge sweep

θ_{LE} –   Compliment of leading-edge-sweep angle, degree

Λ –   Sweep angle, degrees

Λ_F –   Leading-edge-sweep angle of fillet, degrees

$\Lambda_{LE} = \Lambda_W$ –   Leading-edge-sweep angle of basic wing and outboard wing panel, degrees

Λ_{TE} –   Trailing-edge-sweep angle, degrees

$\Lambda_{c/2}$ –   Sweep angle of half chord line, degrees

$\Lambda_{c/4}$ –   Sweep angle of quarter chord line, degrees

$\Lambda_{t/c_{max}}$ –   Sweep angle of maximum thickness line, degrees

λ_W –   Taper ratio of basic wing planform

Ω –   Correlation function for suction ratio in plateau region

Ω_T –   Correlation function for effect of Reynolds number on angle-of-attack boundaries defining regions of linear variation of suction ratio with angle of attack

$\left(\dfrac{dCm}{dC_L}\right)$ –   Longitudinal stability derivative evaluated near zero angle of attack

LIST OF SYMBOLS AND NOMENCLATURE (Concluded)

$$\left(\frac{d \ "R"}{d \ \alpha}\right)_{\substack{(2),3,4, \\ 5,6,7}}$$ - Slope of suction-ratio curve in each region

CODES

Configuration code used in many figures

$$\Lambda_F \quad \Lambda_W \quad .\text{Airfoil}$$
Example 80 45 .0008

Computer Procedure Code

R1T - Air Force version of Aeromodule Computer Procedure (Ref. 8)

X6I - SHIPS Aerodynamic Prediction Procedure for Irregular Planform Wings

Note: Quantities are presented in the International System of Units (U.S. customary units in parenthesis). The work was performed using U.S. customary units.

SCOPE OF THE INVESTIGATION

The scope of this investigation as originally conceived was based on the analysis of wind-tunnel test data from a single parametric experimental investigation of 35 planforms having NACA 0008 airfoils plus a few configurations having NACA 0012 airfoils or sharp leading-edge double-wedge airfoils. The nominal unit Reynolds number range of the test data was from 6.56 million per meter (2 million per foot) to 26.25 million/meter (8 million per foot). The test data base consisted of 131 pitch runs.

Additional tests were tentatively scheduled to provide data to higher Reynolds numbers on a limited series of planforms including variations of airfoil sections. Data from the additional tests were to be considered when and if they became available.

The basic objectives of the investigation were:

(1) To evolve empirical methods from the SHIPS experimental data base for the prediction of first and second order subsonic lift, drag, and pitching-moment characteristics of irregular planform wings of moderate to high thickness ratios having application on possible advanced aerospace vehicles.

(2) To provide correlating parameters and simple predesign charts as well as a rapid and efficient computer program for quick evaluation of new configurational concepts.

The proposed technical approach to meet these objectives had four basic elements.

(1) Existing prediction methods would be examined first to evaluate their applicability.

(2) Where needed, correlations of the SHIPS experimental data would be accomplished to formulate improved methods.

(3) The basic prediction methods would be developed from the data available from the initial test at the maximum unit Reynolds number for the configurations having NACA 0008 airfoils.

(4) Modifications to the basic methods to account for Reynolds number effects and airfoil section effects would be sought depending on the scope of data available during the course of the investigation.

In fact, five additional tests were accomplished by NASA which increased the test data base to 452 pitch runs as described in the next section. The additional tests were essential to meet the objectives of the investigation.

Prediction methods were sought for the following elements of the static aerodynamic characteristics in pitch.

- Lift-curve slope near zero lift $\left(C_{L_\alpha}\right)_o$
- Nonlinear lift increment ΔC_L

- Low angle-of-attack stability derivative $\left(\dfrac{dCm}{dC_L}\right)_o$

- Aerodynamic center location - $(x/c)_{a.c.}$
- Angle of attack for stall $-\alpha_{STALL}$

- Pitch-up/pitch-down boundaries

- Drag due to lift - C_{D_L}

- Variation of leading-edge-suction ratio with angle of attack - "R (α)"

It was assumed from previous experience that existing methods of predicting the minimum-drag coefficient were sufficiently accurate to meet the objectives of the investigation if properly applied to the irregular planforms.

The magnitude of the analysis task is illustrated by the fact that more than 4000 curves were plotted during the course of the investigation. Small programmable calculators and desk top computers were beneficial in manipulating and plotting the large mass of data.

EXPERIMENTAL DATA BASE

The scope of the experimental data base is described in this section. The planform study (ref. 4) consisted of 35 planforms illustrated in Figure 1 in which the geometry is shown normalized with respect to the root chord of the basic wings. The detailed geometric characteristics of these planforms are presented in Tables 1 and 2 for the initial series of models. In essence, the planform families started with five basic tapered planforms having leading-edge sweeps of 25, 35, 45, 53 and 60 degrees. The irregular planforms were generated by adding various fillets of increased leading edge sweeps up to a maximum of 80 degrees. The wing area (S_W) and aspect ratio (A_{BASIC} = 2.265) of the basic planforms were constant, and the spanwise location of the intersection of the fillet leading edge and the basic wing leading edges was constant (η_B = 0.41157). The airfoil chordwise thickness distribution was constant across the span.

The models were constructed such that each planform was a separate model which was attached under a minimum cross section balance housing as shown in Figure 2. Nose fairings and constant cross section aft extensions were fitted to the balance housing to produce a "minimum body" for each wing-fillet combination.

Data were supplied from six tests as described below.

(1) Test ARC 086-12-1. Ames Research Center 12-foot pressure tunnel. Planform Study - small models.

   Complete planform matrix (35 planforms) with NACA 0008 airfoils

   3 planforms with NACA 0012 airfoils
   Λ_W = 25°; Λ_F = 25°, 60°, 80°

   4 planforms with 8 percent thick modified double wedge airfoils
   Λ_W = 35°, Λ_F= 35°, 80°

   Λ_W = 60°, Λ_F = 60°, 80°

Boundary-layer transition strips on wings and body nose for most runs.

Mach number = 0.30

Nominal unit Reynolds numbers = 6.56, 13.12, 19.69, 26.25 million per meter (2, 4, 6, 8 million per foot)

NOTE: some planforms were tested at only the two or three highest unit Reynolds numbers.

αRange from -2° to 26°

$\tilde{S}_{REF}$ = total planform area - STRUE
L_{REF} = MGC of total planform = $\bar{c}_{WF}$
X_{CG} = 0.25 MGC

(2) Test 8-ft TPT-780 Langley Research Center Eight-Foot Transonic Pressure Tunnel. Inboard Panel Alone Tests - small models. Zero suction wing test.

AIRFOIL	Λ_F = 65°, 70°, 75°, 80°			
NACA 0012				(x)
NACA 0008	x	x	x	x

THIN MODIFIED DOUBLE WEDGE $\Lambda_W = 45^{\circ}$, $\Lambda_F = 70^{\circ}$

UNIT REYNOLDS NUMBER	9.84	(11.48)	(16.4)	x 10^6/meter
	3.0	(3.5)	(5.0)	x 10^6/foot
MACH NUMBER	0.3	(.6)	(.8)	

NOTE: Conditions in ( ) run only for NACA 0012 model with $\Lambda_F = 80^{\circ}$

Boundary-layer transition strips on body nose and wing surfaces

αRange: -2° to 21.5°

S_{REF} = Total planform area of irregular planform*

L_{REF} = Mean geometric chord of irregular planform*

X_{CG} = 0.25 mean geometric chord of irregular planform

*For fillet-alone tests, planform area was that of Wing II plus fillets.

(3) Test LTPT-255. Langley Research Center Low-Turbulence
     Pressure Tunnel. Airfoil Thickness Study to High Rey-
     nolds Numbers.

     Limited Matrix of Planforms - small models

AIRFOIL SECTION $\Lambda_W = 45°$; $\Lambda_F = 45°$,	65°,	70°,	75°,	80°
NACA 0008	x		x	x	x
NACA 0012	x	x	x	x	x
NACA 0015	x		x	x	x
THIN MODIFIED DOUBLE WEDGE	x			x	x

UNIT REYNOLDS
  NUMBERS   13.12, 19.67, 26.25, 32.81, 39.37, 45.93 x 10^6/M
                 4,   6,   8,   10,   12,   14 x 10^6/FT
MACH NUMBER   .30   .30   .30   .28   .26   .21

   Boundary-layer transition strips on wings and body nose
   for most runs. Complete range of unit Reynolds numbers
   for each configuration.

       αRange from $-2°$ to $26°$
       S_{REF} = basic wing area - S_W
       L_{REF} = Root chord of irregular planforms -C_1
         X_{CG} = 70 percent of root chord

(4) Test LTPT-262. Langley Research Center Low-Turbulence
     Pressure Tunnel. Additional airfoil section studies to
     high Reynolds numbers.

     Limited Planform Matrix - small models

AIRFOIL SECTION $\Lambda_W = 45°$; $\Lambda_F = 65°$,	70°,	75°,	80°
NACA 0008	x			
NACA 0012	x			
NACA 0015	x			
NACA 65A012		x	x	x
NACA 65_1412		x	x	x

UNIT REYNOLDS
   NUMBERS   13.12, 19.67, 26.25, 32.81, 39.37, 45.93 x 10^6/M
                  4   6   8   10   12   14 x 10^6/Ft
MACH NUMBER .30   .30   .30   .28   .24   .21
      Free transition for all runs.

   αRange from -2° to 36°+

   $S_{REF} = S_W$

   L_{REF} = Root chord of irregular planforms -C_1

   X_{CG} = 70 percent of Root chord -C_1

   (5) Test LTPT-266. Langley Research Center Low-Turbulence
       Pressure Tunnel. More additional Airfoil Section
       Studies to High Reynolds Numbers.

            Limited Planform Matrix - small models

AIRFOIL SECTION Λ_W = 45°; Λ_F = 60°, 65°, 70°, 75°, 80°
NACA 0008   x
NACA 0012   x
NACA 0015   x
NACA 0004   x   x   x   x   x   x
UNIT REYNOLDS
   NUMBERS   13.12, 19.69, 22.97, 26.25, 32.81, 39.37 x 10^6/meter
                  4   6   7   8   10   12 x 10^6/Ft
MACH NUMBERS .2   .2   (.2)   .2   .2   .2
             (.3)   .3   (.3)   (.3)

   NOTE: Conditions in (   ) only for NACA 0008, 0012, 0015

   Boundary-layer transition strips on wings and body nose
   for all runs.

   αRange from -2° to 36°+

   $S_{REF} = S_W$
   L_{REF} = Root chord of irregular planform -C_1
   X_{CG} = 70 percent of Root chord -C_1

(6) Test ARC-12-257. Ames Research Center 12-Foot Pressure Tunnel. Airfoil Section Study at High Reynolds Numbers and constant Mach Numbers. Limited Planform Matrix - large models (twice size of small models).

AIRFOIL SECTION $\Lambda_W = 45°$; $\Lambda_F = 60°$, $70°$, $75°$, $80°$

	$60°$	$70°$	$75°$	$80°$
NACA 0008	x	x	x	x
NACA 0012	x	x	x	x
NACA 0015	x	x	x	x
NACA 65A012		x	x	x
NACA 65_1412		x	x	x

UNIT REYNOLDS
NUMBERS   6.56, 13.12, 16.40, 19.69, 22.97, 26.25 X 10^6/Ft
           2*   4*   5,   (6)   7,   8*
MACH NUMBER .3   .3   .3,   (.3)   .3,   .3*

NOTES: (1) NACA 65A012 and NACA 65_1412 configurations run only for conditions in ( ).

(2) Conditions noted by * run for only one configuration.

Free transition for all runs.

αRange - $2°$ to $20°$

$S_{REF} = S_W$

L_{REF} = Root Chord of irregular planform $-C_1$

X_{CG} = 70 percent of Root Chord

The fact that three different test facilities and two different test techniques as well as two different size models were used during the experimental program was considered in the analysis. As a consequence, there are uncertainties in the experimental data which are reflected in the prediction methods.

The use of different sets of reference quantities in the data reduction for the additional tests from those used in the basic planform series test required that pertinent data from the additional test be recalculated to be put on the same basis as data from the basic test.

TABLE 1

GEOMETRIC CHARACTERISTICS OF BASIC WINGS

WING I

Leading-edge sweep, deg	25
Trailing-edge sweep, deg	25
Quarter-chord sweep, deg	13.12427
Half-chord sweep, deg	0.00000
Aspect ratio	2.26500
Taper ratio	.30882
Planform area, ft^2 (m^2)	.52724 (.04898)
Span, ft (m)	1.09279 (.33307)
Root chord, ft (m)	.73726 (.22471)
Tip chord, ft (m)	.22768 (.06939)
Mean aerodynamic chord, ft (m)	.52733 (.16073)
Longitudinal location of mean aerodynamic chord (x), ft (m) . .	.10497 (.03199)
Spanwise location of mean aerodynamic chord (y), ft (m)	.22511 (.06861)
Airfoil sections	NACA 0008, 0012

WING II

Leading-edge sweep, deg	35
Trailing-edge sweep, deg	20
Quarter-chord sweep, deg	23.46871
Half-chord sweep, deg	9.54388
Aspect ratio	2.26500
Taper ratio	.24798
Planform area, ft^2 (m^2)	.52724 (.04898)
Span, ft (m)	1.09279 (.33307)
Root chord, ft (m)	.77320 (.23567)
Tip chord, ft (m)	.19174 (.05844)
Mean aerodynamic chord, ft (m)	.54088 (.16486)
Longitudinal location of mean aerodynamic chord (x), ft (m) . .	.15287 (.04659)
Spanwise location of mean aerodynamic chord (y), ft (m)	.21832 (.06654)
Airfoil sections	NACA 0008, Double Wedge

TABLE 1

GEOMETRIC CHARACTERISTICS OF BASIC WINGS

WING III

Leading-edge sweep, deg	45
Trailing-edge sweep, deg	15
Quarter-chord sweep, deg	34.33357
Half-chord sweep, deg	20.10485
Aspect ratio	2.26500
Taper ratio	.16416
Planform area, ft^2 (m^2)	.52724 (.04898)
Span, ft (m)	1.09279 (.33307)
Root chord, ft (m)	.82887 (.25263)
Tip chord, ft (m)	.13607 (.04147)
Mean aerodynamic chord, ft (m)	.56538 (.17232)
Longitudinal location of mean aerodynamic chord (x), ft (m)	.20782 (.06334)
Spanwise location of mean aerodynamic chord (y), ft (m)	.35351 (.06334)
Airfoil sections	NACA 0008

WING IV

Leading-edge sweep, deg	53
Trailing-edge sweep, deg	7
Quarter-chord sweep, deg	43.96733
Half-chord sweep, deg	31.05545
Aspect ratio	2.26500
Taper ratio	.098334
Planform area, ft^2 (m^2)	.52724 (.04898)
Span, ft (m)	1.09279 (.33307)
Root chord, ft (m)	.87856 (.26778)
Tip chord, ft (m)	.08639 (.02633)
Mean aerodynamic chord, ft (m)	.59086 (.18009)
Longitudinal location of mean aerodynamic chord (x), ft (m)	.26339 (.08026)
Spanwise location of mean aerodynamic chord (y), ft (m)	.19844 (.06048)
Airfoil sections	NACA 0008

TABLE 1

GEOMETRIC CHARACTERISTICS OF BASIC WINGS

WING V

Leading-edge sweep, deg 60
Trailing-edge sweep, deg 0
Quarter-chord sweep, deg 52.41091
Half-chord sweep, deg 40.89615
Aspect ratio 2.26500
Taper ratio 00969
Planform area, ft^2 (m^2) . . . . .52724 (.04898)
Span, ft (m) . . . . 1.09279 (.33307)
Root chord, ft (m) . . . . .95566 (.29128)
Tip chord, ft (m) . . . . .00926 (.00282)
Mean aerodynamic chord, ft (m) . . . . .63717 (.19421)
Longitudinal location of mean aerodynamic chord (x), ft (m) . . . .31850 (.09708)
Spanwise location of mean aerodynamic chord (y), ft (m) . . . . . .18389 (.05605)
Airfoil sections . . . . NACA 0008, Double
                                                                          Wedge

TABLE 2

GEOMETRIC CHARACTERISTICS OF WING-FILLET COMBINATIONS TESTED

WING I $\Lambda_{le} = 25°$ $\Lambda_{te} = 25°$ $S_{ref} = .04898\ m^2$ $A_{ref} = 2.26500$

Λ_f, deg	80	75	70	65	60	55	45	35
$\Lambda_{c/4,eff}$, deg	57.9706	49.7656	44.0165	39.0915	34.7258	30.7894	23.9277	18.1252
$\Lambda_{c/2,eff}$, deg	56.2424	46.3857	38.0010	30.8123	24.6805	19.4625	11.1867	4.9436
A_{TRUE}	1.51076	1.72474	1.85838	1.95096	2.01978	2.07369	2.15470	2.21530
S_{TRUE}, m²	.07343	.06432	.05969	.05686	.05493	.05350	.05149	.05008
$C_{R,\ TRUE}$, m	.58147	.44855	.38107	.33974	.31147	.29064	.26129	.24074
$\bar{c}$, eff, m	.32187	.25502	.22362	.20549	.19363	.18522	.17390	.16636
$\bar{x}$, eff, m	.23471	.16664	.12929	.10523	.08816	.07523	.05644	.04286
$\bar{y}$, eff, m	.05337	.05770	.06040	.06227	.06366	.06475	.06639	.06761
$\Delta y/b/2$	.41157	.41157	.41157	.41157	.41157	.41157	.41157	.41157

TABLE 2

GEOMETRIC CHARACTERISTICS OF WING-FILLET COMBINATIONS TESTED

WING II $\Lambda_{le} = 35°$ $\Lambda_{te} = 20°$ $S_{ref} = .04898 \, m^2$ $A_{ref} = 2.26500$

Λ_f, deg	80	75	70	65	60	55	45	35
$\Lambda_{c/4,eff}$, deg	60.6042	53.8730	48.4308	43.7321	39.5459	35.7570	29.1199	
$\Lambda_{c/2,eff}$, deg	57.1494	47.6537	39.6649	32.8715	27.1129	22.2486	14.7040	
A_{TRUE}	1.53370	1.75471	1.89323	1.98940	2.06101	2.11717	2.20169	
S_{TRUE}, m^2	.07233	.06322	.05860	.05577	.05383	.05240	.05039	
$C_{R,TRUE}$, m	.57640	.44348	.37599	.33466	.30639	.28556	.25622	
$\bar{c}$, eff, m	.32144	.25415	.22254	.20426	.19233	.18385	.17245	
$\bar{x}$, eff, m	.23588	.16869	.13186	.10812	.09128	.07853	.05999	
$\bar{y}$, eff, m	.05244	.05670	.05937	.06123	.06261	.06369	.06532	
$\Delta y/_{b/2}$	.41157	.41157	.41157	.41157	.41157	.41157	.41157	

TABLE 2

GEOMETRIC CHARACTERISTICS OF WING-FILLET COMBINATIONS TESTED

WING III $\quad \Lambda_{\ell e} = 45°$ $\quad \Lambda_{te} = 15°$ $\quad S_{ref} = .04898 \ m^2$ $\quad A_{ref} = 2.26500$

Λ_f, deg	80	75	70	65	60	55	45	35
$\Lambda_{c/4,eff}$, deg	64.4756	58.2148	53.0556	48.5494	44.5046	40.8236		
$\Lambda_{c/2,eff}$, deg	58.8962	49.8928	42.4106	36.1350	30.8972	26.5621		
A_{TRUE}	1.5642	1.79470	1.93985	2.04095	2.11639	2.17565		
S_{TRUE}, m^2	.07093	.06182	.05719	.05436	.05242	.05099		
$C_{R,TRUE}$, m	.57282	.43990	.37241	.33108	.30281	.28198		
$\bar{c}$, eff, m	.32345	.25535	.22326	.20470	.19256	.18394		
$\bar{x}$, eff, m	.23575	.16982	.13374	.11048	.09399	.08150		
$\bar{y}$, eff, m	.05081	.05493	.05753	.05933	.06068	.06174		
$\Delta y/b/2$	.41157	.41157	.41157	.41157	.41157	.41157		

TABLE 2

GEOMETRIC CHARACTERISTICS OF WING-FILLET COMBINATIONS TESTED

WING IV $\qquad$ $\Lambda_{\ell e} = 53°$ $\qquad$ $\Lambda_{te} = 7°$ $\qquad$ $S_{ref} = .04898$ m^2 $\qquad$ $A_{ref} = 2.26500$

Λ_f, deg	80	75	70	65	60	55	45	35
$\Lambda_{c/4,eff}$, deg	67.6813	61.8534	56.9821	52.6950	48.8291			
$\Lambda_{c/2,eff}$, deg	61.2200	52.9537	46.2098	40.6503	36.0796			
A_{TRUE}	1.59876	1.84039	1.99335	2.10025	2.18023			
S_{TRUE}, m^2	.06939	.06028	.05565	.05282	.05088			
$C_{R,TRUE}$, m	.56554	.43262	.36514	.32381	.29554			
$\bar{c}$, eff, m	.32354	.25490	.22256	.20384	.19159			
$\bar{x}$, eff, m	.23594	.17117	.13572	.11289	.09669			
$\bar{y}$, eff, m	.04942	.05343	.05597	.05775	.05907			
$\Delta y/_{b/2}$	.41157	.41157	.41157	.41157	.41157			
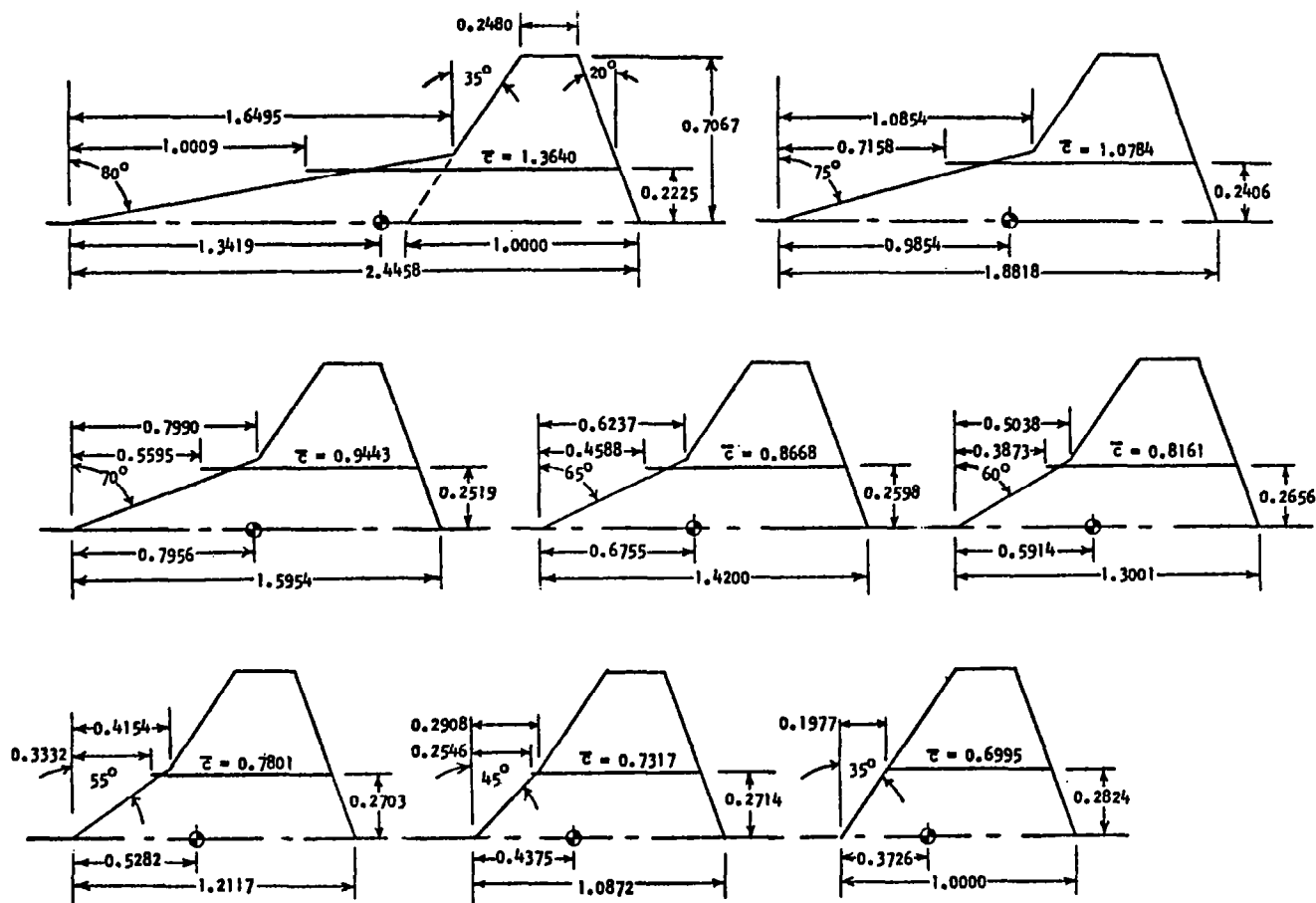
Note: All Dimensions Normalized by Root Chord of Basic Wing

(b)   Wing II; LE = 35°, TE = 20°
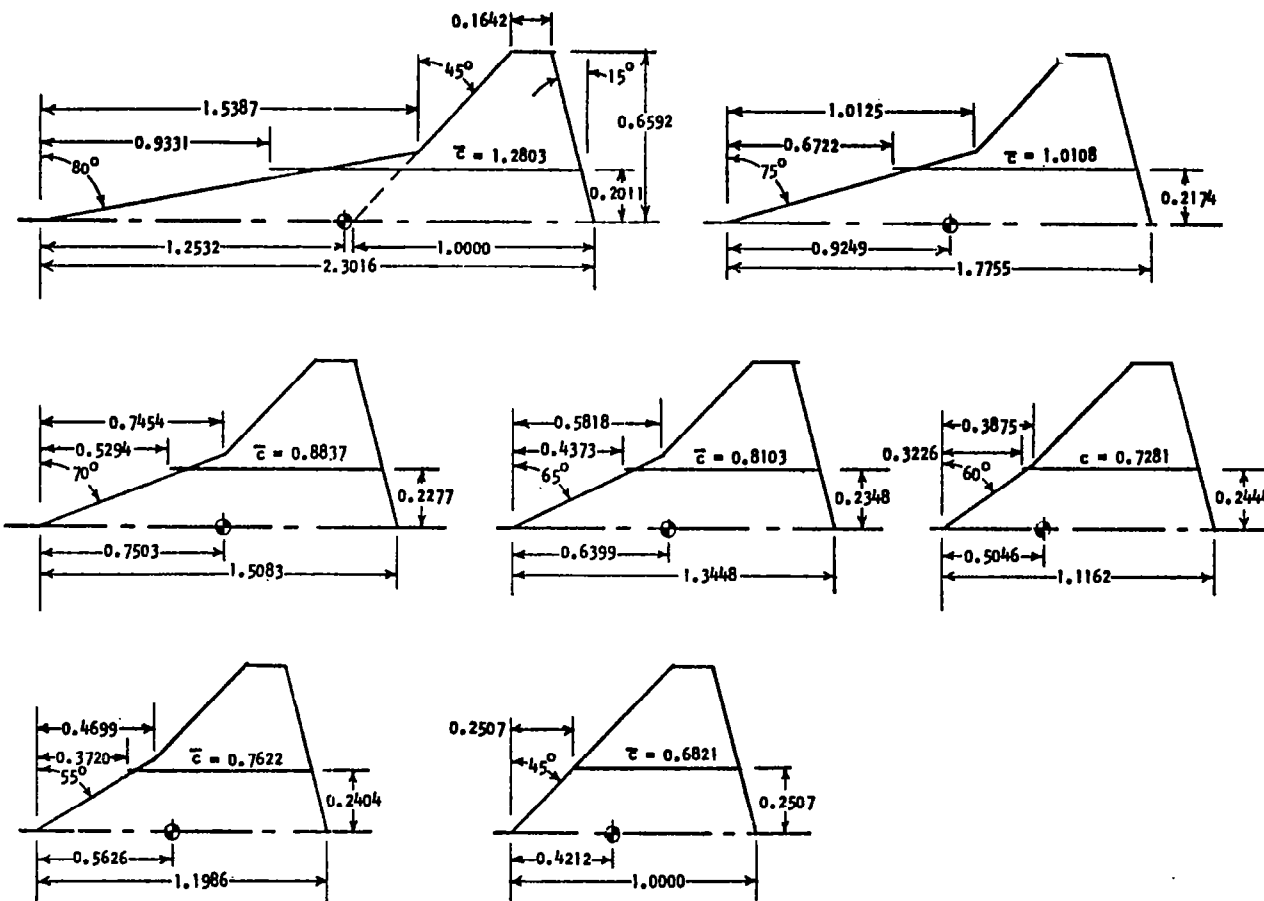
Figure 1. - Continued

Note: All Dimensions Normalized by Root Chord of Basic Wing

(c)   Wing III; LE = 45°, TE = 15°

Figure 1. - Continued
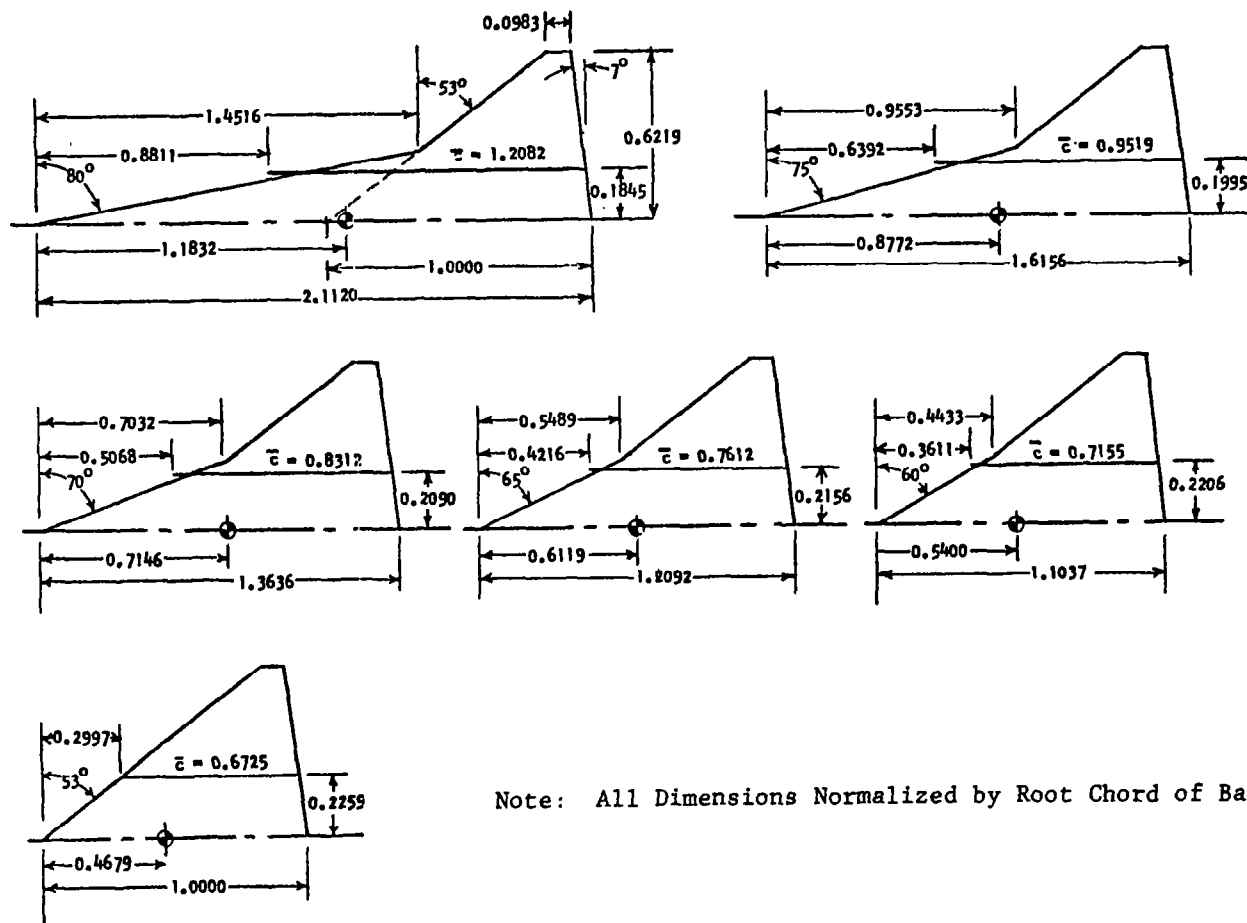
(d)   Wing IV; LE = 53°, TE = 7°

Figure 1. - Continued
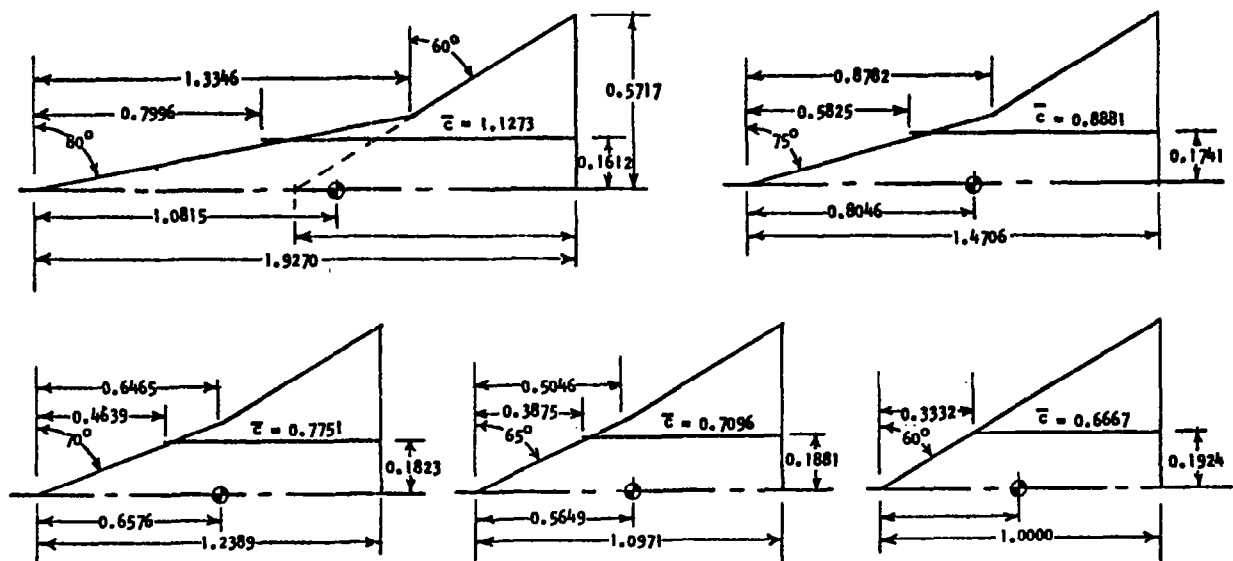
Note: All Dimensions Normalized by Root Chord of Basic Wing

(e)   Wing V; LE = 60°, TE = 0°

Figure 1.- Concluded

FILLET

BASIC WING 1

LONG BODY

SHORT BODY
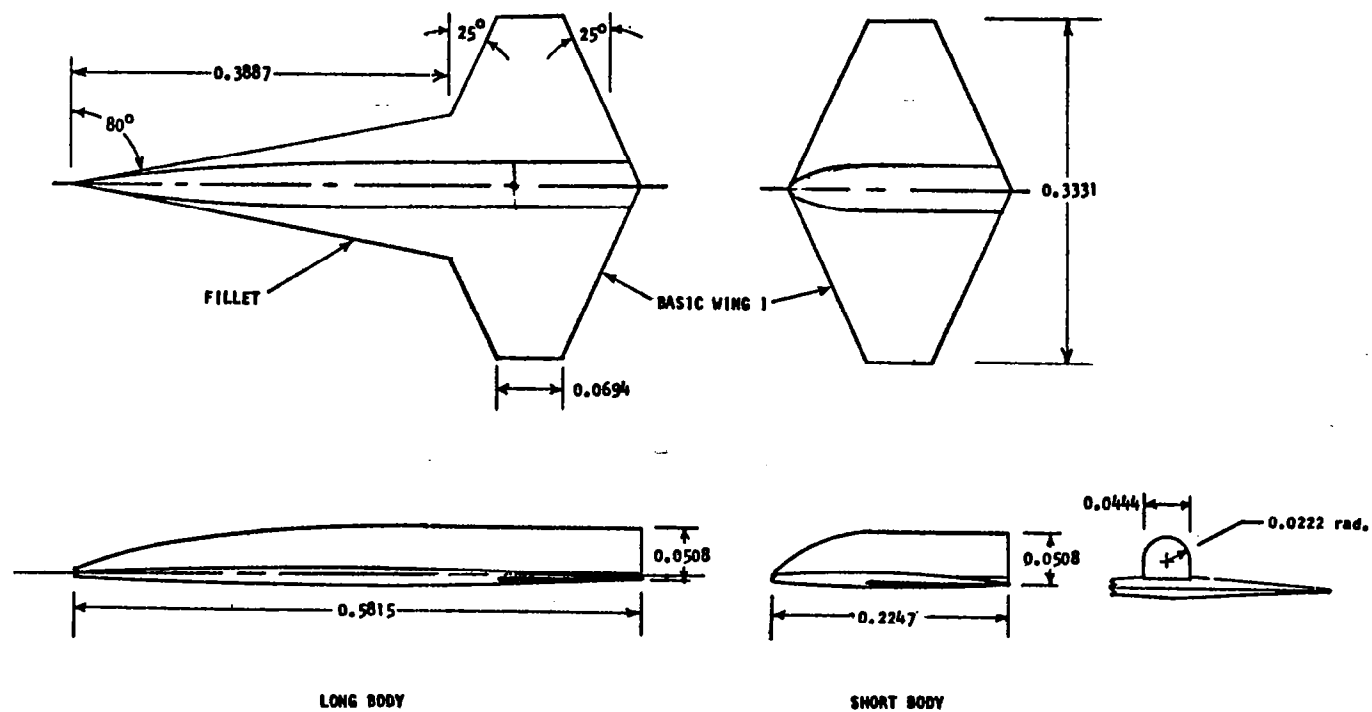
Note: All dimensions in meters

Figure 2. - Sketch showing general arrangement of model used in investigation

GEOMETRIC TERMS AND EQUATIONS USED IN ANALYSES AND PREDICTION METHODS

Many geometric quantities were used in the analysis and in development of the various prediction methods. The terminology and equations needed to compute specific values are presented in this section.

Wing Description

Figure 3 illustrates a typical irregular planform. To generate the families of irregular planforms used in this study, the irregular planforms were considered to be made up of a basic tapered planform, W, to which various fillets were added. The following seven geometric parameters provide sufficient information to allow all other planform parameters to be calculated:

$$\Lambda_{LE}, \quad \Lambda_{TE}, \quad \Lambda_F, \quad S_W, \quad \lambda_W, \quad \eta_B \quad \text{and} \left(\frac{x}{c}\right)_{t/c_{max}}$$

The analyses and prediction methods consider the irregular planforms to be made up of an inboard panel, W_1, and an outboard panel, W_2. The inboard panel consists of the fillet and that portion of the basic wing inboard of the intersection of the fillet leading edge and the basic wing leading edge. The outboard panel consists of the portion of the basic wing outboard of the intersection of the leading edges.

Geometric Equations

Taper ratio of basic wing

$$\lambda_W \equiv c_T/c_R \tag{1}$$
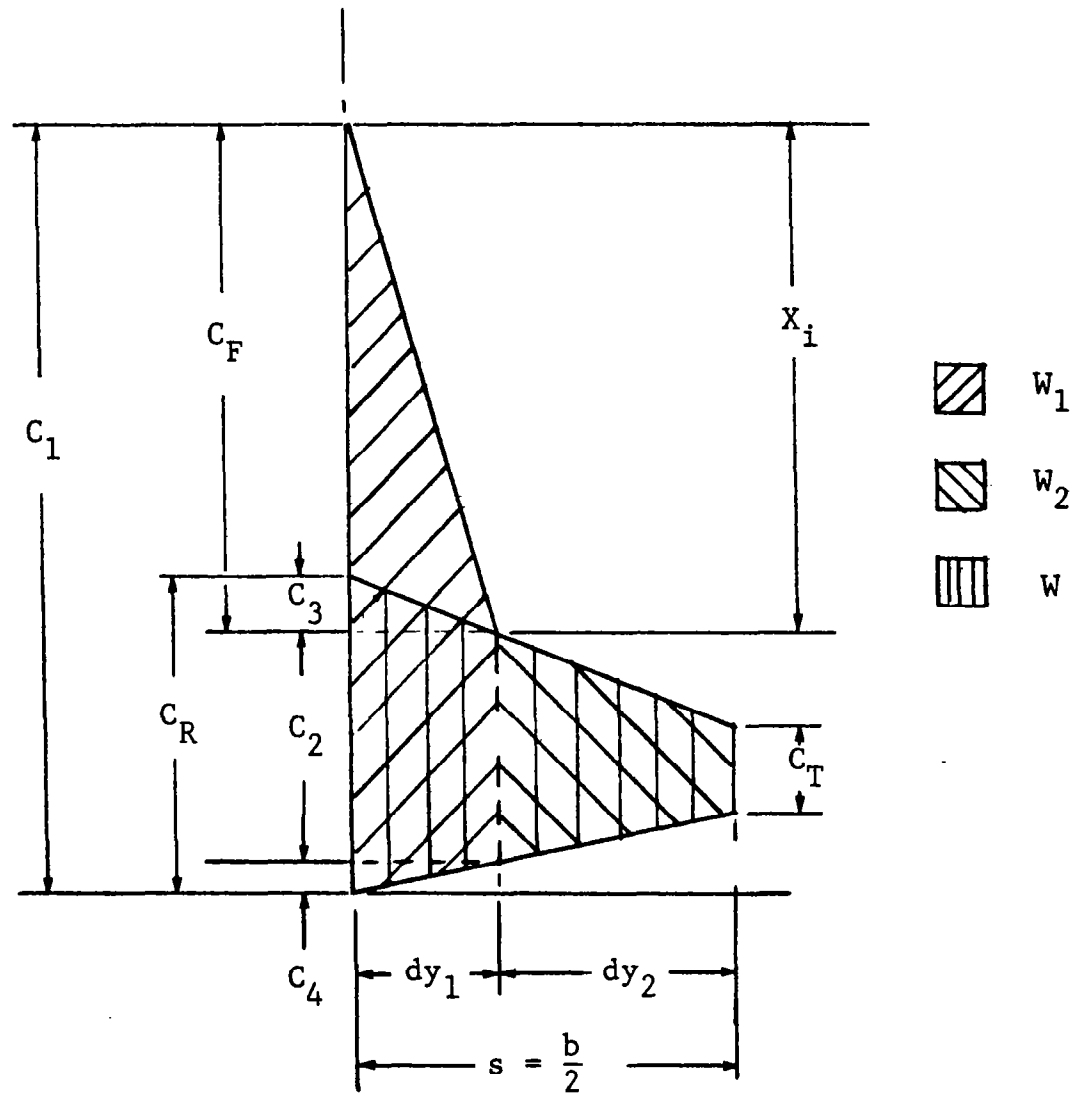
Figure 3. - Wing Planform Geometry Definitions

Nondimensional spanwise location of break in leading edge sweep

$$\eta_B \equiv dy_1/b/2 \tag{2}$$

Root chord of basic wing

$$C_R = \left(\frac{S_W \, (\tan \Lambda_{LE} + \tan \Lambda_{TE})}{1 - \lambda_W^2} \right)^{\frac{1}{2}} \tag{3}$$

Tip chord of basic wing

$$C_T = \lambda_W \, C_R \tag{4}$$

Semispan of basic wing

$$s = b/2 = \frac{S_W}{(C_R + C_T)} \tag{5}$$

Span of basic wing

$$b = 2 \left(\frac{b}{2} \right) \tag{6}$$

Semispan of inboard panel

$$dy_1 = \eta_B (b/2) \tag{7}$$

Semispan of outboard panel

$$dy_2 = \frac{b}{2} - dy_1 \tag{8}$$

Chordwise distance from fillet apex to intersection of fillet leading edge with basic wing leading edge

$$X_i = C_F = (dy_1) \tan \Lambda_F \qquad (9)$$

Chordwise distance from apex of basic wing to leading edge of basic wing at the intersection with the fillet leading edge

$$C_3 = dy_1 \tan \Lambda_{LE} \qquad (10)$$

Chordwise distance from trailing edge of basic wing to trailing edge of root chord of outboard panel

$$C_4 = dy_1 \tan \Lambda_{TE} \qquad (11)$$

Root chord of inboard panel

$$\ell = C_1 = C_R + C_F - C_3 \qquad (12)$$

Root chord of outboard panel

$$C_2 = C_R - (C_3 + C_4) \qquad (13)$$

Chordwise distance of half chord sweep of inboard panel across inboard panel

$$C_5 = \frac{C_1}{2} - \left(\frac{C_2}{2} + C_4\right) \qquad (14)$$

Chordwise distance of half chord sweep of basic wing across inboard panel

$$C_6 = \frac{C_R}{2} - \left(\frac{C_2}{2} + C_4\right) \qquad (15)$$

Chordwise distance of quarter chord sweep of inboard panel across inboard panel

$$C_7 = .75C_1 - (.75C_2 + C_4) \qquad (16)$$

Chordwise distance of quarter chord sweep of basic wing across inboard panel

$$C_8 = .75C_R - (.75C_2 + C_4) \qquad (17)$$

Chordwise distance of maximum thickness sweep of inboard panel across inboard panel

$$C_9 = \left[1 - \left(\frac{X}{C}\right)_{t/c_{max}}\right] C_1 - \left\{\left[1 - \left(\frac{X}{C}\right)_{t/c_{max}}\right] C_2 + C_4\right\} \qquad (18)$$

Chordwise distance of maximum thickness sweep of basic wing across inboard panel

$$C_{10} = \left[1 - \left(\frac{X}{C}\right)_{t/c_{max}}\right] C_R - \left\{\left[1 - \left(\frac{X}{C}\right)_{t/c_{max}}\right] C_2 + C_4\right\} \qquad (19)$$

Sweep angle of quarter-chord of inboard panel

$$(\Lambda c/_4)_1 = \tan^{-1} (C_7/dy_1) \qquad (20)$$

Sweep angle of quarter-chord of basic wing or outboard panel

$$(\Lambda c/4)_2 = \tan^{-1} (C_8/dy_1) \qquad (21)$$

Sweep angle of half-chord of inboard panel

$$(\Lambda c/_2)_1 = \tan^{-1} (C_5/dy_1) \qquad (22)$$

Sweep angle of half-chord of basic wing or outboard panel

$$(\Lambda c/2)_2 = \tan^{-1} (C_6/dy_1) \qquad (23)$$

Sweep angle of maximum thickness line of inboard panel

$$(\Lambda_{t/c_{max}})_1 = \tan^{-1} (C_9/dy_1) \tag{24}$$

Sweep of maximum thickness line of basic wing or outboard panel

$$(\Lambda_{t/c_{max}})_2 = \tan^{-1} (C_{10}/dy_1) \tag{25}$$

Average chord of inboard panel

$$C_{AV_1} = \frac{1}{2} (C_1 + C_2) \tag{26}$$

Average chord of outboard panel

$$C_{AV_2} = \frac{1}{2} (C_2 + C_T) \tag{27}$$

Effective quarter chord sweep of irregular planform

$$(\Lambda_{C/4})_{eff} = \frac{(\Lambda_{C/4})_1 (C_{AV_1})(dy_1) + (\Lambda_{C/4})_2 (C_{AV_2})(dy_2)}{(C_{AV_1})(dy_1) + (C_{AV_2})(dy_2)} \tag{28}$$

Cosine of effective half chord sweep of irregular planform

$$(\text{Cos } C/2)_{eff} = \frac{\left[\text{Cos}(\Lambda_{C/2})_1\right] (C_{AV_1})(dy_1) + \left[\text{Cos}(\Lambda_{C/2})_2\right] (C_{AV_2})(dy_2)}{(C_{AV_1})(dy_1) + (C_{AV_2})(dy_2)} \tag{29}$$

Total planform area of irregular planform

$$S_{TRUE} = 2 \left[(C_{AV_1})(dy_1) + (C_{AV_2})(dy_2)\right] \tag{30}$$

Aspect ratio of irregular planform

$$A_{TRUE} = b^2 / S_{TRUE} \qquad (31)$$

Aspect ratio of basic wing

$$A_W = b^2 / S_W \qquad (32)$$

Aspect ratio of inboard planform

$$A_1 = \frac{(2 dy_1)^2}{2 (C_{AV_1})(dy_1)} \qquad \frac{2 dy_1}{C_{AV_1}} \qquad (33)$$

Mean geometric chord of basic wing

$$\bar{c}_W = \frac{2}{3} C_R \left(\frac{1 + \lambda_W^2}{1 + \lambda_W} \right) \qquad (34)$$

Mean geometric chord of inboard panel

$$\bar{c}_{W_1} = \frac{2}{3} C_1 \left[1 + \frac{(C_2 / C_1)^2}{1 + (C_2 / C_1)} \right] \qquad (35)$$

Mean geometric chord of outboard panel

$$\bar{c}_{W_2} = \frac{2}{3} C_2 \left[1 + \frac{(C_T / C_2)^2}{1 + (C_T / C_2)} \right] \qquad (36)$$

Mean geometric chord of irregular planform

$$\bar{c}_{WF} = \frac{\left(\bar{c}_{W_1} \right)\left(C_{AV_1} \right)\left(dy_1 \right) + \left(\bar{c}_{W_2} \right)\left(C_{AV_2} \right)\left(dy_2 \right)}{\left(C_{AV_1} \right)(dy_1) + \left(C_{AV_2} \right)(dy_2)} \qquad (37)$$

Spanwise location of mean geometric chord of basic wing

$$\bar{y}_W = \frac{1}{3} \left[\frac{1 + 2 \, (\lambda_W)}{1 + \, (\lambda_W)} \right] \, (b/2) \tag{38}$$

Spanwise location of mean geometric chord of inboard panel

$$\bar{y}_{W_1} = \frac{1}{3} \left[\frac{1 + 2 \, (C_2/C_1)}{1 + \, (C_2/C_1)} \right] (dy_1) \tag{39}$$

Spanwise location of mean geometric chord of outboard panel from root of outboard panel

$$\bar{y}_{W_2} = \frac{1}{3} \left[\frac{1 + 2 \, (C_T/C_2)}{1 + \, (C_T/C_2)} \right] (dy_2) \tag{40}$$

Spanwise location of mean geometric chord of irregular planform

$$\bar{y}_{WF} = \frac{\left(\bar{y}_{W_1} \right) \left(C_{AV_1} \right) \left(dy_1 \right) + \left[\left(dy_1 \right) + \left(\bar{y}_{W_2} \right) \right] \left(C_{AV_2} \right) \left(dy_2 \right)}{\left(C_{AV_1} \right) \left(dy_1 \right) + \left(C_{AV_2} \right) \left(dy_2 \right)} \tag{41}$$

Chordwise location of leading edge of mean geometric chord of basic wing from apex of basic wing

$$\bar{x}_W = \bar{y}_W \, \tan\Lambda_{LE} \tag{42}$$

Chordwise distance of leading edge of mean geometric chord of irregular planform from apex of fillet

$$\bar{X}_{WF} = \frac{\left(\bar{y}_{W_1}\right)\left(\tan\Lambda_F\right)\left(C_{AV_1}\right)\left(dy_1\right) + \left[\left(dy_1\right)\left(\tan\Lambda_F\right) + \left(\bar{y}_{W_2}\right)\left(\tan\Lambda_{LE}\right)\right]\left(C_{AV_2}\right)\left(dy_2\right)}{\left(C_{AV_1}\right)\left(dy_1\right) + \left(C_{AV_2}\right)\left(dy_2\right)} \tag{43}$$

Leading-edge radius of mean geometric chord of basic wing

$$LER_{\bar{C}_W} = (100\ r/C)\left(\frac{\bar{c}_W}{100}\right) \tag{44}$$

Leading edge radius of wing tip chord

$$LER_{C_T} = (100\ r/C)\left(\frac{C_T}{100}\right) \tag{45}$$

Chordwise location of moment reference point

$$X_{CG} = \bar{X}_{WF} + \frac{\bar{c}_{WF}}{4} \tag{46}$$

Body Description

The models had a "minimum body" on the upper wing surface to house a strain-gage balance. The body consisted of a nose fairing, the balance housing and a constant crosssection aft extension which reached to the wing trailing edge at the centerline. Body geometric parameters are shown in Figure 4. The nose fairing contour lines consisted of circular arcs in the longitudinal direction in both the vertical and horizontal planes. The cross-sections of the balance housing and aft extension consisted of flat vertical sides plus a half circle. The nose fairing cross-sections matched the balance housing at the point of tangency.
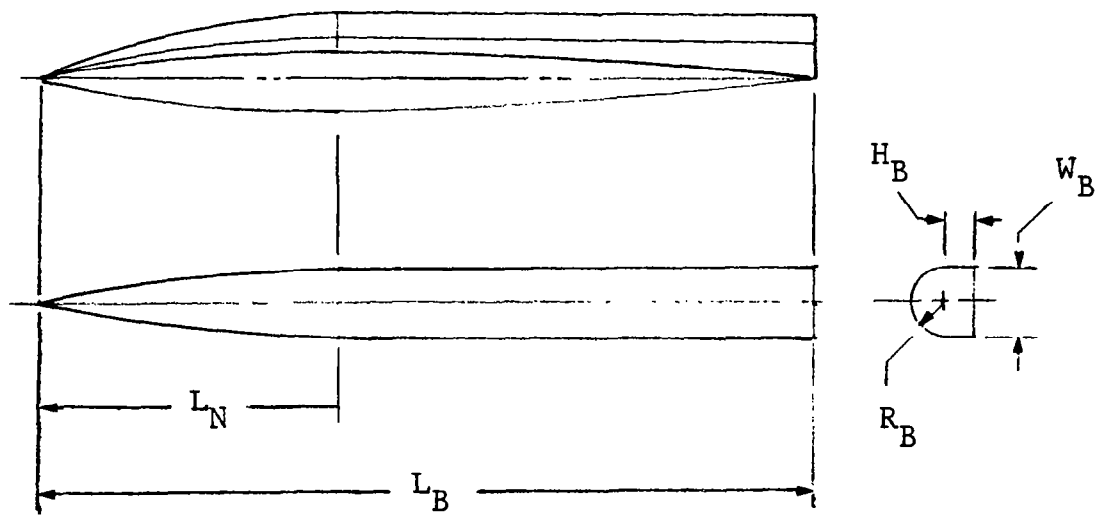
Figure 4. Body Geometry

The geometric data needed for the analyses are the surface wetted area and the effective fineness ratio of the bodies.

The body wetted area can be approximated by:

$$S_{WET_B} = L_N \left(\frac{4}{3} H_B + \frac{2\pi}{3} R_B \right) + \left(L_B - L_N \right) \left(2 H_B + \pi R_B \right) \tag{47}$$

Note:

The effective fineness ratio is defined by:

$$FR = \frac{L_B}{\sqrt{\left(W_B \right) \left(H_B + R_B \right)}} \tag{48}$$

Wing Wetted Area

Inboard Panels

$$S_{WET_1} = 4 \left(C_{AV_1} \right) \left(dy_1 \right) - L_N \left(\frac{4}{3} R_B \right) - \left(L_B - L_N \right) \left(2 R_B \right) \tag{49}$$

Outboard Panels

$$S_{WET_2} = 4 \left(C_{AV_2} \right) \left(dy_2 \right) \tag{50}$$

EVALUATION OF EXISTING METHODS

The initial task in this investigation was to evaluate existing methods of predicting the aerodynamic characteristics of wings at low speed. Most of the existing aerodynamic prediction methods were developed for thin sharp-edged wings of slender planform, for moderately thick wings of variable-sweep planform, or for moderately thick to thick wings of conventional planform. None of these methods was expected to apply directly to the configurations tested in the SHIPS program without additional correlation effort. Thus, the objective of the study of existing methods was to define the limits of applicability when applied to moderately thick to thick wings of slender irregular planform.

While methods were sought for predicting all of the steady-state forces and moments in pitch, the fundamental requirement was to accurately predict the lift and pitching-moment behavior in the region of angle of attack pertinent to approach and landing of an advanced aerospace vehicle. Previous NASA studies indicated this region to be between 15 and 25 degrees of angle of attack. For that region, a significant amount of nonlinear or vortex lift occurs with many of the planforms tested. Therefore, emphasis was placed on examining the ability of existing methods to predict nonlinear lift characteristics.

Early theoretical analyses of the lift produced by "thin" wings were based on linearized potential-flow theory. These analyses produced estimates of the slope of the lift curve ($C_{L\alpha}$) evaluated near zero lift which compared well with test data over a limited range of angle of attack. Deviations from the linear extension of the lift-curve slope at higher angles of attack were attributed to airfoil-thickness effects and flow-separation effects (Figure 5). In recent years, lifting-surface analyses accounting for the true surface boundary conditions have been developed. These analyses show that the potential-flow lift (C_{L_p}) is actually nonlinear with angle of attack such that the curve falls below the linear estimate at all angles of attack above the value for zero lift (Figure 6). In addition, many wings, and particularly those with sharp leading edges, generate leading-edge

flow separation in the form of bubbles (low-sweep planforms) or vortices (swept planforms) and tip vortices which produce lift above that predicted by potential-flow analyses (Figure 7). As the angle of attack is increased, a point is reached at which the bubbles or vortices burst and the lift increases at a lower rate and finally decreases. The angle of attack at which bursting occurs varies with wing planform and airfoil-section geometry.

The preceding discussion indicates that a lift curve is primarily nonlinear. If a particular set of test data shows a linear variation over a significant range of angle of attack, it is apparent now that opposing nonlinear effects compensate each other over that range.

The following existing prediction methods were examined:

1. The WINSTAN nonlinear lift method for slender double-delta wings with sharp leading edges (AFFDL TR-66-73, ref. 5).

2. The Peckham method (WINSTAN) for low-aspect-ratio irregular-planform wings with sharp leading edges (ref. 5).

3. The Peckham method as modified by Ericsson for slender delta-planform wings (AIAA Paper 76-19, ref. 6).

4. The Polhamus leading-edge suction analogy for slender delta wings as modified by Benepe for round-leading-edge airfoils (GDFW ERR-FW 799, ref. 7).

5. The empirically based Aeromodule computer procedure as modified by Schemensky (AFFDL-TR-73-144, ref. 8).

6. The vortex lattice lifting-surface theory computer procedure (including effects of leading-edge suction analogy) developed by Mendenhall et al. (NASA CR 2473, ref. 9).

7. The crossflow drag method for predicting nonlinear lift (NASA TN D-1374, ref. 10).

The different methods were applied either to predict the lift curves for a series of planforms for comparison with test data or

to attempt correlation of the test data. The results for each method are presented in the order listed.

WINSTAN Empirical Method for
Nonlinear Lift of Double-Delta Planforms

This method is based on an empirical correlation of wind tunnel-test data accomplished during the WINSTAN project in 1965 (ref. 5). The method also appears in the USAF Stability and Control DATCOM (ref. 11). The calculation chart is presented in Figure 8. Note that the method requires a value of the linear lift-curve slope as an input.

As a preliminary effort, the Spencer method (ref. 12) was used to estimate C_{L_α} for all 35 SHIPS planforms and compared with test data for a unit Reynolds number of 8 million per foot (evaluated near zero lift). The results are presented in Figure 9. The Spencer method produces a satisfactory preliminary design estimate for C_{L_α}, but additional improvement is possible by applying a simple correction factor. The deviations of predicted values from test data are attributed to interference effects of the minimum bodies of the wind-tunnel models as noted by displacement of C_L amd C_m near zero α, especially for the lower fineness ratio bodies.

It was anticipated that the WINSTAN nonlinear method would predict lift coefficients higher than the test values, since it is known that wings with round-leading-edge airfoils produce less nonlinear lift than do wings with sharp-leading-edge airfoils.

THE WINSTAN nonlinear lift prediction method was applied to two series of SHIPS planforms. One series consisted of the 80-degree leading-edge-sweep fillet and outboard-panel sweeps of 25 to 60 degrees. The other series consisted of an outboard-panel sweep of 25 degrees with various fillet sweeps from 80 to 35 degrees.

Figure 10 presents predicted nonlinear and linear lift variations with angle of attack for the 80-degree-sweep-fillet series of planforms. Also shown is the range of experimental data for this series of planforms at 16 degrees of angle of attack. The experimental data falls between the linear and non-linear estimates for all the outboard-panel sweeps.

All of these planforms have true aspect ratios which are less than 1.65. It is apparent that the basic flow field is dominated by the leading-edge vortices generated by the highly swept fillets; thus, one must expect only a small variation of lift with outboard-panel sweep at a constant angle of attack. Figure 11 illustrates this fact. Note that the round-leading-edge airfoils produce about 50 to 55% of the vortex lift that is estimated by the WINSTAN method for sharp leading edges.

The second series in which the fillet sweep is varied produces considerably larger variations in the lift curves. Figure 12 presents estimates for this series of planforms. The results of the WINSTAN nonlinear method are shown for all the planforms. Note that the planforms with fillet sweeps of 35, 45, and 55 degrees are outside the bounds of the data base for the WINSTAN nonlinear correlation, but the estimates appear quite reasonable. Also shown are linear estimates of lift and the nonlinear potential-flow lift for the three of the planforms. The ranges of SHIPS test data are indicated for 12 and 16 degrees of angle of attack. For fillet sweeps from 35 to 70 degrees, the test data fall below the linear estimates but above the C_{L_p} estimates. Figure 13 shows the variation of lift coefficient with fillet sweep for a constant angle of attack of 16 degrees to illustrate this result more clearly. It is apparent that little vortex lift is produced for fillet sweeps of 60 degrees or less with the 25-degree-sweep outboard panel, which suggests a boundary condition exists with respect to the fillet contribution to nonlinear lift.

It is of interest to plot the ratio of vortex lift produced by the SHIPS wings to the vortex lift predicted by the WINSTAN nonlinear method for sharp-leading-edge wings. Figure 14 shows that when a strong vortex is produced by a high-sweep fillet, there is little variation in the vortex lift at 16 degrees of angle of attack with sweep of the outboard panel. The variation of the vortex-lift ratio with fillet sweep clearly shows that the vortex lift is small up to 60 degrees of fillet sweep and then increases rapidly as fillet sweep is increased to 75 degrees. There is apparently a plateau slightly above 75 degrees.

As expected, the WINSTAN lift prediction method for sharp-leading-edge wings significantly overpredicts the lift generated by the SHIPS models. However there are two possible ways to use the method as a basis for a new method. One way is to derive families of plots similar to those of Figure 14 for various

angles of attack, fillet sweep angles, outboard-panel sweep an-
gles, and Reynolds numbers and then to seek analytical expres-
sions to curve-fit the data. A second way would be to use the
WINSTAN nonlinear-method correlation parameters to define a cor-
relation of the SHIPS data for irregular planforms with round-
leading-edge airfoils. Reynolds number effects would require a
separate correlation chart.

The Peckham Method for Low-Aspect-Ratio
Irregular-Planform Wings with Sharp Leading Edges

The Peckham method as applied to irregular-planform wings
was also investigated during the WINSTAN program (ref. 5). This
method, which is most appropriate for slender wings, consists of
a plot of the correlation parameter $C_L/(s/\ell)^{\frac{1}{2}}$ against angle of
attack, as shown in Figure 15. The parameter s is the wing
semispan and ℓ is the overall length parallel to the plane of
symmetry.

The Peckham method was applied to correlate SHIPS test data
for three series of planforms, as shown in Figures 16, 17, and 18.
The spread of data in these curves is systematic with either
inboard- or outboard-panel sweep. It is apparent that the term
$(s/\ell)^{\frac{1}{2}}$ is too powerful for the round-leading-edge wings.

As an alternate, a weaker relationship, $(s/\ell)^{\frac{1}{4}}$, was at-
tempted. Figure 19 presents the correlation achieved with the
parameter $C_L/(s/\ell)^{\frac{1}{4}}$. Note that below $\alpha = 15^{\circ}$, data for all the
fillet sweeps from 35 to 80 degrees can be represented by a single
curve, whereas above $\alpha = 15^{\circ}$ there is still a systematic spread
in the data. This spread is obviously caused by the variation in
vortex breakdown effects with sweep angle; and, thus, it should be
possible to gain some insight about correlating the effects from
the body of literature covering vortex breakdown. The modified
Peckham method was thus considered a candidate for additional
evaluation.

The Peckham Method as Modified by Ericsson
for Slender Delta-Planform Wings

Ericsson's version of the Peckham correlation method for slender delta wings (ref. 6) uses the parameters

$$C_L / (A/4)^{3/2} = f \ (\alpha / \theta_{LE})$$

where A is the aspect ratio, α the angle of attack, and θ_{LE} is the complement of the leading-edge sweep angle. Note that for a delta wing, $A/4 = s/\ell = \tan \theta_{LE}$. By making the assumption that $\frac{\tan \alpha}{\tan \theta_{LE}} = \frac{\alpha}{\theta_{LE}}$ for slender wings, Ericsson divides each side of the Peckham correlation by θ_{LE}.

Several attempts were made to define an effective θ_{LE} for irregular planforms that would correlate the test data using Ericsson's approach. None were successful. The best of the several that were tried used area-weighted cosine Λ_{LE} to define the θ_{LE} effective. The results are presented in Figure 20 for six of the SHIPS planforms. It is apparent that dividing the angle of attack by the effective θ_{LE} causes the data to spread rather than collapse because the outboard-panel-sweep contribution varies rapidly as the sweep changes. This approach was dropped from further consideration.

The Polhamus Leading-Edge Suction Analogy
as Modified by Benepe for Round-Leading-Edge Airfoils

This method, which was originally developed for round-leading-edge delta wings, is summarized in Figure 21. The method makes use of the leading-edge suction parameter "R," which is defined by the equation:

$$"R" \equiv \frac{C_L \ \tan \alpha + C_{D_{min}} - C_D}{C_L \ \tan \alpha - \frac{C_L^2}{\pi A}}$$

The numerator in this definition represents the equivalent amount of suction actually present while the denominator represents the amount of suction theoretically possible for a wing of the same aspect ratio but having an elliptic loading. In the past, "R" has been successfully used in analyzing and predicting drag-due-to-lift in the lift coefficient range up to polar break.

In the present investigation, it had been proposed to utilize the suction ratio concept to define the nonlinear lift of round leading-edge wings by combining the "R" concept with Polhamus leading-edge suction analogy concept (ref. 12) which is applicable to sharp leading-edge wings. This has successfully been done for low to moderate aspect ratio delta wings (ref. 7).

The lift prediction approach is represented by the following equations:

$$C_L = C_{L_p} + \delta C_{L_{VOR_{SLE}}} \left[1 - \text{"R } (\alpha)\text{"} \right]$$

where C_{L_p} is the nonlinear potential flow lift which is defined by:

$$C_{L_p} = C_{L_\alpha} \sin \alpha \cos^2 \alpha$$

and $\delta C_{L_{VOR_{SLE}}}$ is the vortex lift produced by an equivalent planform having an infinitely thin sharp leading-edge airfoil. According to Polhamus leading-edge suction analogy concept, the leading-edge suction calculated by potential flow theory actually produces a normal force on a sharp thin highly swept wing.

In the present evaluation of existing methods, the $\delta C_{L_{VOR_{SLE}}}$ term is obtained by subtracting C_{L_p} from values of C_L predicted from a correlation of lift of sharp-edged double delta irregular planforms developed prior to the revelation of Polhamus leading-edge suction analogy concept of vortex lift during the WINSTAN project studies (ref. 5). Thus,

$$\delta C_{L_{VOR_{SLE}}} = C_{L_{WINSTAN_{SLE}}} - C_{L_p}$$

For convenience, the C_{L_α} term in the nonlinear potential lift is evaluated by Spencer's method (ref. 12) for irregular planforms:

$$C_{L_\alpha} = \frac{2\pi A}{2 + \sqrt{4 + \left[\dfrac{A}{(\cos\Lambda_{c/2})_{eff}}\right]^2}} \cdot \frac{1}{57.3} \text{ per degree}$$

For wings having round leading-edge airfoils, it is assumed that the difference between full leading-edge suction and the actual leading-edge suction is converted to vortex lift. Thus, the term $\left[1 - "R\ (\alpha)"\right]$ is applied to $\delta C_{L_{VOR_{SLE}}}$ to obtain the vortex lift increments.

This method was applied to analyze data for several SHIPS planforms. The variations of "R" with angle of attack calculated from the test data are presented in Figures 22-24. These variations are typical of the results that can be expected from the SHIPS data. Figure 22 presents data for Basic Wing V at four different unit Reynolds numbers; it illustrates the fact that a significant Reynolds number effect occurs throughout the angle-of-attack range. Figure 23 presents data for two basic planforms and two irregular planforms -- all obtained at the same unit Reynolds number, 3.98×10^6 per foot. Note the significant difference in the shape of the variation of "R" with α for Basic Wings I and V. The variation shown for Wing I is representative of upper-surface flow separation developing on a low-sweep wing and the loss of lift associated with the flow separation. The variation shown for Wing V, on the other hand, is representative of the generation of a vortex-type flow separation, which generates additional lift above that for potential flow. The variation for the combinations of Wing I with a 60-degree fillet shows the general characteristics of that for Basic Wing I; and, thus, one should expect little vortex lift to be generated at high angle of attack. The variation shown for Wing I with the 80-degree fillet also exhibits the dominant effect of the low-sweep outboard panel; but, since a lower level of "R" exists at low to moderate angles of attack, some vortex lift should be present on that wing.

Figure 24 presents the variations of "R" with α for the Basic Wing V and Wing V with an 80-degree fillet. The more rapid de-

crease in "R" at low to moderate angle of attack is indicative of a stronger vortex flow than that occurring on the Basic Wing V, and one would expect a large nonlinear lift contribution for this irregular planform.

The test variations of "R" with α were then used to predict the lift curves for four of the planforms. The linear lift-curve slope was predicted by Spencer's method. The nonlinear potential-flow curves were generated by use of the linear lift-curve slope and the appropriate geometric equation for correcting the linear lift to nonlinear lift. Sharp-edged vortex-lift increments were obtained by estimating the total nonlinear lift for an equivalent sharp-edged thin wing by use of the WINSTAN method and subtracting the nonlinear potential-flow values. The effects of the round leading edges were thus computed by applying 1-"R(α)" values to the sharp-edged vortex-lift increments. The results are presented in Figures 25-28.

Figure 25 is for Basic Wing V. Predictions are compared with test results for two values of unit Reynolds number. Both predictions are slightly higher than test values; however, the correlation of Spencer's $C_{r_{\alpha}}$ prediction with test data shown in Figure 9 indicated the predicted value to be about 6% high. A 6% reduction in the estimates for 20 degrees of angle of attack indicates good correlation between the test data and the estimates. Figures 26 and 27 show the predictions for Wing I with 60- and 80-degree fillets. The predictions are obviously poor above the angle of attack for stall of the low-sweep outboard wing panel. It thus would be necessary to modify the analysis/correlation method to account for the fact that loss of leading-edge suction on the low-sweep outboard panels does not necessarily contribute additional lift.

Figure 28 presents the result for Wing V with an 80-degree fillet. In this case, the prediction compares well with test.

While there were some difficulties associated with this method, it was attractive from the standpoint that defining the variations of "R" with α with the planform geometry parameters, and with leading-edge-radius Reynolds number was also considered the best approach for predicting the drag-due-to-lift.

At this point, several of the SHIPS models were altered to obtain force and moment data with the outborad wing panels removed so that the leading-edge suction parameter variations with α could be determined for use in estimating the fillet contributions. The results of Test 8TPT-780 (inboard panel alone) were initially referenced to the total planform area of the irregular planforms from which they were made. The present analysis required that the lift and drag values be re-referenced to the actual planform areas.

Figures 29 and 30 show typical results for two different fillet sweep angles. Figure 20 presents variations of the leading-edge suction Ratio - "R" for the inboard panel alone, the basic wing and the combined irregular planform for the 80-degree fillet and Wing I with the NACA 0008 airfoil section. On the basis of previous analyses for delta wings, the variation for the inboard panel was expected to have a generally similar shape to that of the irregular planform, but lower values of "R" at each angle of attack. The actual variation was entirely different from what was expected, starting with a low value at low angle of attack and increasing with angle of attack. Figure 30 presents a similar comparison for the 65-degree fillet and Wing I, and the results show the same type of effects. After considerable contemplation of these results, it was concluded that the tip vortex formed along the side edge of the inboard panel models interacts favorably with the leading-edge vortex to enhance the leading-edge suction as angle of attack is increased.

This concept was verified by analyzing test data for delta and cropped delta wings having thin, biconvex airfoils with sharp leading edges (ref. 14). The results are presented in Figure 31. Note that for the cropped wing, the values of leading-edge suction ratio are initially higher than those for the delta wing and increase at higher angles of attack while values for the delta wing decrease throughout the angle-of-attack range.

Further examples of the leading-edge suction ratio data and lift prediction comparisons are presented in Figures 32 and 33, respectively, for the irregular planform consisting of Wing III with 70-degree sweep fillet. Results are shown for both the NACA 0008 airfoil section and the thin modified double wedge airfoil section models.

Figure 32 shows that the variation of "R" with α is significantly different for the wings having an NACA 0008 airfoil and a sharp leading-edge modified double wedge airfoil. Note that the forward facing slopes of the sharp leading-edge airfoil produce significant suction values at low angle of attack. The value of "R" decreases rapidly with increasing α for the sharp wings. At $\alpha = 14.3$ degrees a kink was also noted from the basic data (not presented). The naviation for the round-leading-edge airfoil is much different. "R" remains at relatively high values up to 11.4 degrees α. Above that α, a distinct change occurs in the slope of the curve. These changes, noted for either airfoil, are important clues to a change in flow field which causes the amount of suction to be less than the value $1 - \left["R(\alpha)"\right]$.

Figure 33 presents the buildup of lift predictions and comparisons with test data for the two wings previously discussed. The curves labeled WINSTAN S.L.E., SPENCER LINEAR and C_{L_p} represent elements of the prediction method that are dependent only on the planform and Mach number. The curves labeled SLE and RLE have the term $\left[1-"R(\alpha)"\right]$ applied to determine the vortex lift as explained earlier.

For the sharp-edged airfoil, the agreement between prediction and test is good up to 14.3 degrees when a change in the flow field apparently occurs (probably an outboard panel stall). For the round-leading-edge airfoil, the agreement between prediction and test is good up to 11.4 degrees where again a change in flow field occurs although the effect on the experimental lift curve is not as apparent as it is for the sharp-leading-edge airfoil.

Working the method in reverse order, the suction ratio values required to make the predicted lift match the test data were calculated for these two cases and the results are shown in Figure 34. In essence, the difference between the dashed curves and the test data curves of "R" represents the amount of "lost suction" that is not converted to vortex lift.

In general, the nonlinear method based on the leading-edge suction analogy overpredicted the lift at high angles of attack for the round-leading-edge airfoil irregular planform wings. There is a trend toward better agreement over a larger range of angles of attack as the fillet sweep and outboard panel sweep

increase. The best agreement occurs, as expected, for Wing V with the 80-degree sweep fillet (Fig. 40).

Reynolds number effects were evaluated for the irregular planform consisting of Wing I with 80 degree fillet. Both the NACA 0008 and NACA 0012 airfoil data were analyzed. For the NACA 0008 airfoil, the agreement between prediction and test data improved with decreasing Reynolds number because the test vortex lift increased faster than the predicted vortex lift. For the NACA 0012 airfoil, the agreement between prediction and test improved as the Reynolds number increased because the predicted vortex lift decreased faster than the test vortex lift. (The specific data substantiating these statements are not presented, however the reader is referred to the appendix where the incremental effects of Reynolds number on the finalized lift correlation parameter are presented. The effects are highly configuration dependent.)

It is apparent that for this irregular planform, the effects of Reynolds number are threefold. First, the angle of attack for "stall" of the outboard wing panel is increased as the leading-edge-radius Reynolds number is increased. Second, the strength of the leading-edge vortex flow produced on the inboard panel is reduced substantially as the leading-edge radius Reynolds number is increased. Third, the interaction between the inboard and outboard wing panel flow changes drastically between the two extremes of leading-edge-radius Reynolds number tested.

The obvious difference in inboard panel/outboard panel flow interactions is that at low Reynolds number, the outboard panel having the NACA 0008 airfoil produces a leading-edge flow separation, while at high Reynolds number, the outboard panel having the NACA 0012 airfoil produces a trailing-edge flow separation. It is likely that the wing having NACA 0008 airfoils produces leading-edge flow separation on the outboard panel at all unit Reynolds numbers tested, whereas it is possible that mixed leading-edge and trailing-edge flow separation occurs for the NACA 0012 airfoil at the lowest unit Reynolds number tested.

From this evaluation of applying the leading-edge suction analogy to predict nonlinear lift of the SHIPS planforms, it was concluded that a significant amount of resources and time would be required to make the approach a useful preliminary design tool.

Aeromodule Computer Procedure

The Aeromodule computer procedure was developed to provide a rapid means of assessing the lift, drag and pitching moment characteristics of aircraft configurations, from low speed to supersonic speeds. The basis for the calculations is an extensive set of empirical and semi-empirical methods developed from a data base encompassing fixed wing and variable sweep wing configurations. The computer program has been revised and updated several times since the initial development in 1969 as the data base expanded and improved prediction methods were developed. A version of the program (General Dynamics Procedure Code R1T) developed for the U.S. Air Force (ref. 8) was used in the present investigation.

Aeromodule predictions were obtained for most of the SHIPS planforms during this evaluation. Comparisons between Aeromodule predictions of lift, drag, and pitching moments with the SHIPS wind-tunnel data obtained at 26.25 million per meter unit Reynolds number are presented for a mini-matrix of 9 configurations shown in Table 3. These results adequately illustrate some major points to be made from the Aeromodule prediction evaluation study.

TABLE 3   MINI-MATRIX OF CONFIGURATIONS PRESENTED

Fillet Sweep Deg	Wing Leading-Edge Sweep - Deg.		
	25	45	60
None	Figure 35	Figure 36	Figure 37
80	Figure 38	Figure 39	Figure 40
65			Figure 43
55		Figure 42	
35	Figure 41		

The overall evaluation for the Aeromodule prediction methods indicated that, while there were sometimes significant differences between predicted and test values, the methodologies contained the basic elements that were needed to provide more accurate predictions and could be adapted through data correlations to achieve the necessary accuracy. In general, the discrepancies could be explained by the fact that the SHIPS wings and test conditions fall outside the data base that was available when the empirical methods were developed.

Comparisons for basic Wings I, III, and V are presented in Figures 35, 36, and 37, respectively. These results were informative for they showed that the empirical factors inherent in the computer procedure were not completely satisfactory for the basic planforms. This is not surprising, since the SHIPS basic wings are generally lower in aspect ratio or have thicker airfoils than wings which supplied the data base. In addition, the 26.25 million per meter unit Reynolds number was higher than previously available in any significant parametric study.

The differences between the predicted lift curves and drag curves and the test data were not distressing from a methodology development standpoint. The SHIPS data base could provide adequate information to define new empirical factors. The pitching-moment predictions were actually encouraging even though the discrepancies are quite large.

The fact that the general nonlinear character of the pitching-moment curves also occurred in the predictions was a significant point. Obviously, some alteration to the methodology was required, but again, it could only be a matter of changing the empirical factors to better account for stall progression on the wings with angle of attack. This assumption is borne out by the results shown (Fig. 38, 38, and 40).

Figures 38, 39, and 40 present the comparisons between prediction and test for Wings I, III and V with 80-degree fillets. For all of these irregular SHIPS planforms, the Aeromodule computer program logic selected the WINSTAN nonlinear lift prediction method for sharp leading-edge wings, which does not include the effects of round leading edges or Reynolds number. The predicted lift curves tend toward better agreement with test data as the outer wing panel sweep increases to 60 degrees because the round-leading-edge and Reynolds number effects decrease.

There is an improvement in the agreement between the pitching moments and test data corresponding to the improvement in agreement of the lift predictions.

The drag-polar predictions for the wings with 80-degree sweep fillets all produced higher drag values than test at moderate lift coefficients. These results were also due to the lack of accounting for round-leading-edge and Reynolds number effects.

The third set of 3 configurations for which comparisons are presented between Aeromodule predictions and SHIPS test data consists of Wing I with the 35-degree sweep fillet, Wing III with 55-degree sweep fillet, and Wing V with the 65-degree sweep fillet. The comparisons are shown in Figures 41, 42 and 43, respectively. For the first two cases, the computer program logic initially selected the WINSTAN nonlinear lift method for double-delta planforms, but then attempted to match the USAF DATCOM low-aspect-ratio C_{Lmax} method results and determined that the C_{Lmax} value predicted by that method was lower than the lift predicted by potential flow. The program flow then shifted to the WINSTAN nonlinear lift method for cranked wings and the DATCOM high-aspect-ratio C_{Lmax} method despite the fact that the configuration is a low-aspect-ratio wing. In this case, the procedure computed a C_{Lmax} but did not attempt to fair from the computed lift curve to C_{Lmax}. The user must do that by hand.

The corresponding moment curves in Figures 41 and 42 reflect the use of the C_{Lmax} values above the angle of attack at which the computed lift values exceed C_{Lmax}. The pitching-moment prediction methodology assumes a center of pressure location for a fully separated flow at lift values above C_{Lmax}. A better prediction of the angle of attack at which C_{Lmax} occurs could improve the calculated pitching moments.

It was not at all obvious from the comparisons shown in Figure 43 (for Wing V with 65-degree sweep fillet) what computational path was used by the computer procedure, but it appeared to be the same one as occurred for the configurations presented in Figures 41 and 42. Unfortunately, the specified C_L range for the series of predictions only extended to a value of 1.0, so the pitching-moment curve does not give a clue.

The comparisons between predicted and test drag polars presented in Figures 41, 42 and 43 again show that the predicted drag is too high in the moderate C_L range and too low in the higher C_L range. Improved accounting of Reynolds number effects on the lift coefficient for initial flow separation and the lift coefficient for drag break could lead to significant improvement in both these areas.

The longitudinal stability derivative dC_m/dC_L is compared in Figure 44 with data evaluated in the low lift coefficient range for Wing I combined with several different fillets. The methodology is that of Paniszczyn from the WINSTAN study (ref. 5) which also appears in the USAF Stability and Control DATCOM (ref. 11) in the section on wing-body pitching-moment predictions for double-delta, cranked and curved planforms. The discrepancies which occur are attributable in part to discrepancies in predicting the lift curve slope. The only drawback to the method is the fact that it requires generation of geometry for a fictitious outboard panel.

Comparisons between predicted and test values of the minimum drag coefficient, $C_{D_{min}}$, are presented in Figure 45. In general the discrepancies between predicted values and test values were much larger than was anticipated from previous experience. The variations of the experimental data with fillet sweep show some significant deviations from smooth curves. Some of this type of discrepancy was found to be attributable to the effects of the different forebody shapes on the measured base pressures. In addition, the inherent lack of sensitivity at low angle of attack of a wind-tunnel balance when designed to measure large forces at high angle of attack contributed to the "scatter." Investigation as to why the predicted values were so much higher than expected revealed that the geometry calculations contained in the Aeromodule program could not properly account for the fact that the body existed only on the upper surface, so the calculated wetted areas for the body contributions to minimum drag were too large. When the predicted values were corrected to account for the actual wetted areas, the agreement between prediction and test values was much better and within the expected accuracy.

In summary, an extensive evaluation of the Aeromodule prediction methods was completed, and the conclusion was that the methods contain most of the necessary elements to produce accurate predictions for the SHIPS planforms. The discrepancies that did occur are primarily due to an inadequate data base which the SHIPS test data could remedy. The Aeromodule methods were used as guidelines during the data correlation efforts.

Lifting-Surface Theory of Mendenhall, et al.,
Including Effect of Leading-Edge Suction Analogy

This method (ref. 9) was included in a preliminary study be-
cause it offers a convenient way to obtain theoretical values of
the nonlinear lift contribution for sharp leading edges and also
because the amount of leading-edge suction converted to lift can
be arbitrarily applied for each wing panel of a two-panel irregular-
planform wing. Analysis of Wing I with a 60-degree fillet
was tried, first, by using full-leading-edge suction analogy and,
then, by arbitrarily assigning various amounts of leading-edge
suction to the inboard and outboard panels at each angle of at-
tack. Guidance in selecting the applied amounts was obtained
from the plot of $R(\alpha)$ for the configuration. The results are
presented in Figure 46.

The plot shows the variation of C_{L_p}, the WINSTAN sharp-
leading-edge prediction, the Mendenhall predictions for full and ar-
bitrary amounts of suction assigned, and the test data. The Men-
denhall result for full suction conversion to vortex lift agrees
with the WINSTAN prediction. The result with partial suction
conversion agrees better than when the test value of suction was
applied to the WINSTAN increment. The reason is that at $\alpha = 15^\circ$
and above the outboard-panel suction ratio was set to zero since
lift data for Basic Wing I indicated wing stall at about $\alpha = 15^\circ$.

The next step was to apply the same technique as had been
done in the WINSTAN study for cranked wings of moderate thickness,
that is, to assume that at 15 degrees of angle of attack the
potential-flow contribution had ceased to grow and the only addi-
tional lift was that caused by the vortex flow on the inboard
panel. This result is shown by the symbol x in Figure 46. The
agreement with test data is excellent. The choice of 15 degrees
was arbitrary in this case; what is needed is a valid correlation
of α for $C_{L_{BREAK}}$ as a function of planform parameters, airfoil
suction parameters, and Reynolds number. The basis for such cor-
relations is contained in the Aeromodule methods, but data perti-
nent to the SHIPS planforms would be helpful to refine the
approach.

The Crossflow Drag Method

The crossflow drag method for predicting nonlinear lift (ref.10) assumes that the total lift is obtained by a relation of the form

$$C_L = C_{L_\alpha}(\alpha) + C_{D_C} \left(\frac{\alpha}{57.3}\right)^2$$

where the term C_{D_C} is the planform drag coefficient evaluated at $\alpha = 90^\circ$ at high Reynolds number and α units are degrees.

Although this method is useful for very preliminary estimates of the nonlinear lift, the C_{D_C} term is relatively insensitive to wide differences in planform shape for low-aspect-ratio wings. Values in the literature vary from about 1.15 to 1.30 for wings with round-leading-edge airfoils. In addition, the available data are not systematic with planform shape, so it would be difficult to apply the method with sufficient accuracy to differentiate between the effects for the various SHIPS planforms.
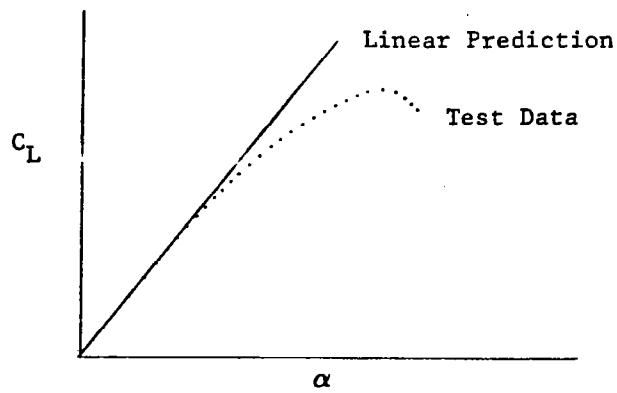
Figure 5. Early Analysis Approach
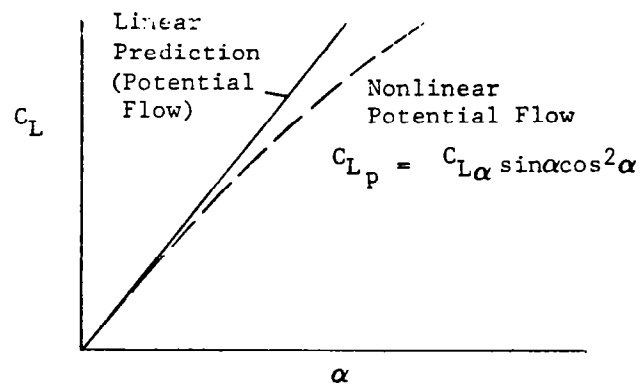
Figure 6. Recent Potential Flow (Lifting-Surface Theory) Analysis
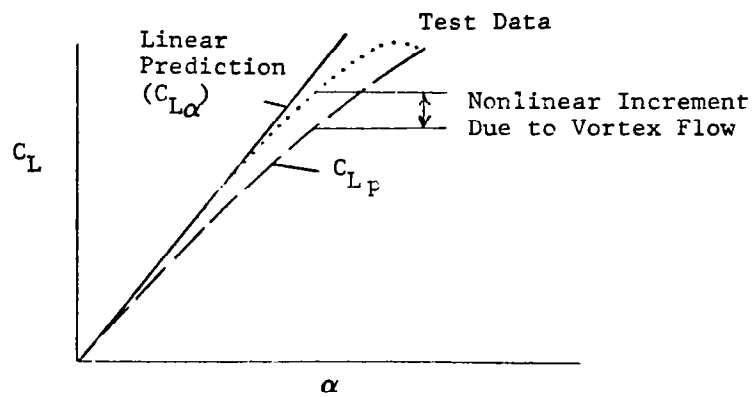
Figure 7. Analysis Including Effect of Vortex Flow
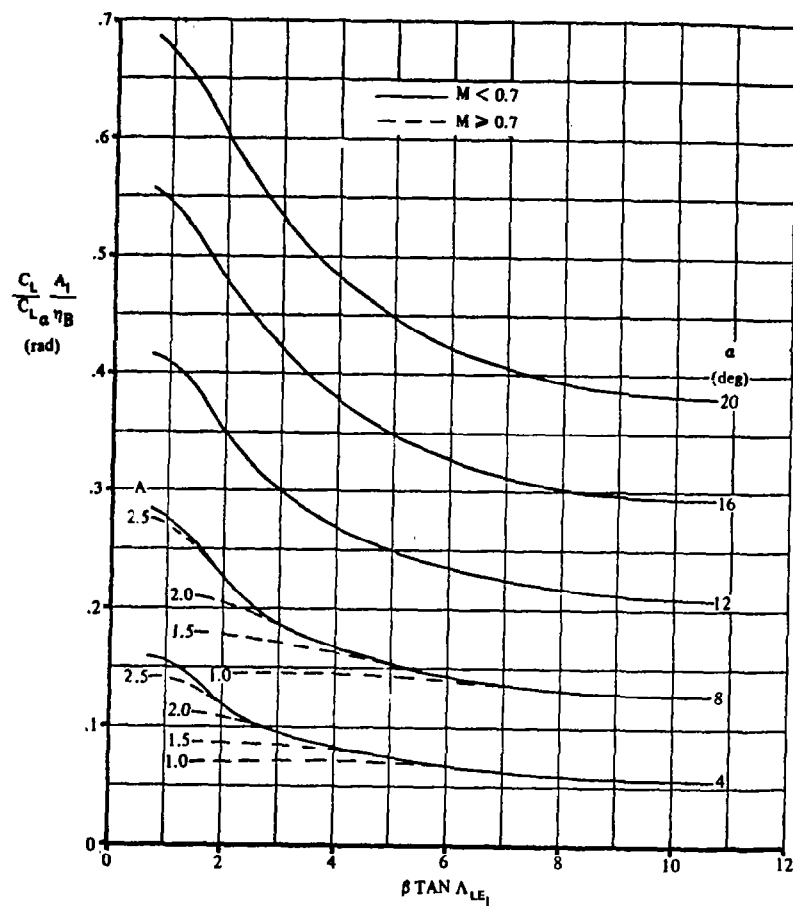
Figure 8. Calculation Chart for Prediction of Nonlinear Lift of Double-Delta Platforms at Subsonic Speeds
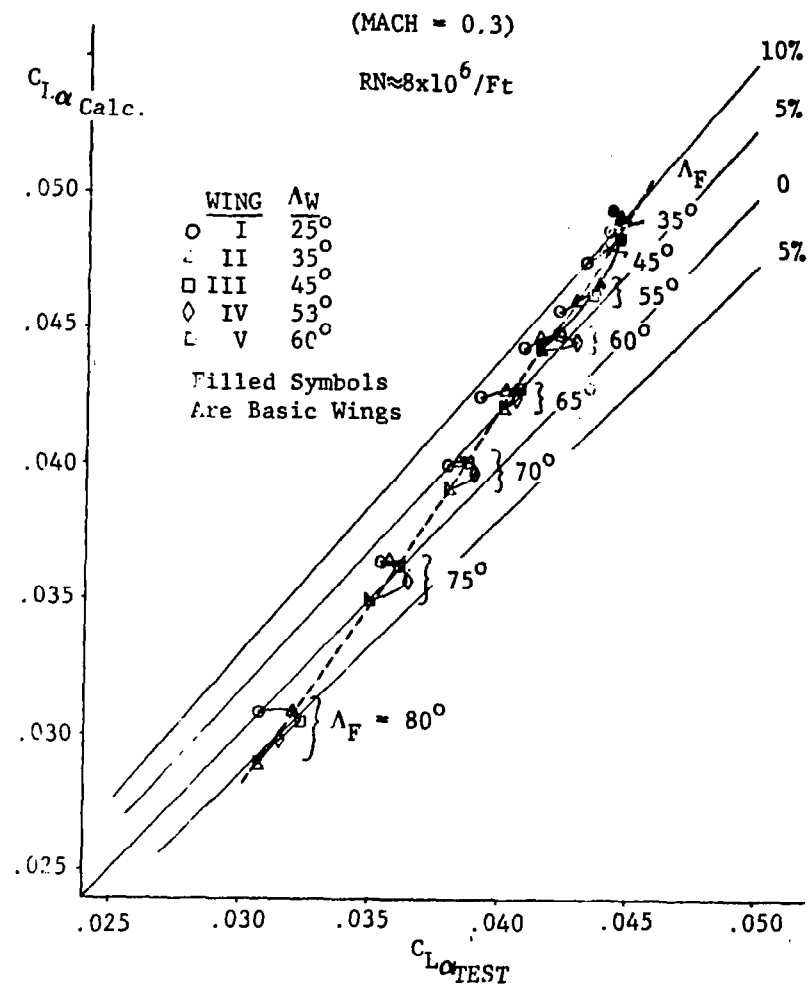
Figure 9. Comparison of Spencer C_{L_α} Prediction With Test Data
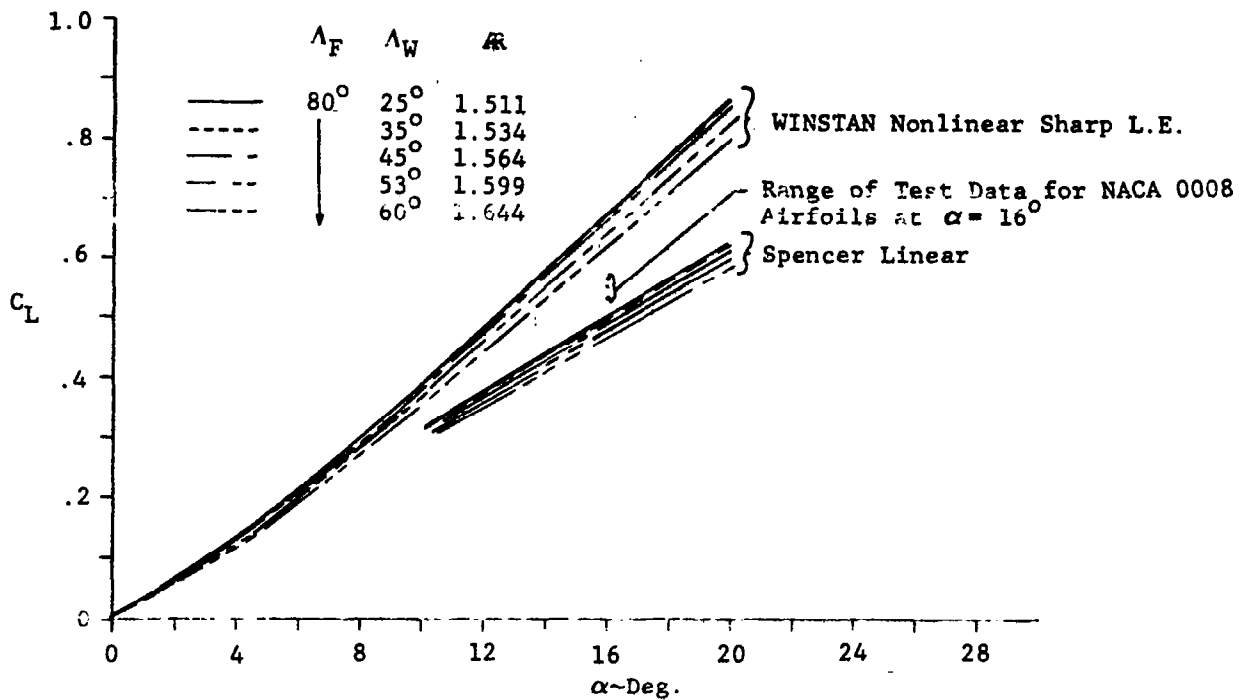
Figure 10. Effect of Outboard-Panel Sweep on Lift
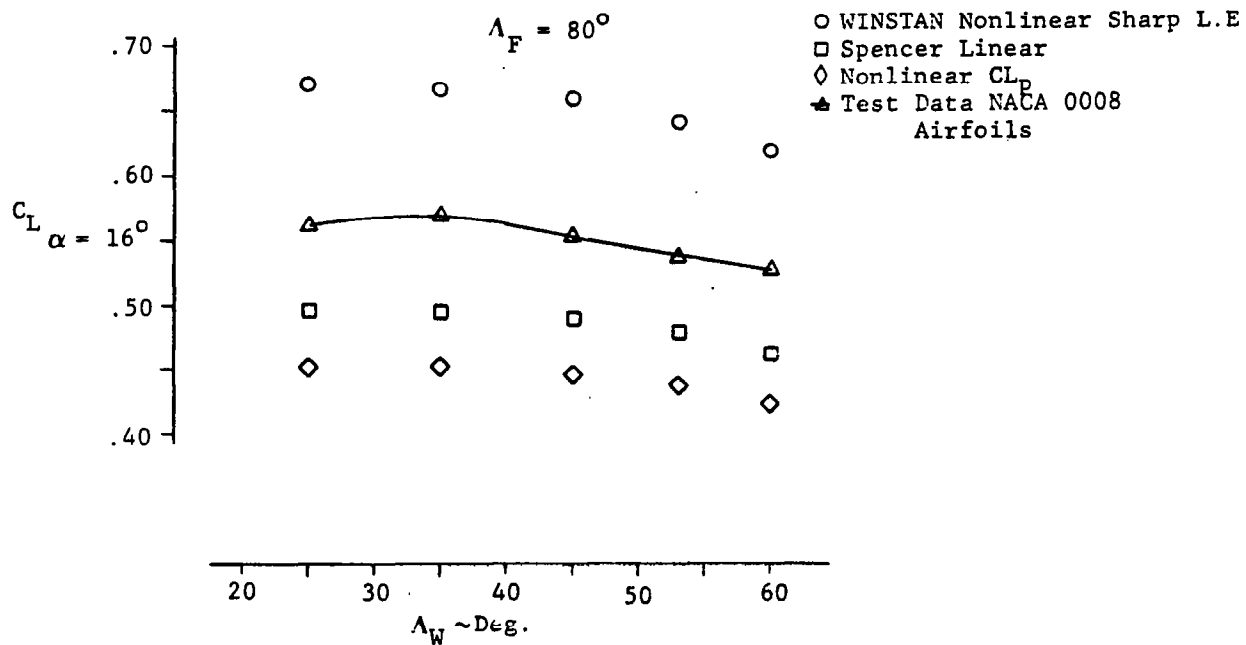
Figure 11. Effect of Outboard-Panel Sweep on Lift at $\alpha = 16°$
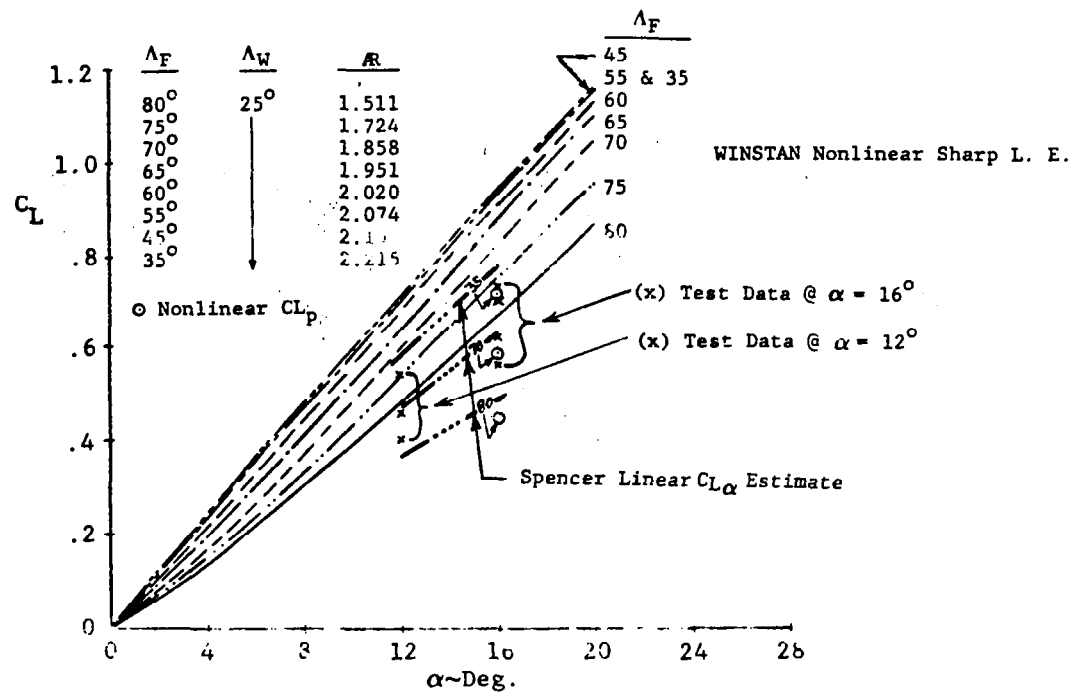
Figure 12. WINSTAN Nonlinear Predictions Wing I Planforms
(Sharp Thin Airfoils)
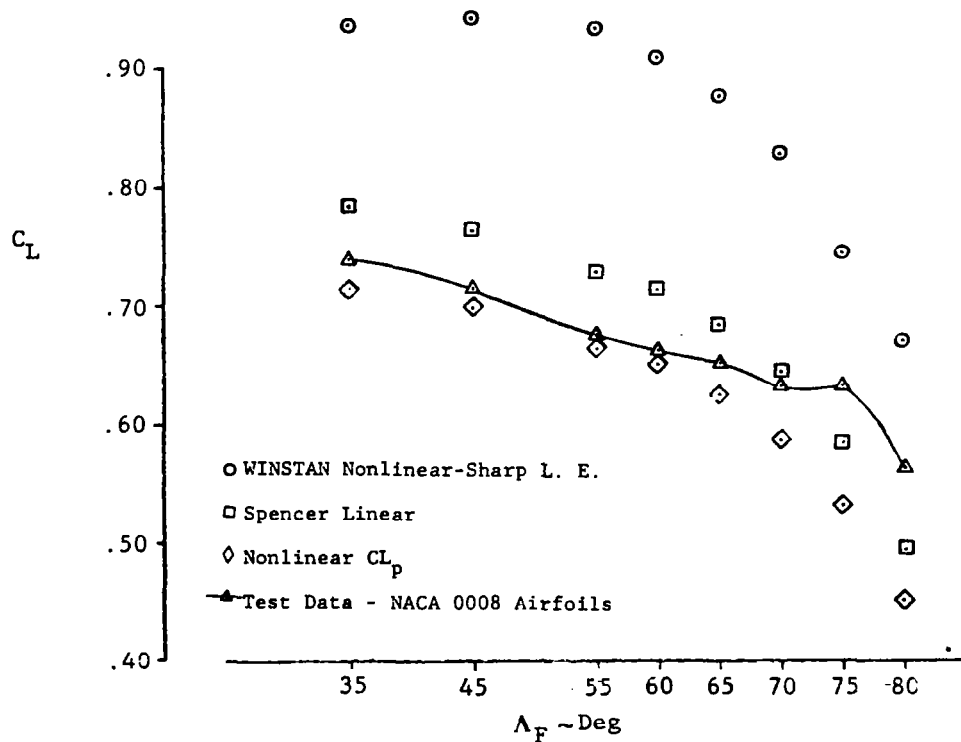
Figure 13. Effect of Fillet Sweep on Lift of
Wing Planforms at $\alpha = 16°$
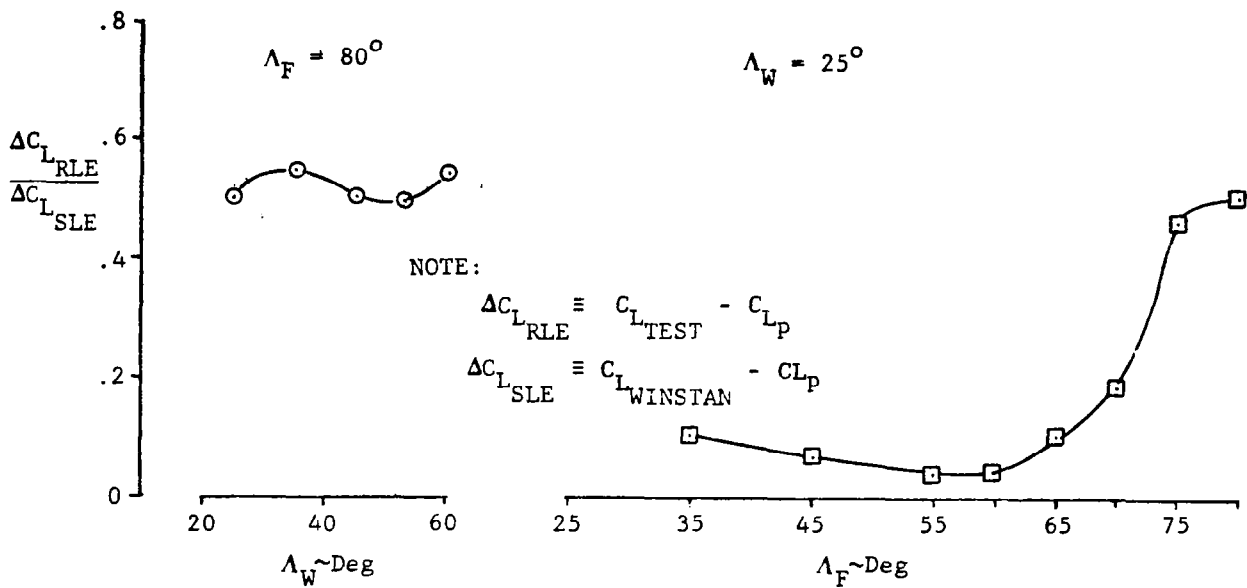
Figure 14.   Effect of Round Leading Edges on Vortex Lift
             at $\alpha = 16^{\circ}$

NOTE:

$$\Delta C_{L_{RLE}} \equiv C_{L_{TEST}} - C_{L_p}$$

$$\Delta C_{L_{SLE}} \equiv C_{L_{WINSTAN}} - CL_p$$
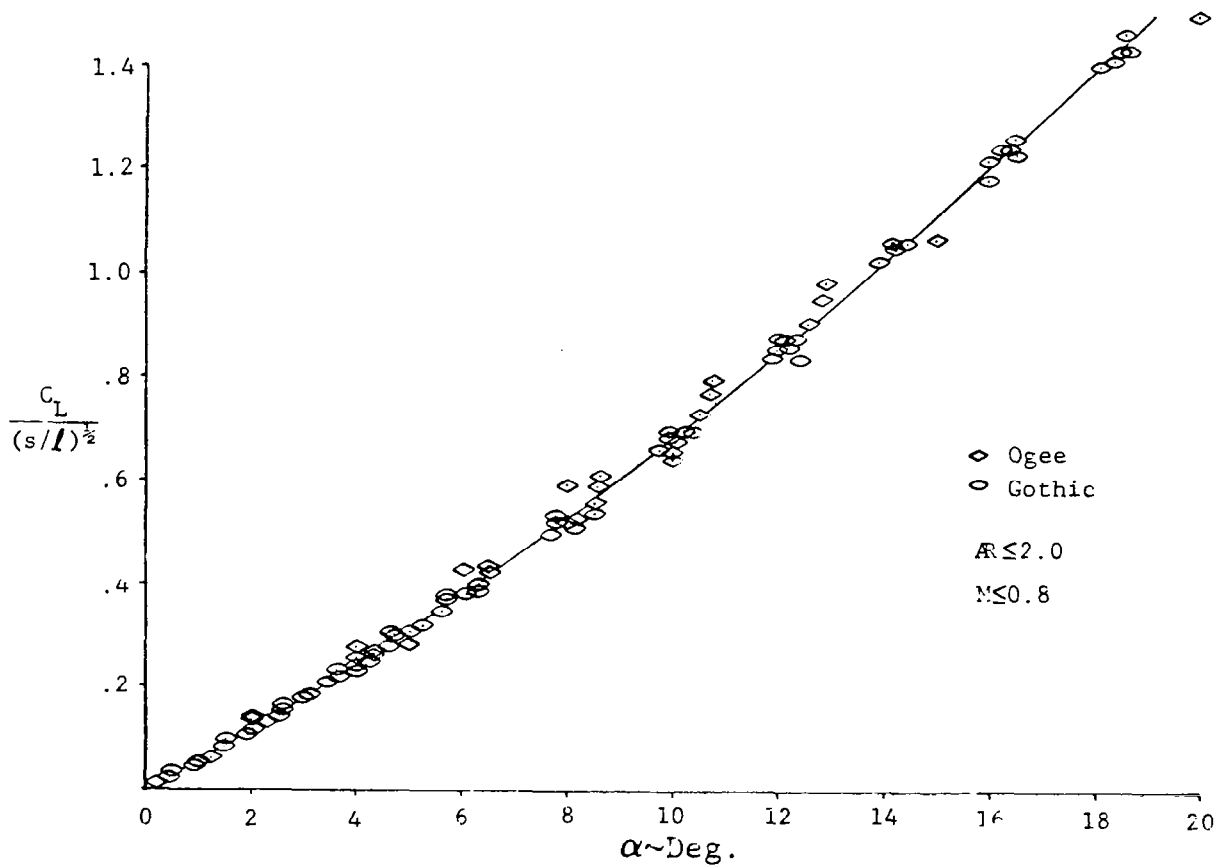
Figure 15.   Correlation of Lift Curves of Gothic and
             Ogee Planforms

◇ Ogee
○ Gothic

$\cancel{R} \leq 2.0$

$M \leq 0.8$
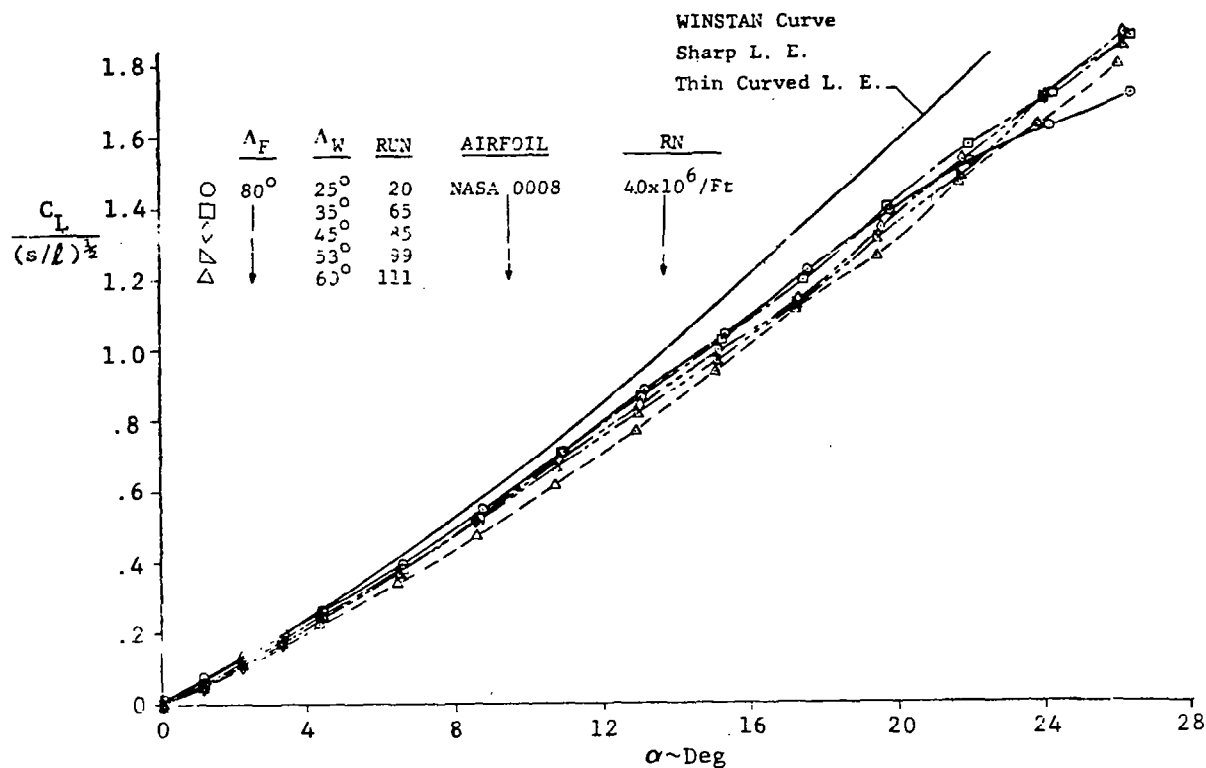
Figure 16. Effect of Outboard Panel on Peckham-Type
C_L Correlation ($\Lambda_F = 80°$)
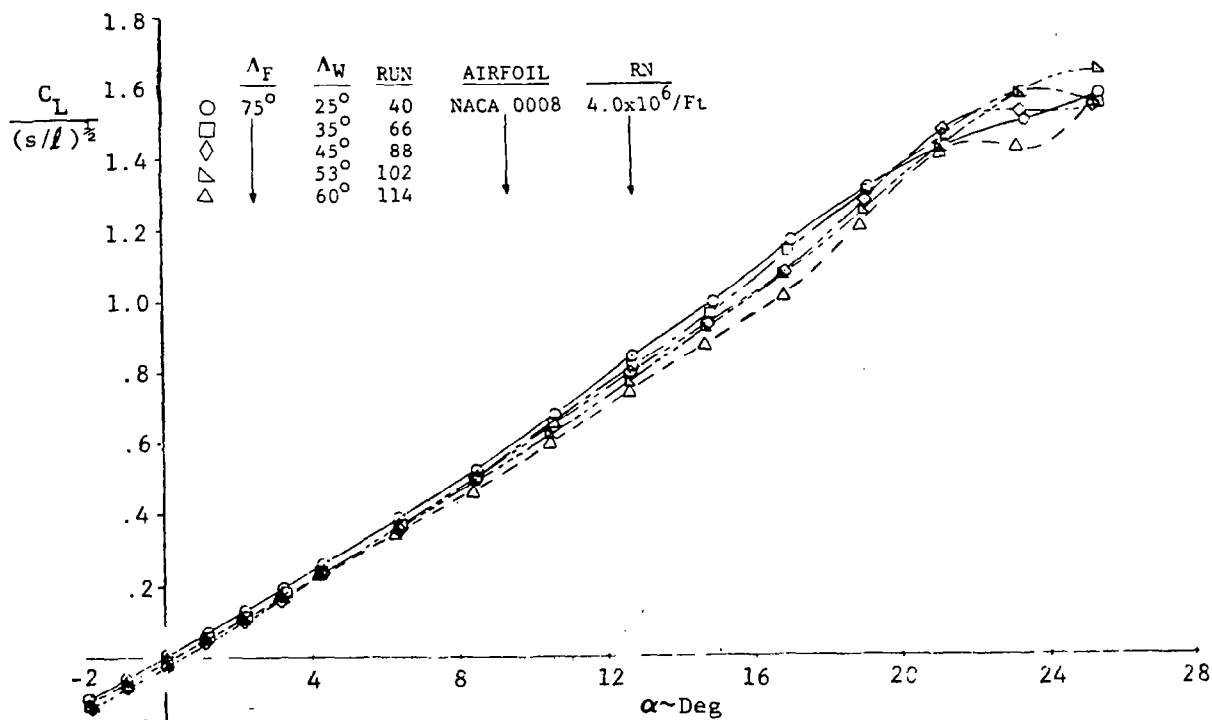
Figure 17. Effect of Outboard Panel on Peckham-Type
C_L Correlation ($\Lambda_F = 75°$)
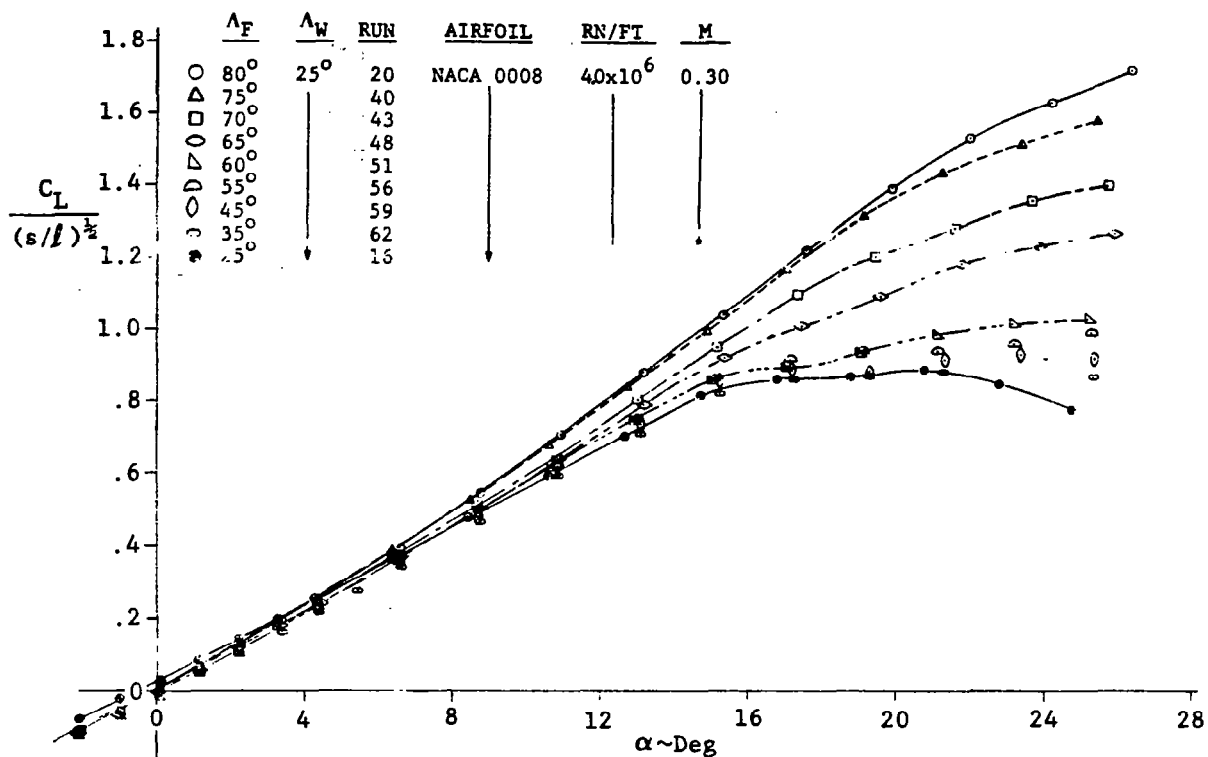
Figure 18. Effect of Inboard Panel on Peckham-Type
C_L Correlation. $(\Lambda_W = 25^{\circ})$
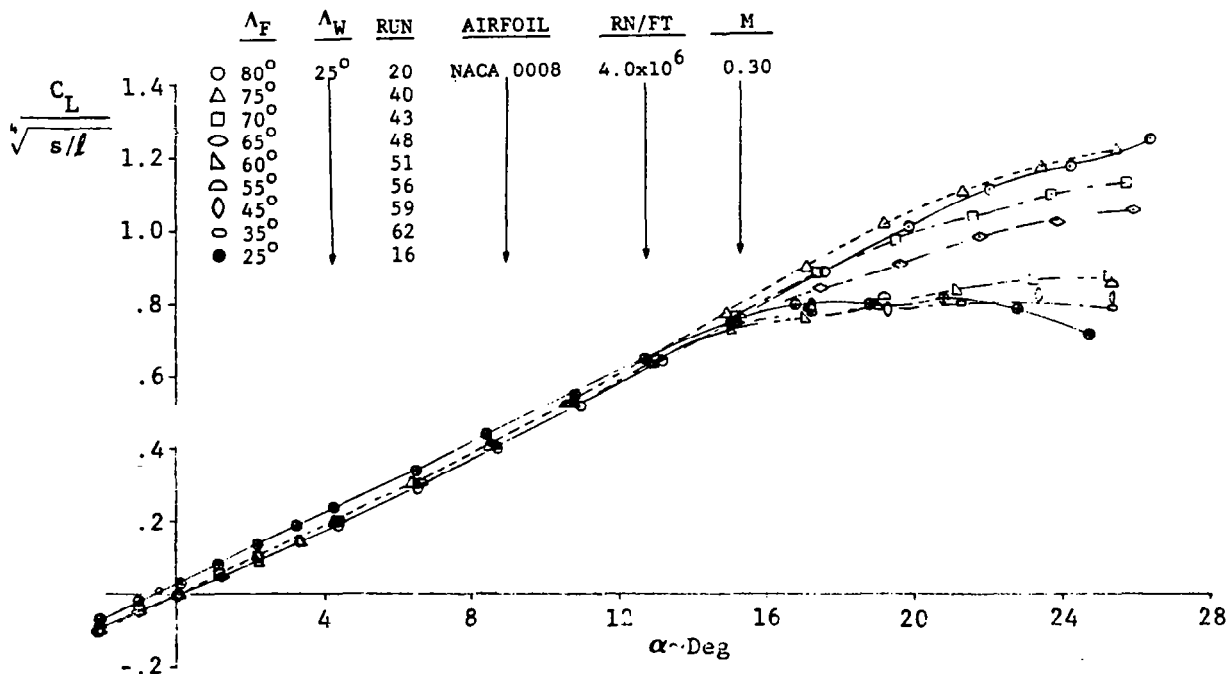
Figure 19. Modified Peckham Correlation for SHIPS Wing I Planforms
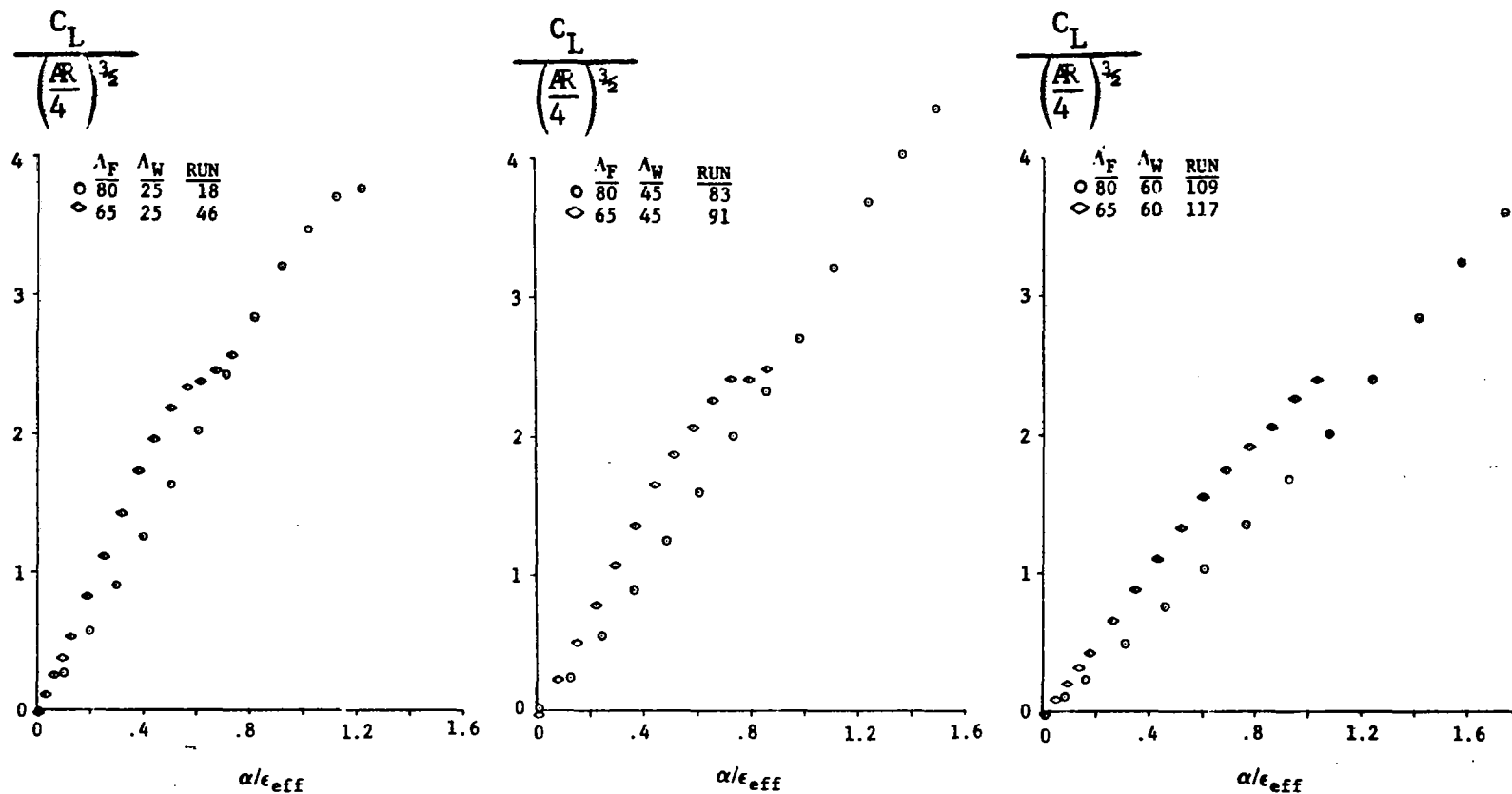
Figure 20.   Ericsson Version of Peckham Method - Area- Weighted Cosine $\Lambda_{LE_{eff}}$
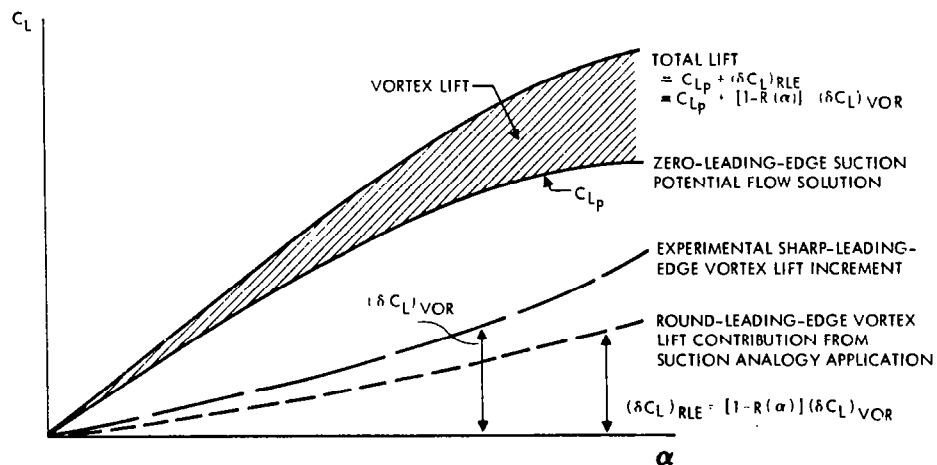
Figure 21. Analysis Method for Round Leading Edges
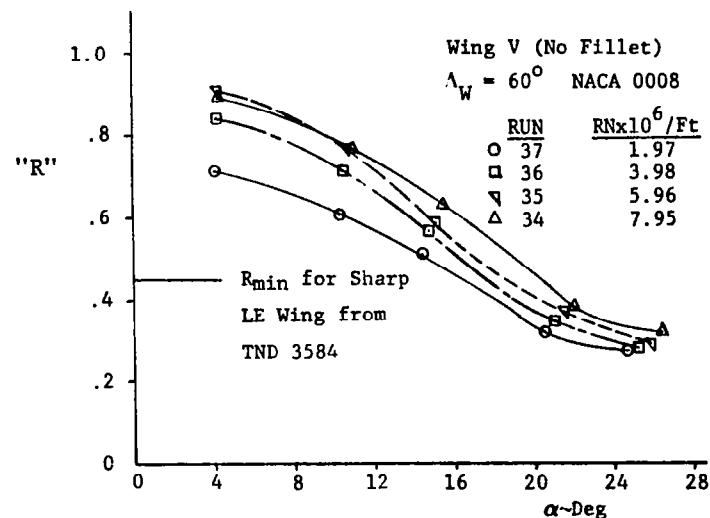
Figure 22. Variations of Suction Ratio With Angle of Attack for Various Reynolds Numbers
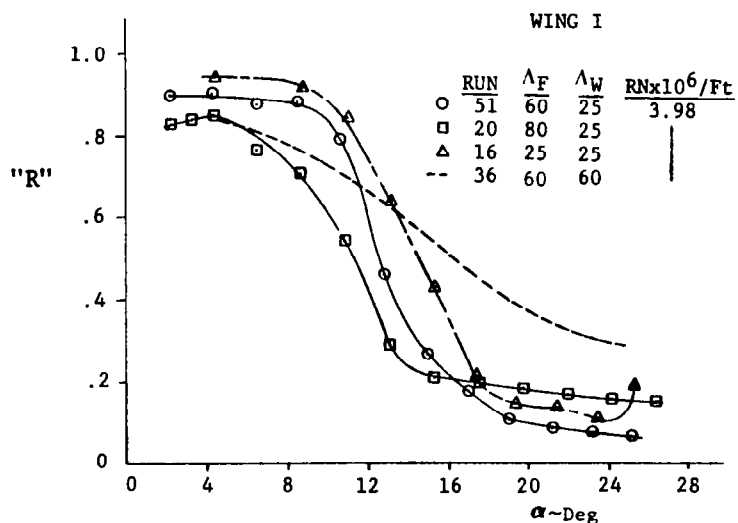
Figure 23. Variations of Suction Ratio with Angle of Attack for Various Planforms at Unit Reynolds Number of 4.0×10^6/Ft
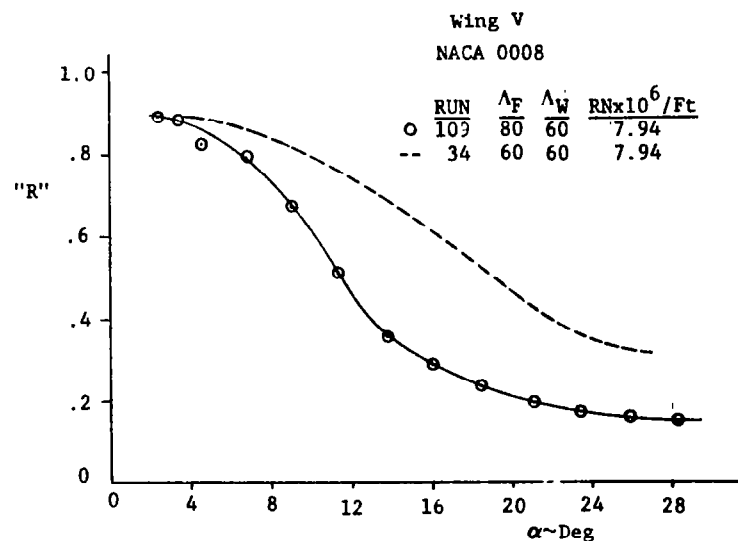
Figure 24. Variations of Suction Ratio With Angle of Attack Showing Effect of Fillet
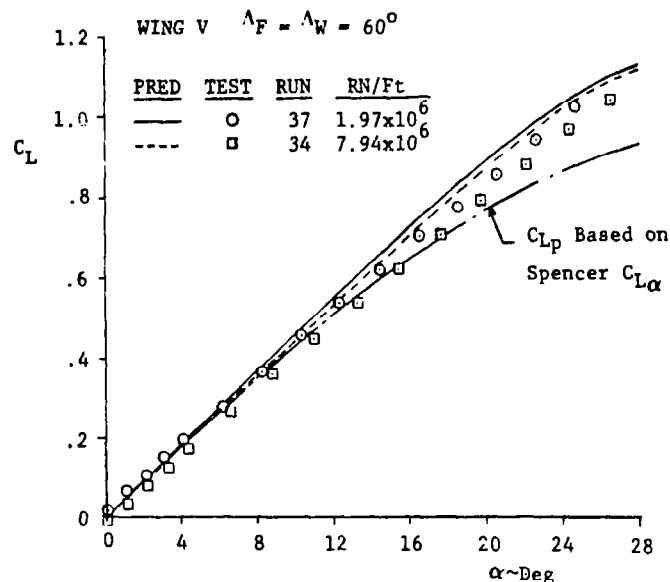
Figure 25. Prediction of Nonlinear Lift Using Test Values of Suction Ratio for Various Reynolds Numbers
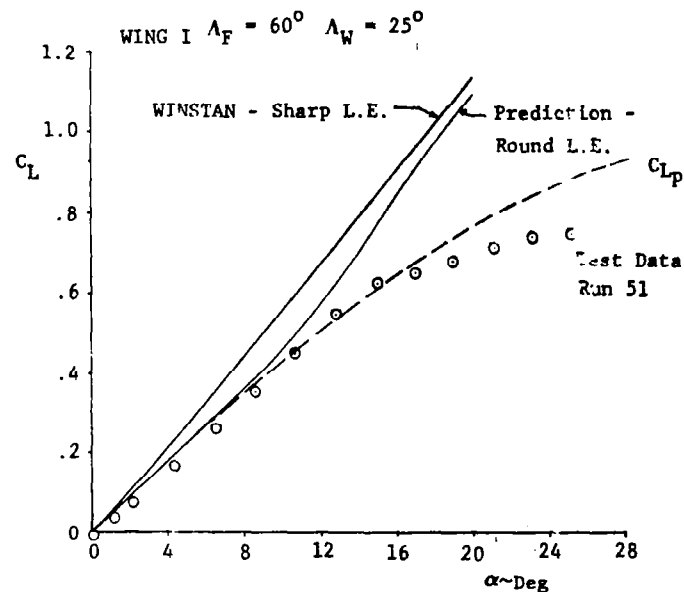
Figure 26. Prediction of Nonlinear Lift Using Test Values of Suction Ratio for Wing I With 60° Fillet
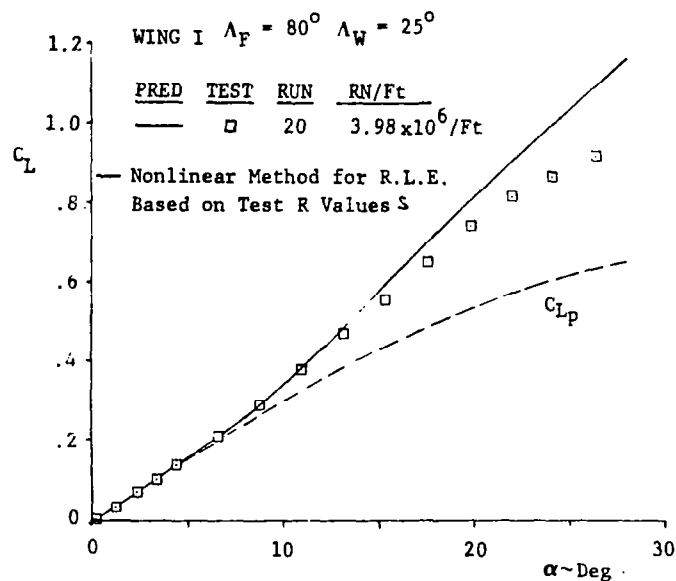
Figure 27. Prediction of Nonlinear Lift Using Test Values of Suction Ratio for Wing I with 80° Fillet
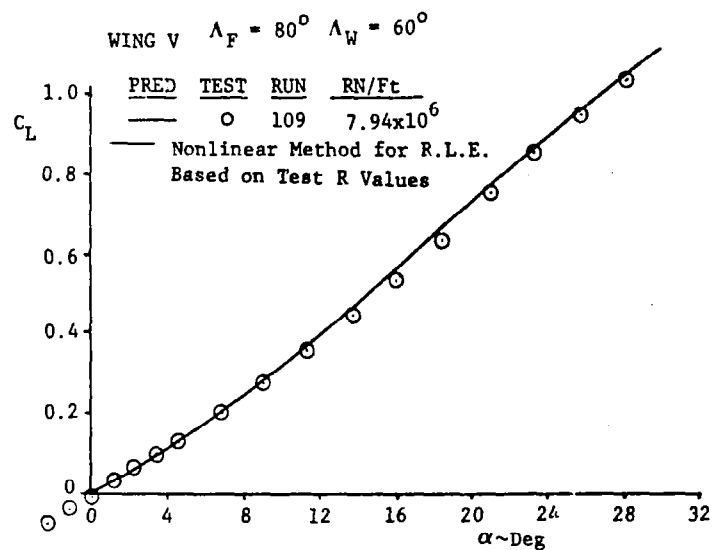
Figure 28. Prediction of Nonlinear Lift Using Test Values of Suction Ratio for Wing V with 80° Fillet

TEST	RUN	M	$R_N \times 10^{-6}$/FT	Λ_F Λ_W	AIRFOIL
○ TPT 780	9	.3	1.9	80 -- .0008	Inboard Panel
□ 12-086	21		1.9	80-25 .0008	Irregular Planform
△	17		1.97	25-25 .0008	Basic Wing I
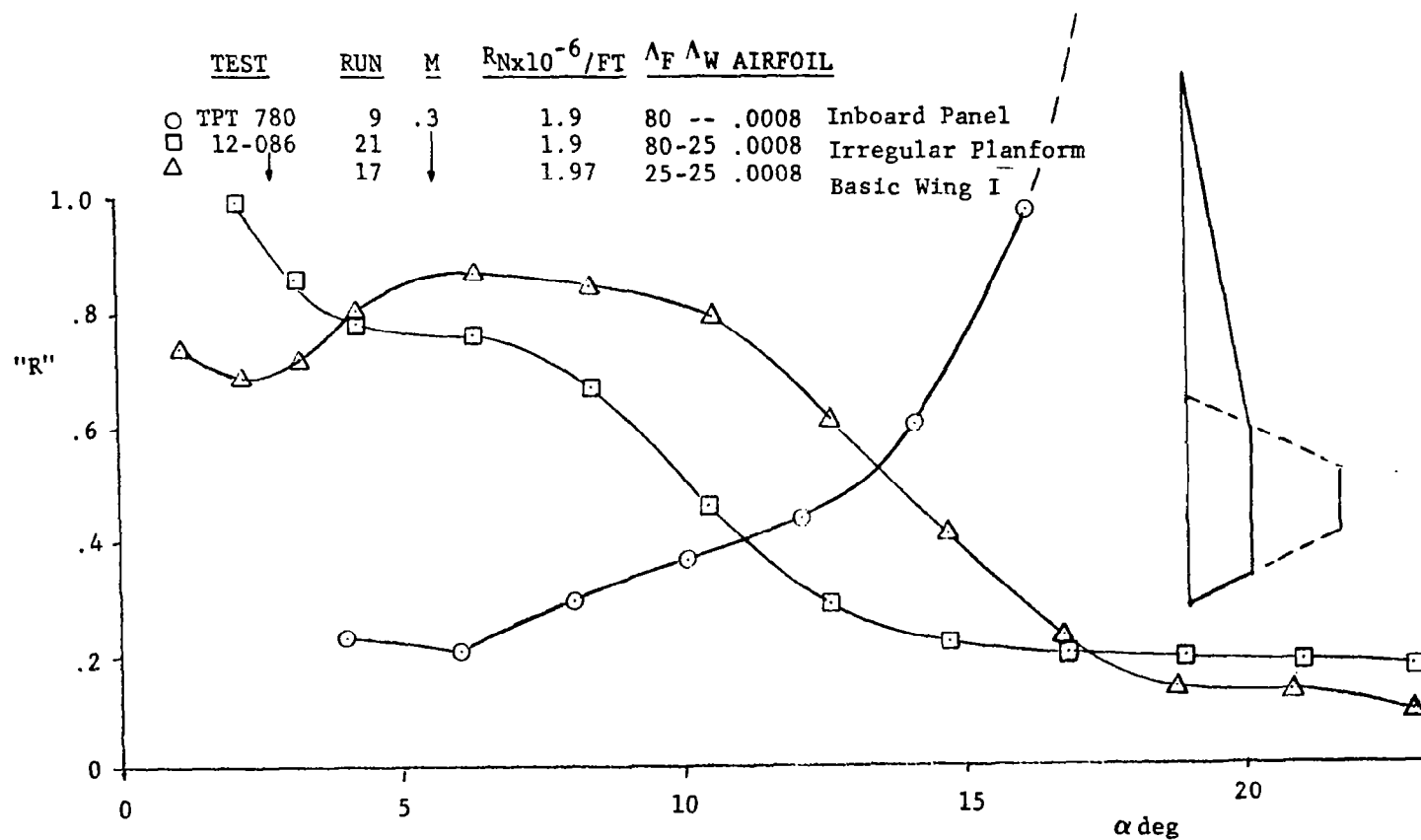
Figure 29.   Variation of Leading-Edge-Suction Ratio With Angle
of Attack - Wing I With 80° Fillet

"R"

	TEST	RUN	M	RNx10^6/Ft	Λ_F Λ_W	AIRFOIL	
○	TPT 780	15	.3	1.9	65 --	.0008	Inboard Panel
□	12-086	48		4.0	65-25	.0008	Irregular Planform
△		16			25-25	.0008	Basic Wing I

α Deg
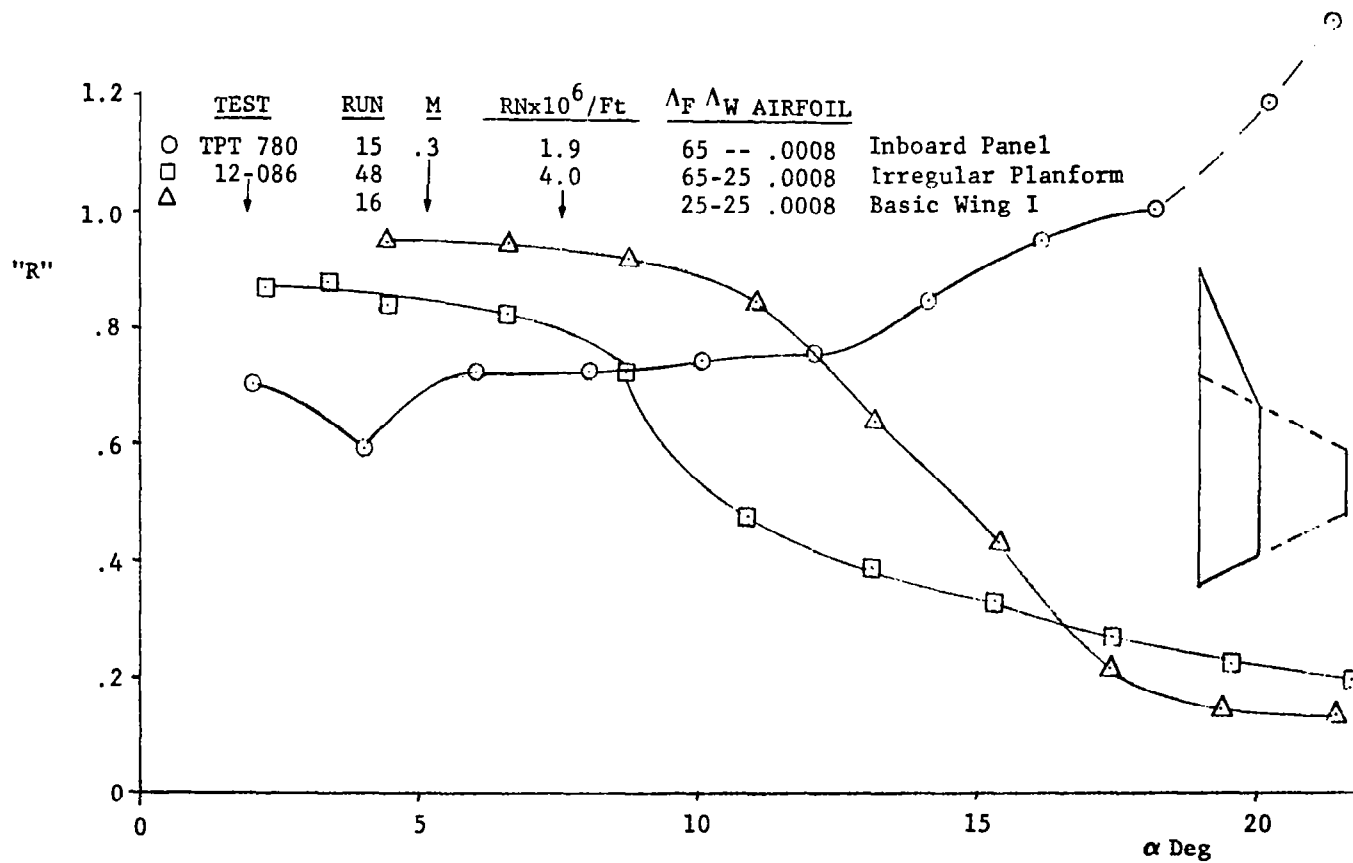
Figure 30.   Variation of Leading-Edge-Suction Ratio With Angle
of Attack - Wing I with 65° Fillet
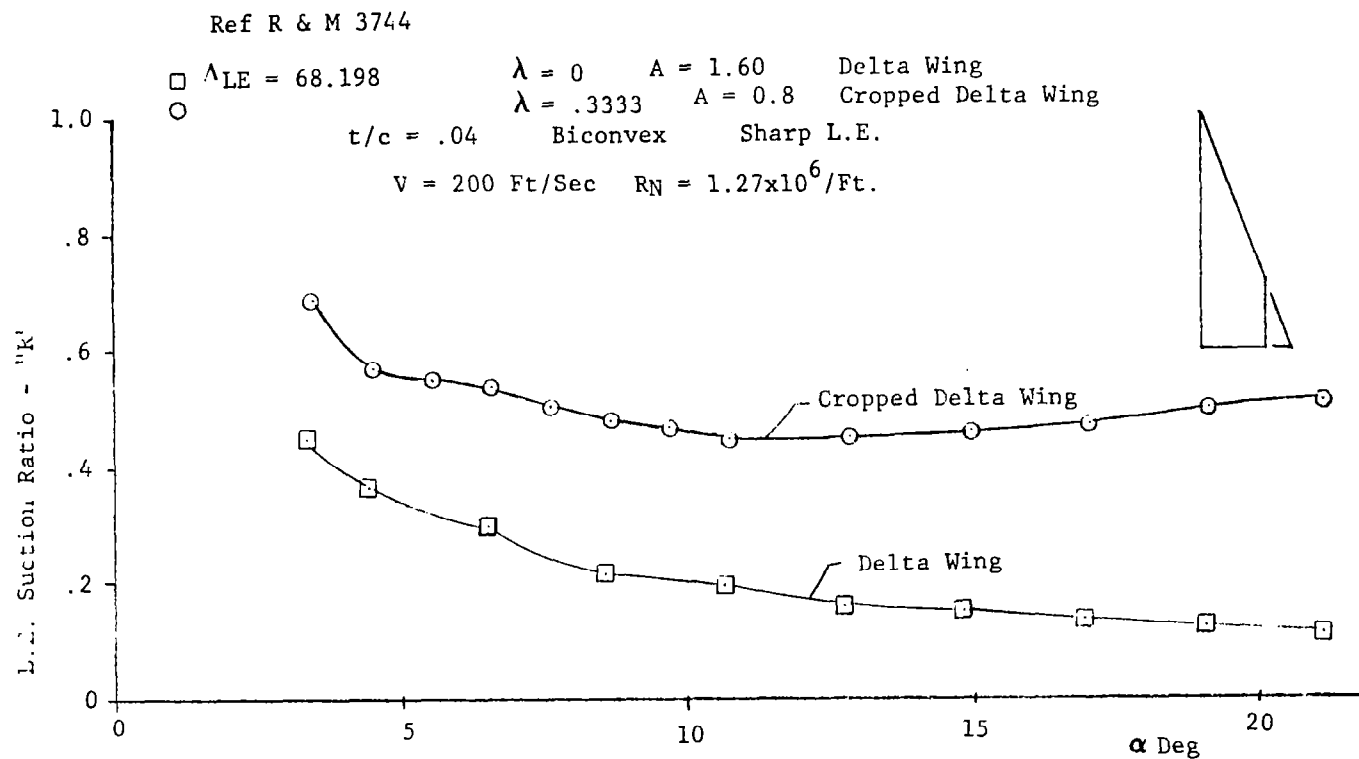
Figure 31.   Variation of Leading-Edge-Suction Ratio With Angle
             of Attack - Delta and Cropped Delta Wings
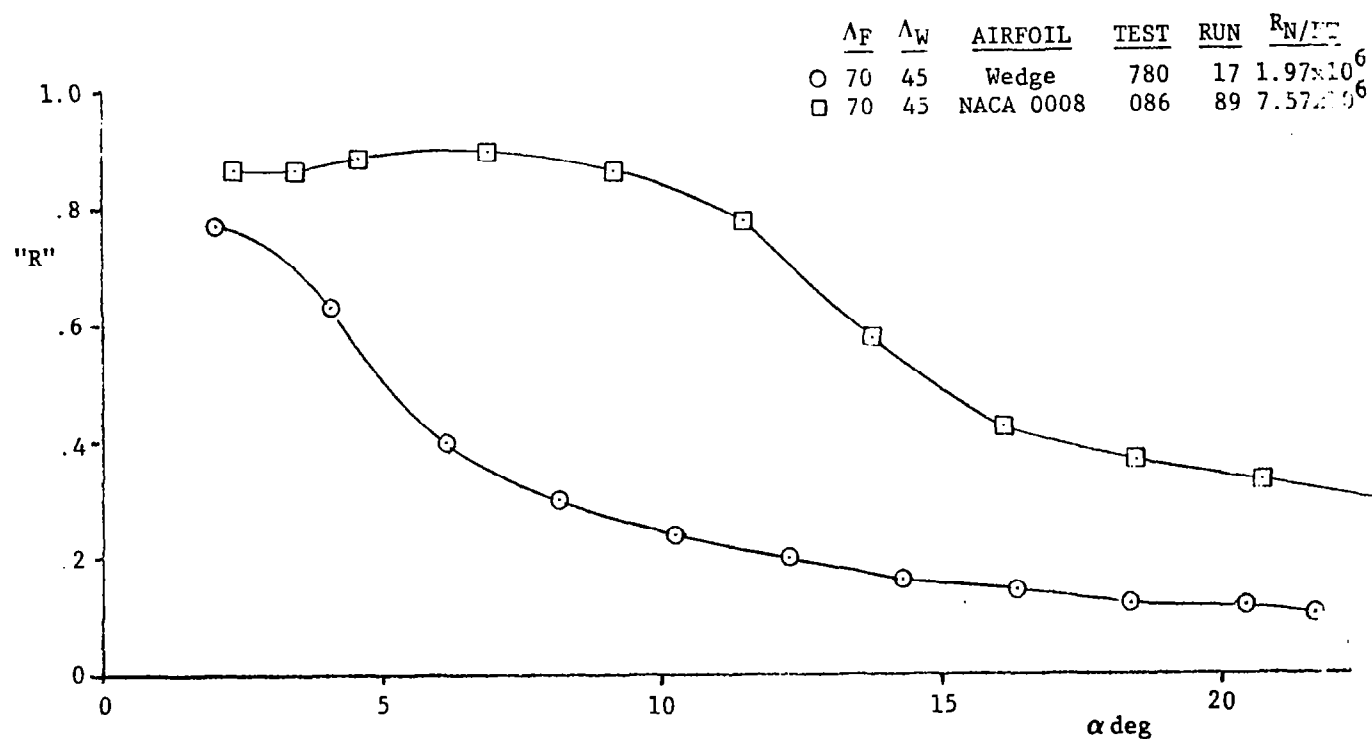
Figure 32.   Leading-Edge-Suction Values Calculated From Test
Data - Wing III With 70° Fillet

Λ_F	Λ_W	AIRFOIL	TEST	RUN	R_N/FT
O 70	45	Wedge	780	17	1.97×10^6
□ 70	45	NACA 0008	086	89	7.97×10^6
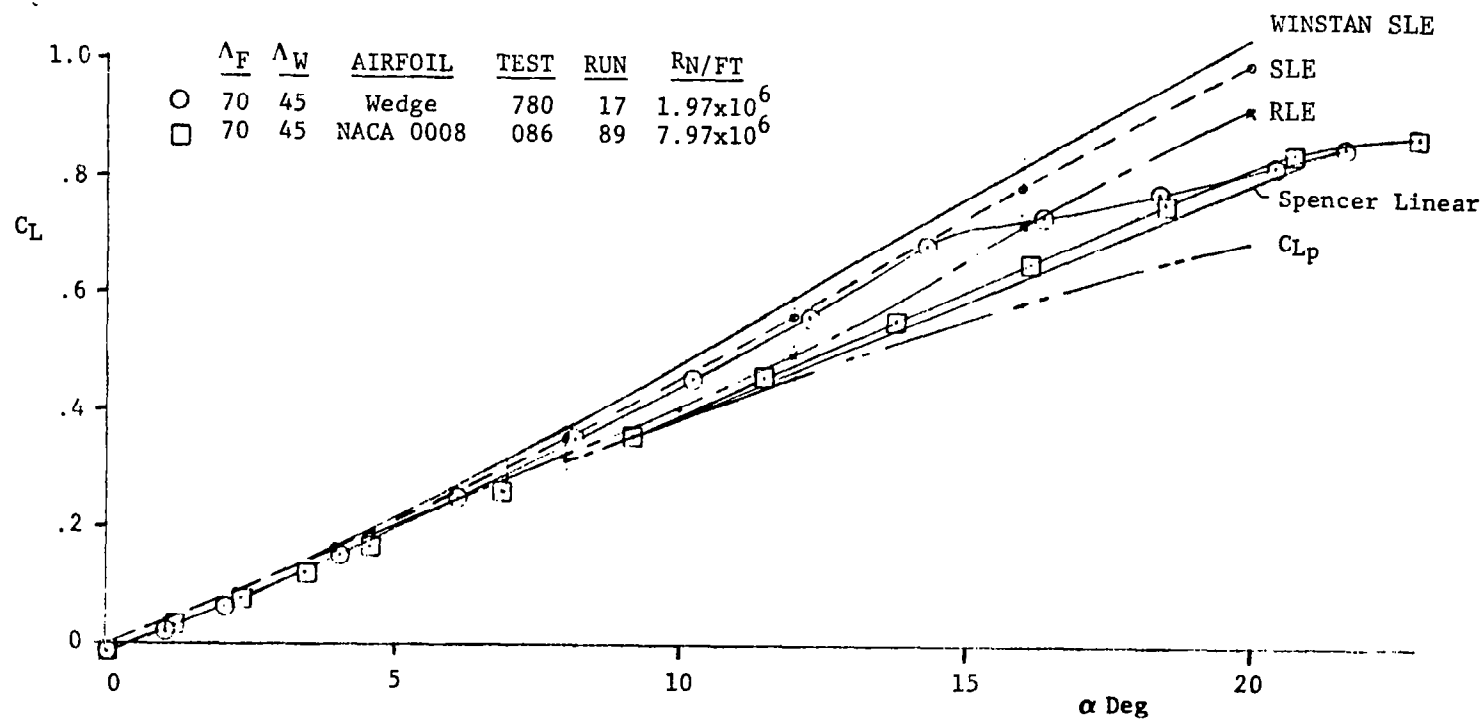
Figure 33.   Comparisons of Predicted and Test Lift Curves - Wing III With 70° Fillet
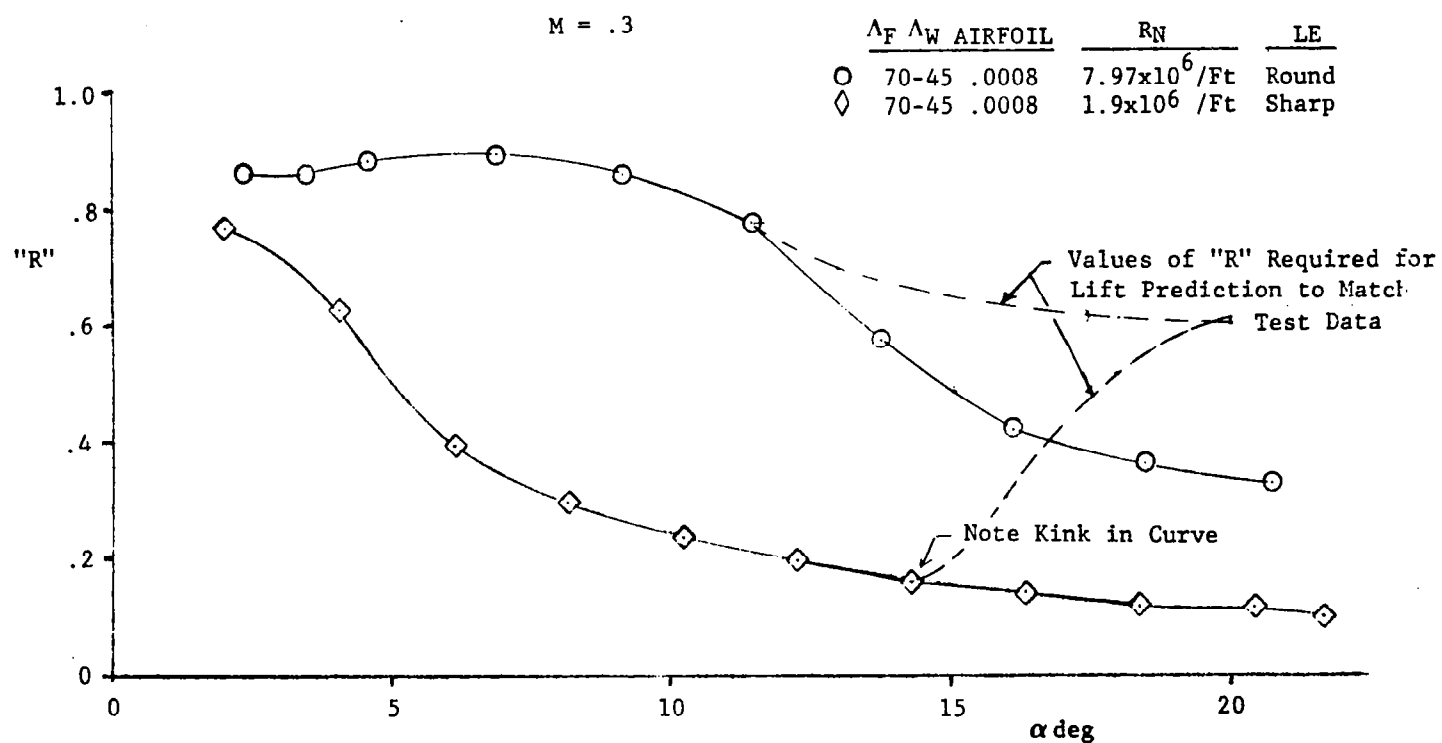
Figure 34.   Modified Variations of Leading-Edge-Suction Ratio -
Wing III With 70° Fillet

82
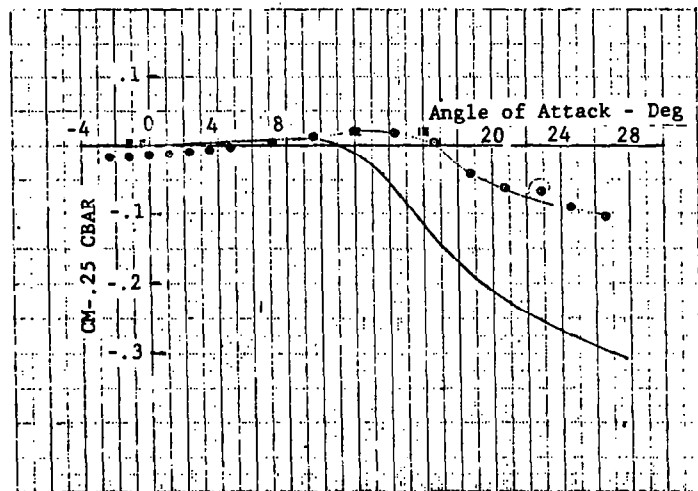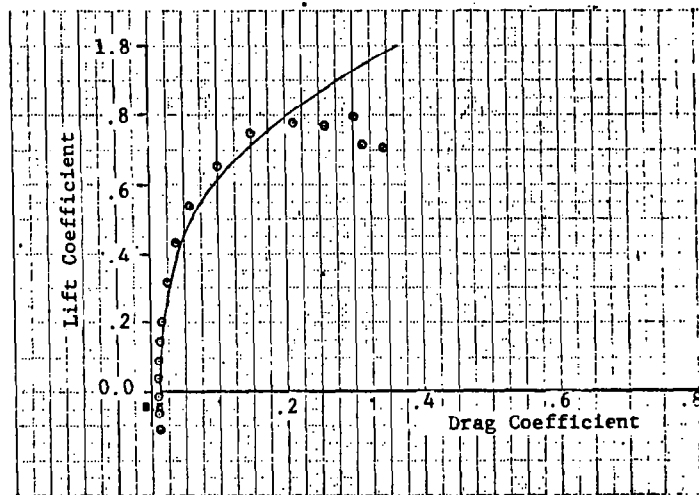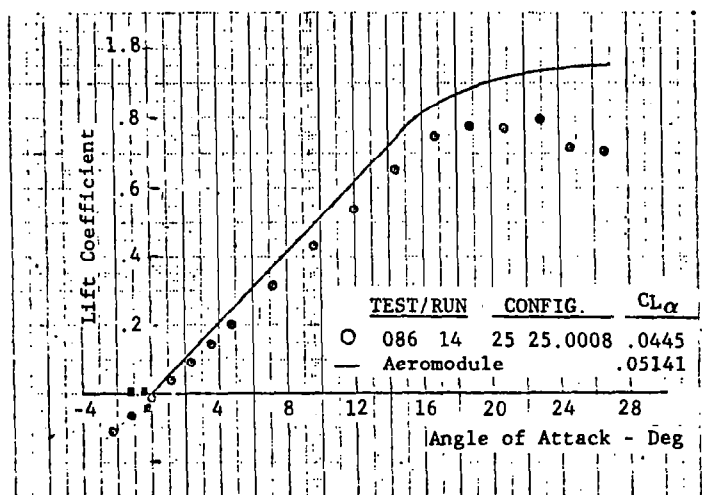
Figure 35. Comparisons of Aeromodule Predictions With Test
Data - Configuration 25 25.0008
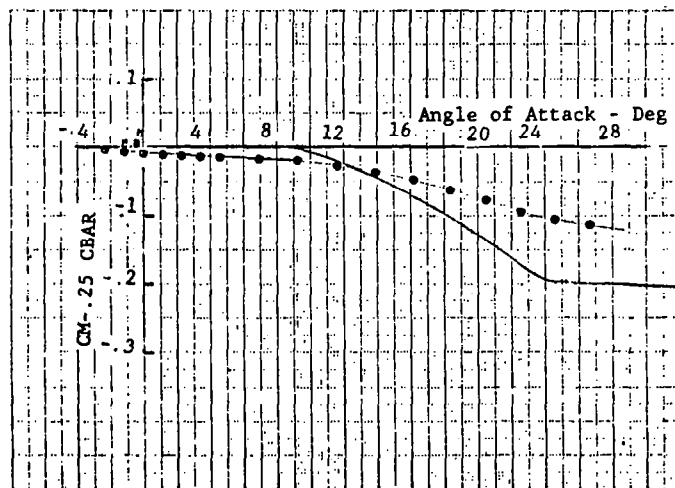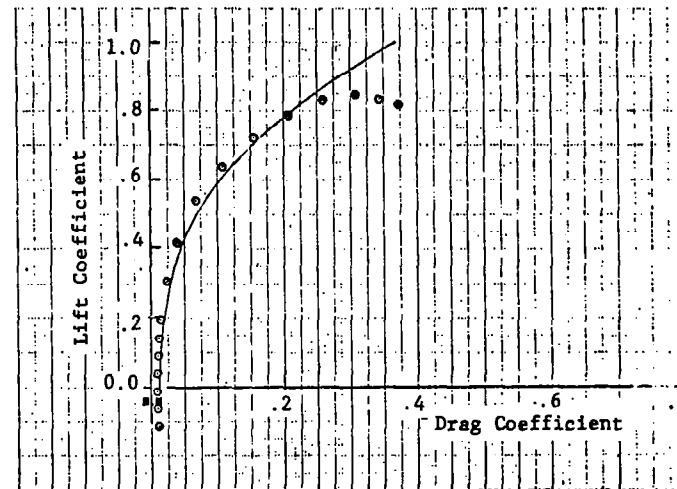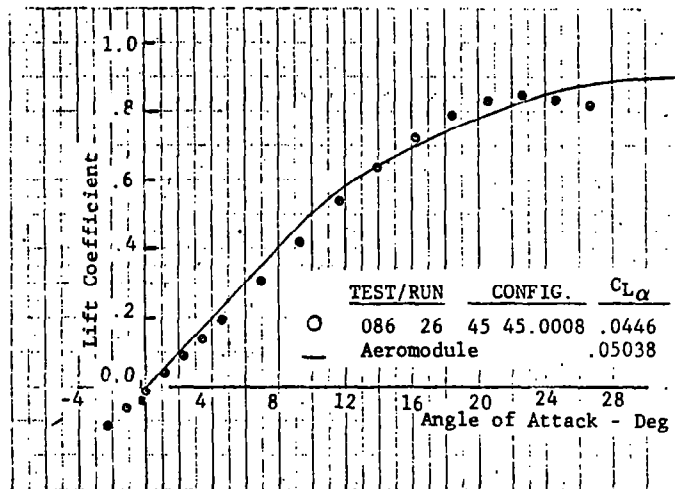
Figure 36.   Comparisons of Aeromodule Predictions With Test
              Data - Configuration 45 45.0008

TEST/RUN		CONFIG.	C_{L_α}
O	086 34	60 60.0008	.0416
— Aeromodule			.04651
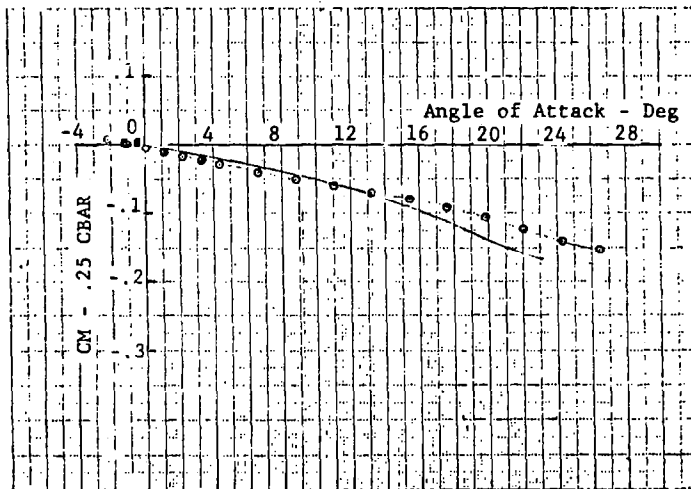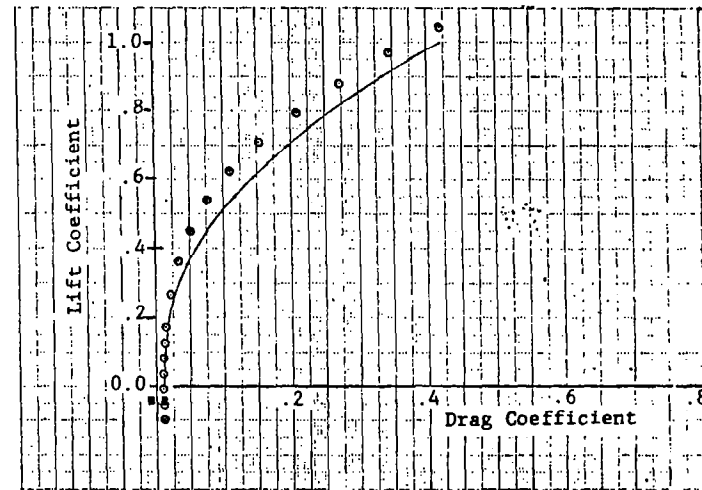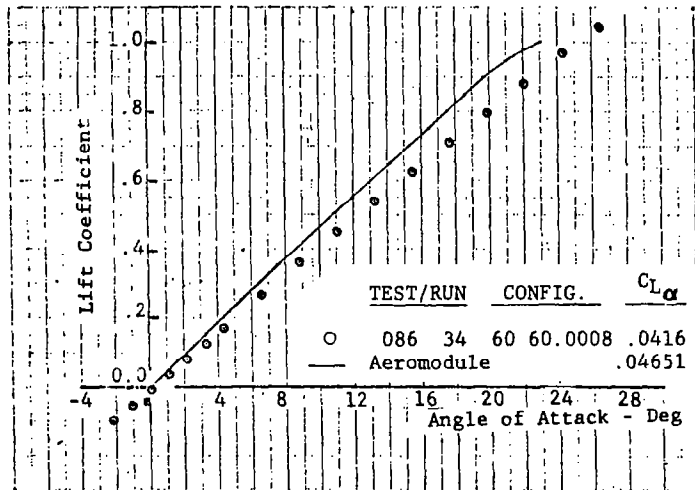
Figure 37.   Comparisons of Aeromodule Predictions With Test
Data - Configuration 60 60.0008
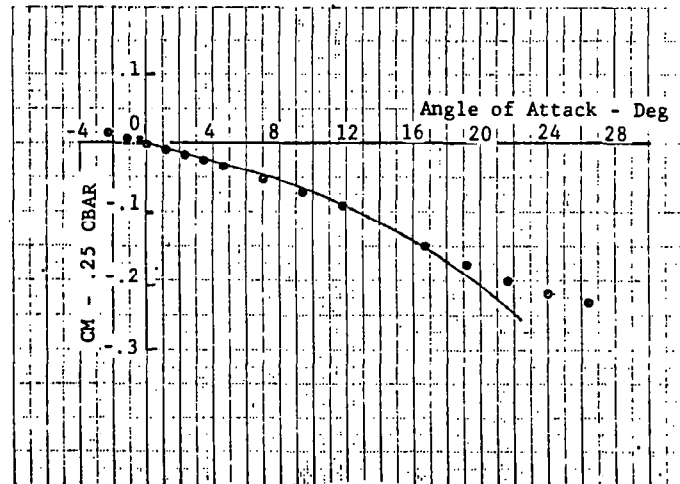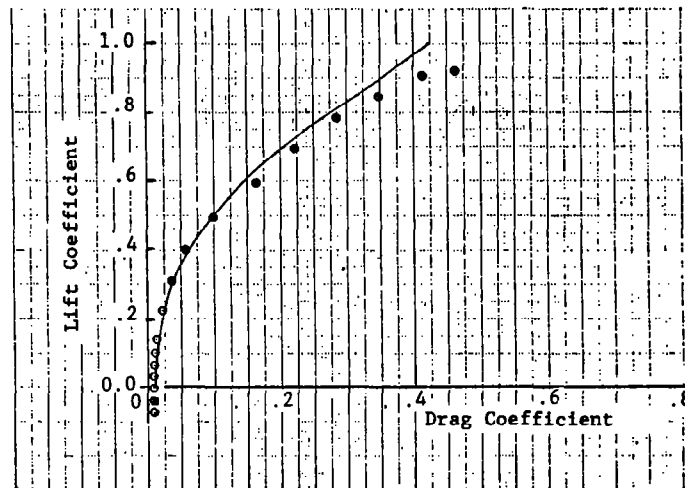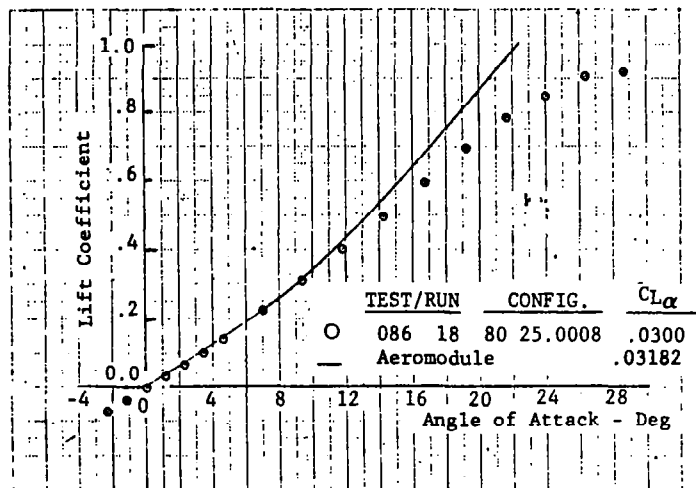
Figure 38.   Comparisons of Aeromodule Predictions With Test
Data - Configuration 80 25.0008
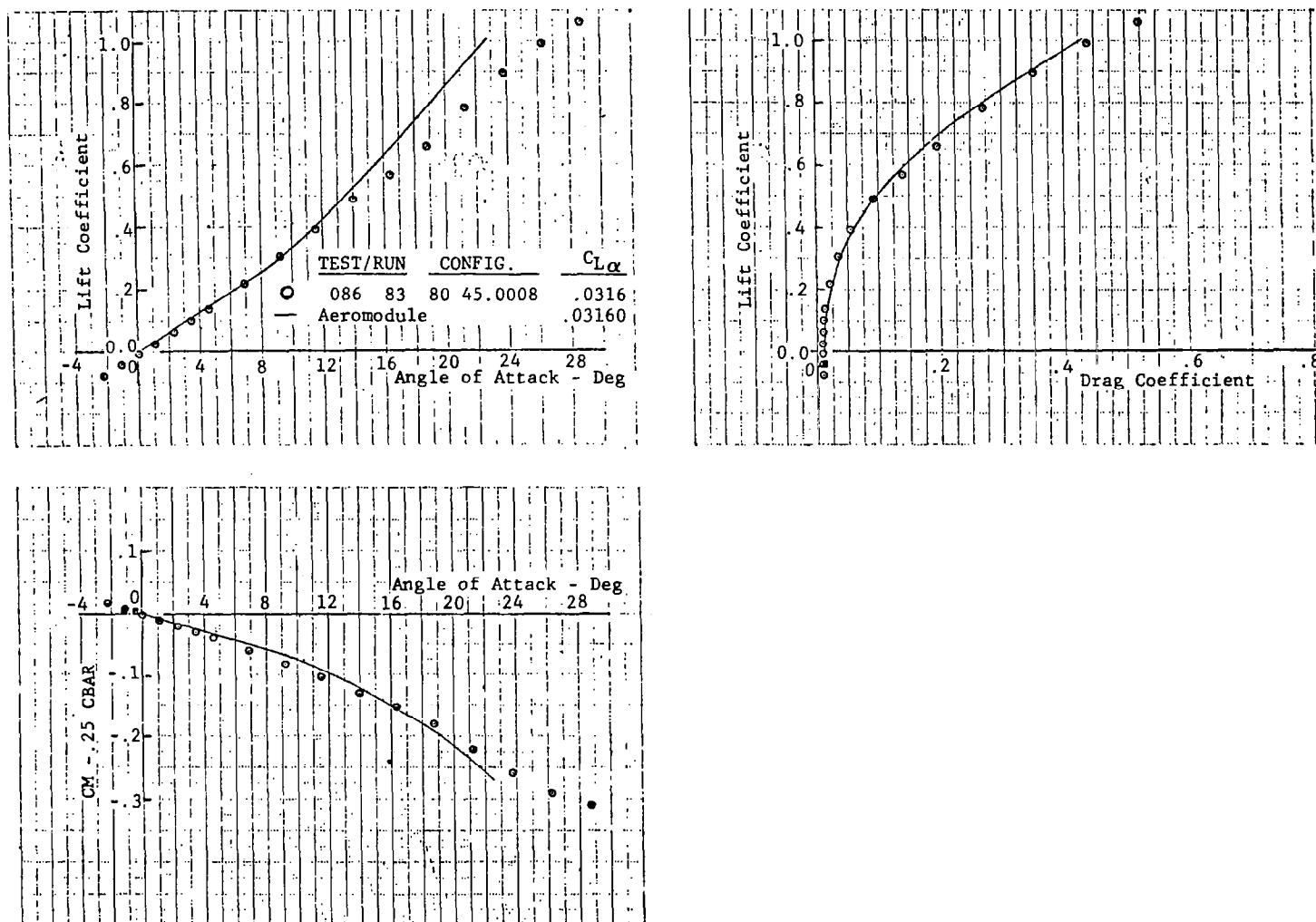
Figure 39. Comparisons of Aeromodule Predictions With Test Data - Configuration 80 45.0008
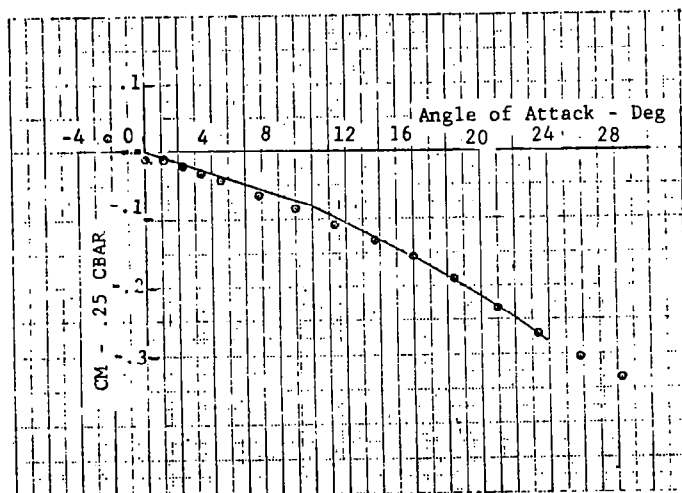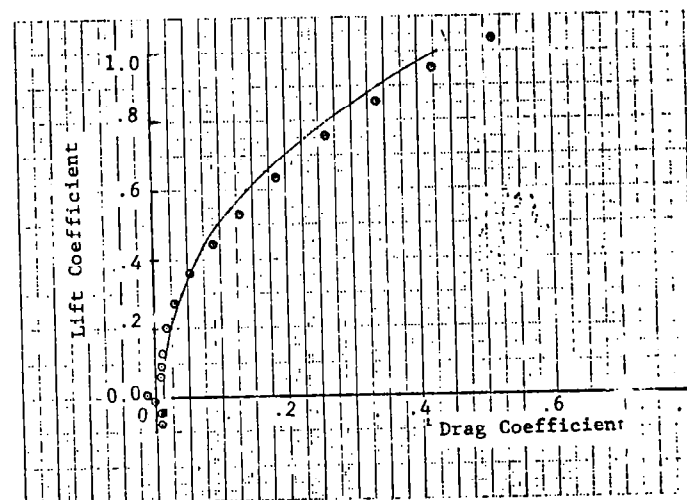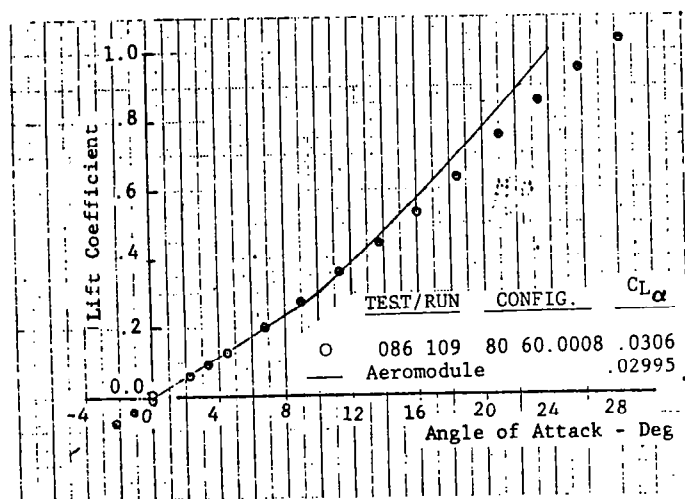
Figure 40.   Comparisons of Aeromodule Predictions With Test
             Data - Configuration 80 60.0008

TEST/RUN	CONFIG.	C_{L_α}
⊙ 086 60	35 25.0008	.0435
— Aeromodule		.05060
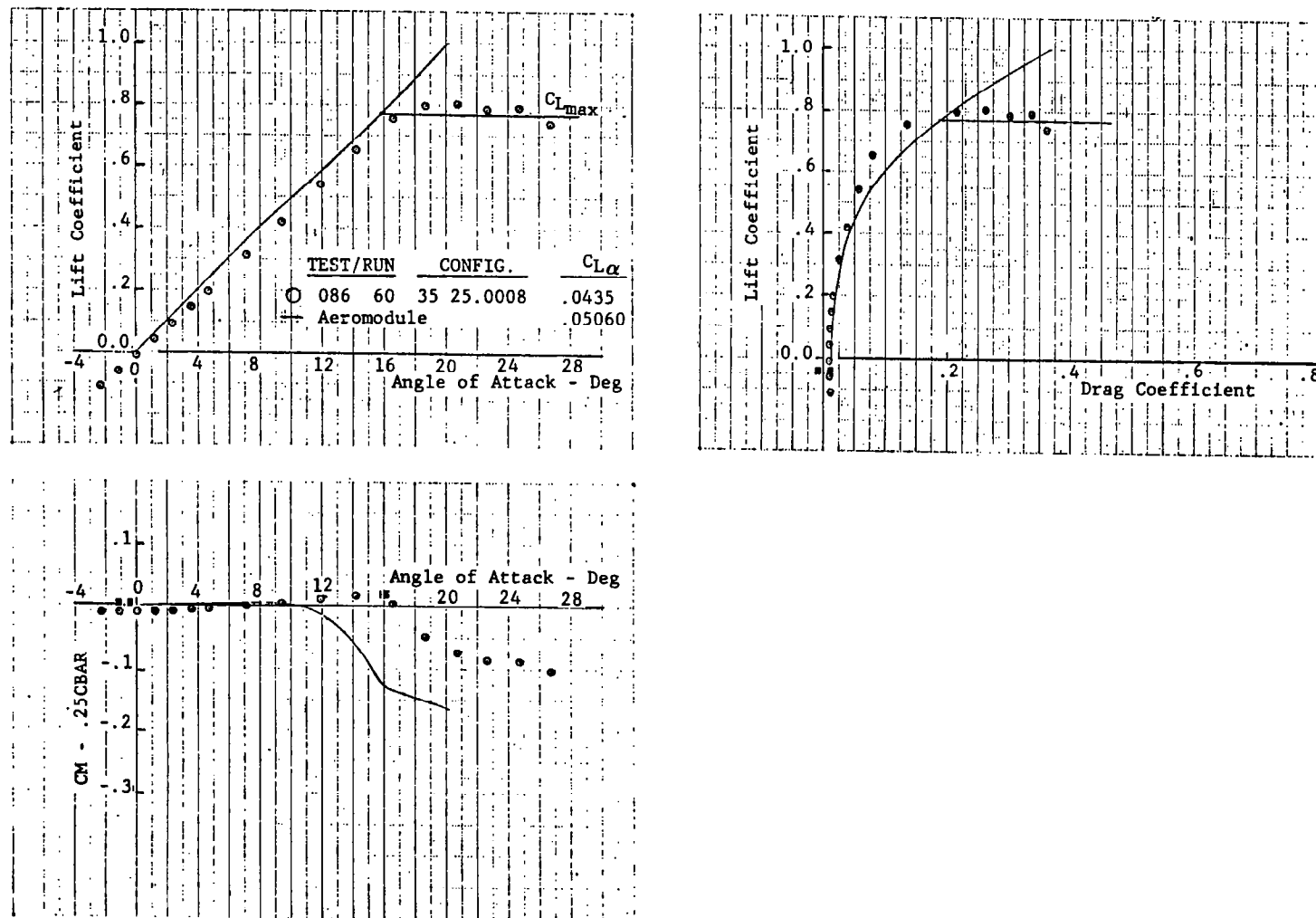
Figure 41.   Comparisons of Aeromodule Predictions With Test
Data - Configuration 35 25.0008
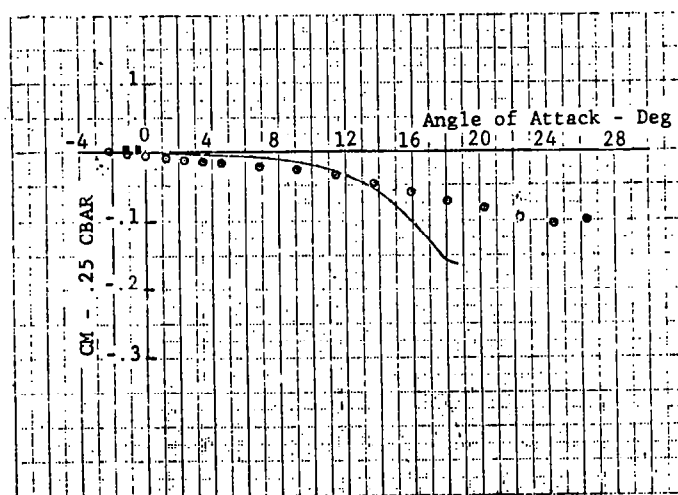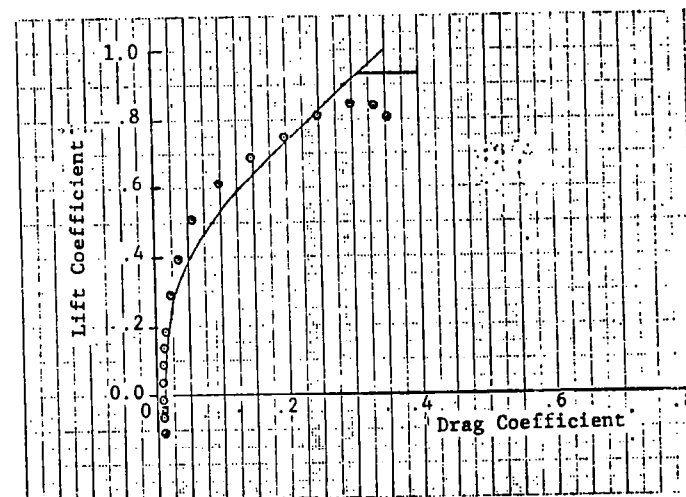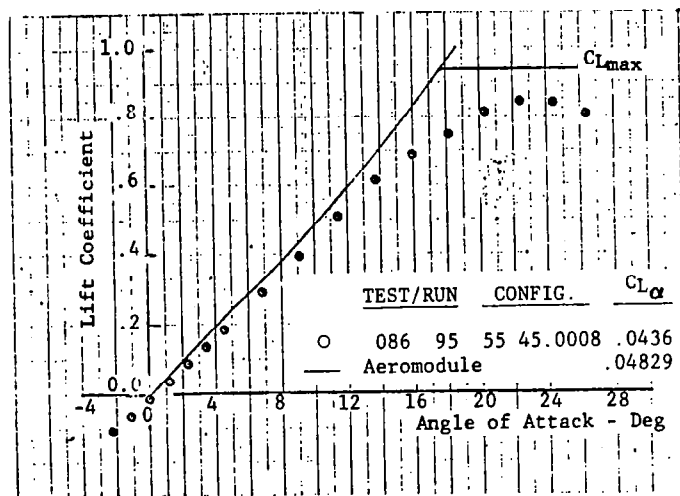
Figure 42.   Comparisons of Aeromodule Predictions With Test
              Data - Configuration 55 45.0008
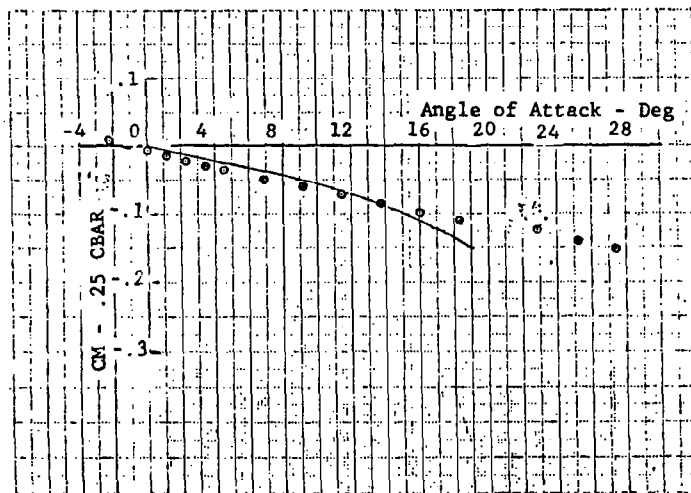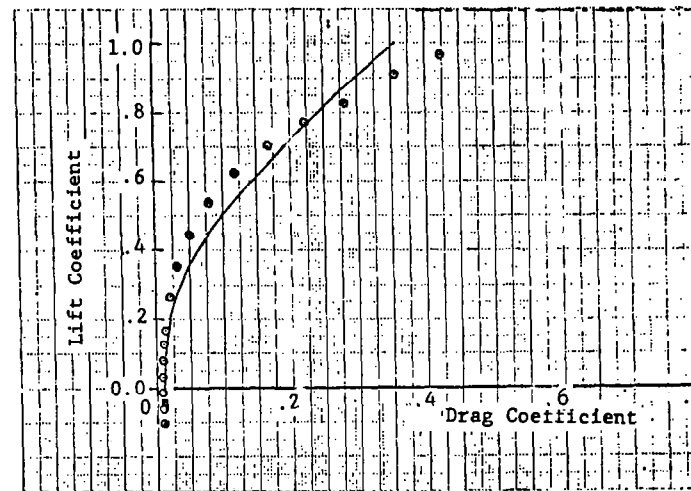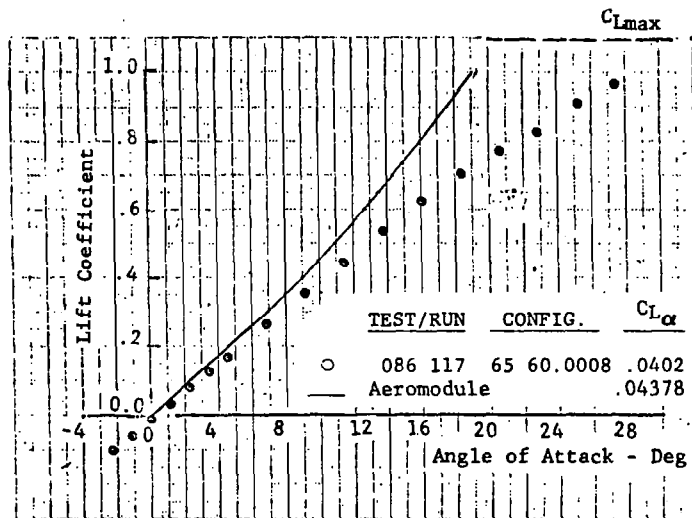
Figure 43.   Comparisons of Aeromodule Predictions With Test
Data - Configuration 65 60.0008
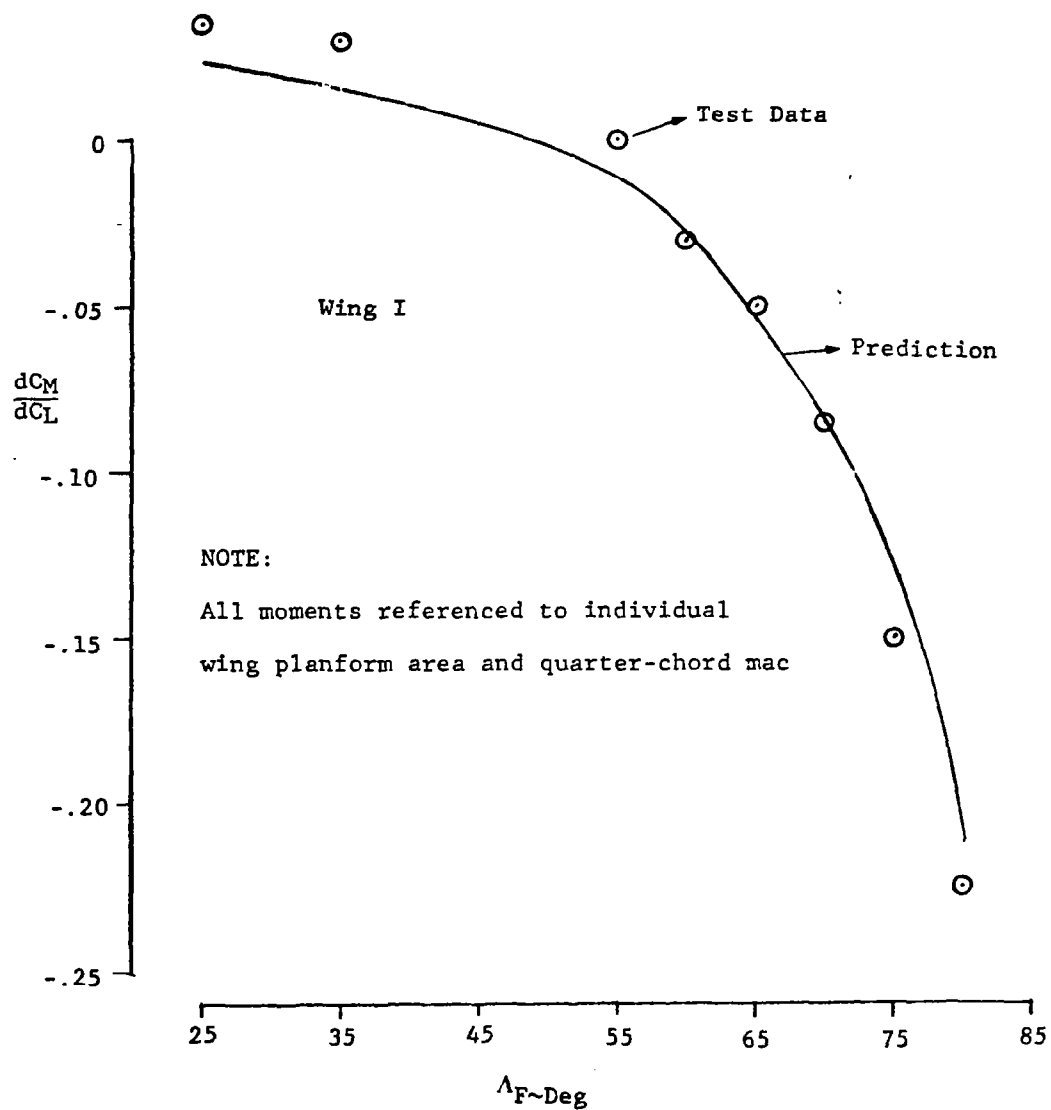
Figure 44. Comparison of Aeromodule Longitudinal Stability Derivative With Test Data for Wing I With Various Fillets
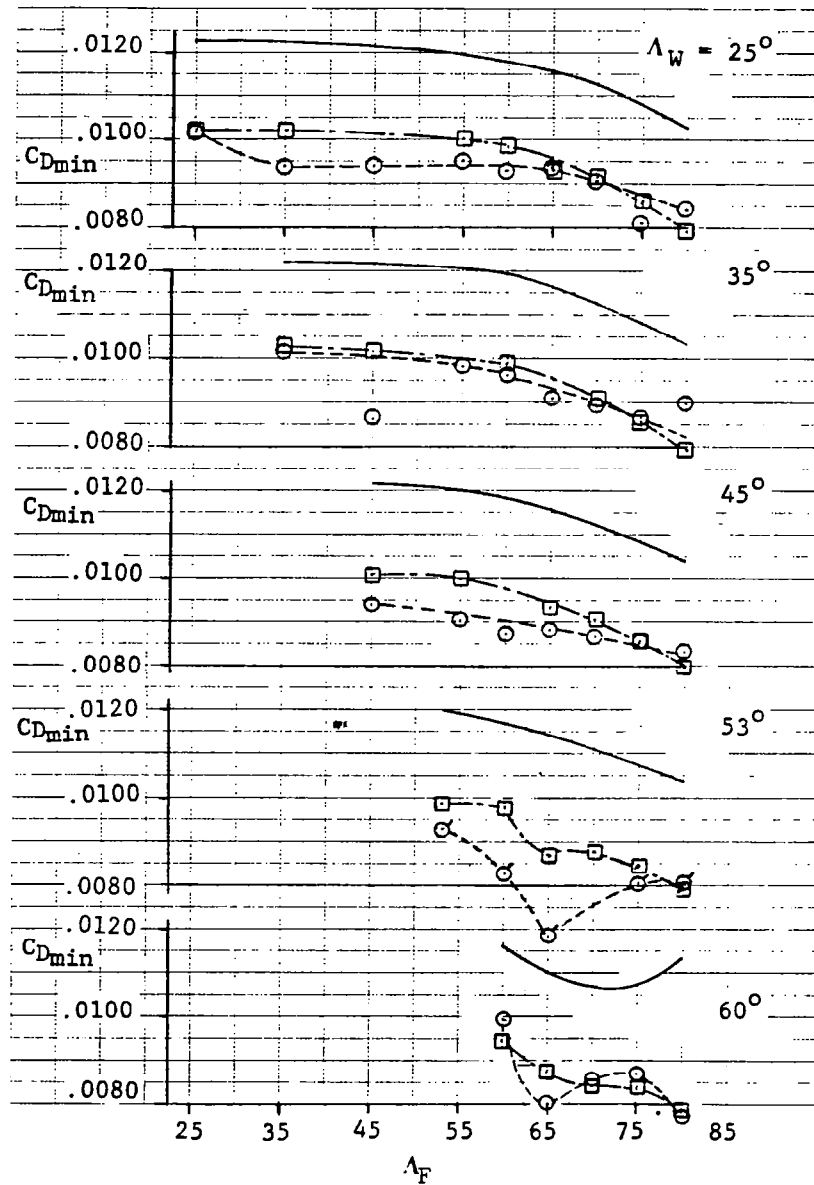
Figure 45. Minimum Drag Test-to-Theory Comparisons
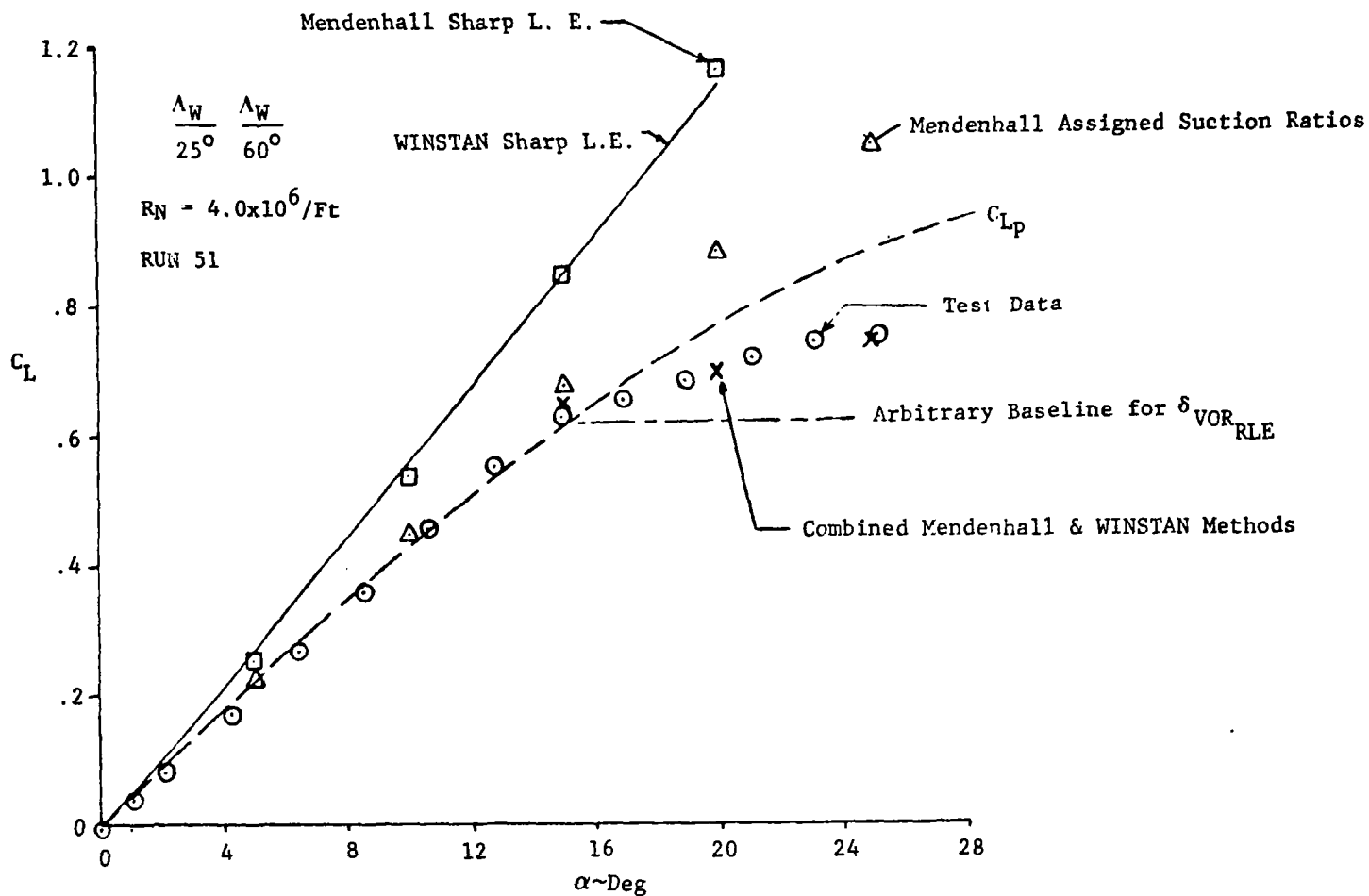
Figure 46. Results of Analysis Using Mendenhall Lifting
Surface Plus Suction Analogy Computer Proce-
dure and WINSTAN Methods

DATA CORRELATIONS

The goals of the data correlation efforts were twofold:

(1) to provide a means of removing the deficiencies and limitations of existing prediction methods or developing new empirical methods, and (2) to generate simplified design guides for evaluating new configuration concepts.

The specific objective of the task was to obtain combinations of planform geometric parameters, airfoil section parameters and flow parameters that would correlate the SHIPS lift, drag, and moment data.

The evaluations of existing prediction methods indicated that new or revised correlations were needed for the following elements of the aerodynamic characteristics:

(1) Second order (nonlinear) lift

(2) Drag due to lift

(3) Aerodynamic-center location

(4) High angle-of-attack pitching moment characteristics (pitch-up boundaries).

The approach used was to obtain the basic effects of planform parameters from the test data obtained at 26.25 million per meter unit Reynolds number with the NACA 0008 airfoils and then examine the effects of Reynolds number and airfoil section parameters. The efforts will be described in the order listed above.

Nonlinear Lift

The analysis of existing methods indicated that accurate prediction of nonlinear lift was perhaps the most essential ingredient in the development of an improved prediction methodology.

Therefore, a considerable amount of effort was devoted to investigating different correlation approaches for lift.

A plot showing the spread of the lift coefficient data for all 35 SHIPS planforms with NACA 0008 airfoils is presented in Figure 47. The coefficients are referenced to the total planform area. What is desired is to find correlation parameters that will coalesce these data into either a single line or a family of lines. From previous work it was known that plotting data for constant values of fillet sweep would reduce scatter considerably. Figure 48 which presents the data for SHIPS planforms with 80 degree fillets illustrates this fact. Note that the remaining scatter is systematic with outboard panel sweep. A further reduction in scatter for angles of attack below 20 degrees was obtained by dividing the test lift coefficient (C_L) by the lift curve slope per degree angle of attack C_{L_α} (estimated by the Spencer method) as illustrated in Figure 49. Figure 50 presents the same correlation parameter applied to the lift data for the Basic Wings. The reduction in scatter is excellent below 16 degrees angle of attack.

The WINSTAN correlation parameter for lift of double delta planforms was examined next. The parameter combines C_L/C_{L_α} with two irregular planform geometric parameters: (1) A_1 the aspect ratio of the inboard panel and (2) η_B, the spanwise location of the break in leading-edge sweep as a fraction of semispan. The parameter is

$$\left(\frac{C_L}{C_{L_\alpha}} \quad \frac{A_1}{\eta_B} \right)$$

In this case, the lift-curve slope is per radian.

Figures 51 through 58 present correlations of SHIPS lift data for each of the fillet sweeps starting with the 80-degree sweep fillet wing combinations. In each case, the correlation produces a satisfactory collapse of the data up to 16 degrees angle of attack and a reasonably systematic spread of the data above that angle, which is dependent on outboard panel sweep.

The data were then further correlated using the second correlation parameter from the WINSTAN double-delta lift-prediction

method. Curves of $\left(\dfrac{C_L}{C_{L\alpha}} \dfrac{A_1}{\eta_B}\right)$ as functions of $\beta \tan\Lambda_F$ were established at constant angles of attack as shown in Figure 59. The curves for angles of attack from 0 to 16 degrees apply to all outer panel sweeps. The curves above 16 degrees apply only for $\Lambda_W = 45$ degrees.

Further effort to account for other outboard panel sweeps was held in abeyance until other correlations of lift were achieved. It was obvious, however, that the WINSTAN double-delta method was a prime candidate for developing a SHIPS lift prediction technique.

The next lift correlation technique investigated was the modified Peckham method in which the parameter $C_L/(s/\ell)^{\frac{1}{4}}$ is plotted against angle of attack. Figure 60 is a plot showing the spread of data for all 35 SHIPS planforms. The collapse of data below 16 degrees angle of attack is remarkable considering the simplicity of this correlation. The spread of data above 16 degrees reflects, of course, the differences in stall progression among the many wing planforms. Figures 61, 62 and 63 present individual correlations for the basic wings and for the fillet wing combinations with 65-degree and 80-degree fillets. The data collapse up to 16 degrees angle of attack is not significantly better than that of the overall correlation. The data above 16 degrees do indicate definite families of curves for the various outboard panel sweeps.

A further modification of the Peckham method was also evaluated. The previously described correlation parameter was divided by the lift-curve slope, per degree, as predicted by the Spencer method. The new parameter

$$\left(\dfrac{C_L}{(s/\ell)^{\frac{1}{4}}}\right)\left(\dfrac{1}{C_{L\alpha}}\right) \quad \text{or} \quad \left(\dfrac{C_L}{C_{L\alpha}} \dfrac{1}{(s/\ell)^{\frac{1}{4}}}\right)$$

is plotted against angle of attack in Figures 64 through 72 for the basic wings and then for wing fillet combinations for constant values of fillet sweep. The data collapse for angles of attack below 16 degrees is much improved compared to using only $\dfrac{C_L}{(s/\ell)^{\frac{1}{4}}}$ except for fillet sweeps of 65 and 70 degrees where the improvement is less significant. In addition, correlation curves

representing these results have different initial slopes. A plot similar to the WINSTAN double-delta method presented earlier would be needed to have a viable prediction technique. Although the correlations do not appear to be quite as good as those of the WINSTAN method, this approach did offer an alternative to the WINSTAN method.

The many different approaches presented thus far were aimed specifically at trying to develop correlations that could evolve into a prediction method. The next two analyses were intended primarily to evolve design guidelines.

First, the SHIPS lift data were plotted using the parameter

$$\frac{C_L}{C_{L_{SPENCER}}}$$

in which $C_{L_{SPENCER}}$ is the linear estimate of lift variation with angle of attack. Figures 73 through 81 present the plotted calculations for the basic wings first and then the fillet-wing combinations for constant fillet sweeps. The primary use of these curves would be to establish the upper limit of angle of attack for quasi-linear lift for each configuration. Rather than provide arbitrary boundaries, it was decided to allow the designer to exercise some judgment as to how much nonlinearity would be acceptable for a given situation. The design guide would consist of faired curves grouped like the test data plots.

The final correlation parameter examined is the ratio of test lift coefficient to the nonlinear potential flow lift coefficient, C_L/C_{L_p}

where

$$C_{L_p} = C_{L_\alpha} \cos \alpha \sin^2 \alpha \text{ and } C_{L_\alpha} \text{ is the Spencer value}$$

per degree. Typical variations of this parameter with angle of attack are shown in Figures 82 and 83. The results for 80 degree sweep fillets (Figure 83) show large contributions due to vortex lift, whereas the results for the basic wings exhibit little vortex lift except on the 60-degree sweep wing.

Drag Due to Lift

The basic approach to developing correlations for drag due to lift was the analysis of the leading-edge-suction ratio, "R", as a function of angle of attack, planform parameters, airfoil section parameters, and Reynolds number. The basis of the approach was the fact that for low to moderate angles of attack, correlation of leading-edge-suction ratio with planform parameters and the effective leading-edge radius Reynolds number had been achieved and verified for both swept and irregular planforms during the WINSTAN investigation (Ref. 5).

As an initial step in the analysis, values of the suction ratio were calculated for all runs of test ARC 12-086-1 and plotted versus angle of attack. Figure 84 presents a typical family of suction ratio data for the SHIPS planforms with 75 degree fillet sweeps obtained at unit Reynolds number of 26.25 million per meter (8 million per foot) and illustrates a fact noted in most of the plotted data. There are six distinct regions to the variations with angle of attack. At low angles of attack the variations are erratic because the analysis is extremely sensitive to the value selected for $C_{D_{min}}$ and the test values of lift and drag coefficients are not sufficiently accurate to define specific data trends. At angles above about 4 degrees, a plateau value is apparent which has been used in previous work to define the basic drag polar shape for attached flow. For analysis purposes, the lower limit of the plateau region was defined as α_1 and the upper limit as α_2. Next there is a slight decrease in the slope of the variations which is apparently caused by the initial development of flow separation on the wing. While this region is probably a curve, for analysis purposes it is considered to be linear, the upper limit of this region is defined as α_3. The flow separation then develops more rapidly causing a marked decrease in the value of the suction ratio with angle of

attack, which again appears to be nearly linear. The upper limit of this region is defined as α_4. Next, there is a reduction in the rate of decrease of the suction ratio with angle of attack as the spread of flow separation slows. The upper limit of this region, which also apparently marks the beginning of a region in which the upper surface flow is fully separated, is defined as α_5.

As an initial step in the analysis the values of the angles of attack bounding each of the regions were determined from the test data obtained on all the planforms at unit Reynolds number of 26.25/million per meter. Typical results are presented in Figure 85 which shows the variations of α_1, α_2, α_3, α_4, and α_5 with fillet sweep angle for the Wing I planforms.

Further examination of the variations of suction ratio with angle of attack for the wings with NACA 0008 airfoils suggested that for prediction purposes the slopes of the variations in a given region could be considered to be the same at each of the Reynolds numbers for a particular planform. Thus it might be possible to establish a prediction method which could account for Reynolds number effects on the angle-of-attack boundaries.

It was first necessary to establish a correlation of the plateau values with planform geometry and Reynolds number. Further consideration of the plotted data led to the following approach:

(1) A correlation of suction ratio would be obtained for the basic wing planforms.

(2) The effect of fillet sweep would be accounted for by a correction term.

Two correlations of the basic wing data were achieved. The first correlation uses the effective leading-edge radius Reynolds number in which the velocity and radius are both taken normal to the swept leading edge. The results are compared in Figure 86 with the band of data presented by W. P. Henderson in NASA TN D-3584 (Ref. 15) for wings of 4 to 6 percent thickness ratio and boundary-layer transition fixed by the Braslow technique (Ref. 16). The SHIPS data agree quite well with the earlier data, but there is slightly more scatter. The reason for the

scatter is most likely the fact that the balance axial-force sensitivity is lower than those used for the data presented in TN D-3584, because the balance had to be capable of handling loads at high angles of attack, high values of dynamic pressure and across the speed range.

The second correlation used the WINSTAN correlation parameter (Ref 5).

$$\Omega \equiv R_{LER} \ COT\Lambda_{LE} \ \sqrt{1-M^2\cos^2\Lambda_{LE}}$$

where: R_{LER} is the leading-edge radius Reynolds number based on the streamwise velocity and radius measured at the mean geometric chord. The other two terms provide an empirical fit for sweep and Mach number effects. The original WINSTAN correlation also used another parameter $\dfrac{A\lambda}{\cos\Lambda_{LE}}$ to further account for planform effects.

The results of applying this approach to the SHIPS basic wing test data are presented in Figure 87 along with the original WINSTAN correlation curves for $\dfrac{A\lambda}{\cos\Lambda_{LE}}$ values of 0 and 1 which bound the SHIPS planform values. The SHIPS data which were obtained with fixed transition form a different correlation band than the original WINSTAN data which were obtained with free transition. In addition, the planform correlation does not appear to be appropriate for the SHIPS data.

Figure 88 presents a comparison of correlated values of suction ratio with test data assuming the long dash short dash line in Figure 87 represents a correlation curve for the effects of Reynolds number and leading-edge sweep, $"R"_{BW}$, for the basic wings.

Using the premise that the data correlation curve, $"R"_{BW}$, shown in Figure 87 should form the basis for evaluation of the effects of Reynolds number on the leading-edge suction ratio at low lift coefficients for the irregular planforms, it was possible to establish families of straight line "curves" (shown in Figure 89) with fillet sweep angle and unit Reynolds number as the parameters.

The families of curves presented in Figure 89 can be represented by another family of curves shown in Figure 90 which present the curve slopes $\dfrac{\Delta "R"}{\Lambda_F - \Lambda_W}$ as functions of outer panel leading-edge sweep angle, Λ_W, for parametric values of leading-edge radius Reynolds number based on streamwise velocity and radius measured at the mean geometric chord of the basic wing. Thus, the leading-edge suction ratio at low lift coefficients can be predicted using a relatively simple equation:

$$"R"_1 = "R"_{0<\alpha<\alpha_2} = "R"_{BW} + \left[\dfrac{\Delta "R"}{(\Lambda_F - \Lambda_W)}\right] (\Lambda_F - \Lambda_W)$$

where $"R"_{BW}$ is obtained from Figure 87 and the term in brackets is obtained from Figure 90. For simplicity the "plateau value" of "R" is assumed to apply from zero angle of attack to the boundary α_2.

With a satisfactory methodology in hand for predicting the suction ratio in the plateau region, attention was then turned to refining the evaluation of the angle-of-attack boundaries and slopes for the other regions. Despite several iterations between selections of the boundaries and slopes, no satisfactory correlation could be achieved when using the boundaries directly, except for α_2. The curves defining α_2 are presented in Figure 91. However, it was finally noted that incremental values of angle of attack between each boundary formed reasonable sets of curves for regions 2 and 3 as shown in Figure 92 and 93. The incremental values for region 4 were somewhat erratic but definable as shown in Figure 94.

It therefore appeared that a workable prediction method for the variation of suction ratio with angle-of-attack was achievable if a suitable correlation could be found for the effect of Reynolds number on the angle-of-attack boundaries. That aspect of the methodology was completed in the following way.

First, plots were made of the values of the α boundaries as functions of fillet sweep with parametric variations of unit

Reynolds number. Figure 95 is a typical example. After much thought, it was decided to attempt to correlate the boundaries for the basic wings as functions of Reynolds number and then apply a ratio term to the increment in α for the basic wings to account for the effect of fillet planforms.

A clue to a possible method of correlating the data for the basic wings was obtained from a paper by Chappell of the Royal Aero Society's Engineering Services Data Unit (Ref. 17). He had correlated the angle of attack for initial separation, α_s, of swept, tapered wings by plotting $\alpha_s \cos\Lambda_{LE}$ against the leading-edge radius Reynolds number evaluated normal to the wing at the tip. Figure 96 shows α_2 for each of the basic wings correlated using Chappell's approach and comparisons of his results for airfoil thickness ratios of .08 and .10. The results were encouraging.

Then a form of the Ω function was tried in which the streamwise leading-edge radius Reynolds number at the tip was substituted for the value based on the mean geometric chord. The results are presented in Figure 97. This approach was tried with all the α boundaries. There was enough consistency to the resulting plots to attempt to pursue this approach.

Since a correction term was sought rather than the absolute values, the individual values for each basic wing sweep were shifted along the ordinate axis to form a reasonably smooth envelope curve encompassing the data obtained at the maximum unit Reynolds number of 26.25 million per meter (8.0 million per foot). Figures 98 through 101 show the results for each angle-of-attack boundary. The correction terms $\Delta(\delta\alpha_{(\ )}\cos\Lambda_W)$ due to Reynolds number effects are obtained from Figures 98 through 101 by first calculating values of Ω_T at a reference Reynolds number and the Reynolds number appropriate to the conditions to be evaluated, then subtracting the value of $(\delta\alpha_{(\ )}\cos\Lambda_W)$ ref from the value $(\delta\alpha_{(\ )}\cos\Lambda_W)$ as illustrated in Figure 98.

The reference value of Reynolds number is evaluated assuming a unit Reynolds number of 26.25 million per meter (8.0 million per foot) and a tip leading-edge radius corresponding to a wing span of 0.33307 meters (1.09279 feet). If the reference value of Ω_T is less than the value of Ω_T for the condition to be evaluated, then $\Delta(\delta\alpha_{(\ )}\cos\Lambda_W)$ will have a positive value.

The next step was to obtain the effect of the irregular planforms by forming ratios of the increments in angle of attack due to Reynolds number at the various values of fillet sweep to the increments measured for each basic wing planform. The results are shown in Figure 102. These ratios are applied to the increments produced by the previous step to obtain the final result for the effect of Reynolds number on the angle-of-attack boundaries for each region.

Aerodynamic-Center Location

The initial step in the pitching-moment analysis was to survey the C_M - C_L curves for each configuration for the data obtained from test 12-086 at unit Reynolds number of 26.247 million per meter (8.0 million per foot). In this initial survey, 3 distinct quasilinear regions were observed for many of the wings: A small region near zero lift, a "primary-slope" region generally falling between lift coefficients of 0.1 and 0.5, and a region at high lift coefficients.

The aerodynamic-center locations (referenced to the mean geometric chord of each planform) for each region are presented in Figures 103 through 107. The angle of attack and lift coefficient envelopes for the primary slope region are shown in Figures 108 and 109. In general, the variations of a.c. location with fillet sweep in the low-lift and "primary-slope" regions are smooth curves, whereas the variations for the high-lift region are irregular for fillet sweeps in the neighborhood of 60 to 70 degrees. The envelope curves for the upper and lower limits of the "primary-slope" region also shows distinct irregularities in the region of fillet sweep from 60 to 70 degrees. It is apparent that when a significant amount of vortex flow is present on the fillet there is a definite reduction in the shift of a.c. location between the primary-slope region and the high angle-of-attack region. In a few cases, the shift in a.c. location is actually destabilizing at higher lift coefficients.

Emphasis was then placed on attempting to correlate the a.c. location in the "primary-slope" region. One approach was to modify the Panisczcyn method of predicting the a.c. location (developed in the WINSTAN investigation, Ref. 5) by applying a multiplying factor k to the lift prediction for the inboard panel. A parametric evaluation was conducted for a range of k values from 0 to 2. The results are presented in Figures 110 through 114. The comparisons with test data indicated that weighting

factors (k) in the range from .9 to 1.1 would give good correlation.

In seeking an alternative to the Panisczcyn method which might be more simple to apply, the a.c. locations in the "primary-slope" region were analyzed and plotted in several different formats as presented in Figures 115 through 121. None of these formats provided a significant collapse of the data, but in each case the data form families of curves for parametric values of either fillet sweep or outboard panel sweep. Eventually, Figures 120 and 121 were curve fitted to produce simple and useful prediction techniques.

The effects of Reynolds number on the a.c. location in the low and high-lift-coefficient regions and the "primary-slope" regions are shown in Figures 122 through 126. The effects were small in both the low-lift and "primary-slope" regions for all configurations, but are quite pronounced for some of the configurations at high lift coefficients. In general, an increase in unit Reynolds number produces an aft shift in a.c. location. Figure 125 for example shows that for Wing IV with 65 degree fillet an increase in unit Reynolds number from 19.67 million per meter (6.0 million per foot) to 26.25 million per million(8.0 million per foot) changes a pitch-up trend to a pitch-down trend.

As a consequence, efforts to analyze pitch-up/pitch-down characteristics were initially concentrated on the data obtained at 26.25 million per meter unit Reynolds number.

High Angle-of-Attack Pitching-Moment Characteristics

As an aid to describing the pitching-moment characterisitcs, the C_M - C_L curves were reduced in size and assembled on one page for all 35 planforms (Figure 127). At low angles of attack, the change in the static stability derivative dC_m/dC_L is in the negative direction with increasing values of either fillet sweep or outboard panel sweep. At high angles of attack, the changes in dC_m/dC_L are in the opposite direction. All of the planforms with

fillet sweep of 60 degrees or less and outboard panel sweep of 53 degrees or less exhibit a definite pitch-down tendency at high angles of attack. As the fillet sweep or the outboard panel sweep is increased, the trend at high angle of attack is toward less stability until eventually a definite pitch-up tendency occurs. The moment reference point is $0.25\bar{c}_{WF}$ in Figure 127.

The pitch-up/pitch-down tendencies are summarized in Figure 128 which is a matrix chart having the same arrangement as Figure 127 in terms of the placement of the data for each combination of fillet sweep and outboard panel sweep. Superimposed on the chart are arbitrary boundaries which separate the regions of definite pitch-down and definite pitch-up from the other configurations. In the region between these boundaries, the data does not define whether pitch-up or pitch-down exists.

Some attempts were made to quantify and correlate the shift in a.c. location from the "primary slope" C_L region to higher lift coefficients and the angle of attack and lift coefficient for the break point (upper limit of the primary slope region) of the pitching moment curves. A typical example is shown in Figure 129 in which $\Delta a.c._{BREAK}$, α_{BREAK}, and $C_{L_{BREAK}}$ are plotted against the variable $\beta\tan(\Lambda_F - \Lambda_W)$. This approach produced groupings of the α_{BREAK} and $C_{L_{BREAK}}$ data which showed some promise, so effort was concentrated on the $C_{L_{BREAK}}$ analysis and several correlation parameters were tried and the most promising results (shown in Figure 130) used the parameters $C_{L_{BREAK}}/A_{TRUE}$ and $\tan(\Lambda_F - \Lambda_W)$. Figure 131 presents the same correlation approach after the $C_{L_{BREAK}}$ points had been reviewed and considerable smoothing was applied to the raw results. The smoothed data show two distinctly different trends. Planforms having either Wing I or Wing II outer panels show a decreasing value of $C_{L_{BREAK}}/A_{TRUE}$ as $\tan(\Lambda_F - \Lambda_W)$ increases, whereas planforms having Wing IV and Wing V outer panels show an increasing value of $C_{L_{BREAK}}/A_{TRUE}$.

Planforms having Wing III outer panels apparently are on the borderline between the two trends.

Although this correlation was informative, it did not appear to be easily translated into a prediction method. Shortly thereafter it was noted that the angle-of-attack boundaries obtained in the suction-ratio analysis corresponded closely the break points occurring the plots of pitching-moment variation with angle of attack for many of the planforms. Figures 132 and 133 show typical examples of fitting the experimental pitching moment curves with linear segments between the angle-of-attack boundaries established from the suction-ratio analysis.

This approach was adopted and it was found that two additional angle-of-attack boundaries were needed for the pitching-moment analysis: α_1 which corresponded to the lower limit of the plateau region of the suction-ratio analysis and α_6 which occurred at high angle of attack for a few configurations. Thus, it appeared possible to produce prediction methods for lift, drag, and pitching-moment variations with angle of attack which would produce consistent results.

The analysis of pitching-moment variations with angle of attack also brought to mind an alternate approach to developing a design guide for the high angle-of-attack pitching behavior. The author remembered a comment in a British paper on the use of irregular planforms to minimize the aerodynamic-center travel which occurs between subsonic and supersonic flight. The comment warned that along with the favorable reduction in a.c. travel

came a tendency toward pitch-up at high angles of attack at low speed.

This author interpreted that comment to mean that a correlation between a.c. location at low lift coefficients and high angle-of-attack pitchup might exist. Such a correlation was attempted, and the results presented in Figure 134 show that it is possible to define a boundary between pitch-up and pitch-down behavior as a function of outboard panel sweep and aerodynamic-center location in terms of percent mean geometric chord of the irregular planforms.

One of the goals of the overall SHIPS program is to provide a guide for using irregular planforms yielding desired improved C_L, reduced transonic a.c. shift, while avoiding pitch-up. Figures 128 and 134 provide one element of the overall design guide appropriate to the landing condition. Note that the design guides do not rule out any configuration, they merely point out that certain configurations must be evaluated in more detail than others.
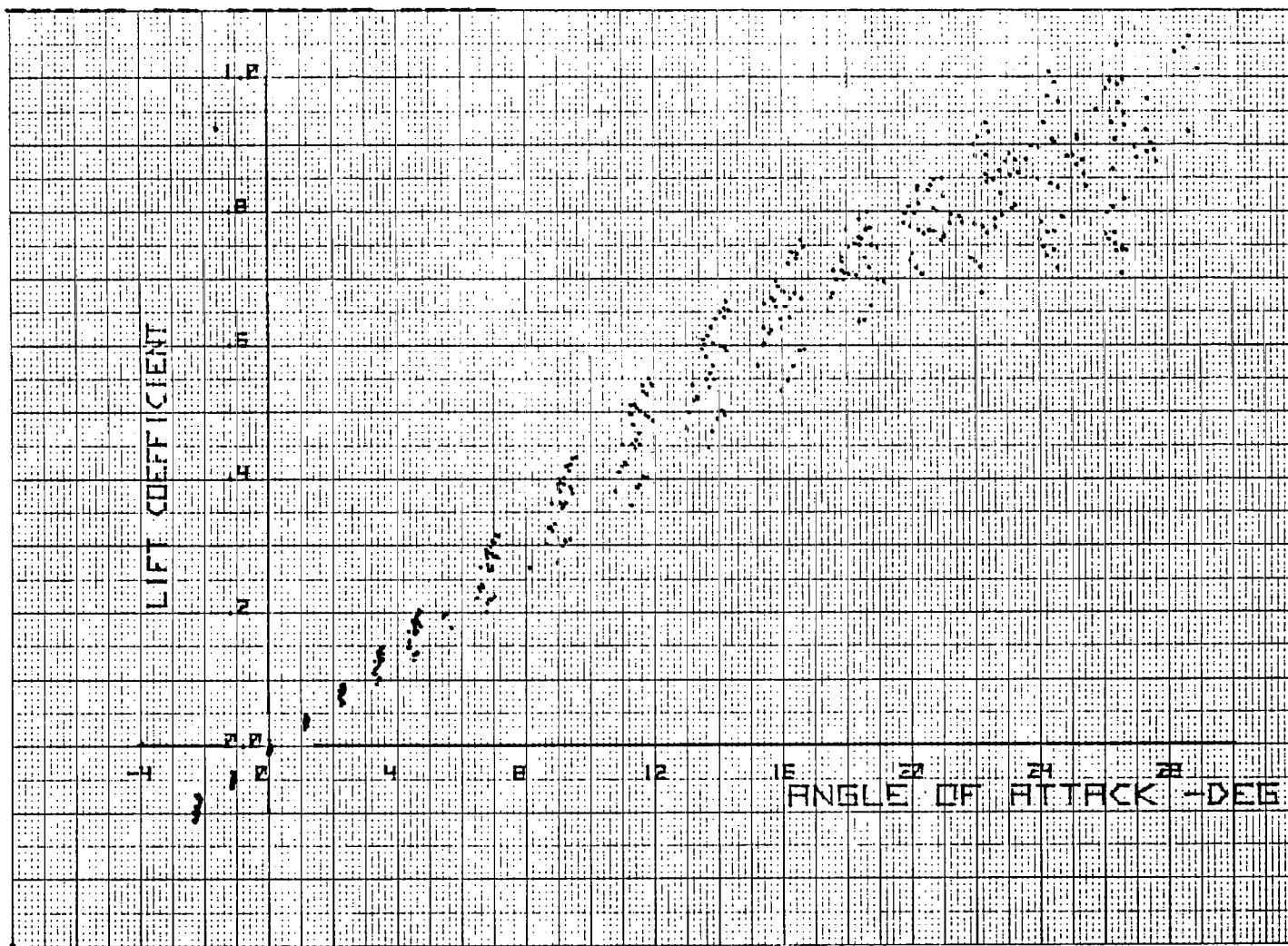
Figure 47.   Scatter Plot Showing Spread of Lift Data for all
35 SHIPS Planforms
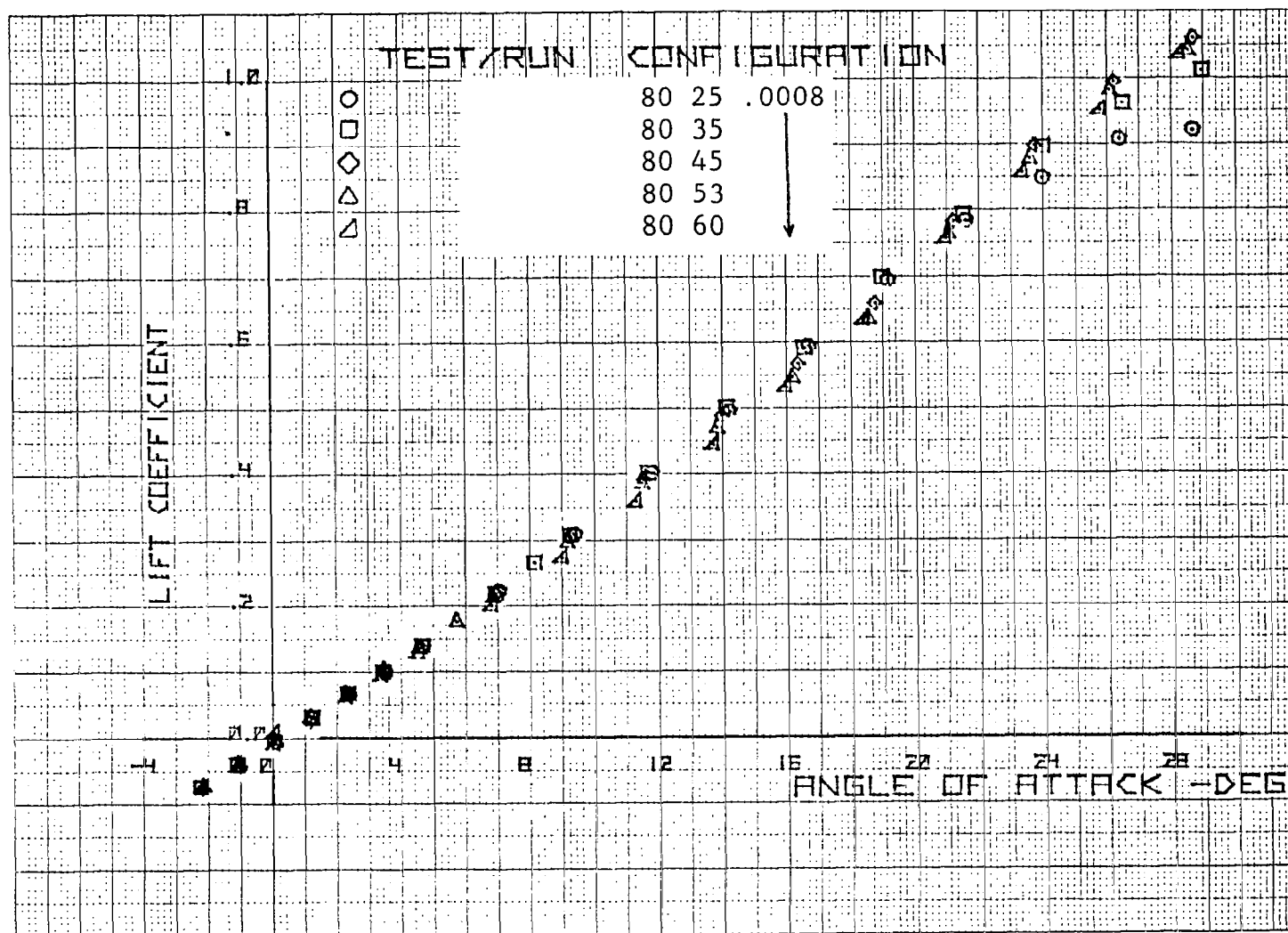
Figure 48. Plot Showing Spread of Lift Data for Constant Fillet
Sweep

TEST/RUN CONFIGURATION

80 25 .0008
80 35
80 45
80 53
80 60
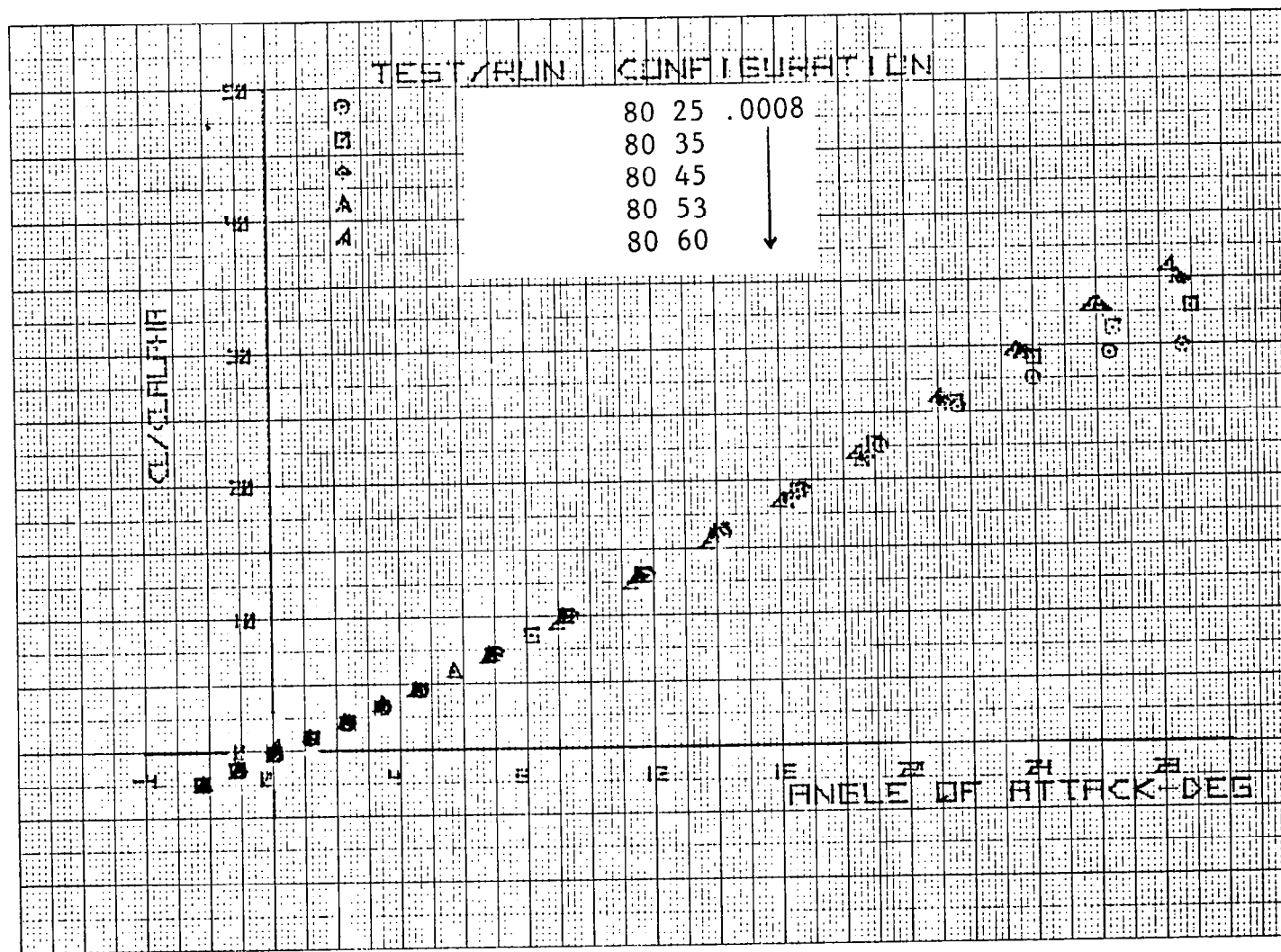
Figure 49.   Example of Lift Data Collapse Using C_L/C_{L_α} Parameter
for 80° Fillet Sweep

Figure 50.   Example of Lift Data Collapse Using $C_L/C_{L\alpha}$ Parameter
for Basic SHIPS Planforms
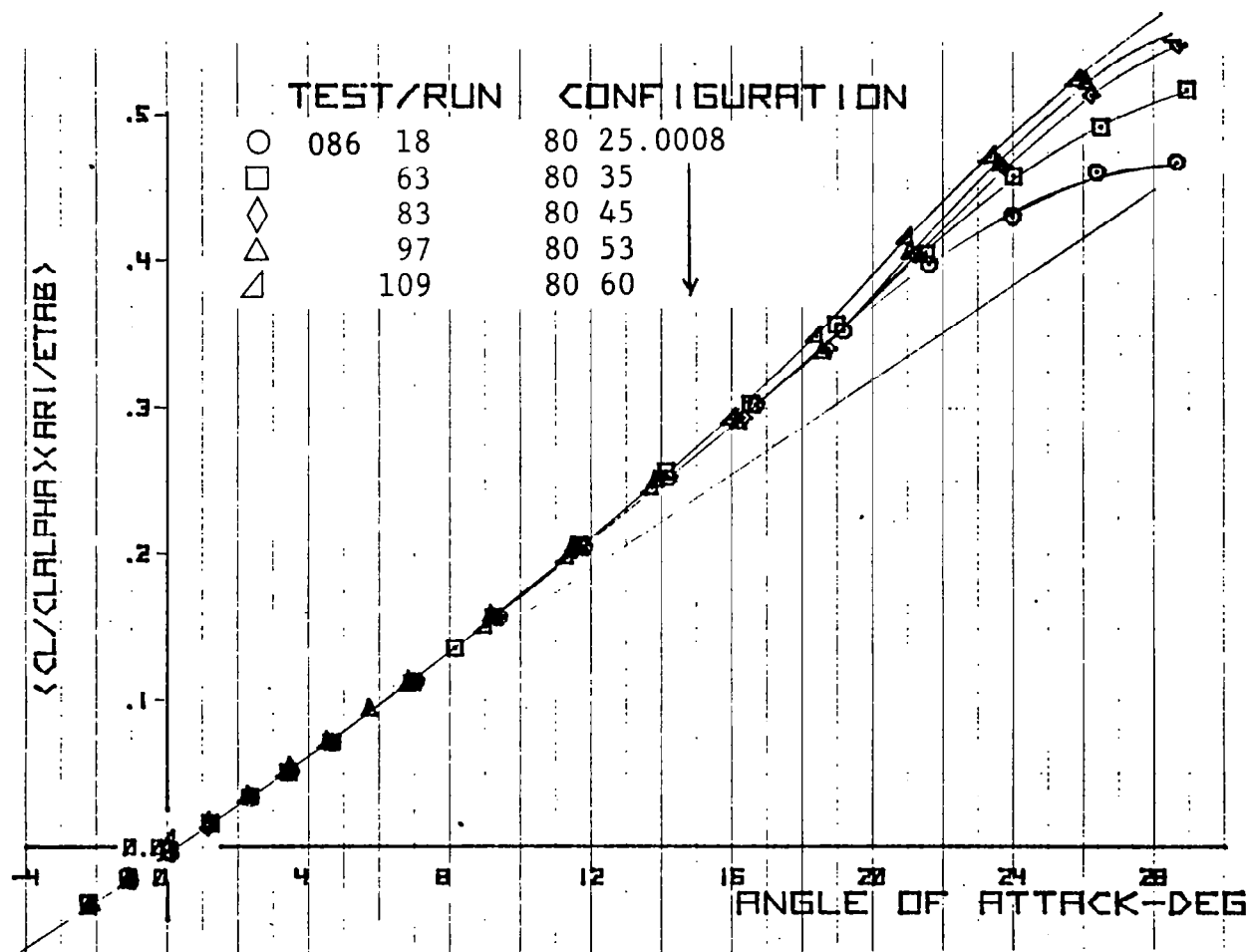
Figure 51. Correlation of SHIPS Test Data Using WINSTAN Correlation Parameter for Nonlinear Lift of Double-Delta Wings - Wings with 80° Fillet Sweep
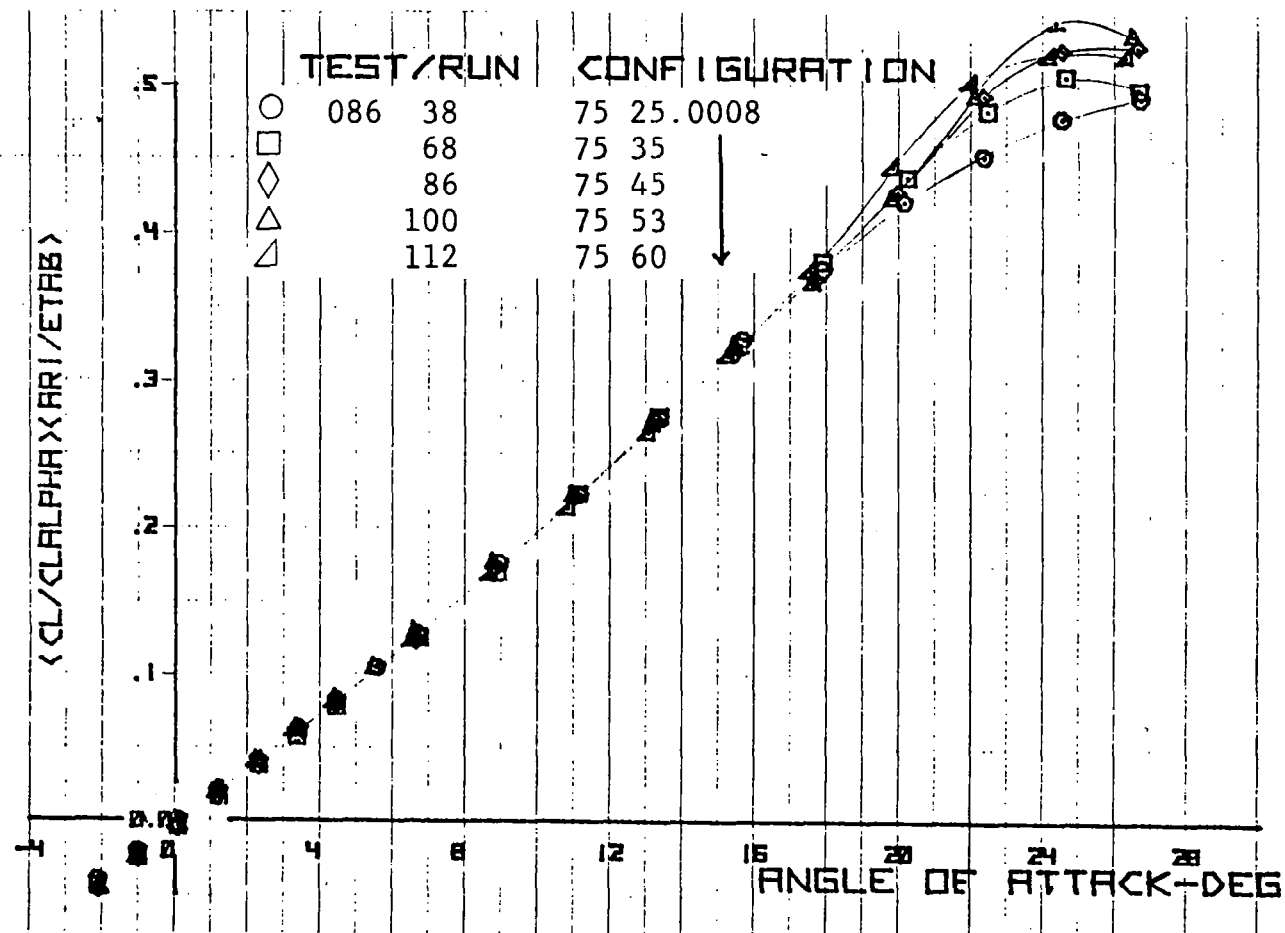
Figure 52.   Correlation of SHIPS Test Data Using WINSTAN Corre-
lation Parameter for Nonlinear Lift of Double-Delta
Wings - Wings With 75°-Sweep Fillets
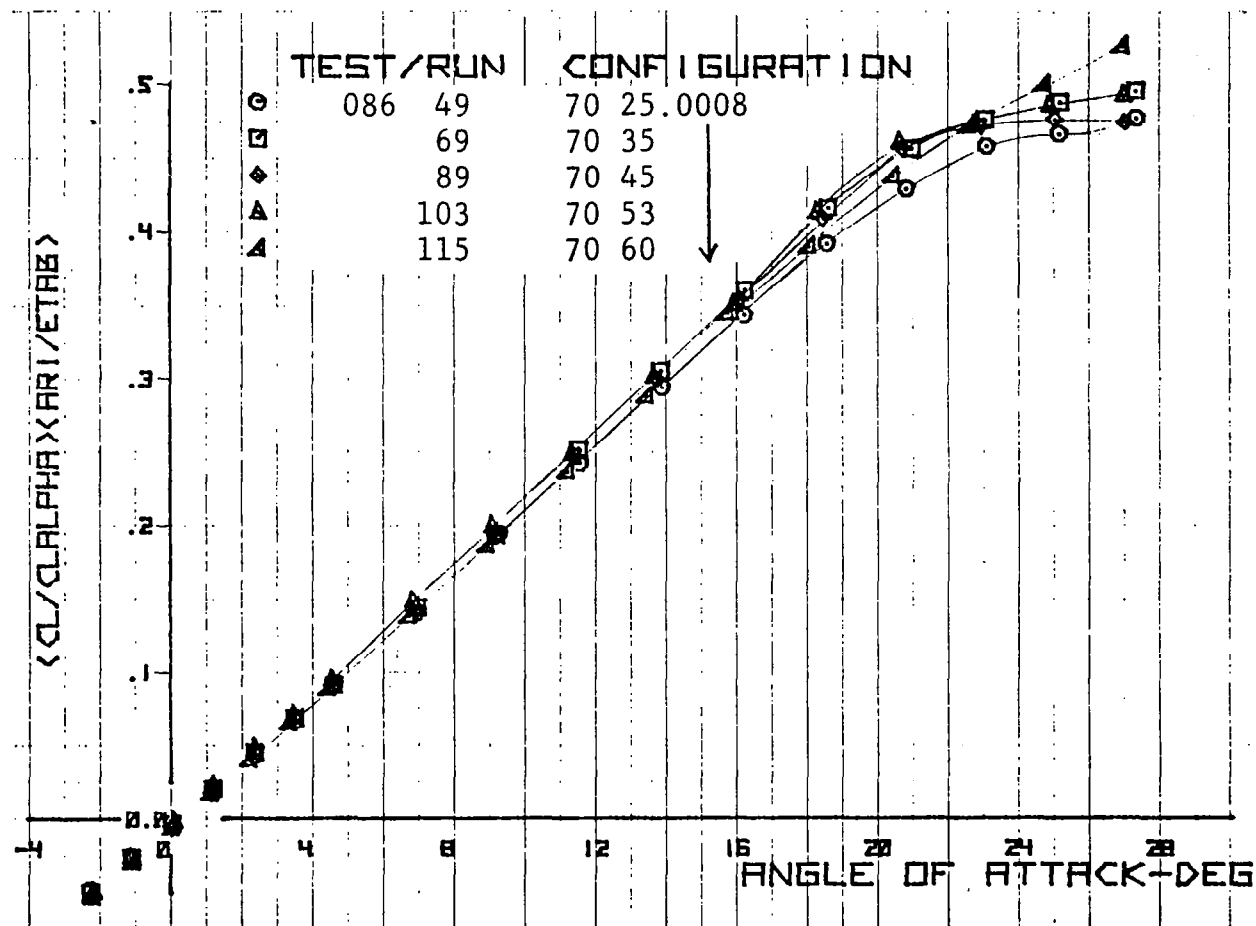
Figure 53. Correlation of SHIPS Test Data Using WINSTAN Correlation Parameter for Nonlinear Lift of Double-Delta Wings - Wings With 70°-Sweep Fillets
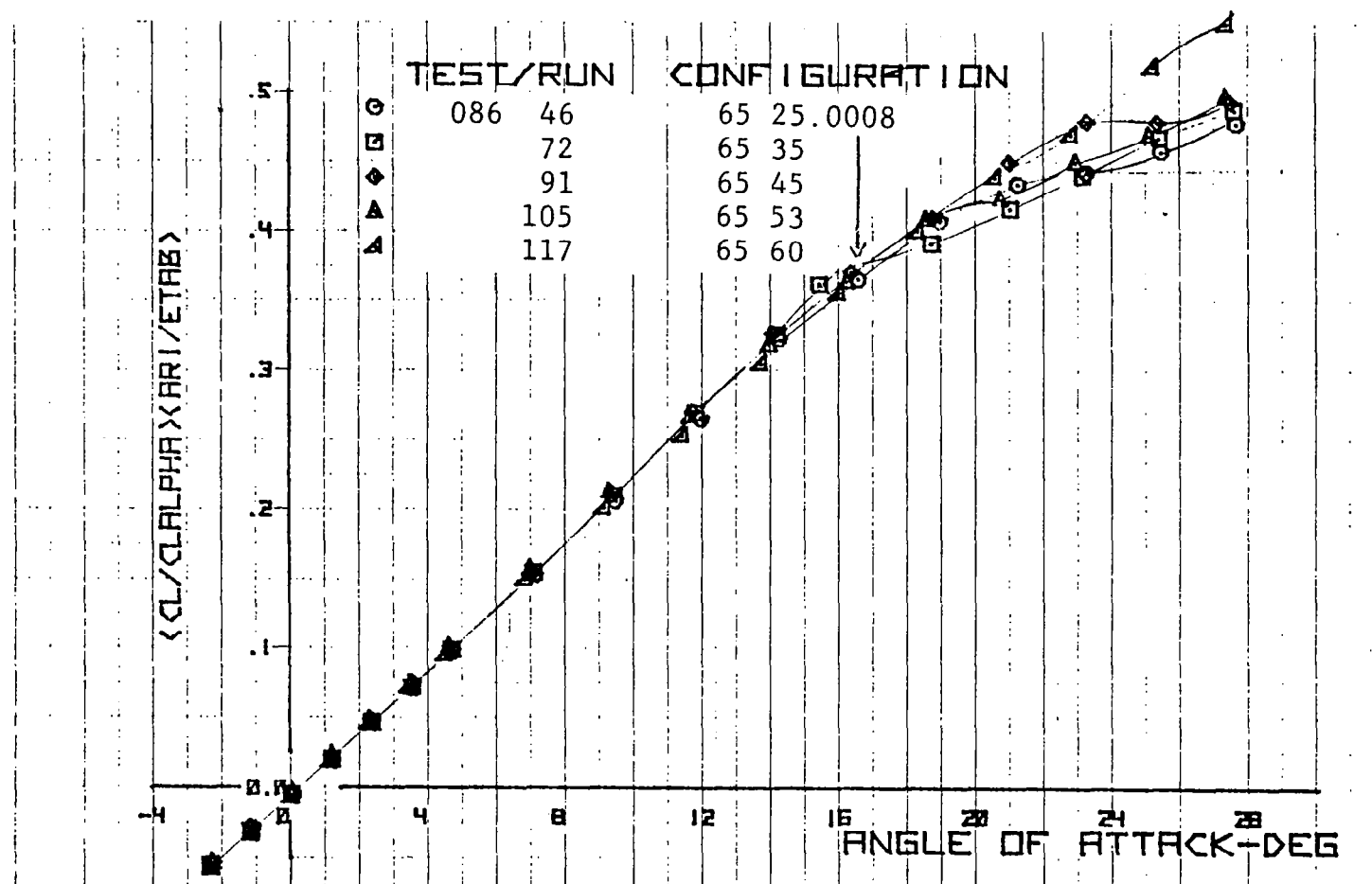
Figure 54. Correlation of SHIPS Test Data Using WINSTAN Corre-
lation Parameter for Nonlinear Lift of Double-Delta
Wings - Wings With 65°- Sweep Fillets
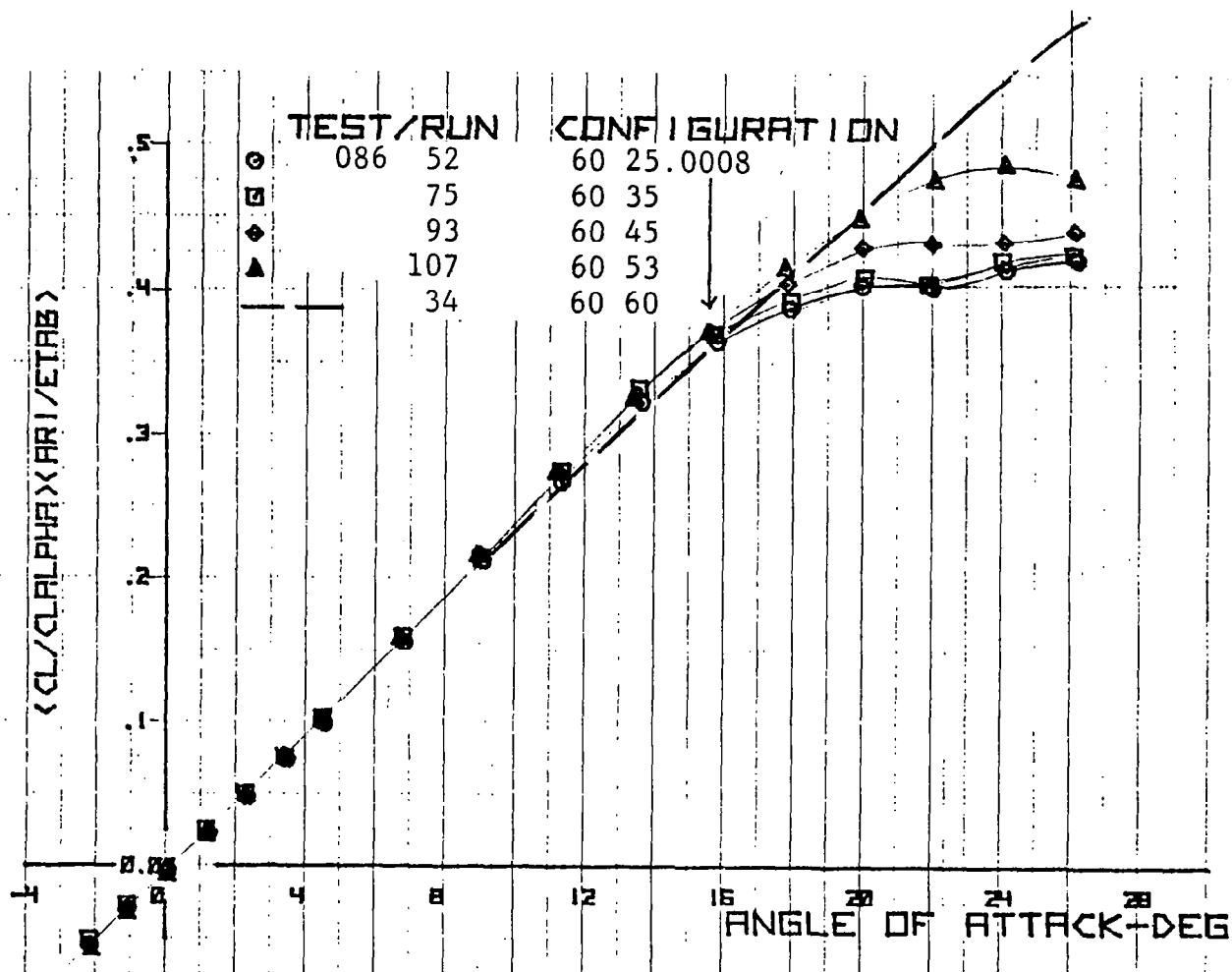
Figure 55.   Correlation of SHIPS Test Data Using WINSTAN Correlation Parameter for Nonlinear Lift of Double-Delta Wings - Wings With 60°- Sweep Fillets
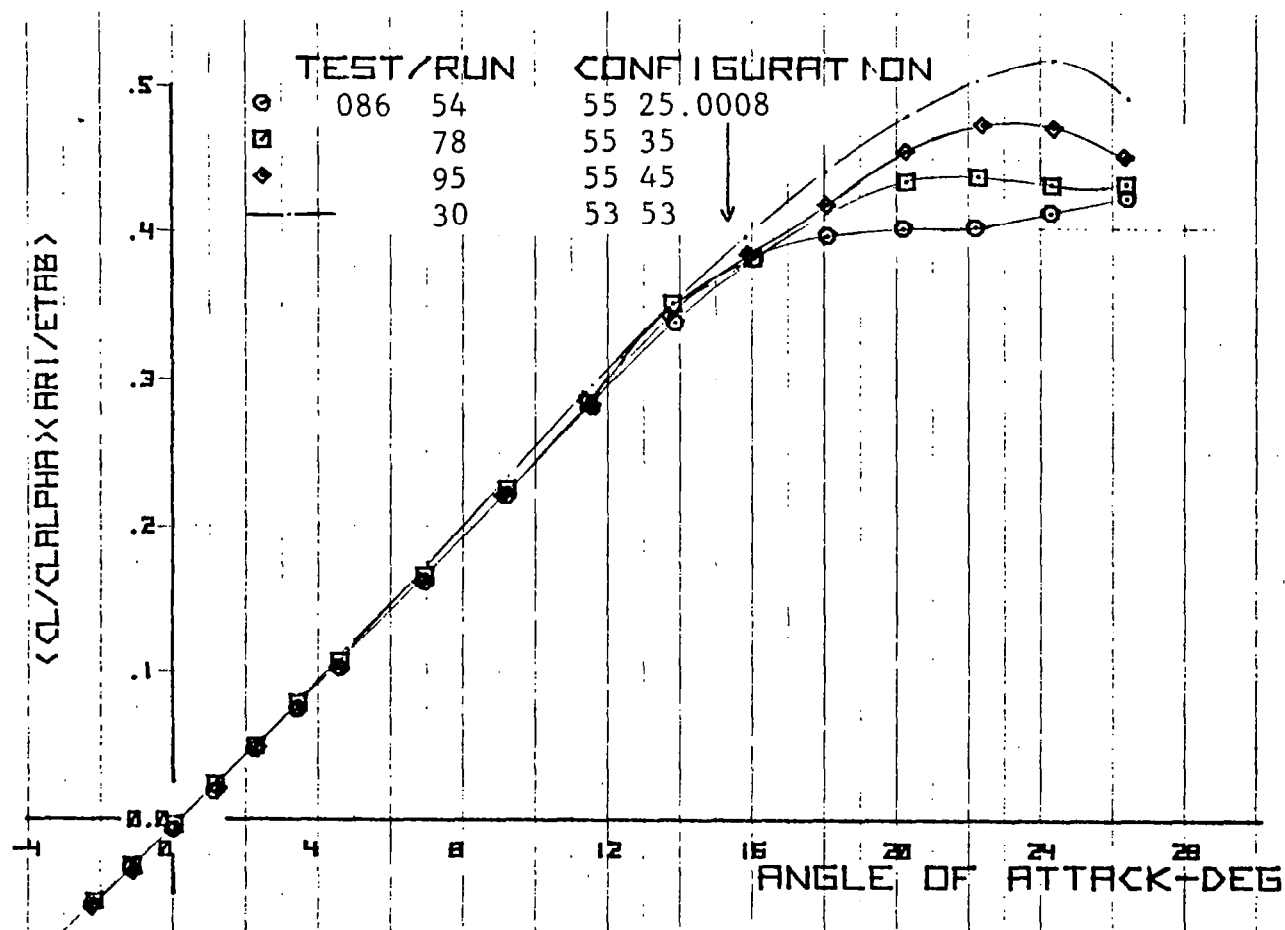
Figure 56. Correlation of SHIPS Test Data Using WINSTAN Corre-
lation Parameter for Nonlinear Lift of Double-Delta
Wings - Wings with 55°-Sweep Fillets and Basic Wing IV
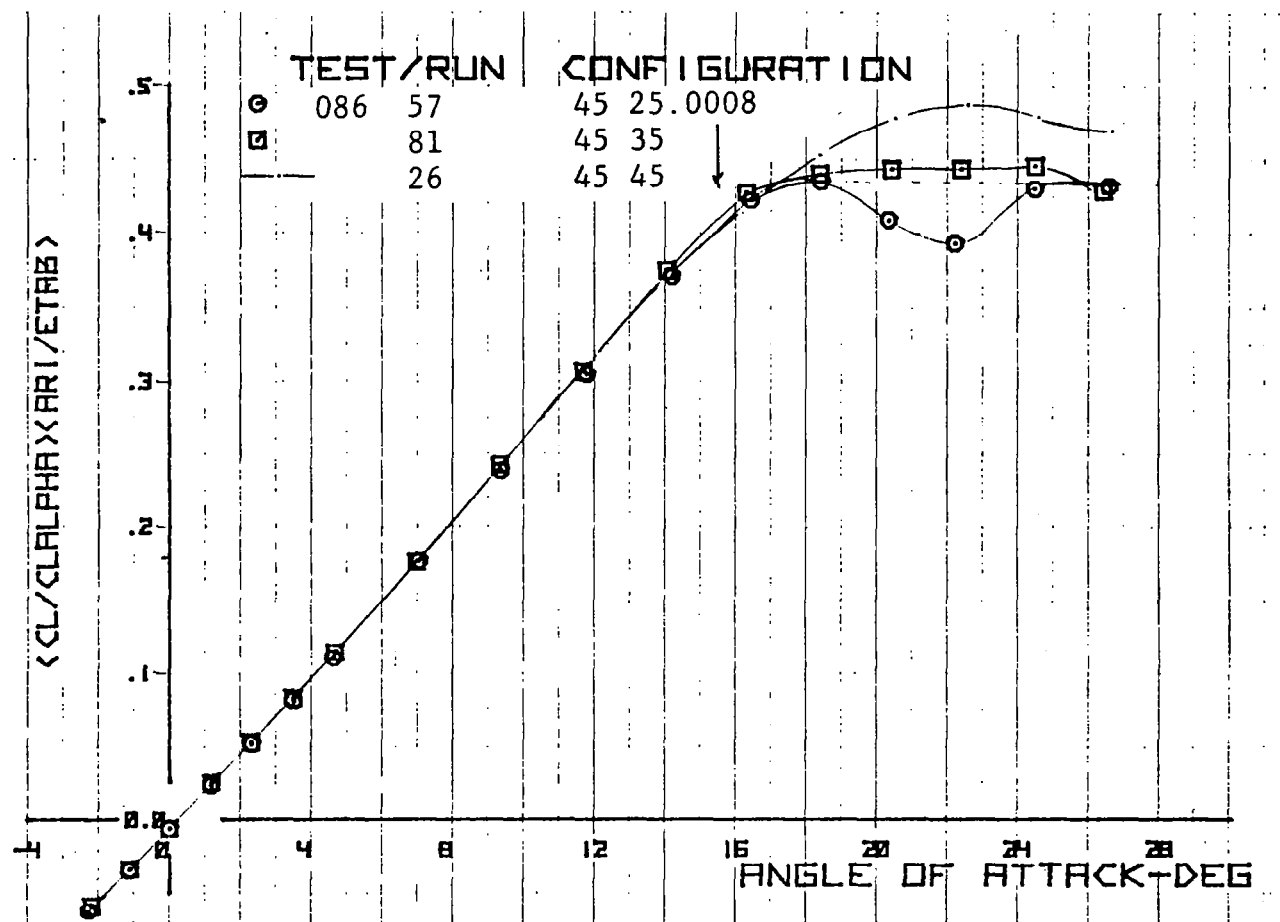
Figure 57. Correlation of SHIPS Test Data Using WINSTAN Correlation Parameter for Nonlinear Lift of Double-Delta Wings - Wings With 45°- Sweep Fillets
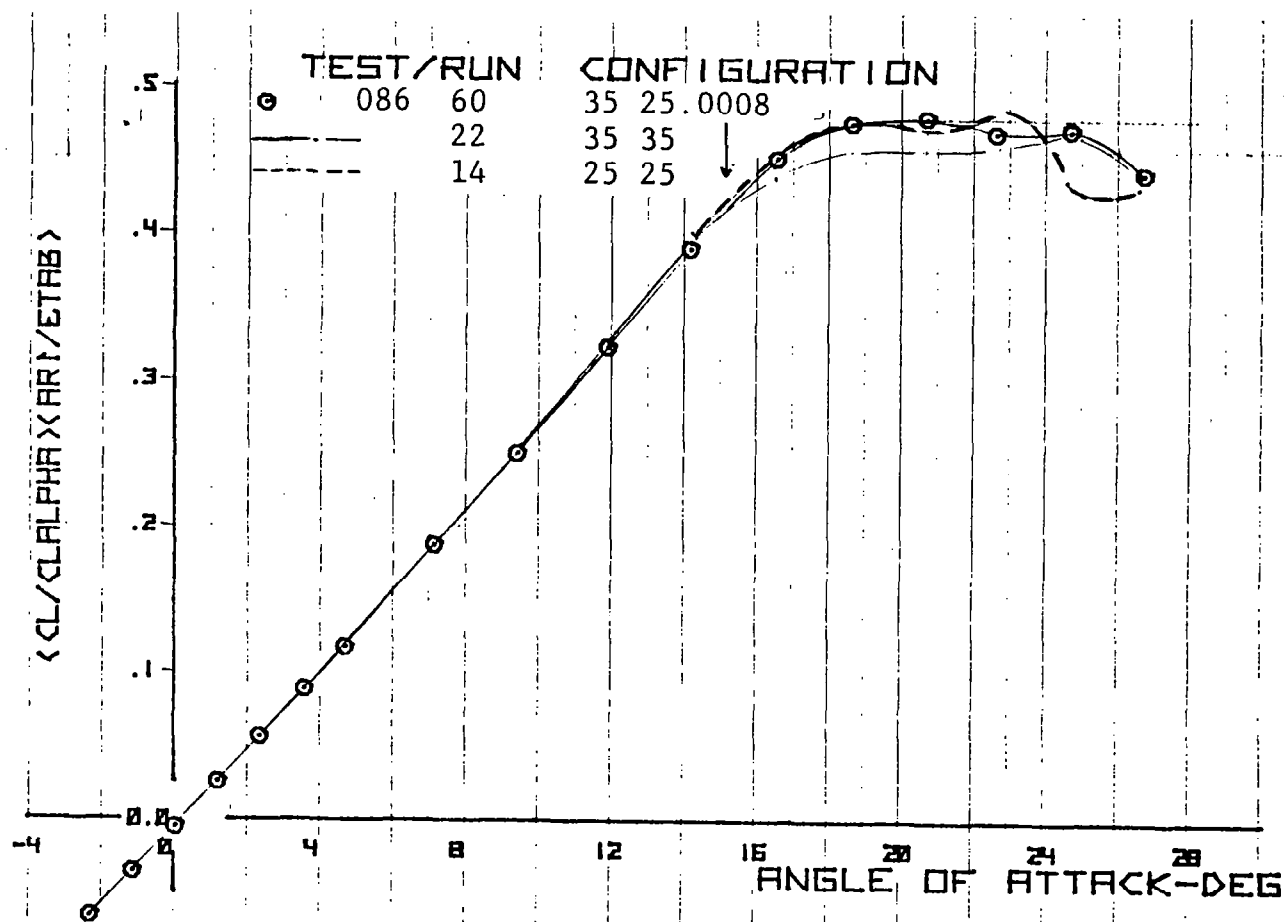
Figure 58. Correlation of SHIPS Test Data Using WINSTAN Correlation Parameter for Nonlinear Lift of Double-Delta Wings - Wings With 35° Sweep Fillets and Basic Wing I
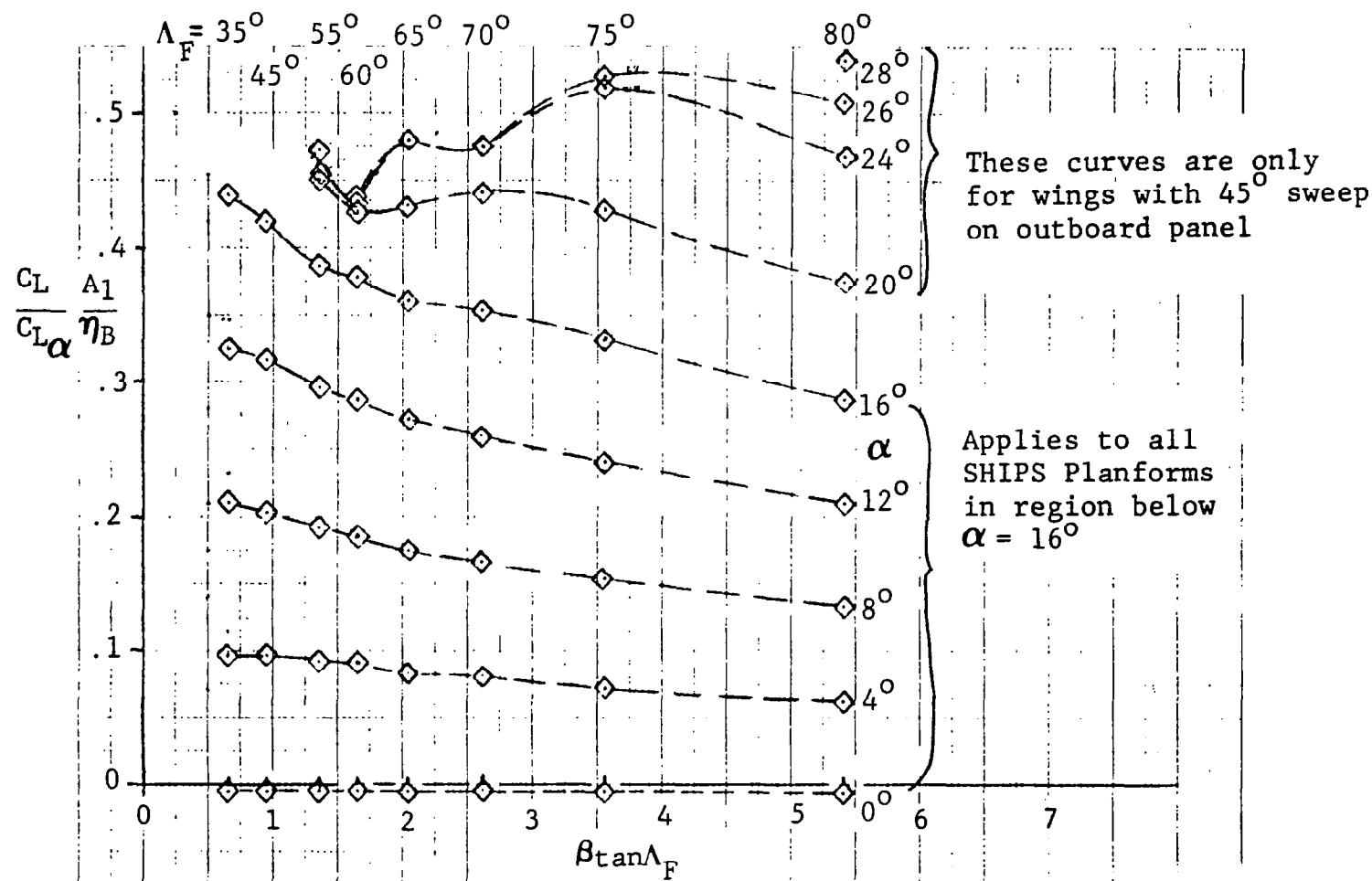
Figure 59.   SHIPS Lift Data Correlation Using WINSTAN Method
for Double-Delta Wings (Preliminary)
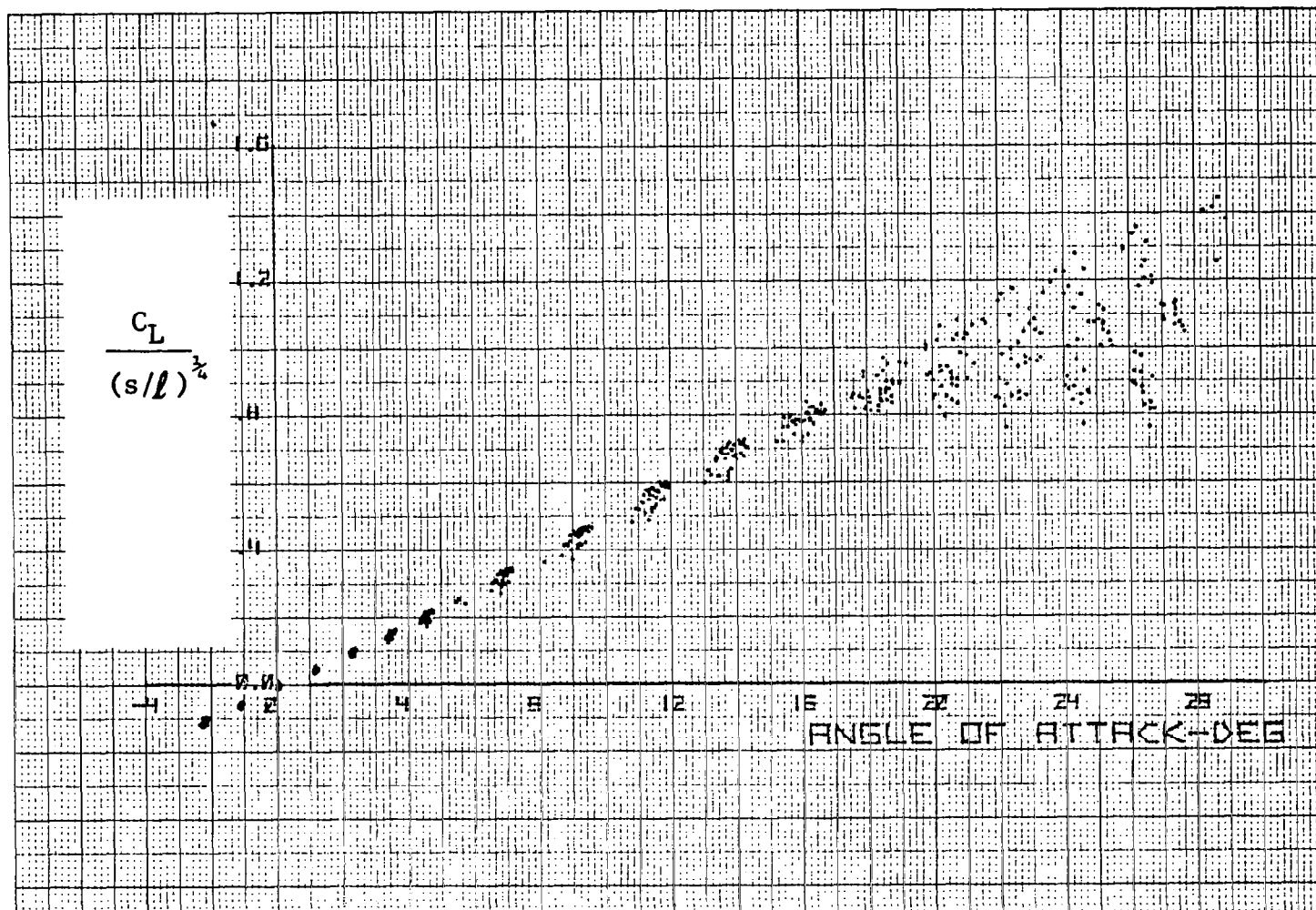
Figure 60.   Scatter Plot for Modified Peckham Lift Correlation
Parameter for All 35 SHIPS Planforms
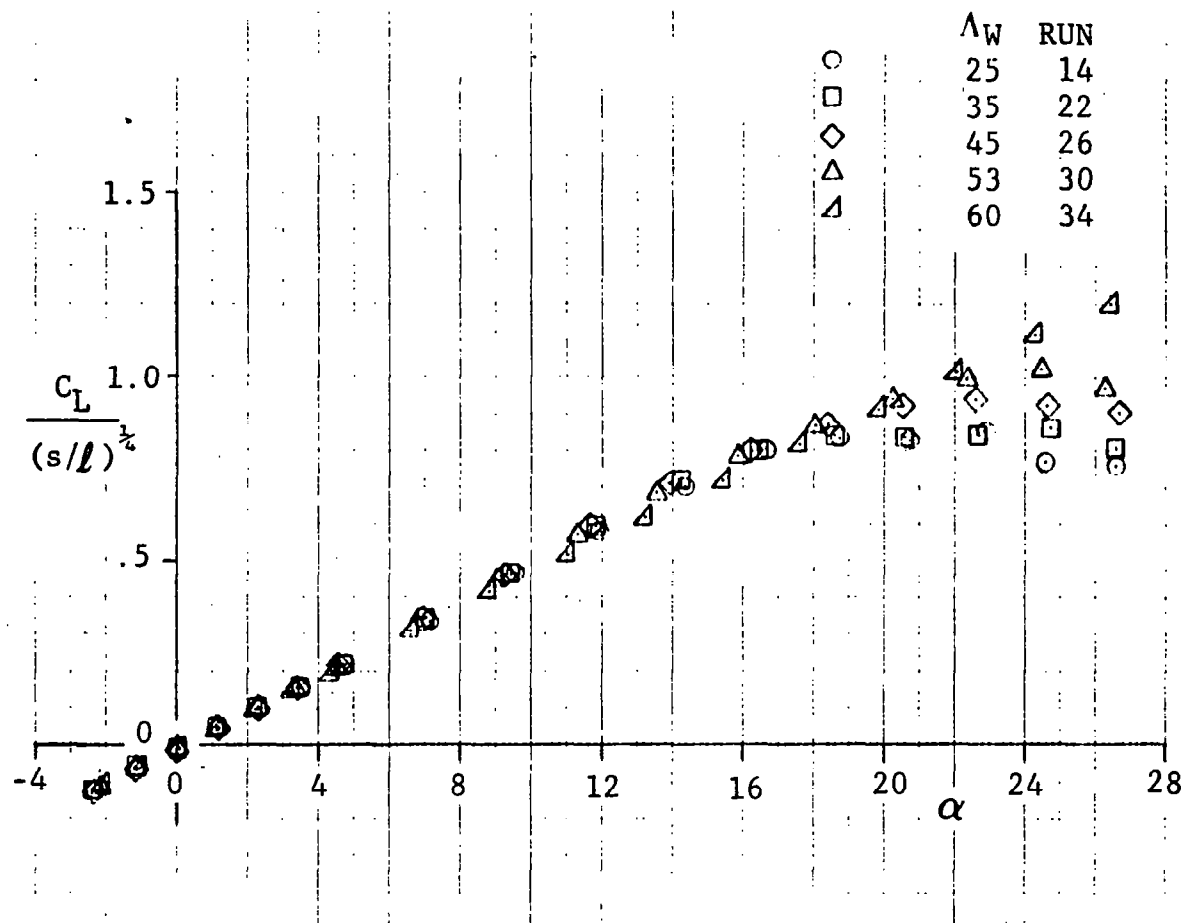
Figure 61. Modified Peckham Correlation of Lift Data - Basic Wings
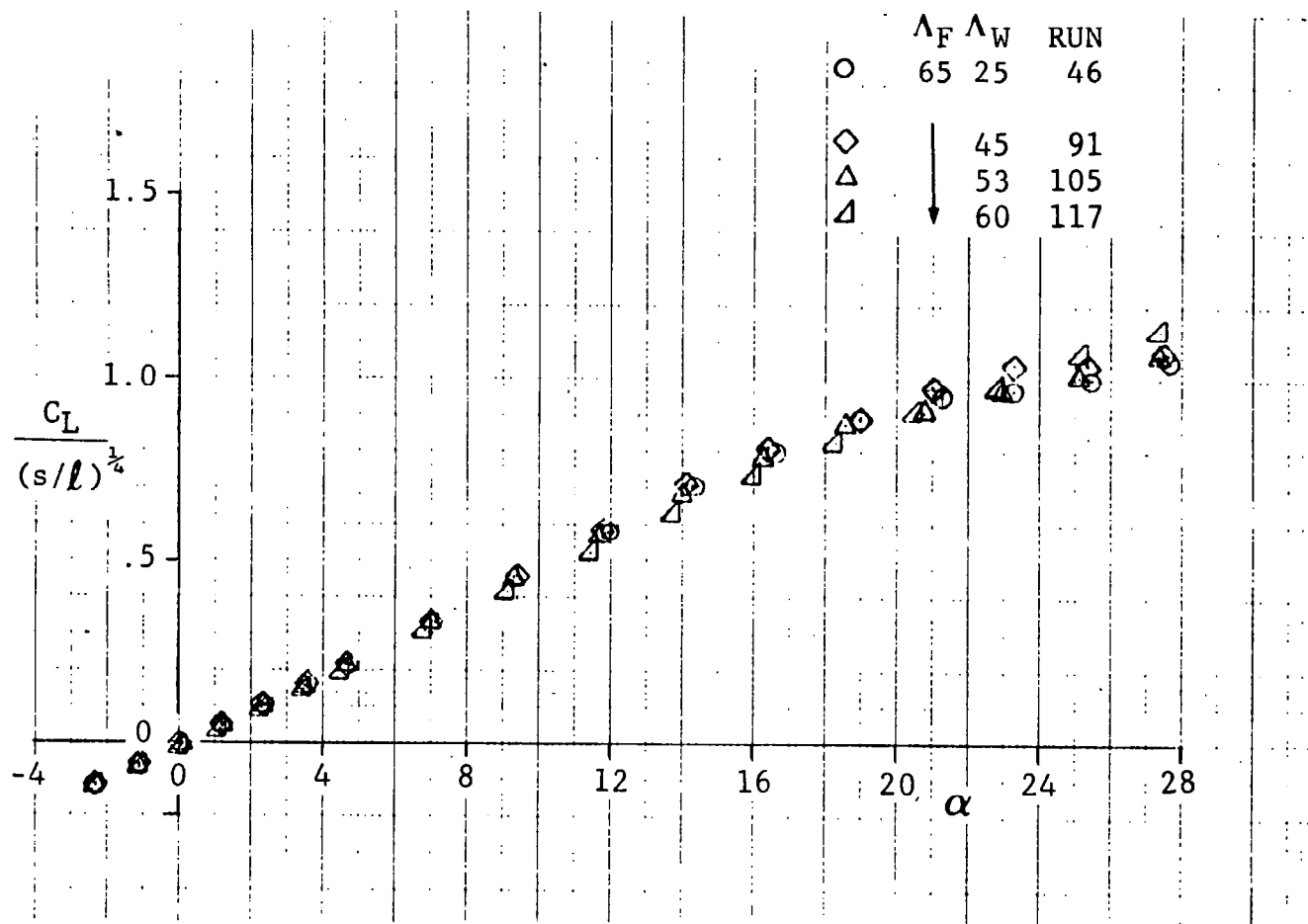
Figure 62. Modified Peckham Correlation of Lift Data - $\Lambda_F = 65^\circ$
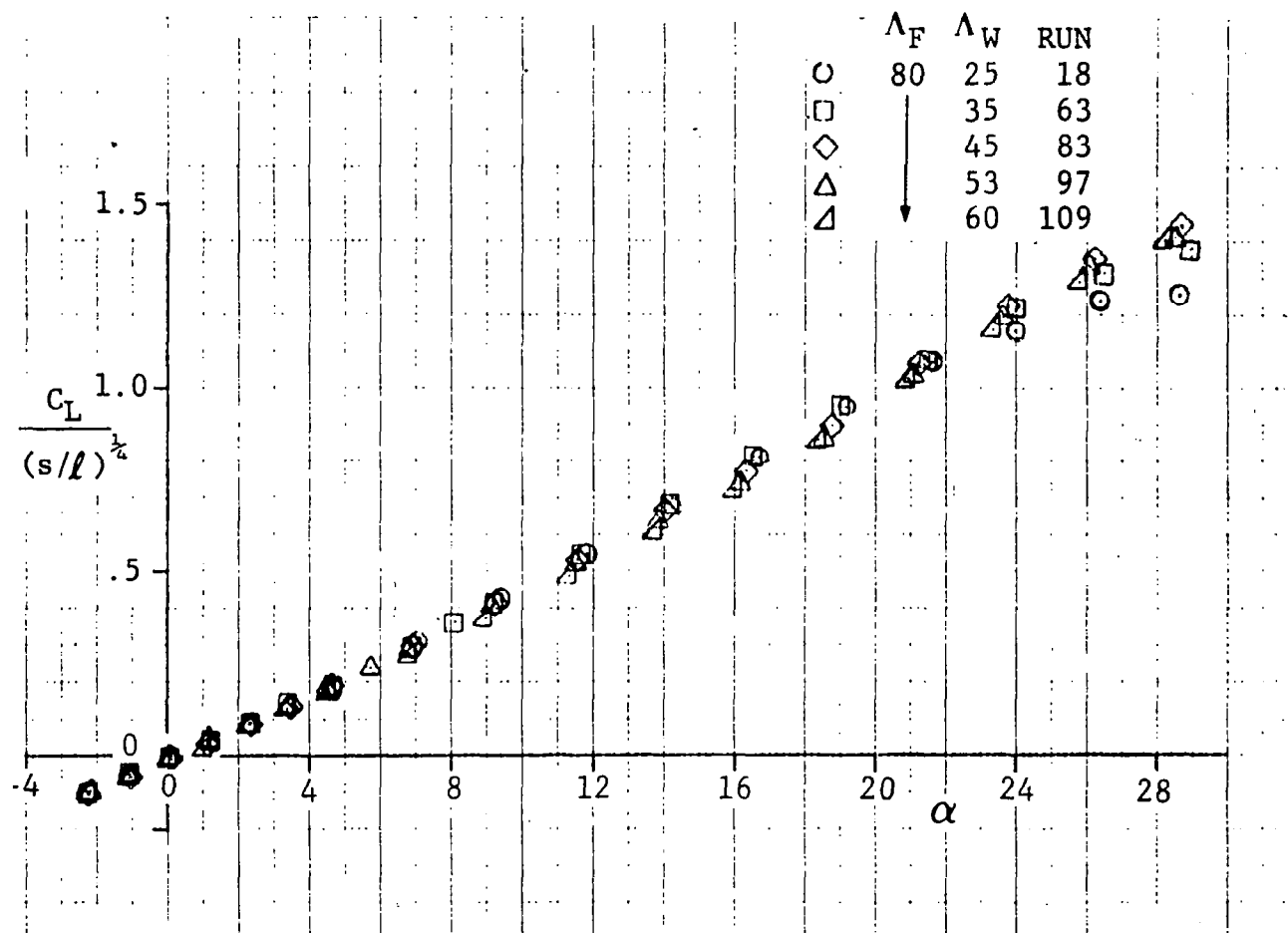
Figure 63.   Modified Peckham Correlation of Lift Data – $\Lambda_F = 80^o$

TEST/RUN   CONFIGURATION

	TEST/RUN	CONFIGURATION
⊙	25	25.0008
⊡	35	35
◇	45	45
▲	53	53
⊿	60	60

(CL/X S/L)EXP0.25 X 1/CLALPHA)

50

40

30

20

10

-4   4   8   12   16   20   24   28

ANGLE OF ATTACK-DEG
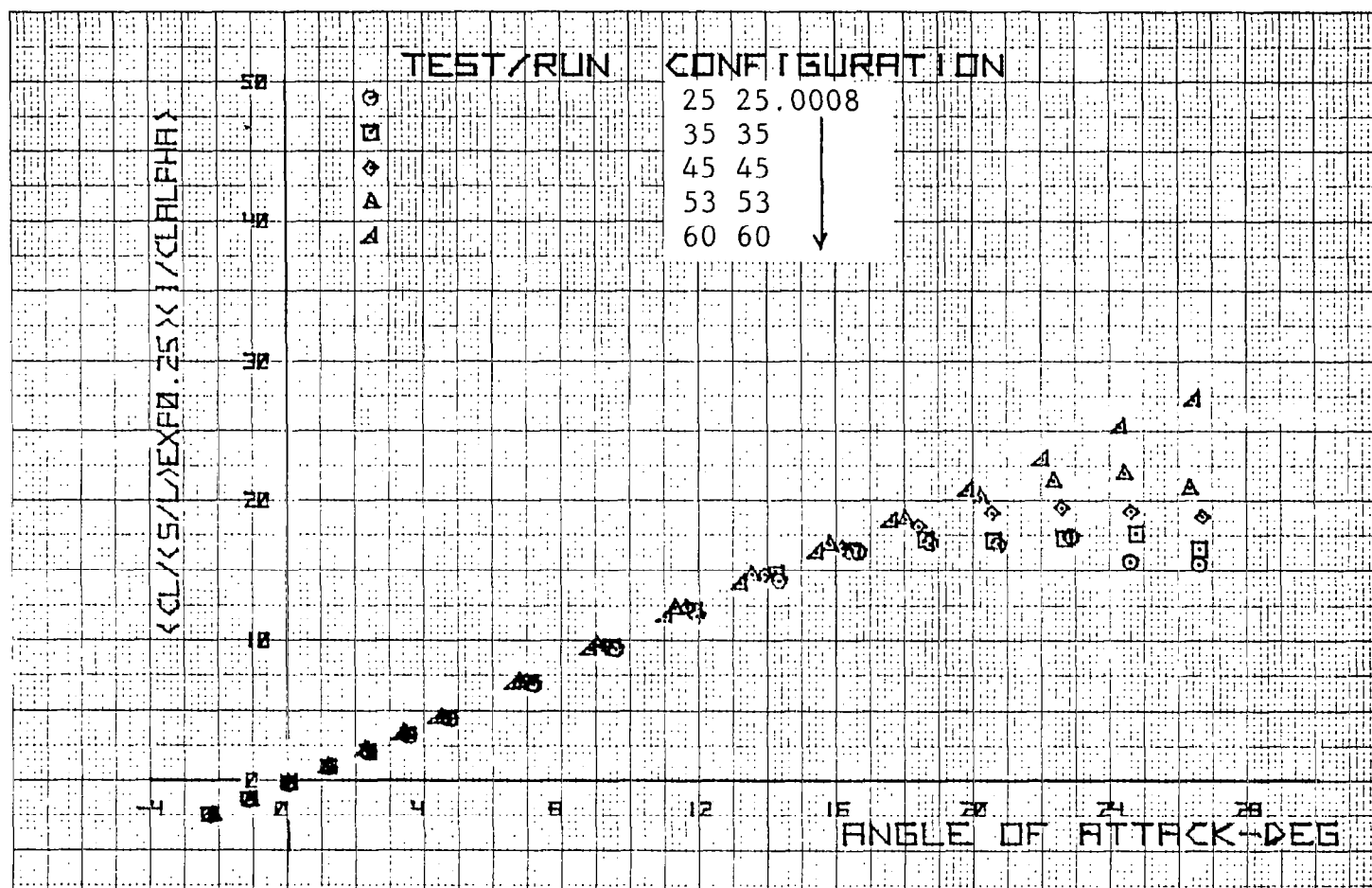
Figure 64.   Data Collapse With Further Modification of Peckham
Lift Correlation Parameter - Basic Wings
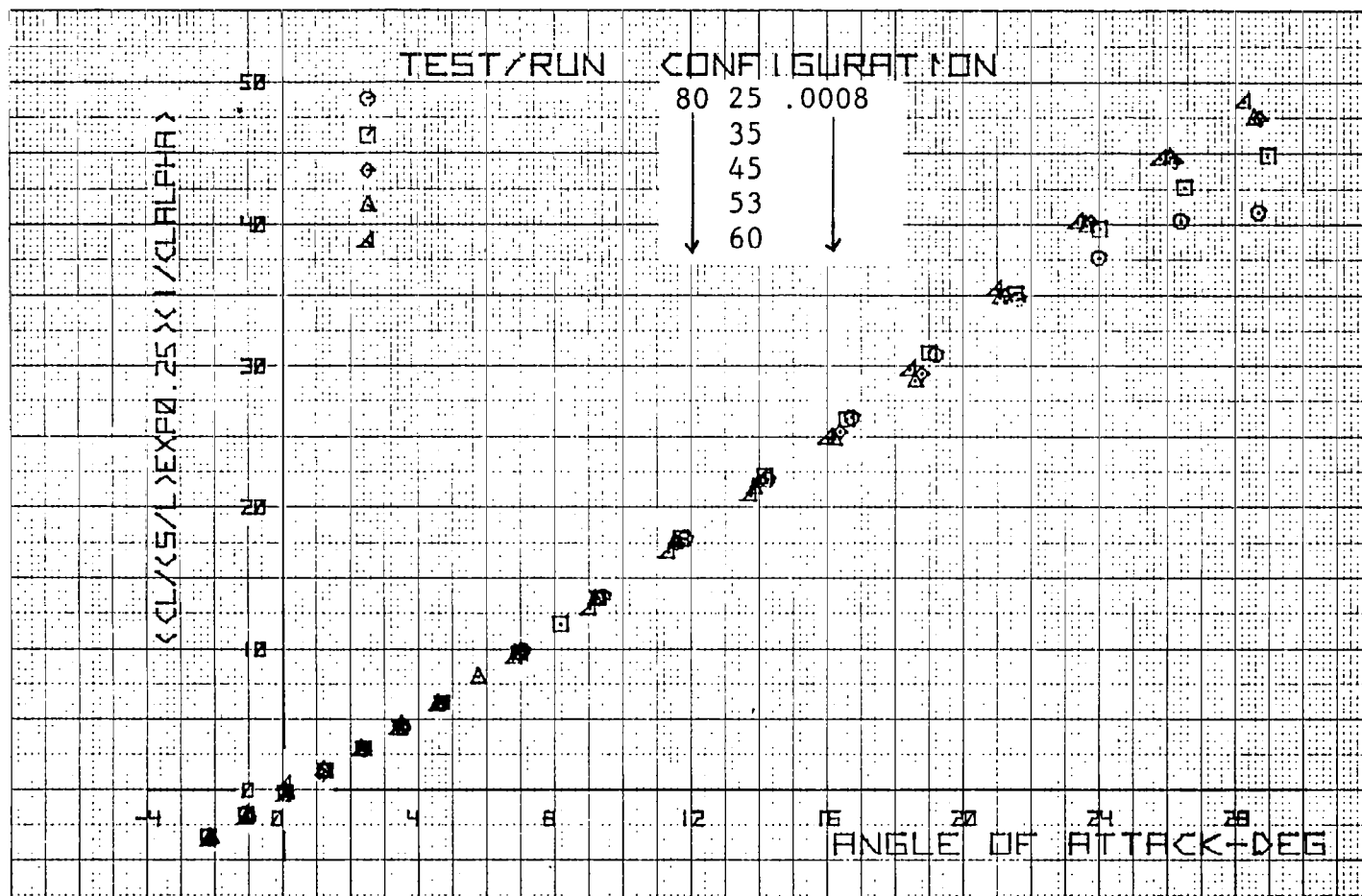
Figure 65.   Data Collapse With Further Modification of Peckham
             Lift Correlation Parameter - Λ_F = 80°
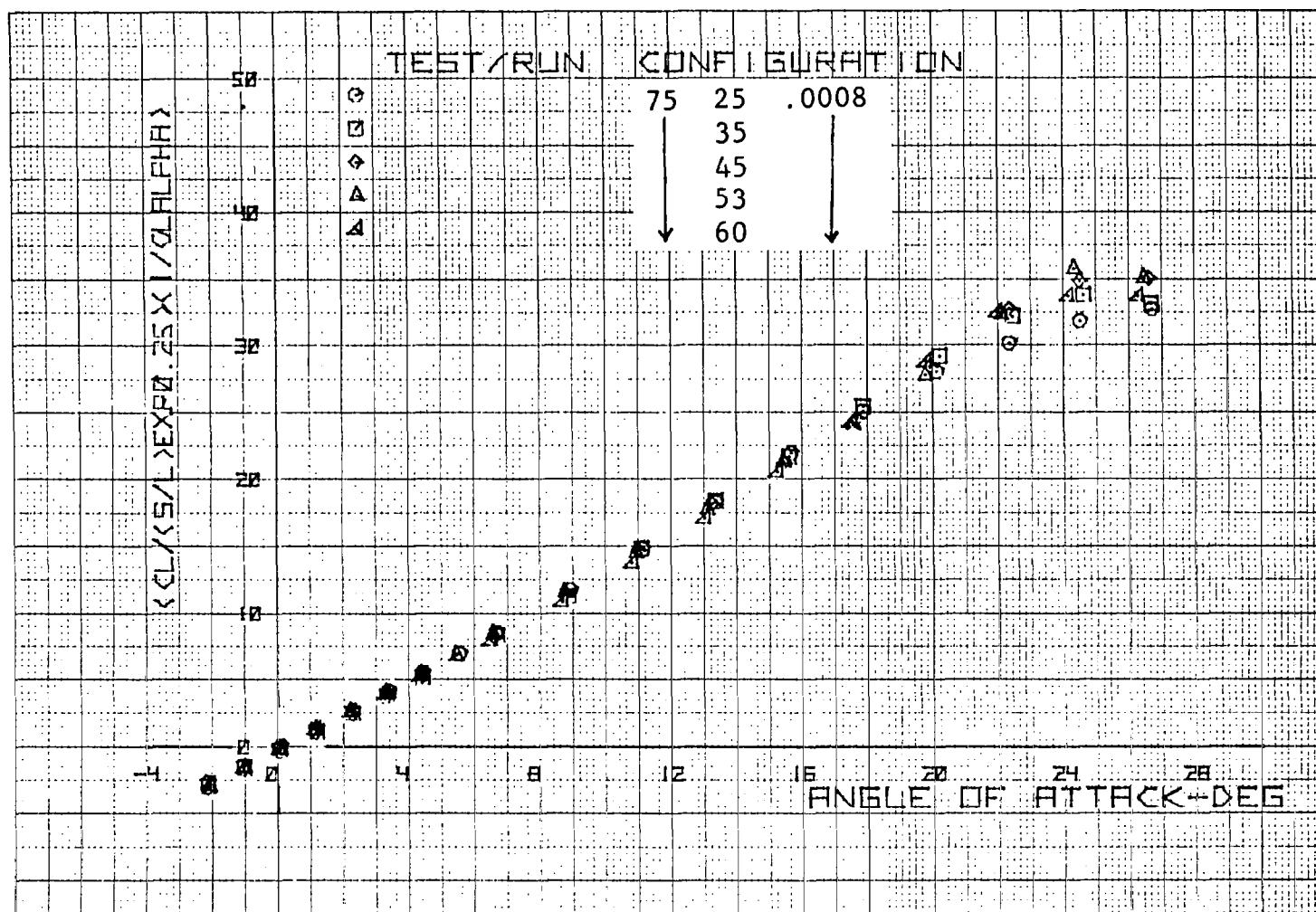
Figure 66.   Data Collapse With Further Modification of Peckham
Lift Correlation Parameter - $\Lambda_F = 75^o$
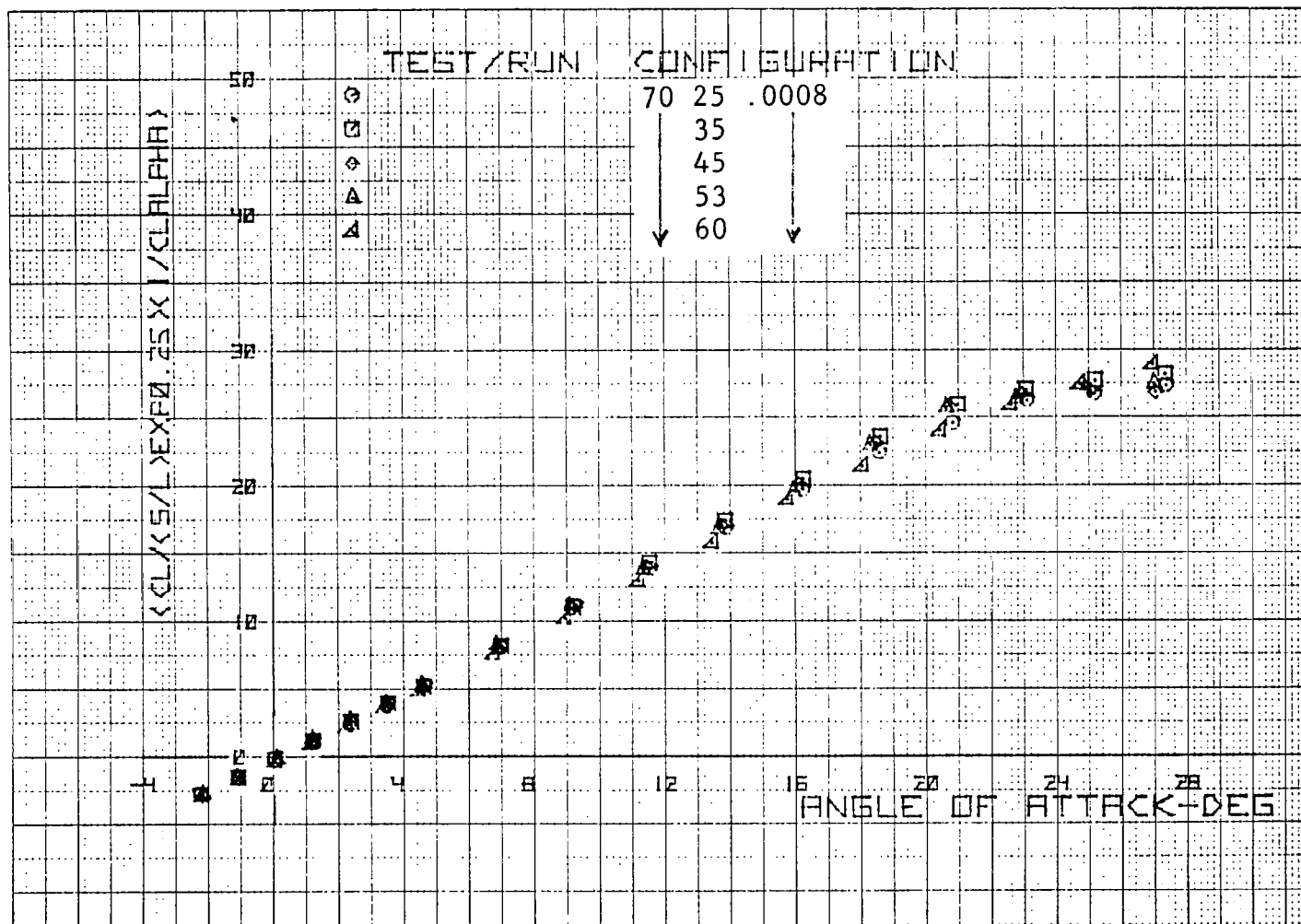
Figure 67. Data Collapse With Further Modification of Peckham
Lift Correlation Parameter - $\Lambda_F = 70°$
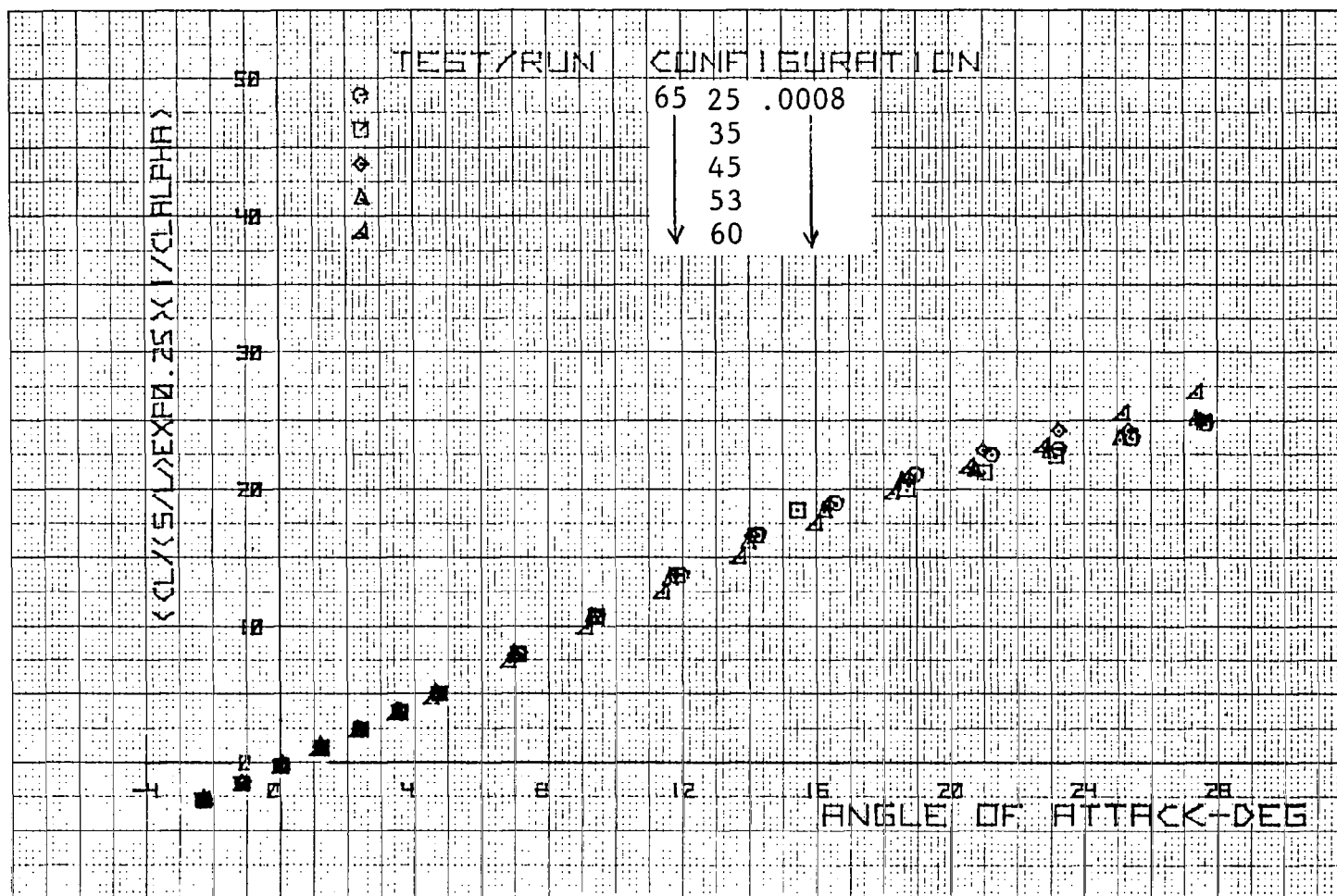
Figure 68.   Data Collapse With Further Modification of Peckham
Lift Correlation Parameter - $\Lambda_F = 65^o$
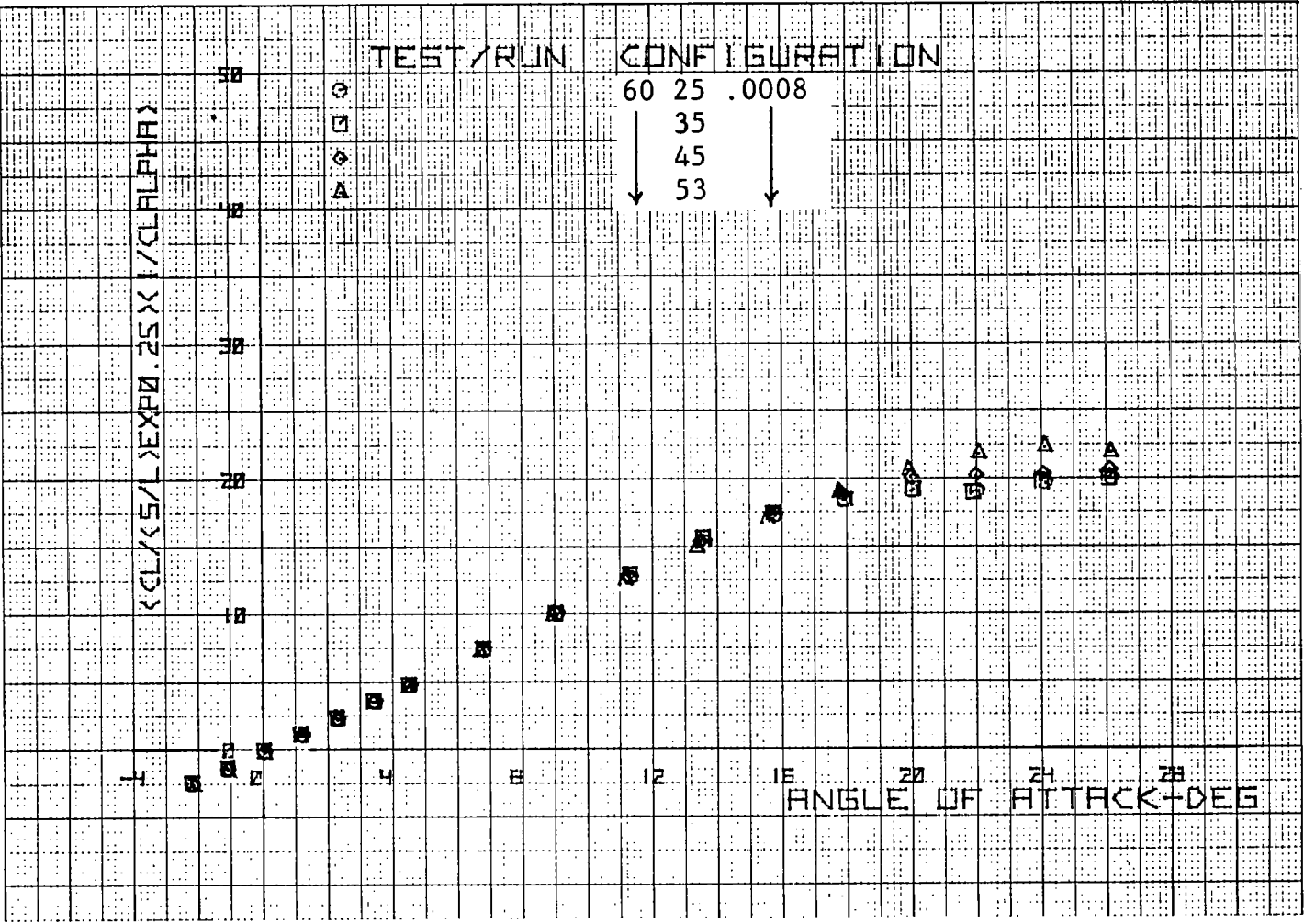
Figure 69.   Data Collapse With Further Modification of Peckham
             Lift Correlation Parameter - $\Lambda_F = 60^o$

TEST/RUN CONFIGURATION

55 25 .0008
   35
   45

⟨CL/⟨S/L⟩EXP∅.25×1/CLALPHA⟩

50

40

30

20

10

-4   0   4   8   12   16   20   24   28

ANGLE OF ATTACK-DEG
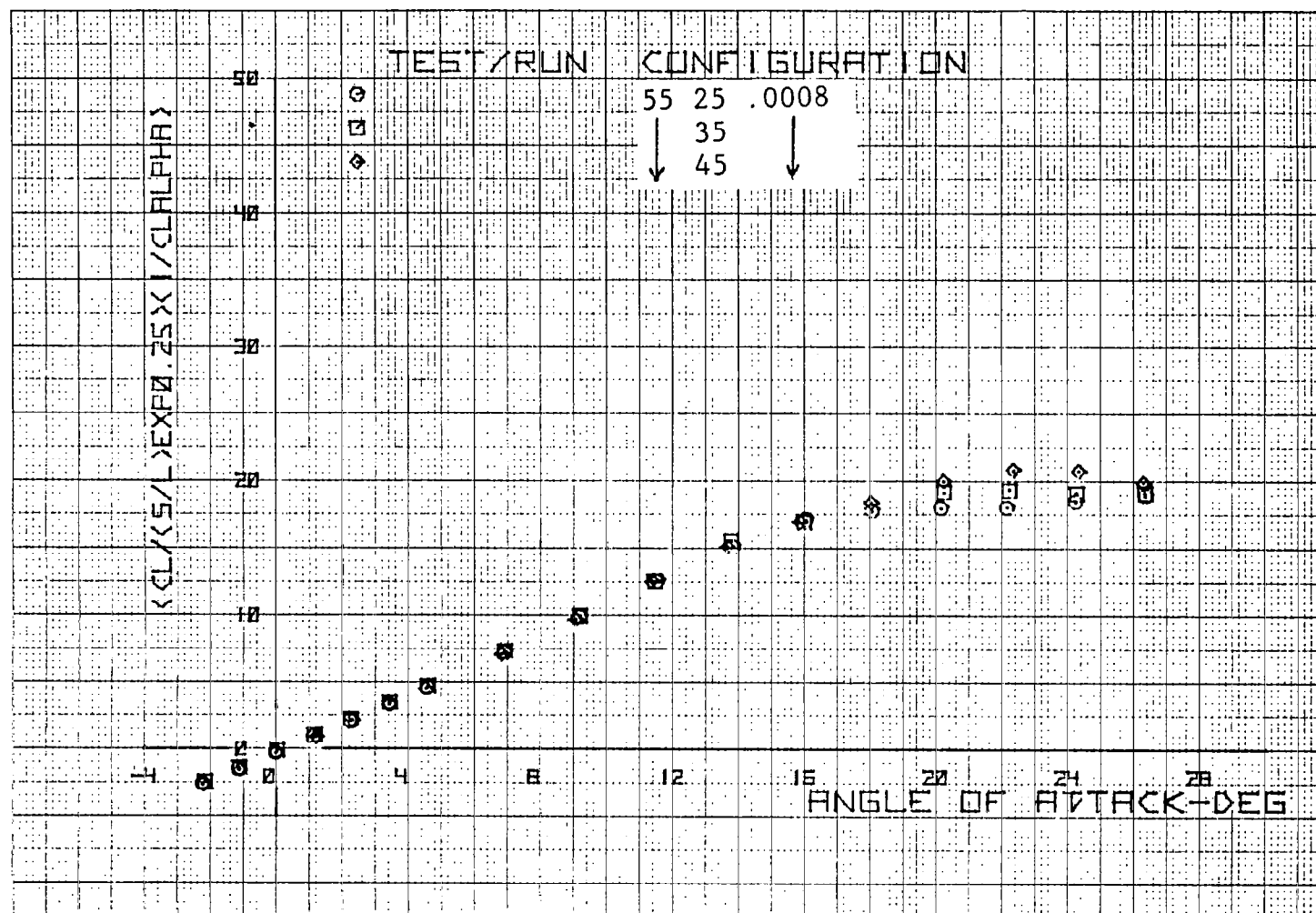
Figure 70.   Data Collapse With Further Modification of Peckham
Lift Correlation Parameter - $\Lambda_F = 55^\circ$
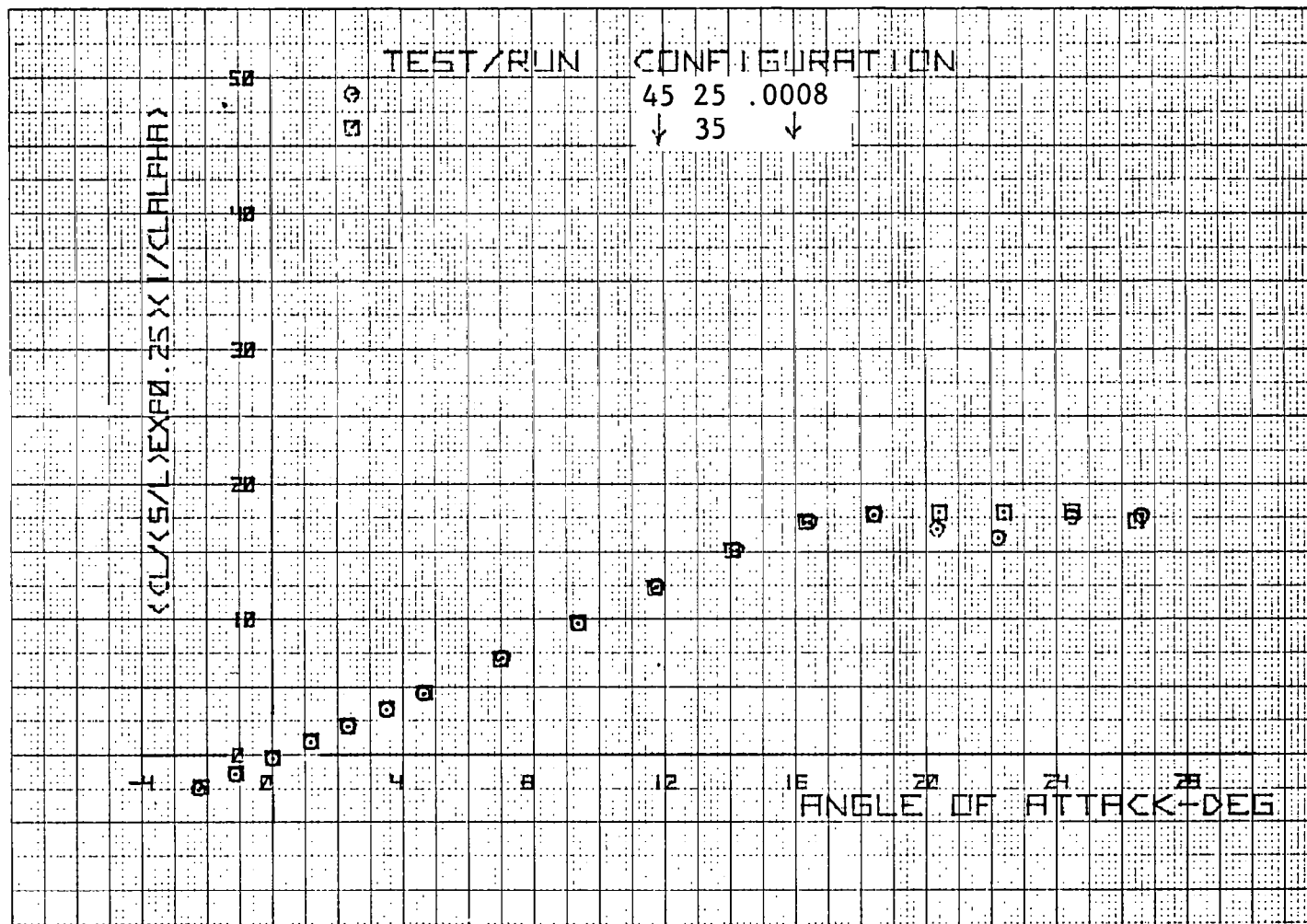
Figure 71.   Data Collapse With Further Modification of Peckham
Lift Correlation Parameter - $\Lambda_F = 45^O$
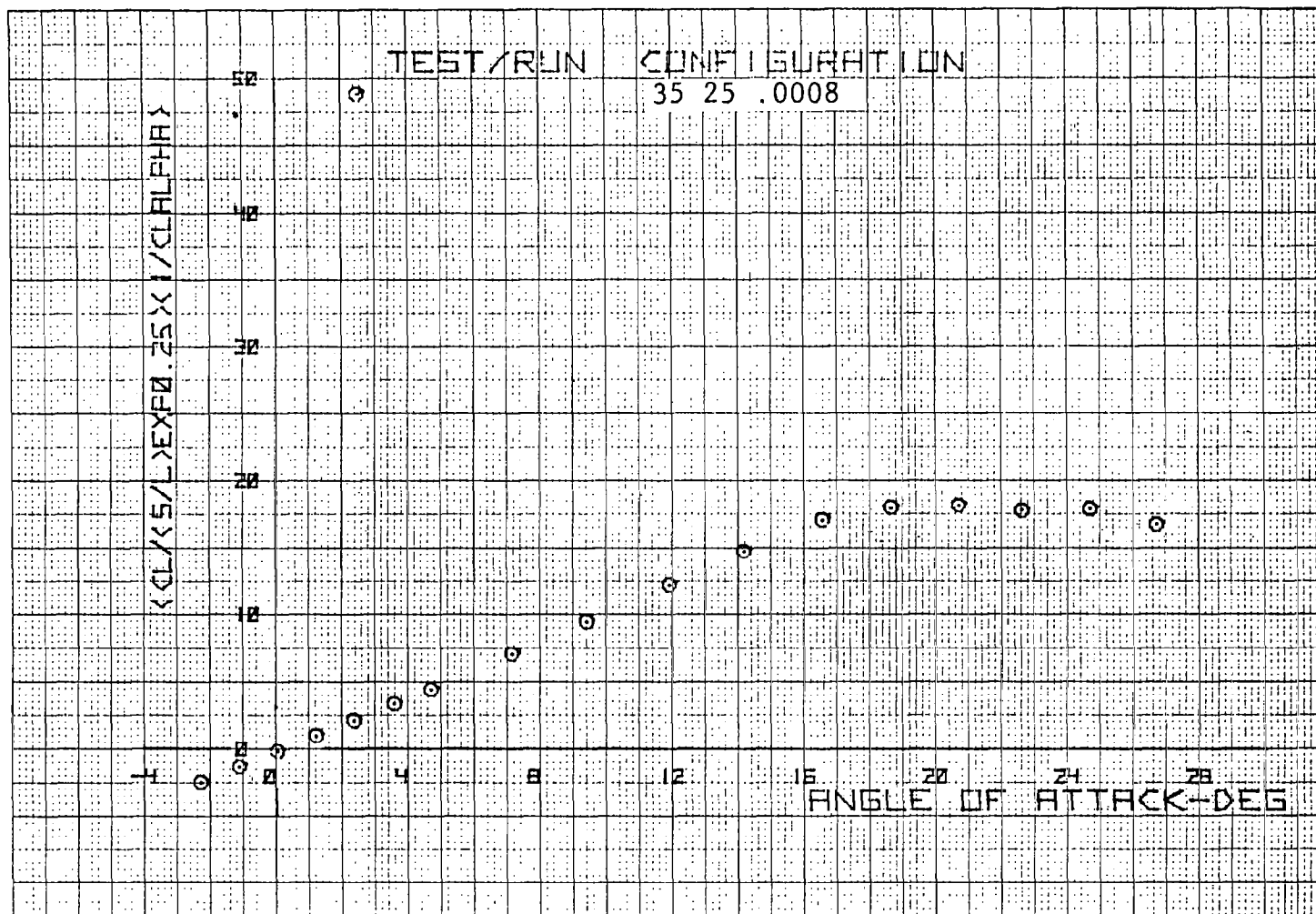
Figure 72. Data Collapse With Further Modification of Peckham
Lift Correlation Parameter - $\Lambda_F = 35^o$
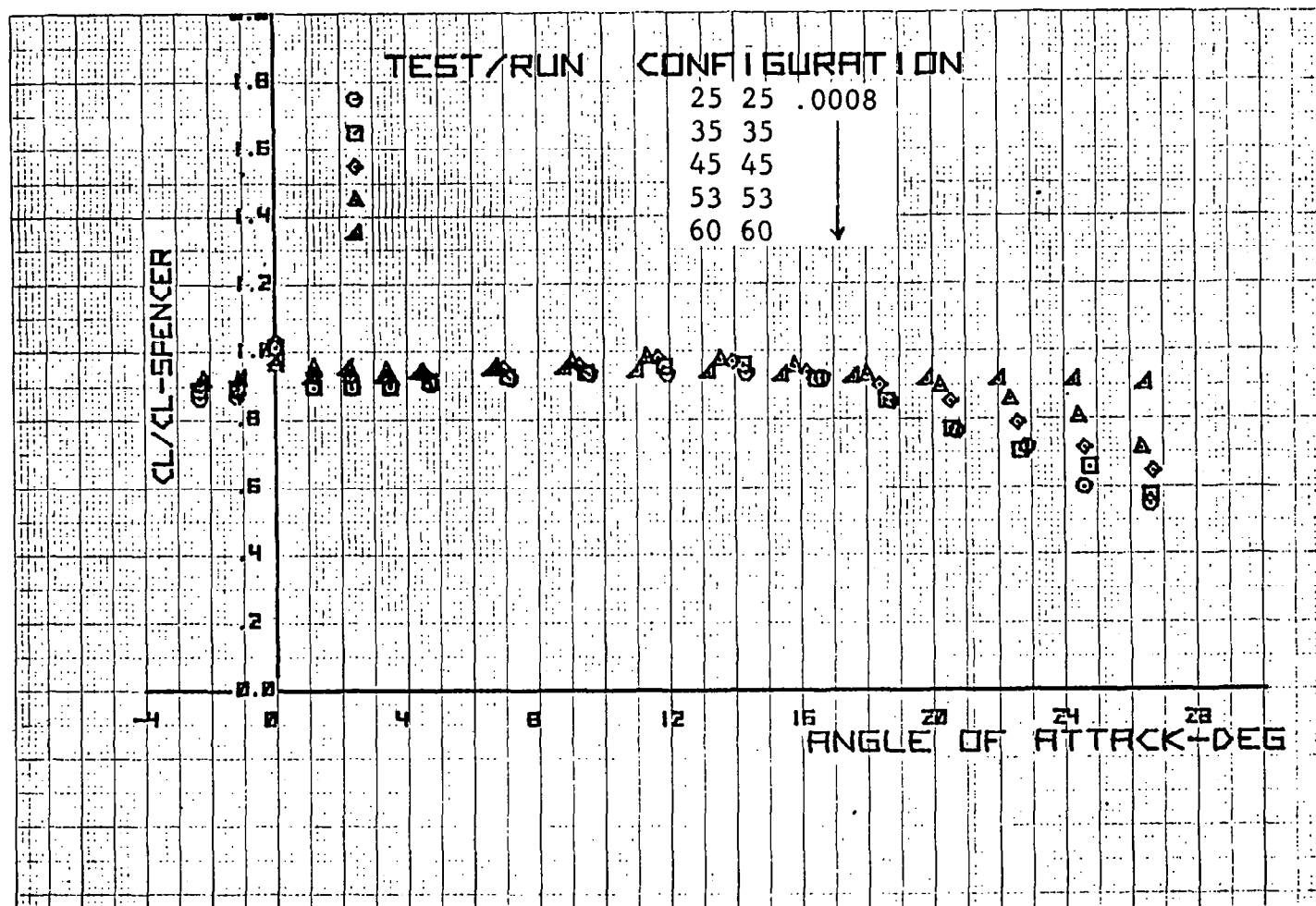
Figure 73. Ratio of Actual Lift to Predicted Linear Lift of SHIPS
Planforms With NACA 0008 Airfoils - Basic Wings
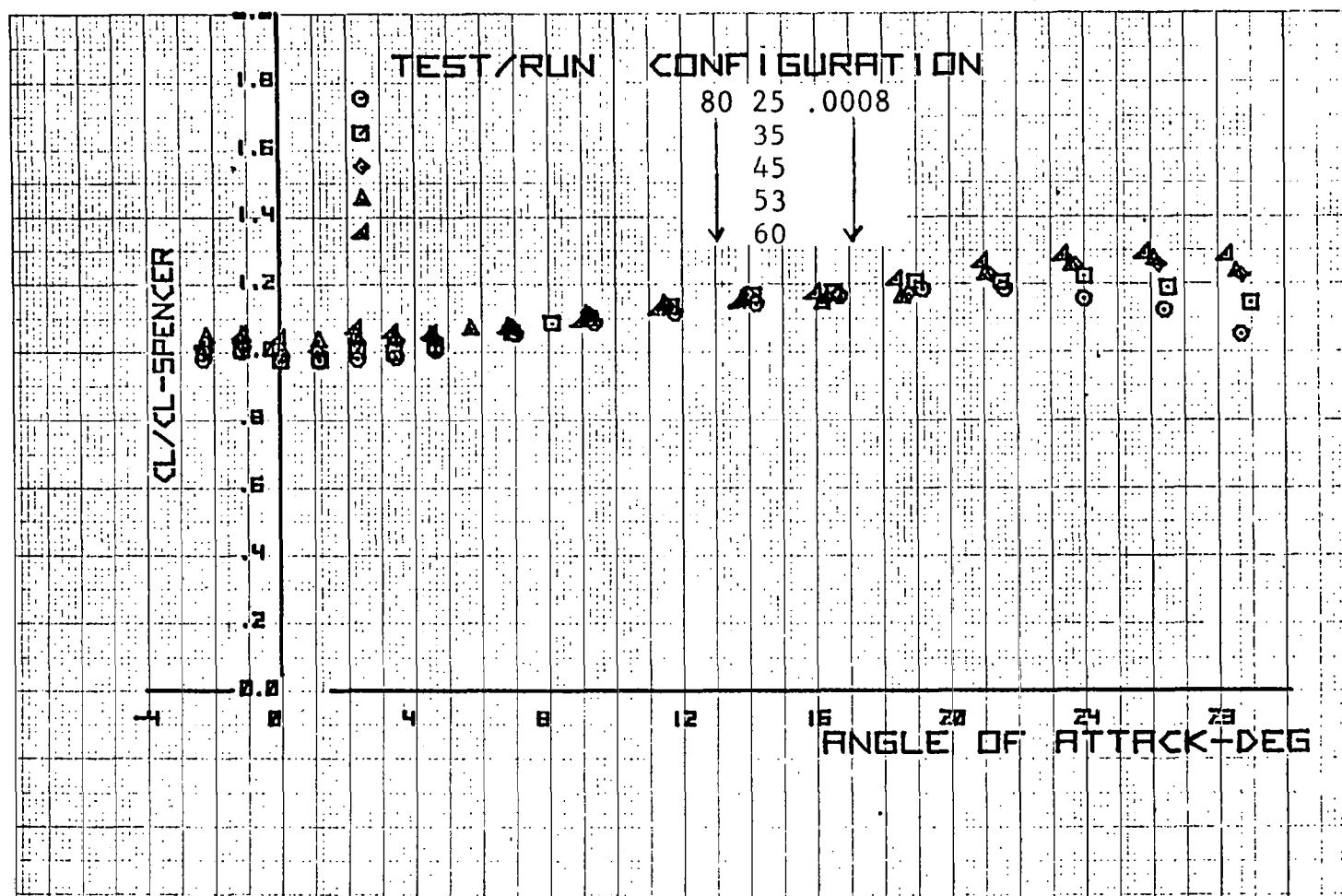
Figure 74. Ratio of Test Lift to Predicted Linear Lift of SHIPS Planforms with NACA 0008 Airfoils - $\Lambda_F = 80^o$
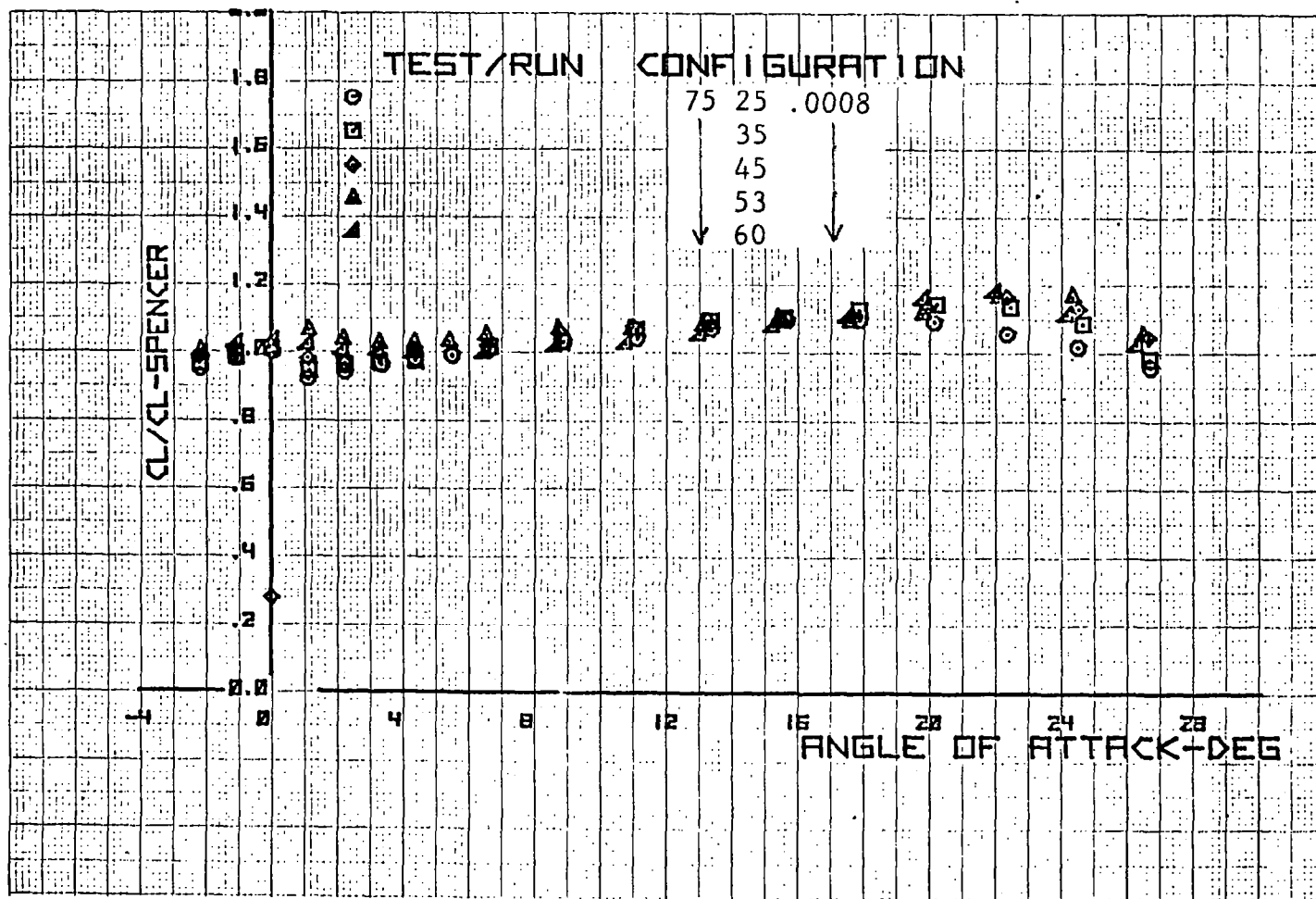
Figure 75. Ratio of Test Lift to Predicted Linear Lift of SHIPS Planforms with NACA 0008 Airfoils - $\Lambda_F = 75°$

TEST/RUN   CONFIGURATION

70 25 .0008
    35
    45
    53
    60

CL/CL-SPENCER

1.8

1.6

1.4

1.2

1.0

.8

.6

.4

.2

0.0

-4   0   4   8   12   16   20   24   28

ANGLE OF ATTACK-DEG
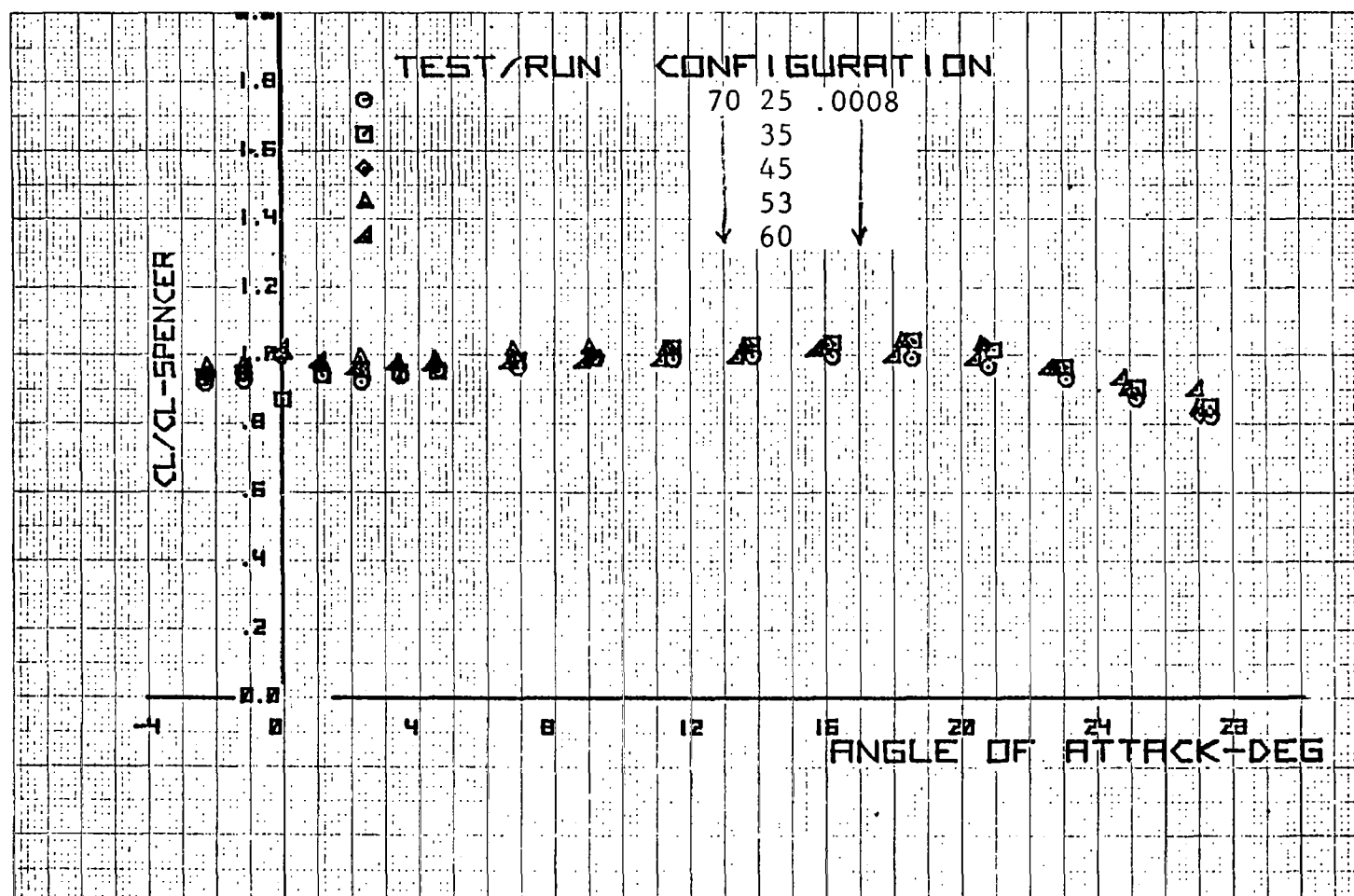
Figure 76.   Ratio of Test Lift to Predicted Lineai Lift of
SHIPS Planforms with NACA 0008 Airfoils - $\Lambda_F = 70^o$
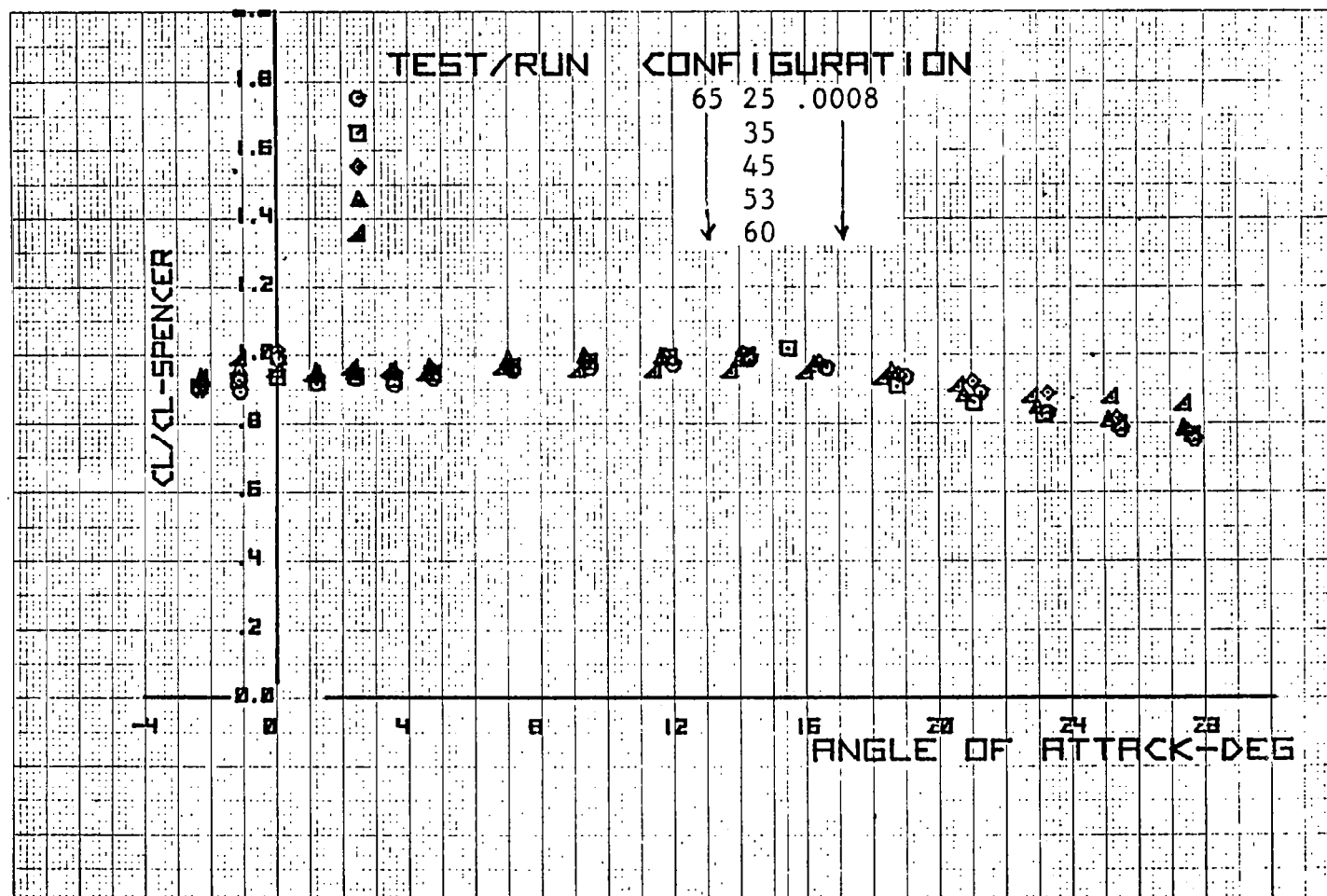
Figure 77. Ratio of Test Lift to Predicted Linear Lift of SHIPS Planforms with NACA 0008 Airfoils - $\Lambda_F = 65^o$
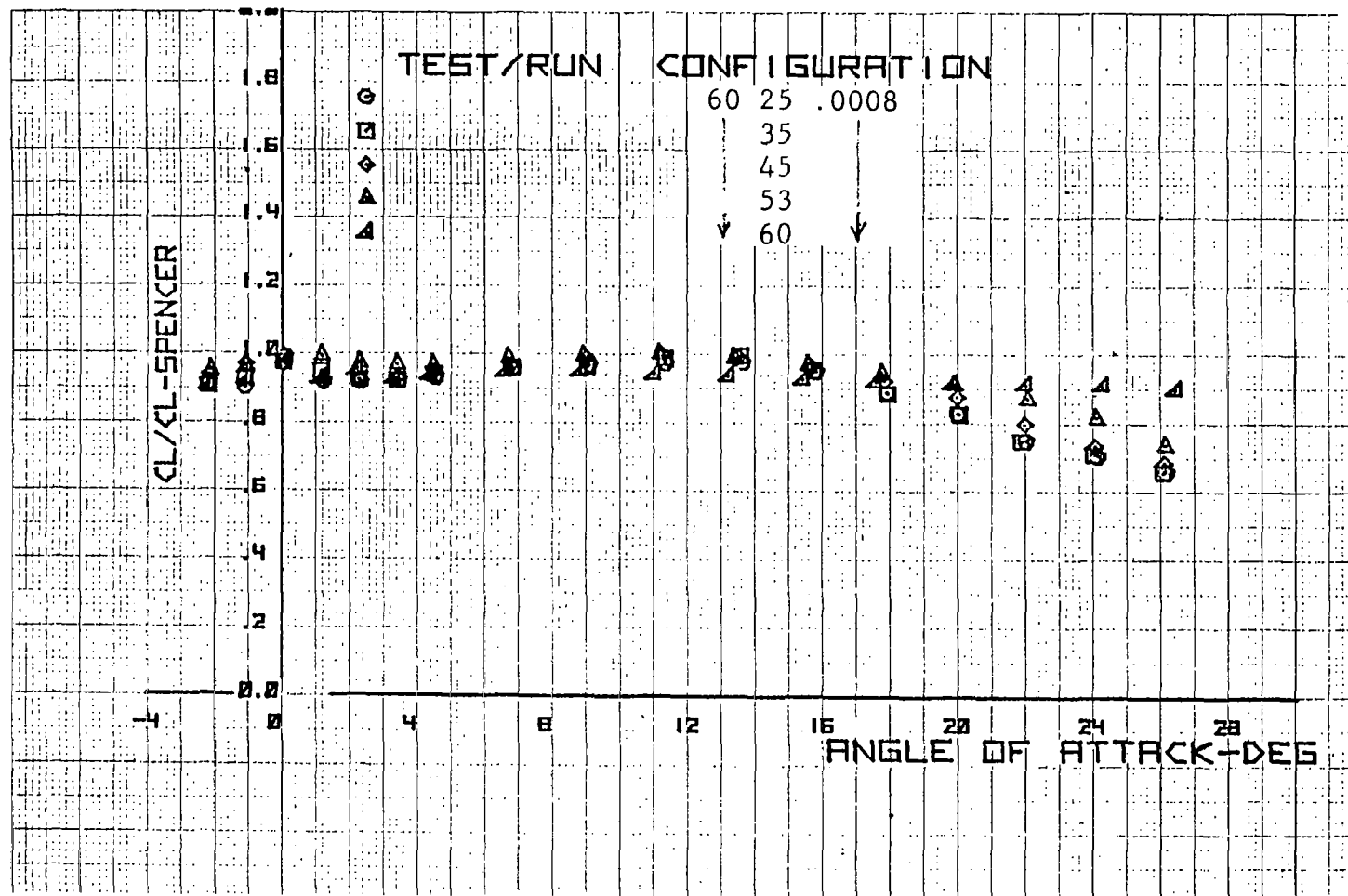
Figure 78. Ratio of Test Lift to Predicted Linear Lift of SHIPS
Planforms with NACA 0008 Airfoils - $\Lambda_F = 60°$
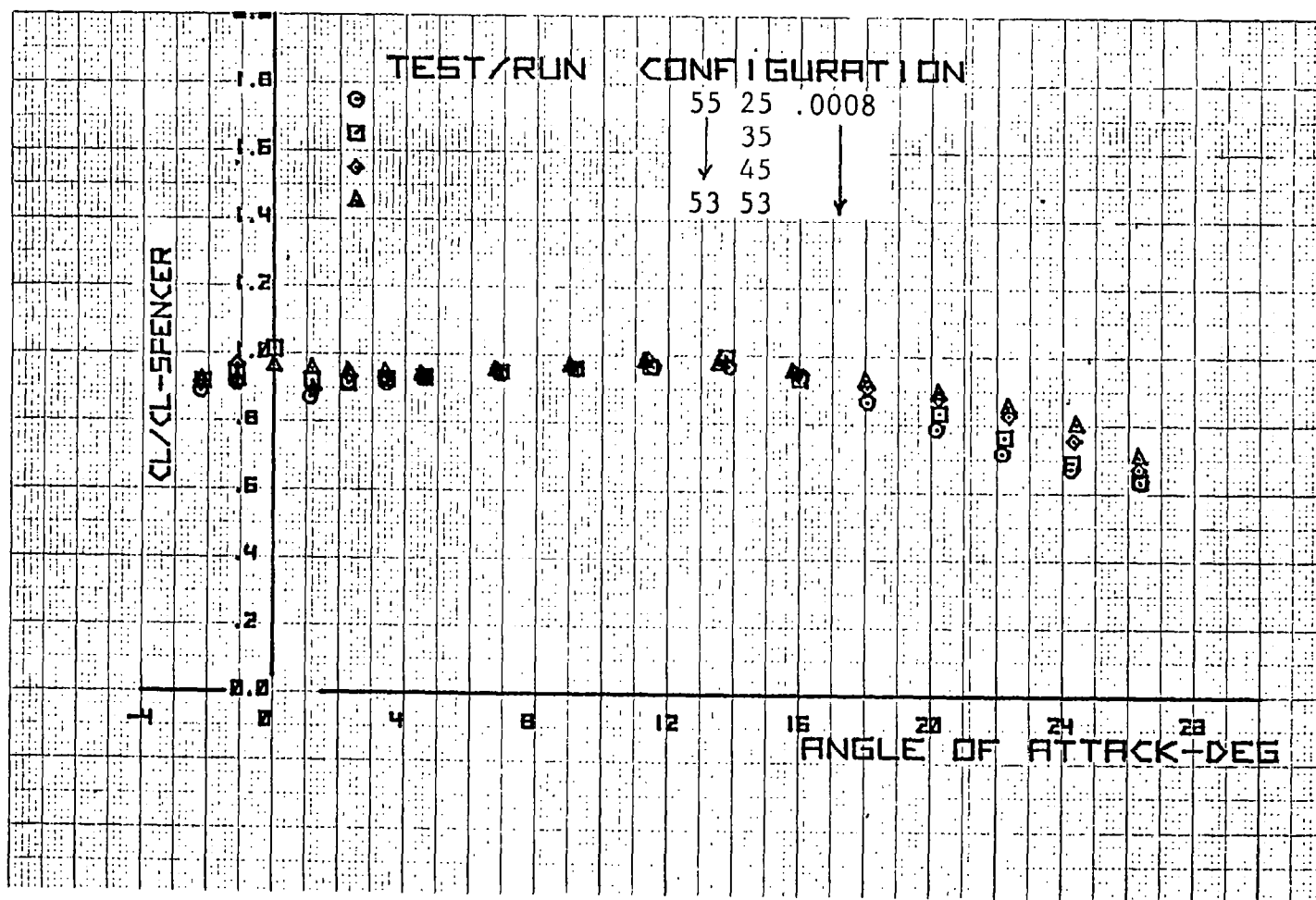
Figure 79. Ratio of Test Lift to Predicted Linear Lift of SHIPS
Planforms with NACA 0008 Airfoils - $\Lambda_F = 55^o$ and 53°
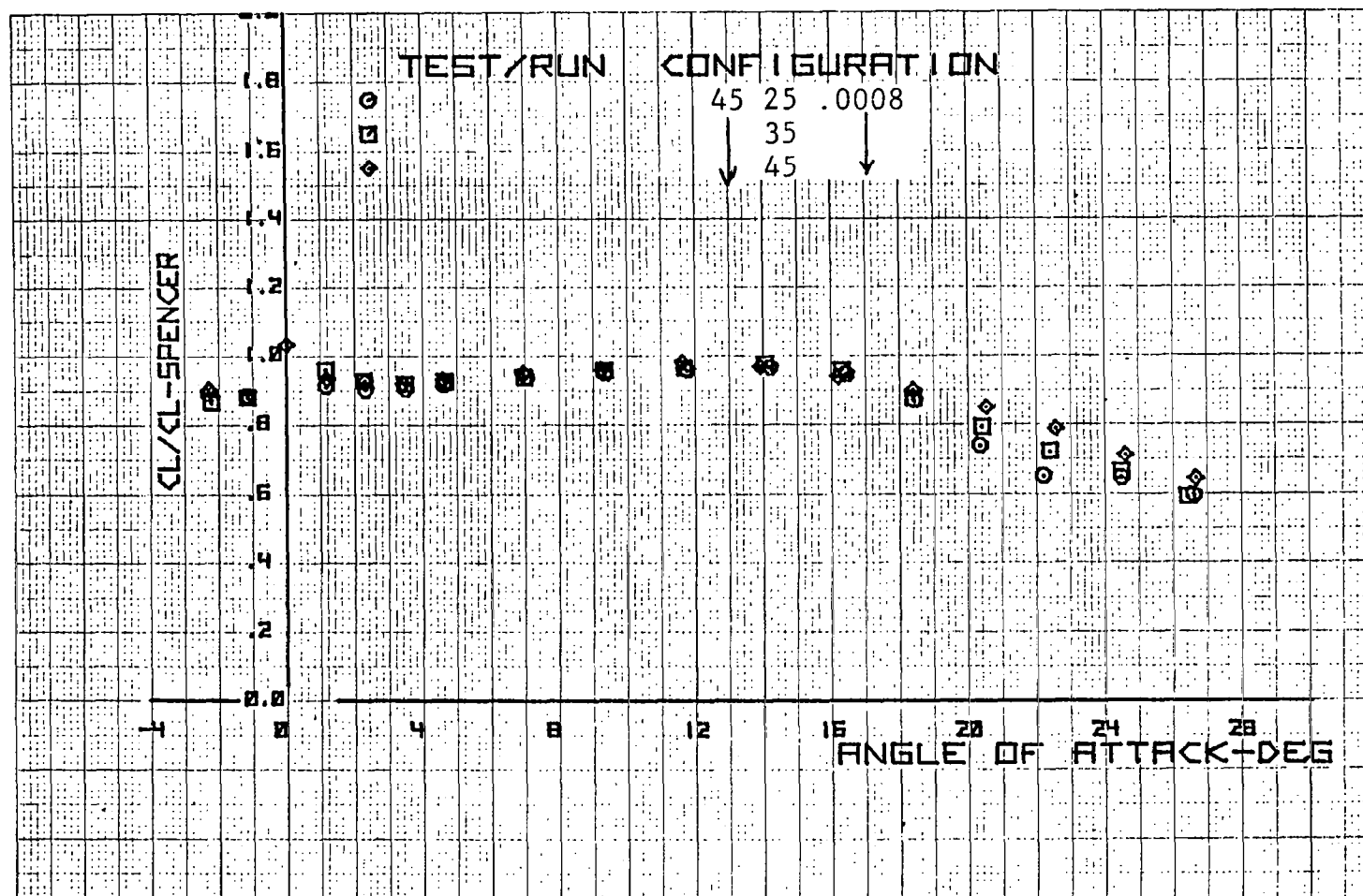
Figure 80. Ratio of Test Lift to Predicted Linear Lift of SHIPS
Planforms with NACA 0008 Airfoils - $\Lambda_F = 45°$
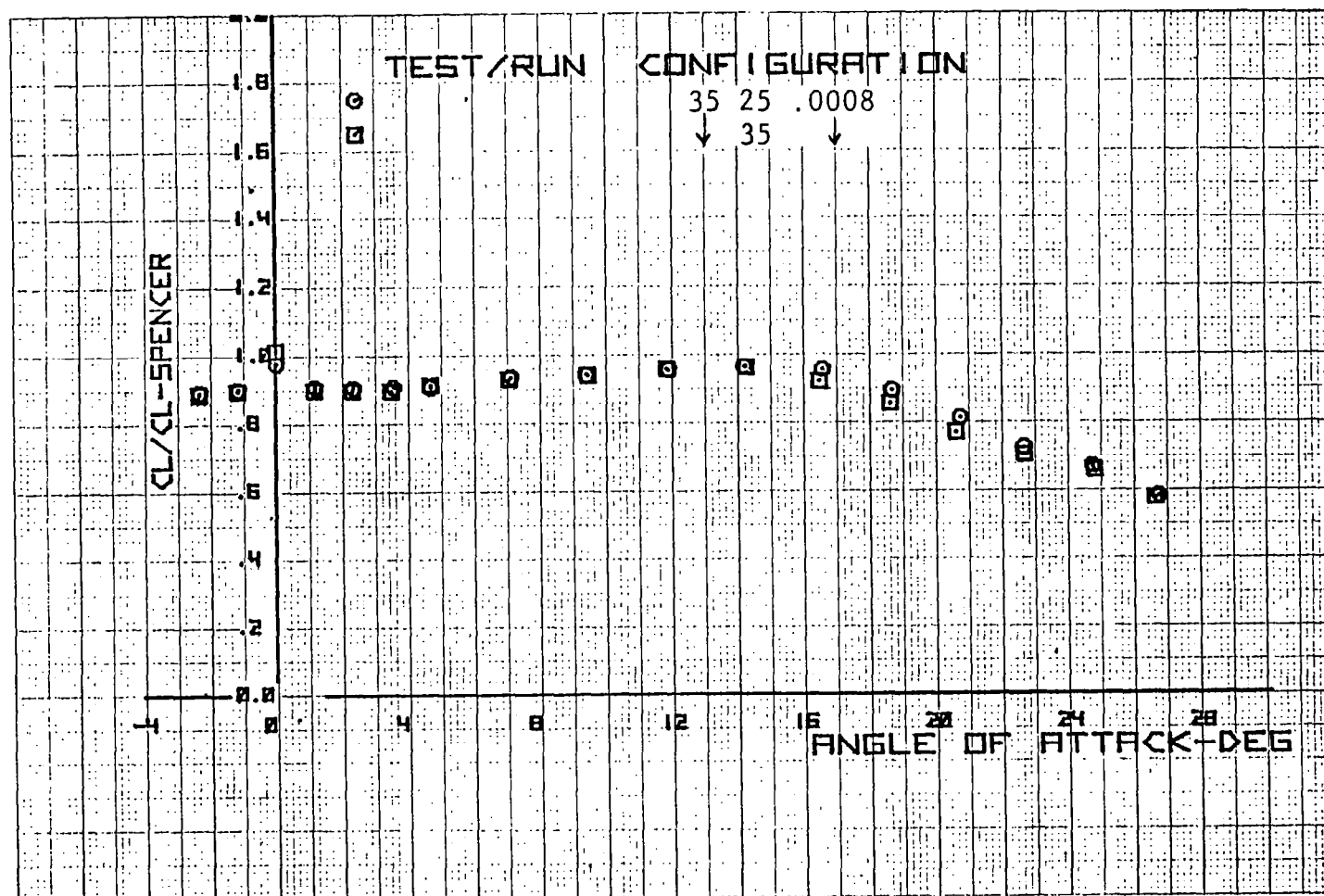
Figure 81.   Ratio of Test Lift to Predicted Linear Lift of SHIPS
Planforms with NACA 0008 Airfoils - $\Lambda_F = 35^\circ$
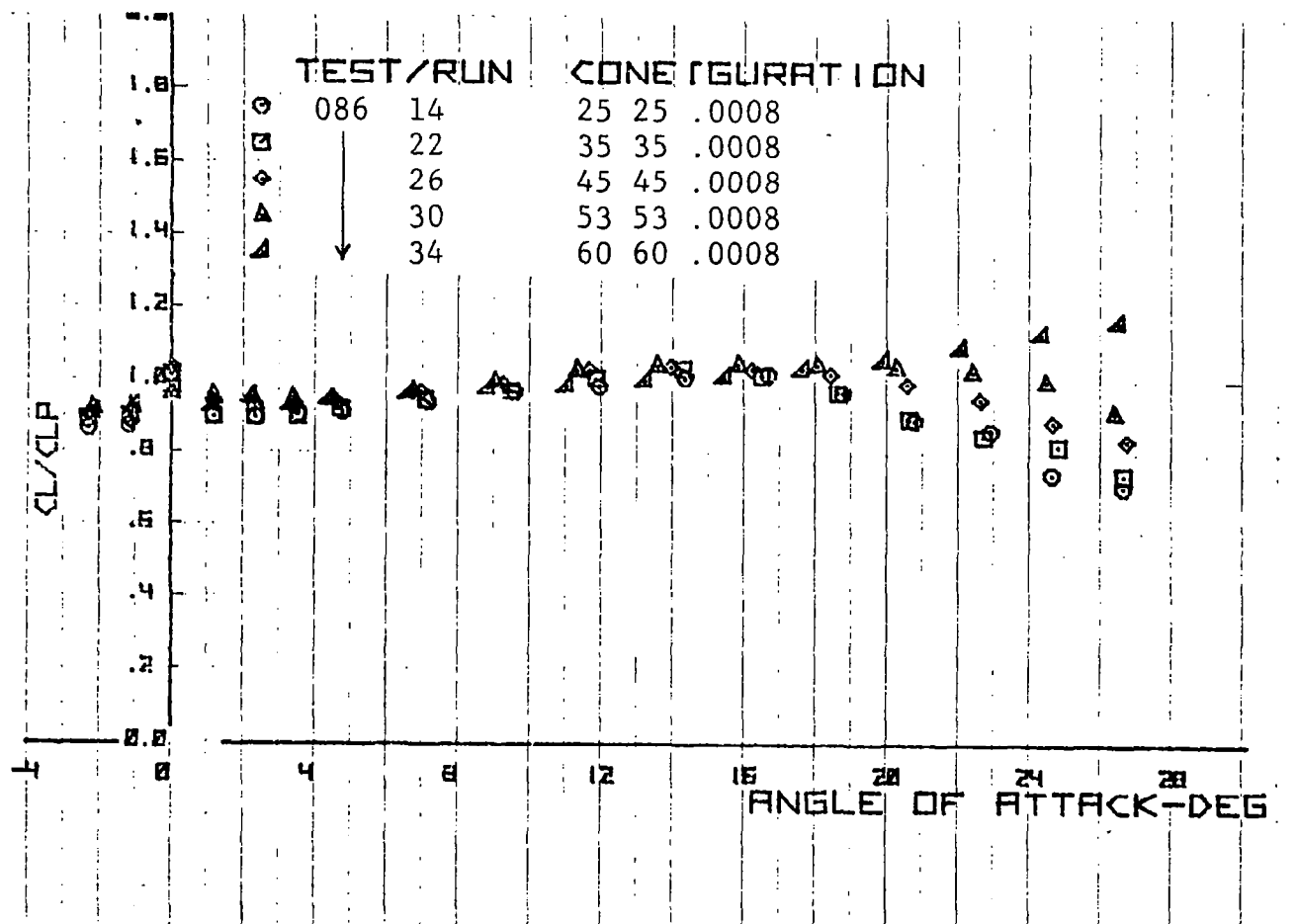
Figure 82.   Ratio of Test Lift to Nonlinear Potential Flow Estimate for Basic SHIPS Planforms
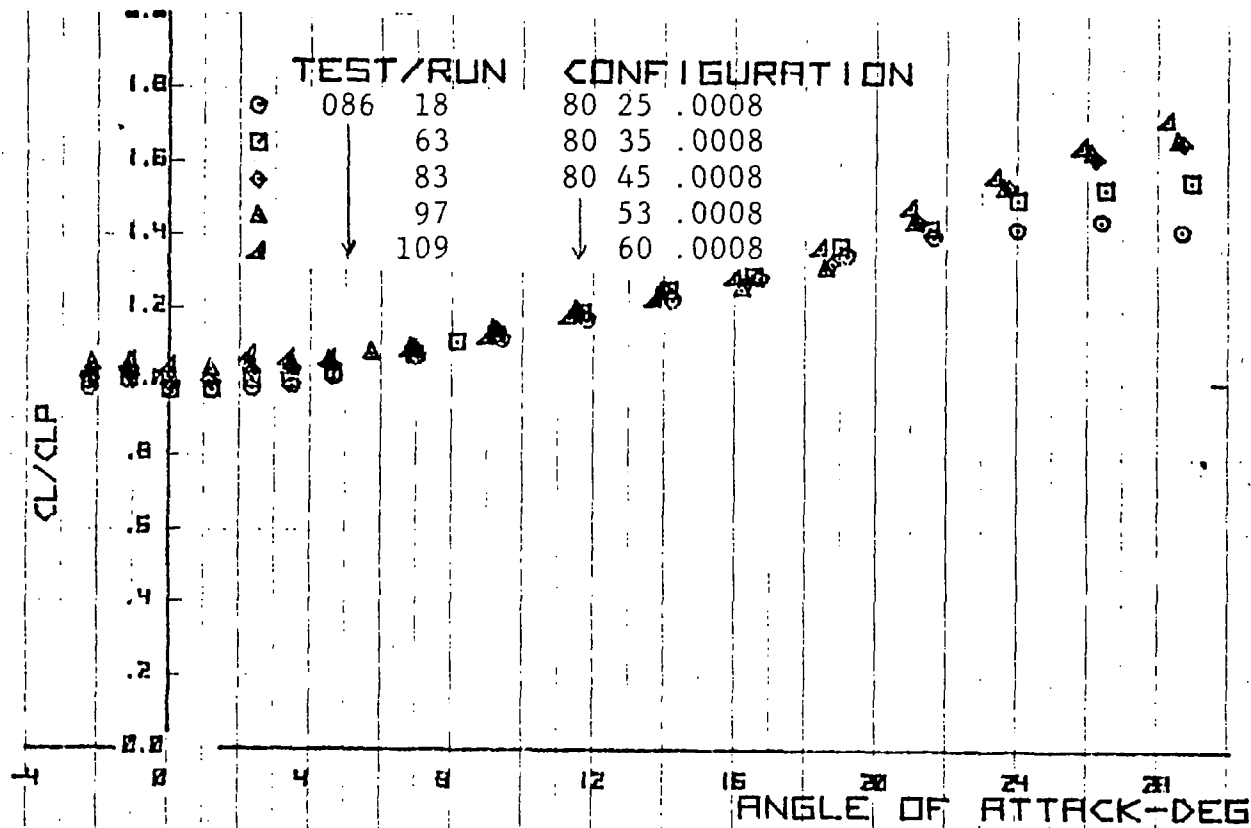
Figure 83.   Ratio of Test Lift to Nonlinear Potential Flow Esti-
mate for SHIPS Planforms Having 80° Fillets.

$$RN = 8.0 \times 10^6/Ft$$
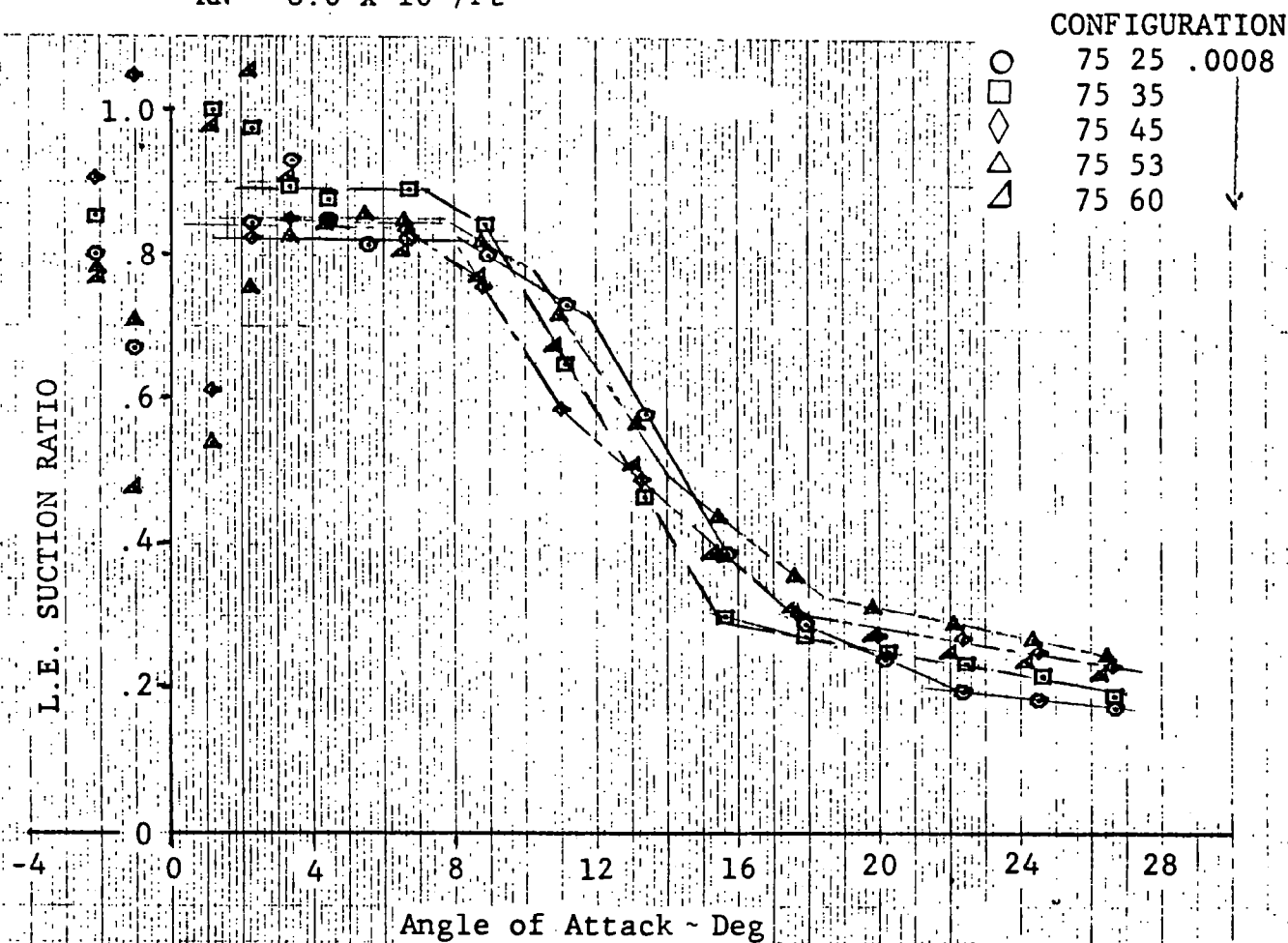
Figure 84.   Variations of Leading-Edge-Suction Ratio with Angle of Attack for Irregular Planforms with 75° Fillet Sweep
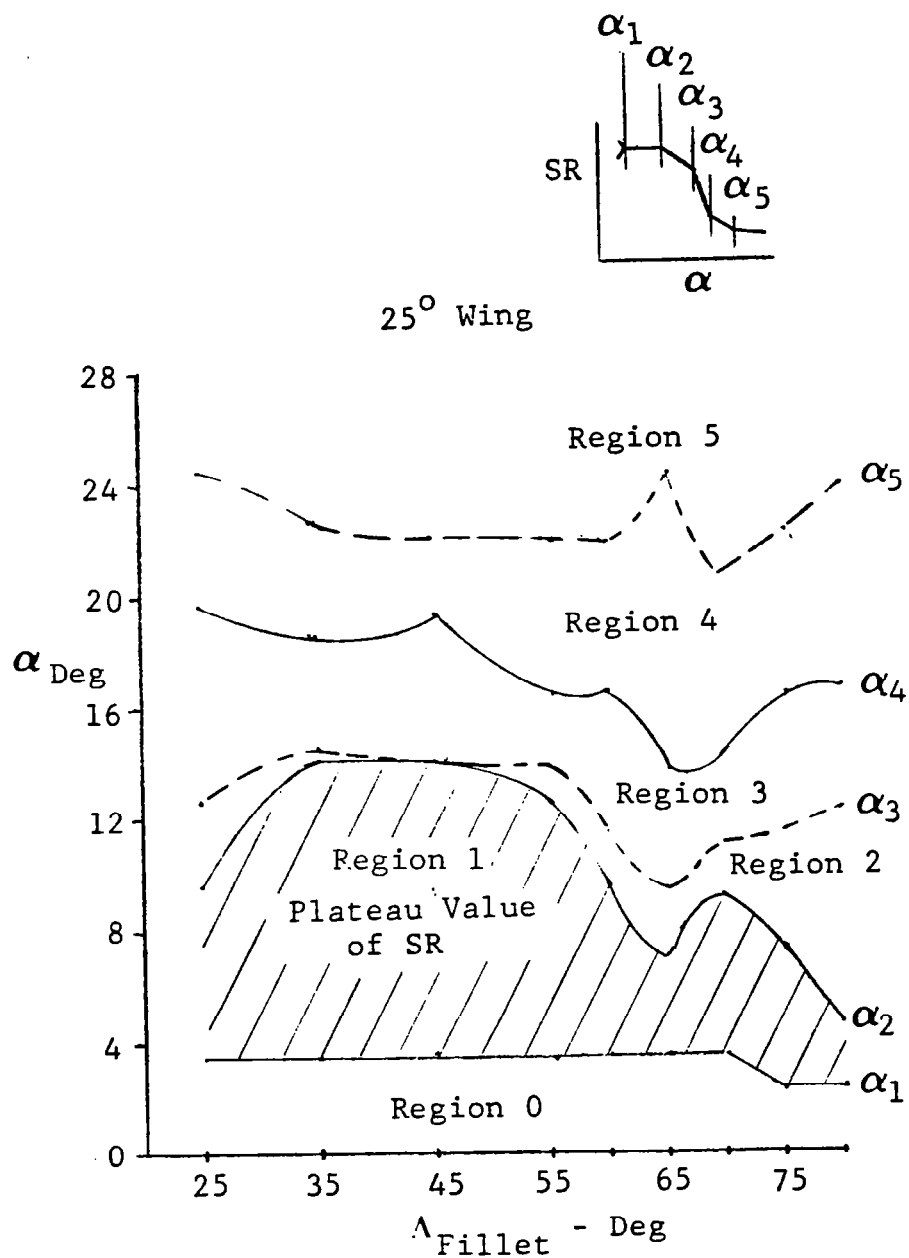
Figure 85.   Example of Angle-of-Attack Boundary Variations with
Fillet Sweep for Wing I Planforms
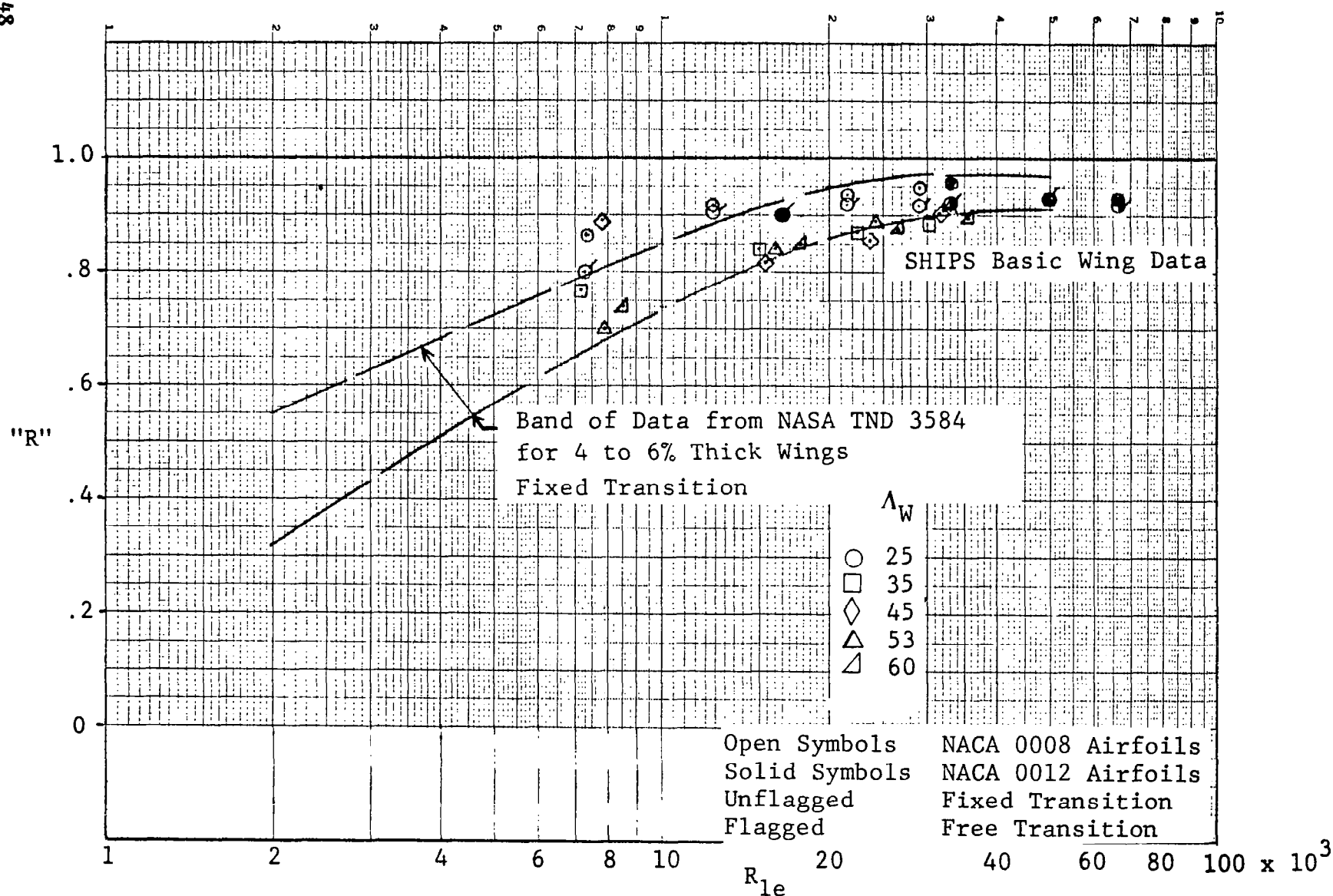
Figure 86.   Correlation of Suction Ratio "R" Using Effective
             Leading-Edge Radius Reynolds Number

"R"

1.0

SHIPS·Basic Wing Data

Correlation

Curve

.8

"R"$_{BW}$

.6

$\dfrac{A\lambda}{Cos\Lambda_{LE}}$

AFFDL TR 66-73(Free
Transition Data)

Λ_W	$\dfrac{A\lambda}{Cos\Lambda_{LE}}$
○ 25	.772
□ 35	.686
◇ 45	.520
△ 53	.370
◿ 60	.044

.4

.2

Open Symbols   NACA 0008 Airfoils
Solid Symbols   NACA 0012 Airfoils
Unflagged   Fixed Transition
Flagged   Free Transition

0

$$\Omega = R_{e_{LER}} \; Cot\Lambda_{LE}\sqrt{1-M^2 Cos^2\Lambda_{LE}}$$

1   2   4 6   10   20   40 60 100   200   400 x 10^3

149
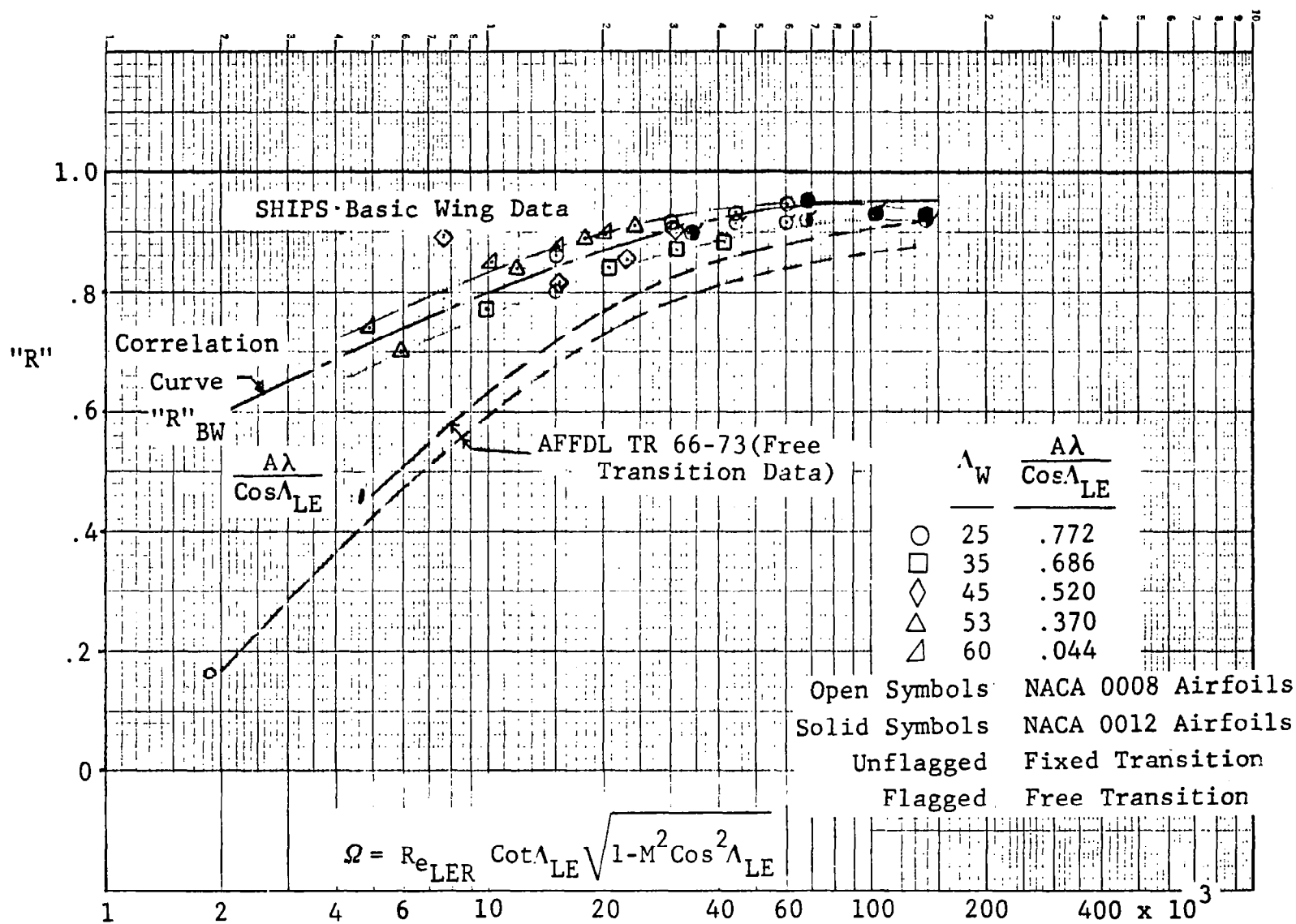
Figure 87.   Correlation of Suction Ratio Using WINSTAN Ω Parameter
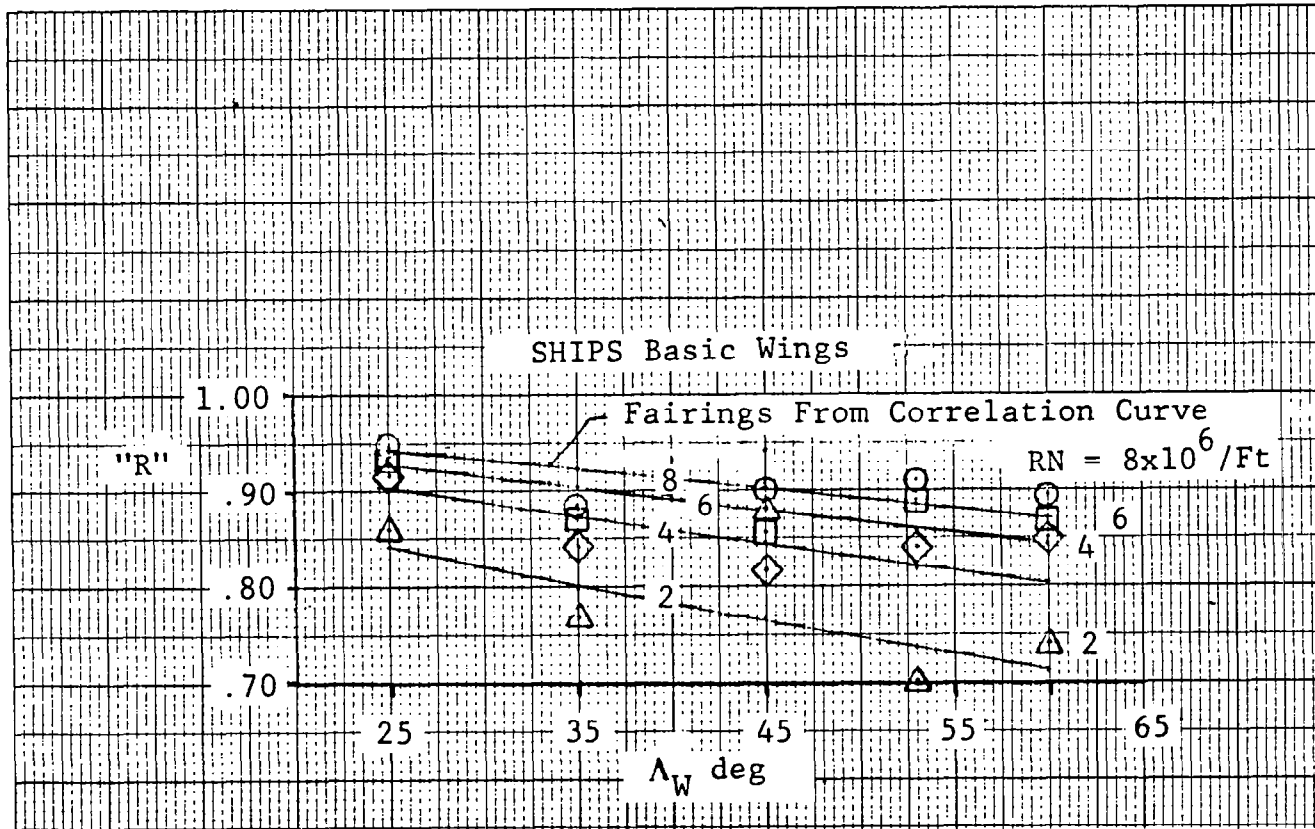
Figure 88. Comparison of Correlation Curve Values of Suction
            Ratio with SHIPS Basic Wing Test Data
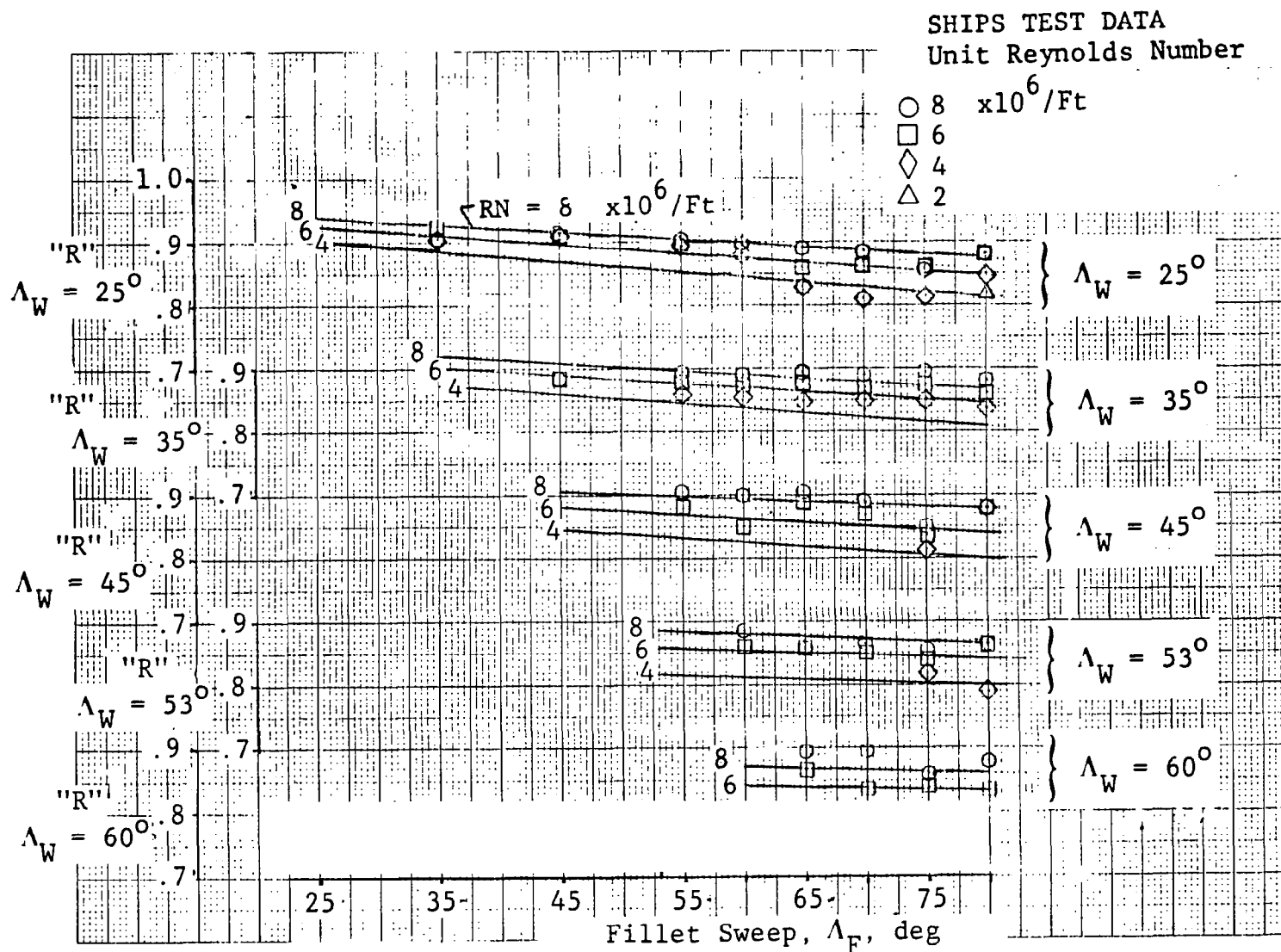
Figure 89   Comparison of Simple Prediction Approach with
Suction Ratio Data
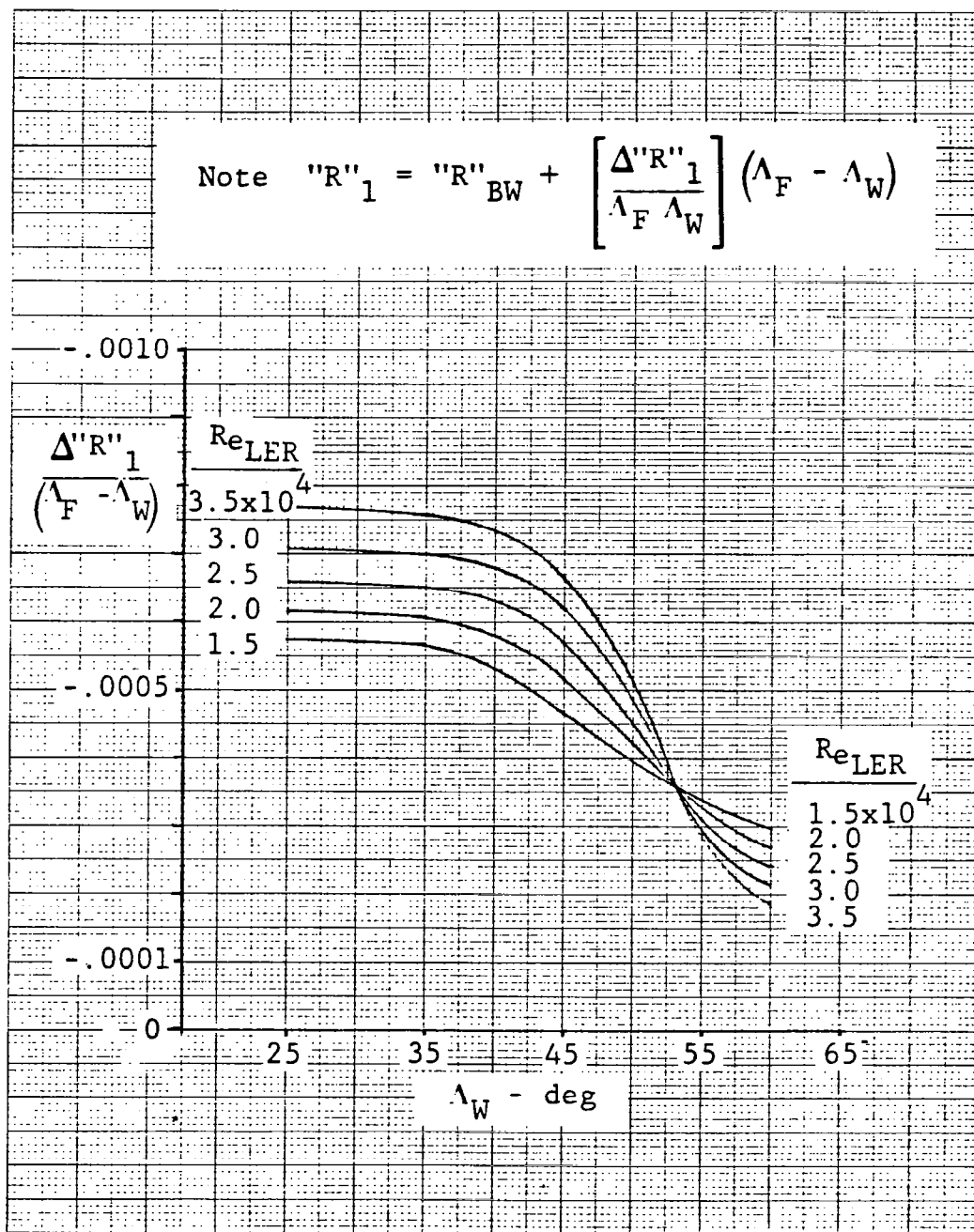
Figure 90. Calculation Chart for Incremental Effect of Fillet Sweep on Suction Ratio in Plateau Region Between $\alpha = 0°$ and α_2
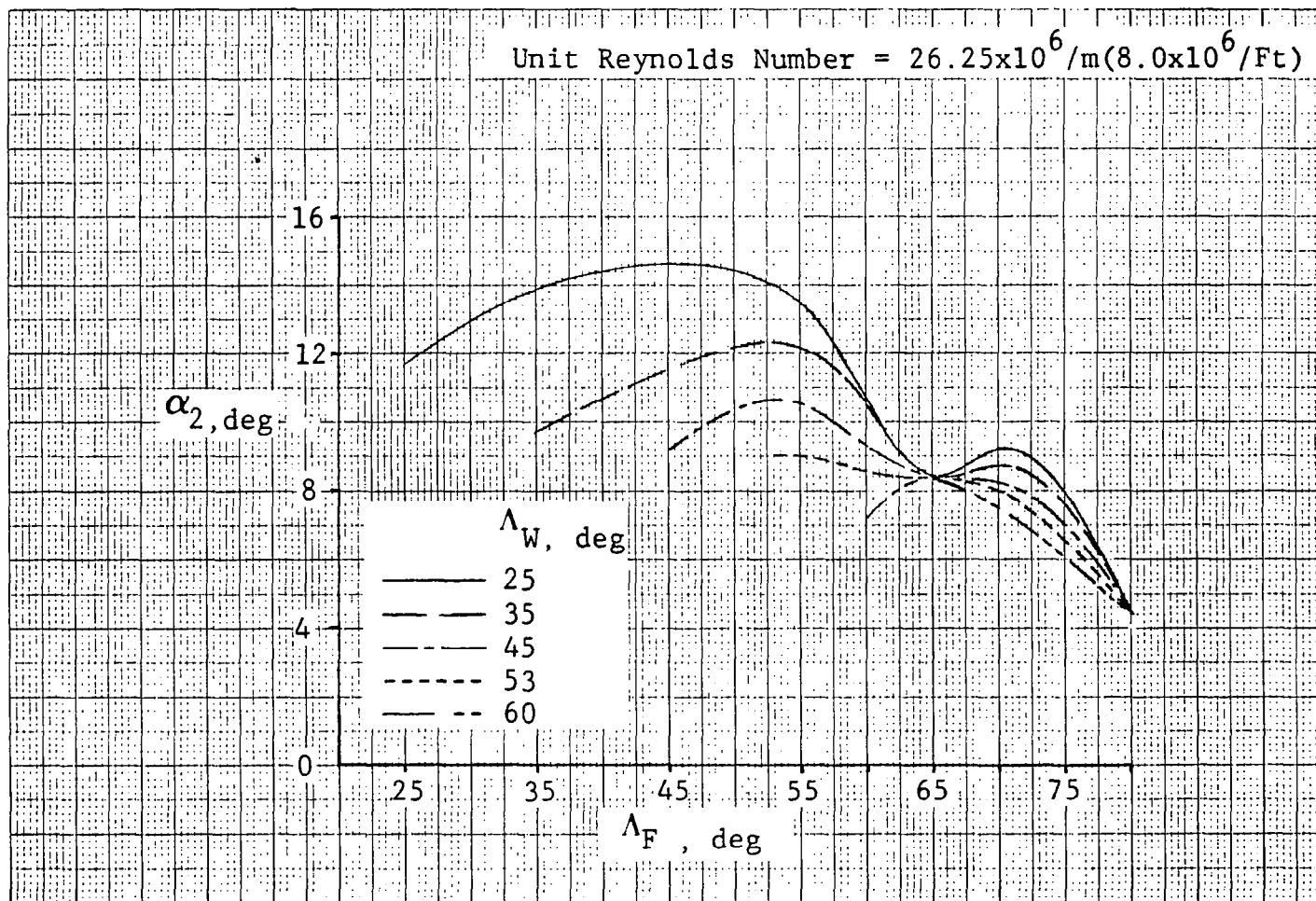
Figure 91. Upper Angle-of-Attack Boundaries for Region 1
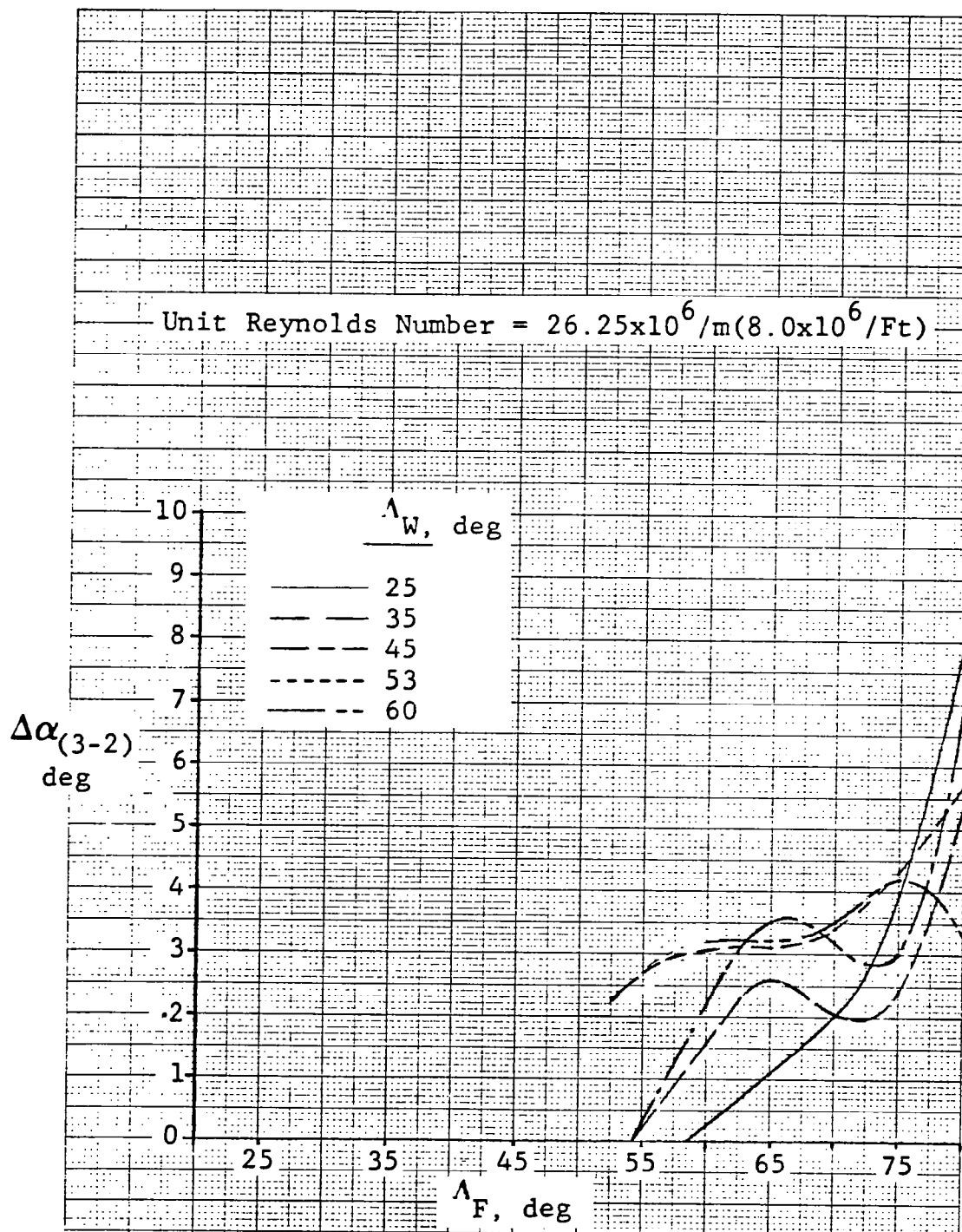
Figure   92.   Incremental Angle of Attack for Region 2

154
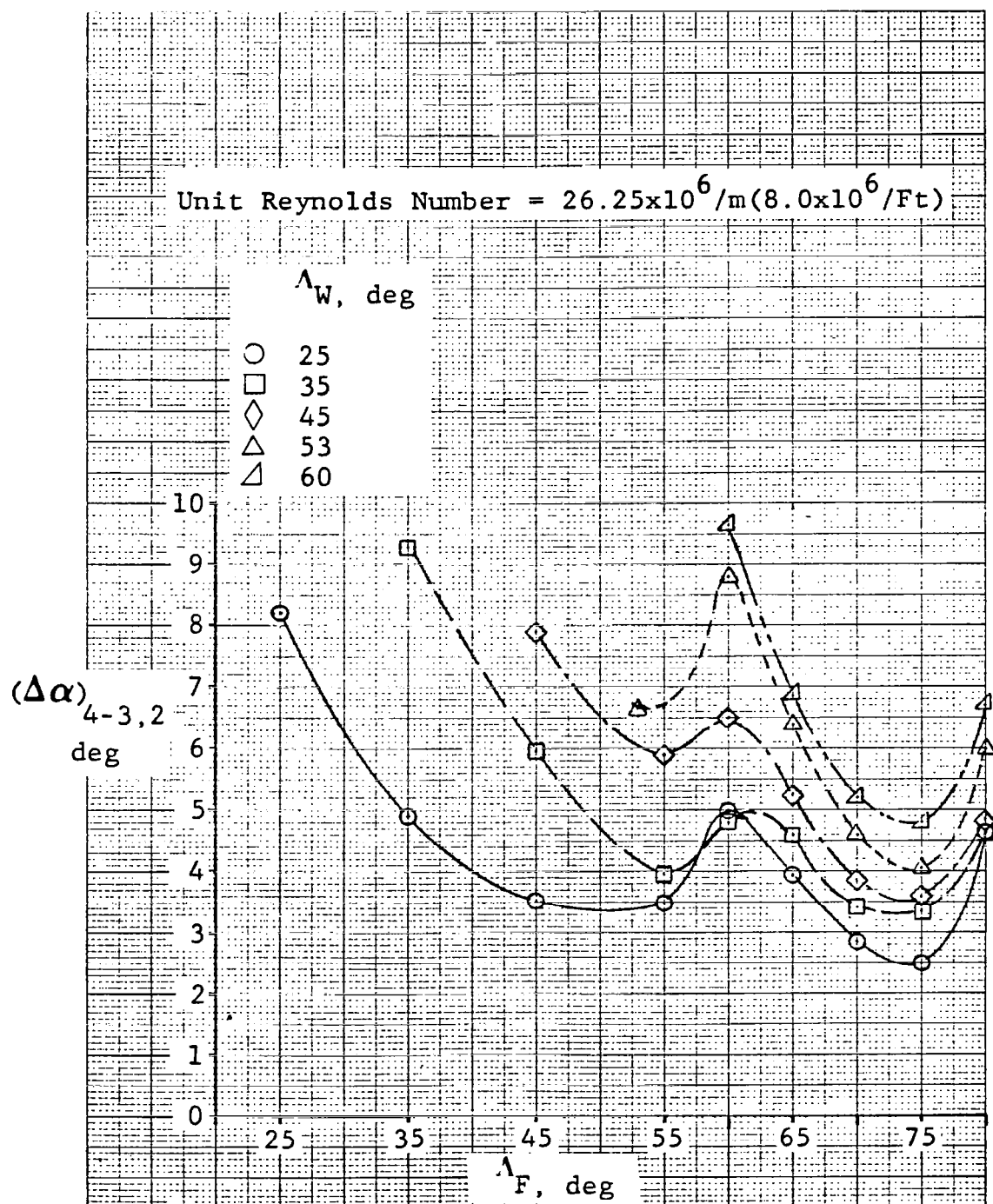
Figure 93. Incremental Angle of Attack for Region 3
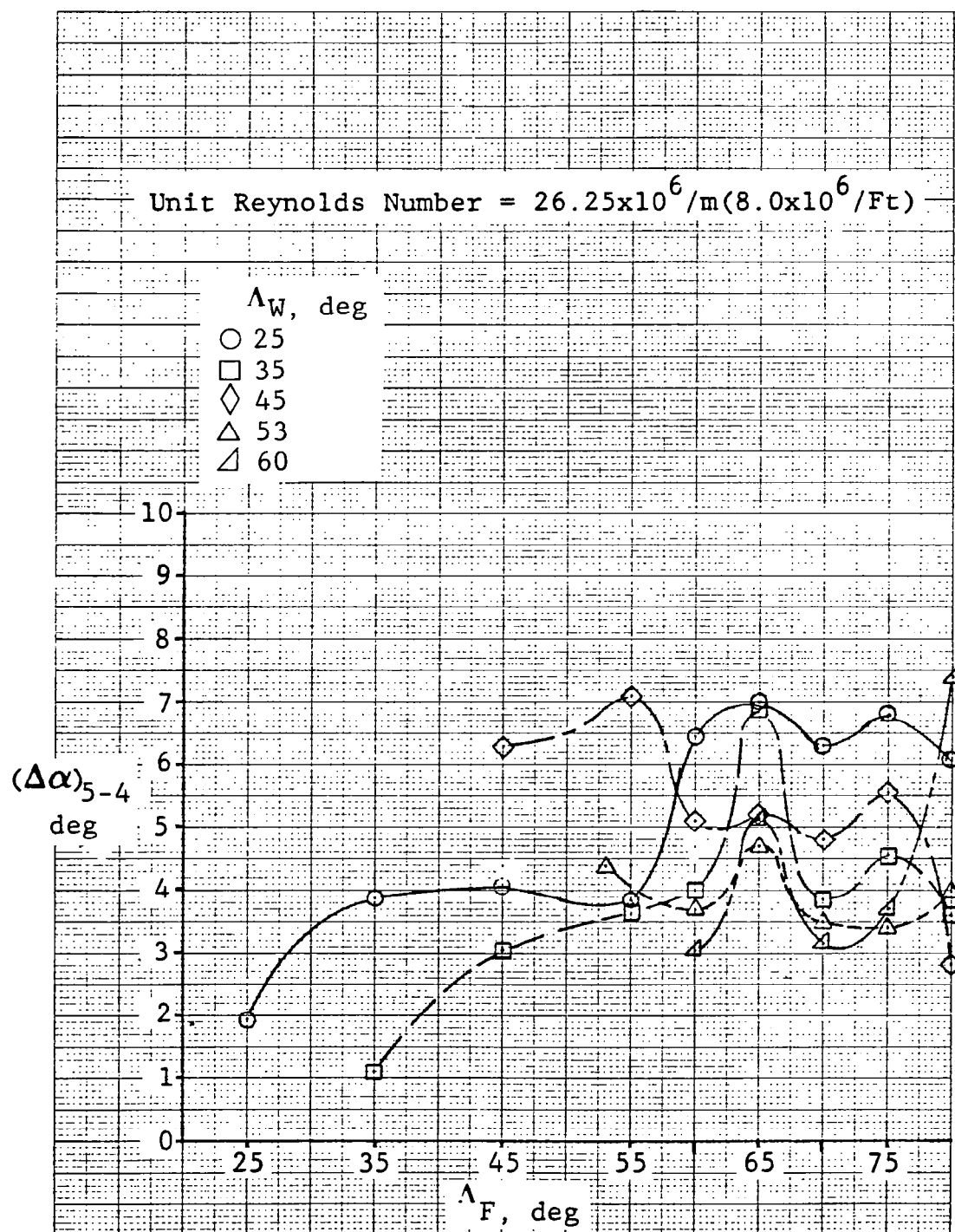
Figure 94. Incremental Angle of Attack for Region 4
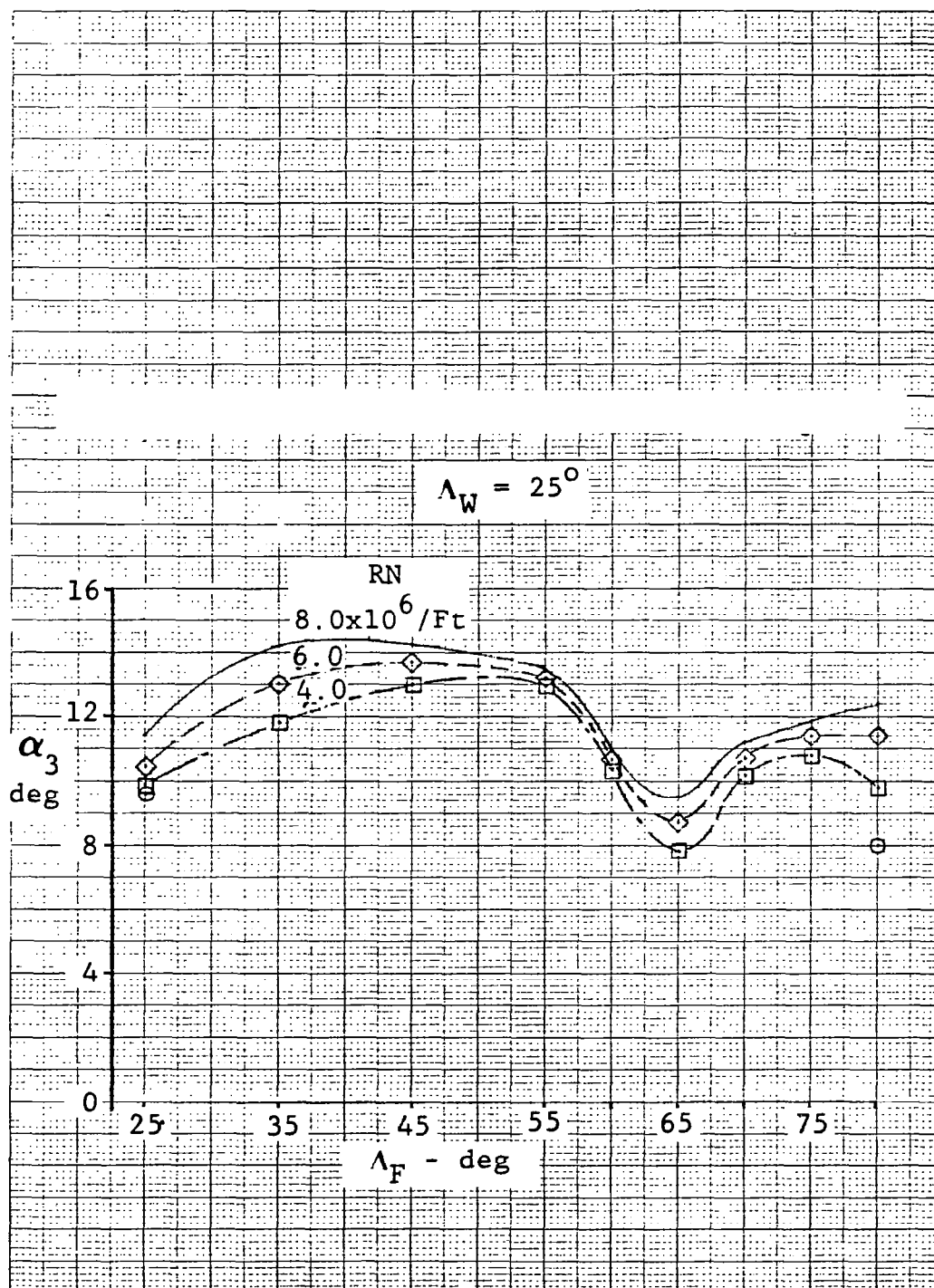
Figure   95.   Effect of Reynolds Number on α_3
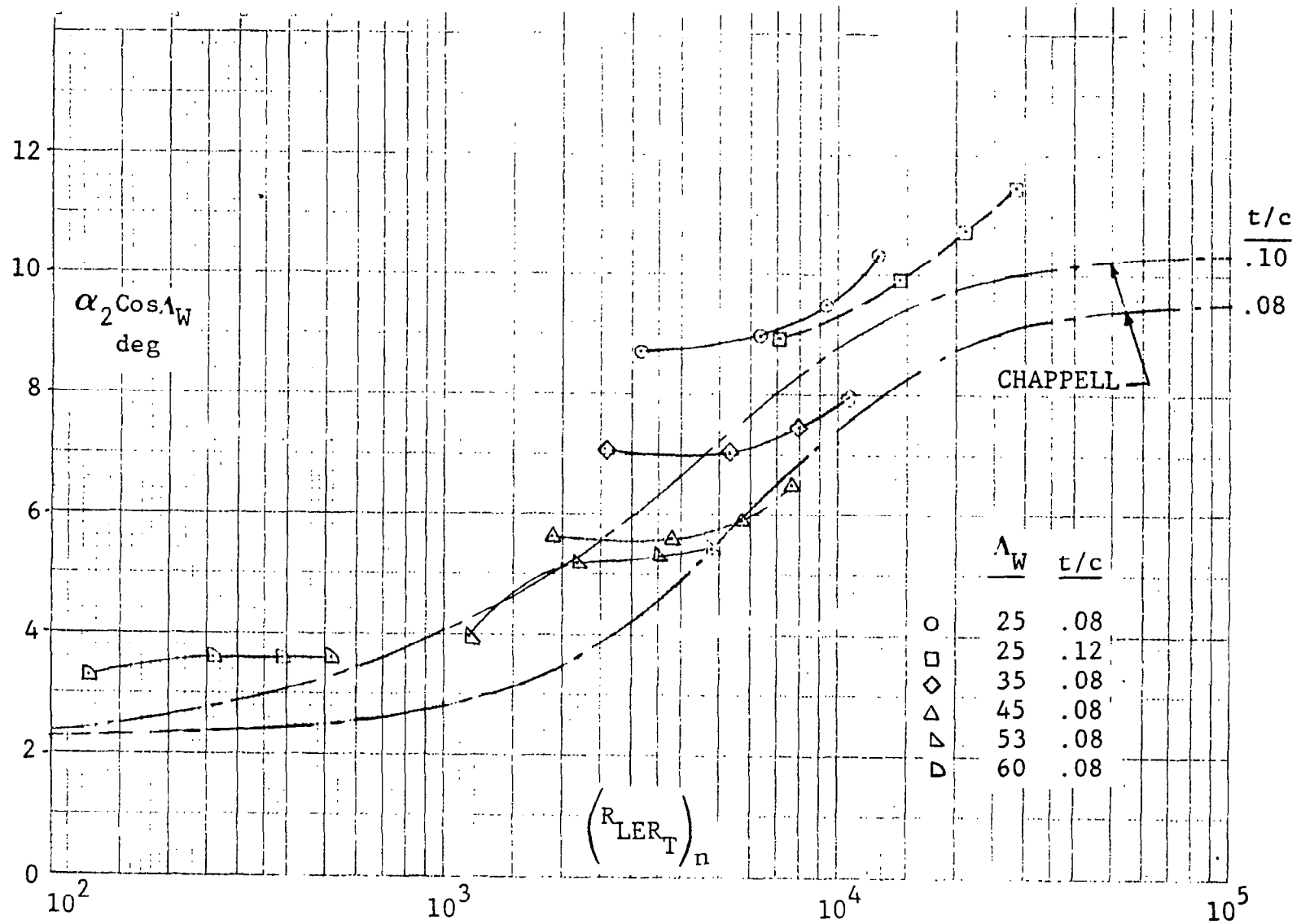
Figure 96. Correlation of Reynolds Number Effects on α_2 for Basic Wings Using Chappell's Correlation Parameter
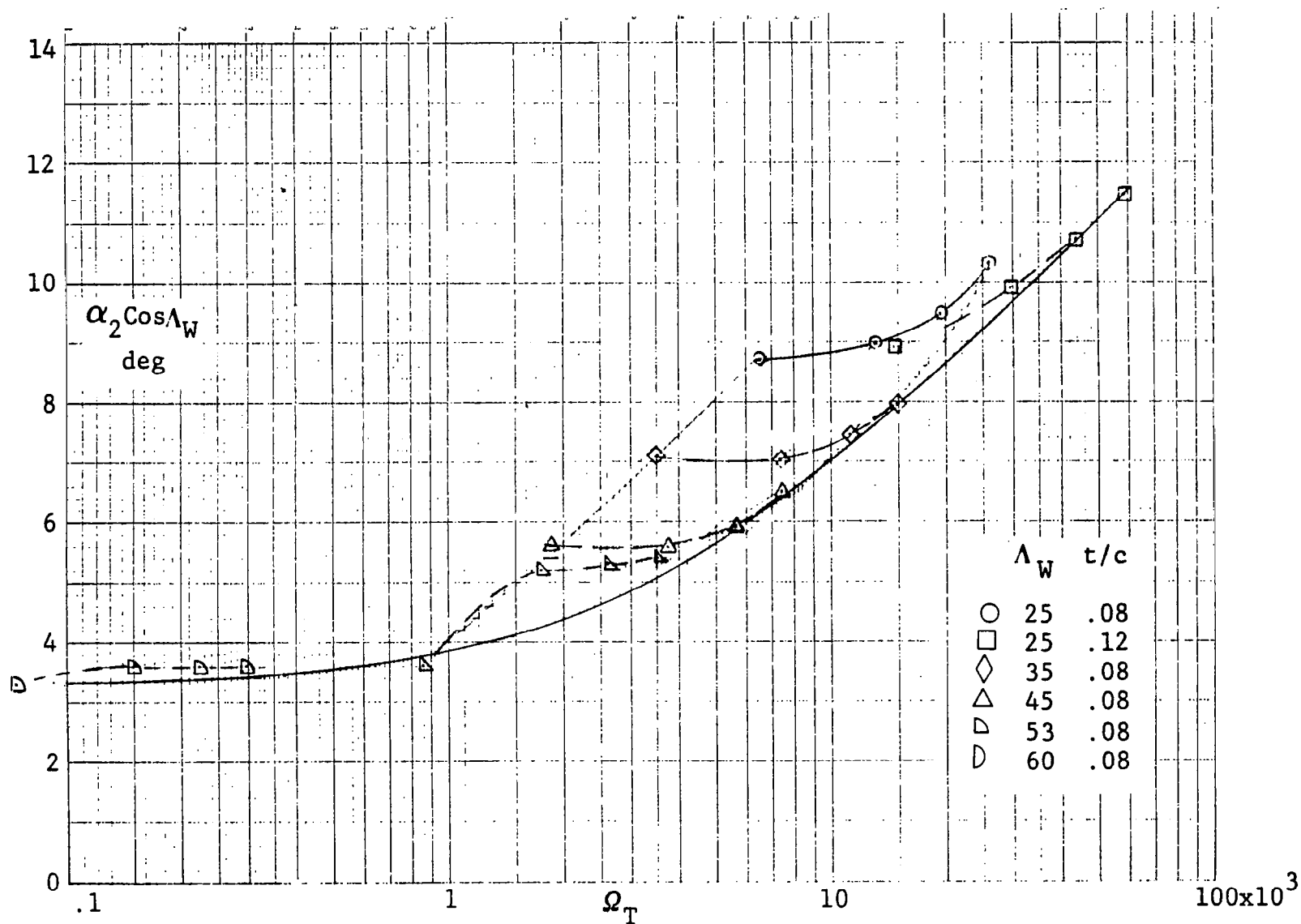
Figure 97.   Correlation of Reynolds Number Effects on α_2 for
Basic Wings Using Ω Function Based on Leading-
Edge Radius at Tip
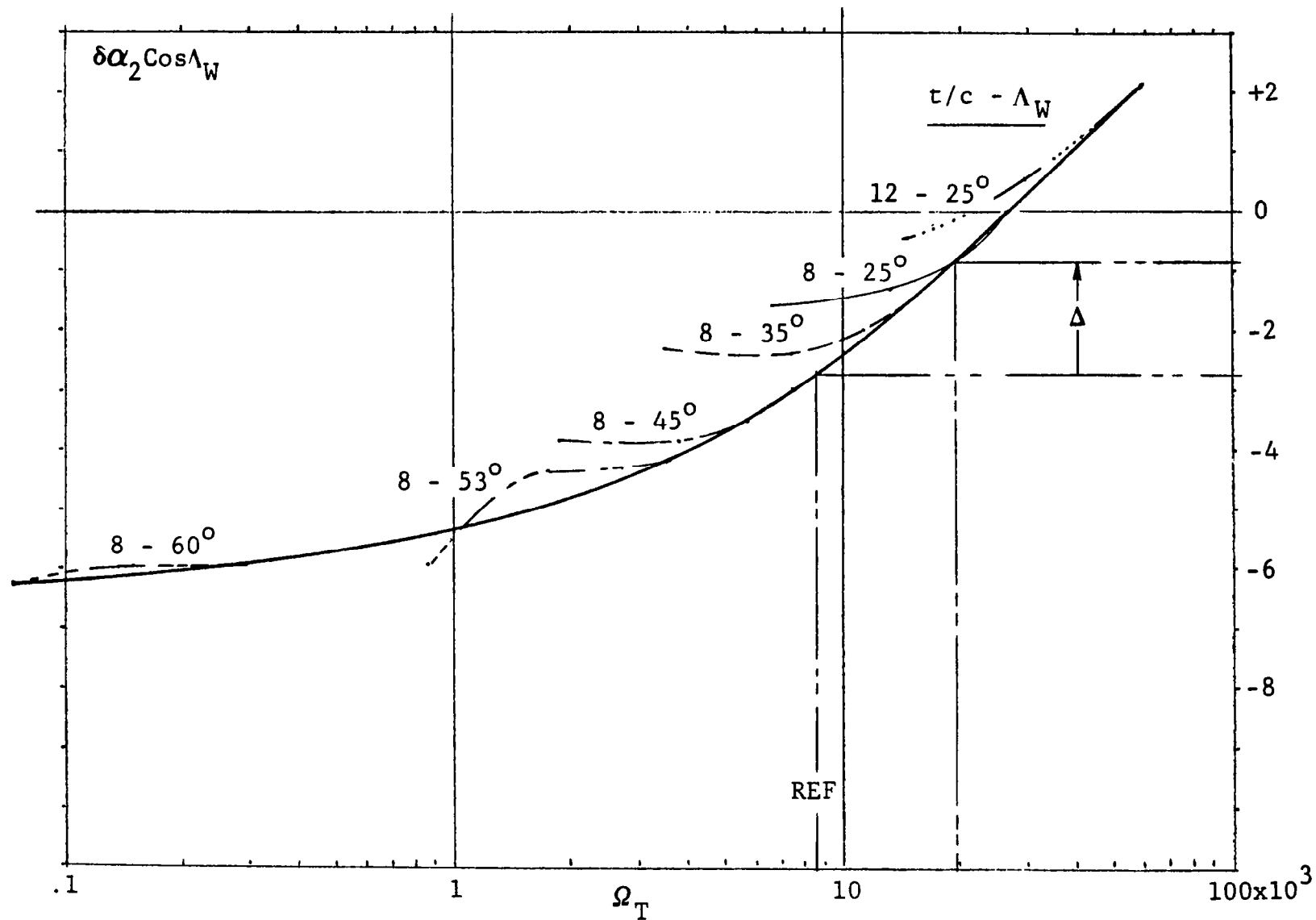
Figure 98. Envelope Correlation Curve for Change in α_2 of Basic Wings Due to Change in Reynolds Number
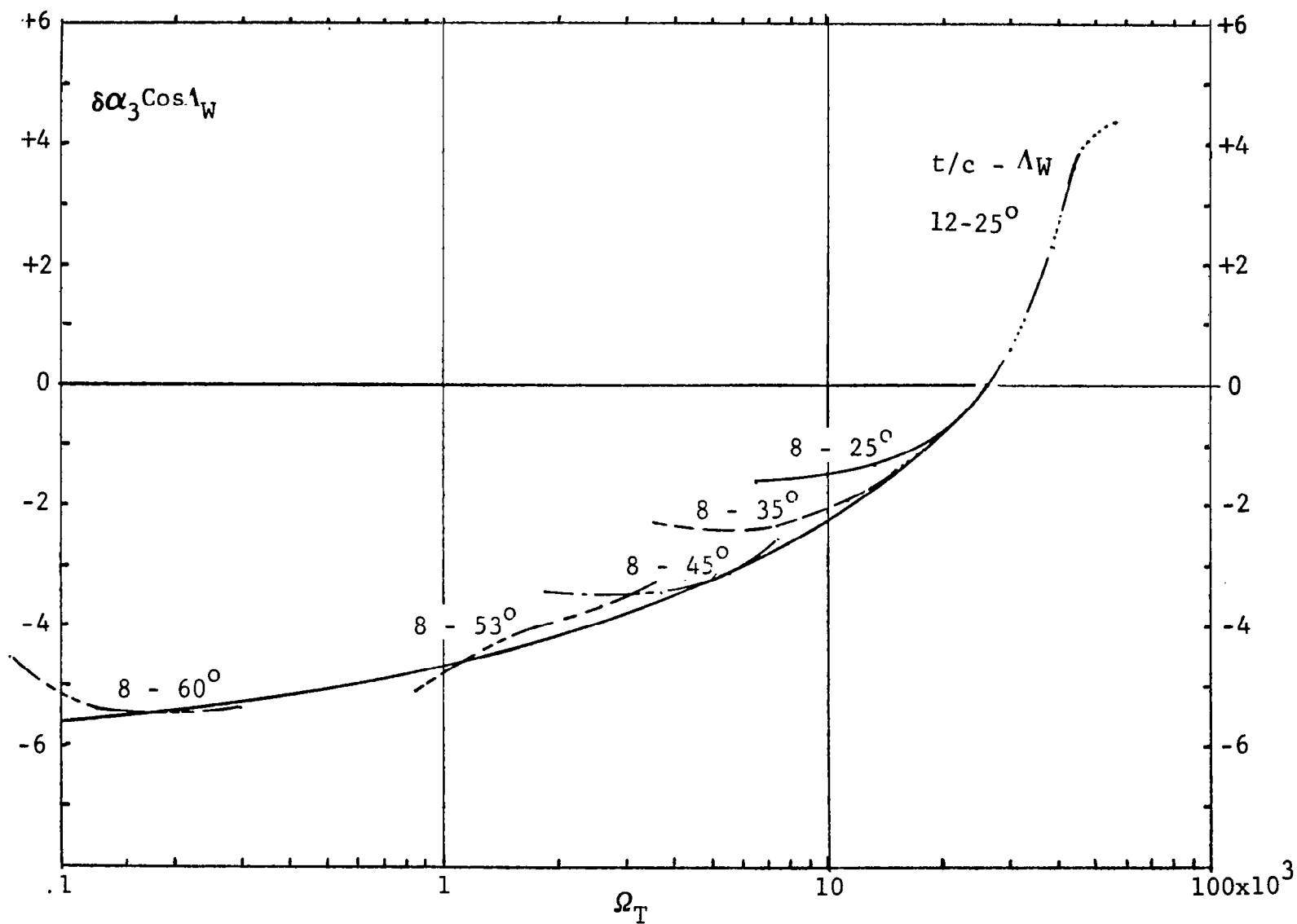
Figure   99.   Envelope Correlation Curve for Change in α_3 of
Basic Wings Due to Change in Reynolds Number
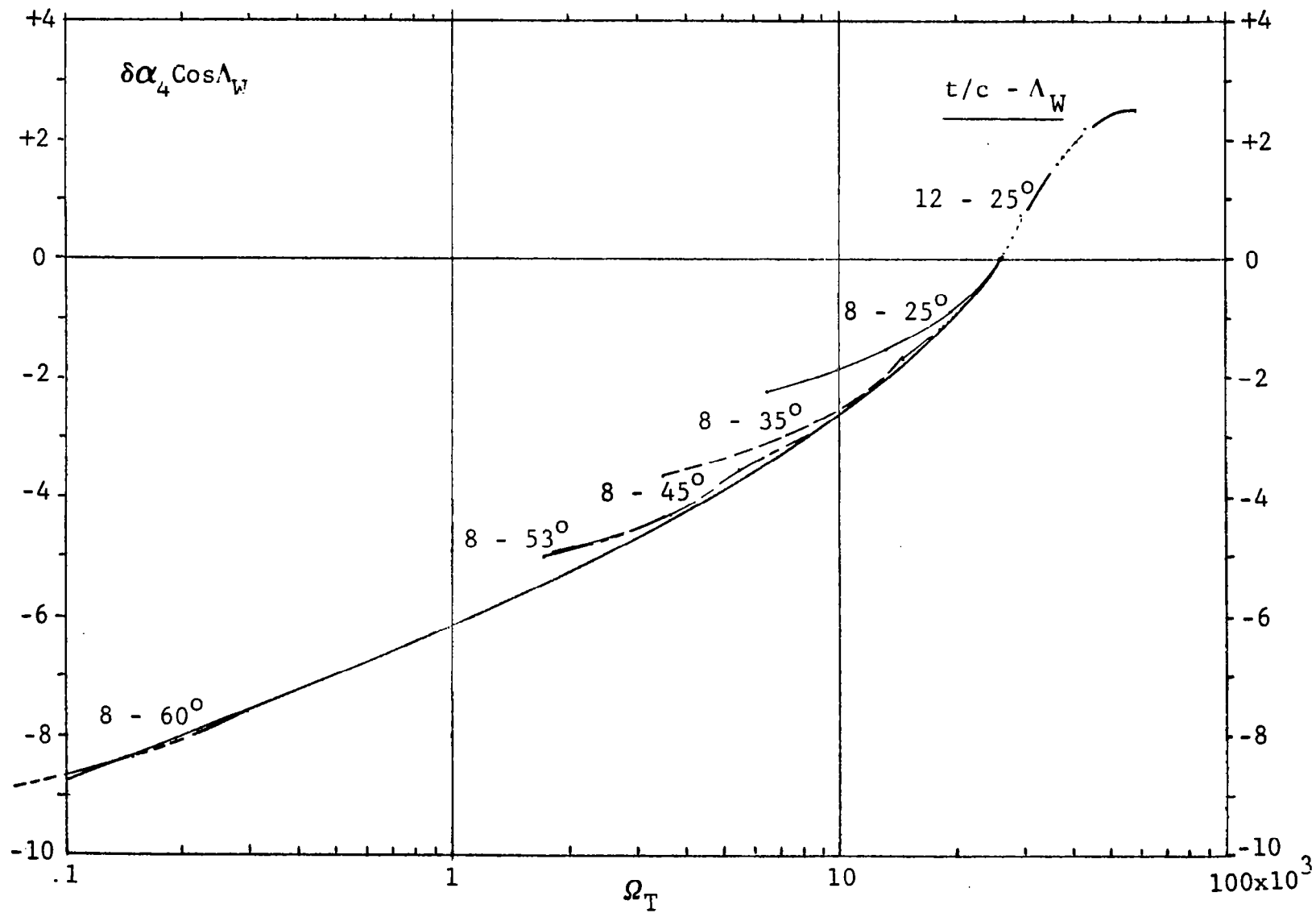
Figure 100.   Envelope Correlation Curve For Change in α_4 of
Basic Wings Due to Change in Reynolds Number
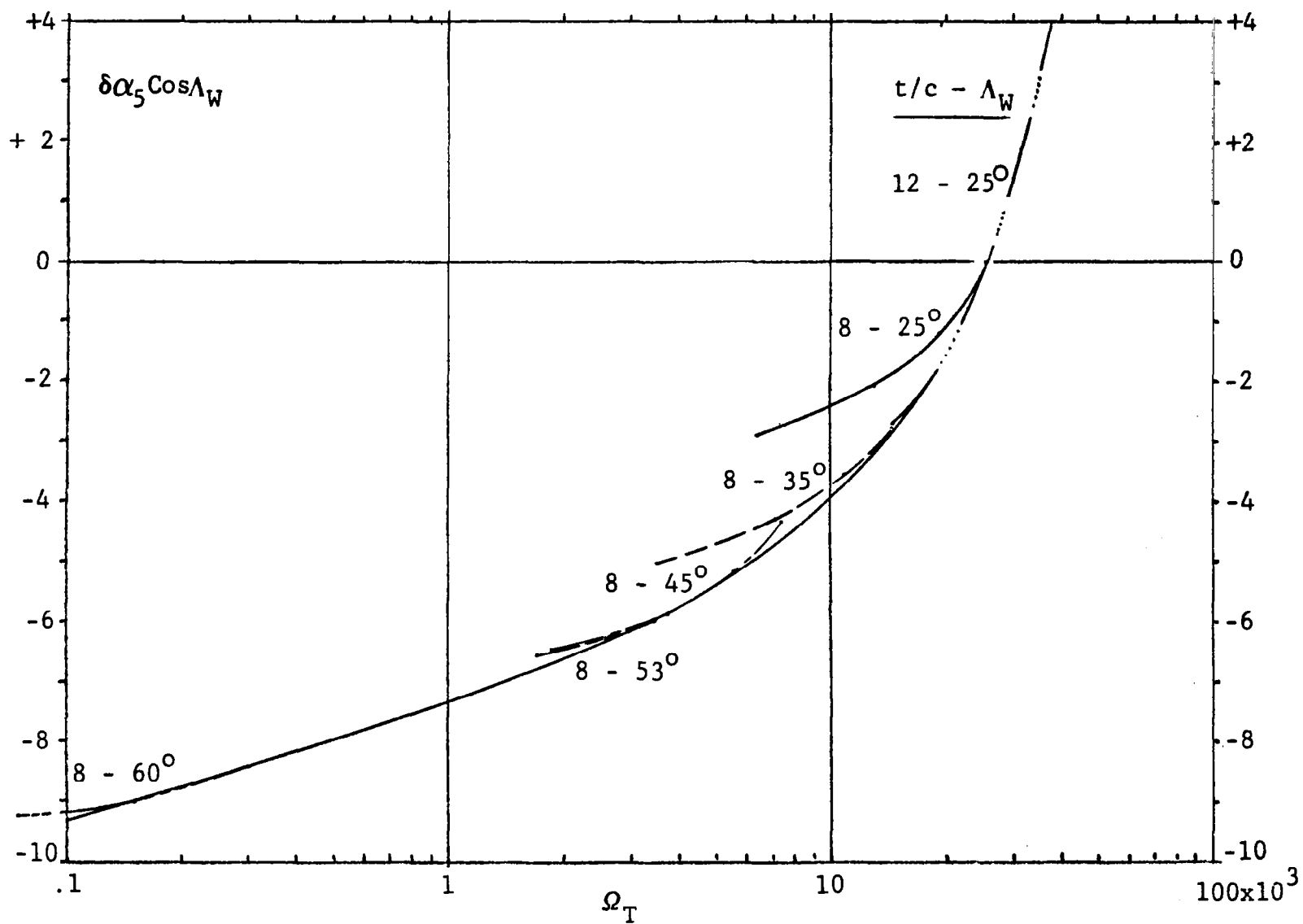
Figure 101.   Envelope Correlation Curve for Change in α_5 of
Basic Wings Due to Change in Reynolds Number
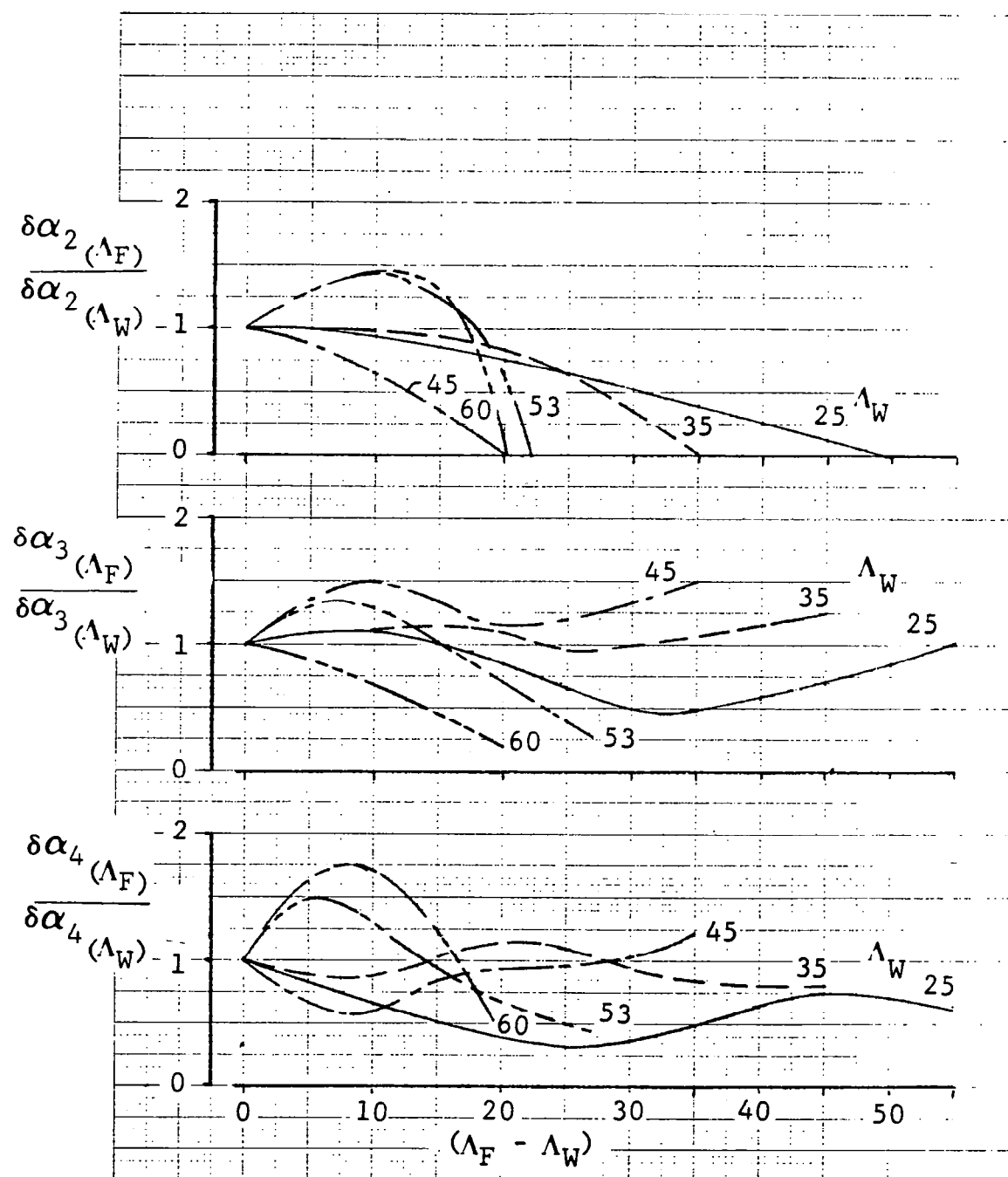
Figure 102. Correction Term for Effect of Fillet Sweep on α Boundaries
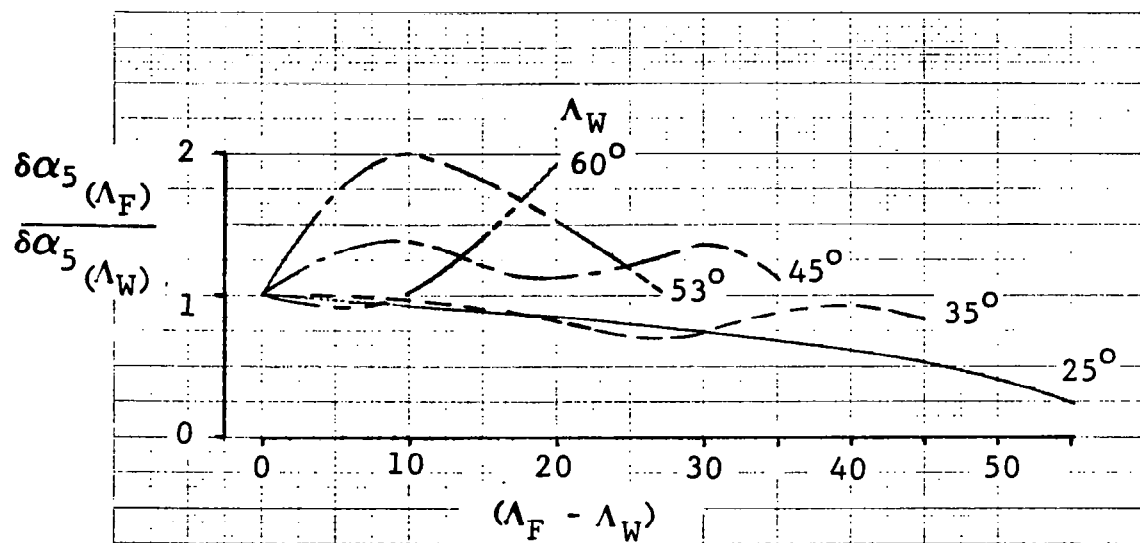
Figure 102. Concluded
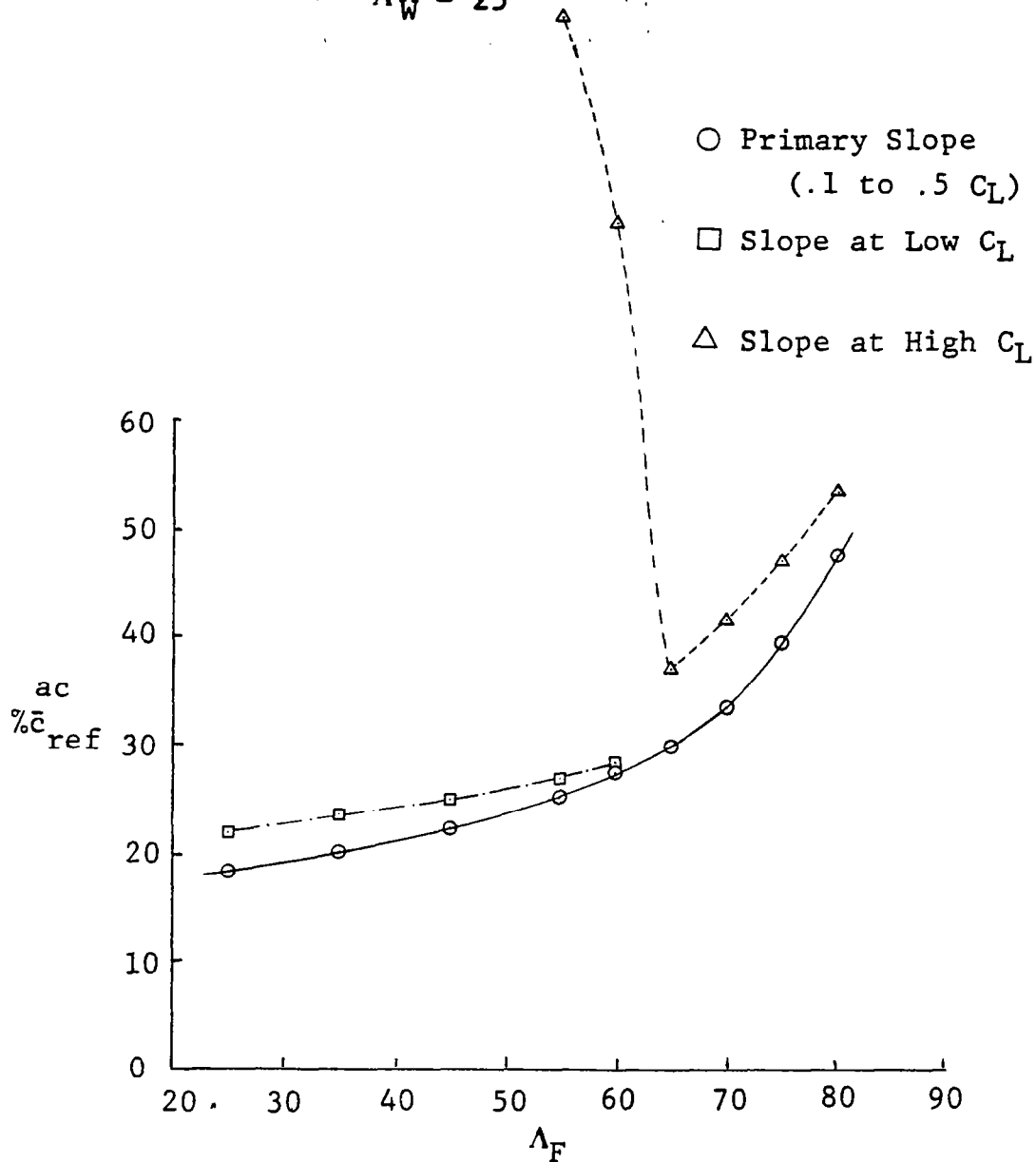
Figure 103. Aerodynamic-Center Locations of SHIPS Wing I Planforms for Various Lift Regions

SHIPS Wind-Tunnel Data

$M = .3$, $R_N = 8.0 \times 10^6 / Ft$

$\Lambda_W = 35^\circ$

○ Primary Slope
(.1 to .5 C_L)

□ Slope at Low C_L

△ Slope at High C_L
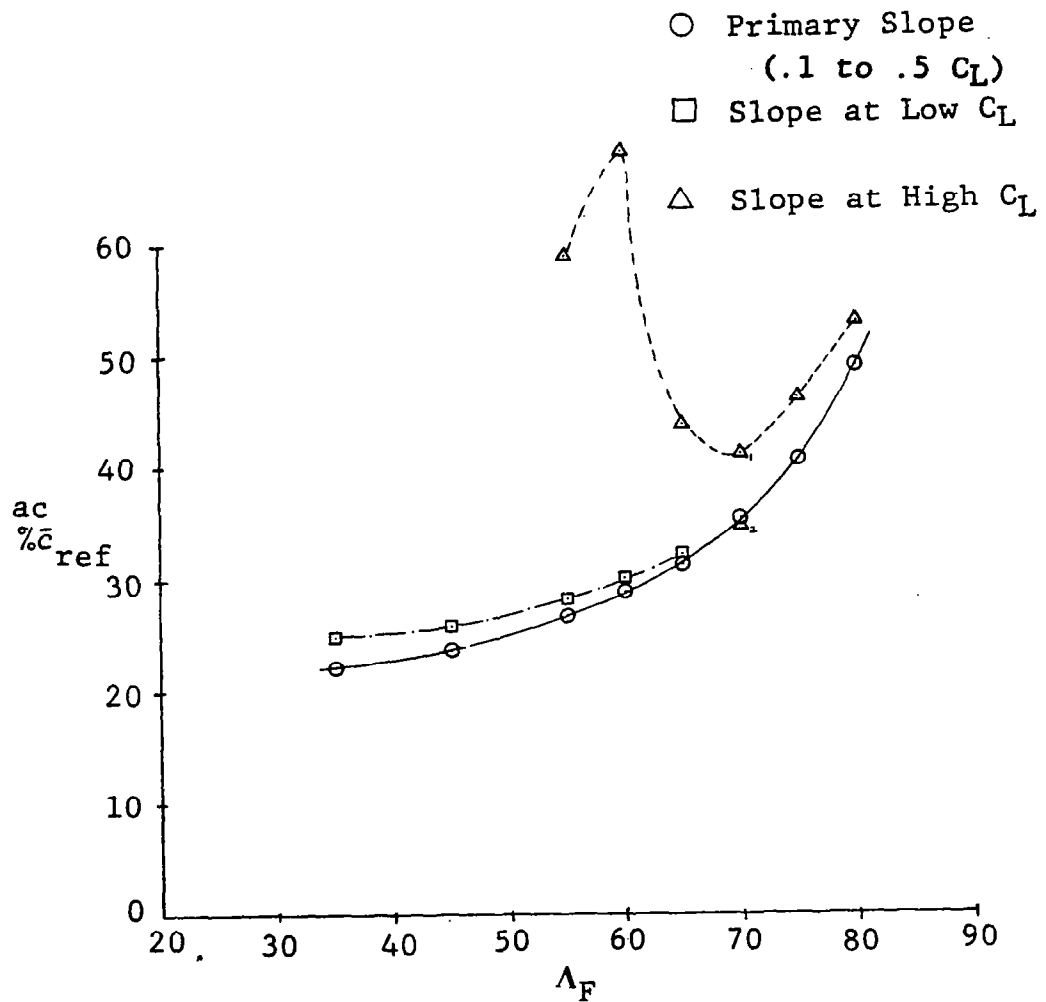
Figure 104. Aerodynamic-Center Locations of SHIPS Wing II Plan-forms for Various Lift Regions
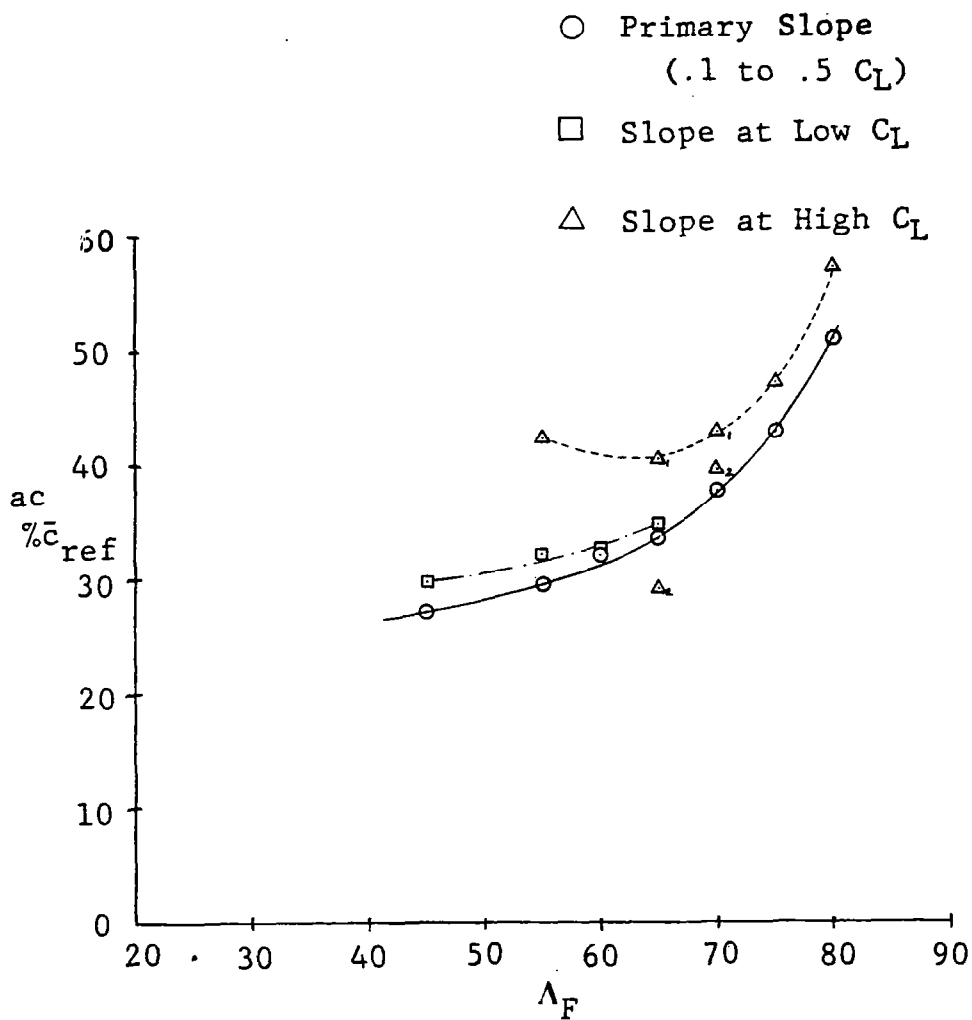
Figure 105. Aerodynamic-Center Locations of SHIPS Wing III Plan-
forms for Various Lift Regions

SHIPS Wind-Tunnel Data

$$M = .3, \quad R_N = 8.0 \times 10^6/\text{Ft}$$

$$\Lambda_W = 53^\circ$$

○ Primary Slope
      (.1 to .5 C_L)
□ Slope at Low C_L
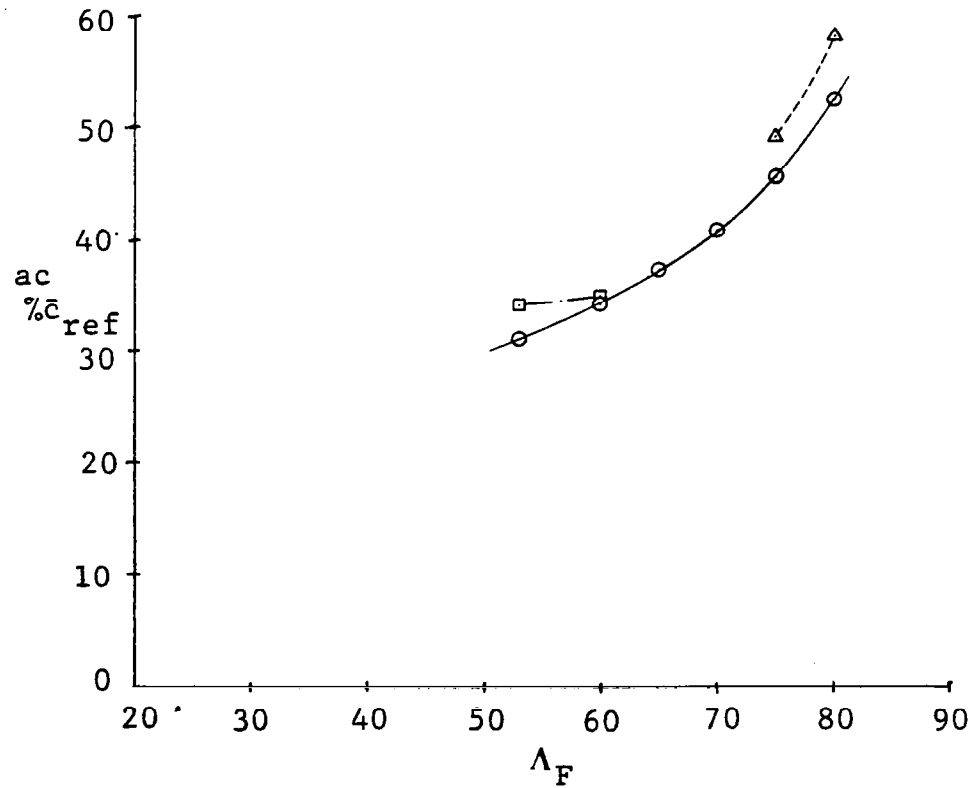
△ Slope at High C_L

Figure 106. Aerodynamic-Center Locations of SHIPS Wing IV Plan-
            forms for Various Lift Regions

SHIPS Wind-Tunnel Data

$M = .3, \quad R_N = 8.0 \times 10^6/\text{Ft}$

$\Lambda_W = 60^\circ$

○ Primary Slope
    $(.1 \text{ to } .5 \text{ C}_L)$
□ Slope at Low C_L

△ Slope at High C_L
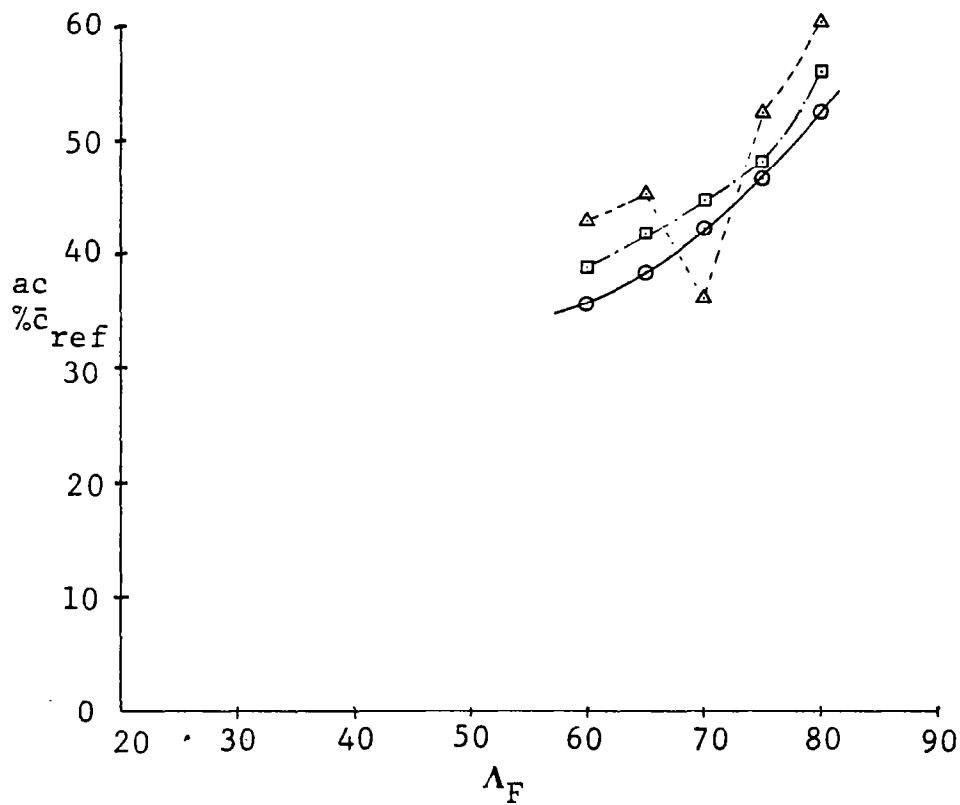
Figure 107. Aerodynamic-Center Locations of SHIPS Wing V Plan-
forms for Various Lift Regions

SHIPS Wind-Tunnel Data

$M = .3$, $R_N = 8.0 \times 10^6/Ft$

SYM	Λ_W
$\bigcirc$	25°
$\square$	35°
$\diamondsuit$	45°
$\triangle$	53°
$\hexagon$	60°
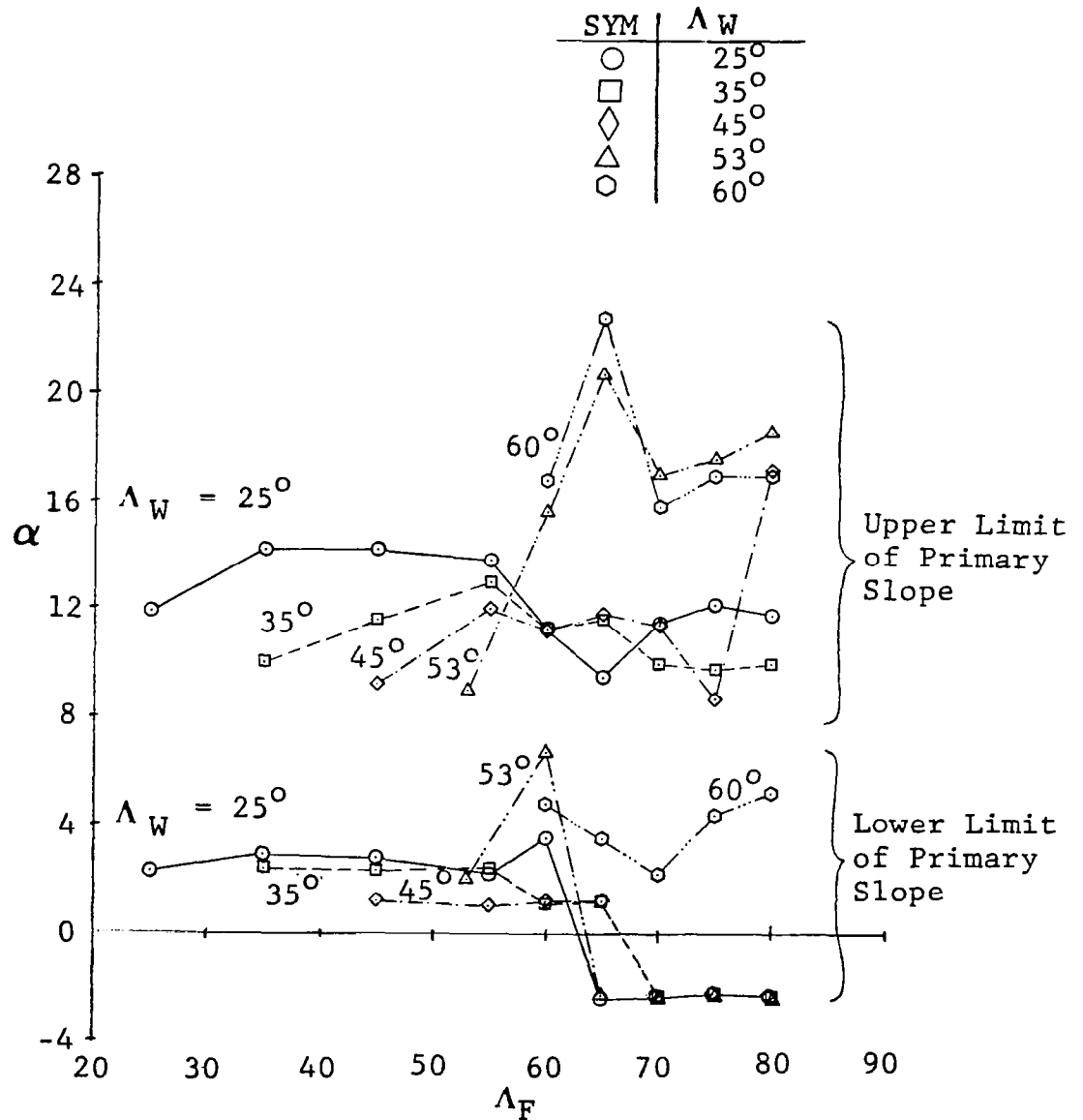
Figure 108. Angle-of-Attack Envelope for Primary Aerodynamic-
Center Location

SHIPS Wind-Tunnel Data

$M = .3, \quad R_N = 8.0 \times 10^6 / Ft$

SYM	Λ_W
○	25°
□	35°
◇	45°
△	53°
⬡	60°
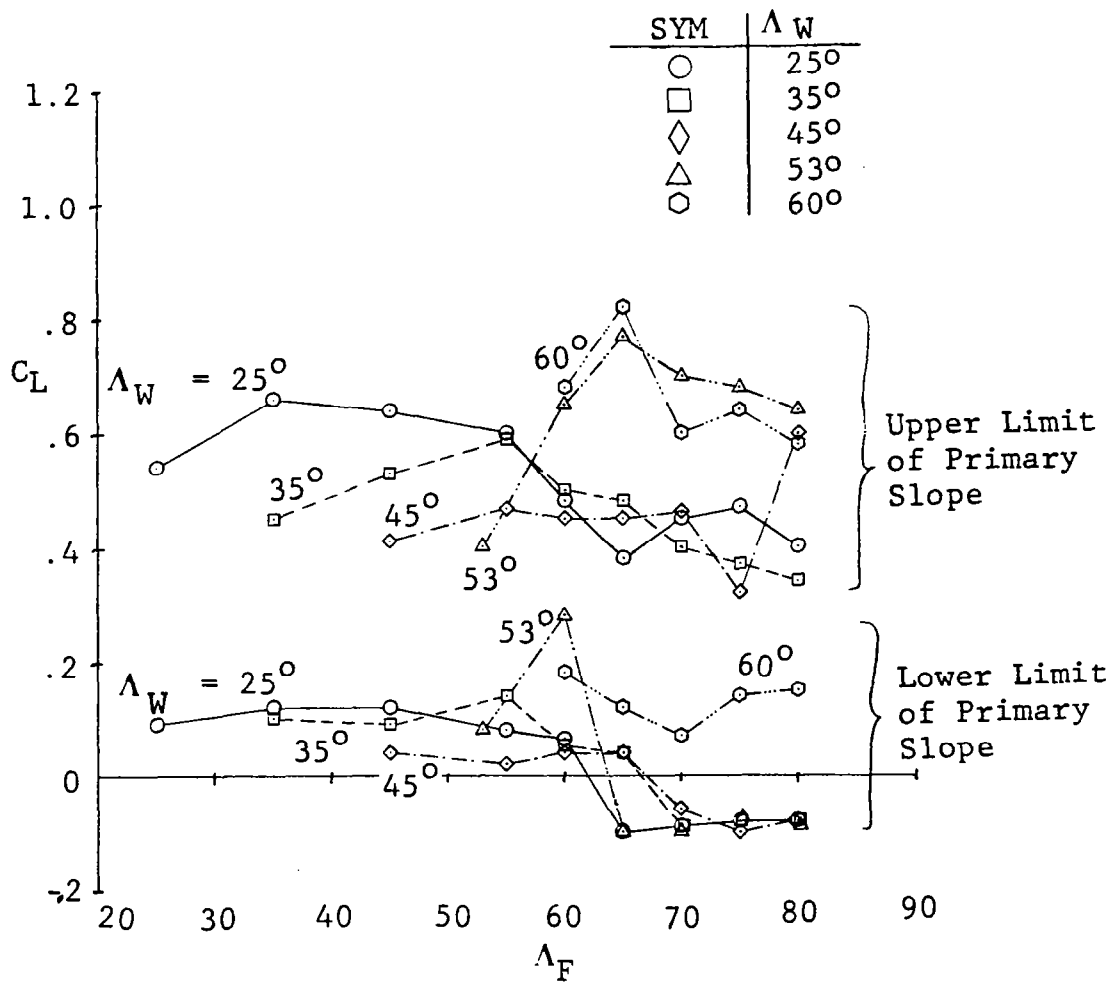
Figure 109.   Lift-Coefficient Envelope for Primary Aerodynamic-Center Location
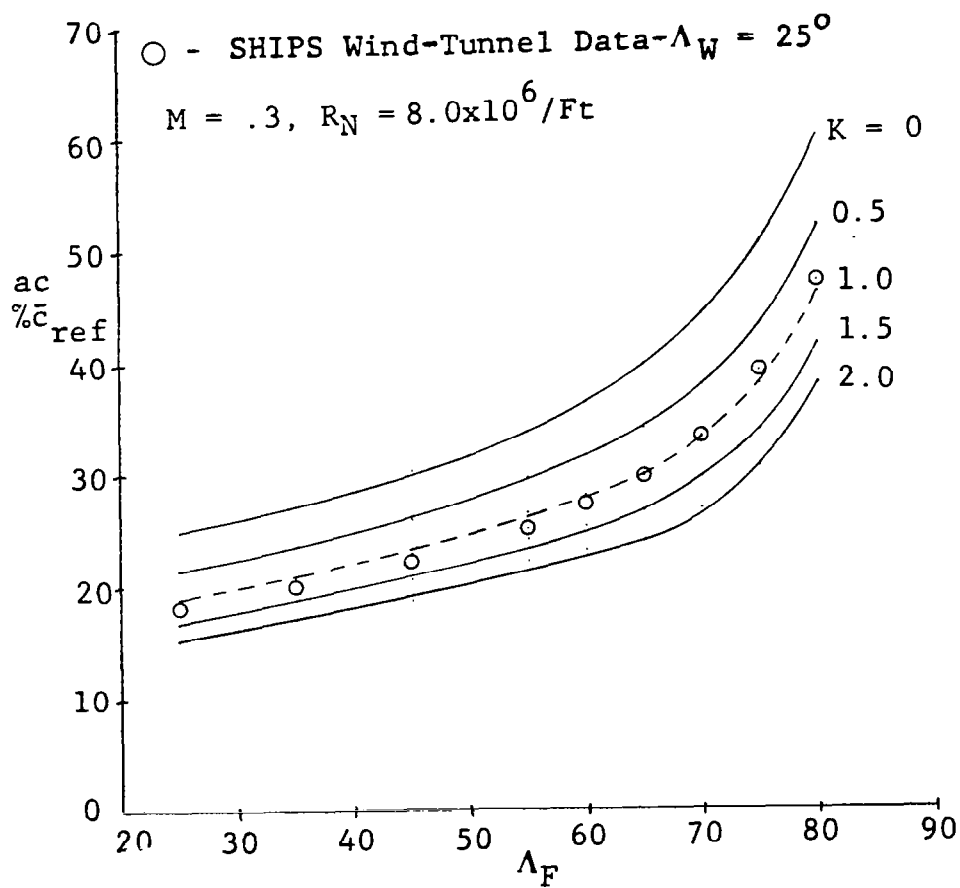
Figure 110. Aerodynamic-Center Prediction - Paniszczyn Method Modified by K Factor Applied to Lift of Inboard Panel - Wing I Planforms
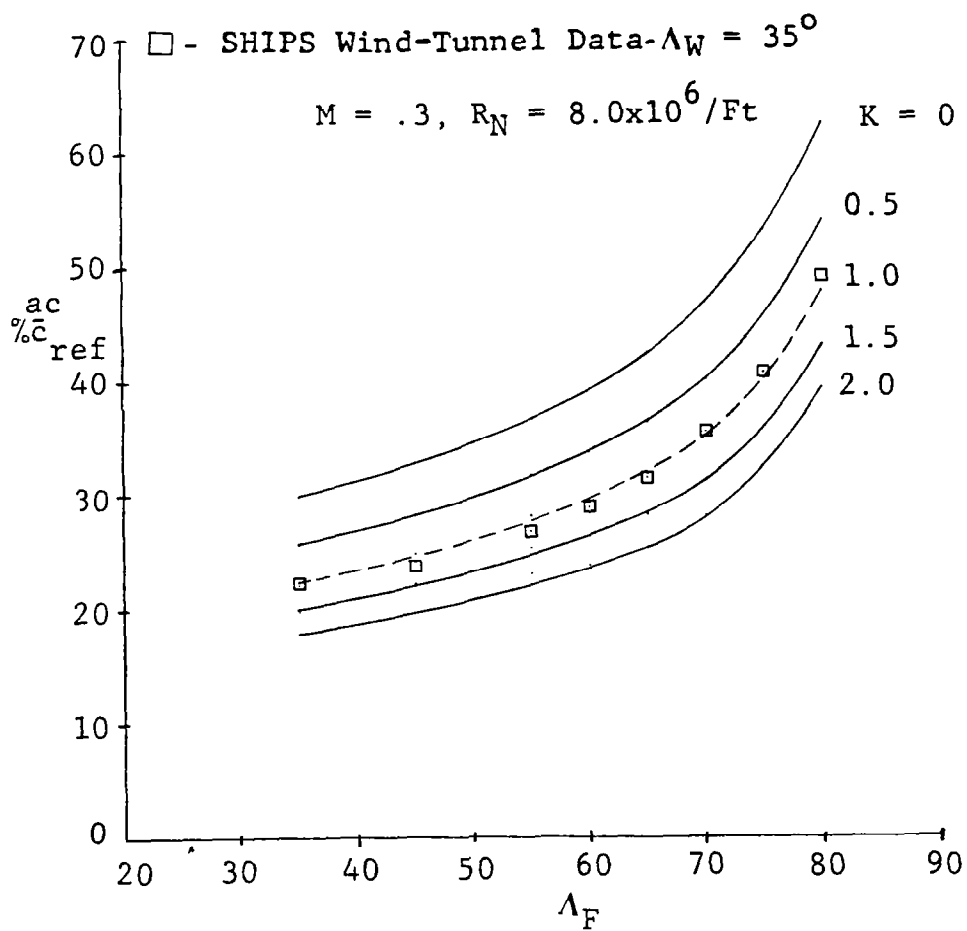
Figure 111.   Aerodynamic-Center Prediction - Paniszczyn Method
Modified by K Factor Applied to Lift of Inboard
Panel - Wing II Planforms
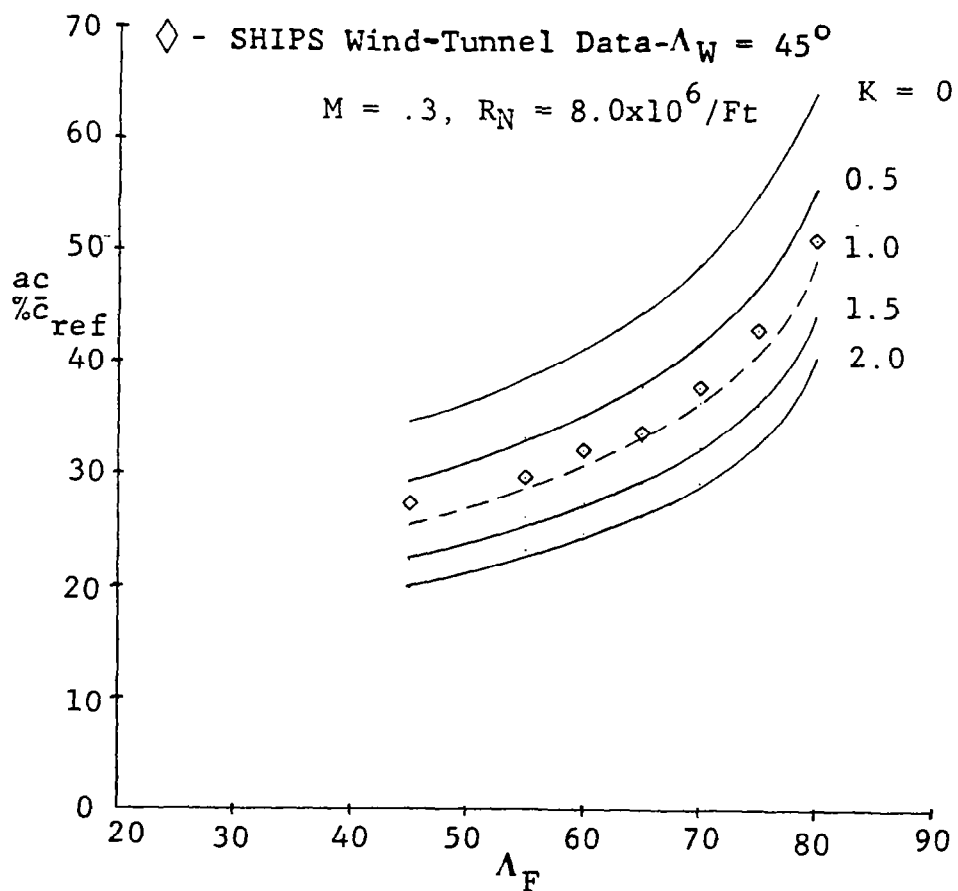
Figure 112.   Aerodynamic-Center Prediction - Paniszczyn Method
Modified by K Factor Applied to Lift of Inboard
Panel - Wing III Planforms
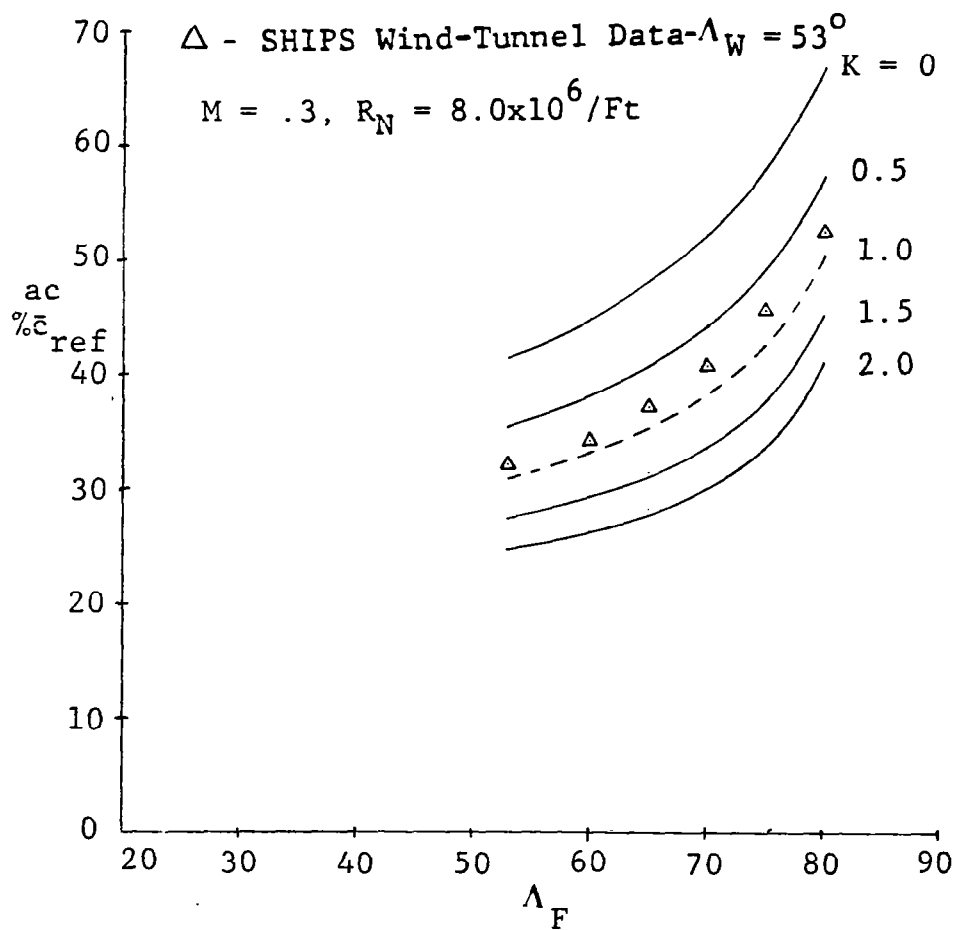
Figure 113. Aerodynamic Center Prediction - Paniszczyn Method
Modified by K Factor Applied to Lift of Inboard
Panel - Wing IV Planforms
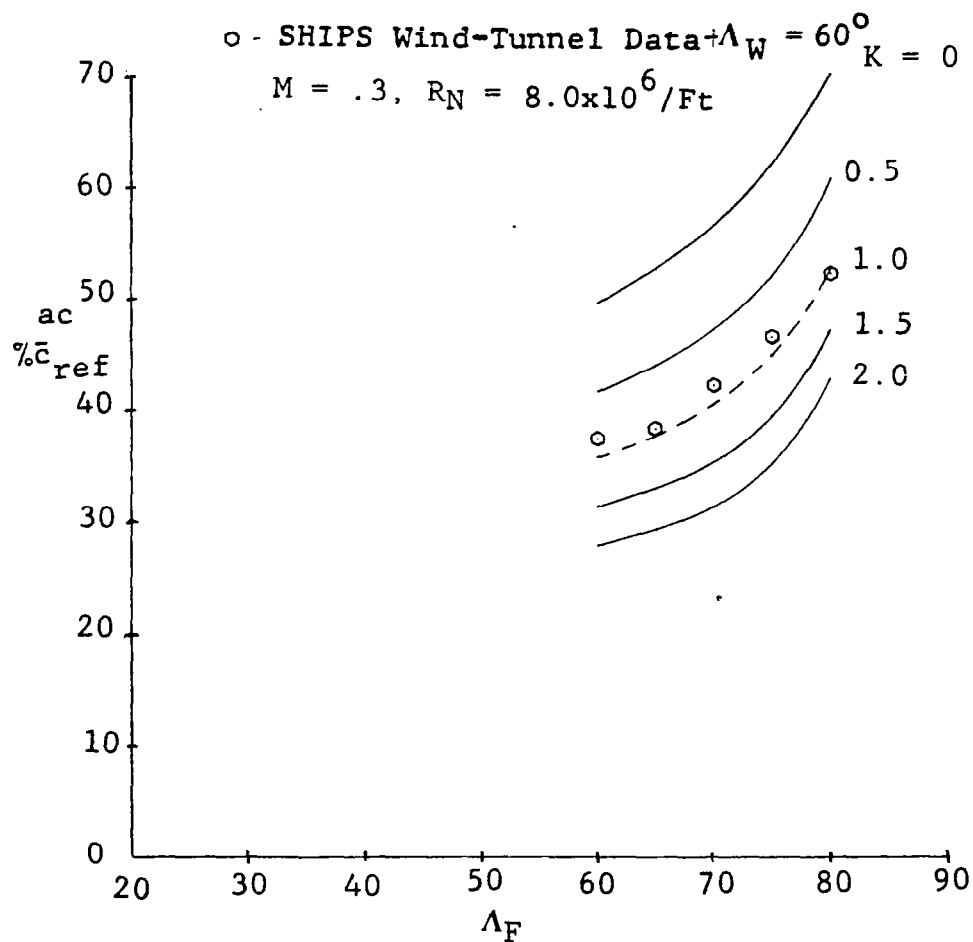
Figure 114. Aerodynamic-Center Prediction - Paniszczyn Method
Modified by K Factor Applied to Lift of Inobard
Planforms - Wing V Planforms

SHIPS Wind-Tunnel Data

$$M = .3, \quad R_N = 8.0 \times 10^6 / Ft$$

Primary Slope

$$(C_L \approx .1 \text{ to } .5)$$

SYM	Λ_W
⭘	60°
△	53°
◇	45°
☐	35°
○	25°

ac
$\%\bar{c}_{ref}$

Λ_F
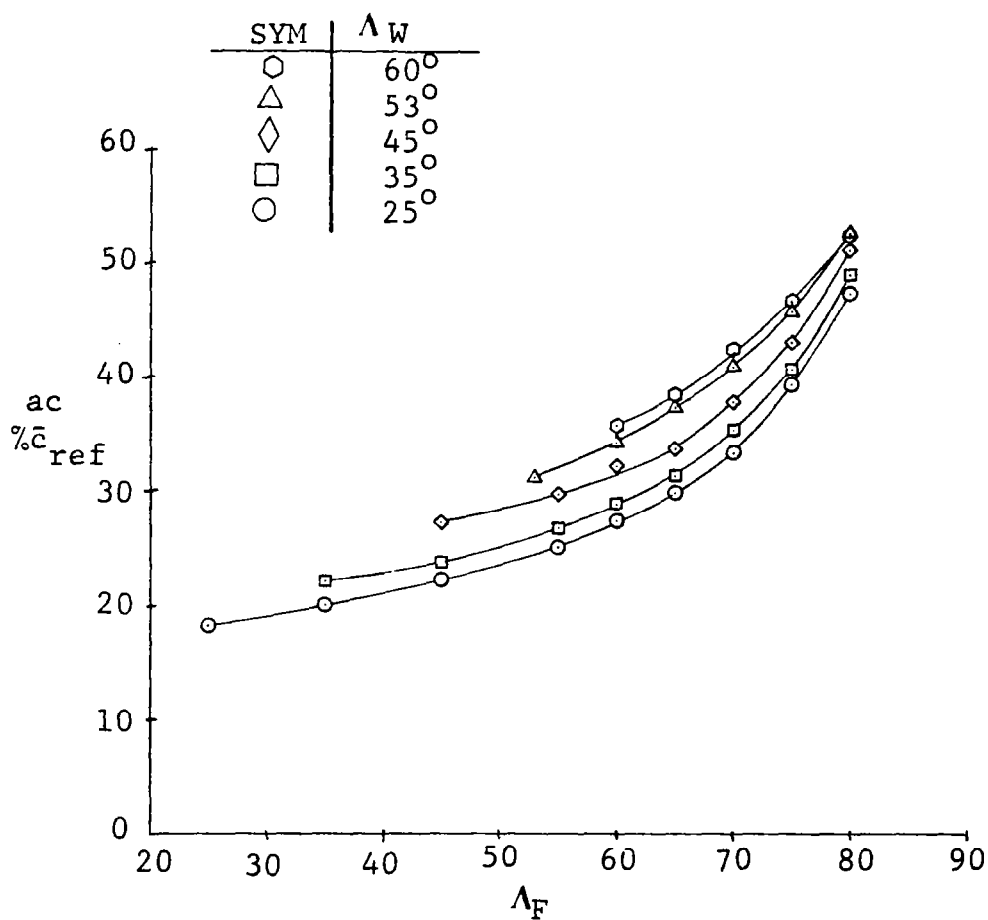
Figure 115. Aerodynamic-Center Location Referenced to Mean
Geometric Chord of Each Irregular Planform

SHIPS Wind-Tunnel Data

$M = .3$, $R_N = 8.0 \times 10^6/\text{Ft}$

Primary Slope

$(C_L \approx .1 \text{ to } .5)$

SYM	Λ_W
◯	60°
△	53°
◇	45°
▢	35°
◯	25°

ac %c̄ of Each Basic Wing

Λ_F
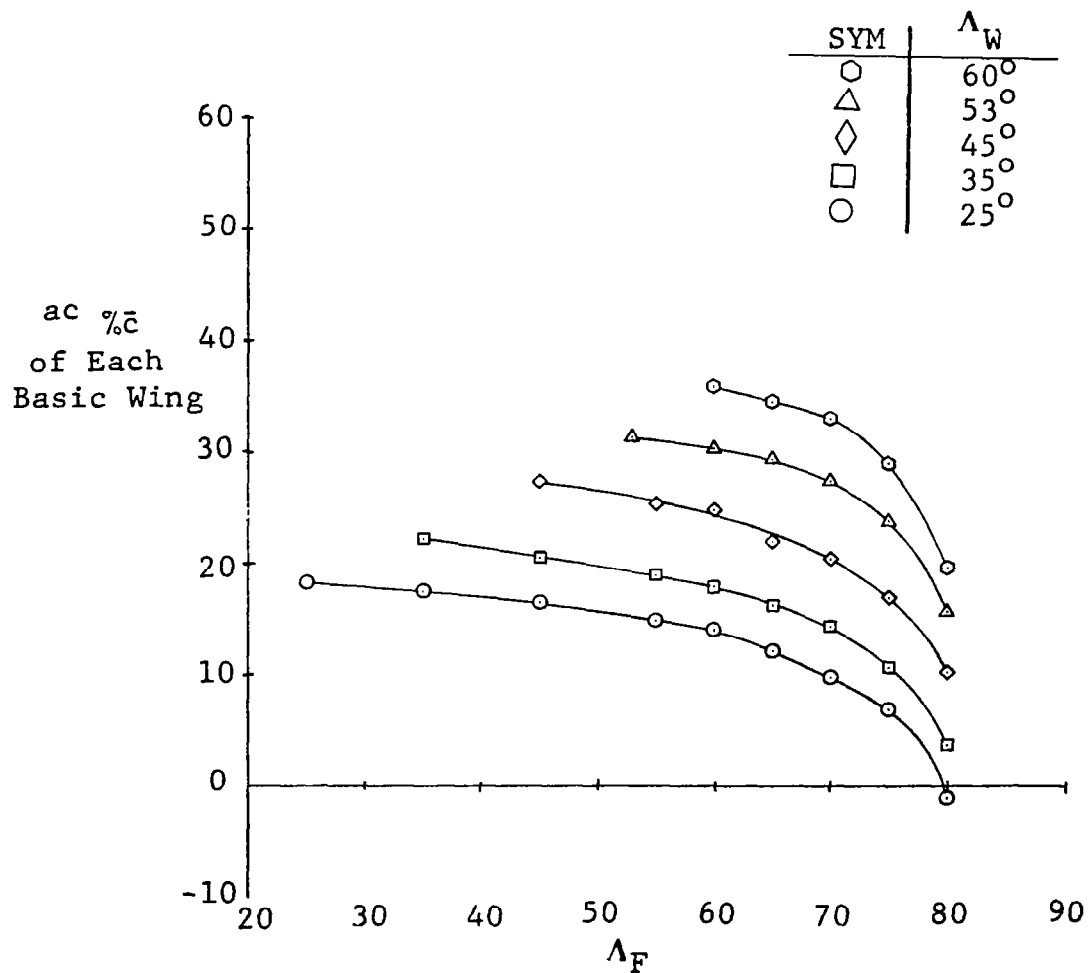
Figure 116. Aerodynamic Center Referenced to Mean Geometric Chord of Each Basic Wing

SHIPS Wind-Tunnel Data

$M = .3$, $R_N = 8.0 \times 10^6$/Ft

Primary Slope

$(C_L \approx .1$ to $.5)$

FS ac from $80°$ apex of each wing

SYM	Λ_W
⬡	$60°$
△	$53°$
◇	$45°$
☐	$35°$
○	$25°$
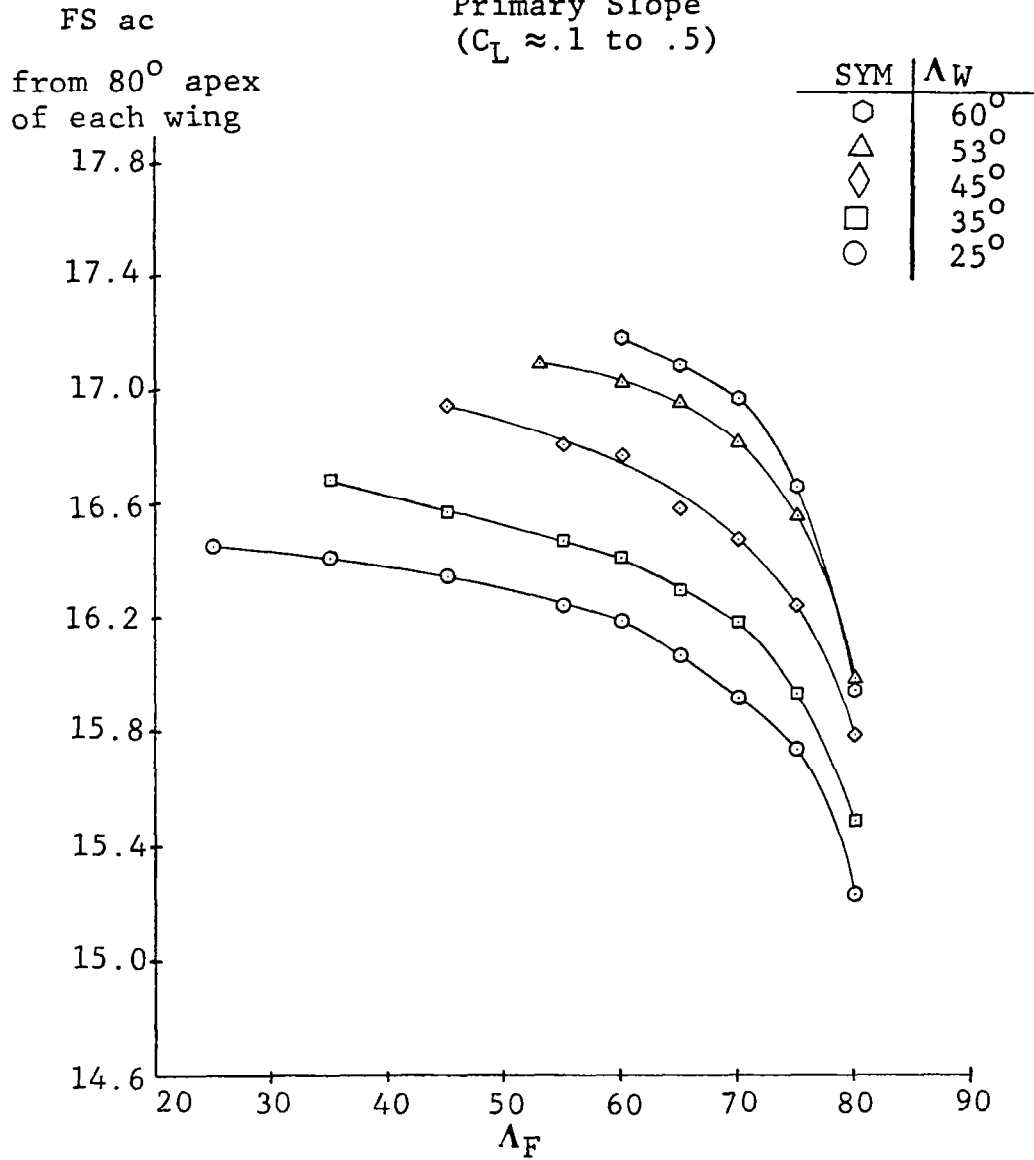
Figure 117.   Aerodynamic-Center Location Referenced to Apex of $80°$ Fillet for Each Planform Family

SHIPS Wind-Tunnel Data

$M = .3$, $R_N = 8.0 \times 10^6$/Ft

Primary Slope

$(C_L \approx .1$ to $.5)$

SYM	Λ_W
$\bigcirc$	60°
$\triangle$	53°
$\diamondsuit$	45°
$\square$	35°
$\bigcirc$	25°

FS$\bar{c}$/4 = 16.887 For all Basic Wings
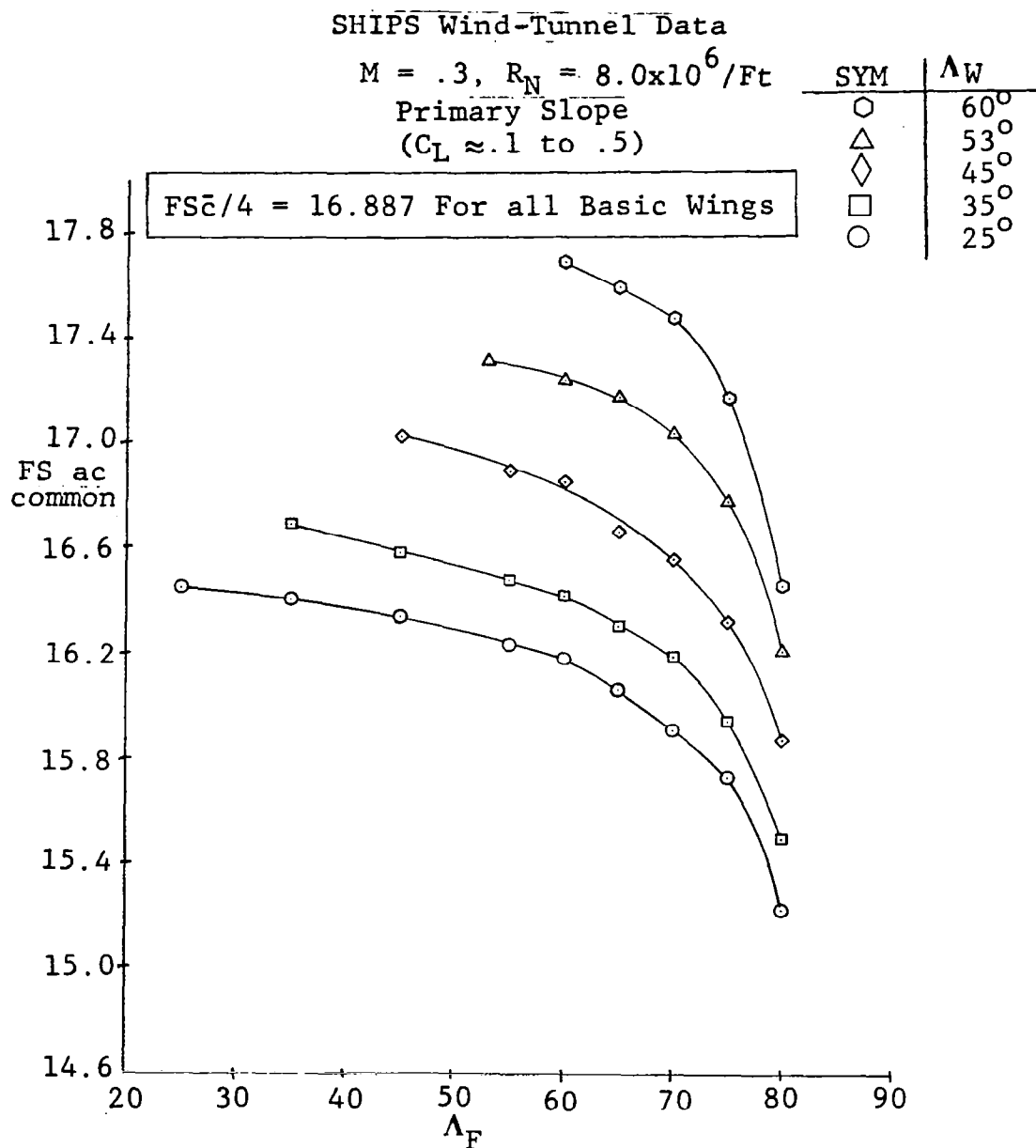
Figure 118. Aerodynamic-Center Location Referenced to Apex of $80^{\circ}/25^{\circ}$ Planform with Common Location of Quarter Chord of MGC of each Basic Wing

SHIPS Wind-Tunnel Data

$$M = .3, \quad R_N = 8(10)^6$$
Primary Slope
$$(C_L \approx .1 \text{ to } .5)$$

SYM	Λ_W
⬡	60°
△	53°
◇	45°
☐	35°
○	25°
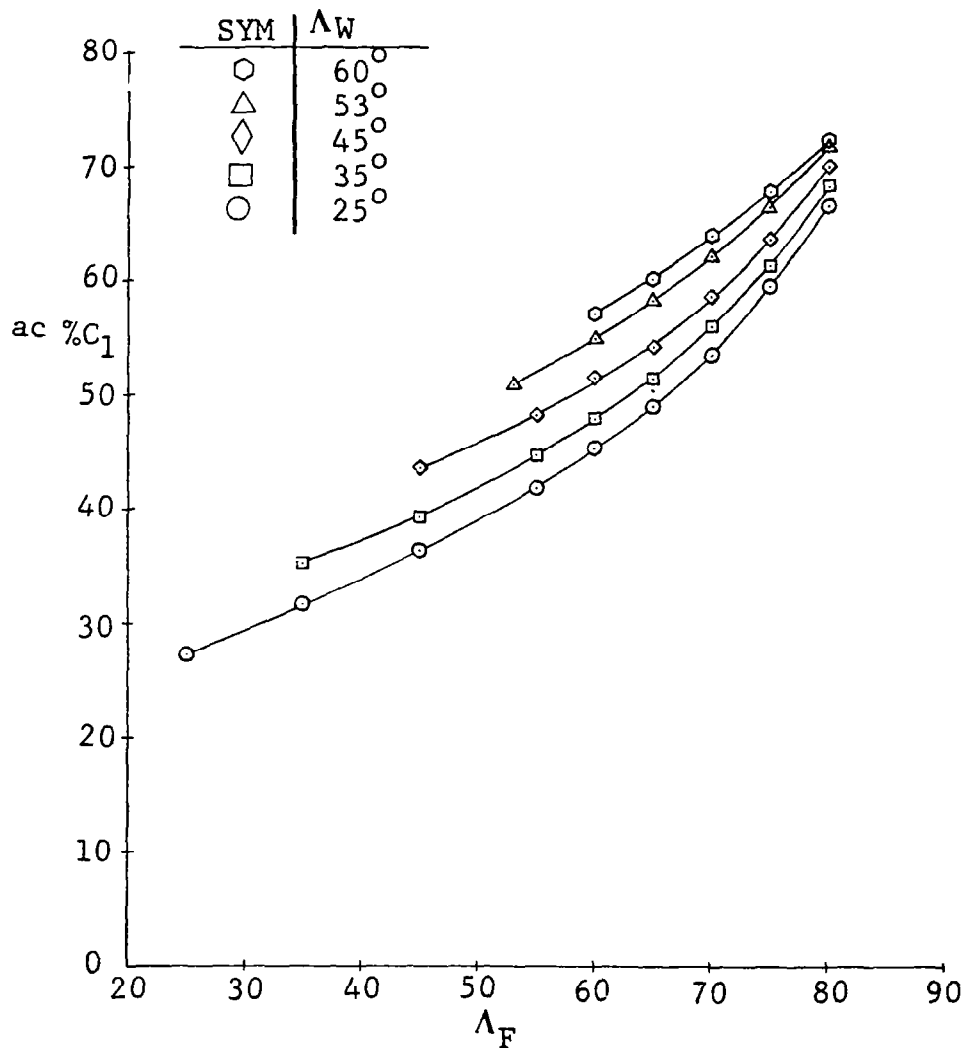
Figure 119. Aerodynamic-Center Location as a Percentage of Root Chord of Each Irregular Planform

SHIPS Wind-Tunnel Data

$M = .3, \ R_N = 8.0 \times 10^6 / Ft$
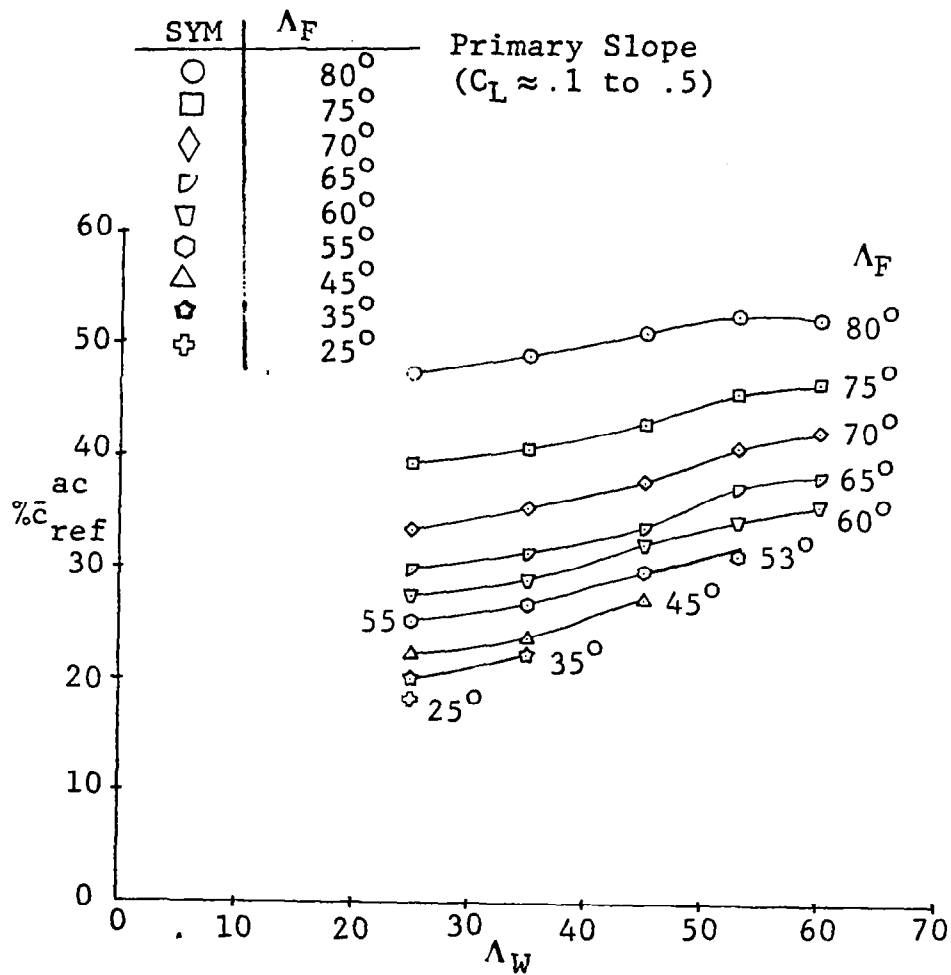
Figure 120. Variation of Aerodynamic-Center Location Referenced
to Mean Geometric Chord of Each Irregular Planform
with Outer Panel Leading-Edge Sweep

SHIPS Wind-Tunnel Data

$M = .3$, $R_N = 8.0 \times 10^6$/Ft

Primary Slope ($C_L \approx .1$ to .5)
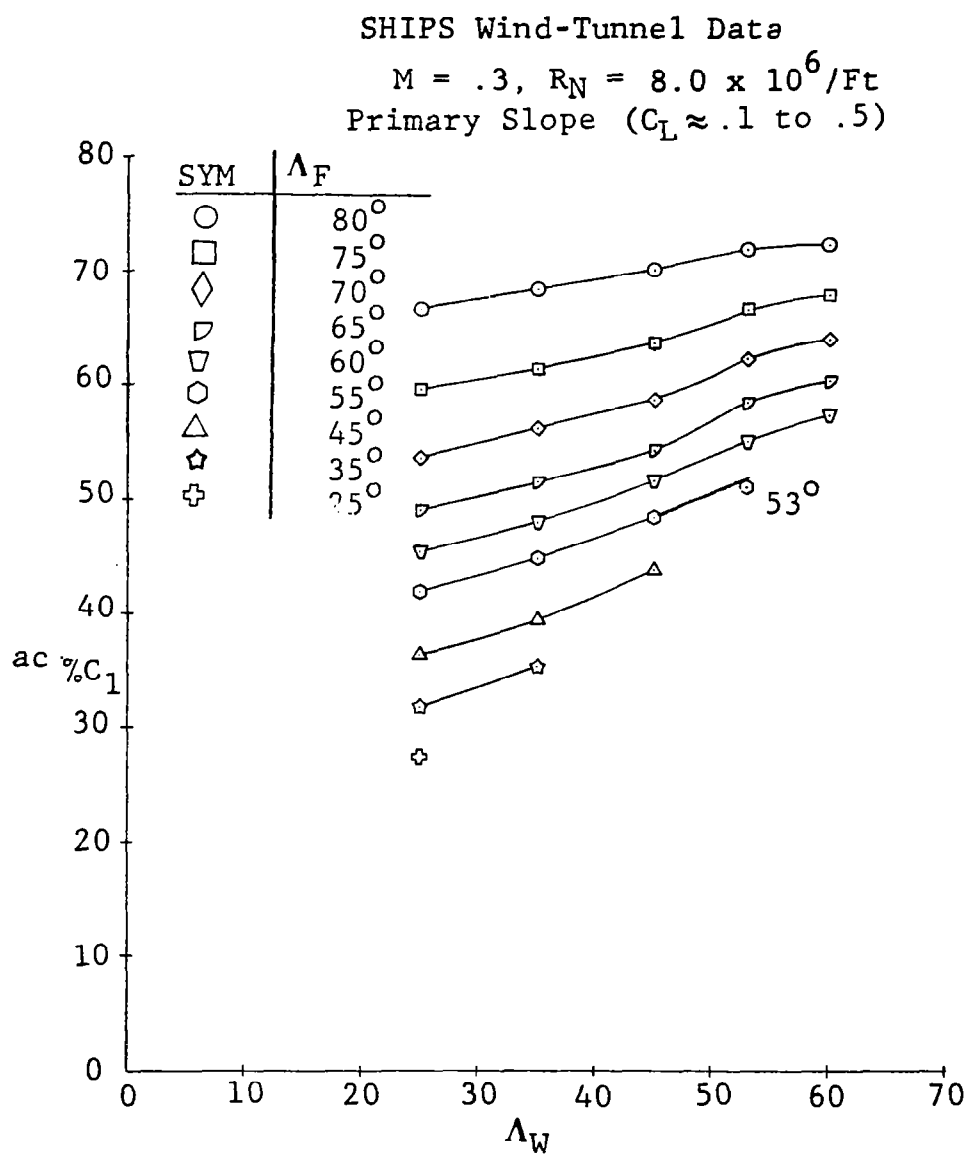
Figure 121. Variation of Aerodynamic-Center Location as a Per-
centage of Root Chord of Each Irregular Planform
with Outer Panel Leading-Edge Sweep

SHIPS Wind-Tunnel Data

M = .3
25° Wing

SYM	R_N /Ft
○	$8 (10)^6$
□	$6 (10)^6$
◇	$4 (10)^6$
△	$2 (10)^6$
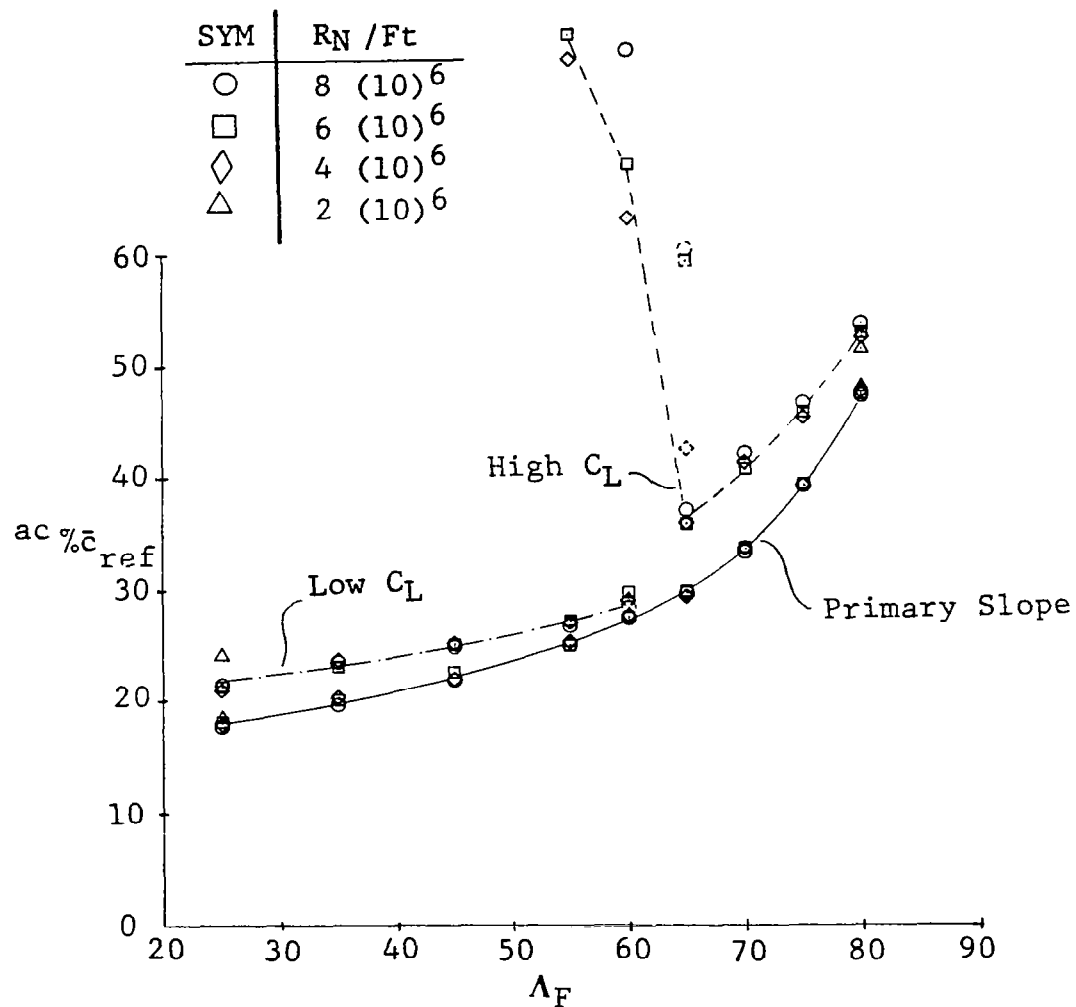
Figure 122. Effect of Reynolds Number on Aerodynamic-Center Location for Various Lift Regions - Wing I Plan-forms

SHIPS Wind-Tunnel Data

M = .3
35° Wing
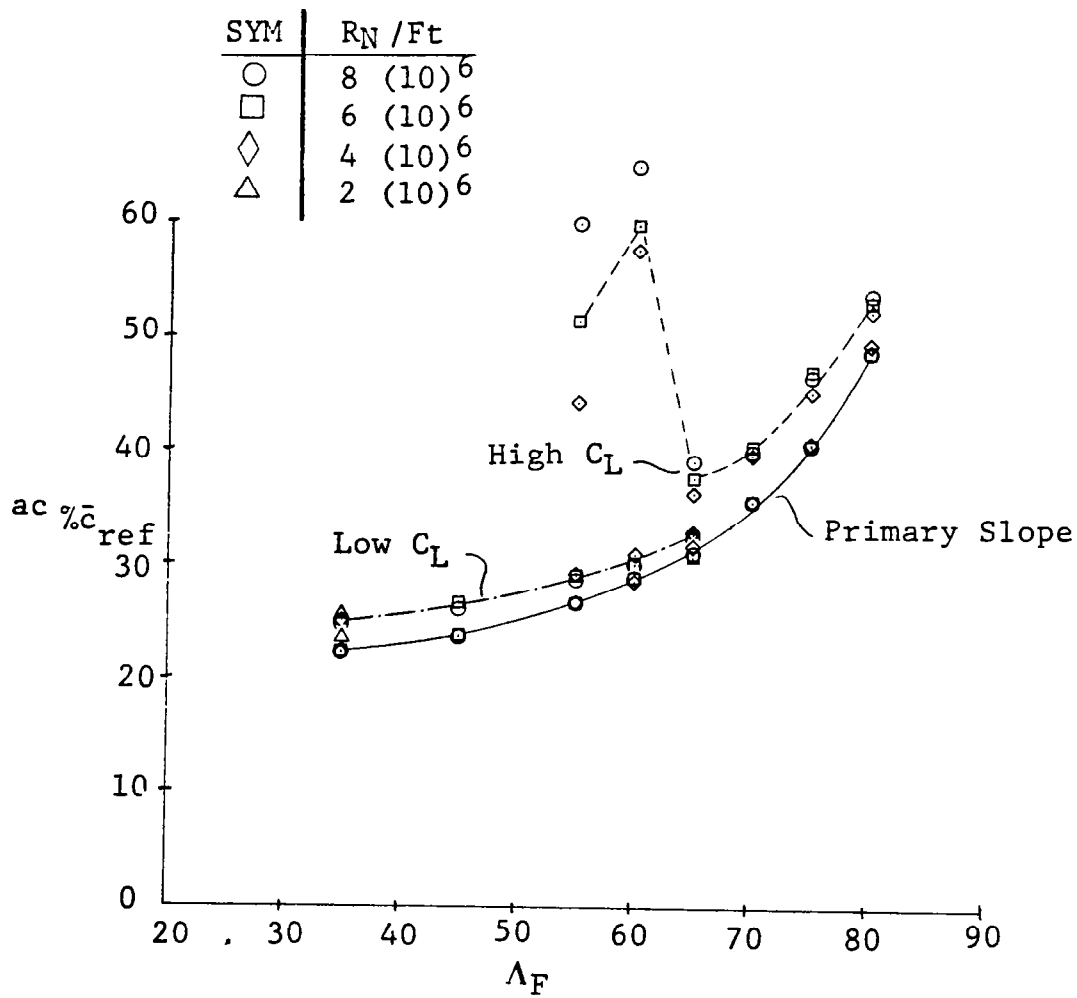
Figure 123. Effect of Reynolds Number on Aerodynamic-Center
Location for Various Lift Regions - Wing II Plan-
forms

SHIPS Wind-Tunnel Data

$$M = .3$$
$$45^{\circ}\ \text{Wing}$$

SYM	R_N /Ft
$\bigcirc$	$8\ (10)^6$
$\square$	$6\ (10)^6$
$\diamondsuit$	$4\ (10)^6$
$\triangle$	$2\ (10)^6$

ac $\%\bar{c}_{ref}$

High C_L

Low C_L

Primary Slope

Λ_F
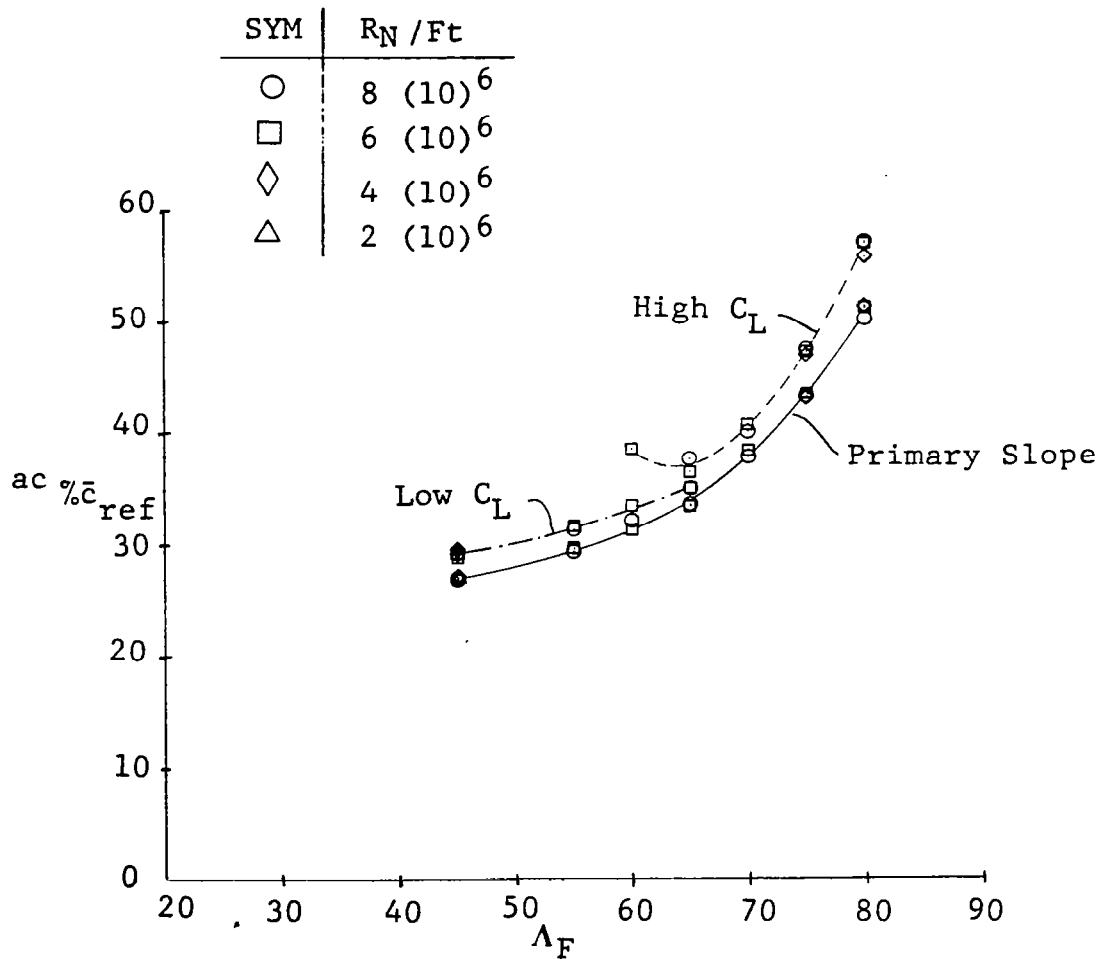
Figure 124. Effect of Reynolds Number on Aerodynamic-Center Location for Various Lift Reigons - Wing III Planforms

SHIPS Wind-Tunnel Data

$$M = .3$$

$$53^{\circ} \text{ Wing}$$
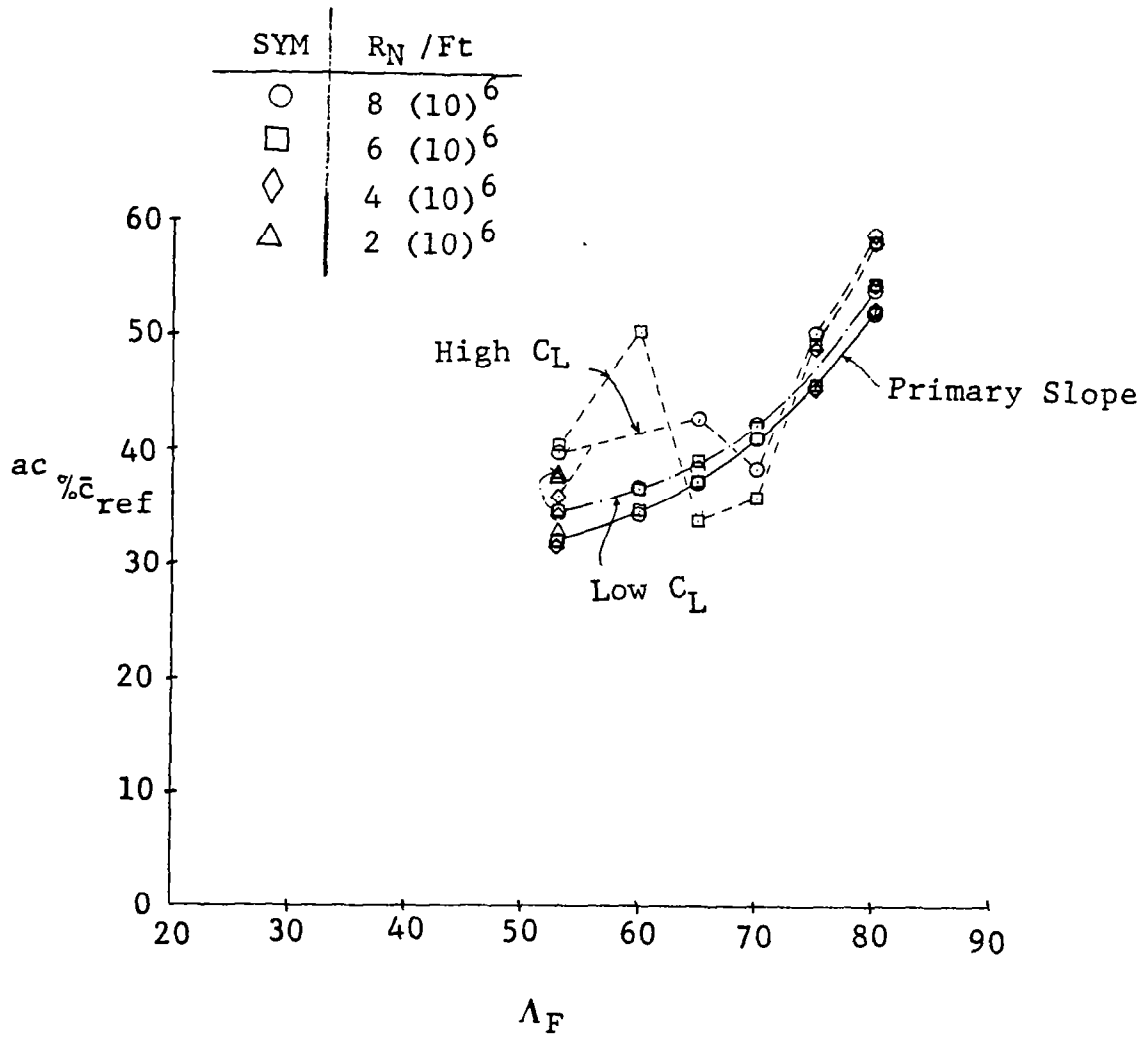
Figure 125. Effect of Reynolds Number on Aero-
dynamic-Center Location for Various
Lift Regions - Wing IV Planforms

SHIPS Wind-Tunnel Data

$M = .3$

60° Wing

SYM	R_N /Ft
○	$8 \ (10)^6$
□	$6 \ (10)^6$
◊	$4 \ (10)^6$
△	$2 \ (10)^6$

High C_L

Low C_L

Primary Slope

ac $\%\bar{c}_{ref}$

Λ_F
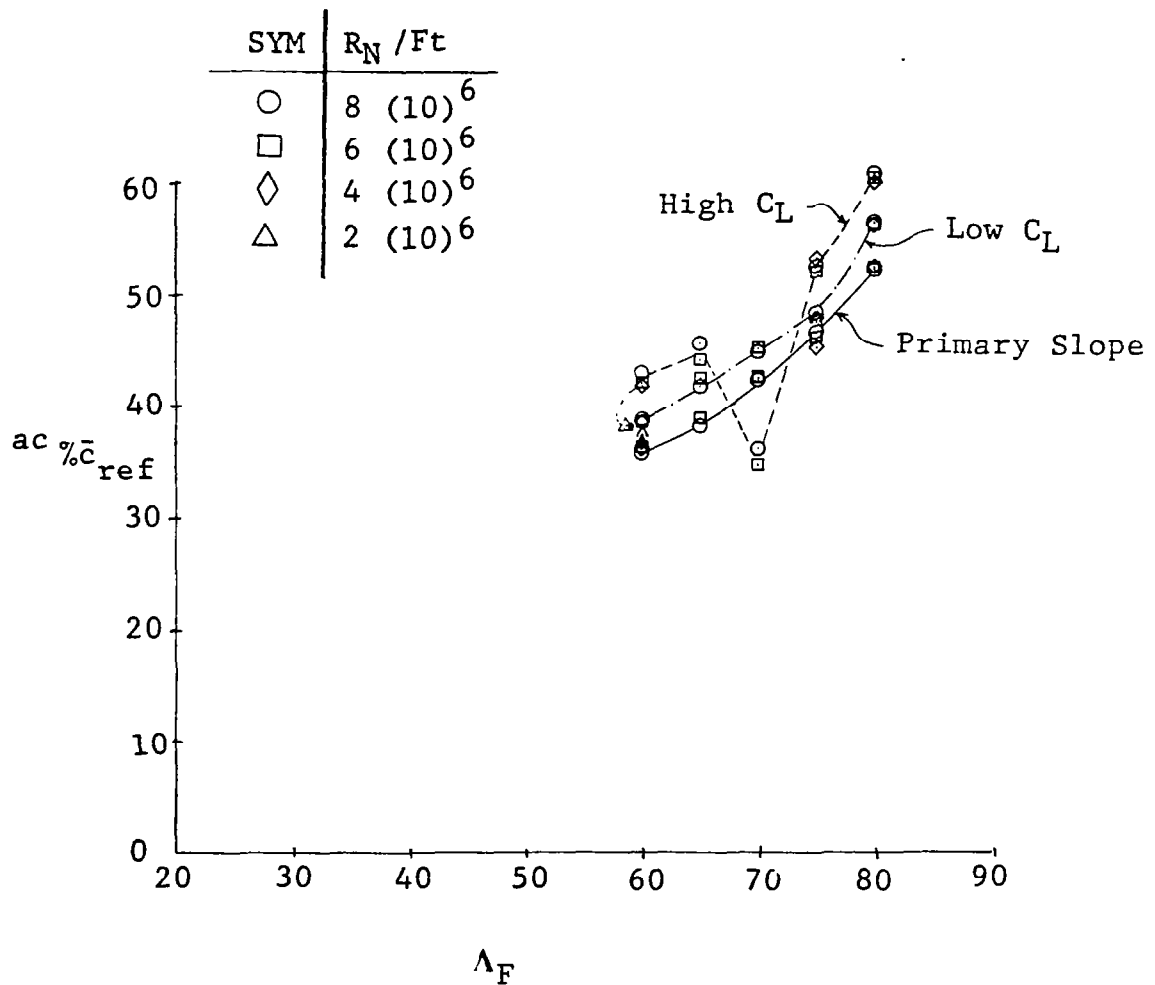
Figure 126.   Effect of Reynolds Number on Aero-
dynamic-Center Location for Various
Lift Regions - Wing V Planforms

Figure 127. C_M - C_L Curve Shape Schematics
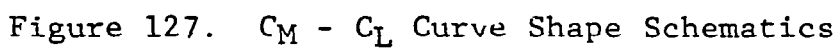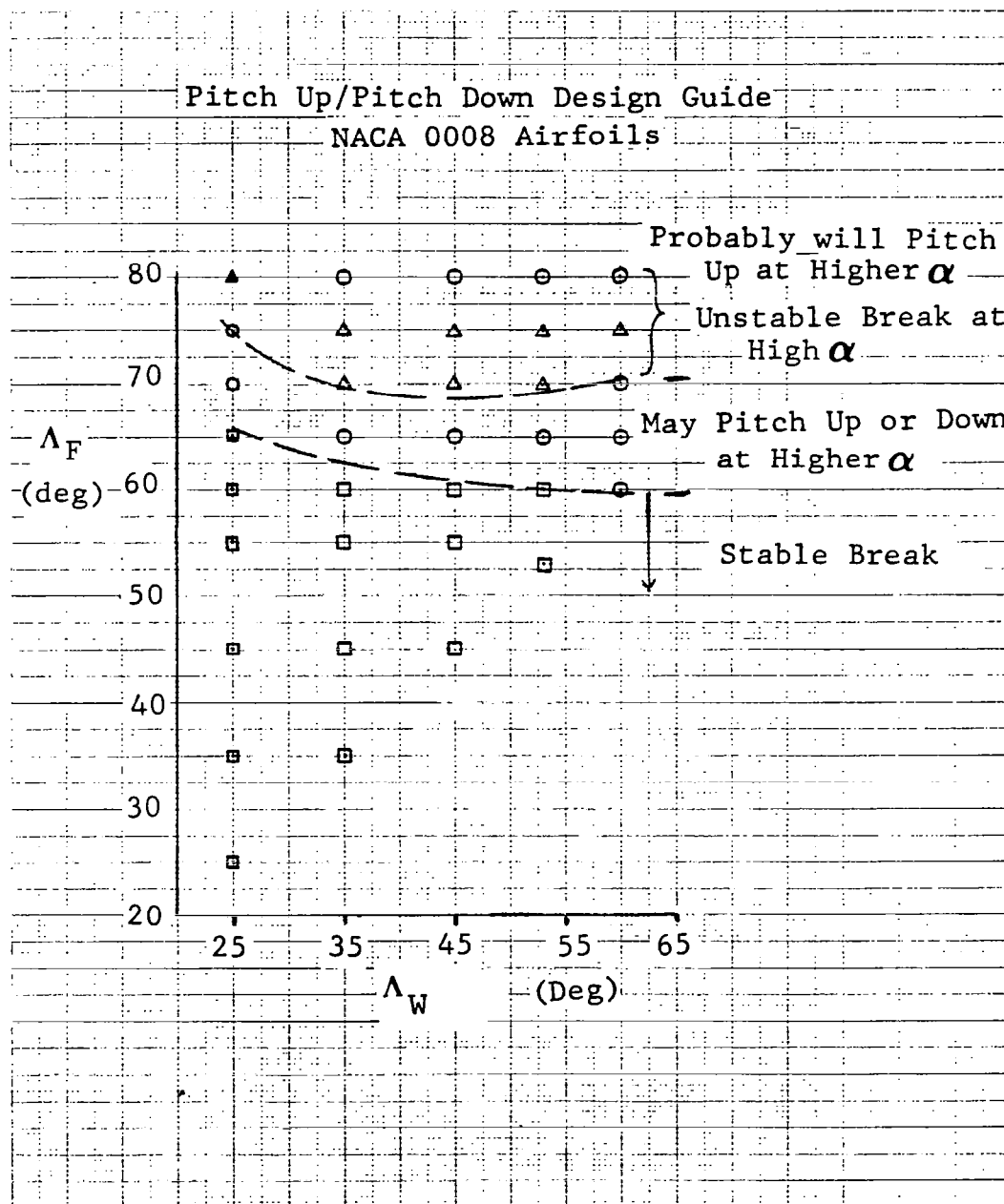
Figure 128. Pitch Up/Pitch Down Tendencies as
Functions of Wing and Fillet Sweep
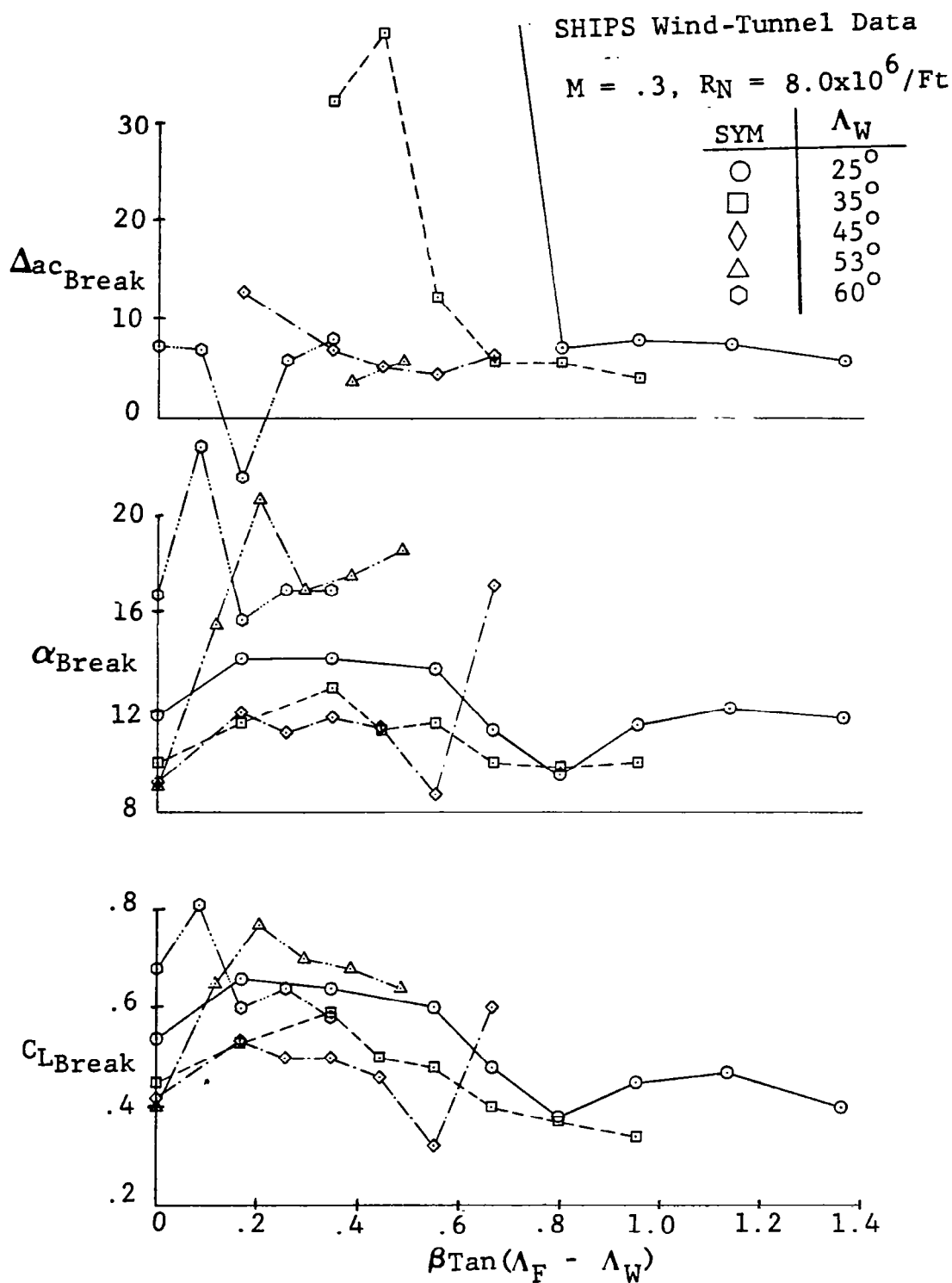
Figure 129. Correlation of Data Related to Shift of Aerodynamic Center in Region Above Primary Slope

SHIPS

Wind-Tunnel Data

$$M = .3, \quad R_N = 8.0 \times 10^6/Ft$$

SYM	Λ_W
◯	25°
☐	35°
◇	45°
△	53°
⬡	60°
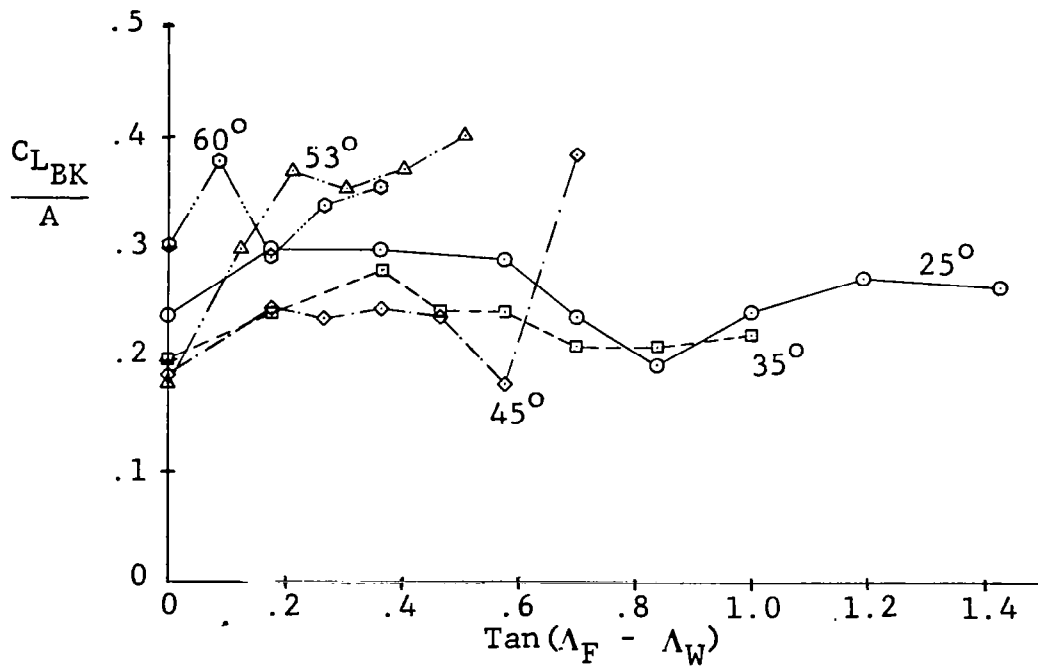
Figure 130. Correlation of Lift Coefficients for Upper Limit
of Primary Slope Region

SHIPS Pitch-Up/Down
Smoothed Wind-Tunnel Data
$$M = .3, \quad R_N = 8.0 \times 10^6 / Ft$$

SYM	Λ_W
◯	25°
□	35°
◇	45°
△	53°
⬡	60°
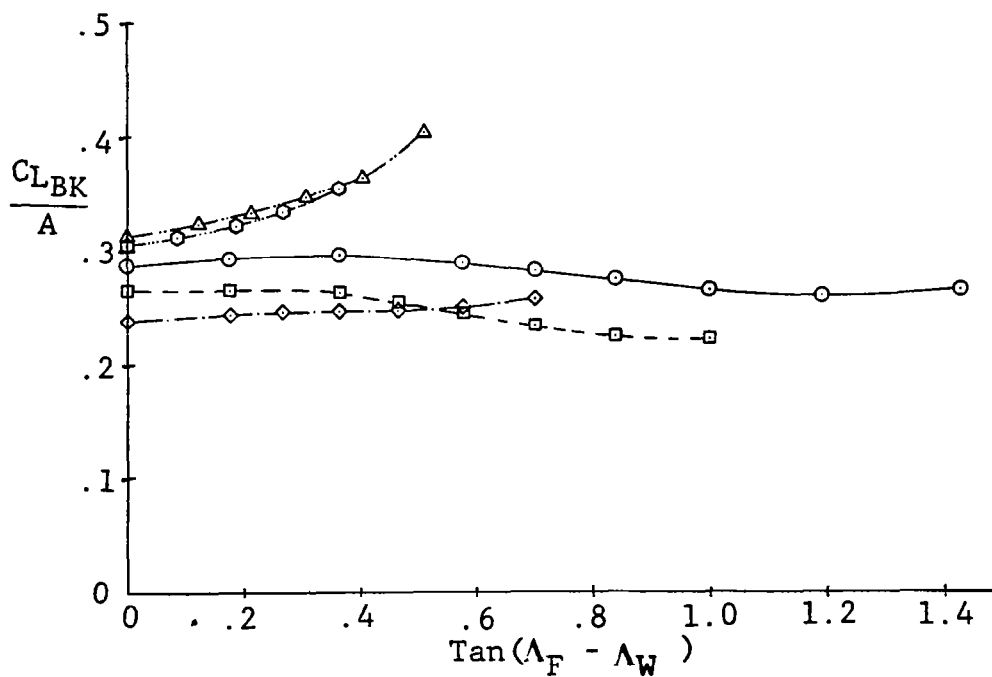
Figure 131. Correlation of Lift Coefficients for Upper Limit of Primary Slope Region Based on Smoothed Wind-Tunnel Data
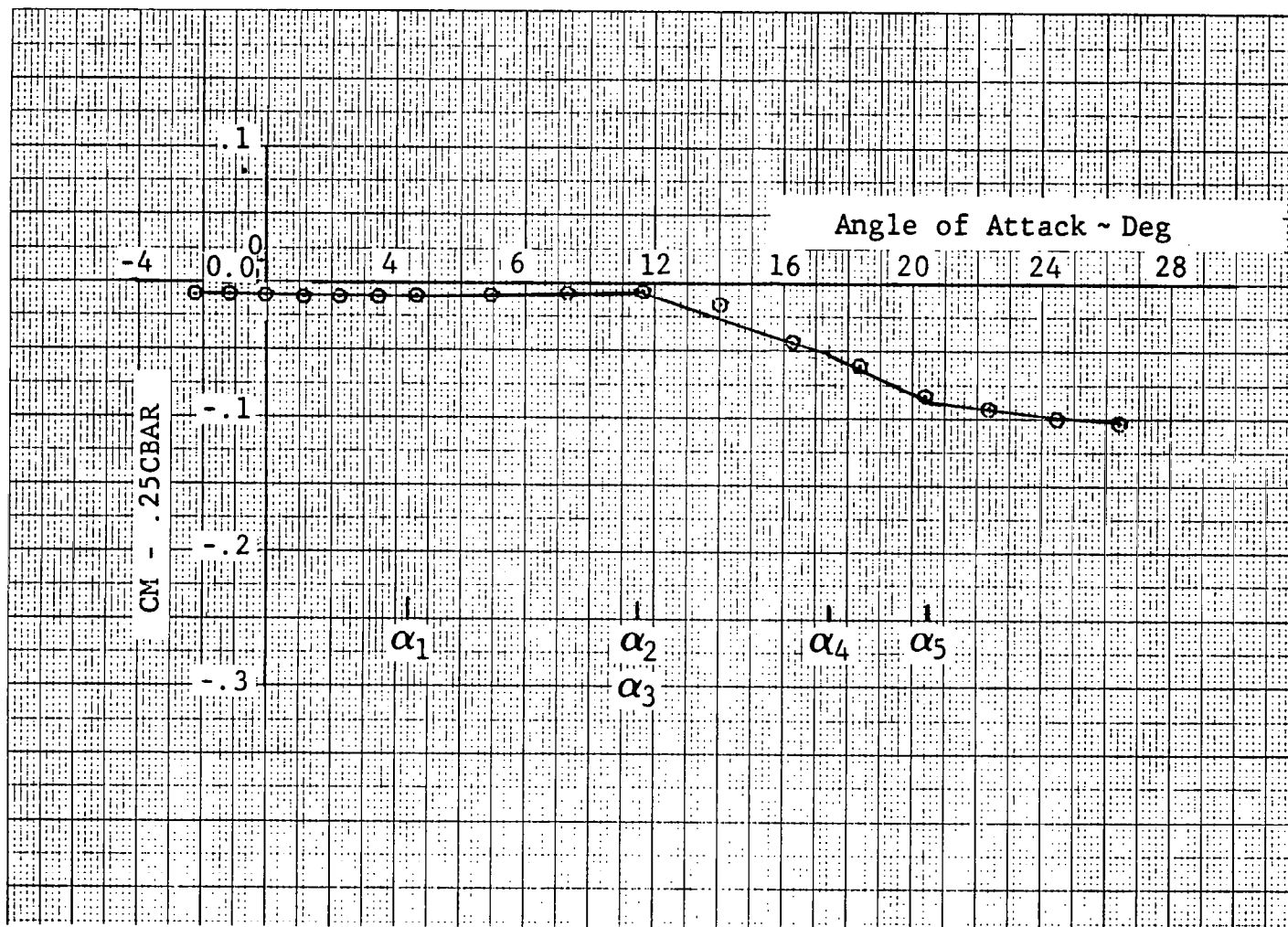
Figure 132. Example of Variation of Pitching Moment with Angle
of Attack Approximated by Linear Segments Between
Angle-of-Attack Boundaries Defined by Suction-Ratio
Analysis - Irregular Planform with Low Fillet Sweep
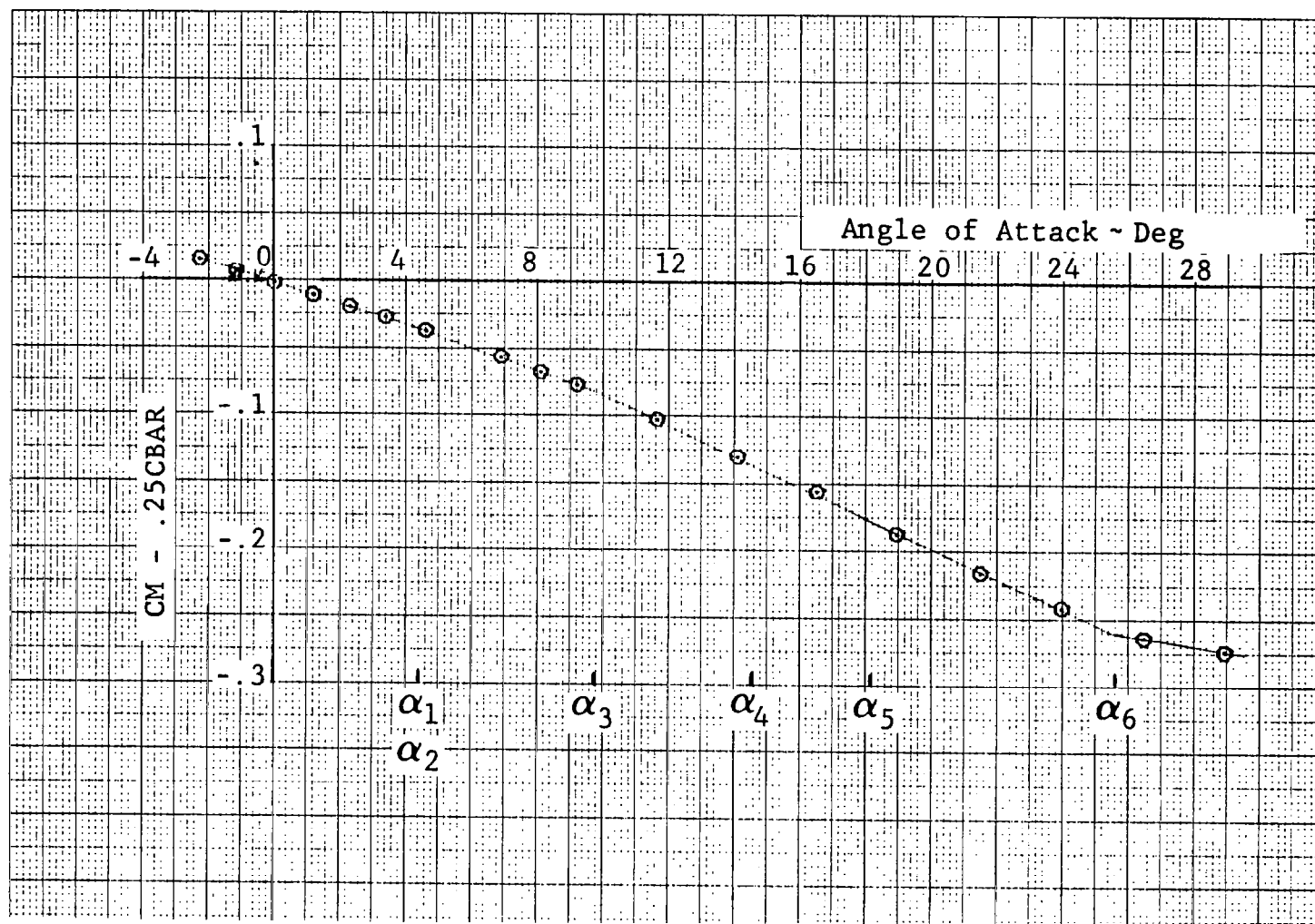
Figure 133. Example of Variation of Pitching Moment with Angle
of Attack Approximated by Linear Segments Between
Angle-of-Attack Boundaries Defined by Suction-Ratio
Analysis - Irregular Planform with High Fillet Sweep
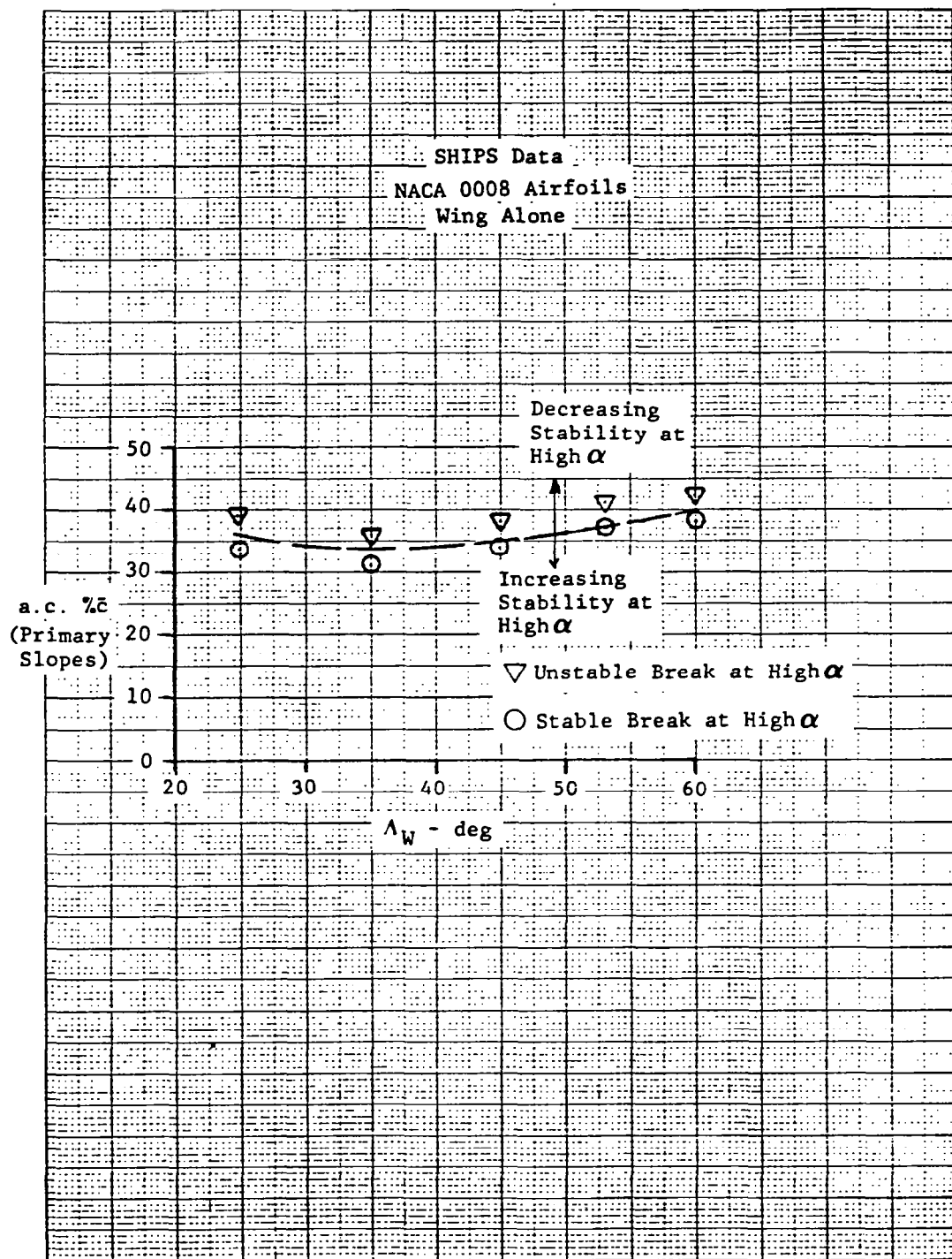
Figure 134.   Pitch-Up/Pitch-Down Design Guide Based on Low
              Angle of Attack Aerodynamic-Center Location

PREDICTION METHOD DEVELOPMENT

The previously described efforts produced several approaches for developing a set of prediction methods for lift, drag, and pitching-moment characteristics, but additional work remained. As discussed earlier, it was intended to devise a basic set of methods from the data obtained at unit Reynolds number of 26.25 million per meter (8.0 million per foot). This section describes how selected approaches for lift, drag, and pitching moment (in that order) were developed into the "basic" prediction technique.

One guideline in the method development process was the fact that eventually prediction methods would be required for transonic and supersonic speeds and compatibility among the methods would be desirable. A second guideline was the desire to computerize the final methods. A third guideline quite obviously was the need to obtain sufficient accuracy from the predictions to be able to represent the differences in the aerodynamic characteristics that occurred between changes in the irregular planforms.

The methods selected for development or modification were:

(1) The WINSTAN nonlinear lift correlation

(2) The Aeromodule prediction method for minimum drag

(3) The leading-edge suction ratio correlation approach for drag due to lift

(4) The quasilinear variation of pitching moment within regions of angle of attack defined from the drag-due-to-lift prediction

The development efforts related to predicting the lift characteristics are presented first, followed in order by those for the drag characteristics and the pitching-moment characteristics.

Lift Characteristics Prediction

While many approaches for correlating the lift characteristics of the SHIPS planforms were examined and several showed promise, the WINSTAN lift correlation approach shown previously in Figure 59 was selected for further development because it had produced the best collapse of data at angles of attack up to 16 degrees and contained parameters which would allow extension to higher Mach numbers. In addition, it was apparent the spread of data above 16 degrees angle of attack was sufficiently systematic in terms of the values of outboard panel leading-edge sweep for each value of fillet sweep that the chances of finding a means of accounting for the effects were good.

The approach taken was to redefine the basic correlation for angles of attack above 16 degrees on the basis of data for the outboard panel sweep equal to 25 degrees. These incremental values of the lift correlation parameter $\Delta\left(\frac{C_L}{C_{L\alpha}} \frac{A_1}{\eta_B}\right)$ were determined for each value of outboard panel sweep. Plots were made of the incremental values as functions of the parameter $\beta\tan\Lambda_F$ for various fixed angles of attack from 16 degrees to 26 degrees. The results were somewhat irregular for fillet sweeps below 65 degrees and angles of attack above 20 degrees, but it proved possible to smooth the baseline curves in a way (Figure 135) which also produced smoother variations of the incremental values with $\beta\tan\Lambda_F$. It was also noted that, if the smoothed incremental values at 22 degrees angle of attack (Figure 136) were used as a basis, the variations of the incremental values with angle of attack at fixed values of $\beta\tan\Lambda_F$ could be reproduced to good accuracy by a correlation curve, f_1, (Figure 137) which represents the stall progression of the family of 35 wing planforms.

The final results provided the following prediction equation:

$$C_L = \frac{C_{L\alpha} \eta_B}{A_1} \left[\left(\frac{C_L}{C_{L\alpha}} \cdot \frac{A_1}{\eta_B}\right)_1 + f_1 \Delta\left(\frac{C_L}{C_{L\alpha}} \frac{A_1}{\eta_B}\right)\right]$$

where the terms in the brackets are read from correlation charts
as follows:

$$\left(\frac{C_L}{C_{L\alpha}} \frac{A_1}{\eta_B}\right)_1 \qquad \text{from Figure 135}$$

$$\Delta\left(\frac{C_L}{C_{L\alpha}} \frac{A_1}{\eta_B}\right) \qquad \text{from Figure 136}$$

$$f_1 \qquad \text{from Figure 137}$$

A_1 is the aspect ratio of the inboard panel

η_B is the non-dimensional spanwise location of the
break in the leading-edge sweep.

The term $\left(\dfrac{C_L}{C_{L\alpha}} \dfrac{A_1}{\eta_B}\right)$ is a function of the parameters $\beta\tan\Lambda_F$
and the angle of attack, α. The term $\Delta\left(\dfrac{C_L}{C_{L\alpha}} \dfrac{A_1}{\eta_B}\right)$ is a function
of $\beta\tan\Lambda_F$ and Λ_W that is applied only for angles of attack
greater than 16 degrees and accounts for the effects of outboard
panel sweep. The factor f_1 varies with angle of attack above 16
degrees to reproduce the incremental effect on stall progression
when applied with the incremental effects caused by variations
with outboard panel sweep.

The lift curve slope, $C_{L\alpha}$, is the incompressible value cal-
culated using Spencer's semi-empirical expression:

$$C_{L_\alpha} = \frac{2\pi A}{2 + \sqrt{4 + \left[\frac{A}{\cos \Lambda_{c/2_{eff}}}\right]^2}} \qquad \text{per radian}$$

where:

        A is the "true" aspect ratio of the irregular planform, and

$$\cos \Lambda_{c/2_{eff}} \equiv \frac{\cos \Lambda_{c/2_{W_1}} \bullet S_1 + \cos \Lambda_{c/2_{W_2}} \bullet S_2}{S_1 + S_2}$$

        The lift values calculated by this method inherently include interference effects of the "minimum fuselages" or balance housings to which the various wings were attached. While the effects are not strictly definable, the basic result is to introduce a slight negative camber to each wing which is manifested in a slightly negative value of lift at zero angle of attack. The method also has the limitations of being applicable strictly to wings with NACA 0008 airfoil sections and Reynolds numbers appropriate to the maximum values tested during ARC Test 12-086-1. However, it will be shown later that the method will provide a reasonable estimate of full-scale lift characteristics for the NACA 0008 airfoils.

Drag Characteristics Prediction

        The approach used to develop a prediction method for the drag characteristics of the irregular planforms consisted of adapting an existing methodology for minimum drag of complete aircraft configurations (Reference 8) and finalizing a drag-due to-lift methodology based on the leading-edge-suction ratio correlation efforts discussed earlier in this report. In both cases it is possible to account for Reynold's number effects.

Minimum Drag

The minimum drag of the irregular planform wings is composed of drag items that are "assumed" to be independent of lift such as friction, form, interference, base, roughness and protuberance drag contributions. The methods used to determine each of the minimum drag contributions are discussed in the following subsections.

Friction, Form, and Interference Drag

A large part of the subsonic minimum drag is comprised of the sum of friction, form, and interference drag of all the configuration components. The drag of each component is computed as

$$C_D = \left(C_f \cdot \frac{S_{wet}}{S_{ref}} \right) \cdot FF \cdot 1F \qquad (3-1)$$

where C_f is the compressible flat-plate skin-friction coefficient, S_{wet} is the component wetted area, and FF and IF are the component form and interference factors.

For emphasis, the specific configuration components considered are illustrated in the sketch below. The pertinent geometric equations are presented in an earlier section

Hidden area
not used in
wetted area
calculation
(Body side
and wing
upper surface
only)

Forebody Nose

Balance
Housing

Base Area

Outboard
Panel

Inboard
Panel
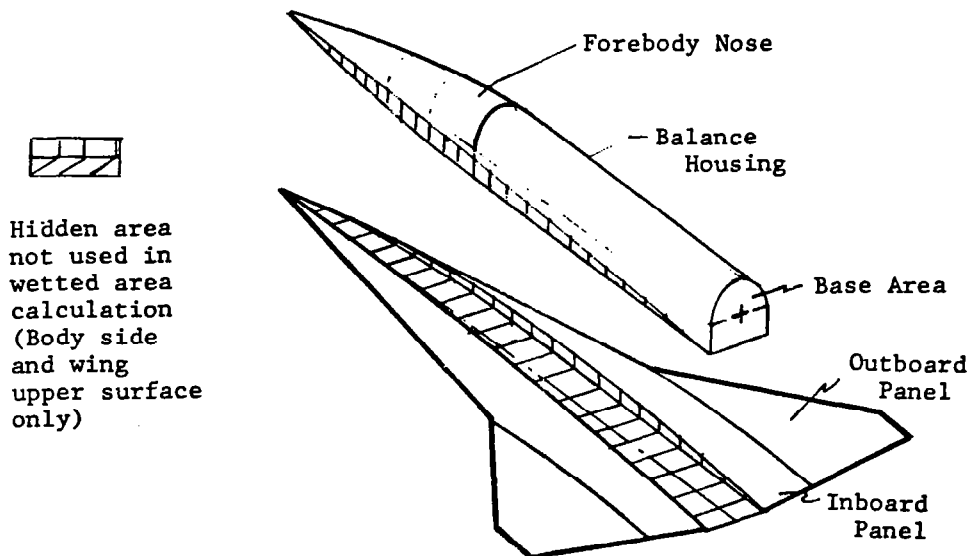
Friction Drag

The flat-plate, compressible, turbulent, skin-friction coefficient is determined from the general equation given in Reference 18

$$C_f = \frac{1}{F_1} \, C_{f_i} \left(R_{N_L} \cdot F_2 \right) \qquad\qquad (3\text{-}2)$$

where F_1 and F_2 are functions of the free-stream Mach number and wall temperature. The incompressible skin-friction coefficient, C_{f_i}, is evaluated at the equivalent Reynolds number, $R_{N_L} F_2$. White and Christoph (Reference 18) developed expressions for the transformation functions F_1 and F_2 along with a more accurate explicit equation, based on Prandtl/Schlichting type relations, for computing the incompressible, turbulent, flat-plate friction coefficient (C_{f_i}) with the following results:

$$F_1 = t^{-1} f^{-1}$$

$$F_2 = t^{1+n} f$$

$$C_{f_i} = \frac{0.430}{\left(\log_{10} R_{N_L} \right)^{2.56}}$$

For an adiabatic wall condition, t and f are given by

$$t = T_\infty / T_{aw} = \left[1 + r \, \frac{\gamma - 1}{2} \, M_\infty^2 \right]^{-1}$$

$$f = 1 + 0.044 \, r \, M_\infty^2 \, t$$

Using a recovery factor r = 0.89 and a viscosity power-law exponent n = 0.67, recommended in Reference 18, results in the following expression for C_f:

$$C_f = t \; f^2 \; \frac{0.430}{\left(\log_{10} \left(R_{N_L} \cdot t^{1.67} \cdot f \right) \right)^{2.56}} \qquad (3\text{-}3)$$

where

$$t = \left[1 + 0.178 \; M_\infty^2 \right]^{-1}$$

$$f = 1 + 0.03916 \; M_\infty^2 \cdot t$$

The Reynolds number, R_{N_L}, is based either on component length or an admissible surface roughness, whichever produces a smaller value of Reynolds number, as follows:

$$R_{N_L} = \text{minimum} \begin{cases} (R_N/\text{ft}) \cdot L \\ K_1 \cdot (L/K)^{1.0489} \end{cases} \qquad (3\text{-}4)$$

where

R_N/ft is determined from standard atmospheric tables or is input.

L is the characteristic length of the component.

K is the admissible surface roughness and is an input quantity.

and,

$$K_1 = 37.587 + 4.615M + 2.949M^2 + 4.132M^3$$

For mixed laminar-turbulent flow, transition location is specified for the upper and lower surfaces of the wing. For the laminar portion of the flow, the Blasius skin-friction relation

$$C_f = 1.328 / \sqrt{R_{N_{X_r}}} \cdot \left(\frac{C_f}{C_{f_i}} \right)_{Laminar} \qquad (3-5)$$

where $C_f / C_{f_i} = (1 + 0.1256M^2)^{-.12}$, is used up to the transition point. At the transition point, X_r, the laminar momentum thickness is matched by an interative process to a turbulent momentum thickness, which begins some fictitious distance, ΔX, ahead of transition. The skin-friction coefficient for the turbulent part of the flow is calculated from Equation 3-3, where the Reynolds number is calculated from

$$R_{N_L} = (\Delta X + L - X_r) \cdot (R_N / ft) \qquad (3-6)$$

The value of C_f with transition is finally given by

$$C_f = \left(\frac{\Delta X}{L} + \frac{L - X_r}{L} \right) C_{f_{Turb.}} \qquad (3-7)$$

Calculated values of C_f versus R_{N_L} are presented in Figures 138 through 143 for mixed laminar-turbulent flow.

Form Factors

The component form factors, FF, account for the increased skin friction caused by the supervelocities of the flow over the body or surface and the boundary-layer separation at the trailing edge. The form factor for the "body" component is computed as

$$FF = 1 + 60/FR^3 + 0.0025 \cdot FR \qquad (3-8)$$

where

$$FR = \frac{\text{Component Length}}{\sqrt{\text{Width x Height}}}$$

For "nacelle" components, the form factor is given by

$$FF = 1 + 0.35/FR \tag{3-9}$$

Equations 3-8 and 3-9 were obtained from the Convair Aerospace Handbook (Reference 19) and also appear in the DATCOM (Reference 11).

The airfoil form factors depend upon airfoil type and streamwise thickness ratio. For 6-series airfoils, the form factor is given by

$$FF = 1 + 1.44(t/c) + 2(t/c)^2 \tag{3-10}$$

For 4-digit airfoils, the form factor is given by

$$FF = 1 + 1.68(t/c) + 3(t/c)^2 \tag{3-11}$$

For biconvex airfoils, the form factor is given by

$$FF = 1 + 1.2(t/c) + 100(t/c)^4 \tag{3-12}$$

And for supercritical airfoils, the form factor is given by

$$FF = 1 + K_1 C_{1d} + 1.44(t/c) + 2(t/c)^2 \tag{3-13}$$

The factor $K_1 C_{1d}$ in Equation 3-13 is an empirical relationship which shifts the 6-series form-factor equation to account for the increased supervelocities caused by the supercritical-section design camber C_{1d}. The factor K_1 (derived from experimental data) is shown plotted in Figure 144 as a function of the Mach number relative to the wing Mach critical. Equations 3-10 and 3-11 were obtained from informal discussions with NASA/LRC personnel; Equation 3-12 appears in both the DATCOM and the Convair Handbook.

Interference Factors

The component interference factors, IF, account for the mutual interference between components. For the fuselage, the interference factor is given by

$$IF = R_{W-B} \tag{3-14}$$

where R_{W-B} is shown plotted in Figure 145 as a function of fuselage Reynolds number and Mach. For other bodies such as stores, canopies, landing-gear fairings, and engine nacelles, the interference factor would be an input factor based on experimental experiences with similar configurations. The Convair Aerospace Handbook (Reference 19) recommends using

IF = 1.0 for nacelles and stores mounted out of
the local velocity field of the wing.

IF = 1.25 for stores mounted symmetrically on
the wing tip.

IF = 1.3 for nacelles and stores if mounted in
moderate proximity of the wing.

IF = 1.5 for nacelles and stores mounted flush
to the wing or fuselage.

The interference factor for the main wing is computed as

$$IF = R_{LS} \cdot R_{W-B} \tag{3-15}$$

where R_{W-B} is the wing-body interference factor presented in Equation 3-14, and R_{LS} is the lifting surface interference factor presented in Figure 146. For supercritical wings the wing interference factor is set equal to one. Other airfoil surfaces such as horizontal or vertical tails use an interference factor determined by

$$IF = R_{LS} \cdot H_f \tag{3-16}$$

where H_f is the hinge factor obtained from input (use $H_f = 1.0$ for an all movable surface, 1.1 if the surface has a flap for control). The factors R_{W-B} and R_{LS} are plotted in Reference 5 and also appear in the DATCOM.

Base Drag

Data presented in Reference 20 were used to establish equations from which the base drag of bodies could be determined. The trends of these data show three different phases: (1) a gradual rise of $C_{D_{Base}}$ at transonic speeds up to $M = 1$, (2) a relatively constant drag level supersonically up to about $M = 1.8$, and (3) a steadily decreasing value of drag above $M = 1.8$. The resulting empirical equations are given as

$$
C_{D_{Base}} = \begin{cases} (0.1 + 0.1222M^8) \dfrac{S_{Base}}{S_{Ref}}, & M \leq 1 \\[2ex] 0.2222 S_{Base}/S_{Ref}, & 1.0 \leq M \leq 1.8 \\[2ex] 1.42 S_{Base}/S_{Ref})/(3.15 + M^2), & M > 1.8 \end{cases} \tag{3-19}
$$

Miscellaneous Drag Items

In the preliminary design stage of aircraft drag estimation, the drag due to surface irregularities such as gaps and mismatches, fasteners, small protuberances, and leakage due to pressurization are estimated by adding a miscellaneous drag increment which is some percentage of the total friction, form, and interference drags. The miscellaneous drag varies between 5 and 20 percent of the total friction, form, and interference drags for typical aircraft.

Drag Due To Lift.

The approach selected for development of a drag-due-to-lift prediction method is based on the concept of the leading-edge suction ratio. The various correlations developed have already been discussed in some detail. The task that remained was to formalize a calculation procedure using forms of the correlations suitable for calculation and define the specific equations to be used. As a consequence, some of the charts presented with the following summary of the prediction method are repeats of previous figures.

The basic equation for drag due-to-lift, C_{D_L}, is:

$$C_{D_L} = C_L \tan\alpha - \text{"R}(\alpha)\text{"} \left[C_L \tan\alpha - \frac{C_L^2}{\pi A} \right]$$

where:

$C_L \tan\alpha$ is the drag due-to-lift with zero leading edge suction

$\dfrac{C_L^2}{\pi A}$ is the drag due-to-lift with full leading edge suction

$\text{"R}(\alpha)\text{"}$ is the ratio of leading-edge suction derived from the test data to the full leading-edge suction value as a function of angle of attack.

A   is the "true" aspect ratio of the irregular planform.

The variation of $\text{"R}(\alpha)\text{"}$ with α typically consists of 5 distinct quasi-linear regions as illustrated in Figure 147.

Region 1 is the plateau region for which $\text{"R}(\alpha)\text{"}$ is a constant for a specific aircraft geometry and test condition, but is a function of leading-edge radius Reynolds number, Mach

number, and leading-edge sweep of both the basic wing planform and the fillet planform.

The value of $"R_1"$ is obtained from the equation:

$$"R_1" = "R_{BW}" + \left[\frac{\Delta"R_1"}{\Lambda_F - \Lambda_W}\right] (\Lambda_F - \Lambda_W)$$

where:

$"R_{BW}"$ is obtained from the correlation curve of $"R_{BW}"$

vs Ω in Figure 148 for

$$\Omega \equiv R_{e_{LER}} \; COT \; \Lambda_W \sqrt{1 - M^2 \cos^2 \Lambda_W}$$

$R_{e_{LER}}$ is the leading-edge radius Reynolds number based on streamwise values of velocity and radius determined at the spanwise location of the mean geometric chord of the basic wing.

and

$$\left[\frac{\Delta"R_1"}{\Lambda_F - \Lambda_W}\right]$$ is obtained from Figure 149.

The upper bound of Region 1 is defined as α_2, which is a function of planform geometry and Reynolds number. The planform effect for 26.25 million per meter (8.0 million per foot) unit Reynolds number on the small-scale models (the "reference values") is presented in Figure 150.

The methodology for determining the other angle-of-attack boundaries and the Reynolds number effect on all the angle-of-attack boundaries requires that "reference values" of α_2, α_3, α_4, and α_5 corresponding to 26.25 million per meter (8.0 million per foot) unit Reynolds number on the small-scale models be computed first. Then the Reynolds number corrections can be applied to the "reference values".

Thus,

$\alpha_{2_{ref}}$ is obtained from Figure 150.

$\alpha_{3_{ref}} = \alpha_{2_{ref}} + \Delta\alpha_{(3-2)}$ from Figure 151.

$\alpha_{4_{ref}} = \alpha_{3_{ref}} + \Delta\alpha_{(4-3)}$ from Figure 152.

$\alpha_{5_{ref}} = \alpha_{4_{ref}} + \Delta\alpha_{(5-4)}$ from Figure 153.

The incremental effect due to Reynolds number requires use of two figures (154 and 155) in which an incremental effect of Reynolds number is first evaluated for the basic wing planform and the effect of irregular planform is applied as a factor. Note that in Figure 154 the Reynolds number parameter Ω_T is based on the leading-edge radius at the wing tip.

The effect of Reynolds number is applied to the α boundary values obtained for 26.25 million per meter (8.0 million per foot) and model scale, i.e.,

$$\alpha_2 = \alpha_{2_{ref}} + \left[\Delta (\delta\alpha_2 \cos \Lambda_W) \right] \left[\frac{\delta\alpha_2 (\Lambda_F)}{\delta\alpha_2 (\Lambda_W)} \right] \frac{1}{\cos \Lambda_W}$$

where

$$\Delta (\delta\alpha_2 \cos \Lambda_W) = (\delta\alpha_2 \cos \Lambda_W)_{\Omega_T} - (\delta\alpha_2 \cos \Lambda_W)_{\Omega_{T_{ref}}}$$

Thus, for a particular design, $\Omega_{T_{ref}}$ must be evaluated at model scale and at a unit Reynolds number of 26.25 million per meter (8.0 million per foot), and Ω_T is evaluated at full scale or other desired conditions.

The other angle-of-attack boundaries α_3, α_4, and α_5 are then calculated in the same way.

$$\alpha_3 = \alpha_{3_{ref}} + \left[\Delta(\delta\alpha_3 \cos \Lambda_W)\right] \left[\frac{\delta\alpha_3(\Lambda_F)}{\delta\alpha_3(\Lambda_W)}\right] \frac{1}{\cos \Lambda_W}$$

$$\alpha_4 = \alpha_{4_{ref}} + \left[\Delta(\delta\alpha_4 \cos \Lambda_W)\right] \left[\frac{\delta\alpha_4(\Lambda_F)}{\delta\alpha_4(\Lambda_W)}\right] \frac{1}{\cos \Lambda_W}$$

$$\alpha_5 = \alpha_{5_{ref}} + \left[\Delta(\delta\alpha_5 \cos \Lambda_W)\right] \left[\frac{\delta\alpha_5(\Lambda_F)}{\delta\alpha_5(\Lambda_W)}\right] \frac{1}{\cos \Lambda_W}$$

The variation of "R(α)" with α is then constructed by sequentially applying the slope functions shown in Figures 156 through 159 in each appropriate angle-of-attack region as follows:

$$\text{"R}(\alpha)\text{"}_1 = \text{"R}_1\text{"} \quad ; \quad 0 \leq \alpha \leq \alpha_2$$

$$\text{"R}(\alpha)\text{"}_2 = \text{"R}(\alpha)\text{"}_1 + \left(\frac{dR}{d\alpha}\right)_2 (\alpha - \alpha_2) \quad ; \quad \alpha_2 \leq \alpha \leq \alpha_3$$

$$\text{"R}(\alpha)\text{"}_3 = \text{"R}(\alpha)\text{"}_1 + \left(\frac{dR}{d}\right)_2 (\alpha_3 - \alpha_2) + \left(\frac{dR}{d\alpha}\right)_3 (\alpha - \alpha_3)$$

$$\alpha_3 \leq \alpha \leq \alpha_4$$

$$\text{"R}(\alpha)\text{"}_4 = \text{"R}(\alpha)\text{"}_1 + \left(\frac{dR}{d\alpha}\right)_2 (\alpha_3 - \alpha_2) + \left(\frac{dR}{d\alpha}\right)_3 (\alpha_4 - \alpha_3)$$

$$+ \left(\frac{dR}{d\alpha}\right)_4 (\alpha - \alpha_4) \quad ; \quad \alpha_4 \leq \alpha \leq \alpha_5$$

$$\text{"R}(\alpha)\text{"}_5 = \text{"R}(\alpha)\text{"}_1 + \left(\frac{dR}{d\alpha}\right)_2 (\alpha_3 - \alpha_2) + \left(\frac{dR}{d\alpha}\right)_3 (\alpha_4 - \alpha_3)$$

$$+ \left(\frac{dR}{d\alpha}\right)_4 (\alpha_5 - \alpha_4) + \left(\frac{dR}{d\alpha}\right)_5 (\alpha - \alpha_5)$$

$$; \quad \alpha_5 \leq \alpha \leq 26 \text{ degrees}$$

In practice, one computes corresponding values of C_L from the lift prediction method and "R(α)" from the above listed equations for a series of angles of attack and solves the basic drag-due-to-lift equation.

Pitching-Moment Characteristics Predictions

The prediction methodology with respect to pitching moments provides three types of information. First, the aerodynamic-center location at low angles of attack can be calculated in terms of percent root chord or in terms of the mean geometric chord from relatively simple curve fits of data obtained at unit Reynolds number of 26.25 million per meter (8.0 million per foot).

Second, the pitch-up/pitch-down tendencies of the irregular planforms at high angles of attack can be assessed on the basis of the a.c. location at low angles of attack calculated in terms of percent effective mean geometric chord.

Third, the complete variation of pitching moment (relative to 25 percent of the effective mean geometric chord) with angle of attack can be constructed.

Aerodynamic Center In Primary Slope Region $(0.1 \leq C_L \leq .5)$

The prediction method for aerodynamic center in terms of percent root chord is based on curve fits of the experimental data for unit Reynolds number of 26.25 million per meter (8.0 million per foot). The plot used (Figure 160) presents the variations of a.c. location with basic wing leading-edge sweep and parametric values of fillet leading-edge sweep.

A cross-plot of the a.c. location variation with fillet leading-edge sweep for a basic wing leading-edge sweep of 45 degrees was fitted with a 4th degree Legendre polynomial. The effects of wing sweep are accounted for by different linear functions in four regions represented by combinations of wing and fillet sweep.

The baseline polynomial for variation of a.c. $\%C_1$ with Λ_F for $\Lambda_W = 45°$ is:

- $(\text{a.c. } \%C_1)_B = 30.10775858 + 0.1524242511 \ \Lambda_F$

$$+ 0.007543290783 \ \Lambda_F{}^2 - 0.0001686738033 \ \Lambda_F{}^3$$

$$+ 0.000001609816225 \ \Lambda_F{}^4$$

- To account for other Λ_W

  - $\Lambda_W < 45°$; Λ_F from $25°$ to $65°$

  $$\text{a.c.} \%C_1 = (\text{a.c.} \%C_1)_B + \frac{d \ \text{ac}}{d \ \Lambda_W} \ (\Lambda_W - 45°)$$

  $$= (\text{a.c.} \%C_1)_B + (\Lambda_W - 45°)(.5700 - 0.004307692308 \ \Lambda_F)$$

  - $\Lambda_W \leq 45°$; Λ_F from $65°$ to $80°$

  $$\text{a.c.} \%C_1 = (\text{a.c.} \%C_1)_B + (\Lambda_W - 45°) \left[.2900 - .007733333333 \ (\Lambda_F - 65°)\right]$$

  - $\Lambda_W > 45°$; Λ_F from $45°$ to $65°$

  $$\text{a.c.} \%C_1 = (\text{a.c.} \%C_1)_B + (\Lambda_W - 45°) \left[.2380 + .01035 \ (\Lambda_F - 45°)\right]$$

  - $\Lambda_W > 45°$; Λ_F from $65°$ to $80°$

  $$\text{a.c.} \%C_1 = (\text{a.c.} \%C_1)_B + (\Lambda_W - 45°) \left[.4450 - 0.017 \ (\Lambda_F - 65°)\right]$$

A comparison of the predicted and test values of aerodynamic center location is presented in Figure 160. A similar approach was used to establish a prediction of the aerodynamic center in terms of the percent of mean geometric chord of the irregular planform.

The baseline polynomial for variation of a.c. $\% \bar{c}$ eff with Λ_F for $\Lambda_W = 45°$ is:

$$(\text{a.c.} \% \bar{c} \text{ eff})_{\substack{\text{Basic} \\ \Lambda_W = 45°}} = 28.61247819 - .9174258792 \ \Lambda_F$$
$$+ .04500815340 \ \Lambda_F^2 - .000803241088 \ \Lambda_F^3$$
$$+ .000005350951339 \ \Lambda_F^4$$

To account for other Λ_W

- $\Lambda_W < 45°$; Λ_F FROM 25° to 60°

  a.c. % $\bar{c}$ eff = (a.c. % $\bar{c}$ eff)$_{BASIC}$ + (Λ_W - 45°)(.275 - .00041666666Λ_F)

- $\Lambda_W < 45°$; Λ_F FROM 60° to 80°

  a.c. % $\bar{c}$ eff = (a.c.% $\bar{c}$ eff)$_{BASIC}$ + (Λ_W - 45°)$\left[.250 - .0024(\Lambda_F - 60)\right]$

- $\Lambda_W > 45°$; Λ_F FROM 45° to 72.5°

  a.c. % $\bar{c}$ eff = (a.c.% $\bar{c}$ eff)$_{BASIC}$ + (Λ_W - 45°)

  $$\left[.125 + .0078181818 (\Lambda_F - 45)\right]$$

- $\Lambda_W > 45°$; Λ_F FROM 72.5° to 80°

  a.c. % $\bar{c}$ eff = (a.c.% $\bar{c}$ eff)$_{BASIC}$ + (Λ_W - 45°)

  $$\left[.340 - .0286666666(\Lambda_F - 72.5)\right]$$

Predicted and test values are compared in Figure 161.

Pitch-Up/Pitch-Down Tendencies

Two forms of design guides are presented. The first, Figure 162, is a simple matrix presentation showing the tendencies for each combination of wing sweep and fillet sweep. While this guide is useful for interpreting the SHIPS data base, it is not necessarily appropriate for analyzing data for other configurations. The second guide, Figure 163, makes use of the aerodynamic-center location in the primary slope region in terms of percent mean geometric chord. For the SHIPS data base it can be used with Figure 161 to assess any pitch-up/pitch-down tendencies. The chart is in the form of a.c. as a percentage of effective mean geometric chord rather than percent root chord, because the MGC is a more descriptive property of the planform than is the root chord.

Pitching-Moment Variation With Angle of Attack

The prediction method for obtaining the variations of pitching moment with angle of attack is directly related to the drag-due-to-lift prediction methodology. It was noted that breaks or kinks in the pitching-moment curves and axial-force curves occurred at or close to the angle-of-attack boundaries established in the drag-due-to-lift analysis. A more extensive study showed that two additional boundaries were required, one at low angle of attack (α_1), Figure 164, and one at high angle of attack (α_6), Figure 165. Both of these boundaries have corresponding points in the drag-due-to-lift analyses, but they were not considered significant because the drag effects are very small. For computational purposes, the data presented in Figures 164 and 165 were simplified or enhanced to produce a useable set of calculation curves.

As in the drag-due-to-lift methodology, the pitching-moment curves are assumed to be linear functions of angle of attack in each region. Except for some irregular planforms which have low values of wing sweep and fillet sweep, the linear assumption provides a quite accurate representation of the actual curves.

The methodology is as follows:

$$C_{m_{.25\,\bar{c}\,eff}} = C_{m_{\alpha=0}} + C_{m_\alpha}(\alpha - 0) \quad ; \quad 0 \le \alpha \le \alpha_1$$

$$= C_{m_{\alpha=0}} + C_{m_{\alpha_0}}\alpha_1 + C_{m_{\alpha_1}}(\alpha - \alpha_1) ; \quad \alpha_1 \le \alpha \le \alpha_{2_{ref}}$$

$$= C_{m_{\alpha=0}} + C_{m_{\alpha_0}}\alpha_1 + C_{m_{\alpha_1}}(\alpha_{2_{ref}} - \alpha_1)$$

$$+ C_{m_{\alpha_2}}(\alpha - \alpha_{2_{ref}}) ; \quad \alpha_{2_{ref}}\bar{c} \le \alpha \le \alpha_{3_{ref}}$$

$$= C_{m_{\alpha=0}} + C_{m_{\alpha_0}}\,\alpha_1 + C_{m_{\alpha_1}}\,(\alpha_{2_{ref}} - \alpha_1)$$

$$+ C_{m_{\alpha_2}}\,(\alpha_{3_{ref}} - \alpha_{2_{ref}}) + C_{m_{\alpha_3}}\,(\alpha - \alpha_{3_{ref}}) \;;$$

$$\alpha_{3_{ref}} \;\; \alpha \leq \alpha_{4_{ref}}$$

$$= C_{m_{\alpha=0}} + C_{m_{\alpha_0}}\,\alpha_1 + C_{m_{\alpha_1}}\,(\alpha_{2_{ref}} - \alpha_1)$$

$$+ C_{m_{\alpha_2}}\,(\alpha_{3_{ref}} - \alpha_{2_{ref}}) + C_{m_{\alpha_3}}\,(\alpha_{4_{ref}} - \alpha_{3_{ref}})$$

$$+ C_{m_{\alpha_4}}\,(\alpha - \alpha_{4_{ref}}) \;;\;\; \alpha_{4_{ref}} \leq \alpha \leq 5_{ref}$$

$$= C_{m_{\alpha=0}} + C_{m_{\alpha_0}}\,\alpha_1 + C_{m_{\alpha_1}}\,(\alpha_{2_{ref}} - \alpha_1)$$

$$+ C_{m_{\alpha_2}}\,(\alpha_{3_{ref}} - \alpha_{2_{ref}}) + C_{m_{\alpha_3}}\,(\alpha_{4_{ref}} - \alpha_{3_{ref}})$$

$$+ C_{m_{\alpha_4}}\,(\alpha_{5_{ref}} - \alpha_{4_{ref}}) + C_{m_{\alpha_5}}\,(\alpha - \alpha_{5_{ref}}) \;;$$

$$\alpha_{5_{ref}} \leq \alpha \leq \alpha_6$$

$$= C_{m_{\alpha=0}} + C_{m_{\alpha_0}}\,\alpha_1 + C_{m_{\alpha_1}}\,(\alpha_{2_{ref}} - \alpha_1)$$

$$+ C_{m_{\alpha_2}}\,(\alpha_{2_{ref}} - \alpha_{3_{ref}}) + C_{m_{\alpha_3}}\,(\alpha_{4_{ref}} - \alpha_{3_{ref}})$$

$$+ C_{m_{\alpha_4}}\,(\alpha_{5_{ref}} - \alpha_{4_{ref}}) + C_{m_{\alpha_5}}\,(\alpha_6 - \alpha_{5_{ref}})$$

$$+ C_{m_{\alpha_6}}\,(\alpha - \alpha_6) \;;\;\; \alpha_6 \leq \alpha \leq 26$$

where:

α_1 and α_6 are obtained from Figures 164 and 165, and the values of $C_{m_{\alpha=0}}$, $C_{m_{\alpha_0}}$, $C_{m_{\alpha_1}}$, $C_{m_{\alpha_2}}$, $C_{m_{\alpha_3}}$, $C_{m_{\alpha_4}}$, $C_{m_{\alpha_5}}$, and $C_{m_{\alpha_6}}$ are obtained from Figures 166 through 172.

The variation of pitching moment at zero angle of attack presented in Figure 167 represents smoothed average values for all outboard panel sweeps. The maximum deviation from the curve was $\pm$ 0.004 at $\Lambda_F=65$, which is well within the desired accuracy.

Note that for the NACA 0008 airfoils the values of $C_{m_{\alpha_1}}$ and $C_{m_{\alpha_2}}$ are identical, but provision has been made in the methodology to account for the fact that for thicker airfoils $C_{m_{\alpha_1}}$ and $C_{m_{\alpha_2}}$ may have different values.

Since the intent of the pitching-moment calculation is primarily to define the stability characteristics of the configuration, the basic prediction method does not account for Reynolds number effects on either the angle-of-attack boundaries or on the pitching-moment slopes because the lift prediction does not include such effects. The effect of Reynolds number on the pitching-moment slopes is small for the NACA 0008 airfoils, but some effect was noted for the thicker airfoils from the basic data plots. These effects were to be accounted for in the final methodology.
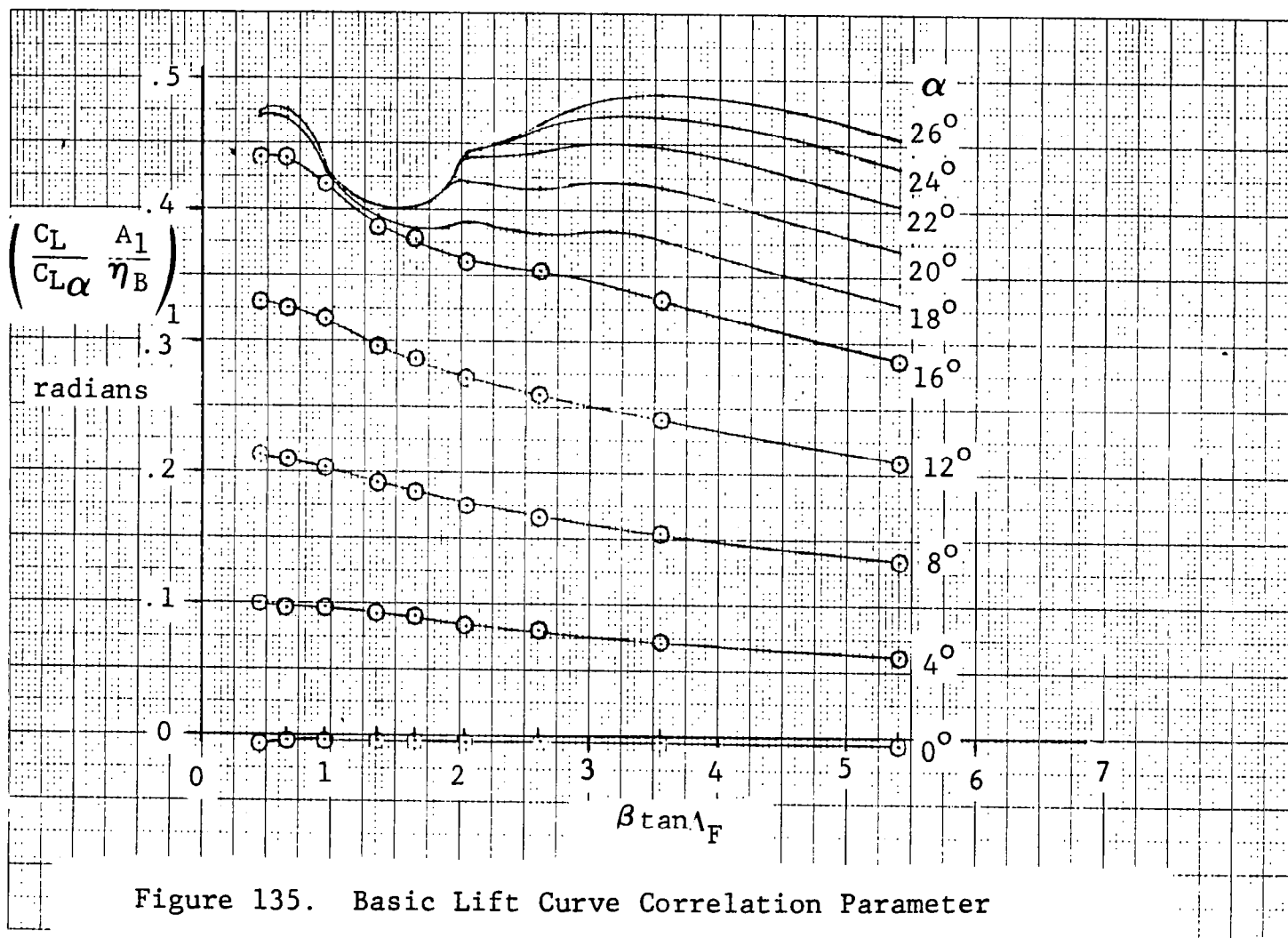
Figure 135. Basic Lift Curve Correlation Parameter
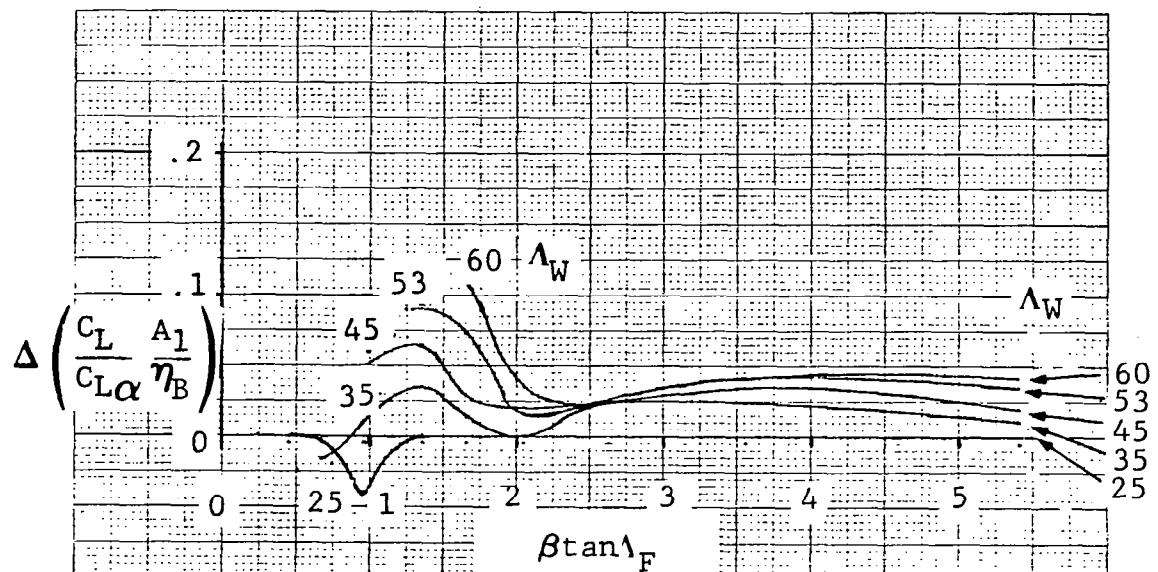
Figure 136. High α Lift Adjustment for Outboard Panel Sweep
Effects to be Applied Above $\alpha = 16^{o}$ only
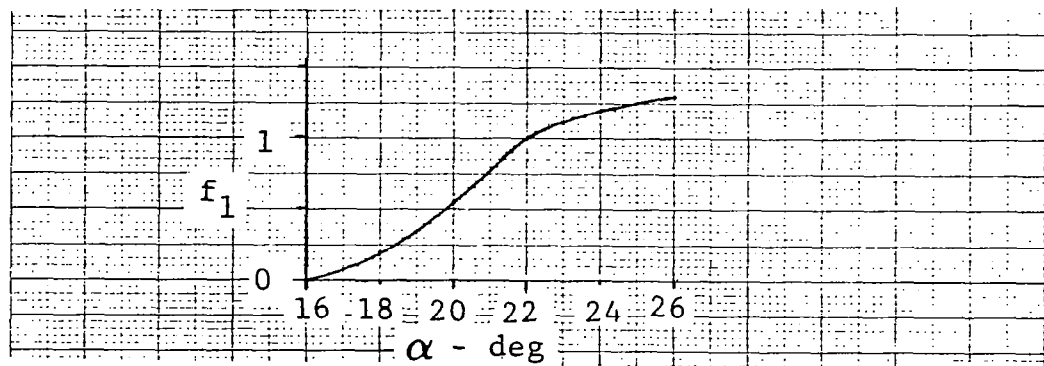
Figure 137. High α Stall Progression Factor

$$C_{L_{\alpha} > 16^{\circ}} = \frac{C_{L_{\alpha}} \eta_B}{A_1} \left[\left(\frac{C_L}{C_{L_{\alpha}}} \frac{A_1}{\eta_B} \right)_1 + f_1 \Delta \left(\frac{C_L}{C_{L_{\alpha}}} \frac{A_1}{\eta_B} \right) \right]$$

Figure 138. Turbulent Skin-Friction Coefficient on an Adiabatic Flat Plate (White-Christoph)

Figure 139. Skin Friction on an Adiabatic Flat Plate, $X_r = 0.1$

224

Figure 140. Skin Friction on an Adiabatic Flat Plate, $X_r = 0.2$

Figure 141. Skin Friction on an Adiabatic Flat Plate, $X_r = 0.3$

225

Figure 142. Skin Friction on an Adiabatic Flat Plate,
$X_r = 0.4$

Figure 143. Skin Friction on an Adiabatic Flat Plate, $X_T = 0.5$

Figure 144.   Supercritical Wing Compressibility Factor
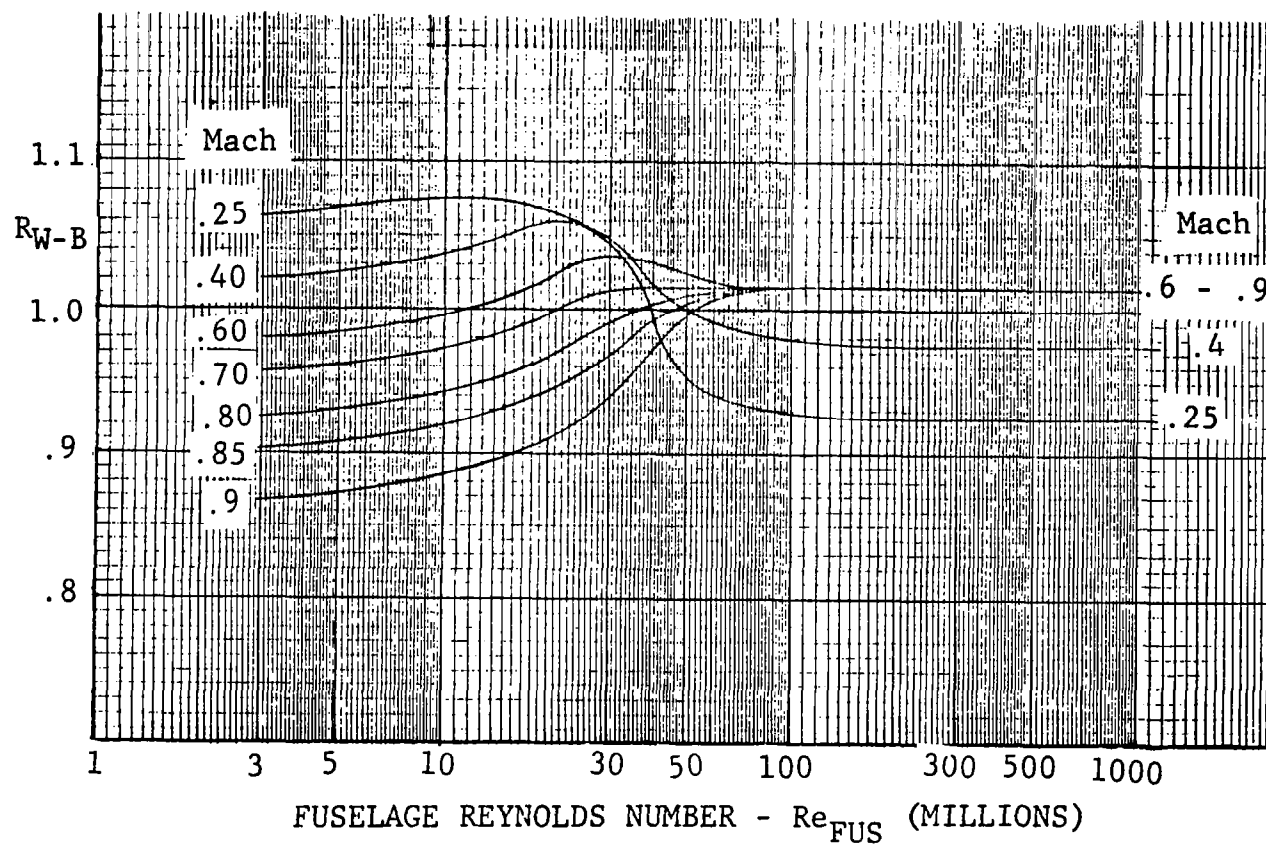
Figure 145. Wing-Body Correlation Factor for Subsonic Minimum Drag
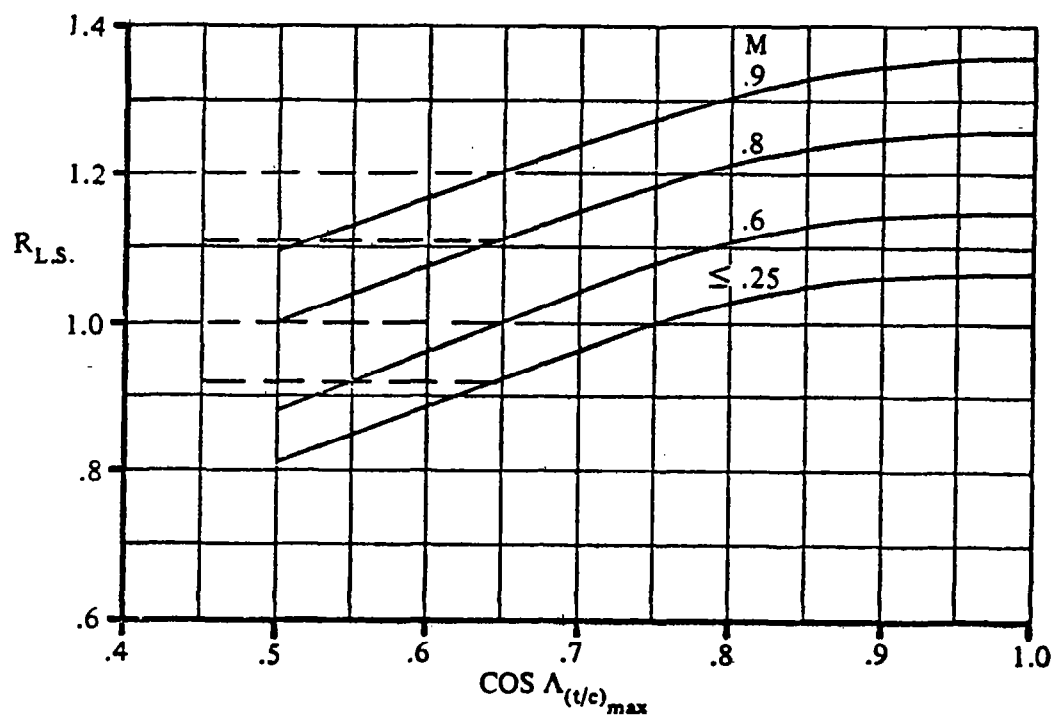
Figure 146. Lifting Surface Correlation Factor for Subsonic Minimum Drag
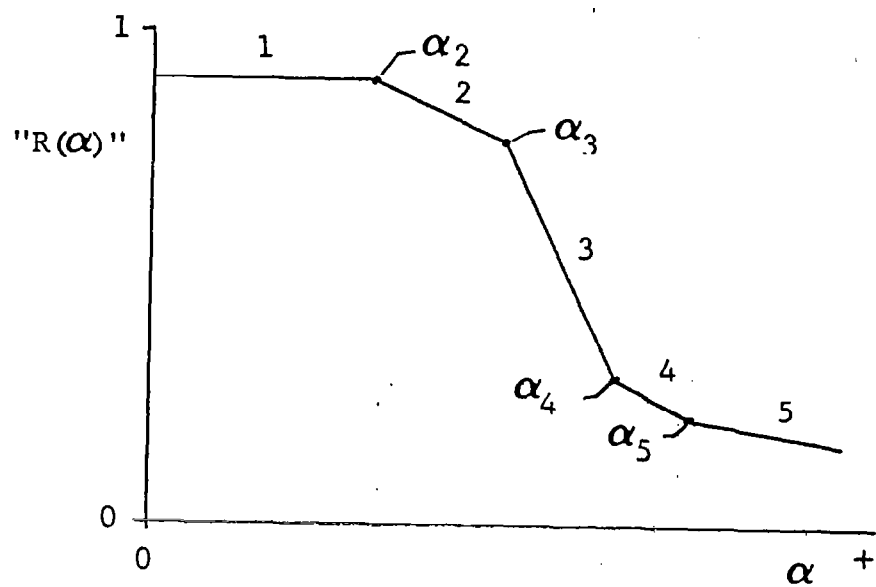
Figure 147. Schematic Variation of Suction Ratio with Angle of Attack

$$\Omega = \text{Re}_{\text{LER}} \; \text{COT}\Lambda_{\text{LE}} \; \sqrt{1 - M^2 \cos^2 \Lambda_{\text{LE}}}$$
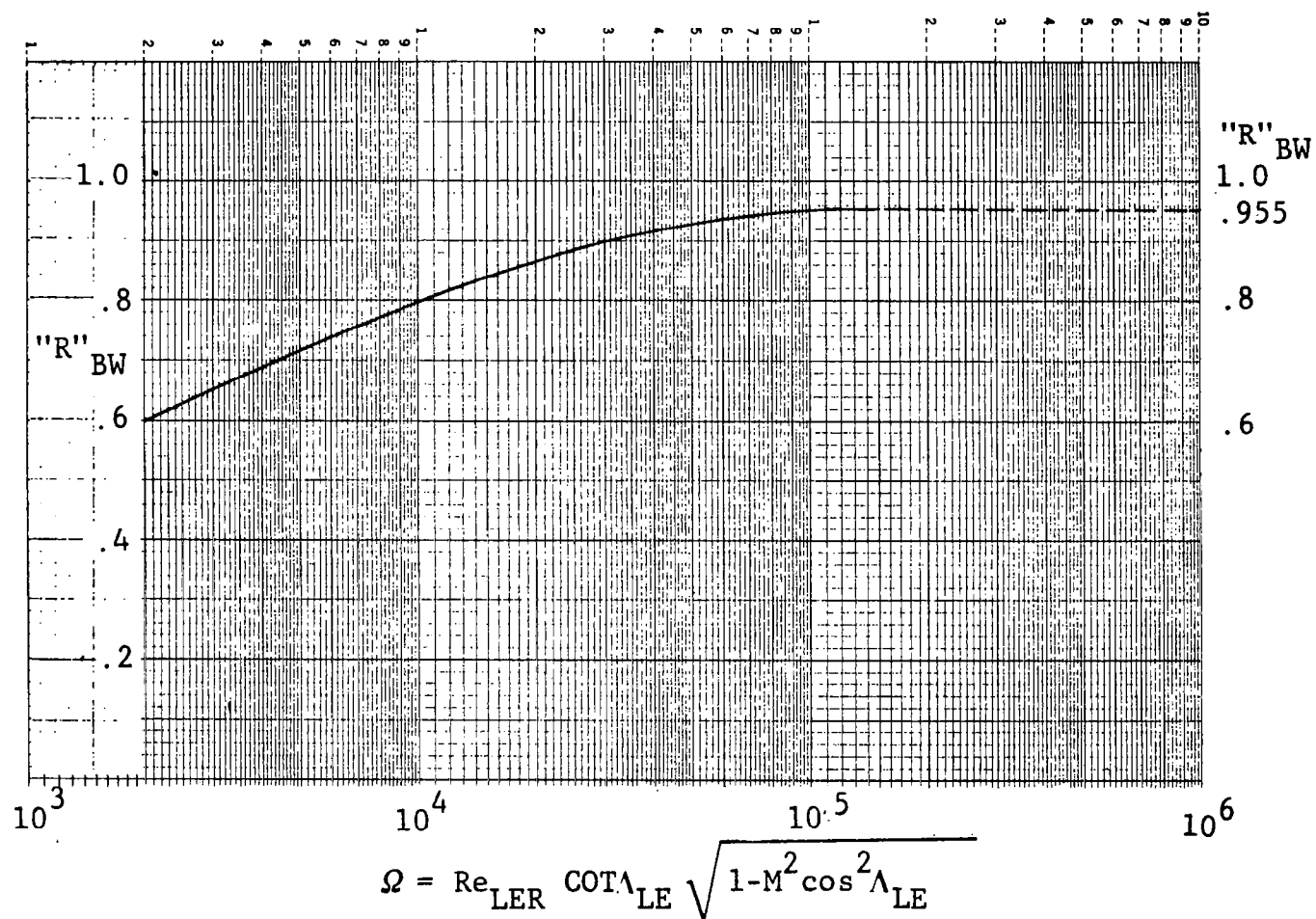
Figure 148.   Correlation Curve for Suction Ratio of Basic Wing
Planforms in Region 1

Note $"R"_1 = "R"_{BW} + \left[\dfrac{\Delta"R"_1}{\Lambda_F - \Lambda_W}\right] (\Lambda_F - \Lambda_W)$
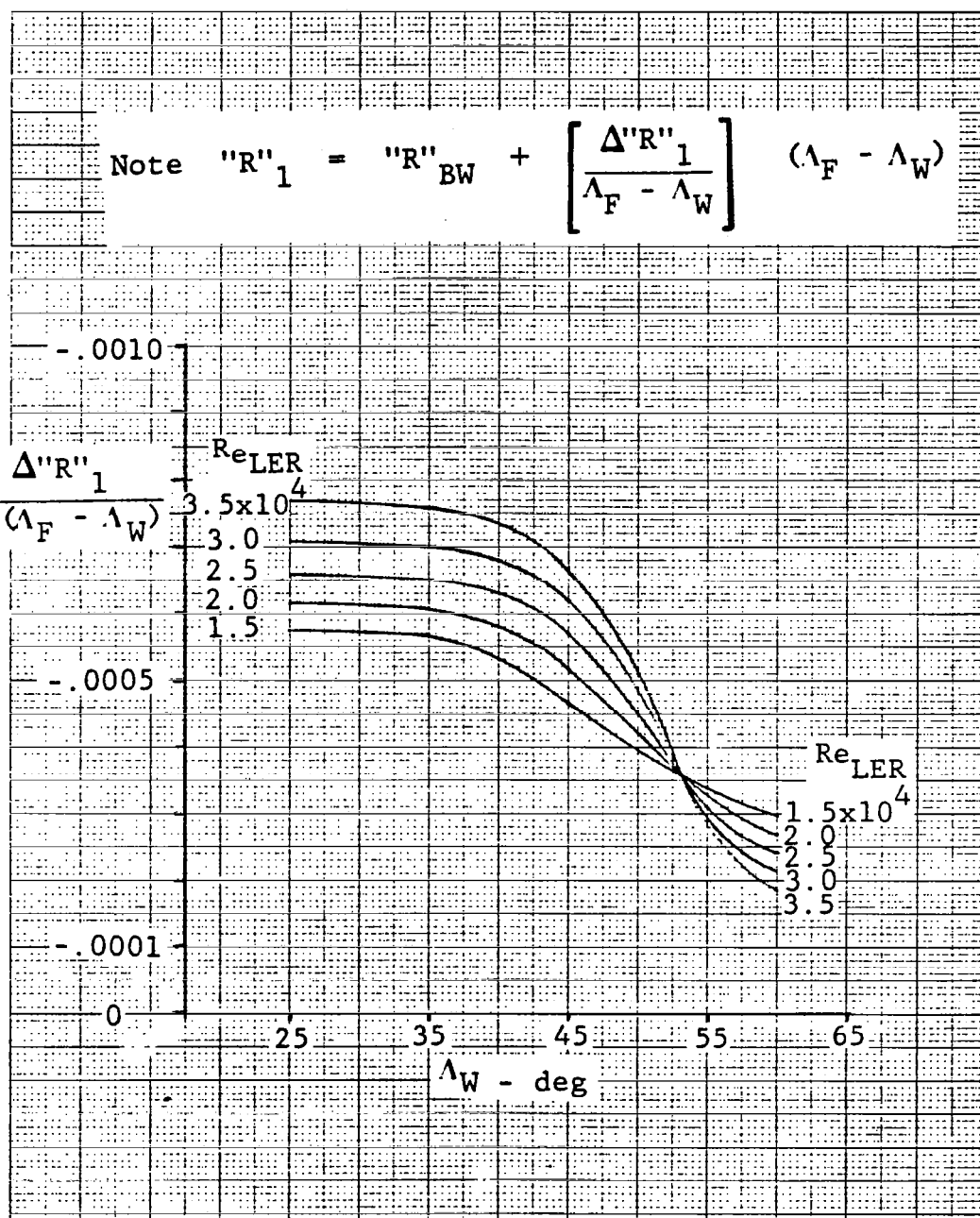
Figure 149. Calculation Chart for Incremental Effect of Fillet
Sweep on Suction Ratio in Region 1
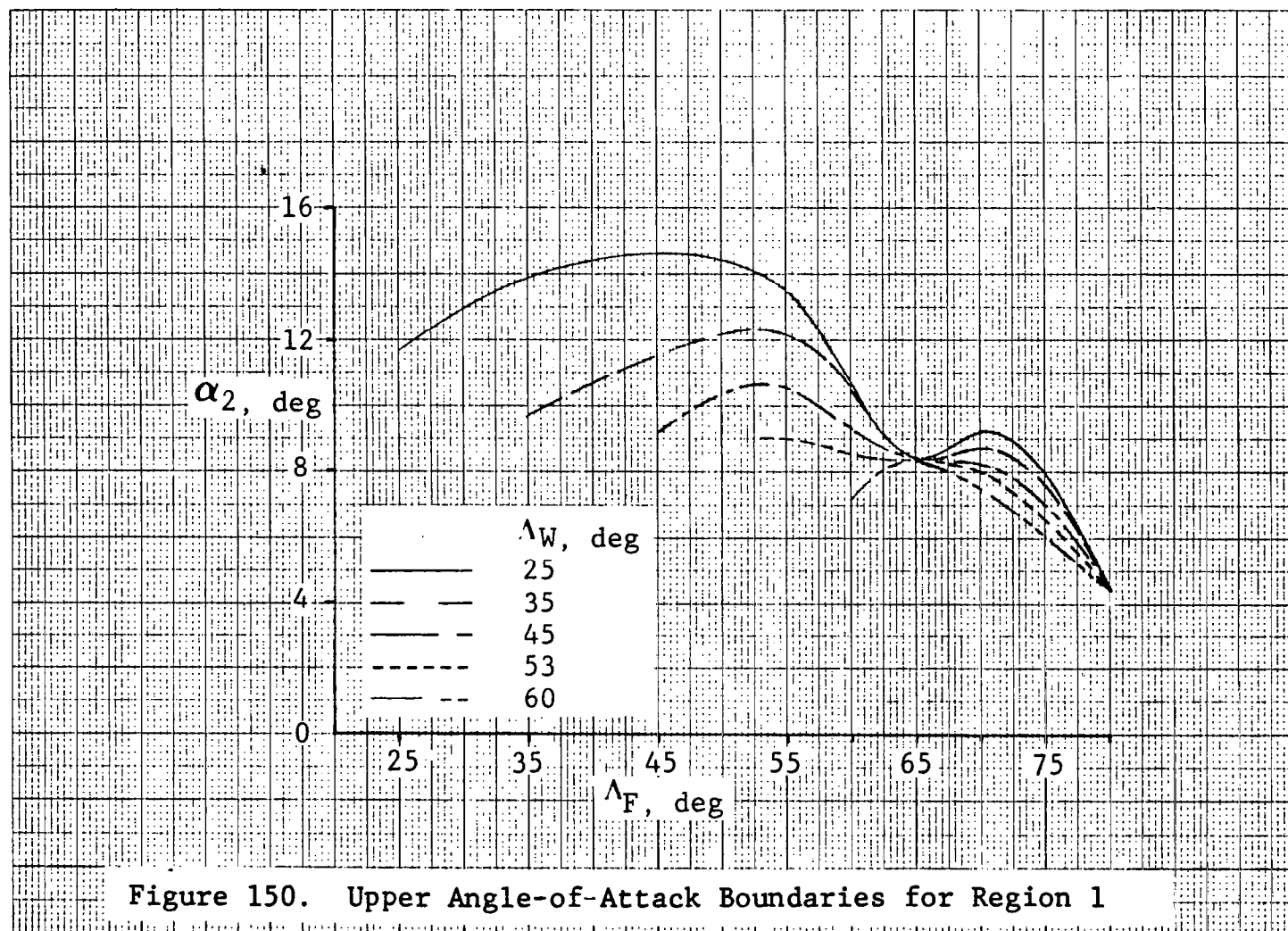
Figure 150. Upper Angle-of-Attack Boundaries for Region 1
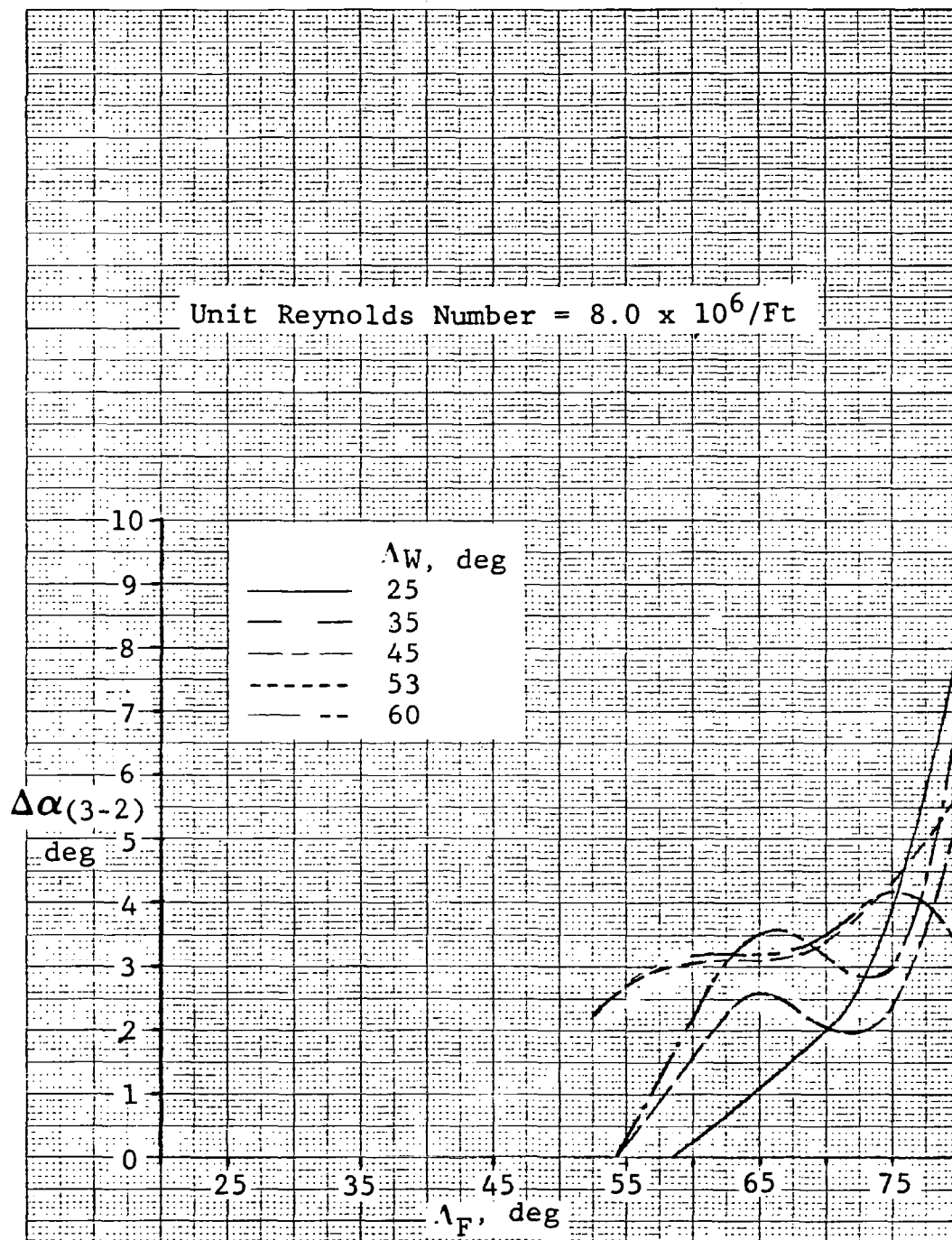
Figure 151. Incremental Angle of Attack for Region 2
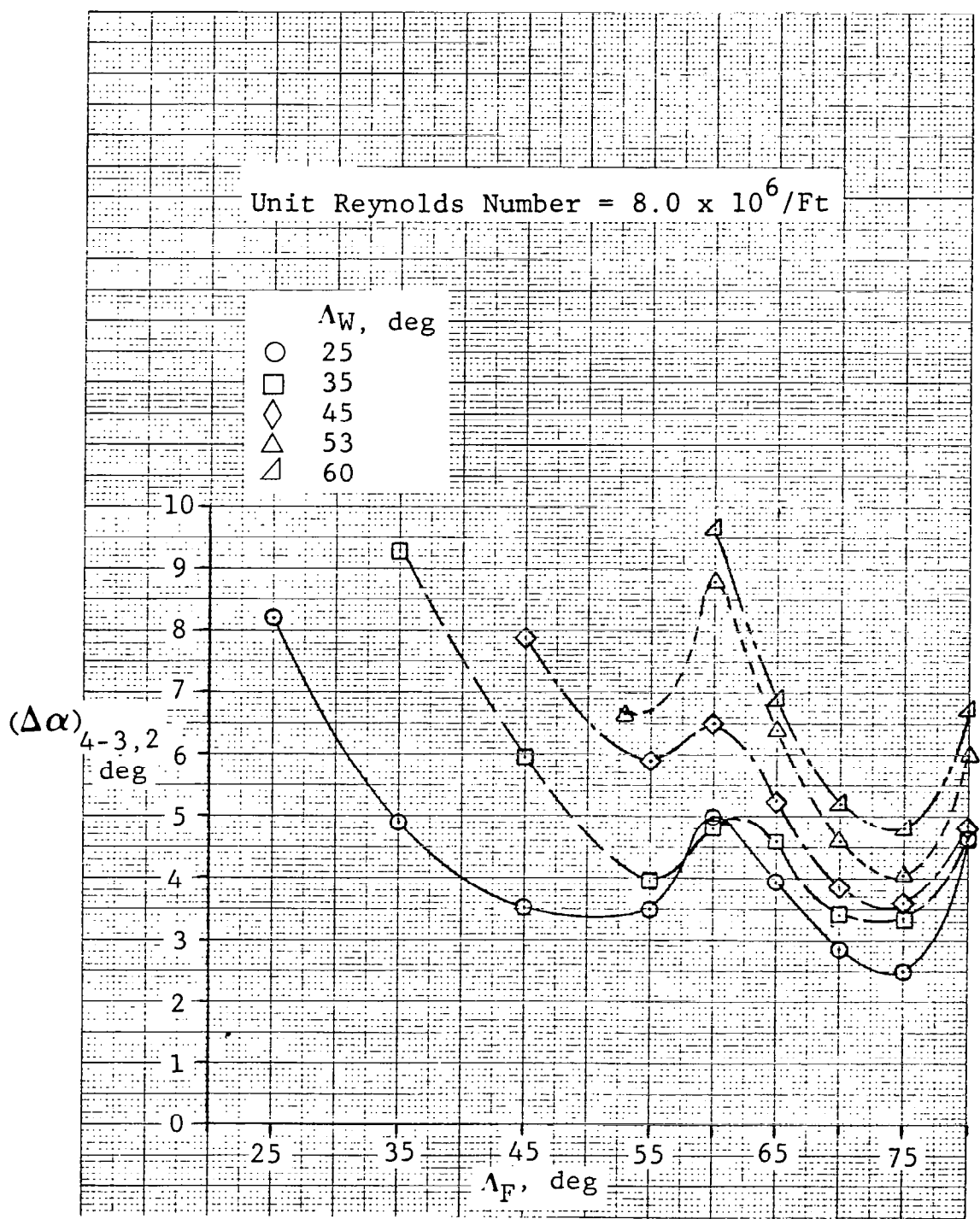
Figure 152. Incremental Angle of Attack for Region 3
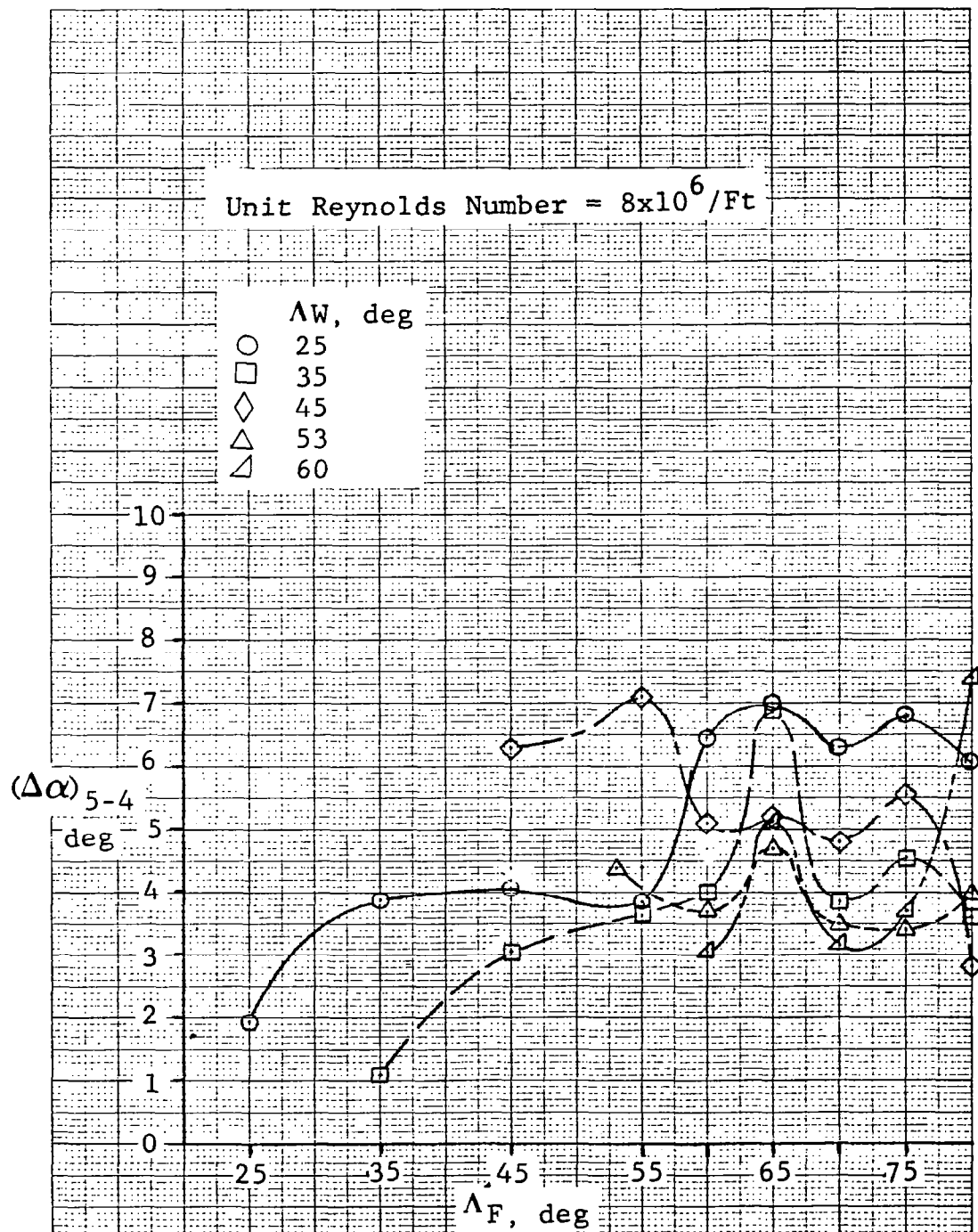
Figure 153. Incremental Angle of Attack for Region 4
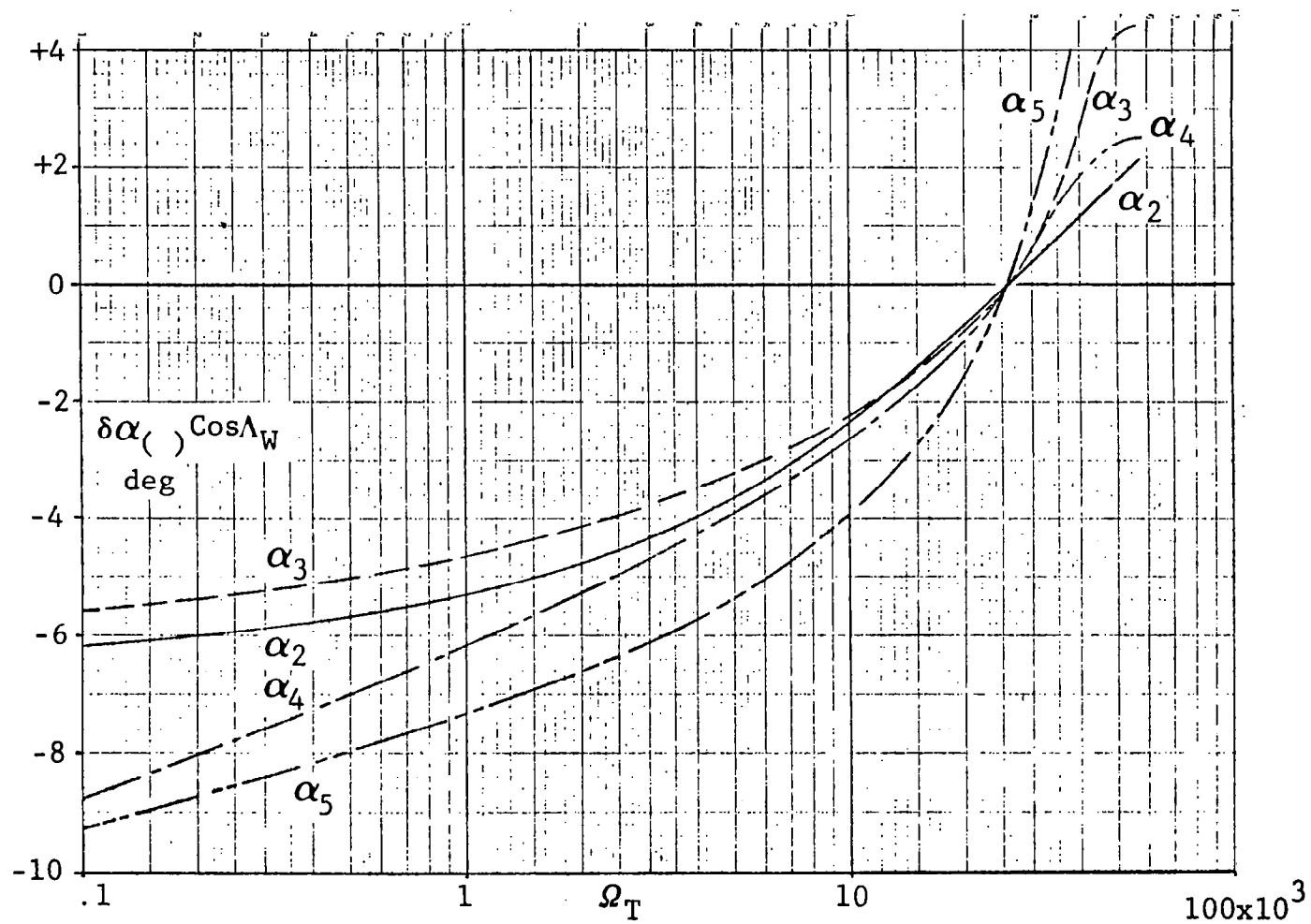
Figure 154. Calculation Chart for Change in α Boundaries of
Basic Wings Due to Change in Reynolds Number
(Ω_T Based on Leading-Edge Radius at Wing Tip)
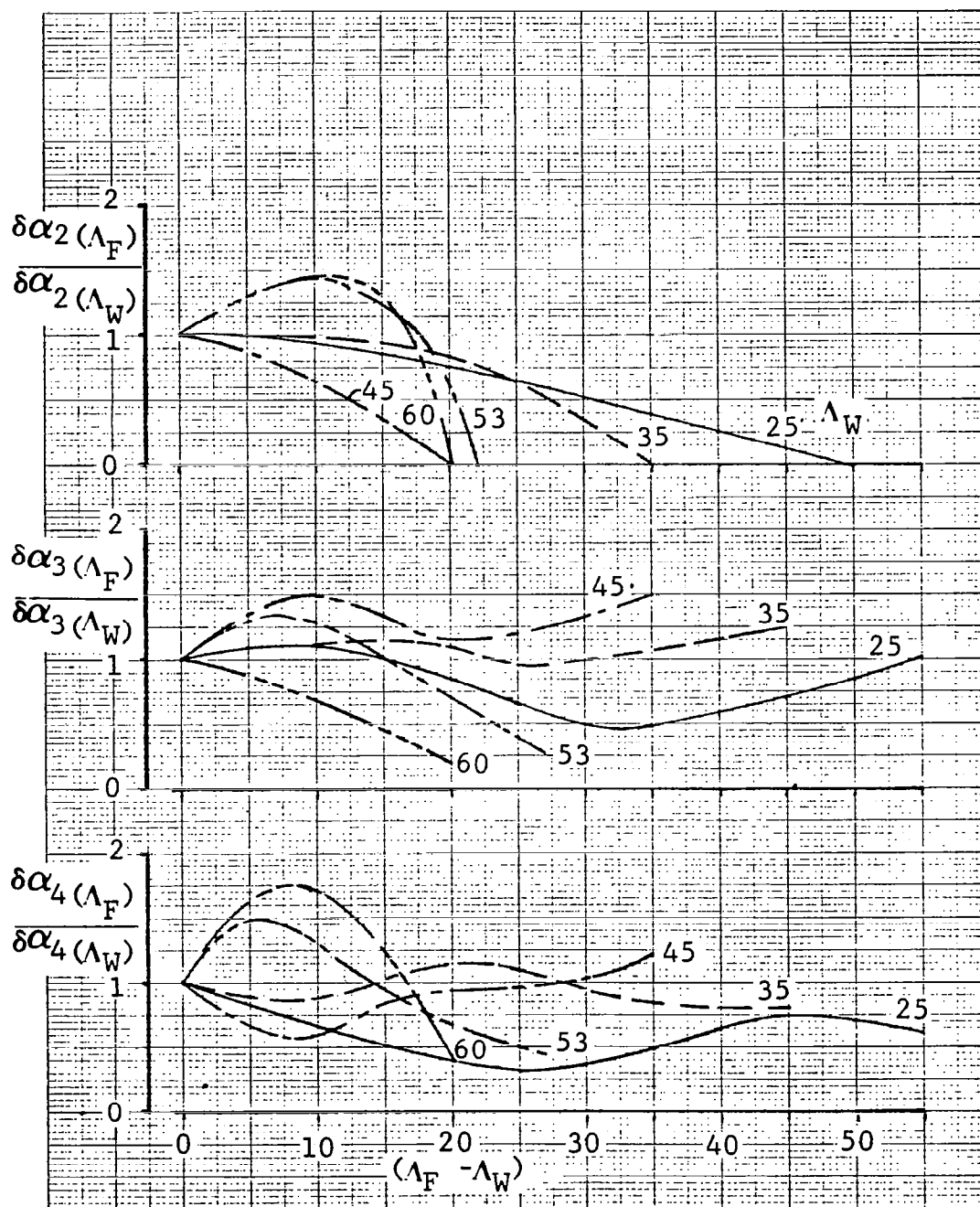
Figure 155. Correction Term for Effect of Fillet Sweep on Boundaries
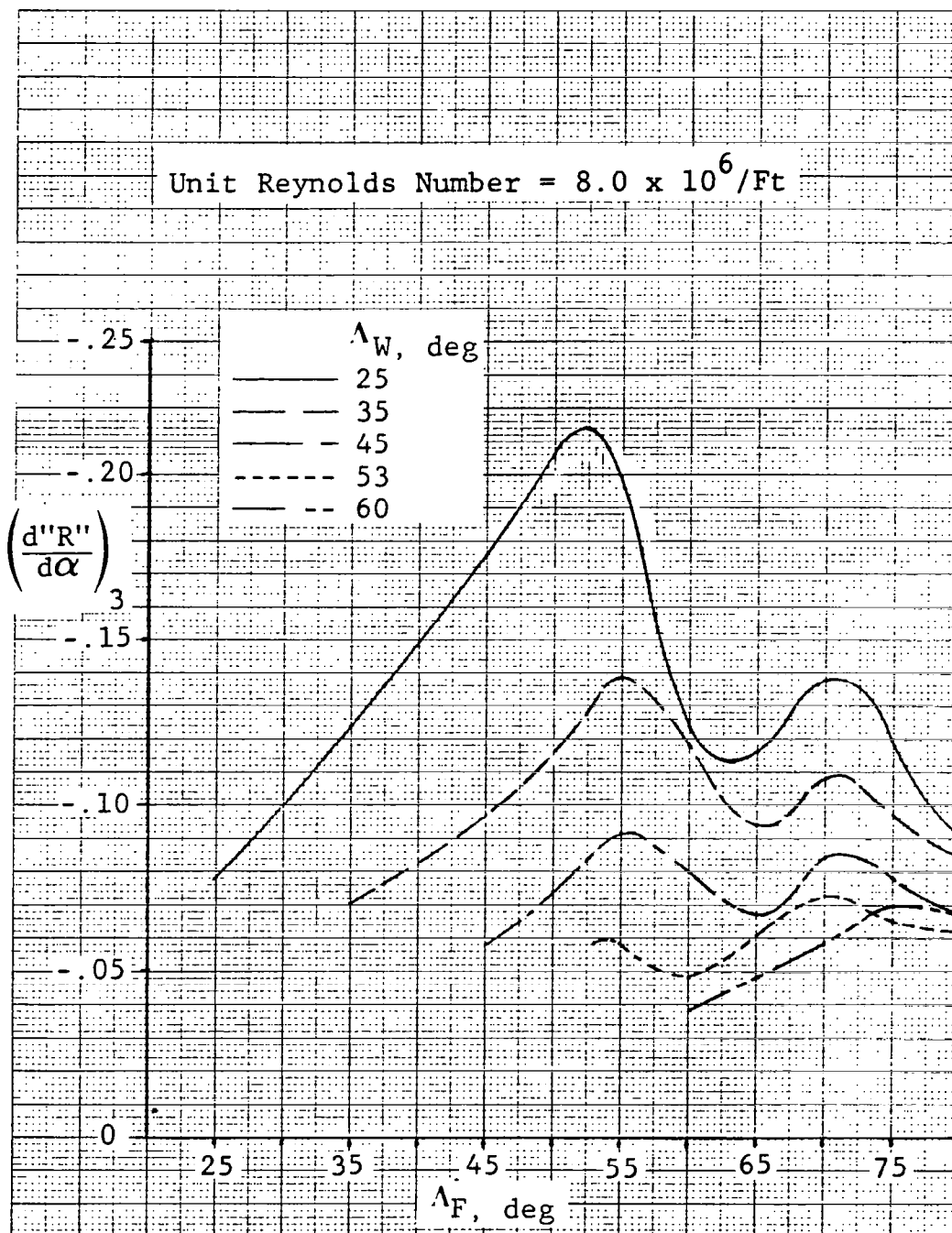
Figure 157. Slopes of Suction-Ratio Curves in Region 3
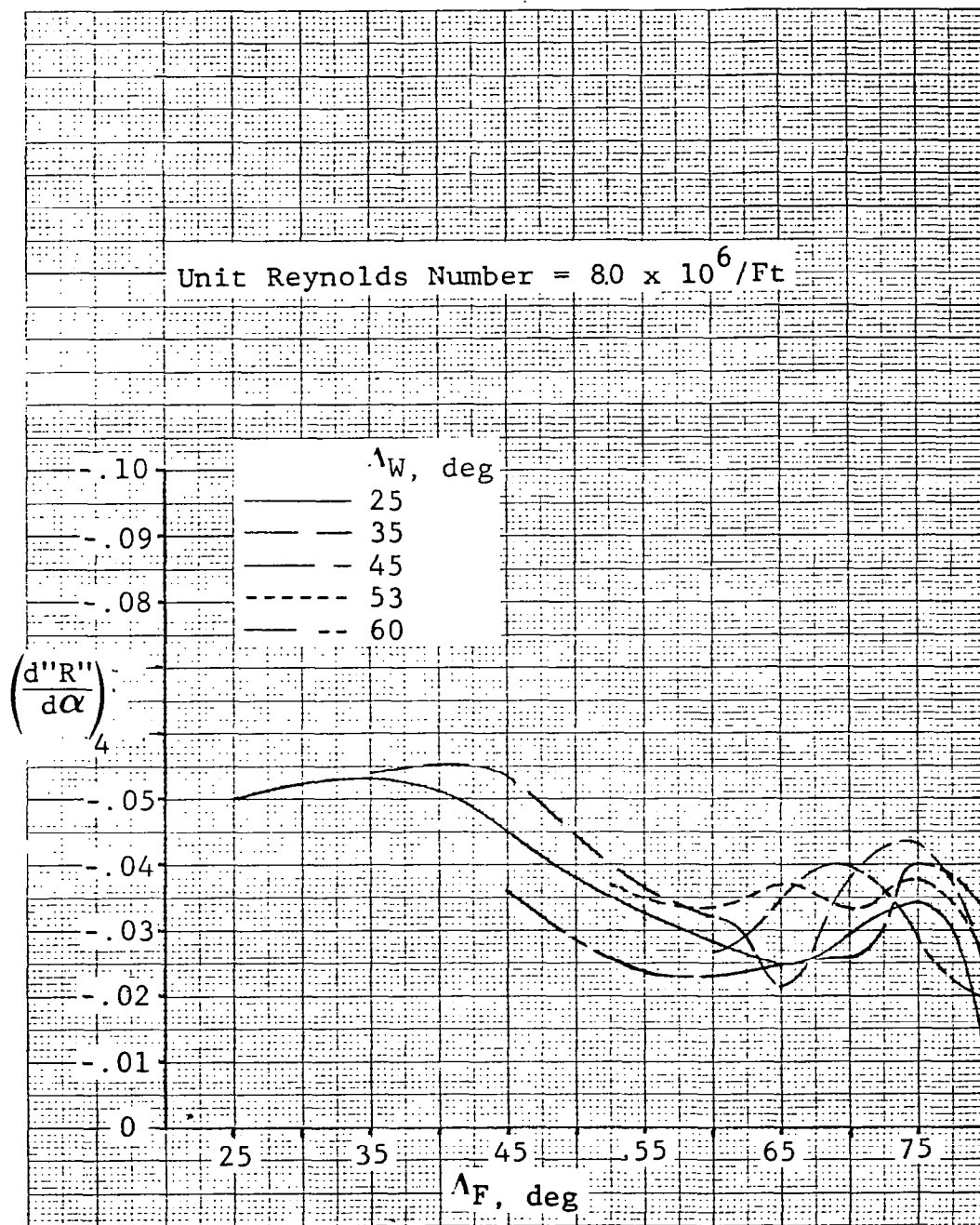
Figure 158. Slopes of Suction-Ratio Curves in Region 4
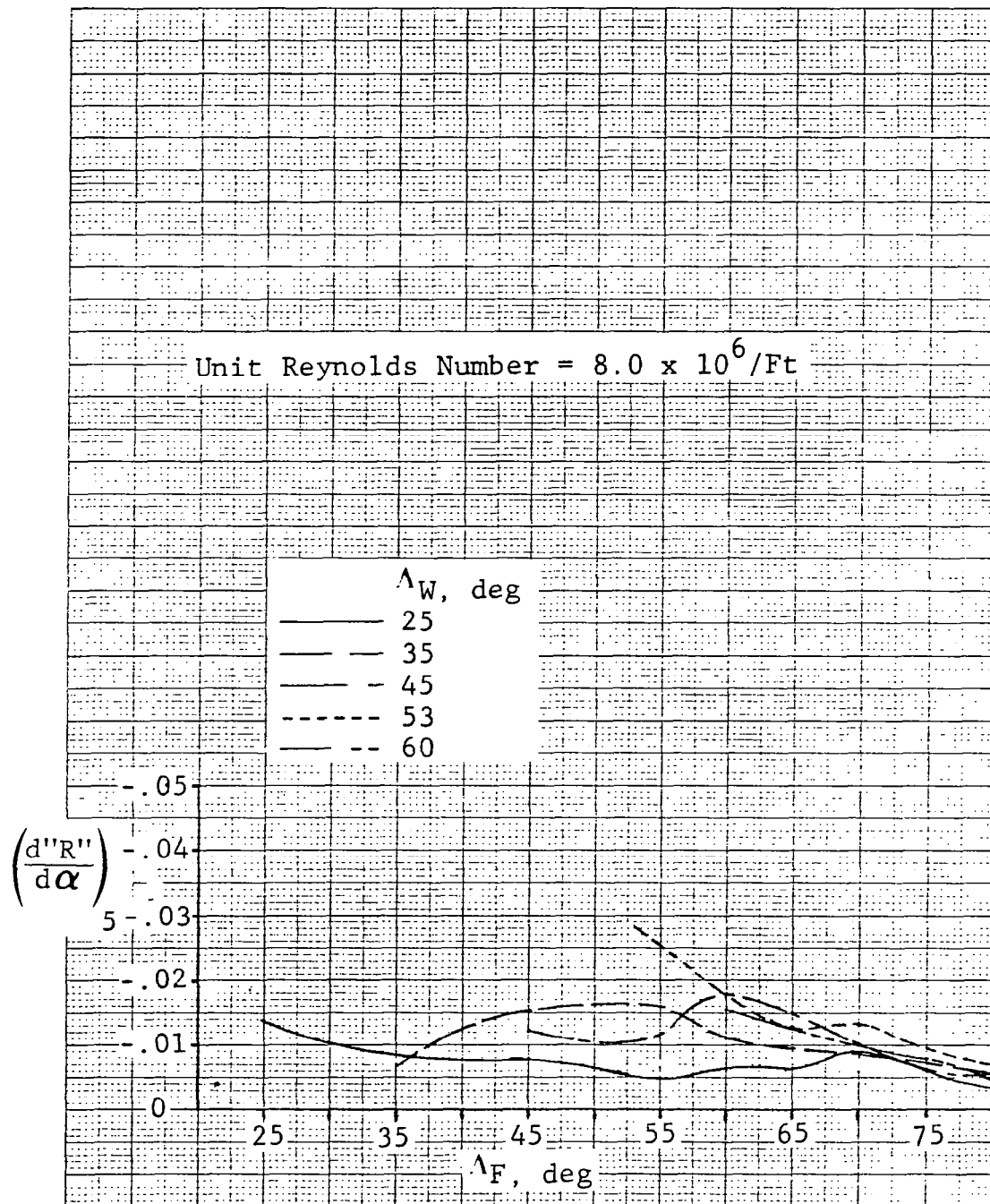
Figure 159.   Slopes of Suction Ratio Curves in Region 5
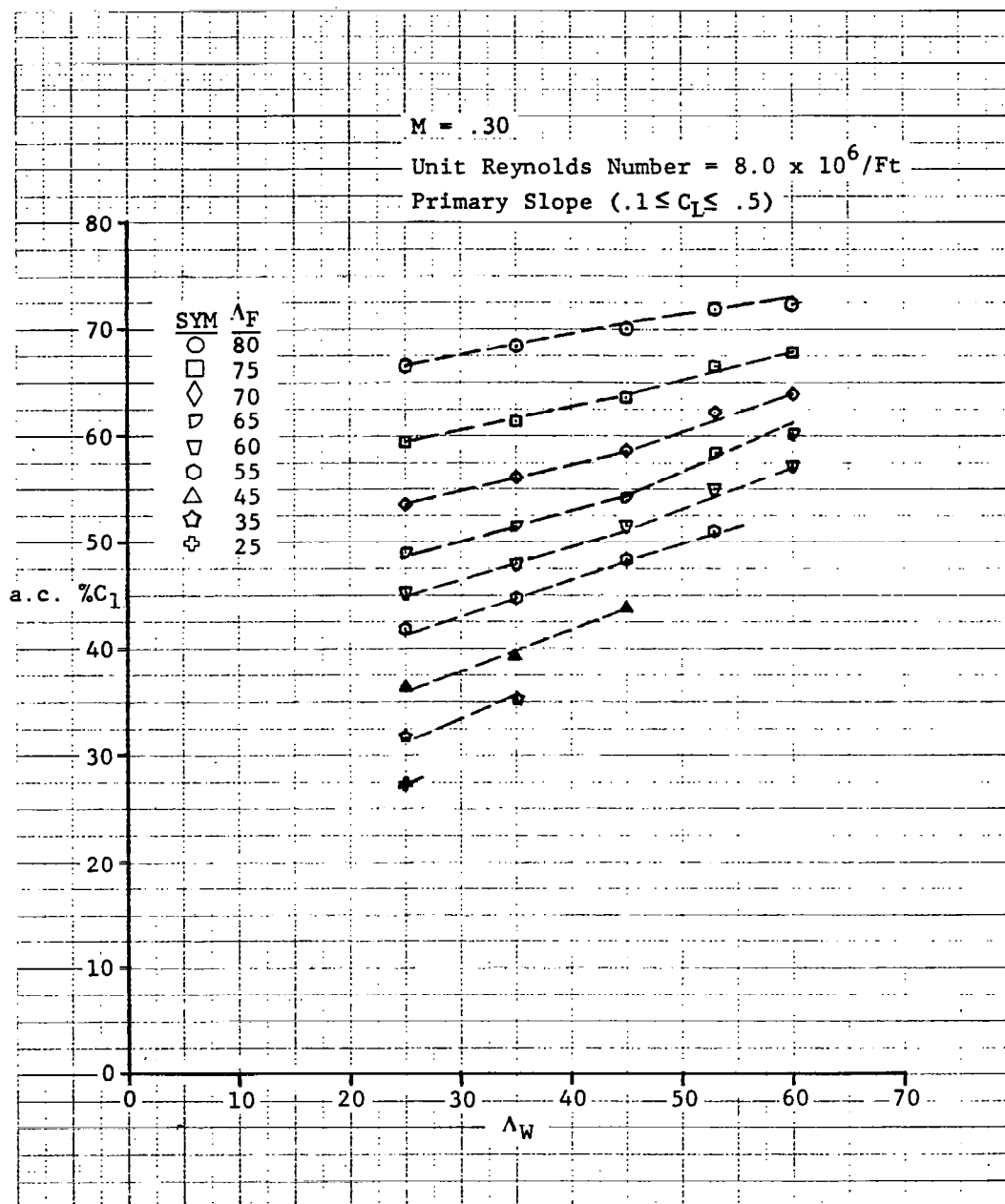
Figure 160. Aerodynamic Center Test-to-Theory Comparison
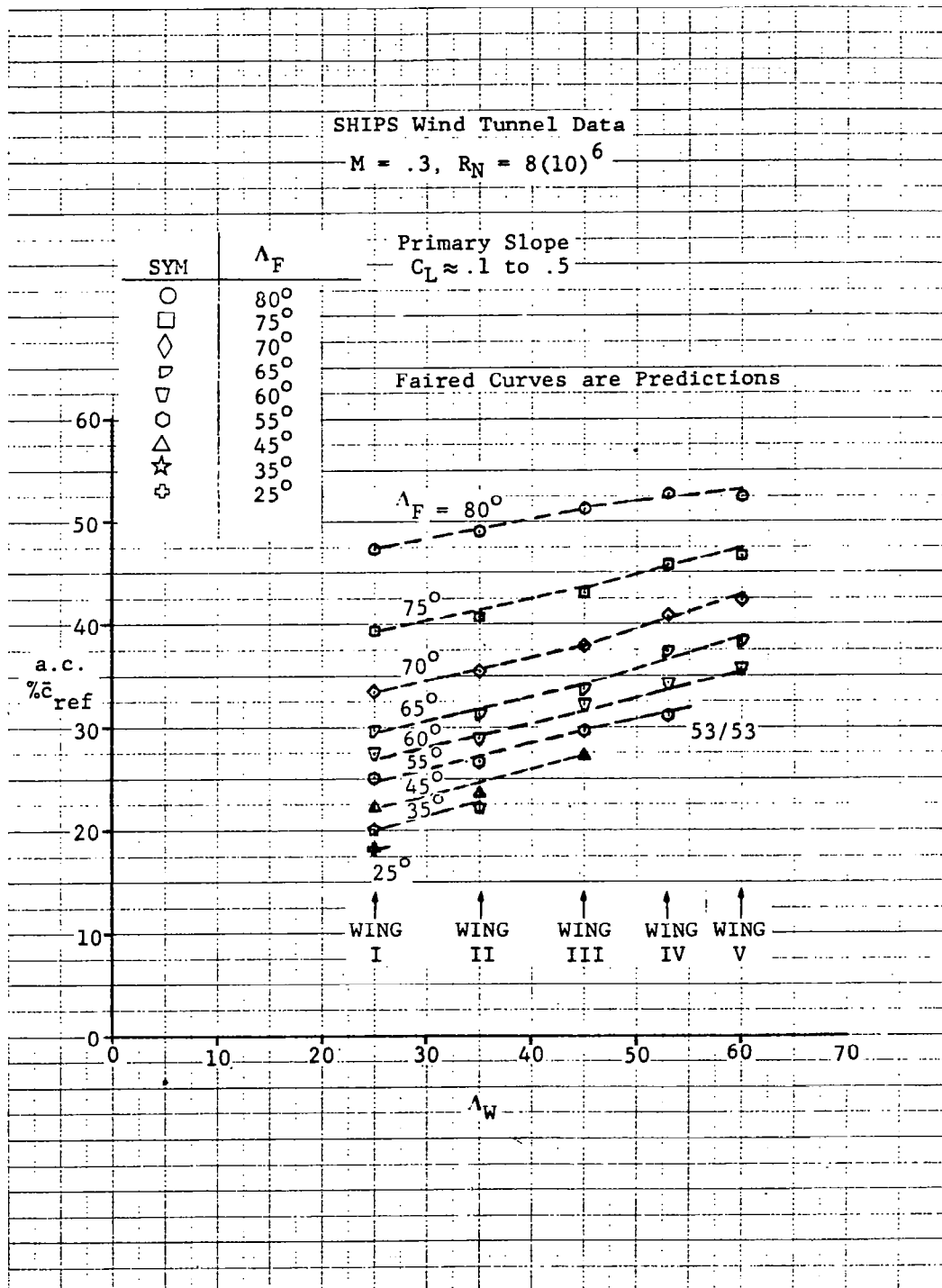
Figure 161. Aerodynamic Center as Percent MCG
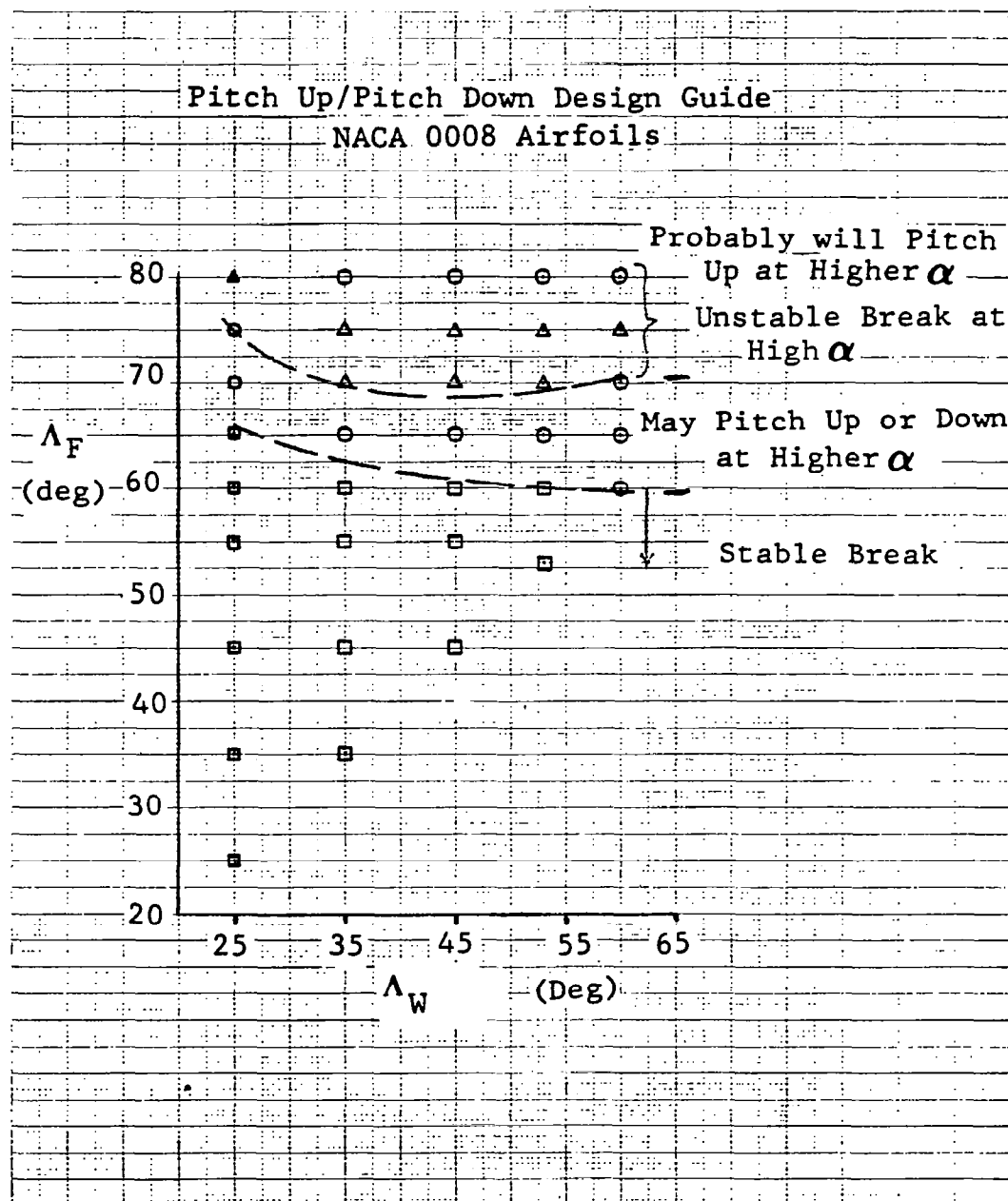
Figure 162. Pitch Up/Pitch Down Tendencies as
Functions of Wing and Fillet Sweep
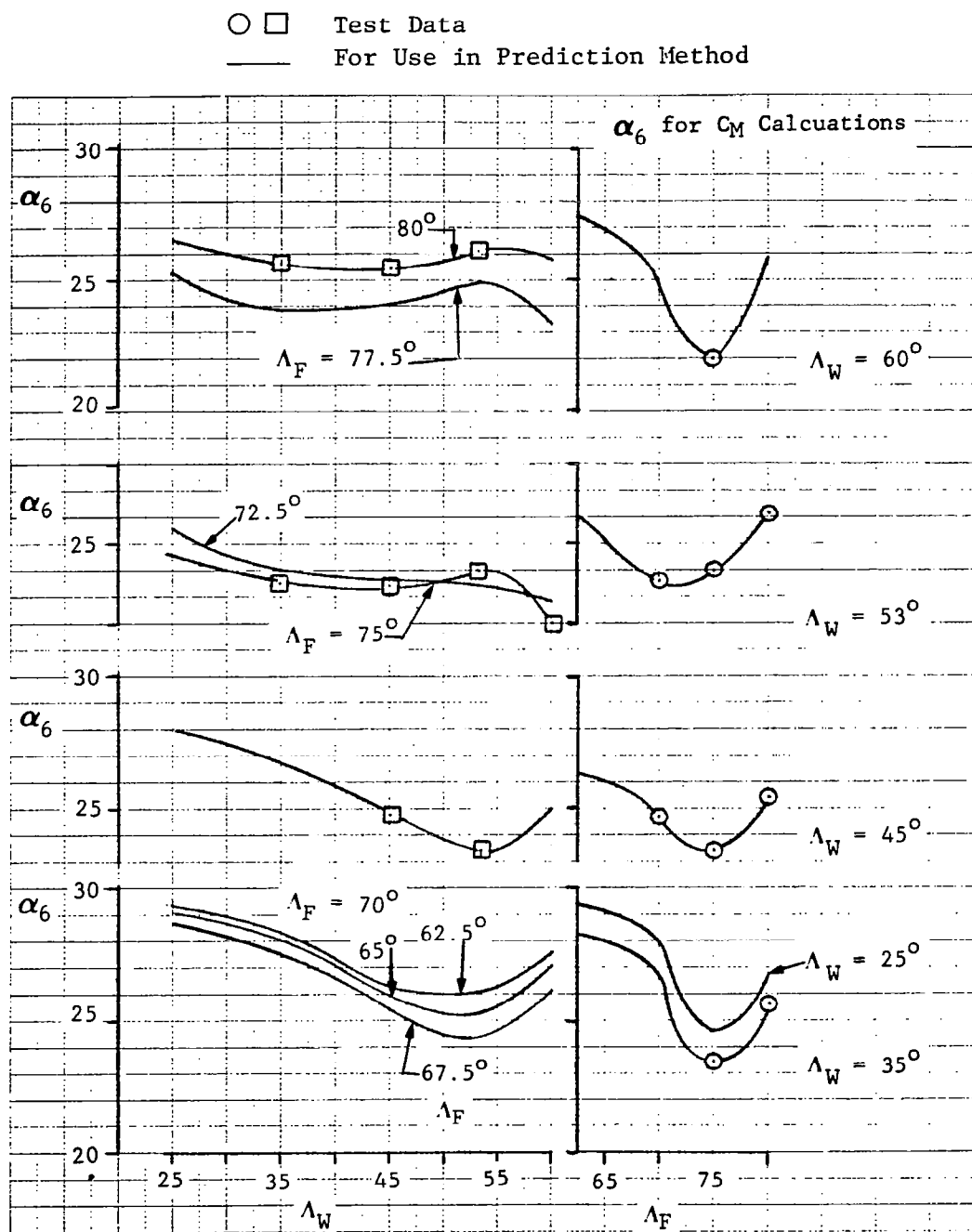
Figure 165. Upper Angle of Attack Boundary for Region 5
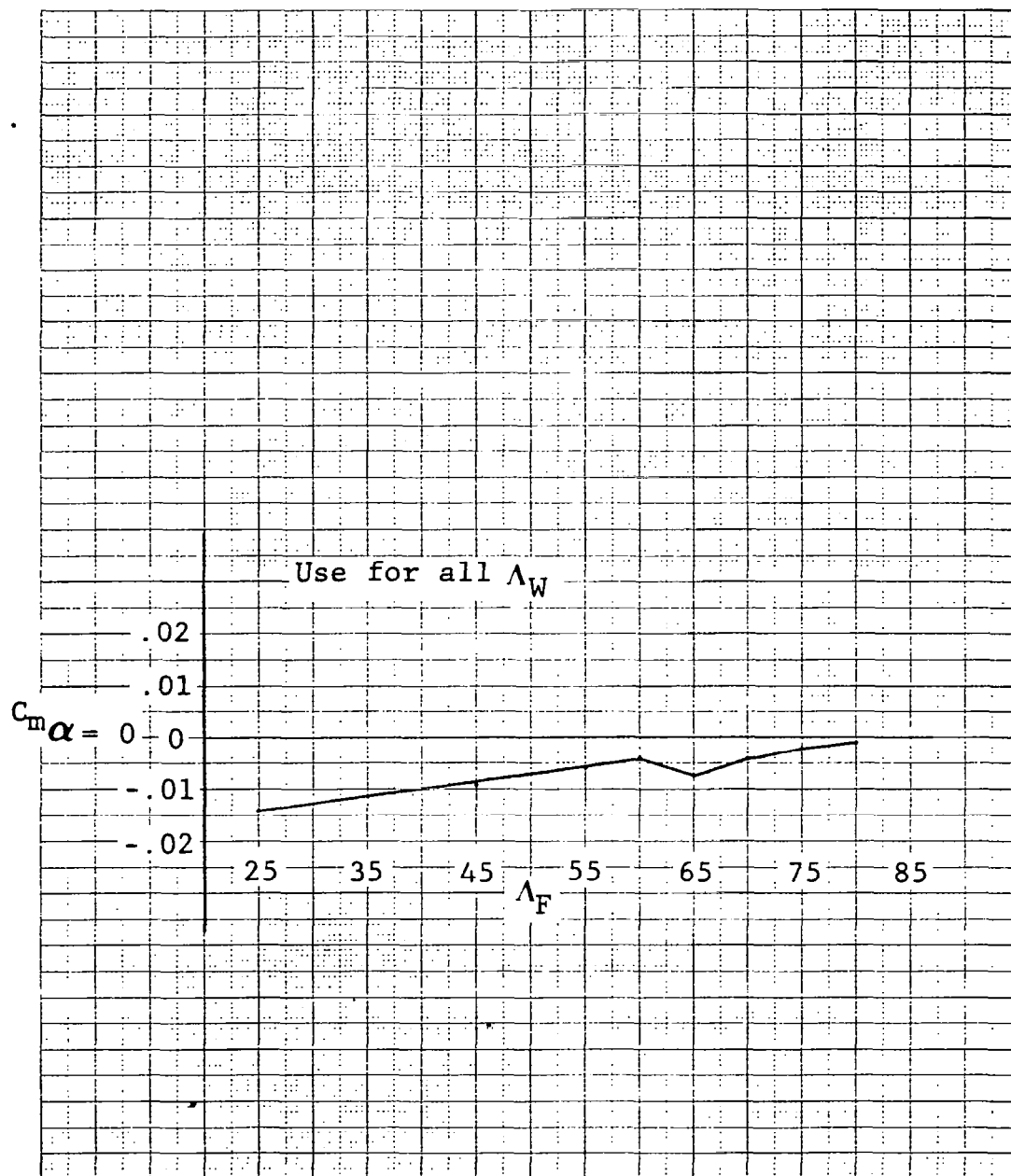
Figure 166. Pitching-Moment Coefficient at Zero Angle of
           Attack
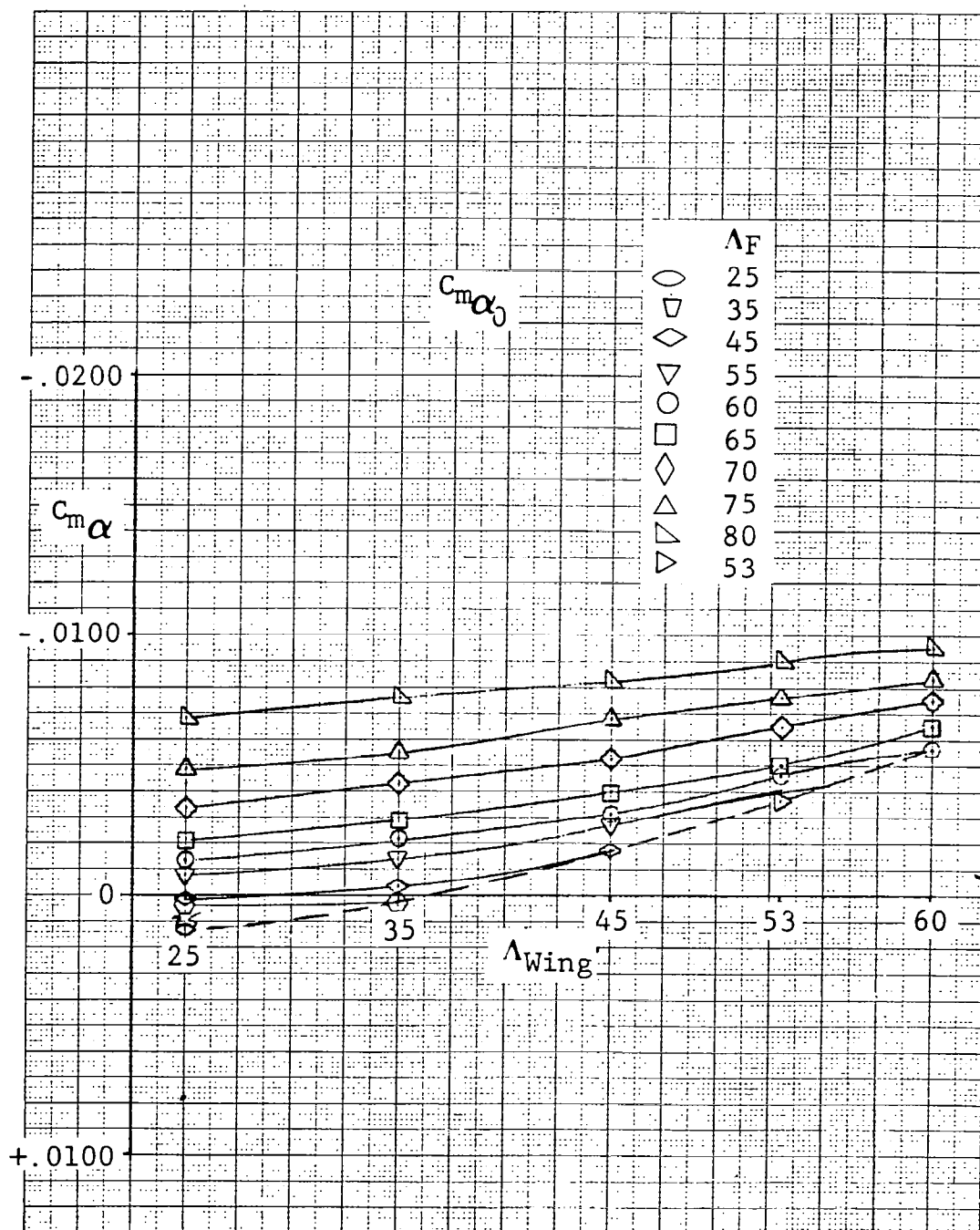
Figure 167. Pitching-Moment Coefficient Derivative for Region 0
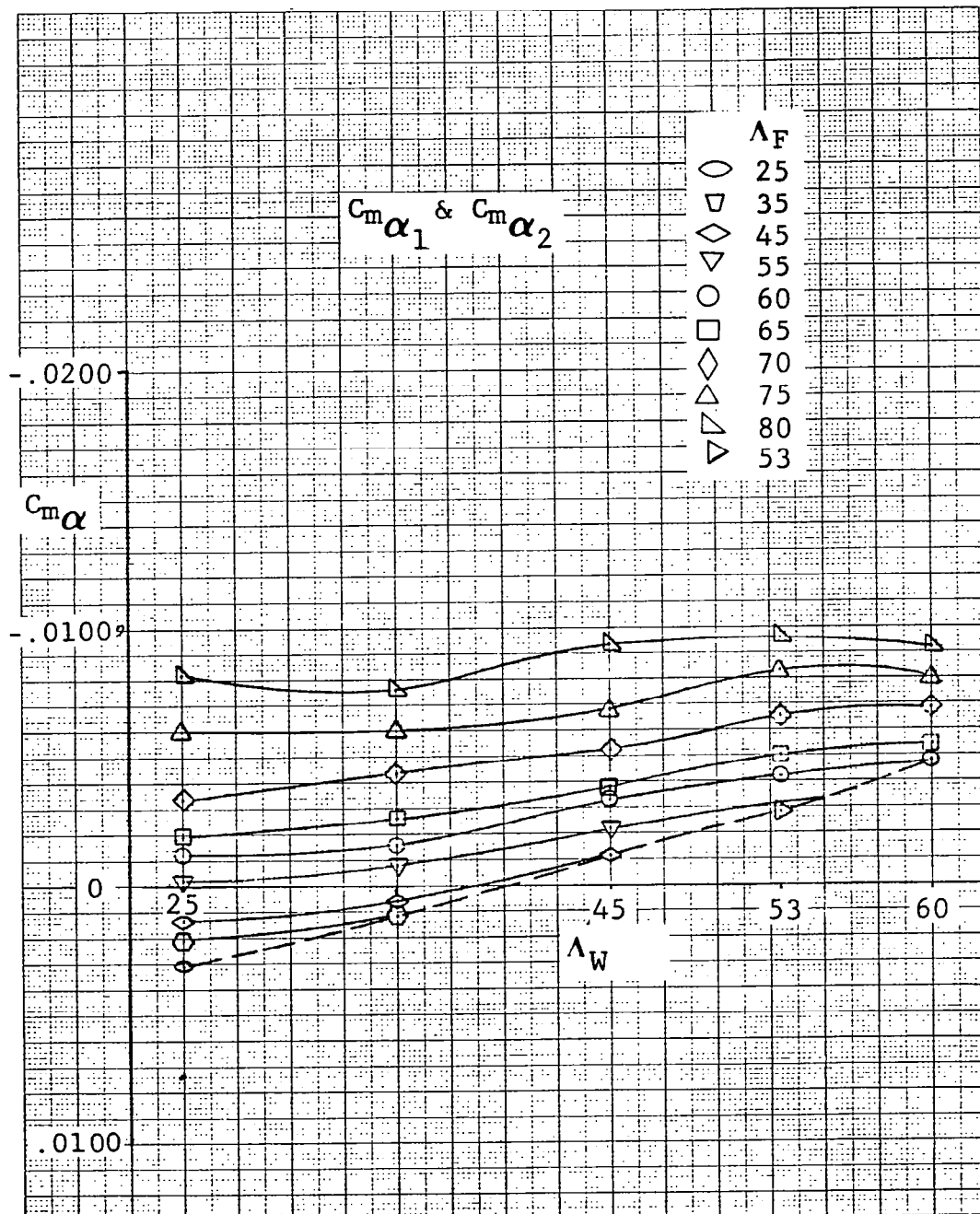
Figure 168.   Pitching-Moment Coefficient Derivatives for
                Regions 1 and 2
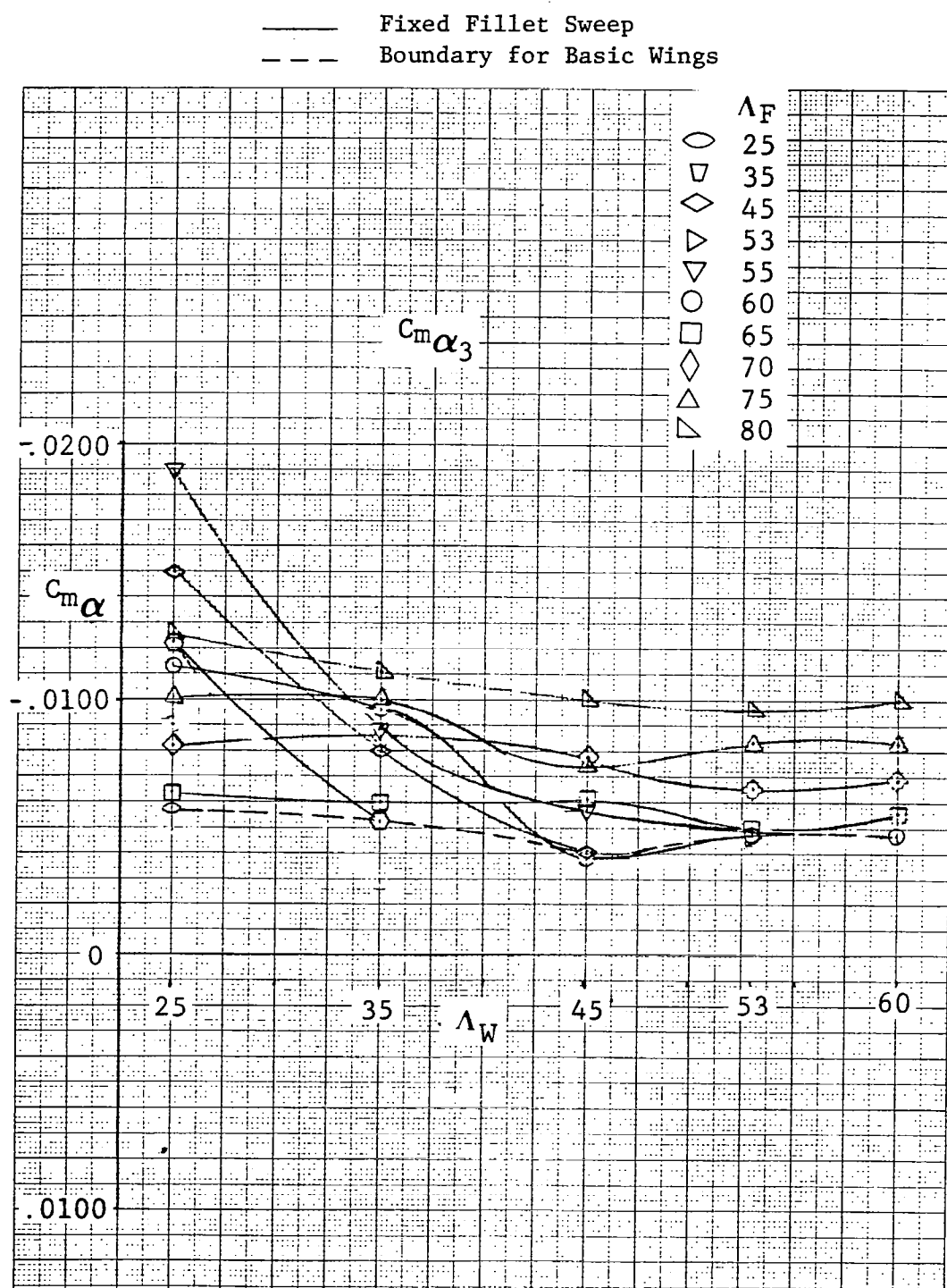
Figure 169. Pitching-Moment Coefficient Derivative for Region 3
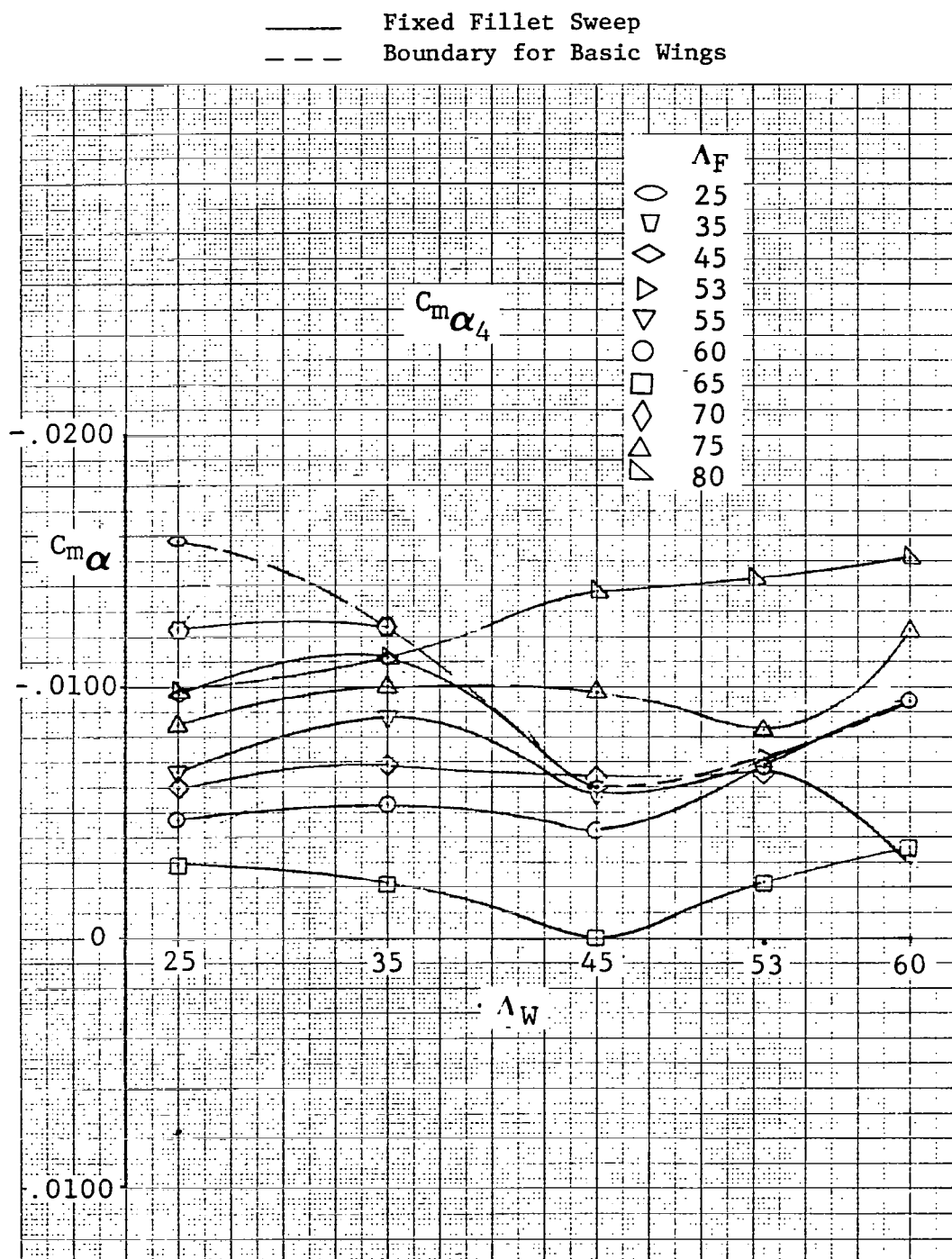
Figure 170. Pitching Moment Coefficient Derivative for Region 4
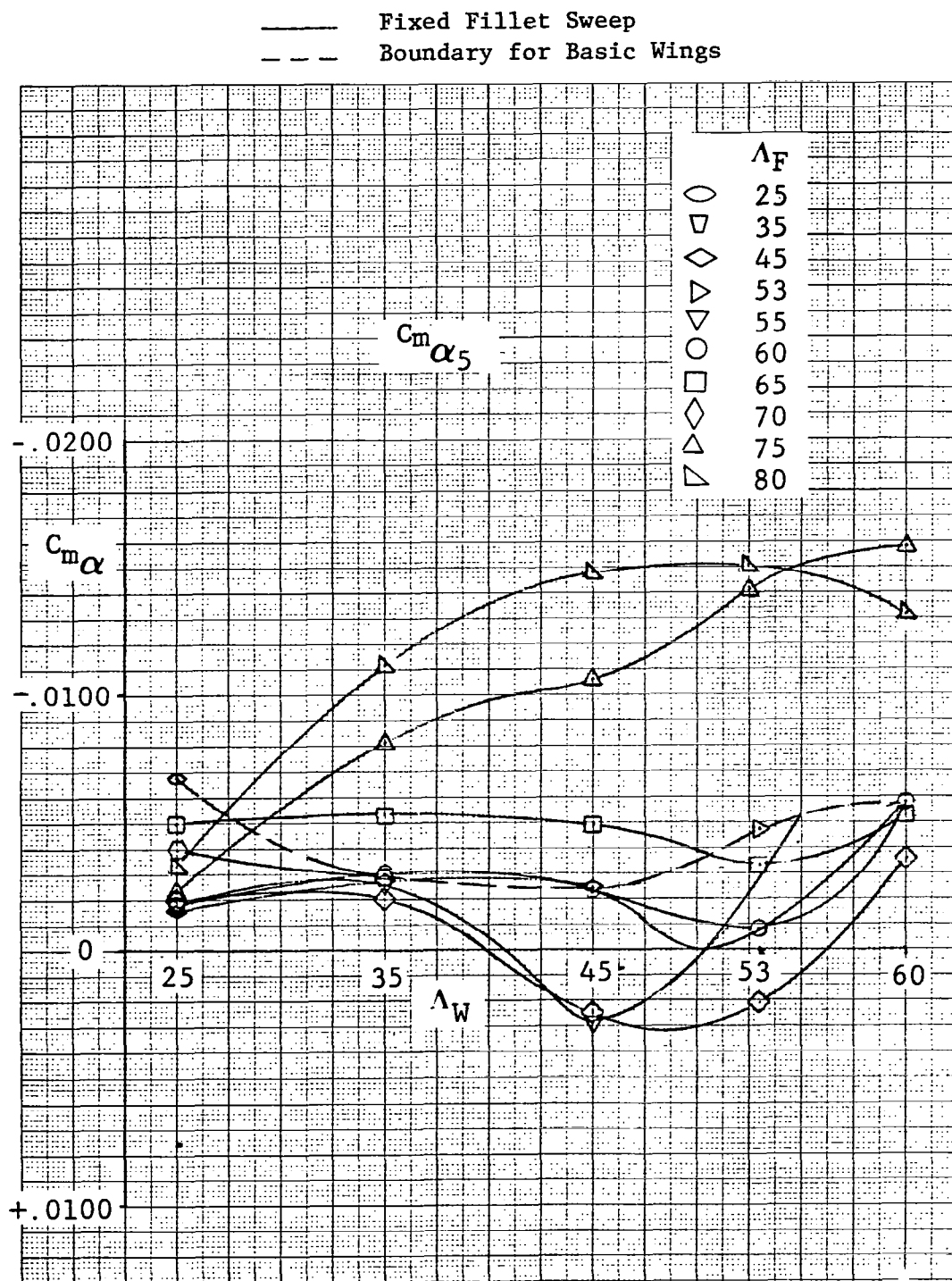
Figure 171.   Pitching Moment Coefficient Derivative for
Region 5
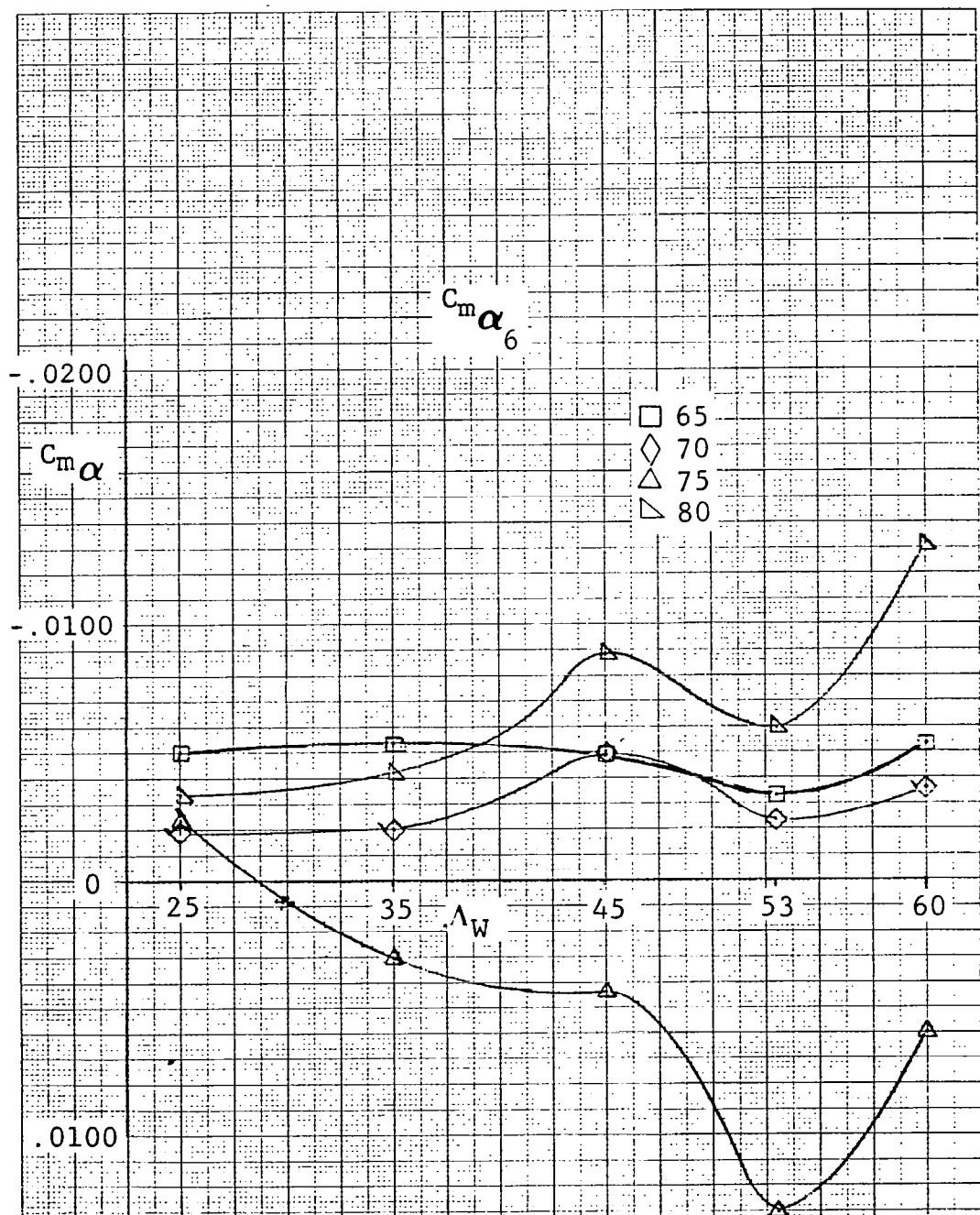
Figure 172. Pitching Moment Coefficient Derivative for Region 6

REVISIONS TO "BASIC" METHODS

The basic prediction methods presented in the previous section partially achieved the objectives of the investigation. Ongoing NASA configuration definition studies of an advanced aerospace vehicle indicated the need for data on configurations with other airfoils than the NACA 0008 airfoil. The very limited data obtained with three configurations having NACA 0012 airfoils indicated that Reynolds number effects might be significant to much larger Reynolds numbers than had been obtained in test ARC 12-086. In addition, limitations on the angles of attack obtained in the first test had left some questions as to the pitching-moment behavior for some configurations. Thus, it was apparent even before the "basic" prediction method task was completed that additional testing would be required to provide data to resolve these issues.

Additional Testing and Analysis

The Vehicle Analysis Branch of the NASA Langley Research Center planned the additional tests of a limited series of planforms (described earlier in the Test Data Base section of this report) to define the effects of different airfoil sections and higher Reynolds numbers, and eventually data were obtained at higher angles of attack. The tests were accomplished in the NASA Langley Research Center Low Turbulence Pressure tunnel with the small models and the NASA Ames Research Center 12-foot tunnel with the large (twice-size) models.

Analysis of the additional data was performed using the same approaches that were used for the "basic" prediction method development. This required that the reference quantities of wing area, moment reference length, and moment reference point be on the same basis, whereas the test data for the additional tests had been reduced originally using different quantities. The neces-

258

sary revisions to the data were made by altering a few equations in the analysis procedures which had been programmed for solution on a Hewlett Packard 9820 desktop computer.

One of the first steps in the analysis was to make comparisons of data obtained in the different facilities to determine if significant differences occurred. An example comparison of the variations of pitching moment with angle of attack is presented in Figure 173. It is apparent that the data for the 65A012 airfoil configuration obtained in LTPT test 262 is significantly different from that for all of the other configurations. In contrast, data from test ARC 12-257 shows only small differences between the pitching-moment curves for 0012 and 65A012 airfoil configurations. It later became apparent that erroneous moment transfer distances had been used in reducing data for four configurations in test LTPT 262, including the 70 and 75 degree fillet configuration with 65A012 and 65_1412 airfoils. It became necessary later to adjust the moment-transfer distances for these configurations in order to complete the pitching-moment predictions. The adjustments were made such that the slopes at low angle of attack agreed with the data from ARC test 12-257.

An overall survey of Reynolds number effects indicated that above a unit Reynolds number of 26.25 million per meter the effects are small in comparison to the effects noted between 13.13 million per meter and 26.25 million per meter for the small models. The configurations with 12 percent thick airfoils show the most sensitivity to Reynolds number. It is apparent that the major effects occur as a result of relatively low leading-edge sweep of the outboard wing panel or of the fillet-outboard panel combination.

A brief look at the suction-ratio data showed that, in general, the values in region 1 are higher than those measured in ARC test 12-086. The reason for this fact is not immediately obvious. It was therefore decided to concentrate first on the lift correlation to see if significant differences occurred between the tests in the different facilities and with the different size models and to look at the effects of airfoil thickness ratio, thickness distribution, and camber.

Some example comarisons are presented in Figures 174 through 179. Figures 174 and 175 illustrate the magnitudes of the differences in the variation of the lift-correlation parameter with angle of attack for three of the 4 tests in which the same configurations were run. Also shown are the predicted values obtained from the overall correlation procedure. It is apparent that measurements made in the Low Turbulence Pressure Tunnel on the small models and in the ARC 12-ft tunnel on the large models produced higher lift coefficients at a given angle of attack than did the original measurements in the ARC 12-foot tunnel on the small models. The differences are of the order of 4 to 7 percent in the regions where the curves are reasonably smooth. It is not at all obvious that any one set of data is more correct than the others.

Figure 176 and 177 present the effects of airfoil-thickness ratio variations as measured in the LTPT and ARC 12-ft facilities on the small and large models of Wing III with the 80 degree fillet. Although there are differences in details of the curves, the general trends of the effects are similar. The same comment applies to the data for the effects of airfoil-thickness ratios presented in Figures 178 and 179 for Wing III with no fillet.

Figures 180, 181 and 182 show the effects of airfoil thickness distribution and camber for the three planforms having Wing III with 80, 75 and 70 degree fillets, respectively. The trends with fillet sweep are consistent. The camber effect decreases with increasing fillet sweep. The large model data produces similar trends.

Figures 183, 184 and 185 show the effect of Reynolds number for Wing III with 70 degree fillet and the three 12-percent thick airfoil sections. Note that the effects are primarily in the stall progression region and, therefore, would affect the stall progression factor and the incremental lift charts.

One approach considered for modifying or revising the prediction methods was to obtain incremental lift curve parameter values from the data obtained on the NACA 0008 airfoil configurations at unit Reynolds number of 26.25 million per meter (8.0 million per foot). Figures 186-190 present the effect of fillet

sweep on the lift curve parameter increments as functions of angle of attack for the different airfoil sections as tested in the LTPT facility. For each airfoil, a reasonably consistent trend exists for the effects of fillet sweep. However, when the effects of Reynolds number are included as in Figure 191 the picture becomes confused.

The approach of trying to use the NACA 0008 airfoil data as a baseline for the airfoil effects and obtain increments for the airfoil effects and other increments for the Reynolds number effects was not successful. There were too many conflicting trends in the data to evolve simple correlations. As a consequence, it was decided to use a more direct approach.

The plots of Reynolds number effects on lift, suction ratio, and pitching moment were reviewed one more time and it was noted that the key results could be represented by defining the characteristics for three values of unit Reynolds number: (1) the minimum value tested (13.13 million per meter or 4.0 million per foot), (2) a "standard" value corresponding to the maximum value tested in the original planform series (26.25 million per meter or 8.0 million per foot), and (3) the maximum value tested in the additional test series (Usually 45.93 million per meter or 14.0 million per foot).

A prediction using the minimum Reynolds number data could be used to help define loads for wind-tunnel models to be tested in facilities having only relatively low unit Reynolds number capabilities.

The use of the "standard" Reynolds number data would allow a tie-in between the airfoil effects and the planform effects obtained from the "basic" prediction method. For practical purposes the maximum unit Reynolds number data might be considered representative of what could be expected for full-scale flight.

This approach was taken and a set of revised prediction methods were developed. The revised methods use slightly different chart formats and equations for two reasons:

(1) The maximum angle of attack was extended from 26 degrees to as high as 32 degrees.

(2) The limited series of planforms tested consisted only of Basic Wing III with various fillets. Thus the effect of outer panel sweep could not be considered in the revised methods.

Revised Lift Prediction Method

The revised prediction method for the lift characteristics uses the same correlation parameter as the basic prediction method, but in a slightly different way. The revised lift prediction equation is:

$$C_L = \frac{C_{L_\alpha} \eta_B}{A_1} \left[\left(\frac{C_L}{C_{L_\alpha}} \frac{A_1}{\eta_B} \right)_{std} + \Delta \left(\frac{C_L}{C_{L_\alpha}} \frac{A_1}{\eta_B} \right)_{RN(\ )} \right]$$

The terms in this equation are the same as for the basic prediction method with the following exceptions:

(1) The terms in brackets are defined by sets of charts appropriate to a specific airfoil section.

(2) The first term in brackets is obtained from a correlation chart which has the lift parameter $\left(\frac{C_L}{C_{L_\alpha}} \frac{A_1}{\eta_B} \right)_{std}$

against the parameter $\beta \tan\Lambda_F$ for parametric values of angle of attack.

The values obtained from this term represent data obtained at the Standard unit Reynolds number of 26.25 million per meter (8.0 million per foot).

(3) The second term in brackets represents the incremental effect of Reynolds number and is obtained from charts

which show the incremental value $\Delta\left(\dfrac{C_L}{C_{L_\alpha}} \dfrac{A_1}{\eta_B}\right)$ for

either RN_{min} or RN_{max} in carpet plot form for various angles of attack.

Table 4 presents a key to the Figures which contain the sets of charts for each airfoil.

TABLE 4   KEY TO REVISED LIFT PREDICTION CHARTS

AIRFOIL SECTION	$\left(\dfrac{C_L}{C_{L_\alpha}} \dfrac{A_1}{\eta_B}\right)_{std}$	$\Delta\left(\dfrac{C_L}{C_{L_\alpha}} \dfrac{A_1}{\eta_B}\right)_{RN_{min}}$	$\Delta\left(\dfrac{C_L}{C_{L_\alpha}} \dfrac{A_1}{\eta_B}\right)_{RN_{max}}$
NACA 0004	Fig 192	N.A.	N.A.
NACA 0008	Fig 193	Fig 194	Fig 195
NACA 0012	Fig 196	Fig 197	Fig 198
NACA 0015	Fig 199	Fig 200	Fig 201
NACA 65A012	Fig 202	Fig 203	Fig 204
NACA 65$_1$412	Fig 205	Fig 206	Fig 207
THIN HEXAGON WITH SHARP L.E.	Fig 208	N.A.	N.A.

Figures 192, 193, 196, and 199 present the lift correlation curves for the NACA 0004, 0008, 0012 and 0015 airfoils, respectively. The NACA 65A012, 65$_1$412, and thin hexagon airfoils were only tested for a few configurations. Figures 202 and 205 show comparisons of the lift correlation curves of the 65A012 and 65$_1$412 airfoils tested with the corresponding curves for the NACA 0012 airfoil, and Figure 208 shows comparison of the lift correlation curves of the 4 percent thick hexagon airfoils with corresponding curves for the NACA 0004 airfoils. If for some reason it were necessary to estimate the lift curve of a configuration having the 65A012 or 65$_1$412 airfoils with a fillet sweep less than 70 degrees, the appropriate correlation curves could be extended to lower values of $\beta \tan \Lambda_F$ using the NACA 0012 curves as a guide.

With respect to the incremental values due to Reynolds number, it was found that for the 4-percent thick airfoils

the effects of Reynolds number were not significant.

The prediction method consists of calculating C_L values for several values of angle of attack using the appropriate set of charts for the desired configuration and airfoil section. The charts are set up to produce lift curves for any thickness ratio between .04 and .15.

In order to provide a tie-in to the "basic" prediction method, data for the Wing III series of planforms with NACA 0008 airfoils from test ARC 12-086 were plotted in the format used for the revised prediction method. The resulting chart is presented in Figure 209.

Figure 209 can be of value in two ways. First, it can be used to establish the uncertainties in lift predictions for the family of irregular planforms having Wing III as the basic planform, by comparing results obtained using Figure 209 and Figure 193. Second, it provides a means of applying the incremental effects of airfoil thickness ratio, airfoil shape, and Reynolds number determined from the revised prediction method to a broader range of planforms. It is likely that reasonable estimates of the lift curves could be made for irregular planforms having basic planforms in the range from Wing II to Wing IV, by applying the increments to results obtained from the "basic" prediction method for the desired planform.

Revised Drag-Prediction Method

Revisions to the drag prediction methodology affected only the drag-due-to-lift part of the method. Revisions were required for three reasons:

(1) The plateau values of suction ratio for the basic wings of different thickness ratios, as tested in the LTPT facility, were significantly higher and formed a different correlation curve as a function of the Ω parameter from the curve developed for the basic prediction method.

(2) The slopes of the suction-ratio curves in the various regions varied significantly with Reynolds number for the thicker airfoils for some of the planforms.

(3) The approach used to predict the effects of Reynolds number on lift was not compatible with the method used to account for Reynolds number effects on drag due to lift in the original formulation used in the basic prediction method.

The revised method still makes use of the suction-ratio concept and the representation of the variation of suction ratio with angle of attack by a series of linear segments as illustrated in Figure 210. The angle-of-attack boundaries defining the segments also apply to the pitching-moment prediction and in fact some iteration between values appropriate to the suction-ratio curves and those appropriate for the pitching-moment curves was required to produce compatible results.

As many as 7 linear segments were required to produce reasonable fits to the experimental suction ratio and/or pitching moment data because the angle-of-attack range for the prediction was extended from 26 to 32 degrees. Some of the configurations did not require 7 segments. In those cases, fictitious boundaries were defined to allow a single generalized equation to represent all the configurations.

The basic drag-due-to-lift equation is the same as used for the "basic" prediction method.

$$C_{D_L} = C_L \tan \alpha - "R(\alpha)" \left[C_L \tan \alpha - \frac{C_L^2}{\pi A} \right]$$

but for the revised method

$$"R(\alpha)" = R_1 \qquad ; \ 0 \leq \alpha \leq \alpha_2$$

$$= R_1 + \left(\frac{d"R"}{d\alpha}\right)_2 (\alpha - \alpha_2) \qquad ; \ \alpha_2 \leq \alpha \leq \alpha_3$$

$$= R_1 + \left(\frac{d"R"}{d\alpha}\right)_2 (\alpha_3 - \alpha_2) + \left(\frac{d"R"}{d\alpha}\right)_3 (\alpha - \alpha_3)$$

$$; \ \alpha_3 \leq \alpha \leq \alpha_4$$

$$= R_1 + \left(\frac{d"R"}{d\alpha}\right)_2 (\alpha_3 - \alpha_2) + \left(\frac{d"R"}{d\alpha}\right)_3 (\alpha_4 - \alpha_3)$$

$$+ \left(\frac{d"R"}{d\alpha}\right)_4 (\alpha - \alpha_4) \qquad ; \ \alpha_4 \leq \alpha \leq \alpha_5$$

266

$$"R(\alpha)" = R_1 + \left(\frac{d"R"}{d\alpha}\right)_2 (\alpha_3 - \alpha_2) + \left(\frac{d"R"}{d\alpha}\right)_3 (\alpha_4 - \alpha_3)$$

$$+ \left(\frac{d"R"}{d\alpha}\right)_4 (\alpha_5 - \alpha_4) + \left(\frac{d"R"}{d\alpha}\right)_5 (\alpha - \alpha_5)$$

$$; \quad \alpha_5 \leq \alpha \leq \alpha_6$$

$$= R_1 + \left(\frac{d"R"}{d\alpha}\right)_2 (\alpha_3 - \alpha_2) + \left(\frac{d"R"}{d\alpha}\right)_3 (\alpha_4 - \alpha_3)$$

$$+ \left(\frac{d"R"}{d\alpha}\right)_4 (\alpha_5 - \alpha_4) + \left(\frac{d"R"}{d\alpha}\right)_5 (\alpha_6 - \alpha_5)$$

$$+ \left(\frac{d"R"}{d\alpha}\right)_6 (\alpha - \alpha_6) \quad ; \quad \alpha_6 \leq \alpha \leq \alpha_7$$

$$= R_1 + \left(\frac{d"R"}{d\alpha}\right)_2 (\alpha_3 - \alpha_2) + \left(\frac{d"R"}{d\alpha}\right)_3 (\alpha_4 - \alpha_3)$$

$$+ \left(\frac{d"R"}{d\alpha}\right)_4 (\alpha_5 - \alpha_4) + \left(\frac{d"R"}{d\alpha}\right)_5 (\alpha_6 - \alpha_5)$$

$$+ \left(\frac{d\text{"R"}}{d\alpha}\right)_6 (\alpha_7 - \alpha_6) + \left(\frac{d\text{"R"}}{d\alpha}\right)_7 (\alpha - \alpha_7)$$

$$; \quad \alpha_7 \leq \alpha \leq 32$$

The values of the α boundaries, the plateau value of the suction ratio, R_1, and the values of the slopes of the suction ratio curves in each region, $\left(\frac{d\text{"R"}}{d\alpha}\right)$ were determined for each configuration for each of the three Reynolds number conditions used in the revised lift prediction method. The α boundaries are tabulated in Tables 5 through 8, and the plateau values of suction ratio and the slopes of the various segments of the suction ratio variations with angle of attack are tabulated in Tables 9 through 12.

To use the prediction method, the calculations are made for a series of angles of attack using compatible values for the various terms, i.e., the planform, airfoil section, and Reynolds number condition must be the same for both lift and the drag-due-to-lift conditions. If the user wishes to predict full-scale flight characteristics, the lift and drag-due-to-lift terms for $R_{N_{max}}$ conditions should be used. The minimum-drag term should be calculated for the actual flight Reynolds number condition.

Revised Pitching-Moment Prediction Method

The only revisions to the pitching-moment prediction method are those required to extend the angle-of-attack range from 26 to 32 degrees and to make the method consistent with the revised lift and drag-due-to-lift predictions.

The equation for the variation of pitching moment with angle of attack is:

$$C_{m_{.25\bar{c}}} = C_{m_{\alpha=0}} + C_{m_{\alpha_0}}(\alpha-0) \quad ; \quad 0 \le \alpha \le \alpha_1$$

$$= C_{m_{\alpha=0}} + C_{m_{\alpha_0}}(\alpha_1-0) + C_{m_{\alpha_1}}(\alpha-\alpha_1) \quad ; \quad \alpha_1 \le \alpha \le \alpha_2$$

$$= C_{m_{\alpha=0}} + C_{m_{\alpha_0}}(\alpha_1-0) + C_{m_{\alpha_1}}(\alpha_2-\alpha_1)$$
$$+ C_{m_{\alpha_2}}(\alpha-\alpha_2) \quad ; \quad \alpha_2 \le \alpha \le \alpha_3$$

$$= C_{m_{\alpha=0}} + C_{m_{\alpha_0}}(\alpha_1-0) + C_{m_{\alpha_1}}(\alpha_2-\alpha_1)$$
$$+ C_{m_{\alpha_2}}(\alpha_3-\alpha_2) + C_{m_{\alpha_3}}(\alpha-\alpha_3) \quad ; \quad \alpha_3 \le \alpha \le \alpha_4$$

$$= C_{m_{\alpha=0}} + C_{m_{\alpha_0}}(\alpha_1-0) + C_{m_{\alpha_1}}(\alpha_2-\alpha_1)$$
$$+ C_{m_{\alpha_0}}(\alpha_3-\alpha_2) + C_{m_{\alpha_3}}(\alpha_4-\alpha_3)$$
$$+ C_{m_{\alpha_4}}(\alpha-\alpha_4) \quad ; \quad \alpha_4 \le \alpha \le \alpha_5$$

269

$$C_{m_{.25\bar{c}}} = C_{m_{\alpha=0}} + C_{m_{\alpha_0}}(\alpha_1 - 0) + C_{m_{\alpha_1}}(\alpha_2 - \alpha_1)$$

$$+ C_{m_{\alpha_2}}(\alpha_3 - \alpha_2) + C_{m_{\alpha_3}}(\alpha_4 - \alpha_3)$$

$$+ C_{m_{\alpha_4}}(\alpha_5 - \alpha_4) + C_{m_{\alpha_5}}(\alpha - \alpha_5) \quad ; \alpha_5 \leq \alpha \leq \alpha_6$$

$$= C_{m_{\alpha=0}} + C_{m_{\alpha_0}}(\alpha_1 - 0) + C_{m_{\alpha_1}}(\alpha_2 - \alpha_1)$$

$$+ C_{m_{\alpha_2}}(\alpha_3 - \alpha_2) + C_{m_{\alpha_3}}(\alpha_4 - \alpha_3)$$

$$+ C_{m_{\alpha_4}}(\alpha_5 - \alpha_4) + C_{m_{\alpha_5}}(\alpha_6 - \alpha_5)$$

$$+ C_{m_{\alpha_6}}(\alpha - \alpha_6) \qquad ; \alpha_6 \leq \alpha \leq \alpha_7$$

$$= C_{m_{\alpha=0}} + C_{m_{\alpha_0}}(\alpha_1 - 0) + C_{m_{\alpha_1}}(\alpha_2 - \alpha_1)$$

$$+ C_{m_{\alpha_2}}(\alpha_3 - \alpha_2) + C_{m_{\alpha_3}}(\alpha_4 - \alpha_3)$$

$$+ C_{m_{\alpha_4}}(\alpha_5 - \alpha_4) + C_{m_{\alpha_5}}(\alpha_6 - \alpha_5)$$

$$+ C_{m_{\alpha_6}}(\alpha_1 - \alpha_6) + C_{m_{\alpha_7}}(\alpha - \alpha_7) \quad ; \alpha_7 \leq \alpha \leq 32$$

The angle-of-attack boundaries used for this equation are identical to those used for the suction-ratio calculation which were presented in Tables 5 through 8.

The values of $C_{m_{\alpha=0}}$ and the slopes of the various segments of pitching-moment variations with angle of attack are presented in Tables 13 through 16 for the various combinations of planforms, airfoil section, and Reynolds number condition. Obviously, the pitching-moment prediction requires use of the same planform, airfoil section, and Reynolds number conditions as are used for the lift and drag-due-to-lift calculations.

The "revised" prediction methods are strictly applicable only to the Wing III series of irregular planforms with fillet sweeps between 45 degrees and 80 degrees, whereas the "basic" prediction methods are applicable to a wide range of irregular planforms having NACA 0008 airfoils but only at the standard Reynolds number condition.

It is considered feasible to apply judicious combinations of the two sets of prediction methods to obtain the lift, drag, and pitching-moment variations with angle of attack for configurations which have planforms which are not of the Wing III series but have airfoils other than the NACA 0008 airfoil section.

TABLE 5

Angle-of-Attack Boundaries for Drag Due to Lift and
Pitching-Moment Segments - NACA 00XX Airfoils, $R_{N_{min}}$

CONFIGURATION Λ_F Λ_W AIRFOIL			α_1	α_2	α_3	α_4	α_5	α_6	α_7
45	45	0004	2.4	2.4	7.2	13.4	22.7	26.6	30.5
		0008	4.4	4.4	7.5	15.4	20.6	27.8	31.2
		0012	6.0	6.0	10.8	10.9	17.5	22.0	26.0
		0015	7.0	7.0	12.0	17.7	19.8	25.8	30.0
60	45	0004	3.0	3.0	6.35	15.6	19.3	23.5	30.6
65	45	0004	3.0	3.0	7.0	15.6	19.3	23.5	30.6
		0008	5.6	5.6	10.2	14.2	17.0	22.4	27.0
		0012	7.4	7.4	13.5	15.6	18.0	22.6	29.0
		0015	6.0	6.0	12.2	13.3	20.0	24.0	28.0
70	45	0004	3.6	3.6	6.8	11.5	15.8	18.8	28.3
		0008	6.6	6.6	10.0	14.2	20.2	24.6	28.5
		0012	7.0	7.0	13.5	18.0	22.5	26.6	30.5
		0015	5.6	5.6	14.0	17.2	20.6	27.2	30.0
75	45	0004	3.0	3.0	7.1	12.1	18.4	25.6	29.0
		0008	4.5	4.5	7.1	11.3	17.1	20.8	26.4
		0012	6.0	6.0	8.6	13.2	17.5	21.1	25.0
		0015	4.4	4.4	8.0	13.8	17.9	20.8	30.0
80	45	0004	2.6	2.6	7.95	14.5	17.3	25.5	29.3
		0008	4.8	4.8	7.5	12.5	18.1	23.9	29.3
		0012	6.4	4.8	11.1	15.7	18.7	25.6	30.0
		0015	7.0	7.0	12.0	15.7	20.0	23.0	28.0

TABLE 6

Angle-of-Attack Boundaries for Drag Due to Lift and
Pitching-Moment Segments - NACA 00XX Airfoils, $R_{N_{std}}$

Λ_F	Λ_W	AIRFOIL	α_1	α_2	α_3	α_4	α_5	α_6	α_7
45	45	0004	2.4	2.4	8.4	13.8	22.7	26.6	30.5
		0008	4.4	4.4	9.6	16.9	23.0	27.8	31.2
		0012	6.0	6.0	10.8	14.4	21.0	25.6	31.1
		0015	7.0	7.0	12.0	19.1	21.0	24.2	28.0
60	45	0004	3.0	3.0	6.6	11.7	14.8	19.2	31.2
65	45	0004	3.0	3.0	7.0	15.6	19.3	23.5	30.6
		0008	5.6	5.6	11.2	16.0	19.6	24.4	28.0
		0012	7.4	7.4	11.7	16.0	20.0	25.2	32.0
		0015	6.0	6.0	12.2	16.0	19.8	24.0	26.4
70	45	0004	3.6	3.6	7.2	12.7	15.8	18.8	28.3
		0008	6.6	6.6	11.0	17.0	21.8	24.6	29.6
		0012	7.0	7.0	13.9	17.5	21.5	25.6	30.0
		0015	5.6	5.6	14.0	18.0	21.0	25.6	30.4
75	45	0004	3.0	3.0	9.4	12.1	18.4	25.6	29.0
		0008	4.5	4.5	8.1	13.8	19.8	23.7	28.0
		0012	6.0	6.0	8.1	14.1	17.8	22.0	28.0
		0015	4.4	4.4	8.0	13.8	17.9	20.8	30.4
80	45	0004	2.6	2.6	8.8	14.5	17.3	25.5	29.3
		0008	4.8	4.8	9.5	12.6	17.4	23.9	28.8
		0012	6.4	6.4	10.8	12.2	17.3	24.0	31.2
		0015	7.0	7.0	10.8	12.0	20.0	27.2	33.0

TABLE 7

Angle-of-Attack Boundaries for Drag Due to Lift and
Pitching-Moment Segments - NACA 00XX Airfoils, $R_{N_{max}}$

Λ_F	Λ_W	AIRFOIL	α_1	α_2	α_3	α_4	α_5	α_6	α_7
45	45	0004	2.4	2.4	9.2	13.8	22.7	26.6	30.5
		0008	4.4	4.4	12.2	16.0	18.4	23.0	27.8
		0012	6.0	6.0	12.6	20.6	22.2	23.5	27.5
		0015	7.0	7.0	12.0	18.2	22.2	23.5	29.5
60	45	0004	3.0	3.0	7.6	11.7	14.8	19.2	31.2
65	45	0004	3.0	3.0	7.0	15.6	19.3	23.5	30.6
		0008	5.6	5.6	11.15	16.0	19.6	24.4	28.0
		0012	7.4	7.4	13.0	17.9	20.8	28.6	32.0
		0015	6.0	6.0	12.2	14.2	18.0	20.3	25.2
70	45	0004	3.6	3.6	7.65	12.7	15.8	18.8	28.3
		0008	6.6	6.6	11.65	16.7	21.0	23.6	27.0
		0012	7.0	7.0	14.7	17.7	21.8	25.3	30.0
		0015	5.6	5.6	14.8	17.6	19.3	27.0	31.0
75	45	0004	3.0	3.0	9.8	12.1	18.4	25.6	29.0
		0008	4.5	4.5	8.0	12.45	19.8	24.0	29.0
		0012	6.0	6.0	8.1	16.6	20.5	24.5	28.6
		0015	4.4	4.4	12.0	16.9	20.1	25.6	29.6
80	45	0004	2.6	2.6	9.1	14.5	17.3	25.5	29.3
		0008	4.8	4.8	9.5	13.1	16.9	22.5	29.1
		0012	6.4	6.4	9.8	16.0	18.9	25.0	28.0
		0015	7.0	7.0	10.8	12.0	20.0	24.4	29.0

TABLE 8

Angle-of-Attack Boundaries for Drag Due to Lift and
Pitching-Moment Segments, NACA 65A012 and 65_1412

Λ_F	Λ_W	AIRFOIL	RN	α_1	α_2	α_3	α_4	α_5	α_6	α_7
70	45	65A012	Min.	7.4	7.4	9.6	15.7	20.3	24.8	27.5
75	45	65A012	Min.	5.4	5.4	9.1	11.1	16.9	22.0	26.1
80	45	65A012	Min.	7.1	7.1	12.2	15.4	20.2	26.0	31.4
70	45	65A012	Std.	7.4	7.4	10.2	14.8	20.4	24.6	30.8
75	45	65A012	Std.	4.6	4.6	9.6	17.0	20.8	24.6	27.8
80	45	65A012	Std.	5.8	5.8	10.8	15.1	20.0	27.2	31.0
70	45	65A012	Max.	7.4	7.4	10.2	15.8	20.1	25.0	28.6
75	45	65A012	Max.	4.8	4.8	10.0	16.2	18.4	21.6	28.2
80	45	65A012	Max.	6.0	6.0	12.0	15.8	21.2	27.7	32.0
70	45	65_1412	Min.	7.4	7.4	10.7	13.8	17.7	22.8	27.2
75	45	65_1412	Min.	6.9	6.9	14.4	18.2	20.7	27.3	32.0
80	45	65_1412	Min.	5.6	5.6	13.0	18.9	23.5	28.0	30.5
70	45	65_1412	Std.	7.6	7.6	10.3	14.1	19.1	25.6	32.4
75	45	65_1412	Std.	6.9	6.9	15.3	17.8	22.4	28.4	31.0
80	45	65_1412	Std.	5.5	5.5	10.8	15.4	20.6	25.7	30.1
70	45	65_1412	Max.	7.4	7.4	11.0	15.4	19.2	22.6	28.6
75	45	65_1412	Max.	6.9	6.9	13.6	16.2	19.2	24.0	29.0
80	45	65_1412	Max.	5.6	5.6	13.0	16.0	22.8	28.0	32.0
45	45	00SLE	Std.	2.4	2.4	7.2	15.8	20.0	22.9	26.9
75	45	00SLE	Std.	2.0	2.0	7.0	13.0	18.2	23.4	31.6
80	45	00SLE	Std.	2.0	2.0	7.9	11.6	17.2	23.8	28.0

TABLE 9

Plateau Values of Suction Ratio and Slopes of
Suction-Ratio Segments - NACA 00XX Airfoils, $R_{N_{min}}$

Λ_F	Λ_W	CONFIGURATION AIRFOIL	R_N	R_1	$\dfrac{dR}{d\alpha_2}$	$\dfrac{dR}{d\alpha_3}$	$\dfrac{dR}{d\alpha_4}$	$\dfrac{dR}{d\alpha_5}$	$\dfrac{dR}{d\alpha_6}$	$\dfrac{dR}{d\alpha_7}$
45	45	0004	Min.	.885	-.0727	-.0355	-.0197	-.0102	-.0070	-.0031
		0008		.967	-.0032	-.0705	-.0443	-.0075	-.0028	-.0028
		0012		.980	-.0040	-.0040	-.0874	-.0488	0	0
		0015		.985	-.0037	-.0037	-.1960	-.0260	-.0238	-.0238
60	45	0004	Min.	.838	-.0893	-.0414	-.0290	-.0158	-.0088	-.0036
65	45	0004	Min.	.835	-.1175	-.0229	-.0103	-.0126	-.0077	-.0048
		0008		.860	-.0048	-.0844	-.0417	-.0215	-.0215	-.0060
		0012		.905	-.0010	-.1484	-.0812	-.0292	-.0012	-.0222
		0015		.940	-.0039	-.0039	-.0470	-.0817	-.0018	-.0018
70	45	0004	Min.	.840	-.1254	-.0315	-.0142	-.0142	-.0092	-.0048
		0008		.950	-.0498	-.0846	-.0102	-.0245	-.0168	-.0087
		0012		.955	-.0067	-.0865	-.0418	-.0101	-.0122	-.0114
		0015		.990	-.0082	-.0082	-.0930	-.0300	-.0140	-.0140
75	45	0004	Min.	.810	-.0943	-.0310	-.0137	-.0068	-.0030	-.0047
		0008		.910	-.0087	-.0931	-.0338	-.0055	-.0166	-.0056
		0012		.955	-.0022	-.0186	-.0638	-.0475	-.0092	-.0182
		0015		.965	-.0120	-.0142	-.0342	-.0906	-.0125	-.0048
80	45	0004	Min.	.882	-.1070	-.0161	-.0096	-.0063	-.0038	-.0078
		0008		.915	-.0337	-.0707	-.0392	-.0055	-.0079	-.0130
		0012		.912	-.0327	-.0327	-.0593	-.0016	-.0016	-.0016
		0015		.915	-.0220	-.0127	-.0378	-.0683	-.0080	-.0080

TABLE 10

Plateau Values of Suction Ratio and Slopes of Suction-Ratio Segments - NACA 00XX Airfoils, $R_{N_{std}}$

Λ_F	Λ_W	AIRFOIL	R_N	R_1	$\dfrac{dR}{d\alpha}_2$	$\dfrac{dR}{d\alpha}_3$	$\dfrac{dR}{\alpha}_4$	$\dfrac{dR}{d\alpha}_5$	$\dfrac{dR}{\alpha}_6$	$\dfrac{dR}{d\alpha}_7$
45	45	0004	Std	.940	-.0727	-.0355	-.0197	-.0102	-.0070	-.0031
		0008		.980	-.0032	-.0705	-.0443	-.0075	-.0028	-.0028
		0012		.990	-.0040	-.0040	-.0721	-.0512	-.0055	-.0061
		0015		.965	-.0037	-.0037	-.1560	-.1032	-.0229	-.0010
60	45	0004	Std	.882	-.0893	-.0414	-.0290	-.0158	-.0088	-.0036
65	45	0004	Std	.900	-.1175	-.0229	-.0103	-.0126	-.0077	-.0048
		0008		.940	-.0048	-.0844	-.0417	-.0153	-.0153	-.0060
		0012		.925	-.0010	-.0010	-.0932	-.0451	-.0163	-.0310
		0015		.940	-.0039	-.0039	-.0145	-.0817	-.0436	-.0146
70	45	0004	Std	.905	-.1254	-.0315	-.0142	-.0142	-.0092	-.0048
		0008		.975	-.0198	-.0924	0	-.0204	-.0167	-.0167
		0012		.960	-.0067	-.0833	-.0429	-.0244	-.0163	-.0118
		0015		.980	-.0082	-.0118	-.0609	-.0431	-.0150	-.0218
75	45	0004	Std	.930	-.0943	-.0310	-.0137	-.0008	-.0030	-.0047
		0008		.945	-.0087	-.0708	-.0465	-.0091	-.0112	-.0180
		0012		.955	-.0022	-.0172	-.0771	-.0473	-.0093	-.0184
		0015		.965	-.0120	-.0142	-.0342	-.0906	-.0125	-.0048
80	45	0004	Std	.960	-.1070	-.0161	-.0096	-.0063	-.0038	-.0078
		0008		.940	-.0337	-.0408	-.0755	-.0057	-.0067	-.0067
		0012		.912	-.0262	-.0262	-.0304	-.0427	-.0027	-.0027
		0015		.915	-.0220	-.0220	-.0127	-.0345	-.0138	-.0072

TABLE 11

Plateau Values of Suction Ratio and Slopes of
Suction-Ratio Segments - NACA 00XX Airfoils, $R_{N_{max}}$

Λ_F	Λ_W	CONFIGURATION AIRFOIL	R_N	R_1	$\frac{dR}{d\alpha}_2$	$\frac{dR}{d\alpha}_3$	$\frac{dR}{d\alpha}_4$	$\frac{dR}{d\alpha}_5$	$\frac{dR}{d\alpha}_6$	$\frac{dR}{d\alpha}_7$
45	45	0004	Max.	.970	-.0727	-.0355	-.0197	-.0102	-.0070	-.0031
		0008		.980	-.0032	-.1048	-.0623	-.0443	-.0075	-.0028
		0012		.982	-.0040	-.0040	-.2470	-.2470	-.0160	0
		0015		.985	-.0037	-.0037	-.1385	-.1385	-.0090	-.0010
60	45	0004	Max.	.925	-.0893	-.0414	-.0290	-.0158	-.0088	-.0036
65	45	0004	Max.	.962	-.1175	-.0229	-.0103	-.0126	-.0077	-.0048
		0008		.956	-.0048	-.0844	-.0417	-.0153	-.0153	-.0150
		0012		.925	-.0010	-.0055	-.1144	-.0225	-.0150	-.0150
		0015		.940	-.0039	0.0039	-.0110	-.2000	-.0101	-.0141
70	45	0004	Max.	.945	-.1254	-.0315	-.0142	-.0142	-.0092	-.0048
		0008		.982	-.0080	-.1073	-.0167	.0197	-.0242	-.0108
		0012		.965	-.0048	-.0829	-.0587	-.0233	-.0150	-.0218
		0015		.990	-.0070	-.0160	-.1060	-.0366	-.0148	-.0148
75	45	0004	Max.	.972	-.0943	-.0310	-.0137	-.0068	-.0030	-.0047
		0008		.970	-.0087	-.0422	-.0685	-.0020	-.0167	-.0167
		0012		.955	-.0070	-.0165	-.0895	-.0255	-.0087	-.0087
		0015		.980	-.0120	-.0120	-.0178	-.0925	-.0214	-.0022
80	45	0004	Max.	1.000	-.1070	-.0161	-.0096	-.0063	-.0038	-.0078
		0008		.940	-.0322	-.0322	-.0965	-.0062	-.0076	-.0076
		0012		.912	-.0262	-.0175	-.0990	-.0320	-.0076	-.0076
		0015		.914	-.0220	-.0220	-.0127	-.0687	-.0100	-.0020

TABLE 12

Plateau Values of Suction Ratio and Slopes of
Suction-Ratio Segments - NACA 65A012 and 65,412

Λ_F	Λ_W	AIRFOIL	R_N	R_1	$\frac{dR}{d\alpha_2}$	$\frac{dR}{d\alpha_3}$	$\frac{dR}{d\alpha_4}$	$\frac{dR}{d\alpha_5}$	$\frac{dR}{d\alpha_6}$	$\frac{dR}{d\alpha_7}$
70	45	65A012	Min.	.880	0	-.0575	-.0765	-.0325	-.0100	-.0205
75	45	65A012		.850	-.0135	-.0967	-.0495	-.0022	+.0004	0.0160
80	45	65A012		.841	-.0775	-.0392	-.0123	-.0004	-.0050	-.0138
70	45	65A012	Std.	.905	0	-.0352	-.0577	-.0167	-.0167	-.0058
75	45	65A012		.900	-.0033	-.0452	-.0613	-.0012	-.0012	-.0180
80	45	65A012		.860	-.0254	-.0492	-.0492	-.0024	-.00054	-.0054
70	45	65A012	Max.	.920	0	-.0202	-.0545	-.0290	-.0240	-.0240
75	45	65A012		.890	-.0042	-.0243	-.0635	-.0575	-.0010	-.0170
80	45	65A012		.880	-.0222	-.0222	-.0677	-.0022	-.0062	-.0062
70	45	65_1412	Min.	.930	-.0047	-.0322	-.1110	-.0020	-.0255	-.0124
75	45	65_1412		.900	-.0080	-.0965	-.0376	-.0070	-.0184	-.0184
80	45	65_1412		.925	-.0156	-.0745	-.0123	-.0080	-.0032	-.0120
70	45	65_1412	Std.	.930	-.0047	-.0027	-.0372	-.0527	-.0098	-.0168
75	45	65_1412		.910	-.0074	-.0618	-.0537	-.0218	-.0153	-.0153
80	45	65_1412		.895	-.0174	-.0174	-.0508	-.0270	-.0098	-.0054
70	45	65_1412	Max.	.910	0	-.0050	-.0282	-.0828	-.0220	-.0220
75	45	65_1412		.890	-.0085	-.0203	-.0328	-.0638	-.0178	-.0202
80	45	65_1412		.895	-.0174	-.0174	-.0572	-.0081	-.0036	-.0036
45	45	00SLE	Std.	.968	-.1003	-.0301	-.0267	-.0123	-.0060	-.0031
75	45	00SLE		.870	-.1170	-.0208	-.0050	-.0084	-.0031	-.0048
80	45	00SLE		.890	-.0988	-.0330	-.0092	-.0048	-.0027	-.0027

CONFIGURATION			$c_{m\alpha=0}$	$c_{m\alpha_{0,1}}$	$c_{m\alpha_2}$	$c_{m\alpha_3}$	$c_{m\alpha_4}$	$c_{m\alpha_5}$	$c_{m\alpha_6}$	$c_{m\alpha_7}$
Λ_F	Λ_W	AIRFOIL								
45	45	0004	-.008	-.0019	-.0030	-.0013	-.0042	-.0010	-.0037	-.0010
		0008	-.005	-.0021	-.0036	-.0043	-.0044	+.0012	-.0005	-.0020
		0012	-.003	-.0014	-.0030	-.0030	-.0047	-.0028	+.0002	+.0006
		0015	+.001	-.0013	-.0025	-.0040	-.0056	+.0003	-.0023	-.0016
60	45	0004	-.007	-.0034	-.0050	-.0026	-.0035	-.0010	-.0017	-.0024
65	45	0004	-.0065	-.0048	-.0058	-.0038	+.0001	+.0001	-.0021	-.0021
		0008	-.005	-.0043	-.0062	-.0057	-.0045	-.0013	+.0012	-.0012
		0012	-.002	-.0039	-.0059	-.0082	-.0054	+.0020	-.0002	-.0008
		0015	+.001	-.0030	-.0052	-.0052	-.0072	+.0016	-.0001	-.0001
70	45	0004	-.003	-.0056	-.0073	-.0056	-.0056	+.0037	-.0029	+.0040
		0008	-.002	-.0058	-.0082	-.0067	-.0065	+.0039	-.0009	+.0010
		0012	-.002	-.0050	-.0068	-.0078	-.0019	+.0017	-.0010	+.0010
		0015	+.002	-.0047	-.0062	-.0088	-.0088	+.0010	+.0010	+.0010
75	45	0004	-.006	-.0070	-.0084	-.0076	-.0118	+.0062	+.0007	+.0007
		0008	+.002	-.0073	-.0092	-.0092	-.0078	-.0132	+.0062	-.0010
		0012	+.005	-.0065	-.0084	-.0084	-.0106	-.0043	-.0108	+.0076
		0015	+.005	-.0062	-.0069	-.0082	-.0106	-.0029	-.0065	+.0090
80	45	0004	+.001	-.0087	-.0098	-.0108	-.0109	-.0126	+.0106	+.0106
		0008	-.002	-.0088	-.0103	-.0103	-.0100	-.0136	-.0092	+.0228
		0012	+.001	-.0083	-.0108	-.0108	-.0078	-.0132	-.0096	+.0137
		0015	+.004	-.0077	-.0103	-.0103	-.0105	-.0068	-.0114	-.0051

280

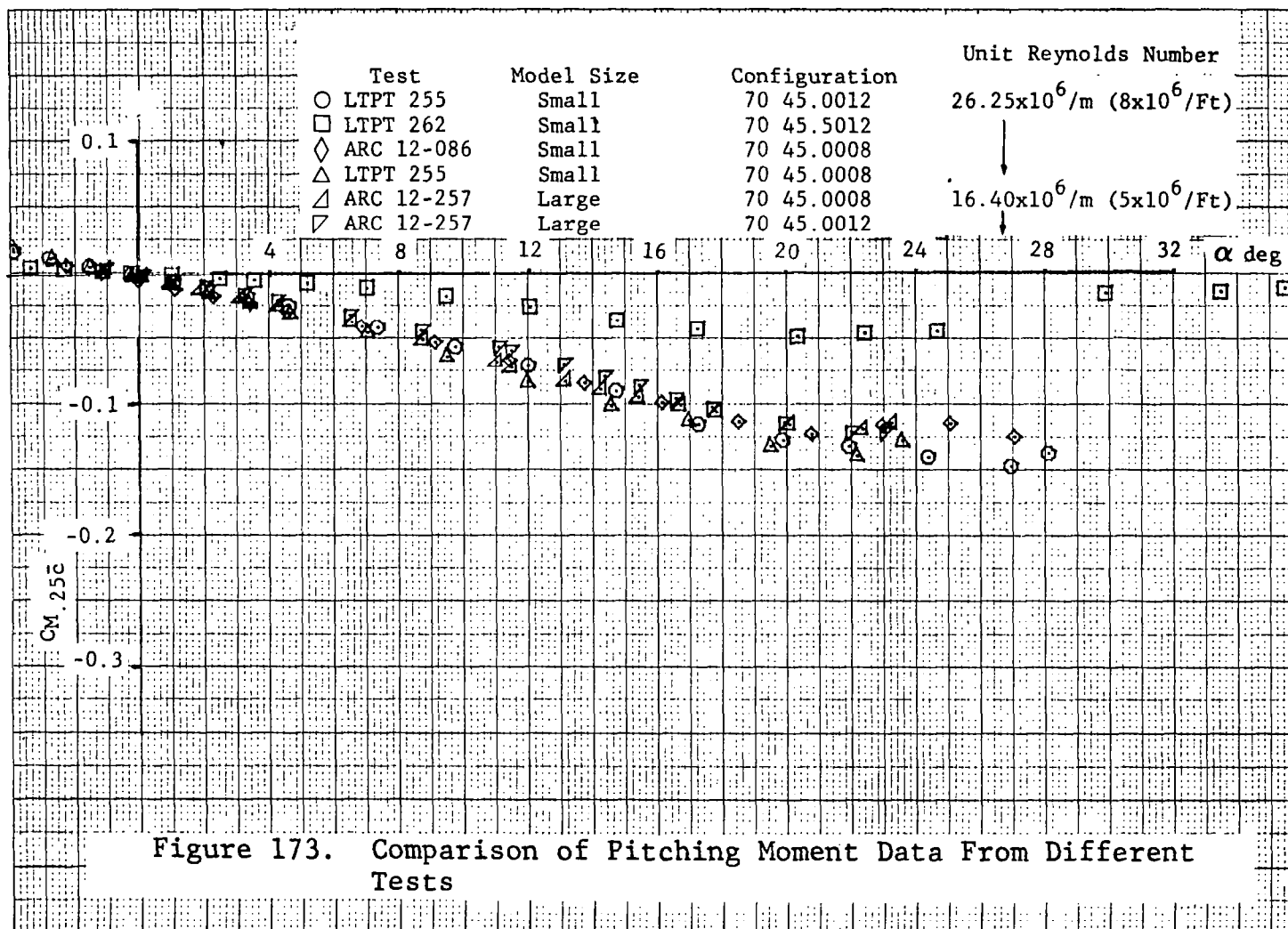TABLE 14 PITCHING-MOMENT INTERCEPTS AND SLOPES OF PITCHING-MOMENT SEGMENTS – NACA 00XX AIRFOILS, RN_{STD}

Λ_F	Λ_W	AIRFOIL	$c_{m_{\alpha=0}}$	$c_{m_{\alpha_{0,1}}}$	$c_{m_{\alpha_2}}$	$c_{m_{\alpha_3}}$	$c_{m_{\alpha_4}}$	$c_{m_{\alpha_5}}$	$c_{m_{\alpha_6}}$	$c_{m_{\alpha_7}}$
45	45	0004	-.008	-.0019	-.0030	-.0013	-.0042	-.0010	-.0037	-.0010
		0008	-.005	-.0021	-.0036	-.0043	-.0044	+.0008	+.0019	-.0002
		0012	-.003	-.0014	-.0033	-.0033	-.0054	-.0008	+.0007	+.0004
		0015	-.001	-.0013	-.0031	-.0043	-.0058	+.0018	+.0002	0
60	45	0004	-.007	-.0034	-.0050	-.0034	-.0017	-.0034	-.0014	-.0029
65	45	0004	-.0065	-.0048	-.0058	-.0043	+.0005	-.0022	-.0004	-.0033
		0008	-.005	-.0043	-.0062	-.0077	+.0010	-.0009	-.0009	+.0005
		0012	-.002	-.0039	-.0059	-.0059	-.0078	0	+.0028	0
		0015	+.001	-.0033	-.0052	-.0064	-.0064	-.0060	+.0049	0
70	45	0004	-.003	-.0056	-.0073	-.0056	-.0090	+.0058	-.0027	+.0005
		0008	-.002	-.0058	-.0082	-.0070	-.0054	-.0077	0	0
		0012	-.002	-.0050	-.0068	-.0088	-.0022	-.0043	+.0080	0
		0015	+.002	-.0047	-.0064	-.0087	-.0087	-.0019	-.0015	+.0088
75	45	0004	-.006	-.0070	-.0084	-.0077	-.0114	+.0062	+.0007	+.0007
		0008	.002	-.0073	-.0077	-.0095	-.0063	-.0128	+.0120	+.0012
		0012	.005	-.0065	-.0084	-.0084	-.0106	-.0010	-.0106	+.0126
		0015	.005	-.0062	-.0069	-.0082	-.0106	-.0029	-.0065	+.0063
80	45	0004	.001	-.0087	-.0098	-.0108	-.0108	-.0126	+.0106	+.0106
		0008	-.002	-.0088	-.0103	-.0103	-.0100	-.0141	-.0117	-.0308
		0012	.001	-.0083	-.0103	-.0103	-.0117	-.0082	-.0123	+.0185
		0015	.004	-.0077	-.0103	-.0103	-.0110	-.0075	-.0102	-.0132

Λ_F	Λ_W	AIRFOIL	$c_{m_{\alpha}}=0$	$c_{m_{\alpha_{0,1}}}$	$c_{m_{\alpha_2}}$	$c_{m_{\alpha_3}}$	$c_{m_{\alpha_4}}$	$c_{m_{\alpha_5}}$	$c_{m_{\alpha_6}}$	$c_{m_{\alpha_7}}$
45	45	0004	-.008	-.0019	-.0030	-.0013	-.0042	-.0010	-.0037	-.0010
		0008	-.005	-.0021	-.0036	-.0049	-.0049	-.0038	+.0006	+.0015
		0012	-.003	-.0014	-.0030	-.0053	-.0045	+.0019	+.0008	+.0002
		0015	-.001	-.0013	-.0031	-.0043	-.0053	+.0065	+.0010	-.0008
60	45	0004	-.007	-.0034	-.0050	-.0034	-.0017	-.0034	-.0014	-.0029
65	45	0004	-.0065	-.0048	-.0058	-.0043	+.0005	-.0034	-.0002	-.0033
		0008	-.005	-.0043	-.0062	-.0041	-.0023	-.0002	-.0017	0
		0012	-.002	-.0039	-.0059	-.0067	-.0064	-.0059	+.0008	+.0018
		0015	+.001	-.0036	-.0049	-.0049	-.0060	-.0036	-.0011	+.0018
70	45	0004	-.003	-.0056	-.0073	-.0057	-.0104	+.0073	-.0027	+.0005
		0008	-.002	-.0058	-.0053	-.0053	-.0051	+.0030	+.0030	-.0005
		0012	-.002	-.0050	-.0068	-.0099	-.0032	-.0048	+.0045	0
		0015	+.002	-.0047	-.0064	-.0092	-.0158	-.0022	+.0050	+.0018
75	45	0004	-.006	-.0070	-.0084	-.0077	-.0114	+.0062	-.0070	-.0070
		0008	+.002	-.0073	-.0077	-.0086	-.0078	-.0133	+.0113	+.0005
		0012	+.005	-.0065	-.0084	-.0093	-.0054	-.0054	-.0100	+.0077
		0015	+.005	-.0062	-.0073	-.0097	-.0054	-.0065	-.0065	+.0072
80	45	0004	+.001	-.0087	-.0098	-.0108	-.0108	-.0126	+.0106	+.0106
		0008	-.002	-.0088	-.0103	-.0103	-.0100	-.0136	-.0120	+.0220
		0012	+.001	-.0083	-.0105	-.0102	-.0106	-.0132	-.0098	-.0040
		0015	+.004	-.0077	-.0103	-.0103	-.0113	-.0045	-.0108	-.0078

TABLE 16   PITCHING-MOMENT INTERCEPTS AND SLOPES OF PITCH-
ING-MOMENT SEGMENTS - NACA 65A012 AND 65_1412

Λ_F	Λ_W	AIRFOIL	R_N	$c_{m\alpha=0}$	$c_{m\alpha_{0,1}}$	$c_{m\alpha_2}$	$c_{m\alpha_3}$	$c_{m\alpha_4}$	$c_{m\alpha_5}$	$c_{m\alpha_6}$	$c_{m\alpha_7}$
70	45	65A012	MIN.	+.005	-.0049	-.0063	-.0048	+.0025	+.0062	+.0005	+.0023
75	45	65A012		+.003	-.0058	-.0070	-.0087	-.0059	-.0072	-.0037	+.0115
80	45	65A012		+.004	-.0079	-.0100	-.0080	-.0108	-.0115	-.0042	+.0153
70	45	65A012	STD.	+.005	-.0048	-.0063	-.0072	-.0056	-.0018	+.0065	0
75	45	65A012		+.006	-.0058	-.0076	-.0080	-.0025	-.0076	-.0025	+.0123
80	45	65A012		+.004	-.0079	-.0100	-.0100	-.0077	-.0128	-.0055	+.0156
70	45	65A012	MAX	+.005	-.0048	-.0063	-.0060	-.0093	-.0039	+.0069	+.0069
75	45	65A012		+.006	-.0058	-.0072	-.0070	-.0088	0	-.0074	+.0175
80	45	65A012		+.004	-.0078	-.0100	-.0100	-.0067	-.0134	-.0067	+.0150
70	45	65_1412	MIN.	-.054	-.0057	-.0074	-.0075	-.0036	-.0036	+.0042	+.0042
75	45	65_1412		-.050	-.0068	-.0072	-.0063	-.0051	-.0034	.0145	+.0081
80	45	65_1412		-.045	-.0087	-.0096	-.0102	-.0100	-.0110	-.0066	+.0123
70	45	65_1412	STD.	-.053	-.0053	-.0072	-.0072	-.00835	-.0011	-.0057	0
75	45	65_1412		-.048	-.0066	-.0076	-.0092	-.0064	0	+.0156	+.0077
80	45	65_1412		-.045	-.0087	-.0096	-.0096	-.0110	-.0082	-.0115	+.0057
70	45	65_1412	MAX.	-.053	-.0053	-.0072	-.0074	-.0056	-.0056	+.0048	+.0048
75	45	65_1412		-.048	-.0066	-.0076	-.0066	-.0092	-.0058	-.0004	+.0162
80	45	65_1412		-.045	-.0087	-.0096	-.0096	-.0106	-.0085	-.0079	+.0095
45	45	00SLE	STD.	+.003	-.0010	-.0025	-.0012	-.0048	+.0003	+.0016	-.0032
75	45	00SLE		+.004	-.0068	-.0080	-.0088	+.0113	+.0082	+.0005	-.0028
80	45	00SLE		-.004	-.0080	-.0105	-.0097	-.0109	-.0136	-.0008	+.0124

Figure 173. Comparison of Pitching Moment Data From Different Tests
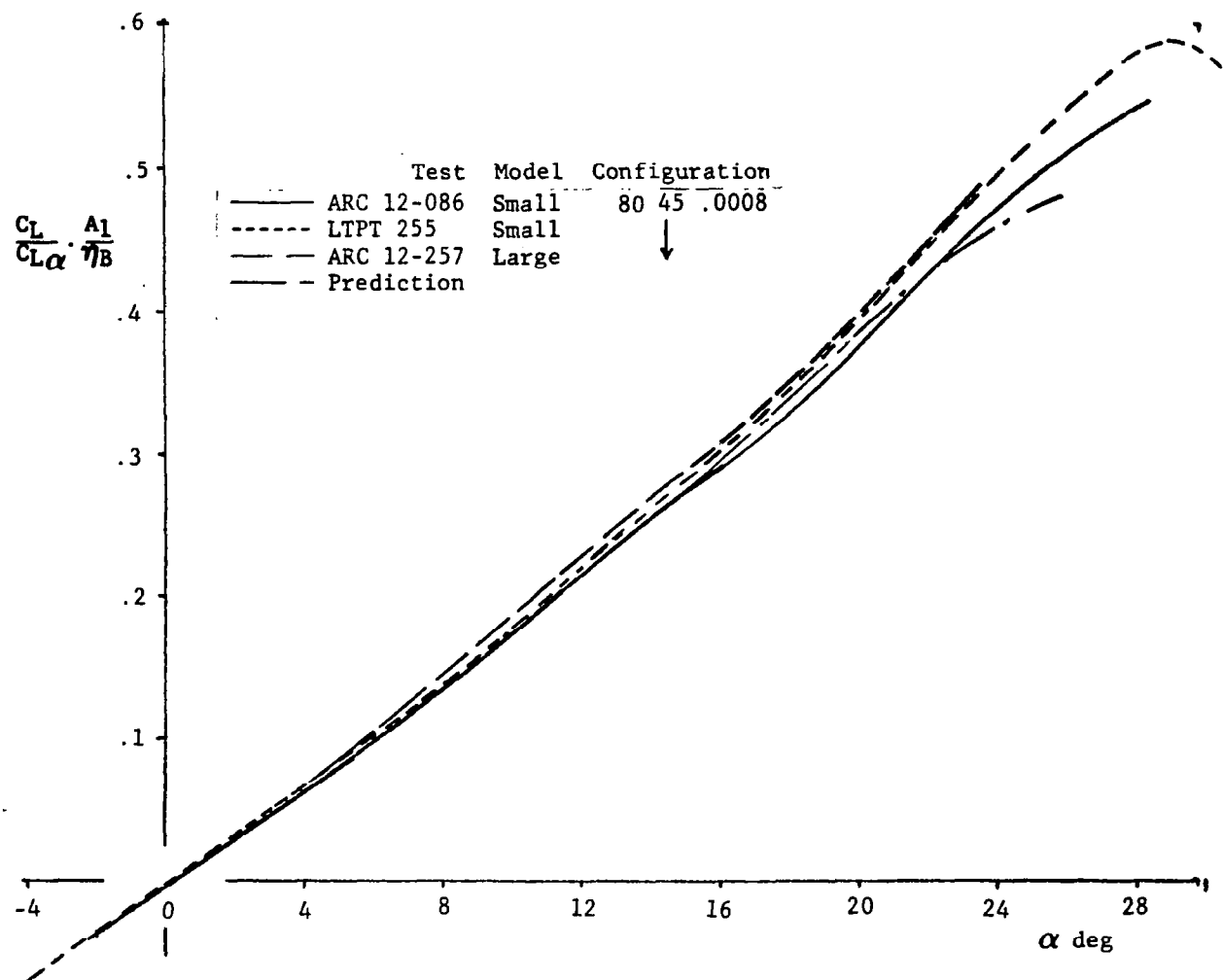
Figure 174. Comparison of Lift Correlation Parameter for Ir-
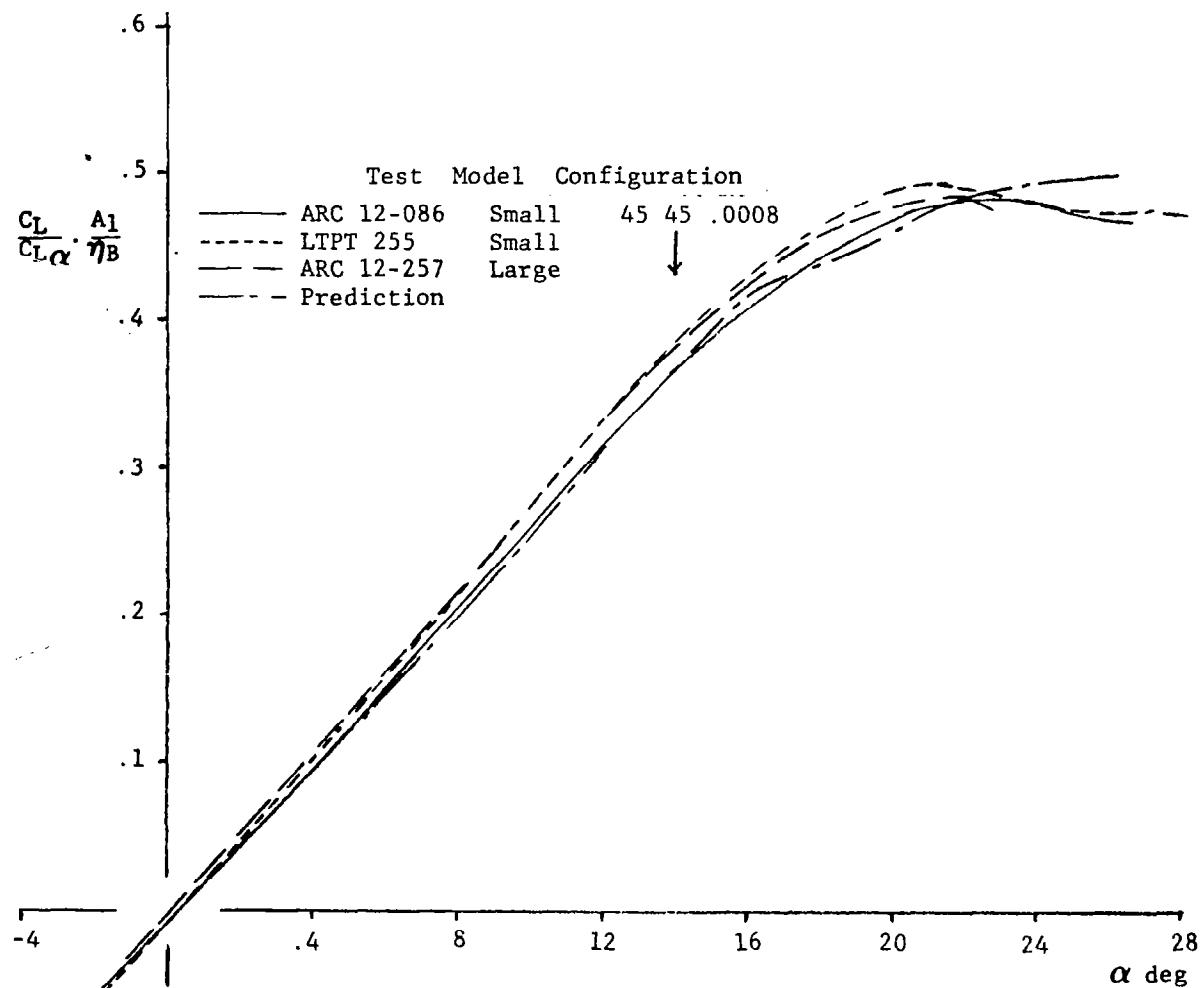regular Planform

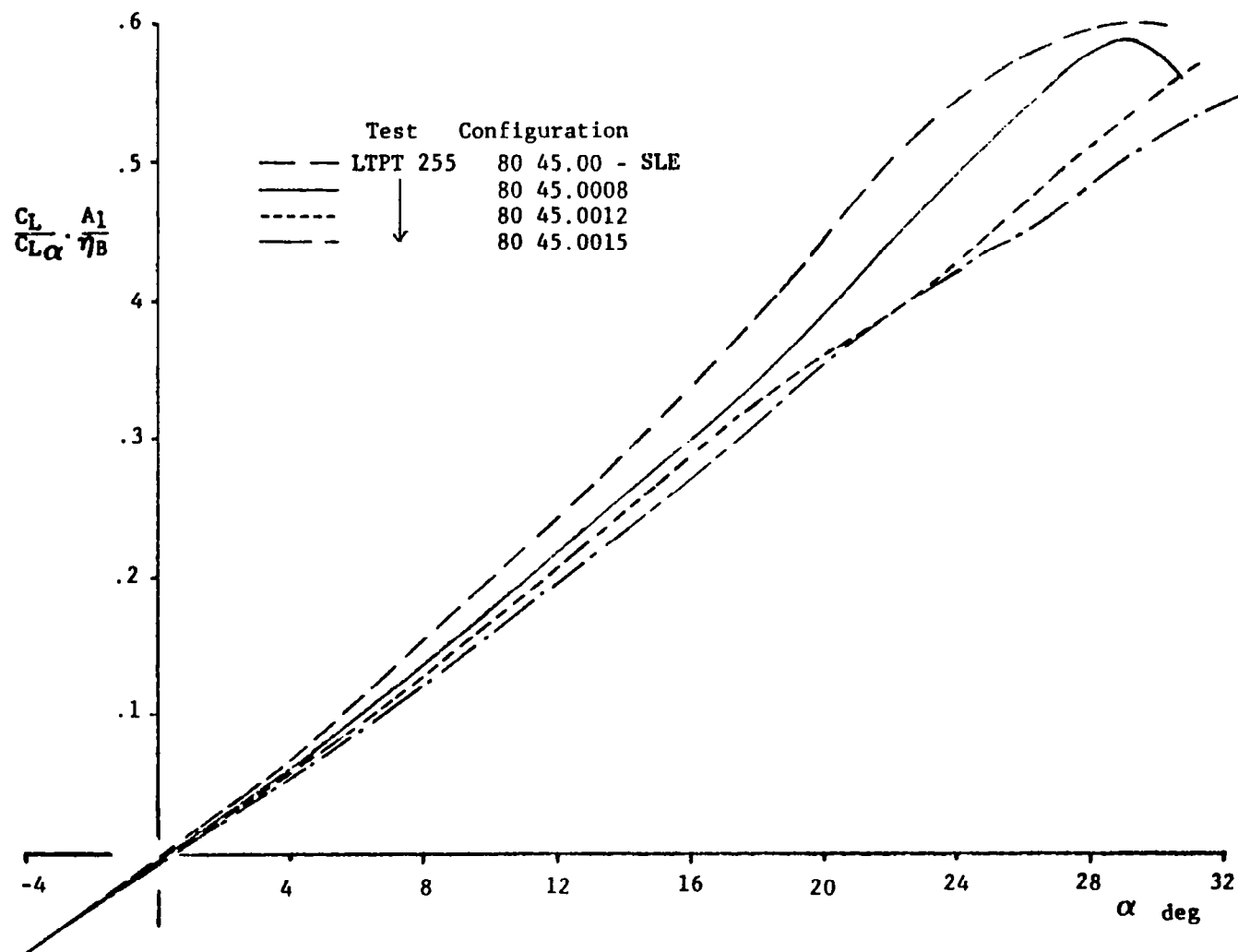Figure 175.   Comparison of Lift Correlation Parameter for Basic Planform

Figure 176.   Effect of Airfoil-Thickness Ratio for Irregular
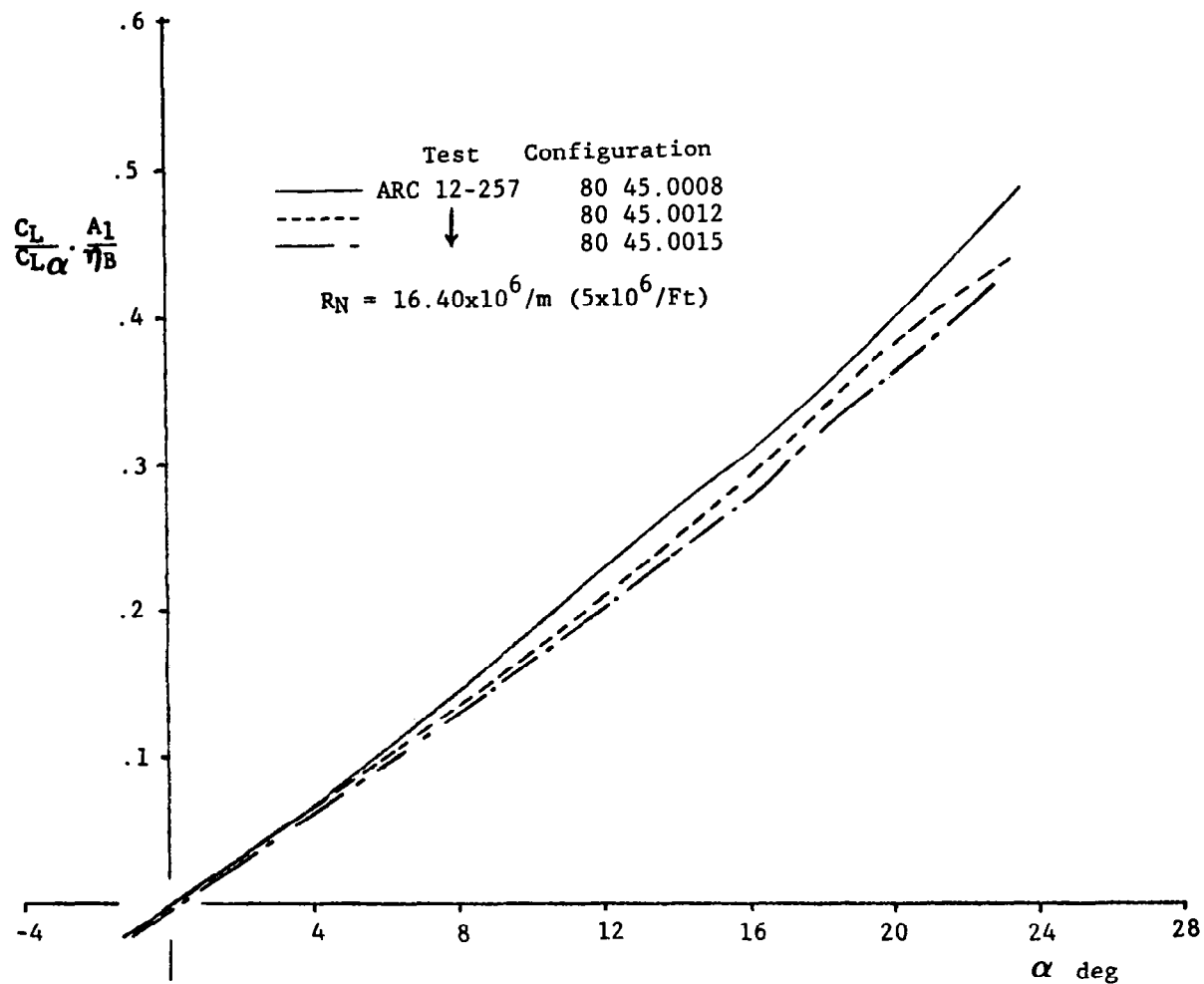Planform From LTPT Facility

Figure 177. Effect of Airfoil-Thickness Ratio for Irregular
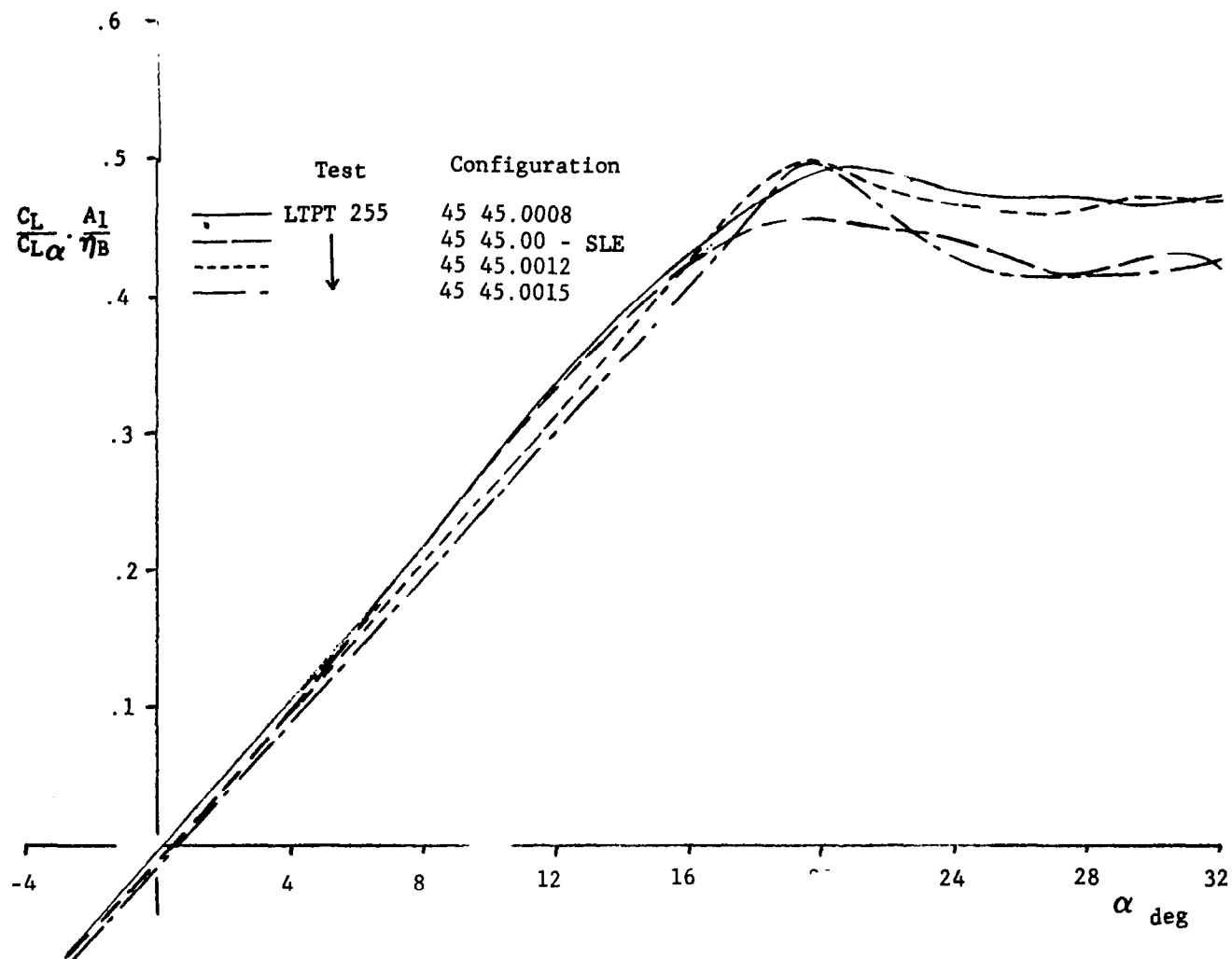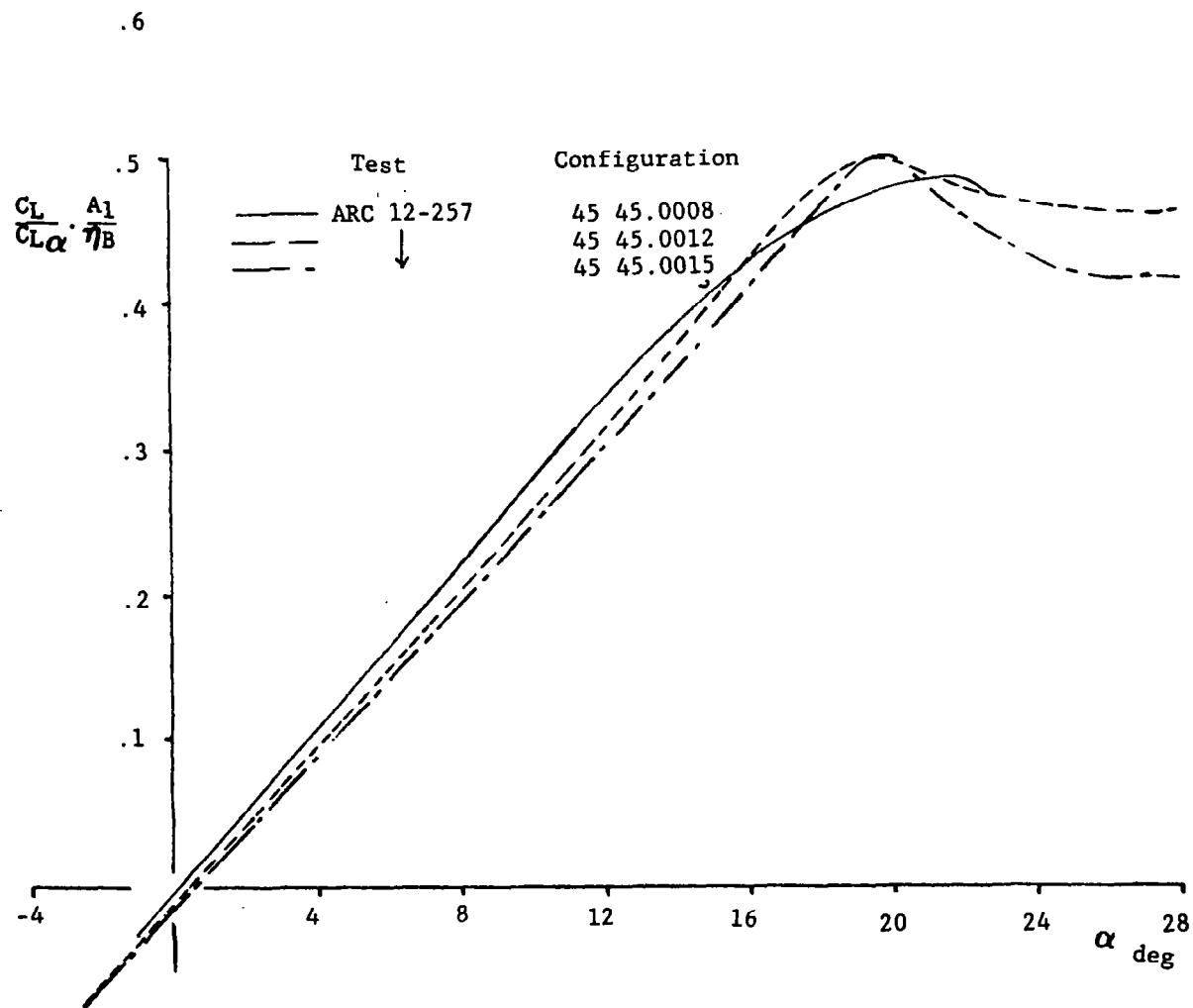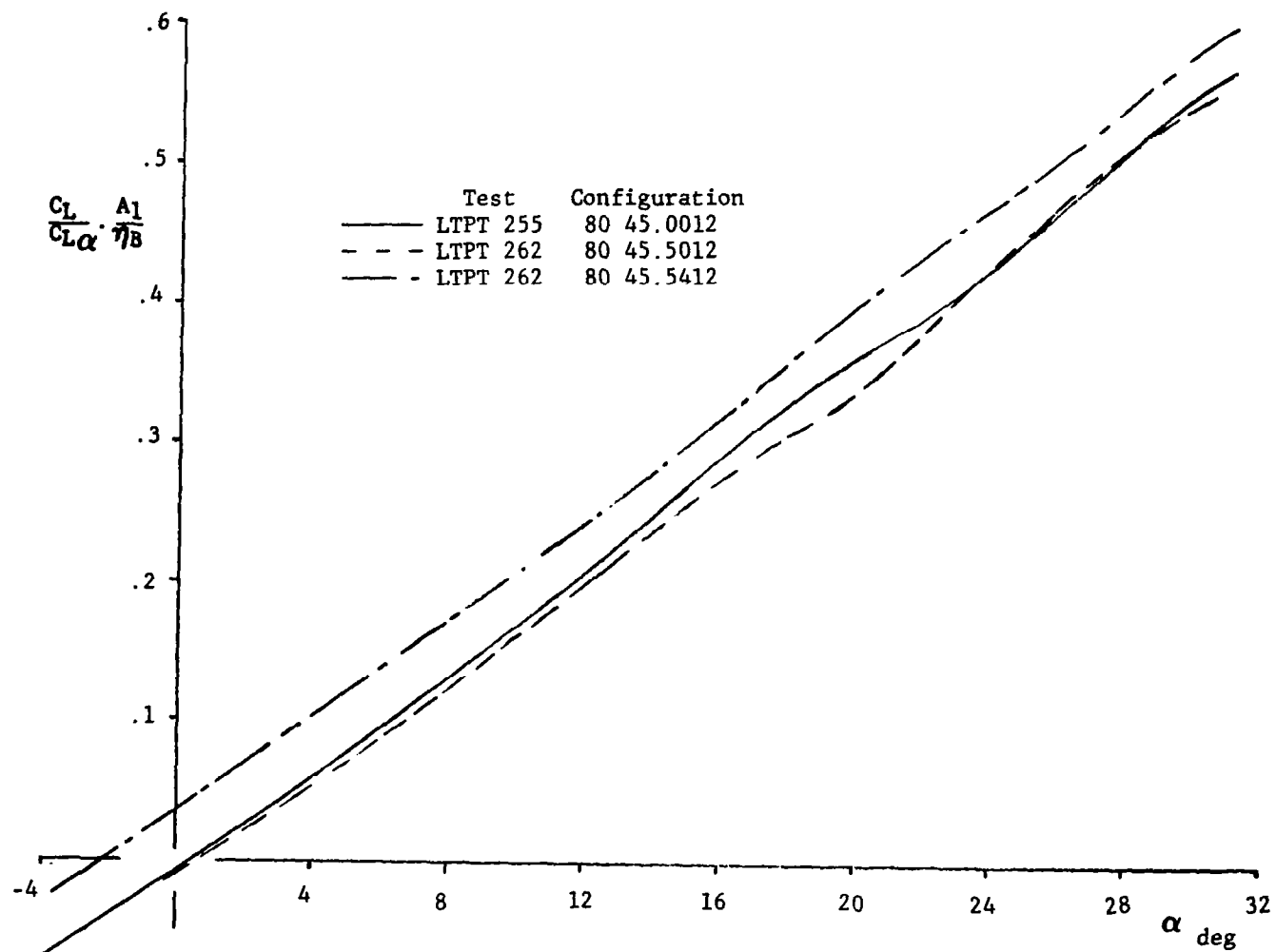Planform From ARC 12-Ft Facility

Figure 178. Effect of Airfoil-Thickness Ratio for Basic Plan-form From LTPT Facility

Figure 179. Effect of Airfoil-Thickness Ratio for Basic Planform
From ARC 12-Ft Facility

Figure 180. Effects of Airfoil Thickness Distribution and Camber for 80-45 Irregular Planform
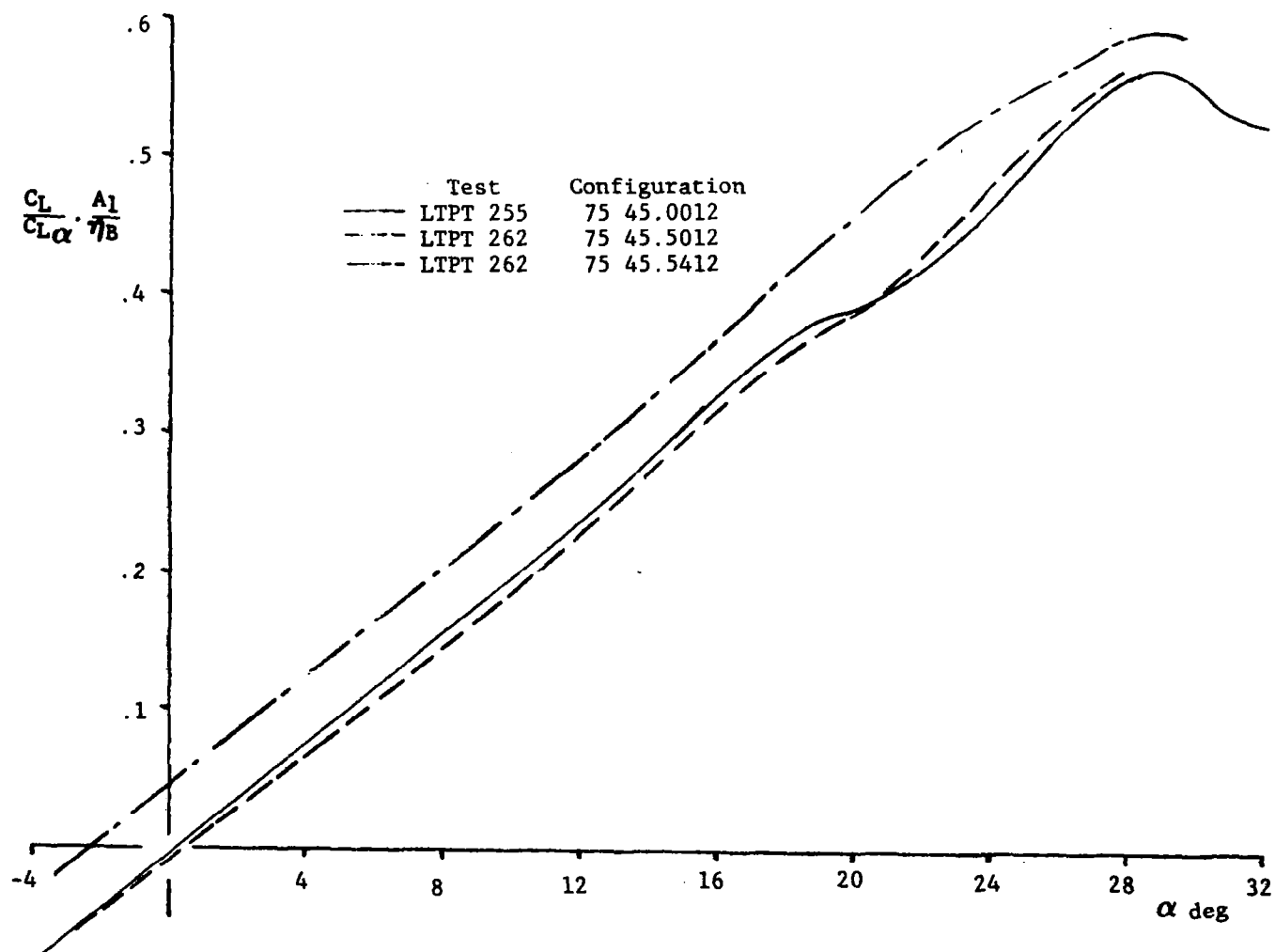
Figure 181. Effects of Airfoil Thickness Distribution and Camber for 75-45 Irregular Planform
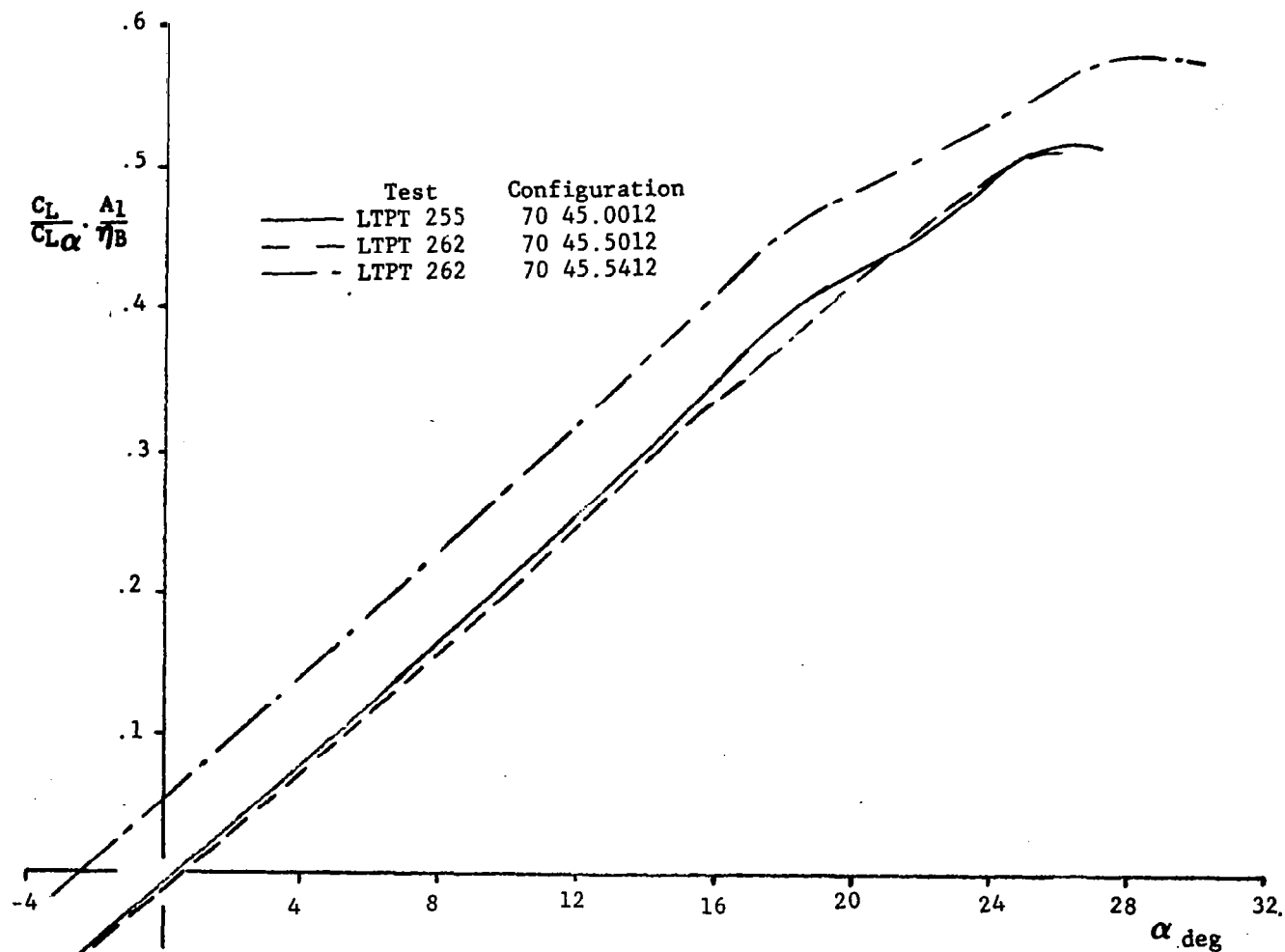
Figure 182.   Effects of Airfoil Thickness Distribution and Camber
for 70-45 Irregular Planform
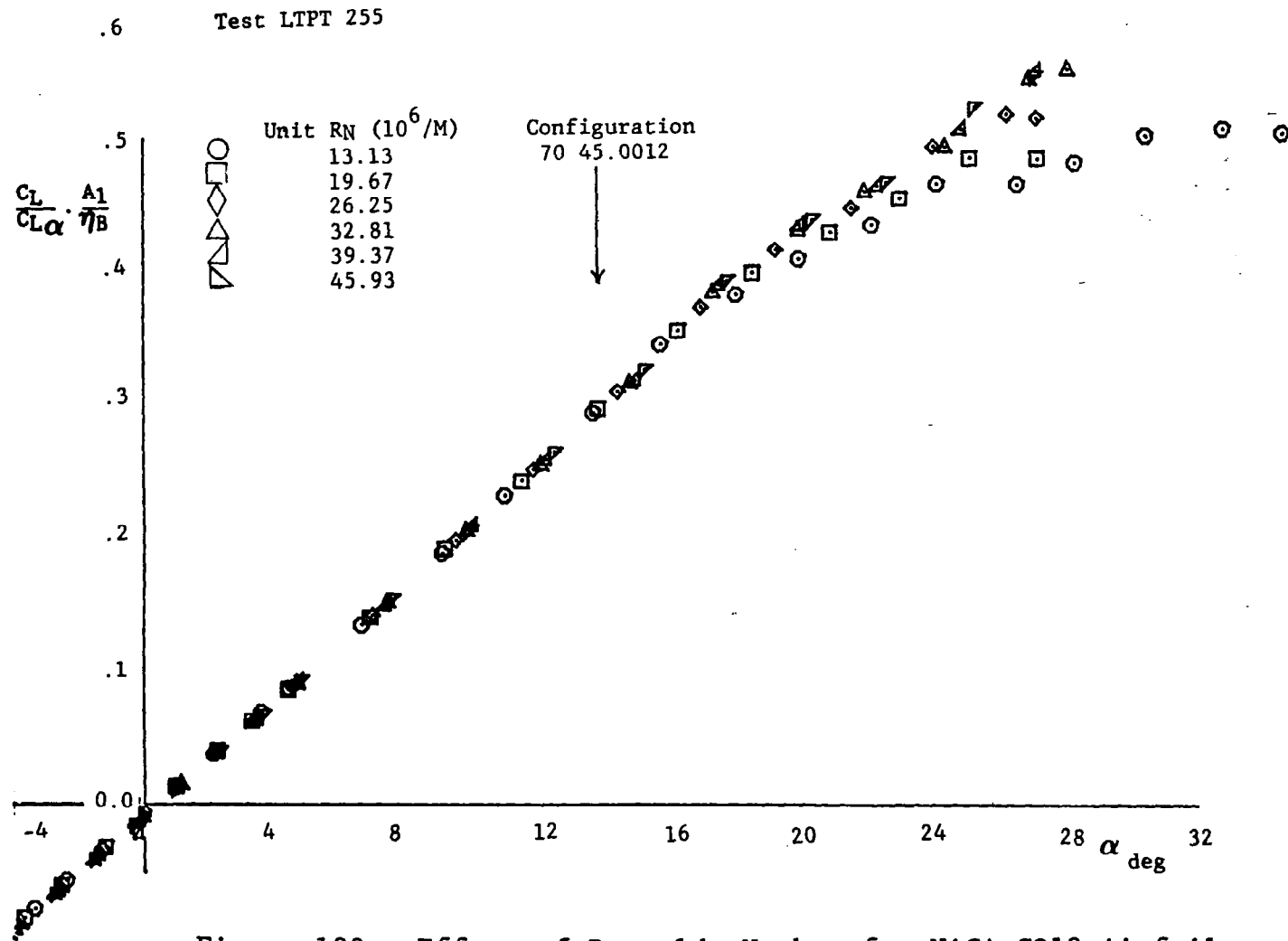
Figure 183. Effect of Reynolds Number for NACA C012 Airfoil
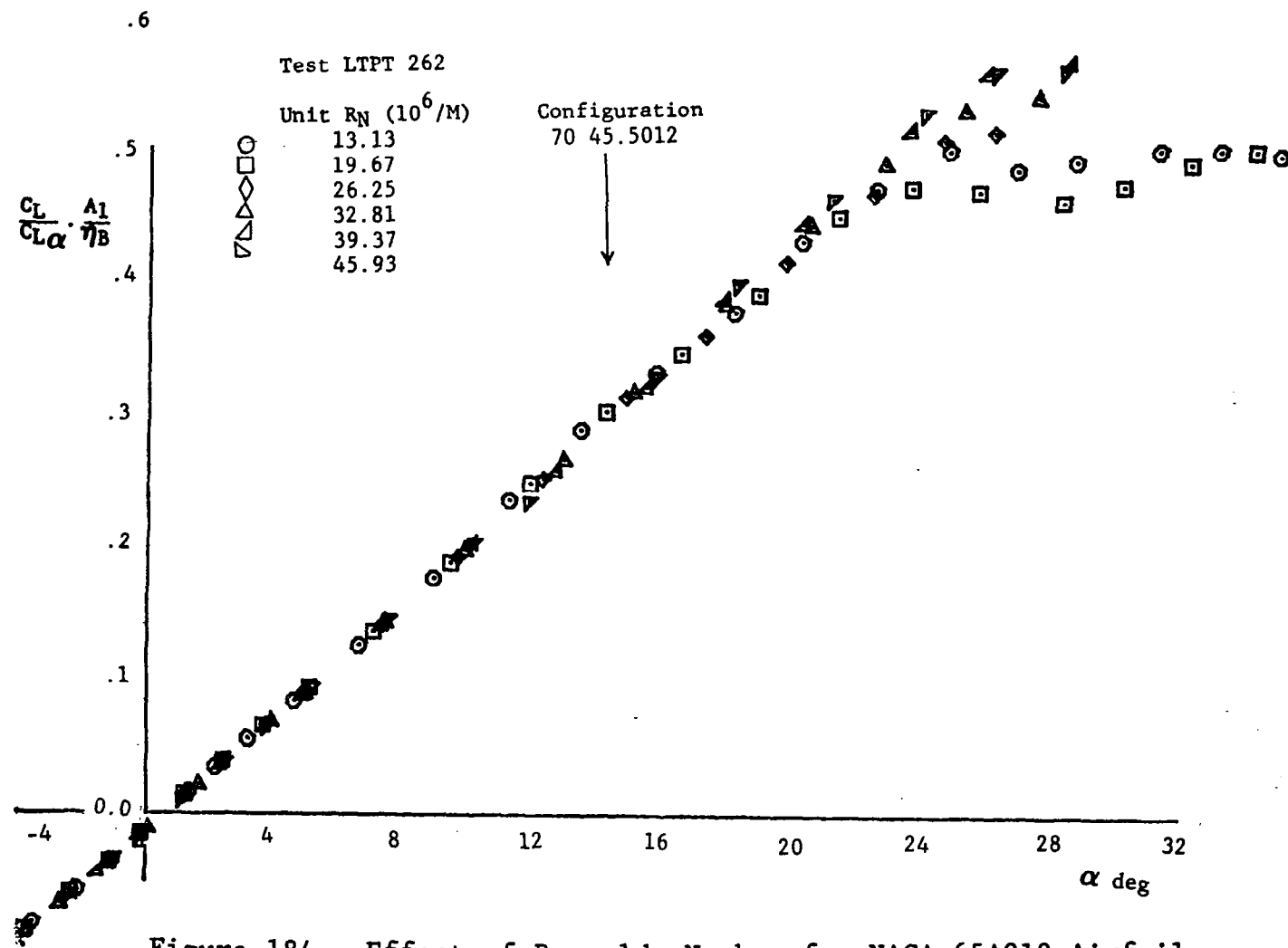
Figure 184.   Effect of Reynolds Number for NACA 65A012 Airfoil

Test LTPT 262

$\dfrac{C_L}{C_{L\alpha}} \cdot \dfrac{A_1}{\eta_B}$

Unit R_N $(10^6/M)$

○ :3.13
□ 19.67
◇ 2b.25
△ 32.81
◁ 39.37
▷ 45.93

Configuration
70 45.5412

.6

.5

.4

.3

.2

.1

0.0

0   4   8   12   16   20   24   28   32

α deg
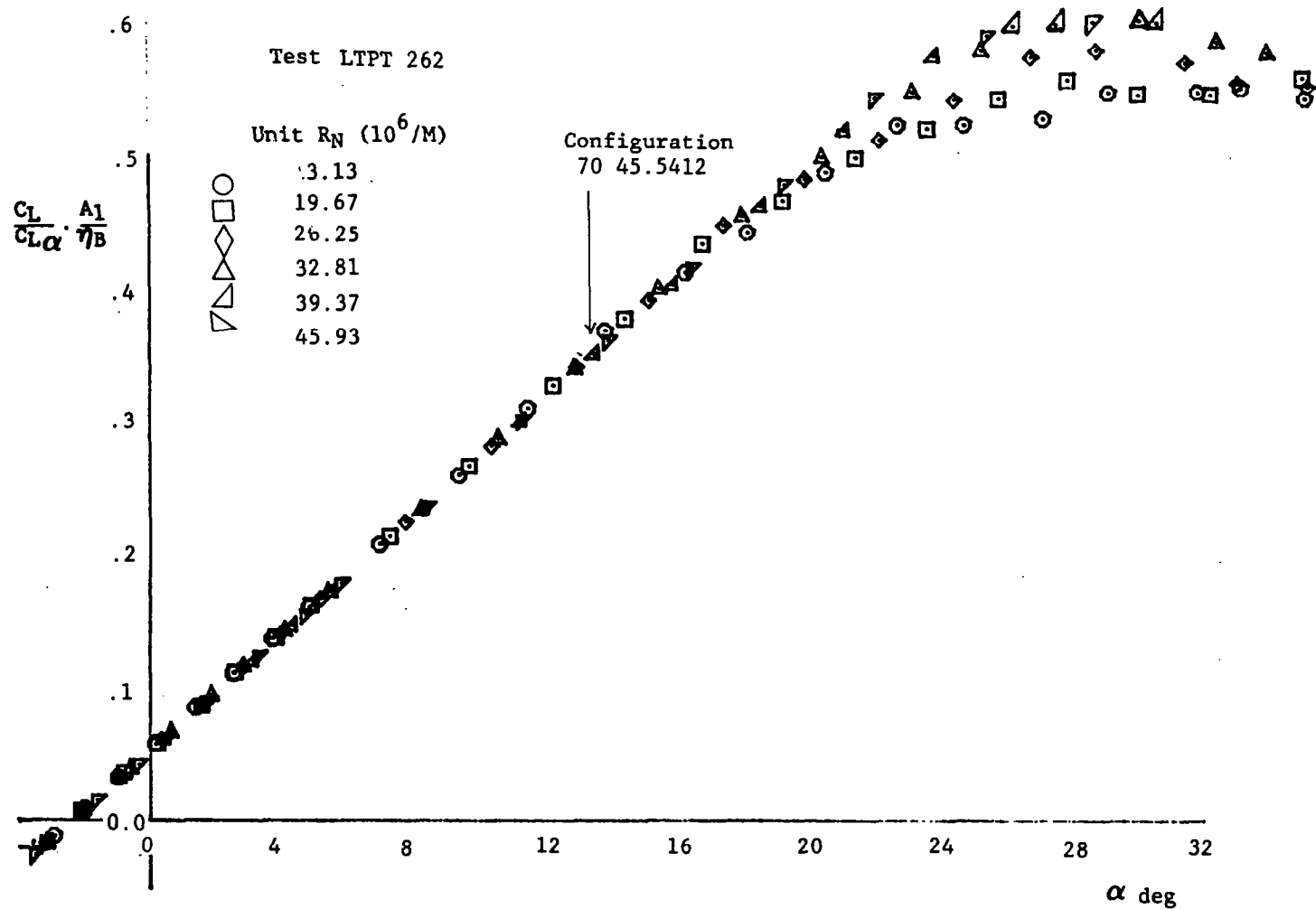
Figure 185.   Effect of Reynolds Number for NACA 65_1412 Airfoil

XX45.00SLE

$$\Delta\left(\frac{C_L}{C_{L_\alpha}}\frac{A_1}{n}\right)$$

Note: Reference Configurations have
NACA 0008 Airfoils at
$R_N = 26.25 \times 10^6/m$

Λ_F
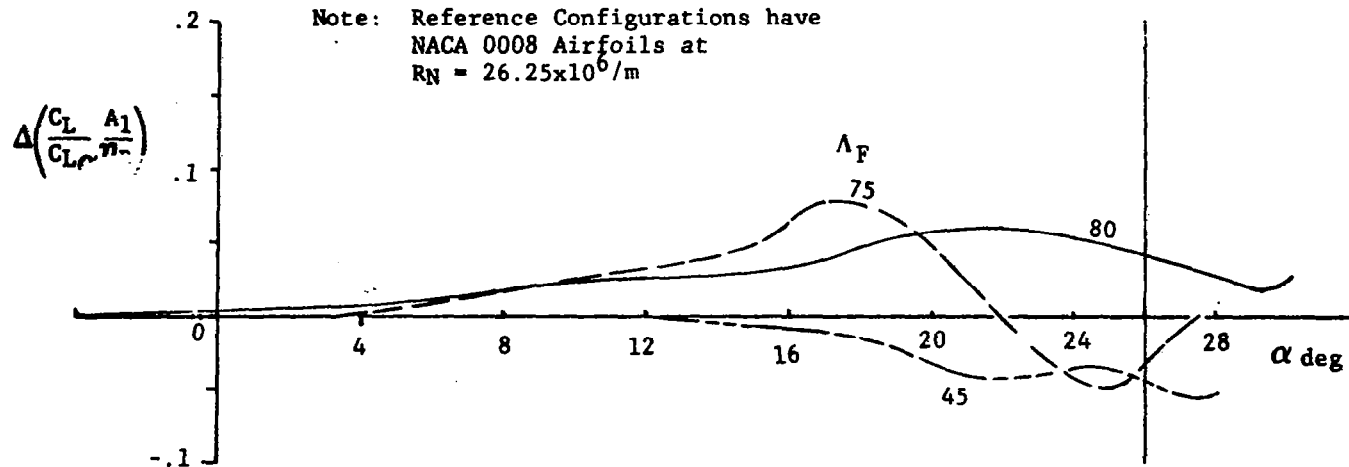
Figure 186. Effect of Fillet Sweep on Lift-Parameter Increment
for Thin Airfoil With Sharp Leading Edge

XX45.0012

$R_N = 26.25 \times 10^6 /m$ $(8 \times 10^6 /Ft)$

$$\Delta\left(\frac{c_L}{c_{L\alpha}}\frac{A_1}{\eta_B}\right)$$

Note: Reference Configurations have NACA 0008 Airfoils
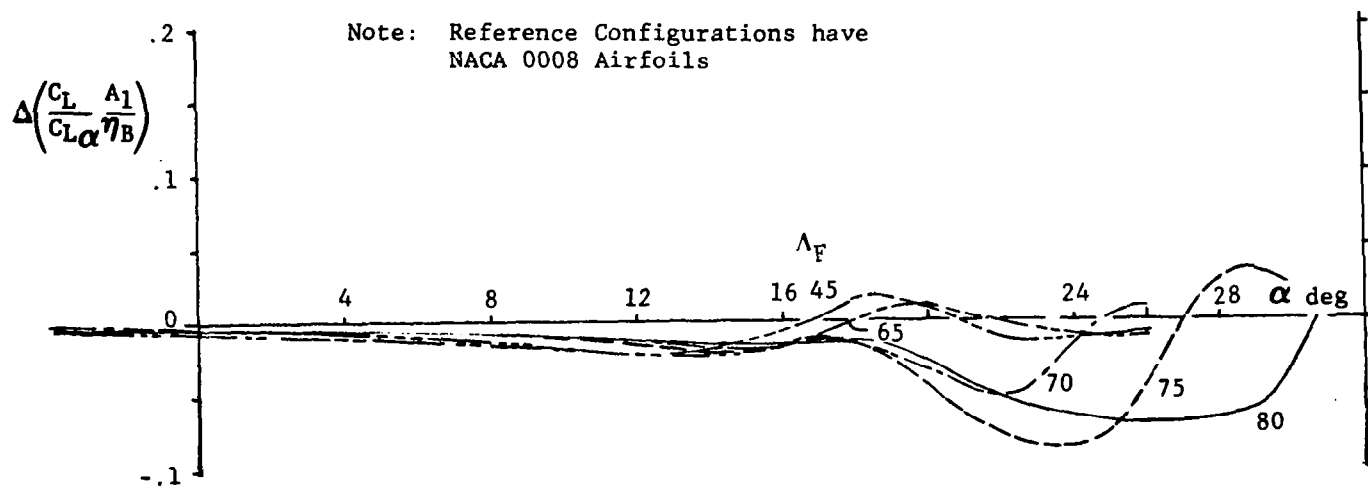
Figure 187. Effect of Fillet Sweep on Lift-Parameter Increment for NACA 0012 Airfoil

XX45.0015 $R_N = 26.25 \times 10^6/m$

Note: Reference Configurations have
NACA 0008 Airfoils

$\Delta\left(\dfrac{c_L}{c_{L\alpha}}\dfrac{A_1}{\eta_B}\right)$
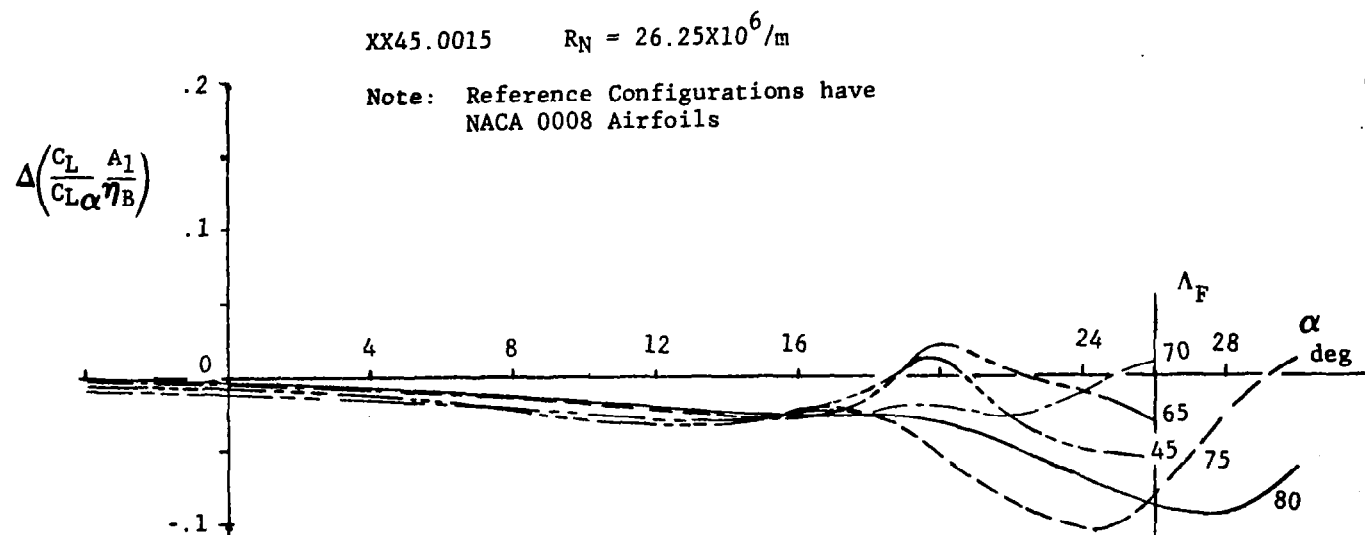
Figure 188.   Effect of Fillet Sweep on Lift-Parameter Increment
for NACA 0015 Airfoil

XX45.5012

$R_N = 26.25 \times 10^6 /m$

Note: Reference Configurations have
NACA 0008 Airfoils

$$\Delta\left(\frac{c_L}{c_{L_\alpha}}\frac{A_1}{\eta_B}\right)$$
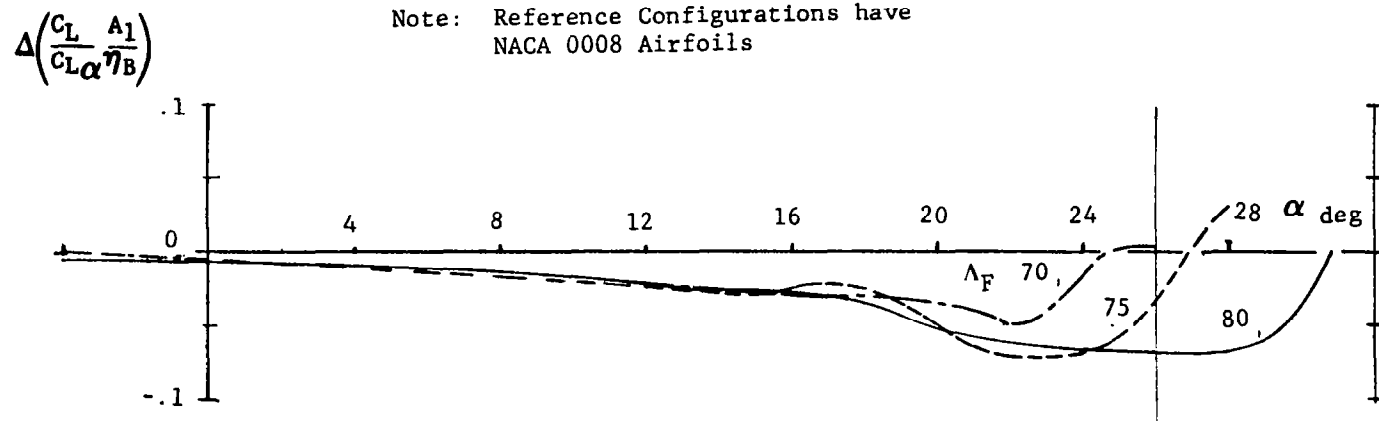
Figure 189. Effect of Fillet Sweep on Lift-Parameter Increment
for NACA 65A012 Airfoil

XX45.5412

$R_N = 26.25 \times 10^6/m$ $(8.0 \times 10^6/Ft)$

Note: Reference Configurations have NACA 0008 Airfoils

$\Delta\left(\dfrac{C_L}{C_{L_\alpha}} \dfrac{A_1}{\eta_B}\right)$

.2

.1

Λ_F

70

75

80

0

4   8   12   16   20   28 α deg

-.1
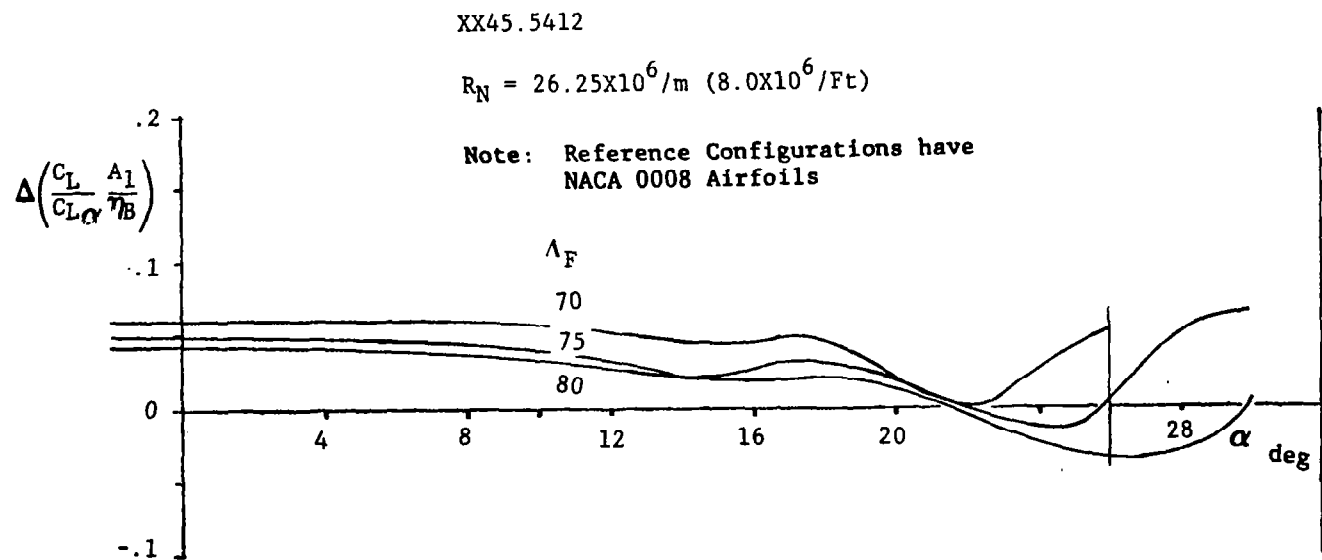
Figure 190.   Effect of Fillet Sweep on Lift-Parameter Increment
for Cambered Airfoil
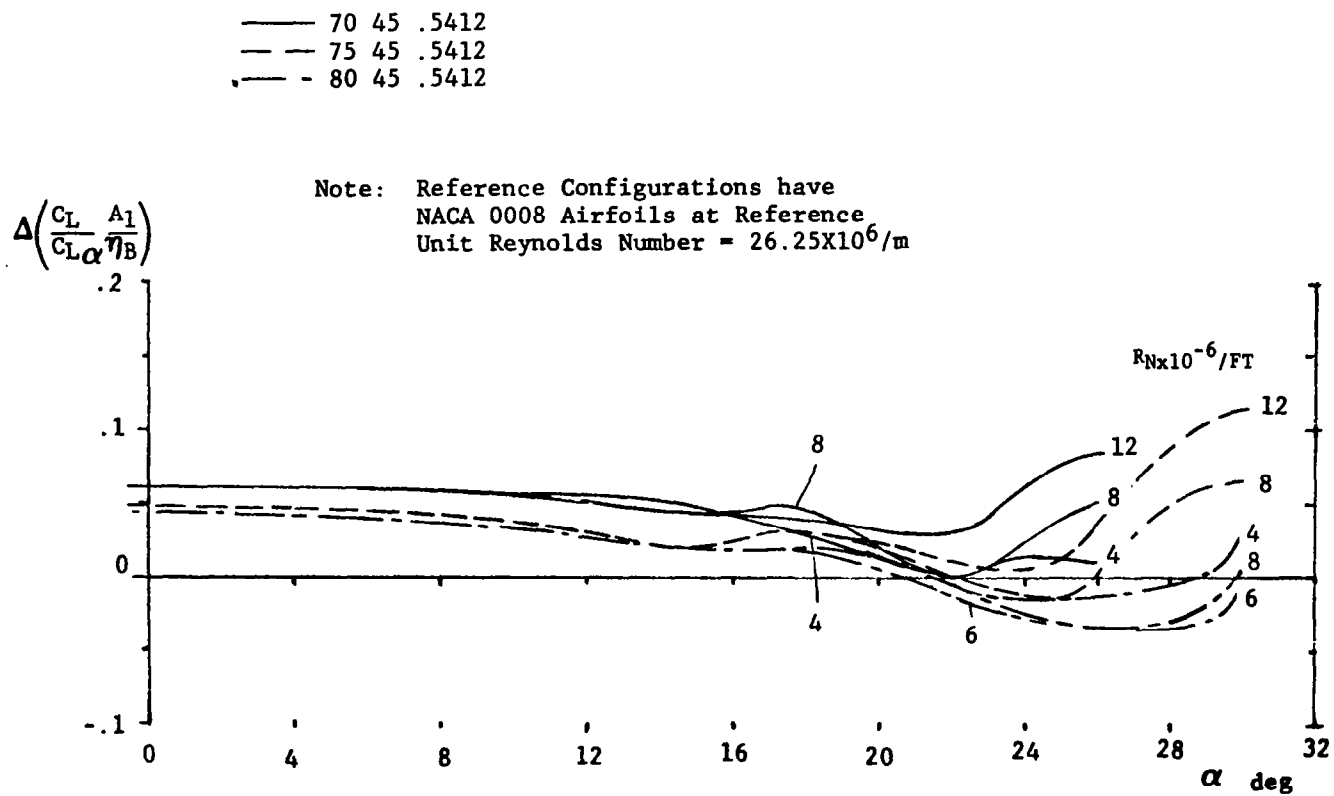
Figure 191. Effects of Reynolds Number Confuse the Situation

Figure 192.   Lift Correlation for NACA 0004 Airfoils

303
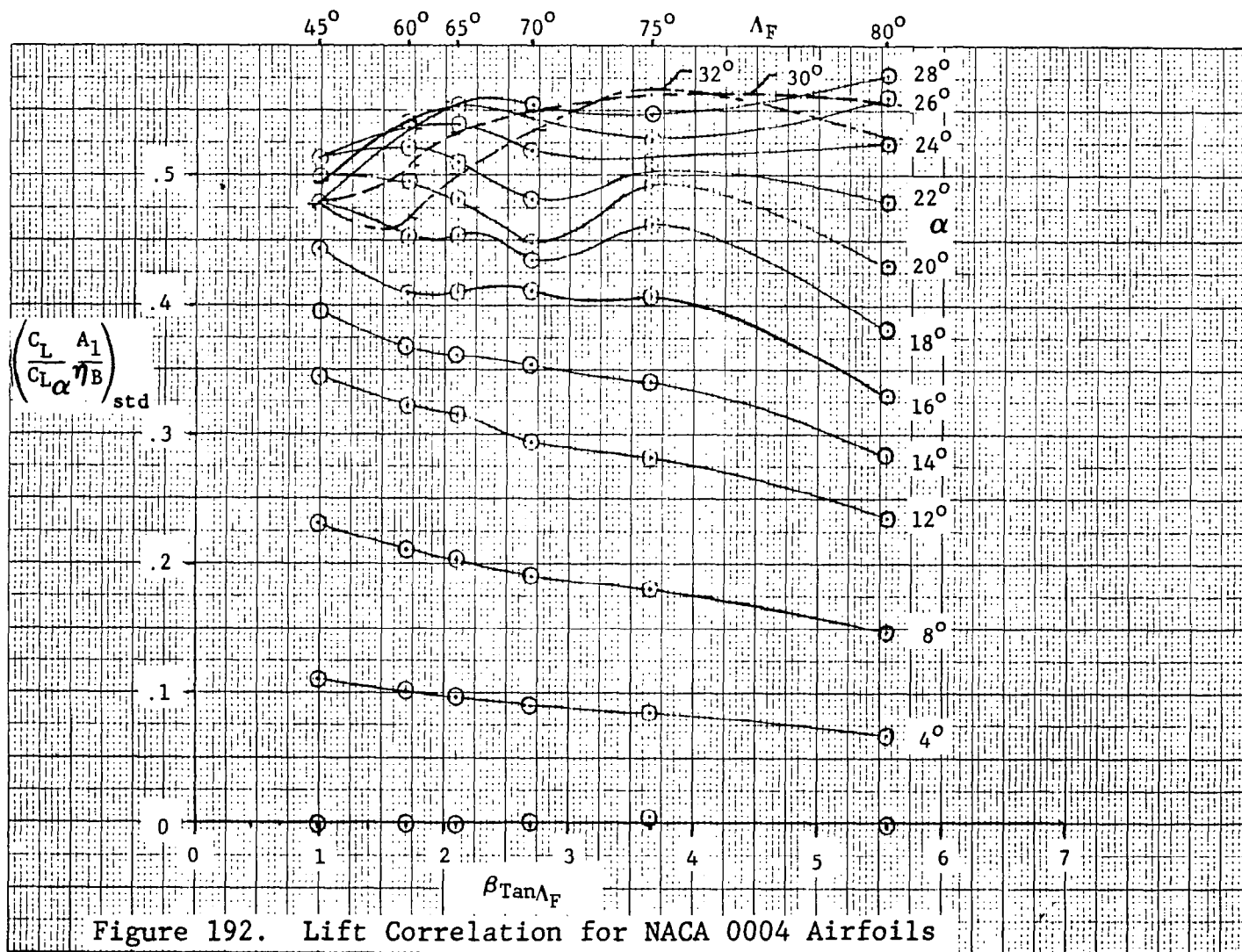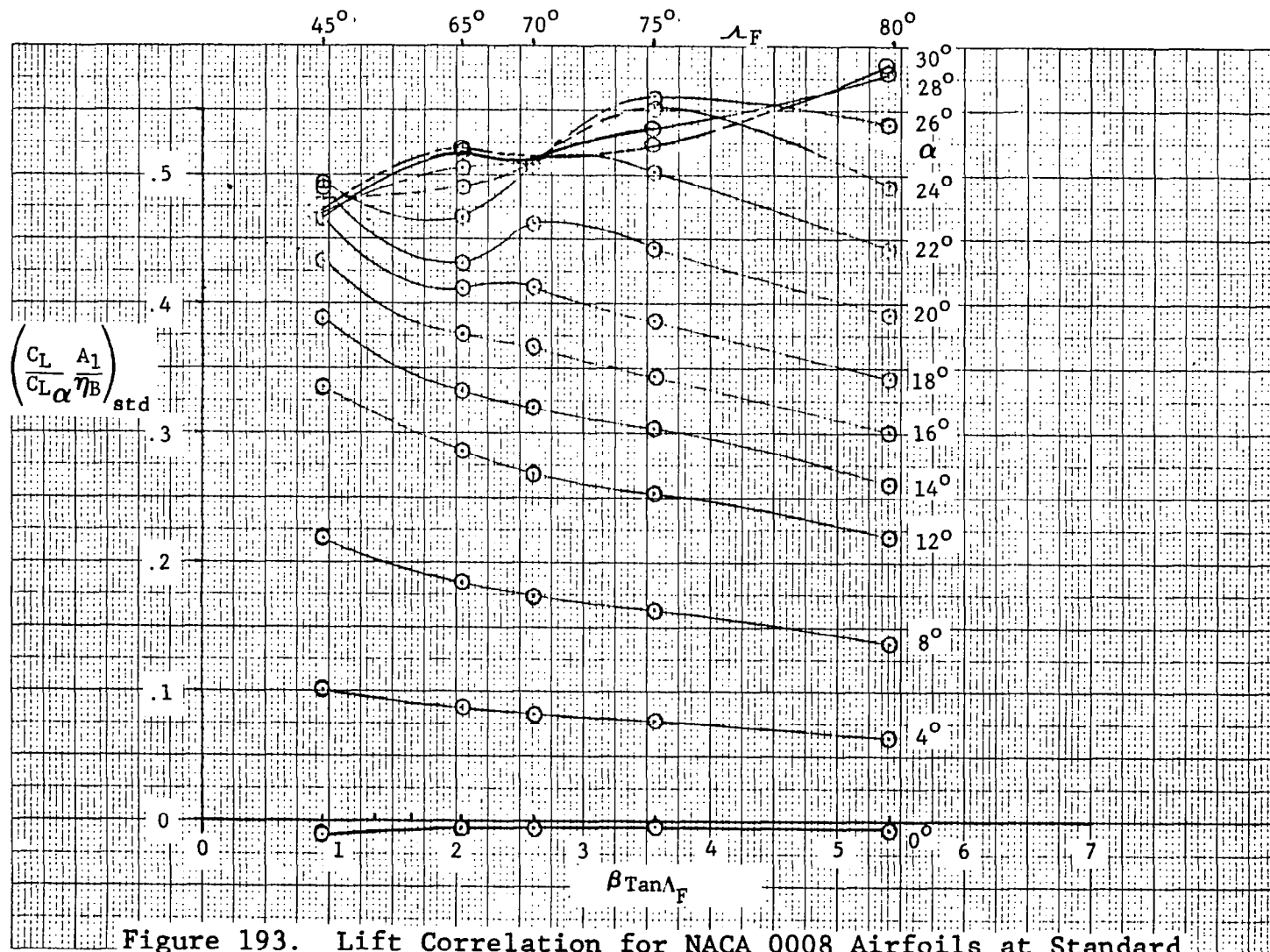
Figure 193. Lift Correlation for NACA 0008 Airfoils at Standard Reynolds Number
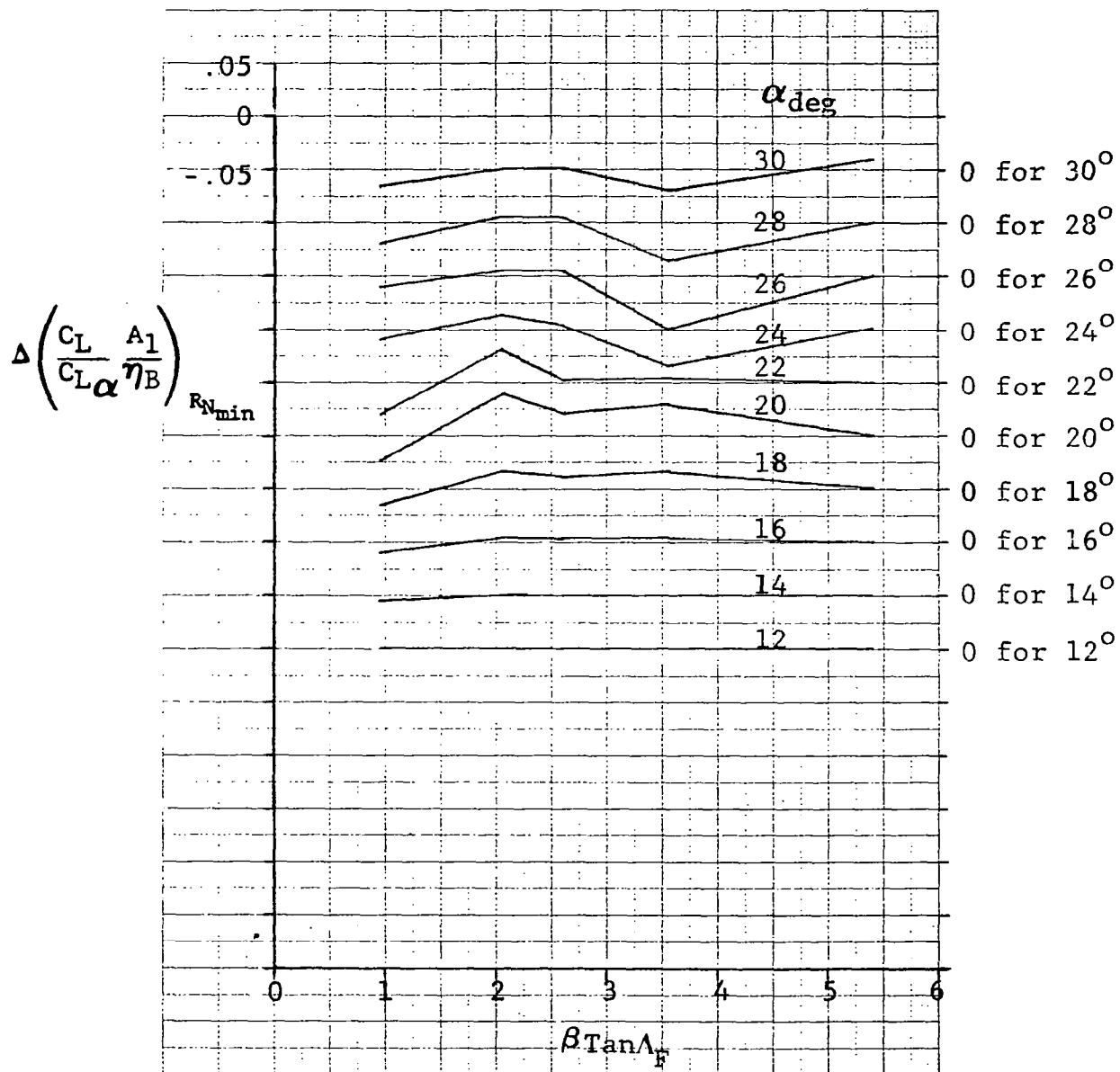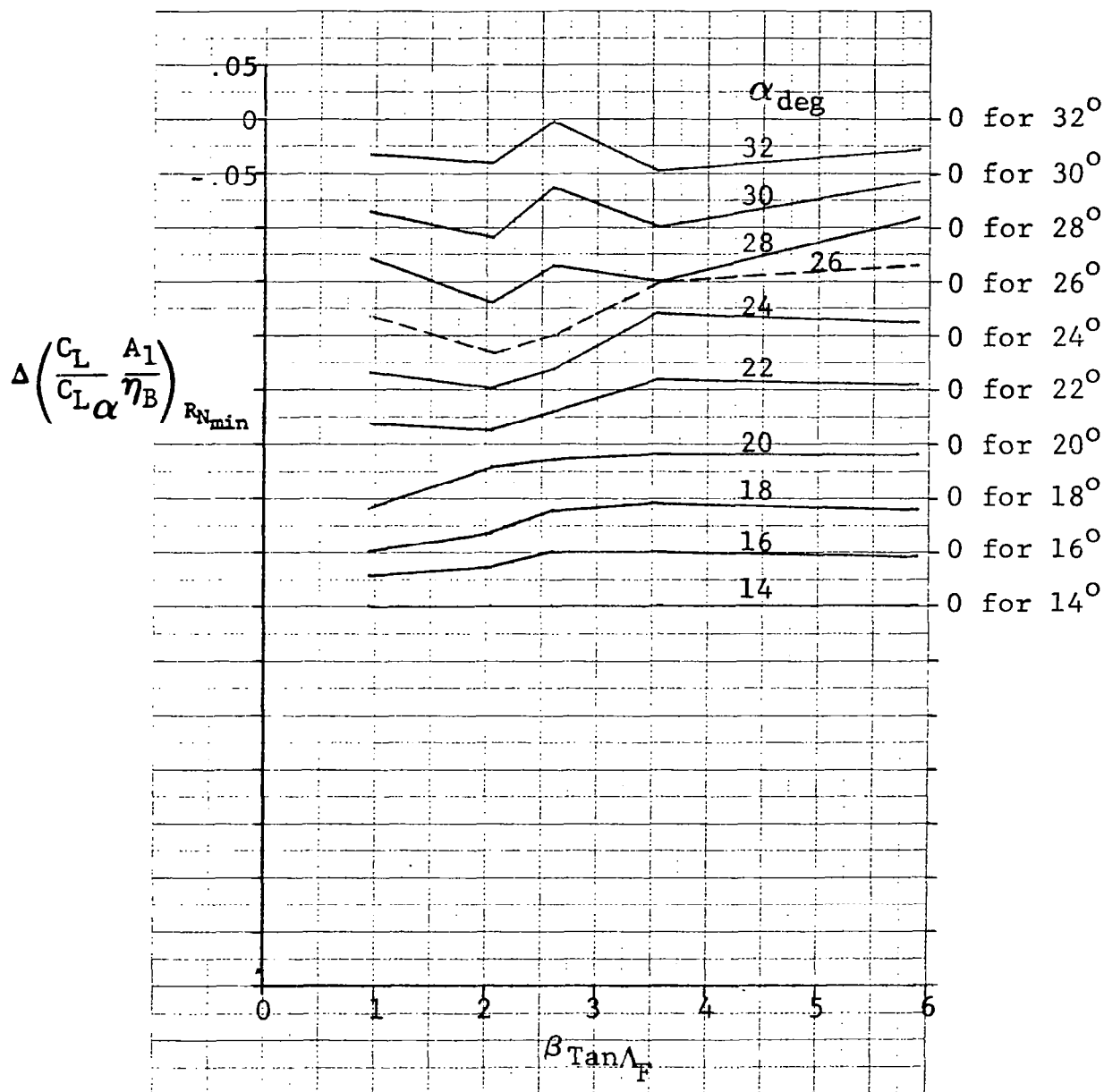
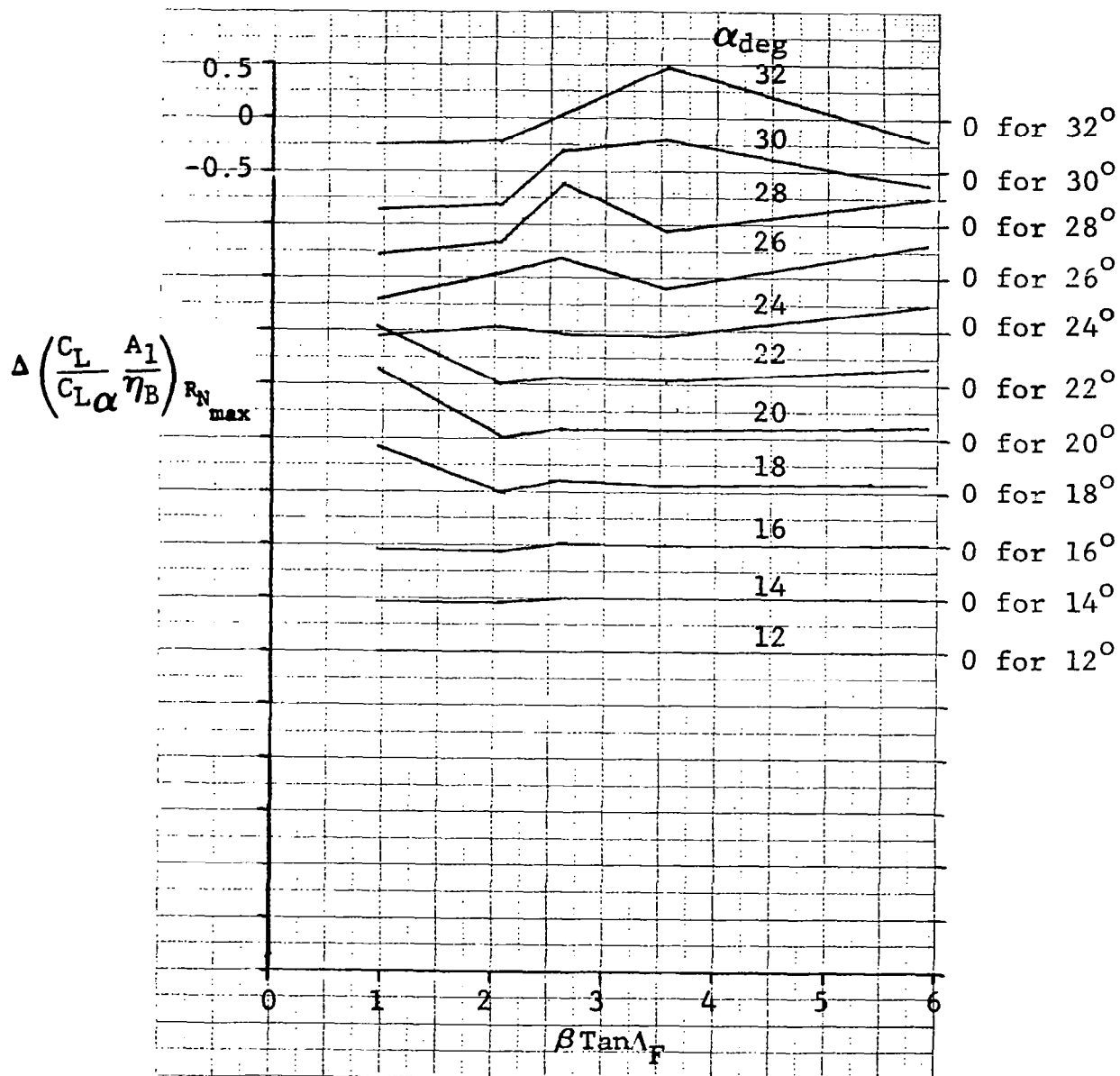Figure 194. Incremental Values of Lift Correlation Parameter for NACA 0008 Airfoils at Minimum Reynolds Number
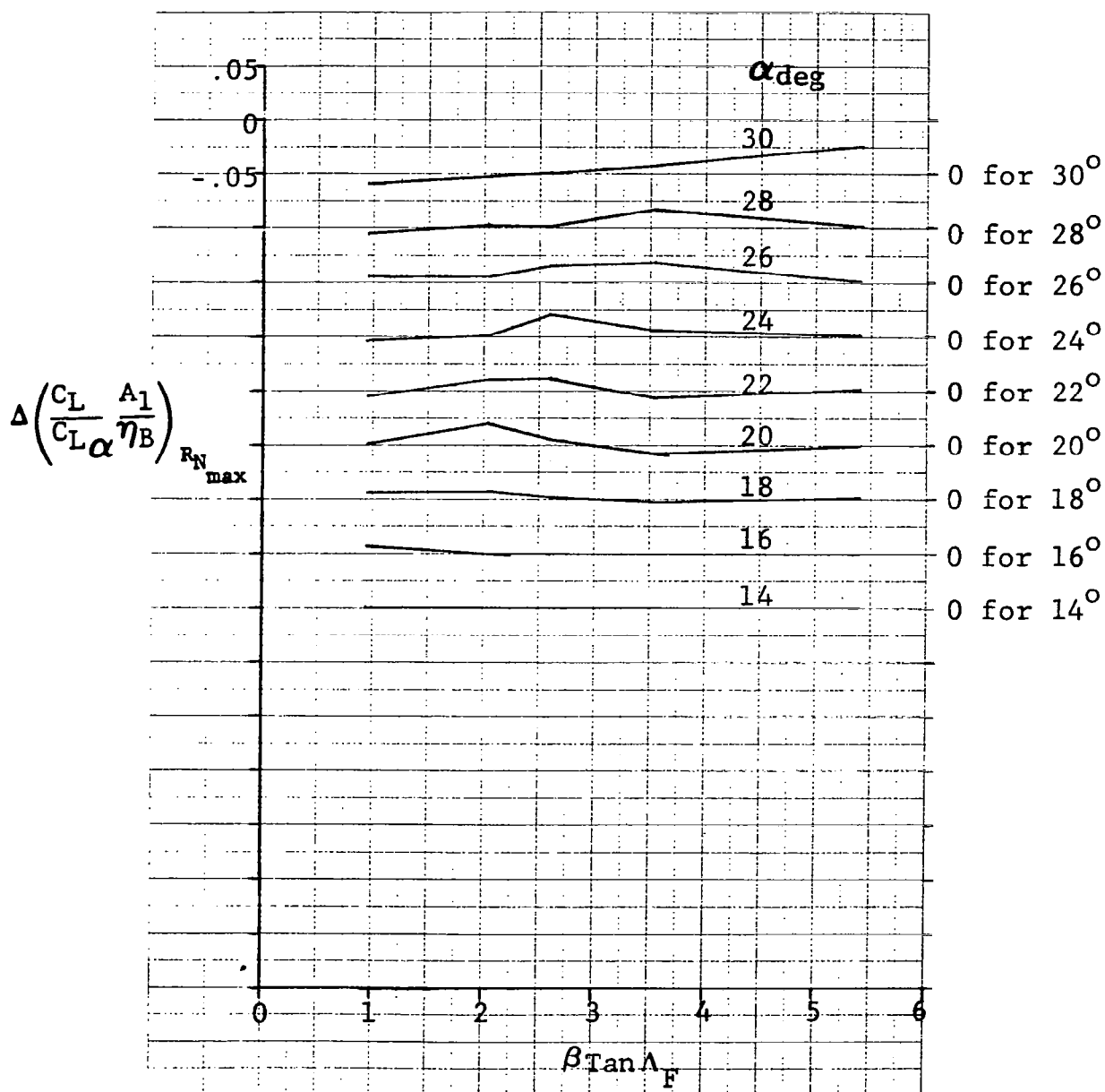
Figure 195.   Incremental Values of Lift Correlation
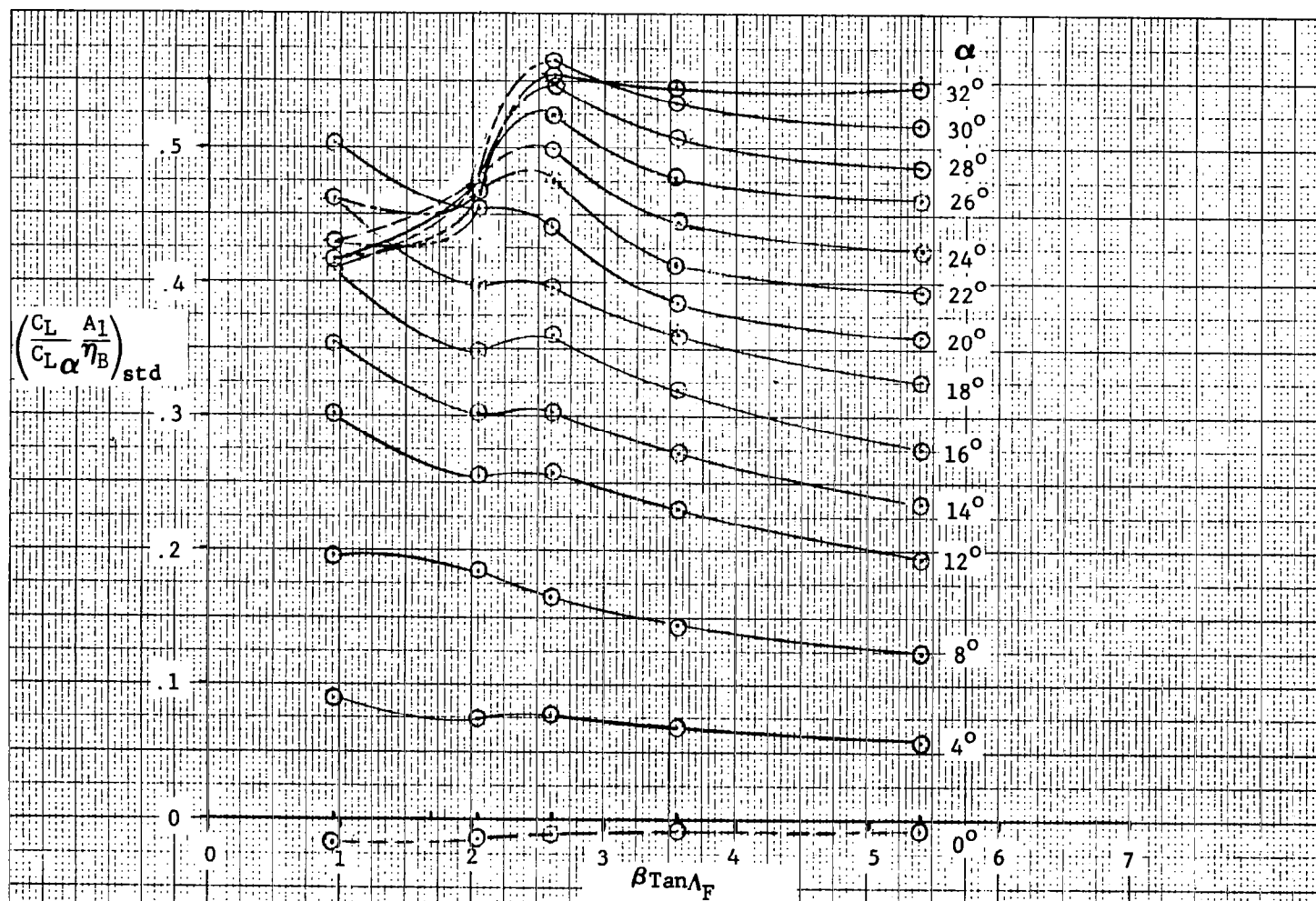Parameter for NACA 0008 Airfoils at
Maximum Reynolds Number
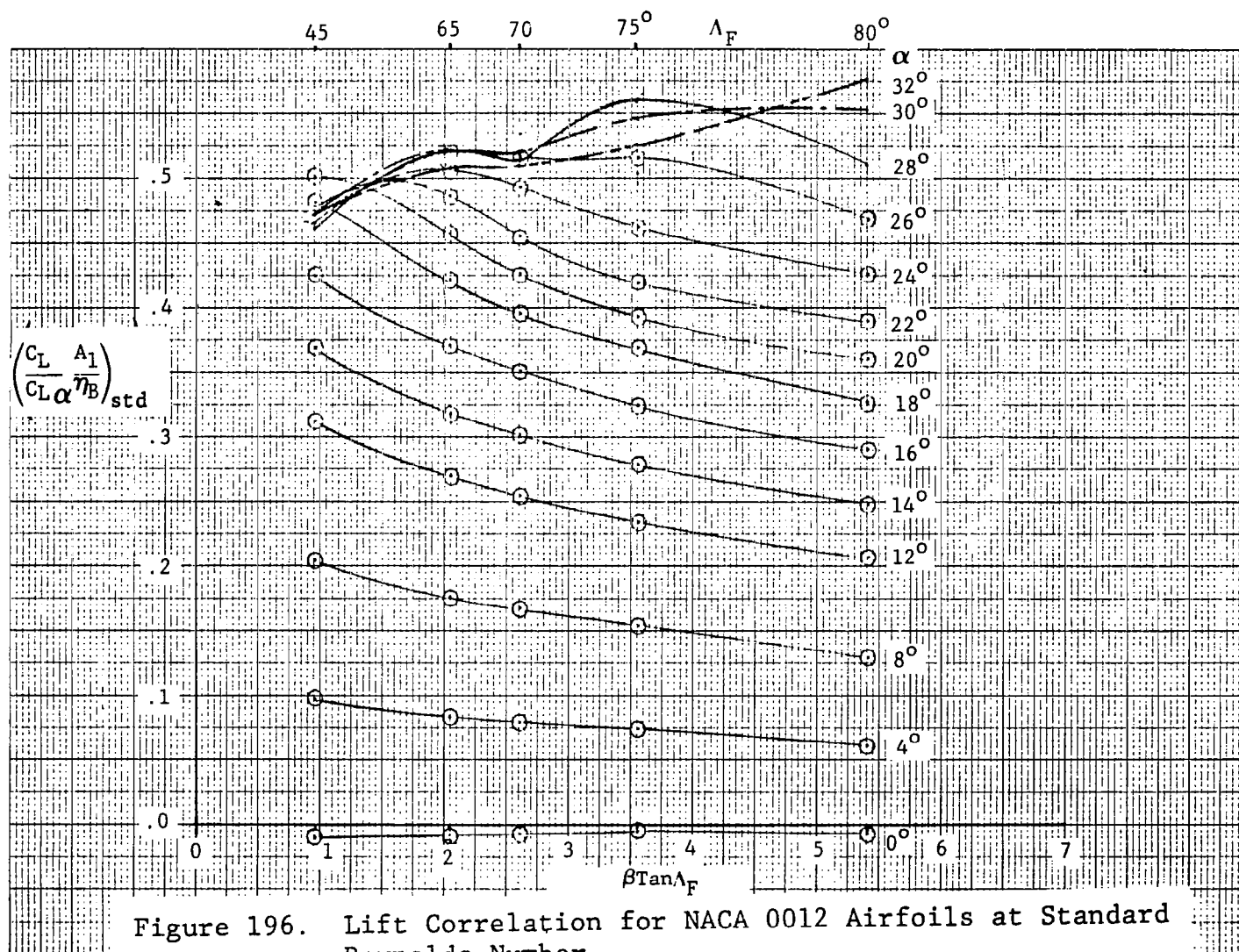
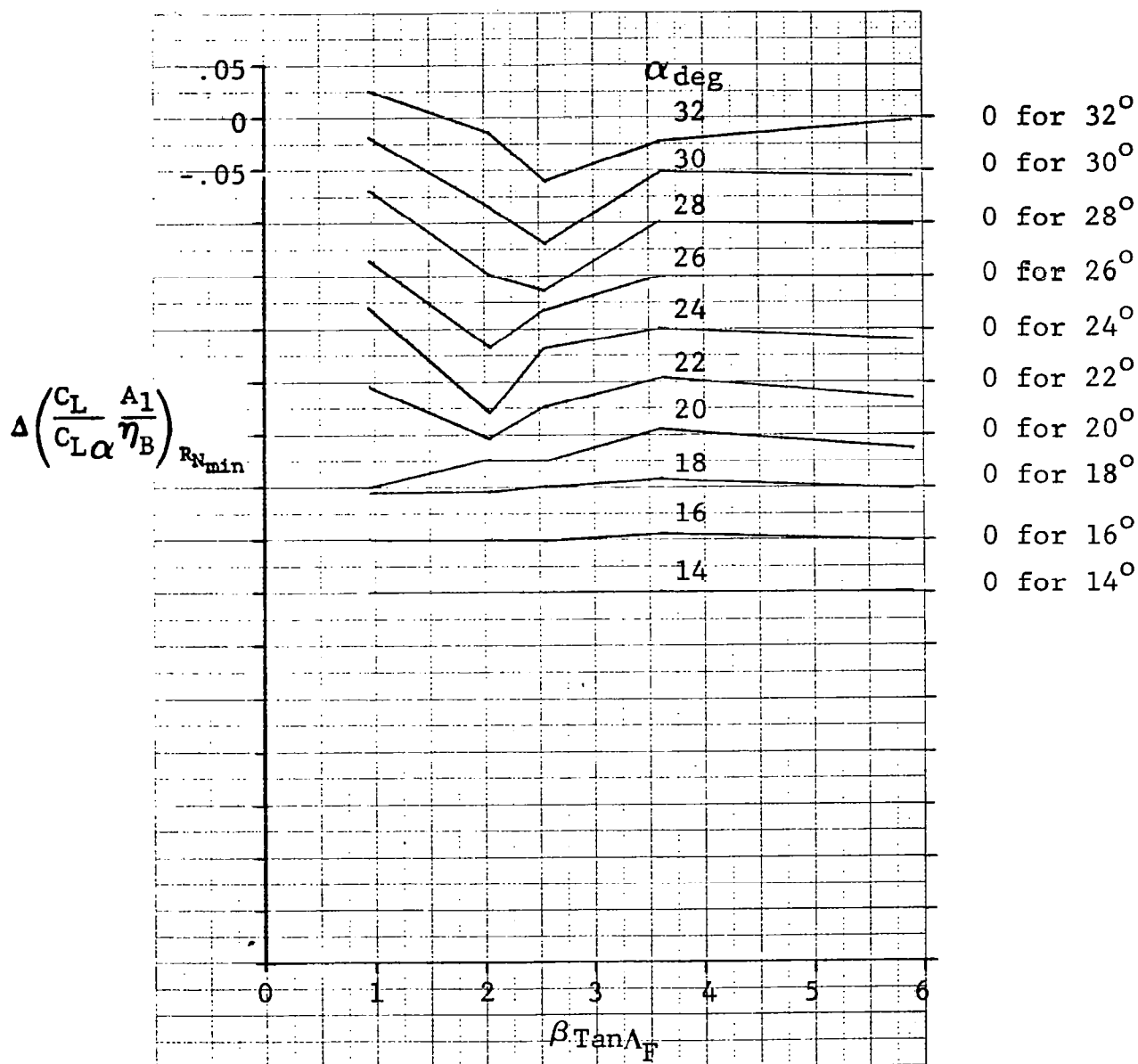Figure 196. Lift Correlation for NACA 0012 Airfoils at Standard Reynolds Number

Figure 197. Incremental Values of Lift Parameter
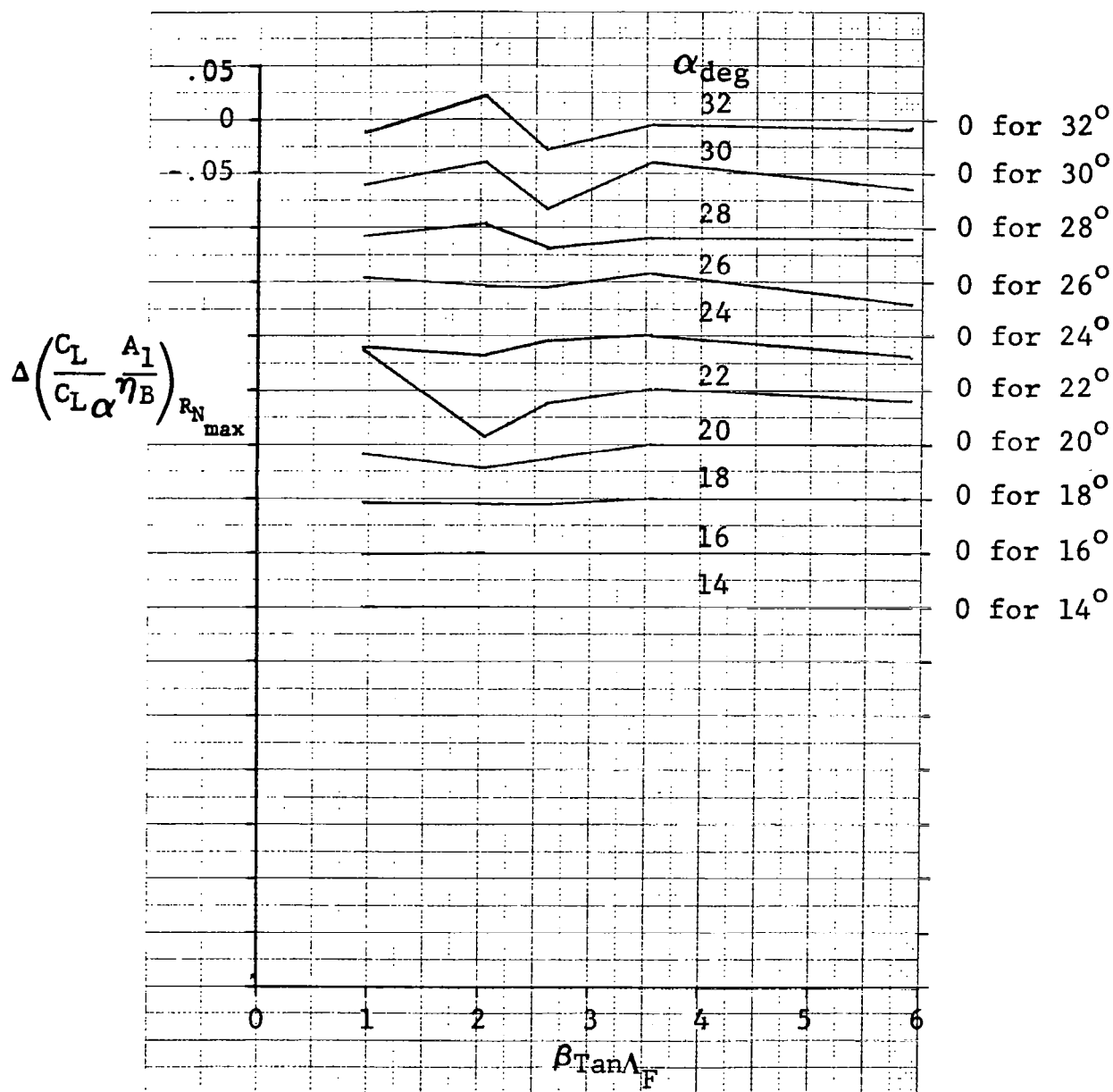for NACA 0012 Airfoils at Minimum
Reynolds Number

Figure 198. Incremental Values of Lift Parameter
for NACA 0012 Airfoils at Maximum
Reynolds Number

Figure 199. Lift Correlation for NACA 0015 Airfoils at Standard Reynolds Number

Figure 200. Incremental Values of Lift Parameter for NACA 0015 Airfoils at Minimum Reynolds Number

Figure 201. Incremental Values of Lift Parameter
for NACA 0015 Airfoils at Maximum
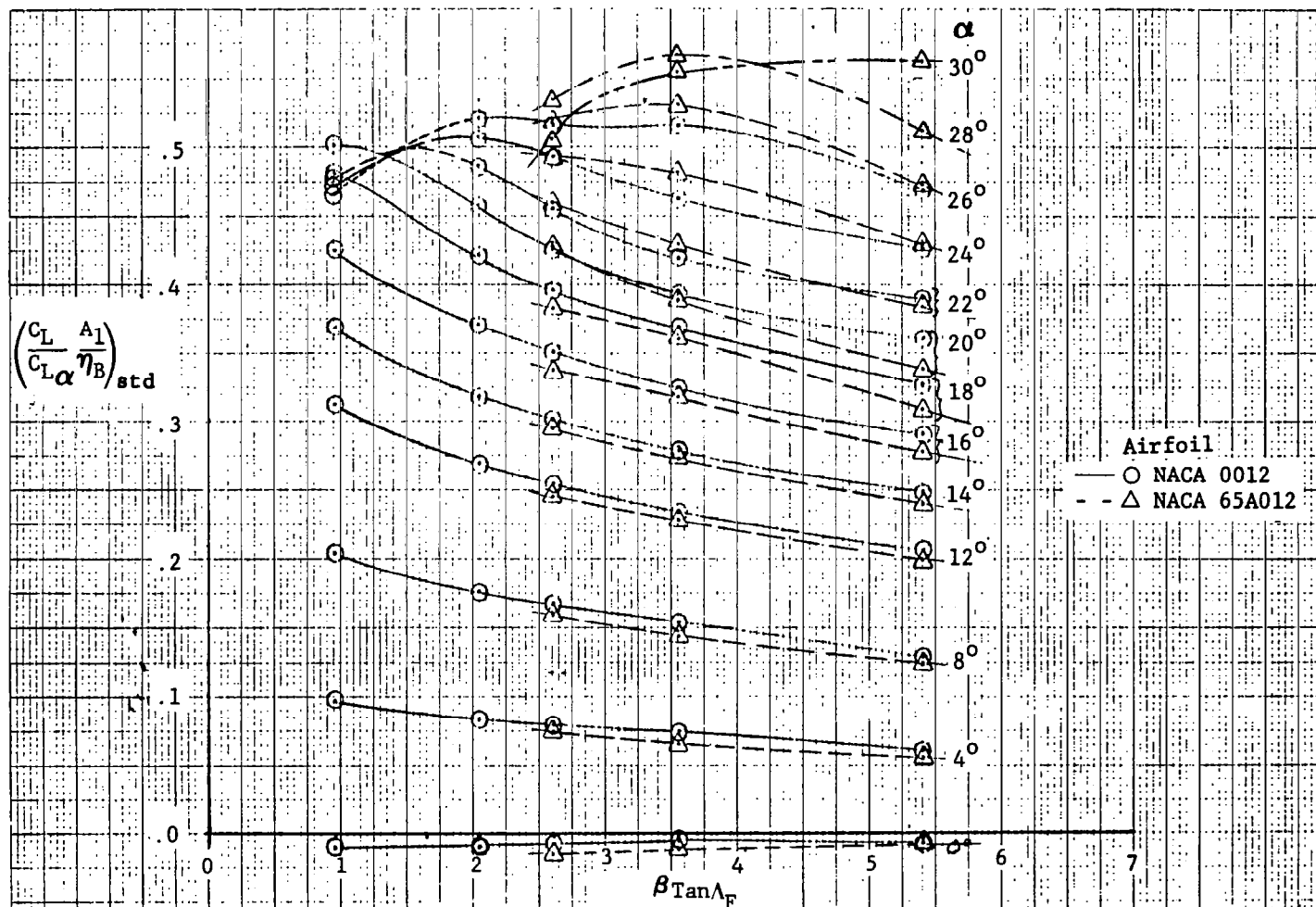Reynolds Number

Figure 202.   Lift Correlation for NACA 65A012 and 0012 Airfoils
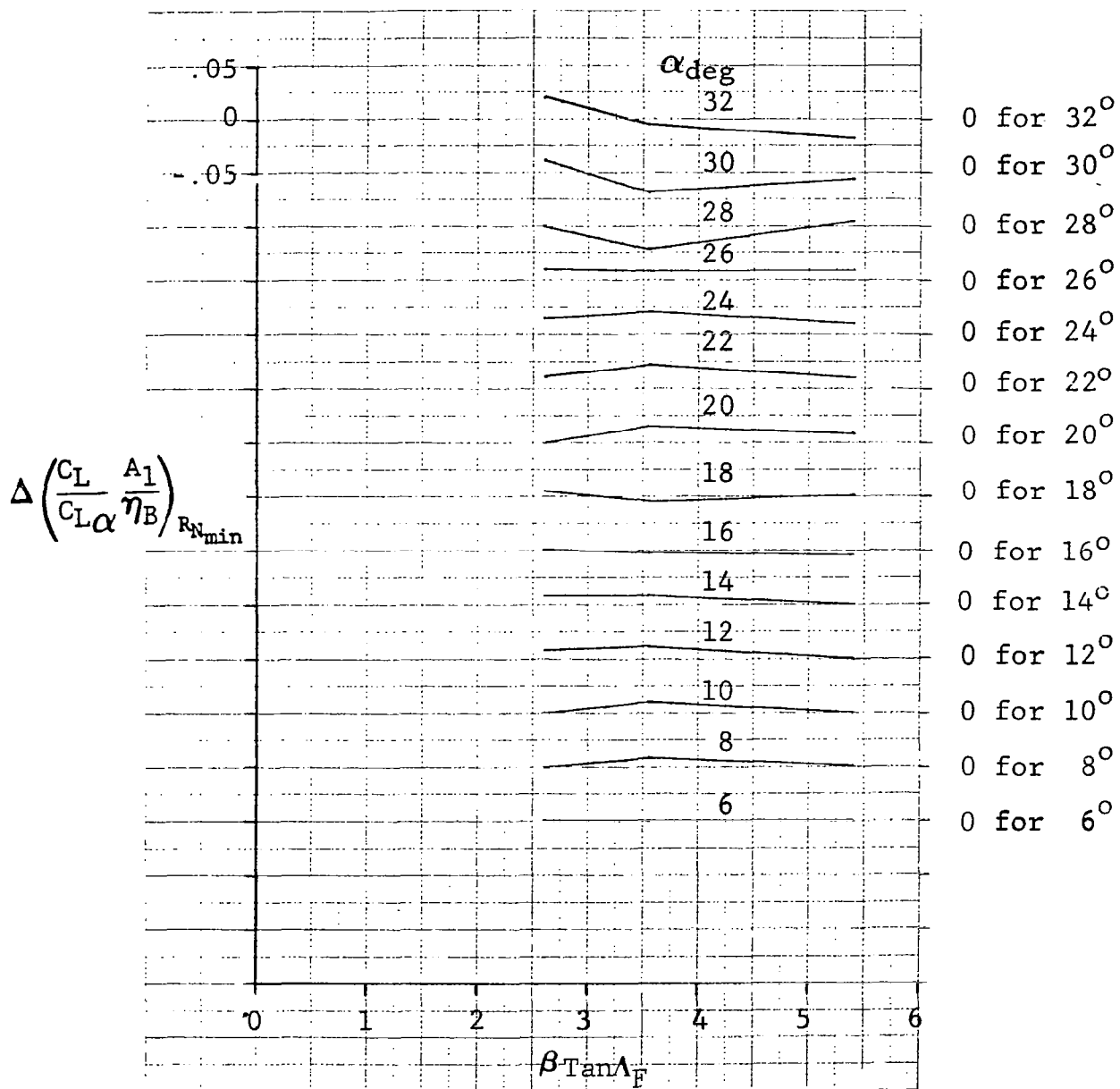at Standard Reynolds Number

Figure 203. Incremental Values of Lift Parameter for NACA 65A012 Airfoils at Minimum Reynolds Number
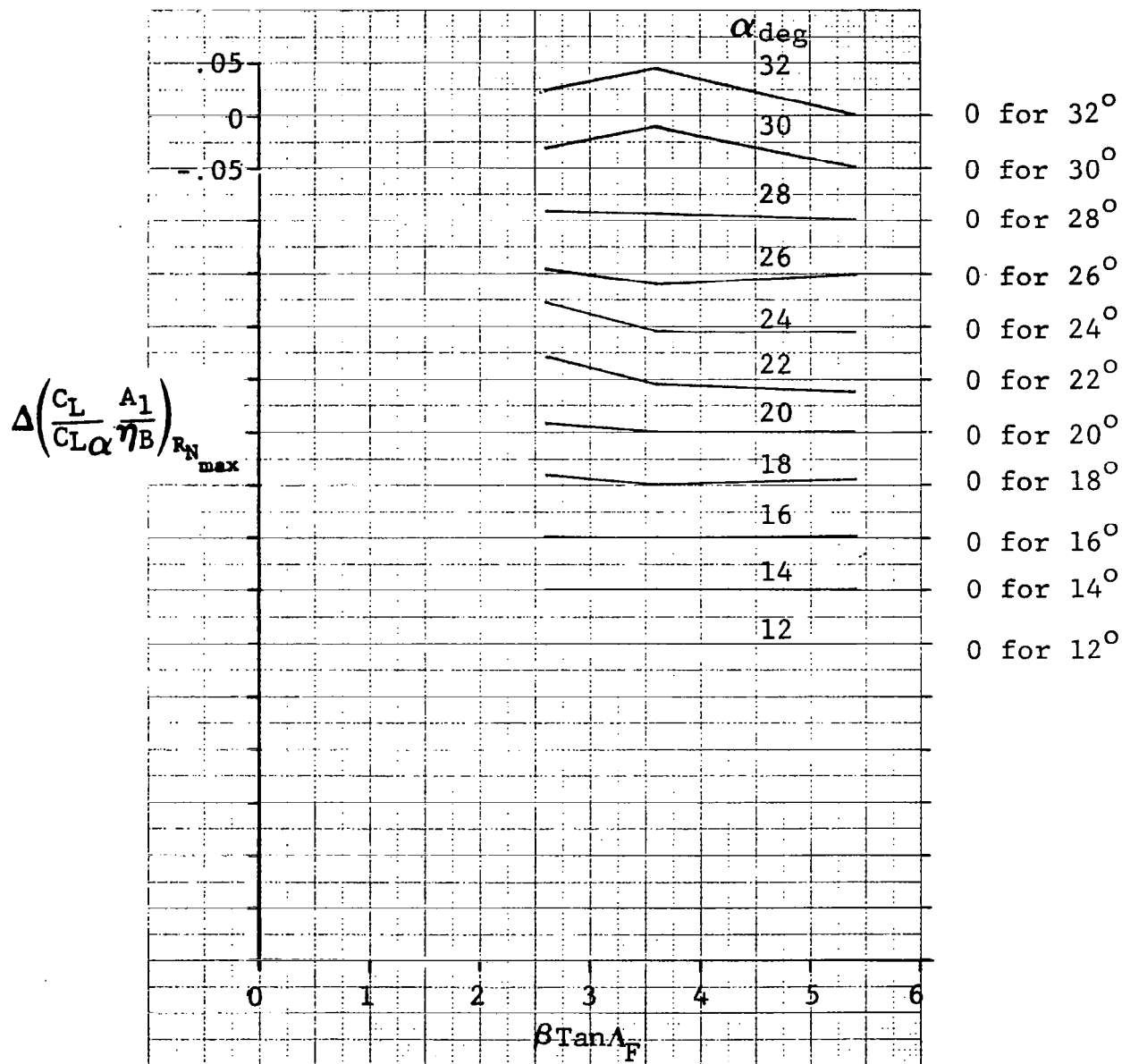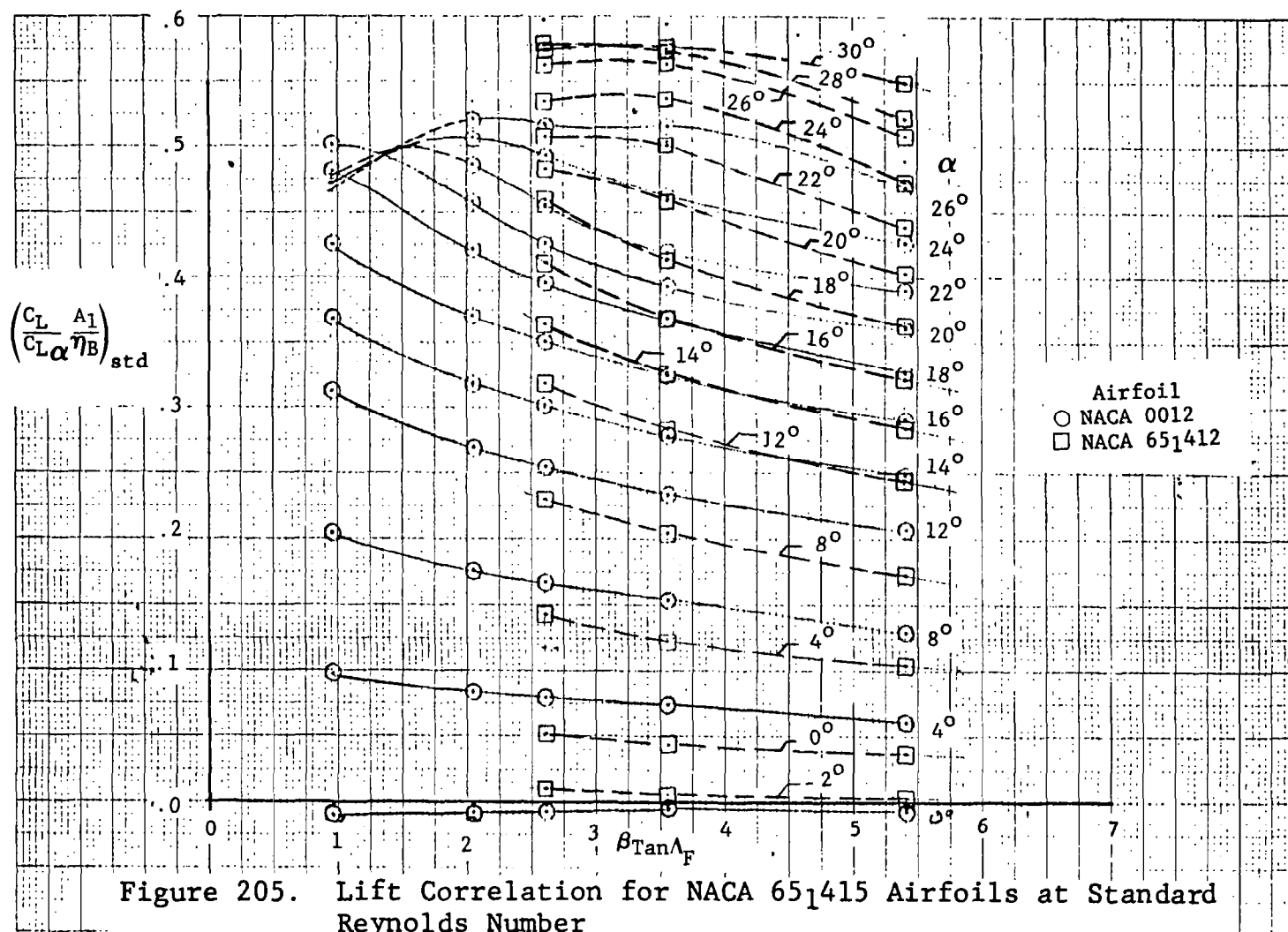
Figure 204. Incremental Values of Lift Parameter
for NACA 65A012 Airfoils at Maximum
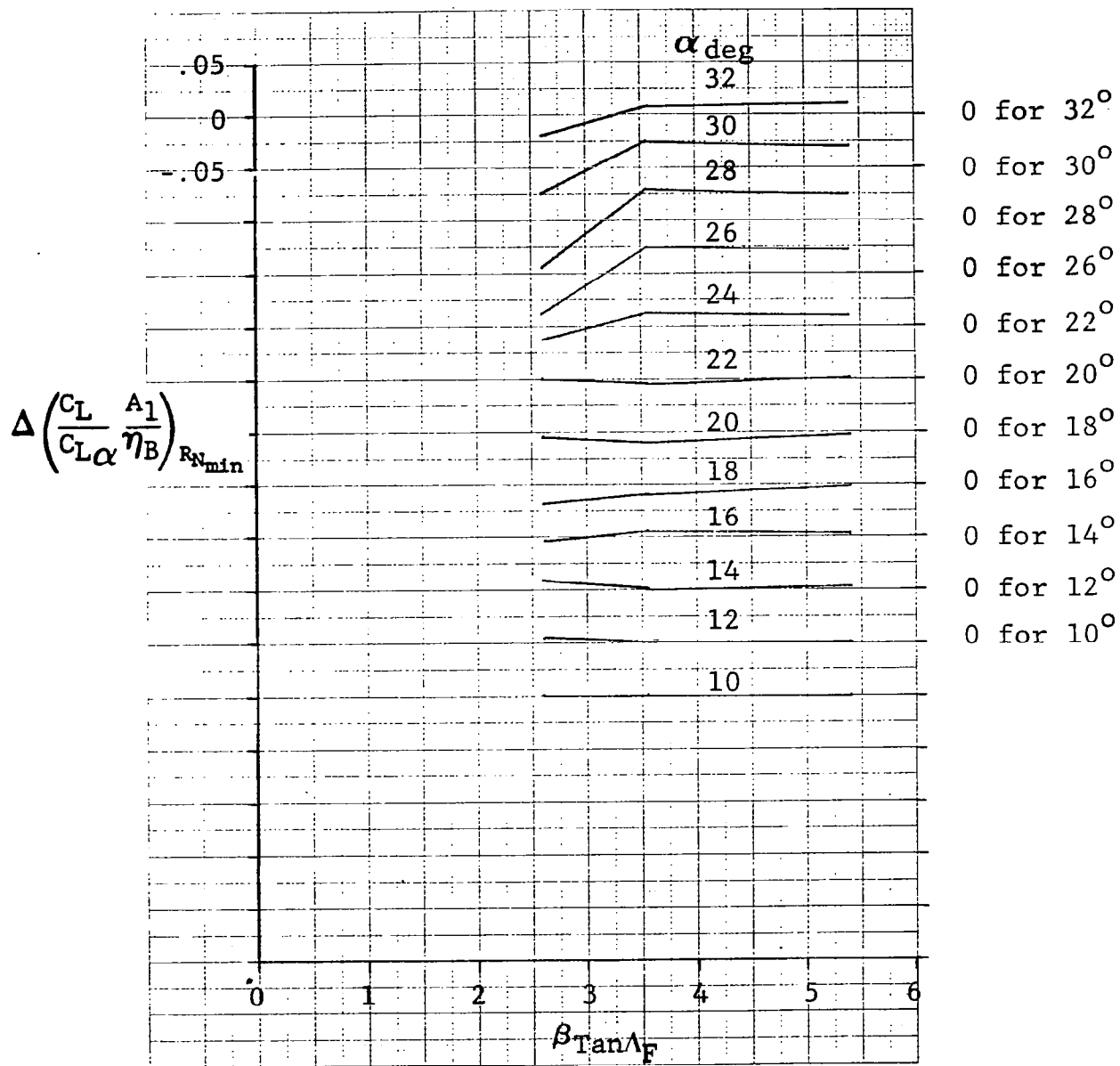Reynolds Number

$$\left(\frac{C_L}{C_{L\alpha}}\frac{A_1}{\eta_B}\right)_{std}$$

Figure 205.   Lift Correlation for NACA 65_1415 Airfoils at Standard Reynolds Number

Figure 206. Incremental Values of Lift Parameter
for NACA 65₁412 Airfoils at Minimum
Reynolds Number

Figure 207.   Incremental Values of Lift Parameter
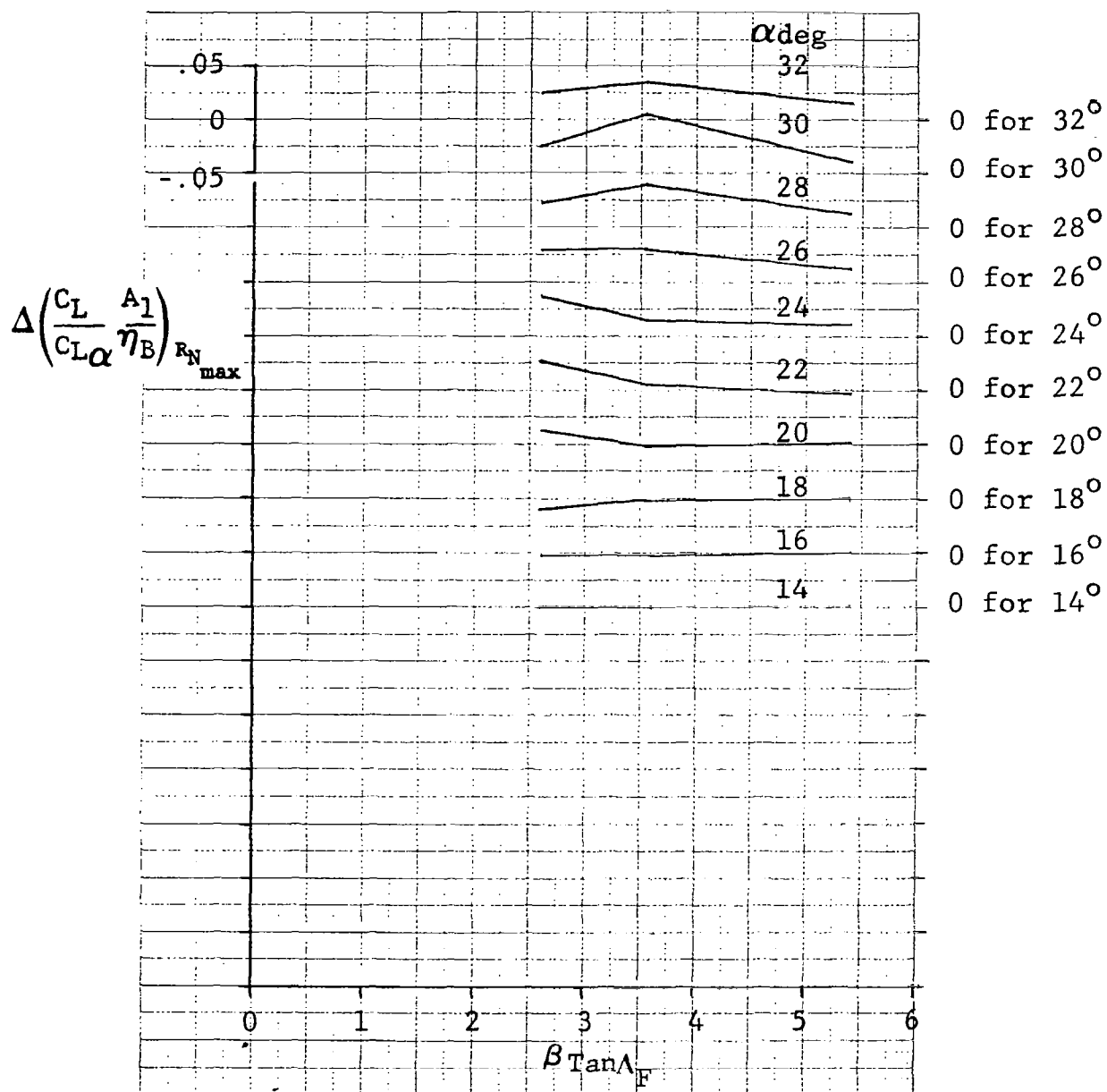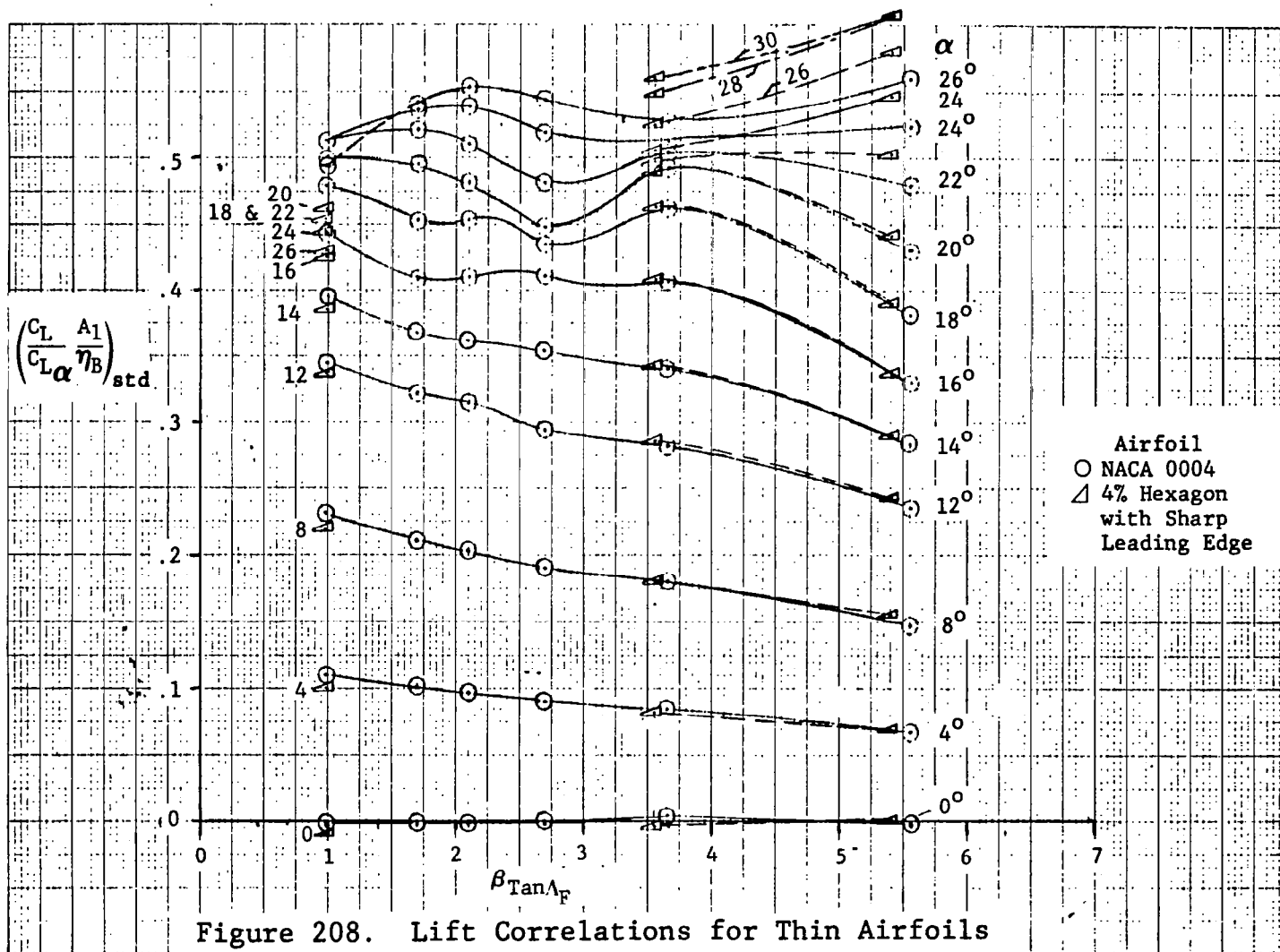for NACA 65$_1$412 Airfoils at Maximum
Reynolds Number

318

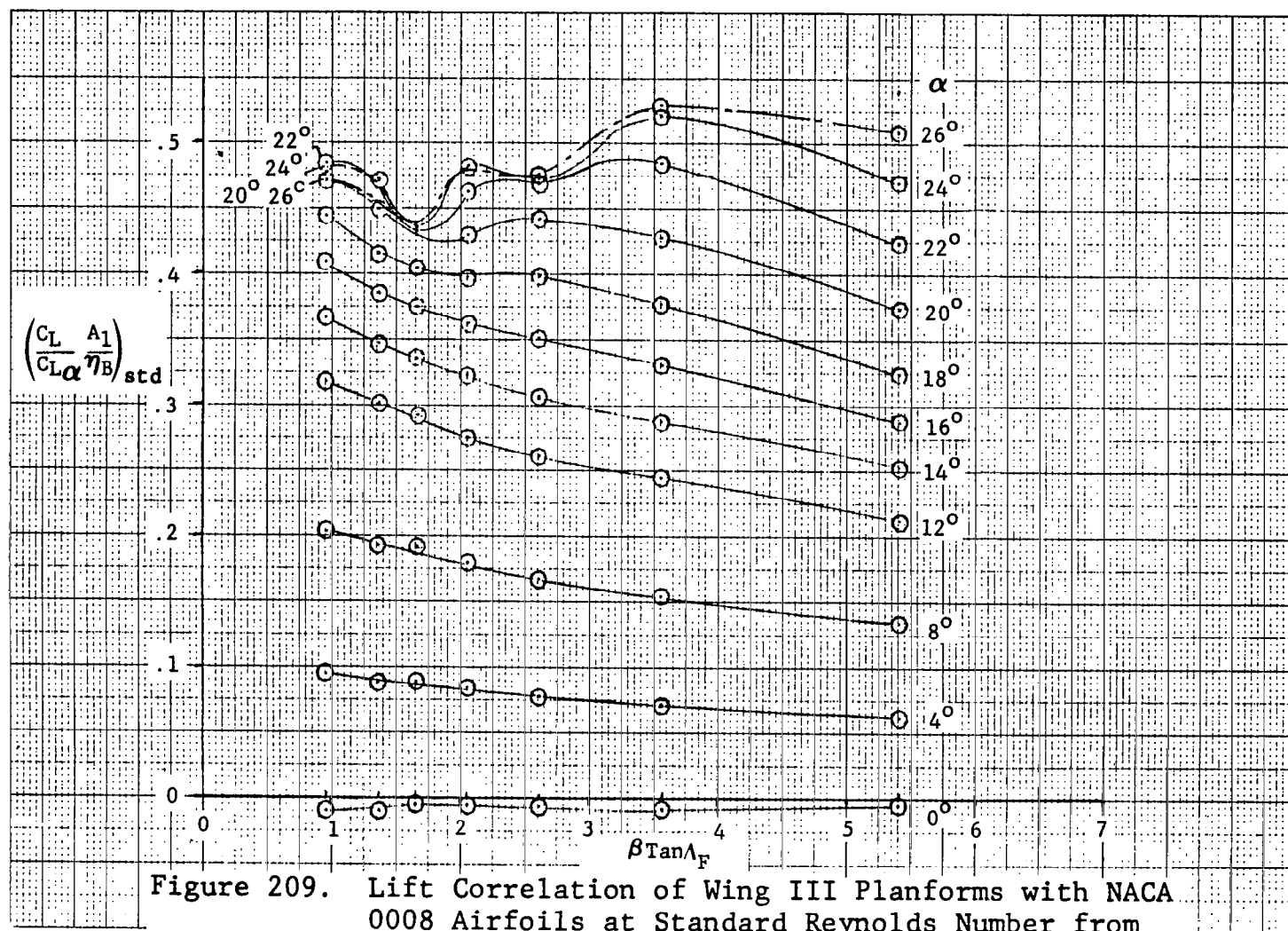Figure 208. Lift Correlations for Thin Airfoils

Figure 209. Lift Correlation of Wing III Planforms with NACA 0008 Airfoils at Standard Reynolds Number from Test ARC 12-086
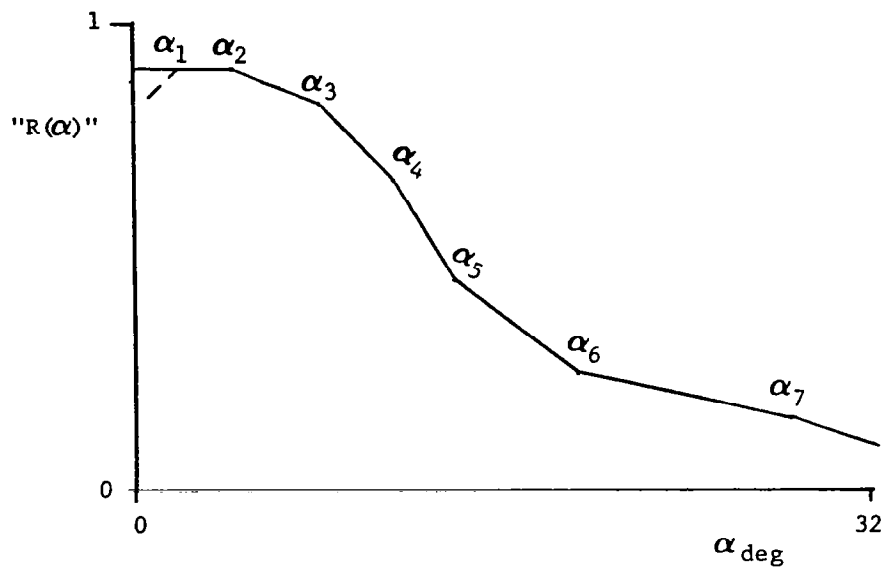
Figure 210.   Schematic of Typical Variation of Suction Ratio
With Angle of Attack Used in Revised Prediction
Method

COMPARISONS WITH TEST DATA

The only evaluation that could be made of the prediction methods described in the previous sections was to compare predictions with test data from which the methods had been derived. In the comparisons which are presented in this section, the predictions were obtained using a computer program written for a CYBER 172 computing system. The computer procedure utilizes simple linear interpolation between tabular data representations of many of the charts and graphs presented in this report. Therefore, one of the objectives of the comparisons of predictions with test data was to evaluate the accuracy of the computer procedure. A second objective was to evaluate what improvements had been achieved over the capabilities to predict the lift, drag, and pitch ing moment that had existed prior to this work.

The first set of comparisons used the "basic" prediction method applied to the 9 configurations which were presented earlier in Figures 35 through 43 of this report as representative of the evaluation of the aeromodule prediction methods. Table 17 identifies the specific figures which present these comparisons.

Table 17   Key to Comparisons Made using the
"Basic" SHIPS Prediction Method

CONFIGURATION			FIGURE NUMBER			
Λ_F	Λ_W	Airfoil	C_L vs α	C_L vs C_D	C_m vs α	C_m vs C_L
25	25	0008	211a	211b	211c	211d
45	45	0008	212a	212b	212c	212d
60	60	0008	213a	213b	213c	213d
80	25	0008	214a	214b	214c	214d
80	45	0008	215a	215b	215c	215d
80	60	0008	216a	216b	216c	216d
35	25	0008	217a	217b	217c	217d
55	45	0008	218a	218b	218c	218d
65	45	0008	219a	219b	219c	219d

Figures 211, 212 and 213 present comparisons of predictions with test data from test ARC 12-086 for the basic Wing configurations W_I, W_{III}, and W_V, respectively. The comparable comparisons with Aeromodule methods were shown in Figures 35, 36, and 37. For each of these configurations, the basic SHIPS prediction method produces much better agreement with test data than the Aeromodule methods for lift and pitching-moment variations with angle of attack and for drag variations with lift coefficient. Also shown for the SHIPS method are comparisons of predicted and test variations of pitching moment with lift coefficient. Despite the fact that some discrepancies occur in the pitching-moment curves, the general character of the variations is well represented.

Figures 214, 215 and 216 present similar comparisons for the irregular planforms consisting of Wings I, III, and V with 80 degree fillets. Corresponding comparisons with Aeromodule predictions were shown in Figures 38, 39 and 40. For these configurations the agreement of the SHIPS predictions with test data is very good for all of the characteristics and again is better than the Aeromodule methods.

Figures 217, 218, and 219 present comparisons for irregular planforms consisting of Wings I, II and III with fillet sweeps of 35, 55, and 65 degrees, respectively. Corresponding comparisons of Aeromodule predictions with test data were presented in Figures 41, 42, and 43. Again, the SHIPS prediction method produces good agreement with the test data and much better agreement than the Aeromodule method for all of the characteristics.

In general, the "basic" SHIPS prediction method produces good agreement with test data and represents a significant improvement over the Aeromodule method from which some of the components of the SHIPS method were adapted. There is one disturbing trend that should be noted in the SHIPS predictions. At the high angles of attack, there is a tendency to predict the lift coefficient slightly lower or slightly higher than the test data. These slight discrepancies are reflected in the pitching-moment variations with angle of attack and sometimes produce an exaggerated or even erroneous change in slope. This situation occurs because the stall progression function used in the lift prediction does not completely account for all of the variations

which occur due to outboard panel sweep variations. As a conse-
quence, the user should pay attention to the pitch-up/pitch-down
design guides when evaluating a specific configuration.

Ten additional comparisons of predictions with test data are
presented, some of which use only the "basic" method, some of
which use both the "basic" and the "revised" methods, and some of
which use only the "revised" method. Table 18 presents a key to
these additional comparisons with test data.

Figure 220 presents comparisons of predictions for an ir-
regular planform having a fillet sweep of 75 degrees, an outboard
panel sweep of 40 degrees, and an NACA 0008 airfoil. The outboard
panel sweep is intermediate between two of the test configura-
tions, and the basic wing planform fits this SHIPS planform family
in terms of half-chord sweep, taper ratio, and aspect ratio. The
test data show that, except for the variation of suction ratio
with angle of attack, the test data bracket the predictions.
The discrepancy for the suction-ratio curve represents one of the
compromises that had to be made during prediction method develop-
ment to achieve smooth variations of the angle-of-attack bound-
aries and slopes in the quasi-linear representation.

Figure 221 presents comparisons of prediction with test for
the irregular planform configuration 60 25.0008 using the basic
SHIPS prediction methods. The comparison for lift, suction ratio,
and drag are very good. The variations of pitching moment with
angle of attack and lift coefficient both show some discrepan-
cies. The discrepancies for the irregular planforms with rela-
tively low values of fillet sweep and outboard panel sweep
occur because the linear segment representations of
the pitching-moment variation with angle of attack requires an
additional segment which is not reflected in the suction-ratio
variation with angle of attack. The "basic" SHIPS method utilized
the angle-of-attack boundaries determined from the suction ratio
analysis, and provisions were made for use of fictitious values to
accommodate the pitching-moment curves only at low and very high
angles of attack.

Figure 222 presents comparisons of predictions made with
both the "basic" and "revised" SHIPS methods and test data from

Table 18

Key to Additional Comparisons of
Predictions Made With the SHIPS Prediction Methods

CONFIGURATION			METHOD		FIGURE NUMBERS				
Λ_F	Λ_W	AIRFOIL	B	R	C_L vs α	"R(α)" vs α	C_L vs C_D	C_m vs α	C_m vs C_L
75	45	0008	✓		220a	220b	220c	220d	220e
60	25	0008	✓		221a	221b	221c	221d	221e
65	45	0008	✓	✓	222a		222b	222c	222d
45	45	0004		✓	223a	223b	223c	223d	223e
45	45	0008	✓	✓	224a		224b	224c	224d
45	45	0012		✓	225a		225b	225c	225d
75	45	0004		✓	226a		226b	226c	226d
75	45	0012		✓	227a		227b	227c	227d
75	45	65_1412		✓	228a		228b	228c	228d
80	45	0008	✓	✓	229a	229b	229c	229d	229e

two different facilities but obtained at the same Reynolds number (26.25 million per meter). The predictions made using the "basic" method slightly undershoot the lift curve at high angles of attack which is reflected in the drag polar and pitching-moment variation with lift coefficient for the irregular planform 65 45.0008. The "revised" prediction method very accurately predicts all three characteristics. The differences between the sets of test data are representative of the magnitudes which occurred for all of the configurations which were tested in both facilities. This is a representation of the uncertainties in wind-tunnel test data historically noted for configurations tested in several facilities.

Figures 223, 224 and 225 present data comparisons with predictions for Basic wing III with NACA 0004, NACA 0008 and NACA 0012 airfoil sections, respectively. The "revised" prediction methods produce accurate representations of the test data for all three airfoil thickness ratios with the exception of the drag at low coefficients for the NACA 0004 airfoil configuration. The measured minimum drag for that configuration appeared to be unusually low at the test Mach number of 0.20, probably due to balance accuracy.

Figure 226 shows the comparisons of predictions using the "revised" prediction method with test data for the irregular planform configuration 75 45.0004. For this case, the method predicts the test data quite accurately even though the prediction was inadvertently made for Mach 0.30 and the data were obtained at M = 0.20. Note that the test minimum drag value is the same for this configuration as it was for the 45 45.0004 configuration which is further evidence that the test value for the 45 45.0004 configuration is unusually low. Of particular importance is the fact that the pitch-up at high angle of attack is accurately predicted.

Figure 227 presents comparisons of predictions with test data for irregular planform 75 45.0012 for the standard and maximum Reynolds number conditions. The revised prediction methods produce good agreement for both Reynolds number conditions and, in particular, reflect the increase in angle of attack for maximum lift coefficient and subsequent pitch-up.

The next comparison of predictions with test data is for the irregular planform consisting of Basic Wing III with 75 degree sweep fillet and having the cambered NACA 65_1412 airfoil and is presented in Figure 228. In this case the effect of camber on the lift, drag, and pitching moment curves are well predicted with the exception of a slight undershoot on the lift curve at the highest angles of attack which is reflected in the drag polar and pitching moment curves. Again the shape of the predicted pitching moment curve reflects the pitch-up characteristic which occurs in the test data.

The last comparisons between predictions and test data presented in Figure 229 use both the "basic" and "revised" prediction methods and are for the irregular planform consisting of Wing III with the 80 degree fillet having the NACA 0008 airfoil. These comparisons show that the "revised" method more accurately predicts the lift curve than does the "basic" method. This improvement is also shown to correct an erroneous occurrence in the pitching-moment variation with lift coefficient in which the "basic" method shows a pitch-down whereas the "revised" method accurately predicts a pitch-up. In retrospect it appears that the simplified representation of the lift curve in the "basic" prediction method using a single curve for the stall progression function should be modified to better account for the effects of outer panel planform effects. The "revised" method is limited in the scope of planforms to which it can be applied, but produces very accurate results and is more applicable when predicting full-scale conditions of airfoils having higher thickness ratios.

The fact that the test results obtained in different facilities are somewhat different reflects the fact that even at low speed there are still uncertainties inherent in the available test techniques.
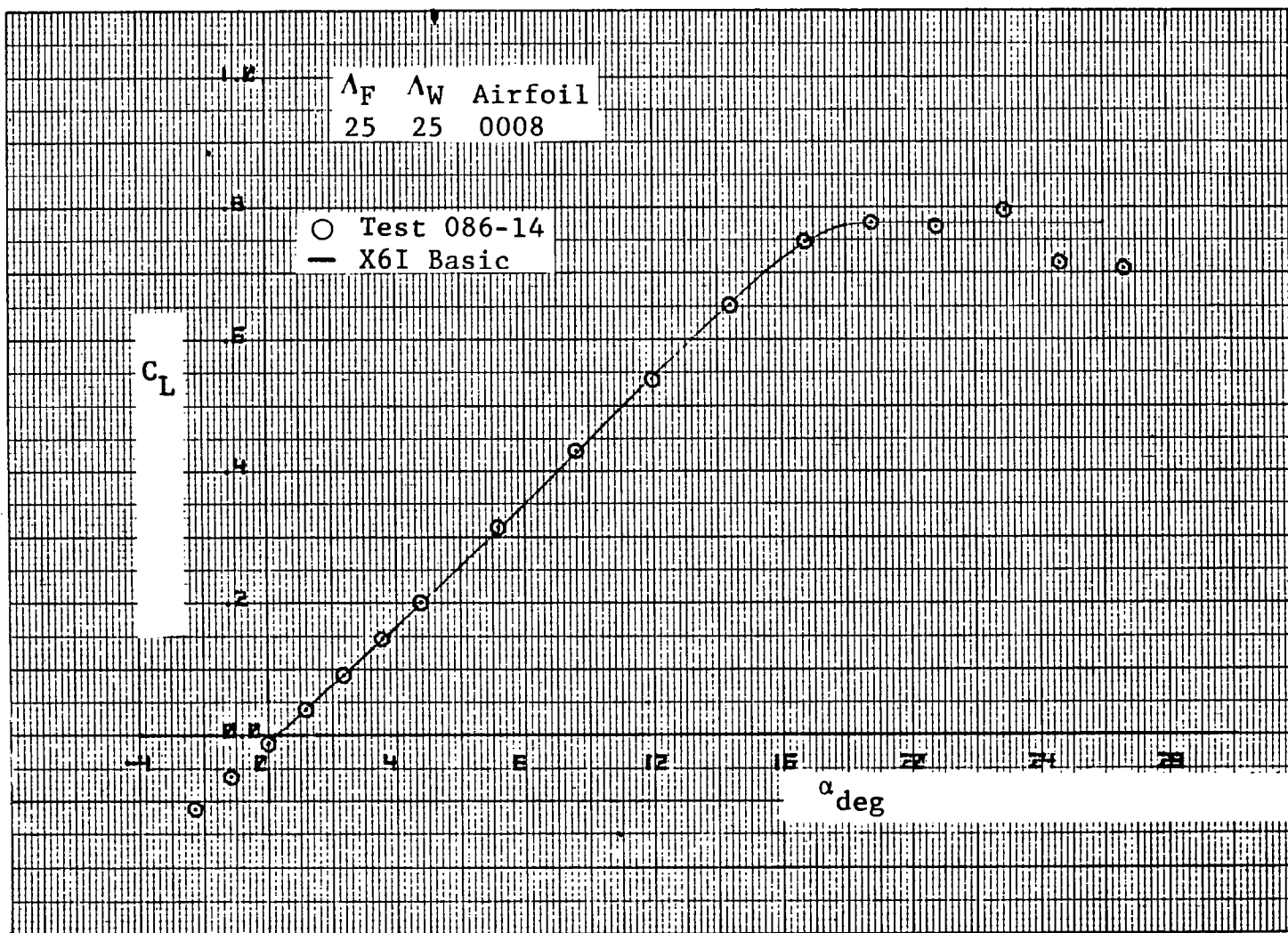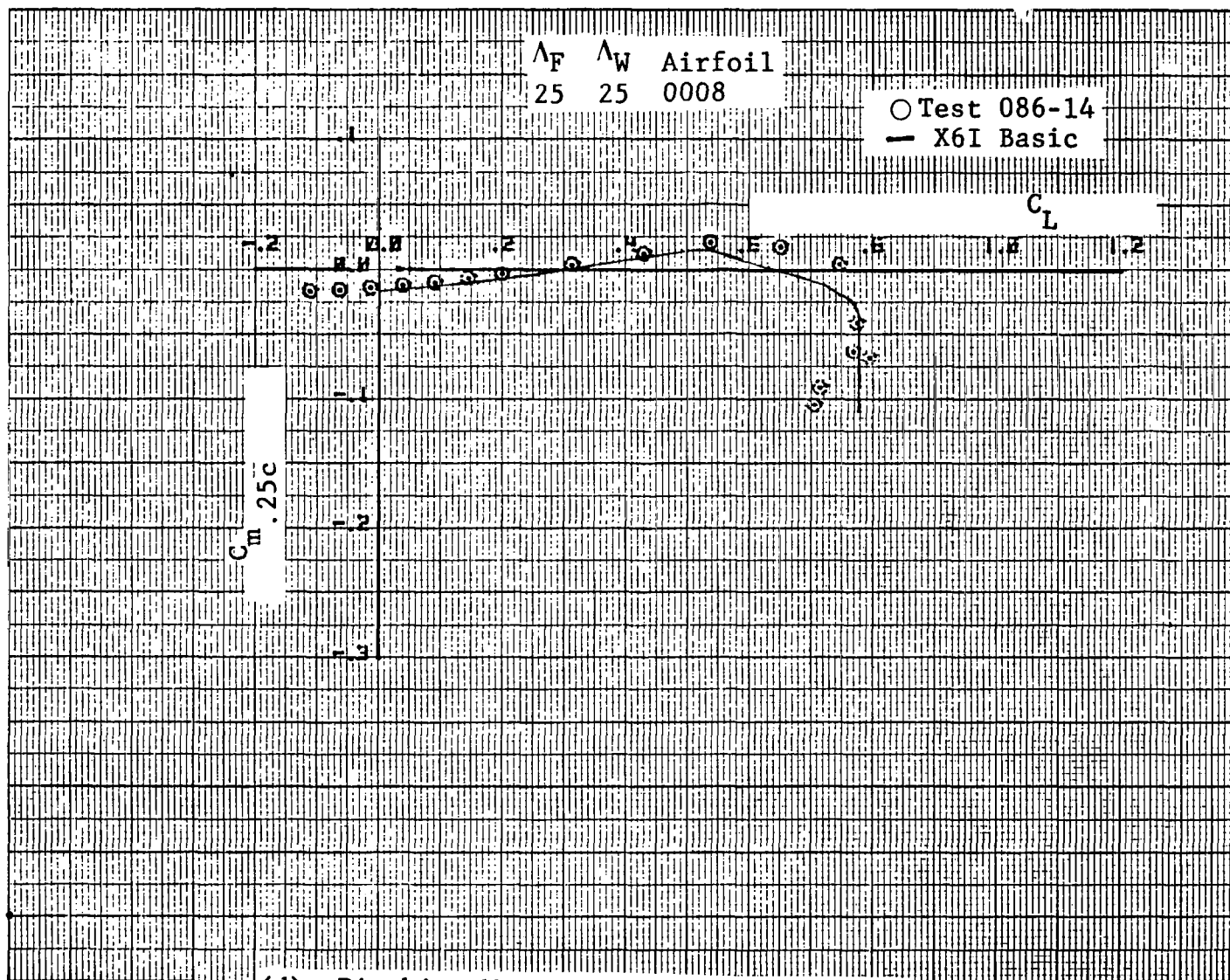
(a) Lift Curve
Figure 211. Comparisons Between Basic SHIPS Prediction and Test
for Basic Wing I
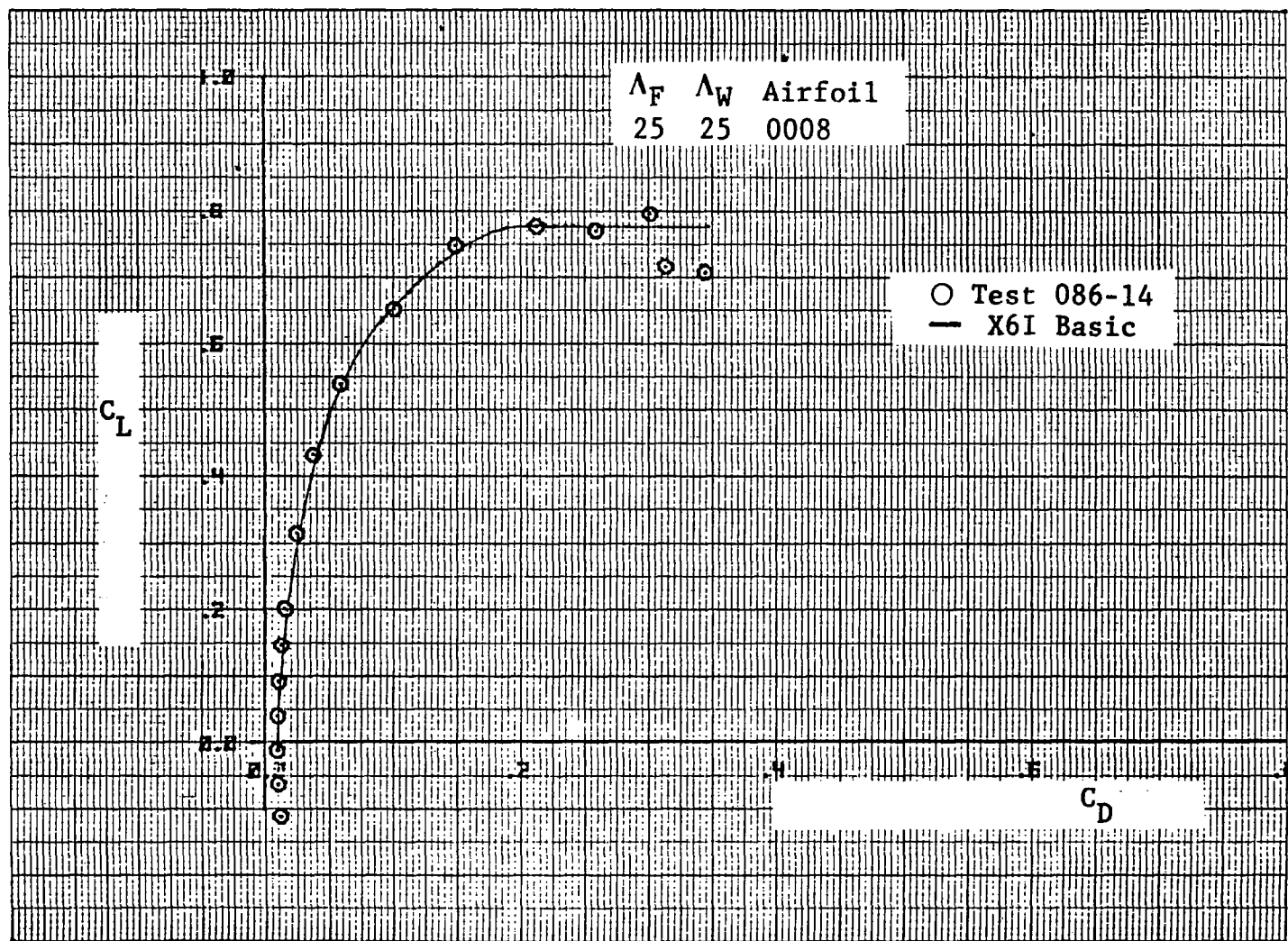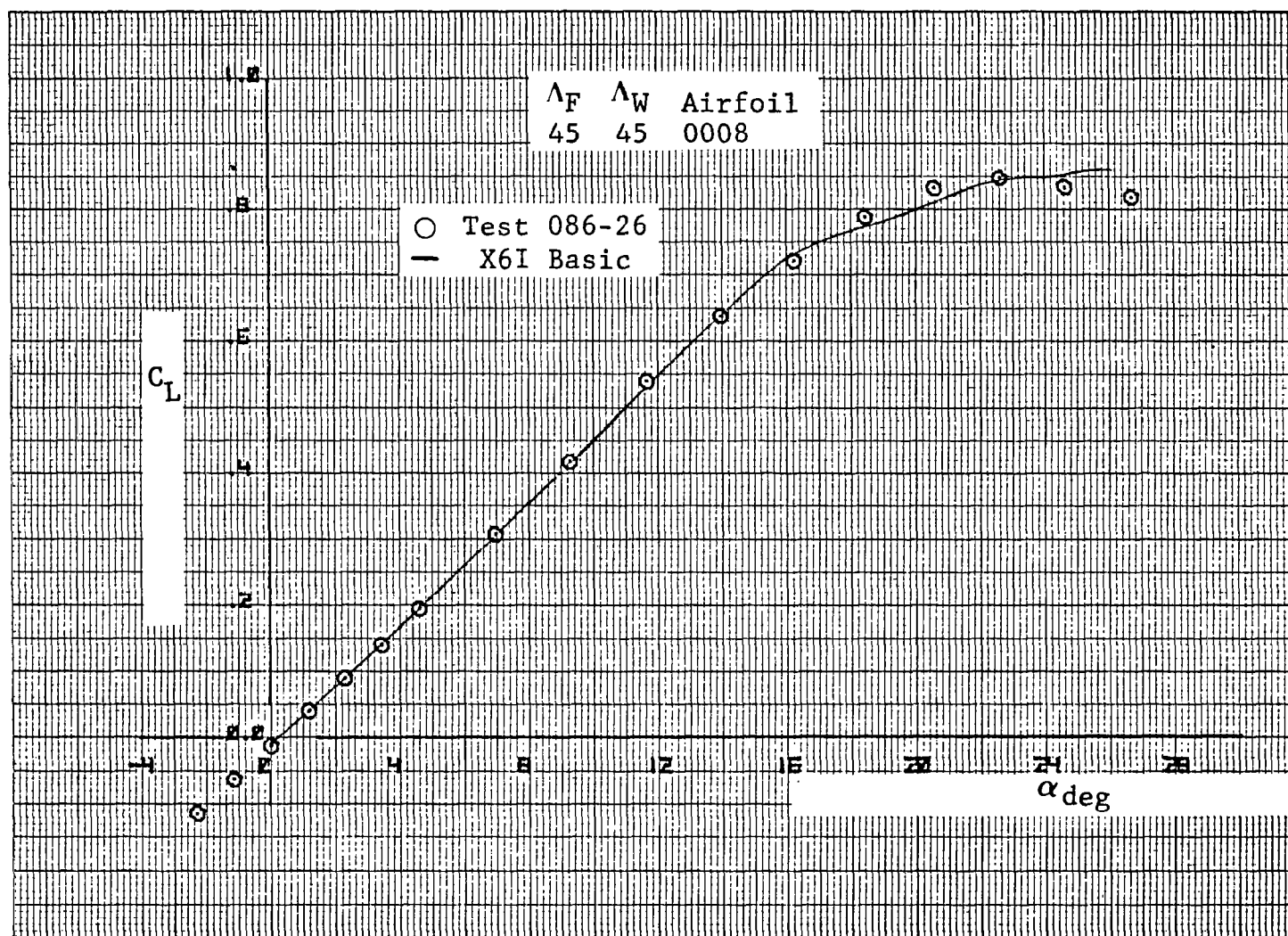
(b) Drag Polar
Figure 211. Continued
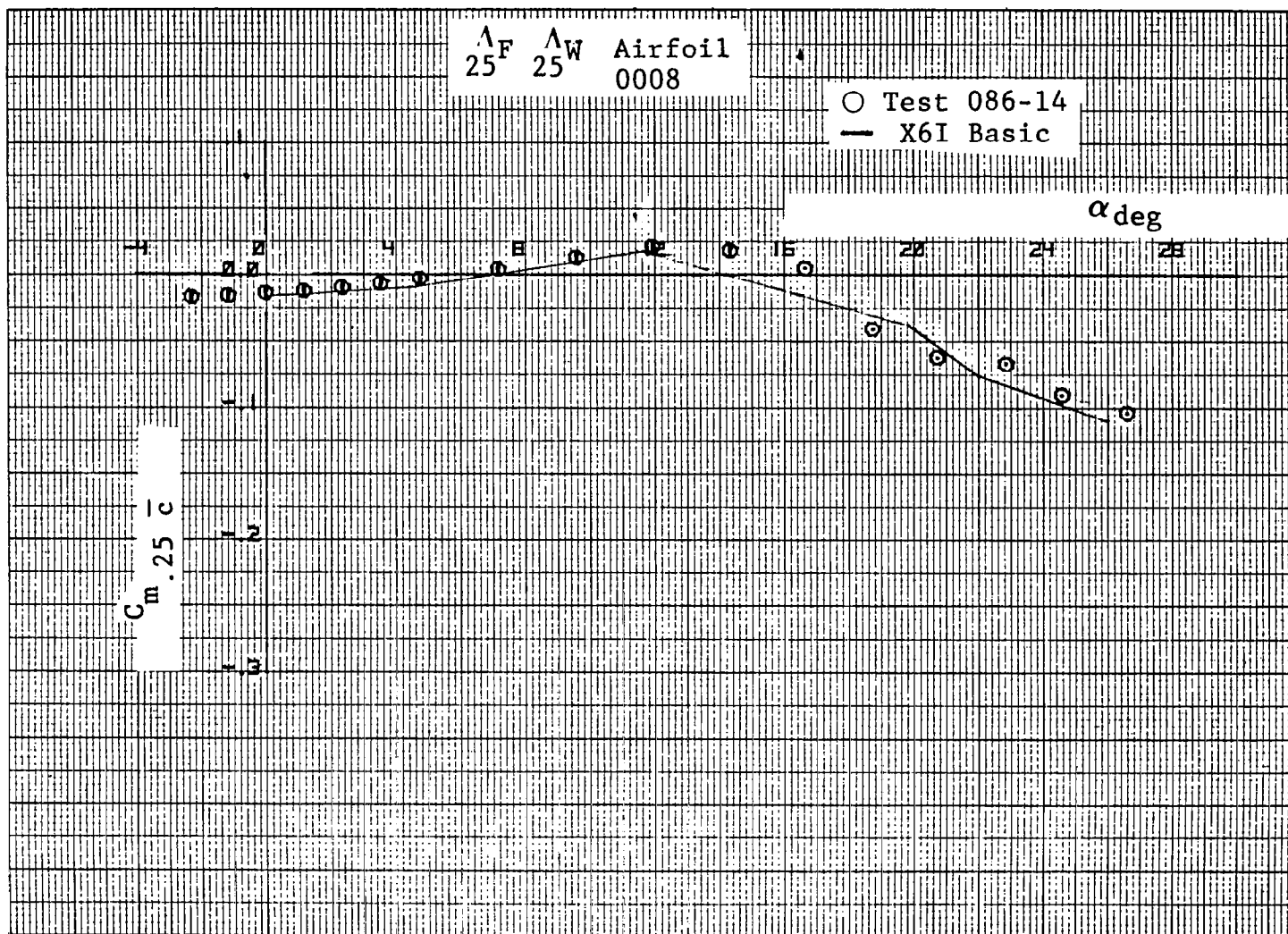
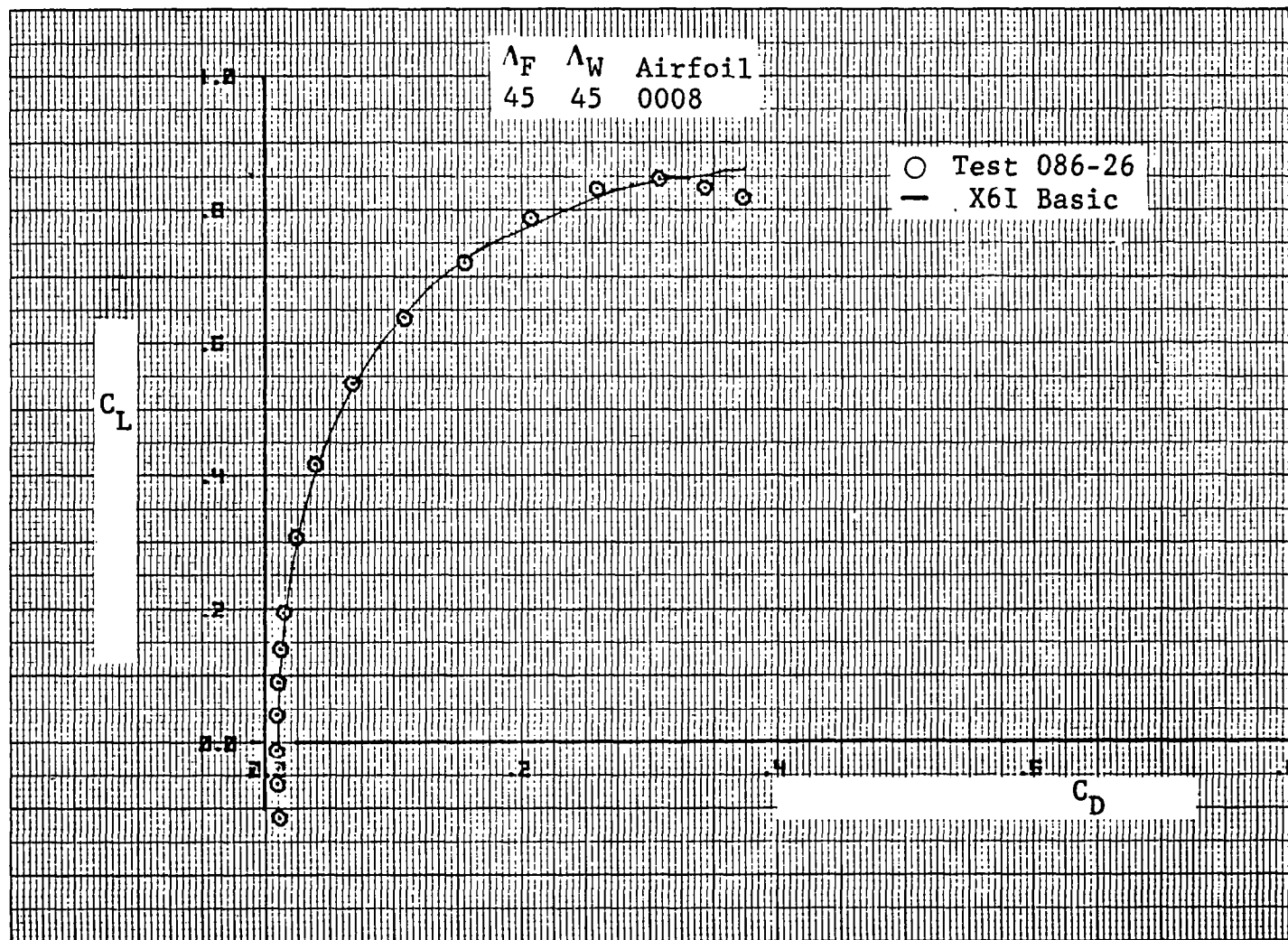(c)   Pitching-Moment Variation with Angle of Attack
Figure 211.   Continued

(d)   Pitching-Moment Variation with Lift
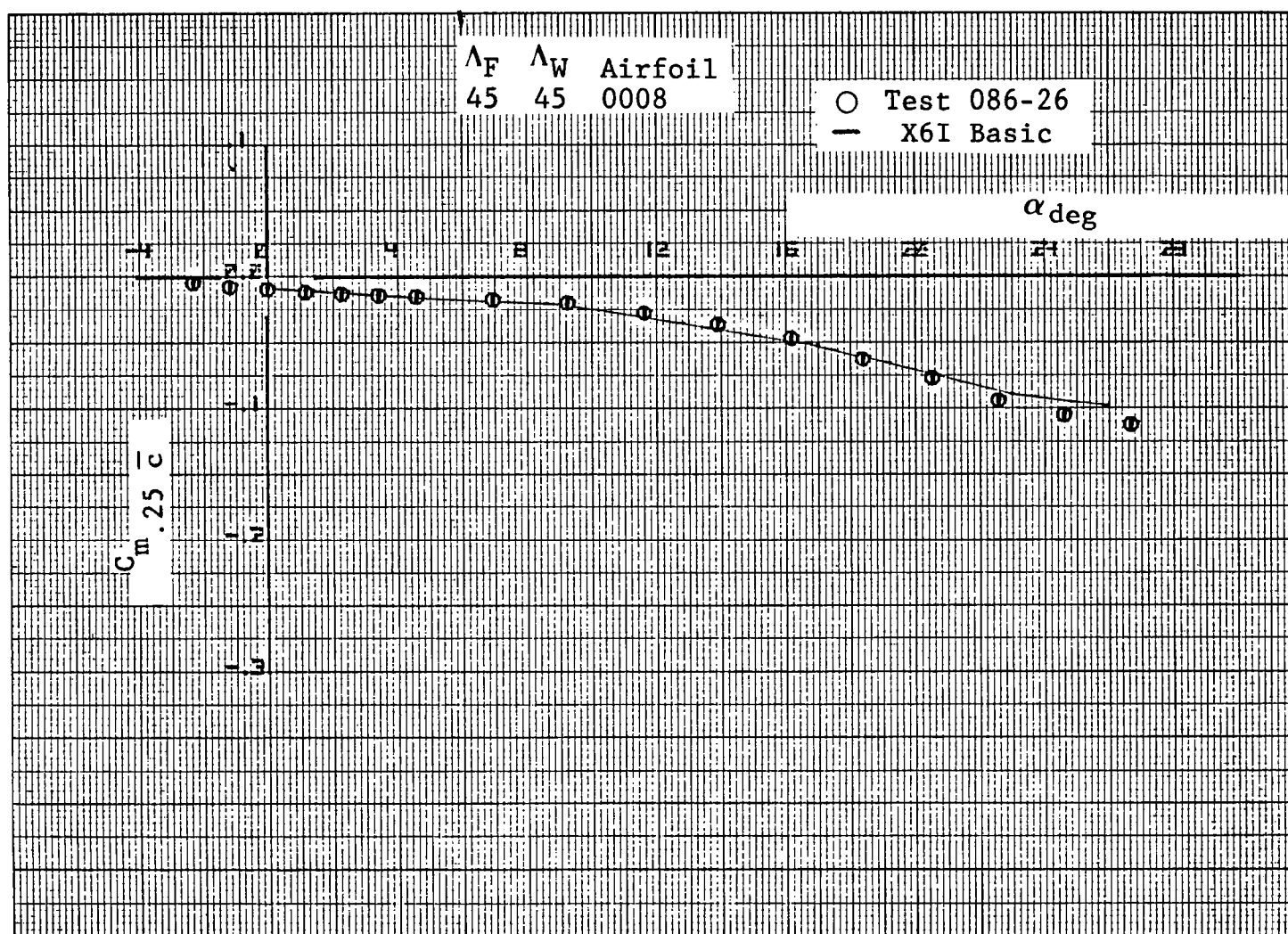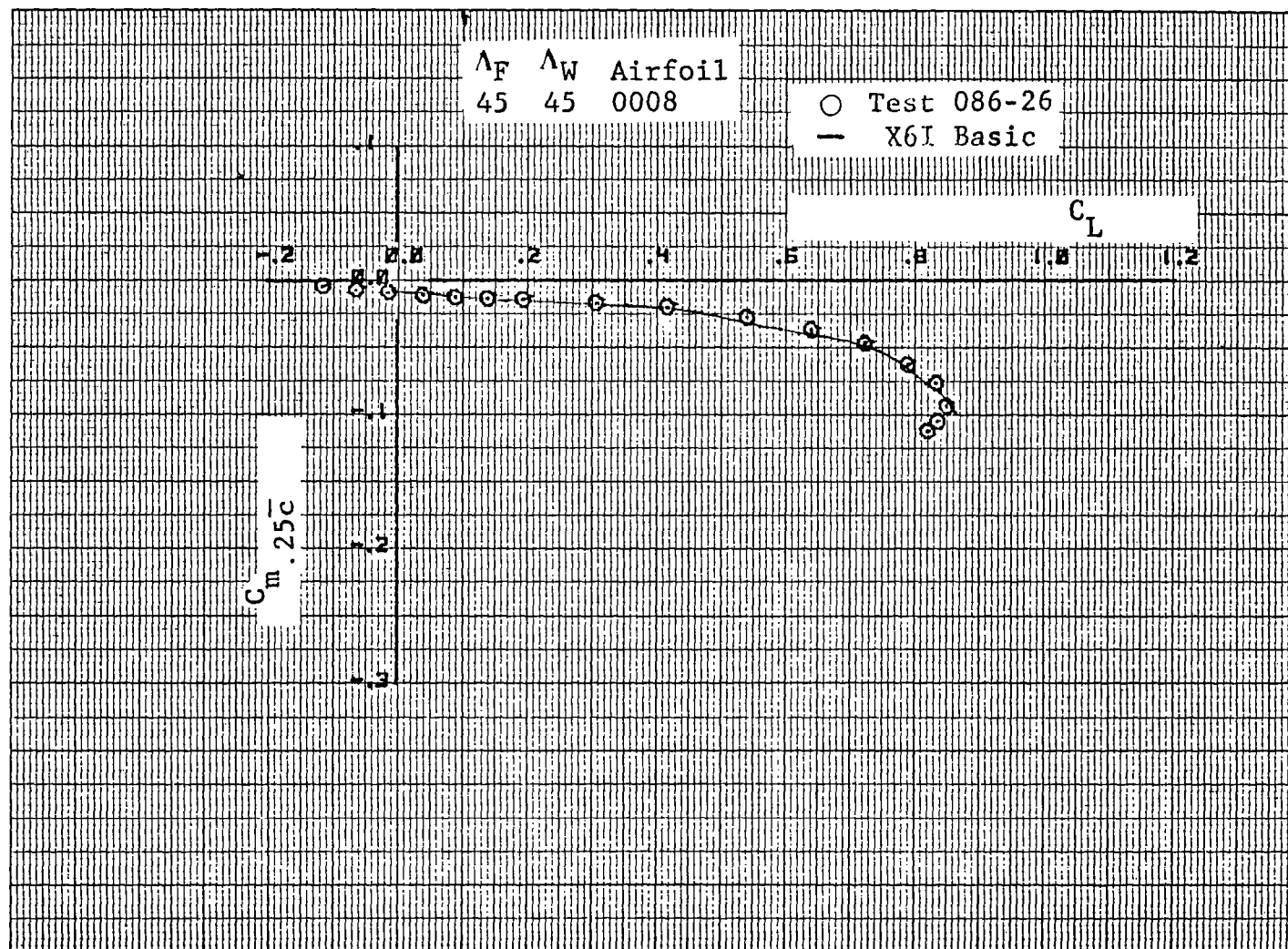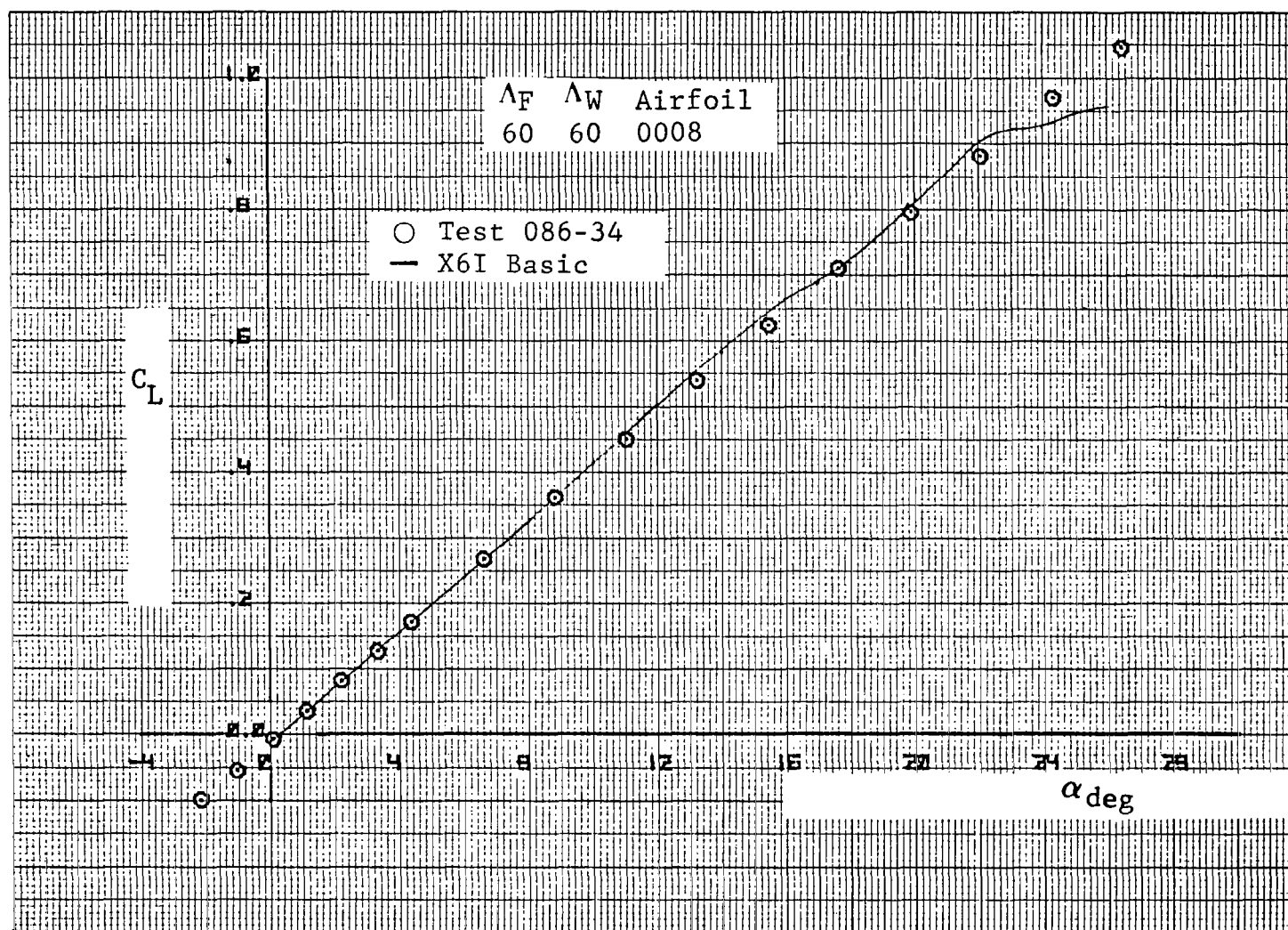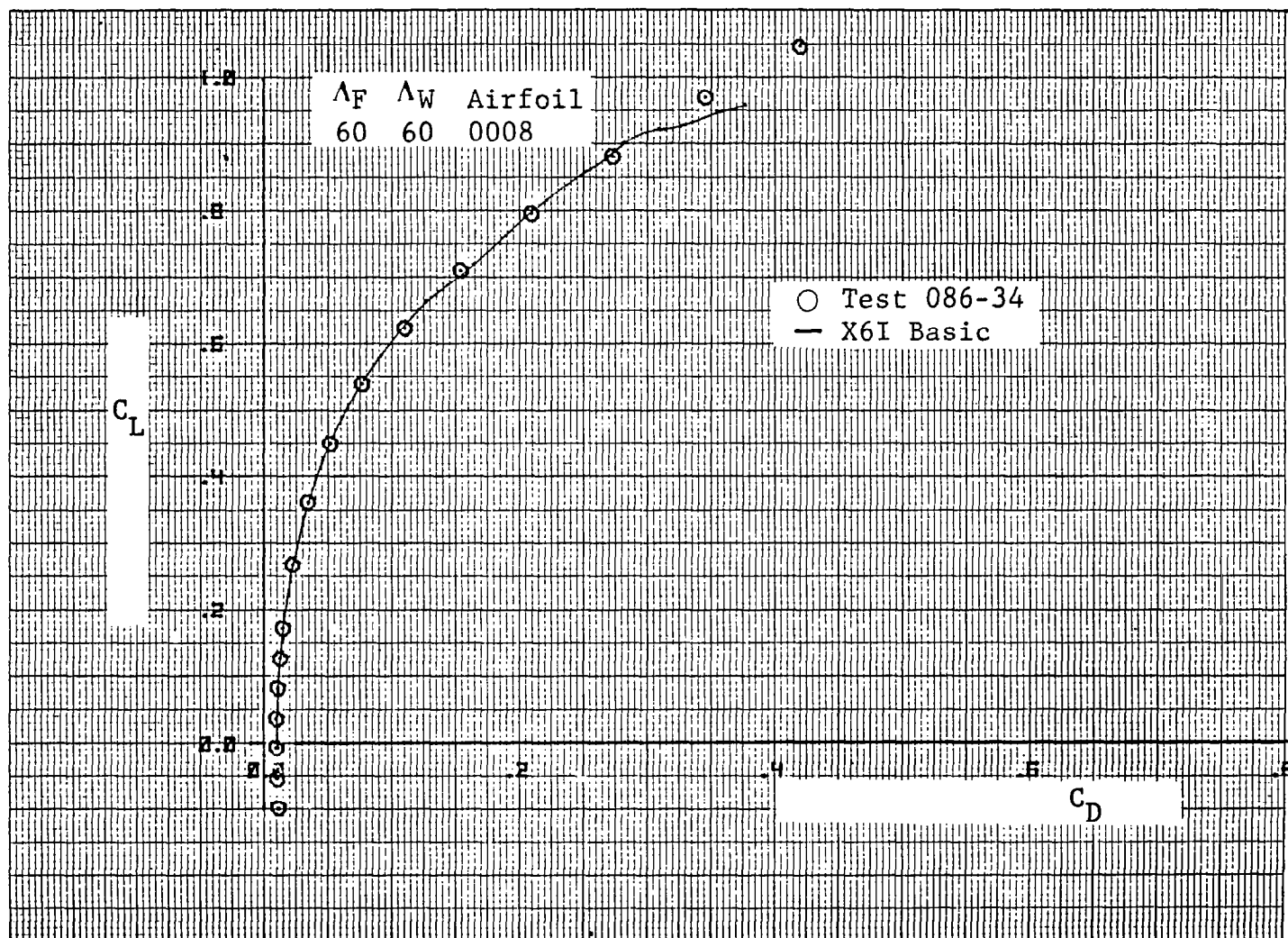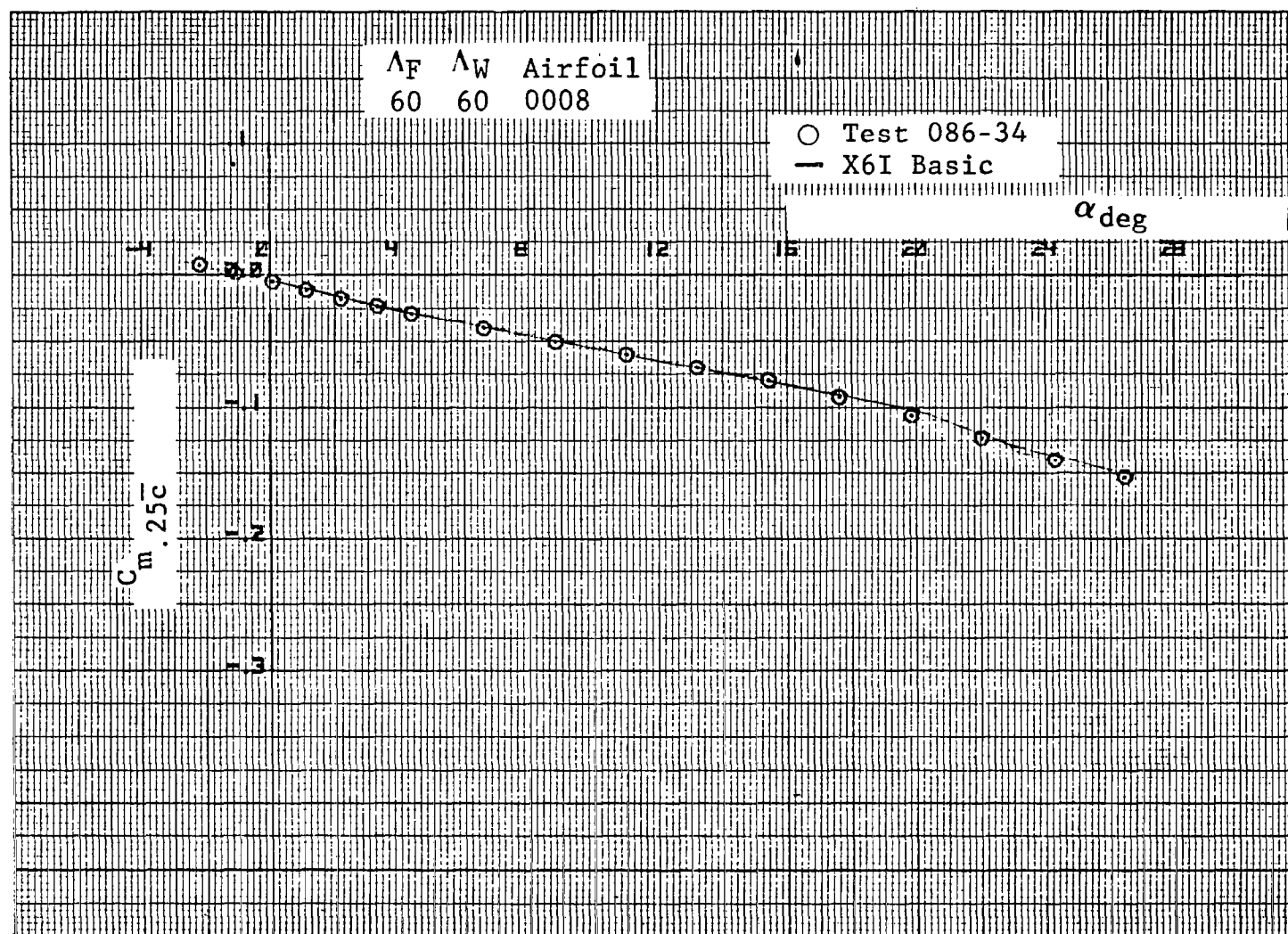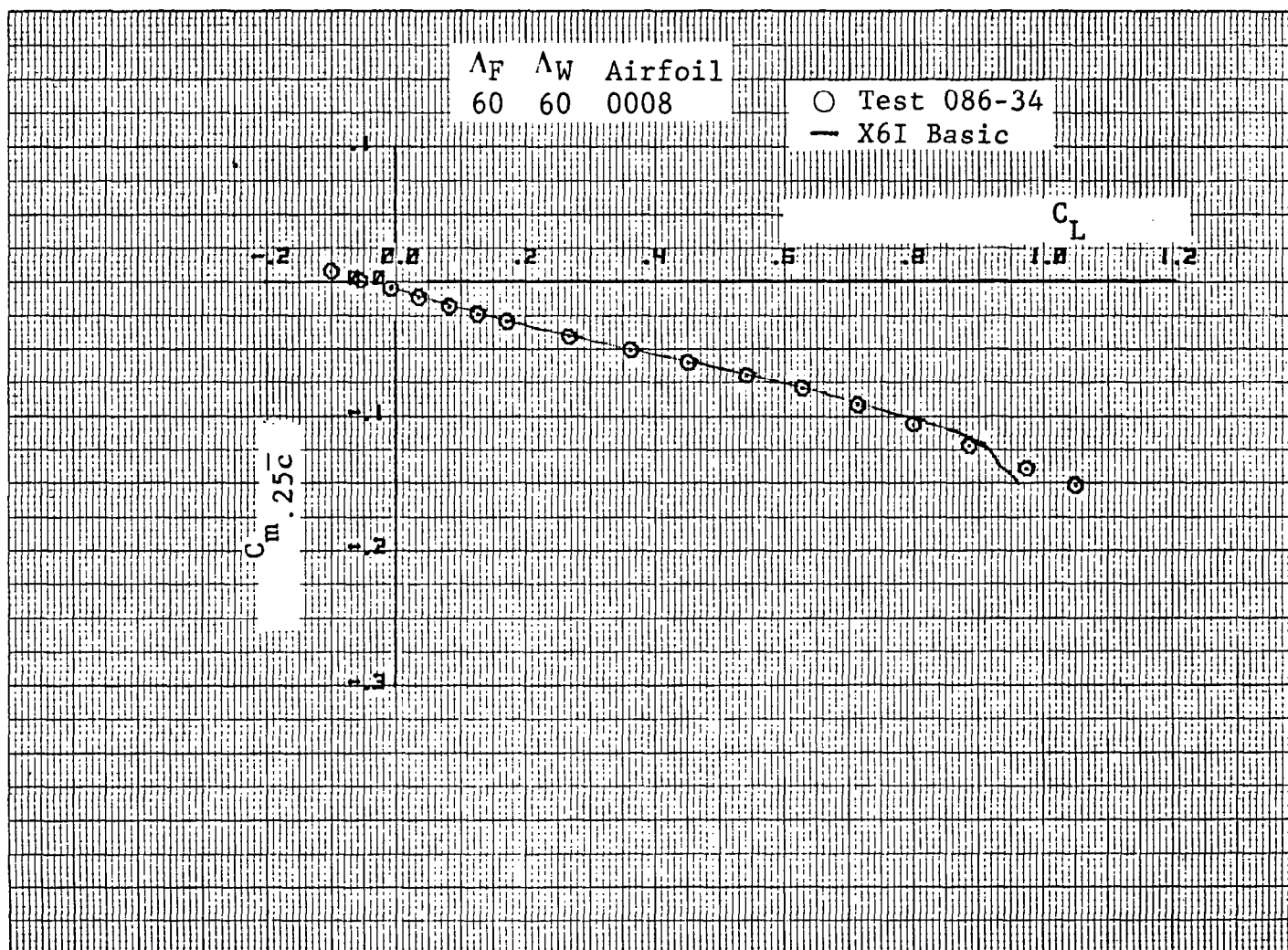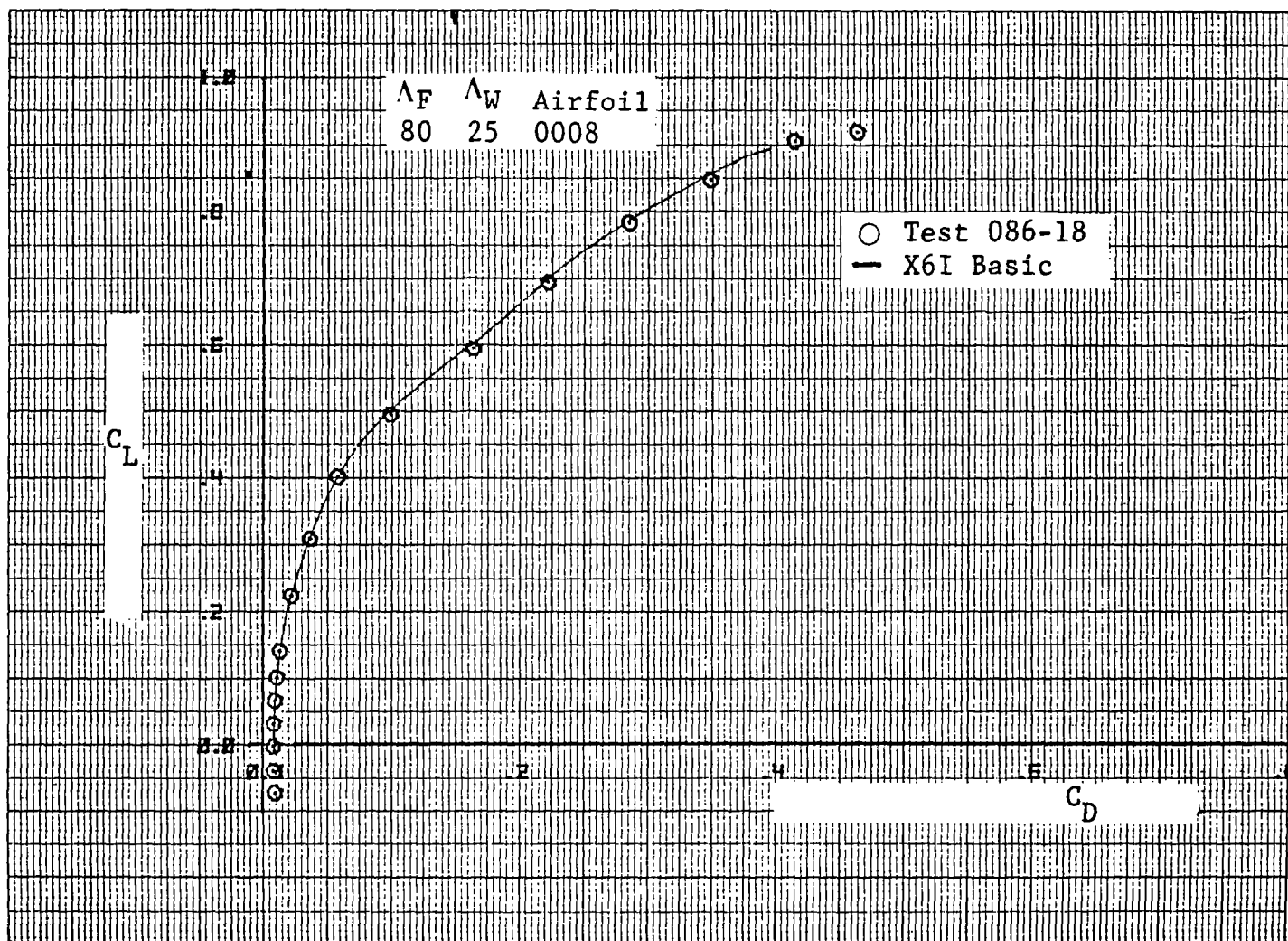
Figure 211.   Concluded.

	Λ_F	Λ_W	Airfoil
	45	45	0008

○ Test 086-26
— X6I Basic

C_L

α_{deg}

(a) Lift Curve

Figure 212. Comparisons Between Basic SHIPS Prediction and Test
for Basic Wing III

(b) Drag Polar

Figure 212. Continued

(c)   Pitching-Moment Variation with Angle of Attack

Figure 212.   Continued

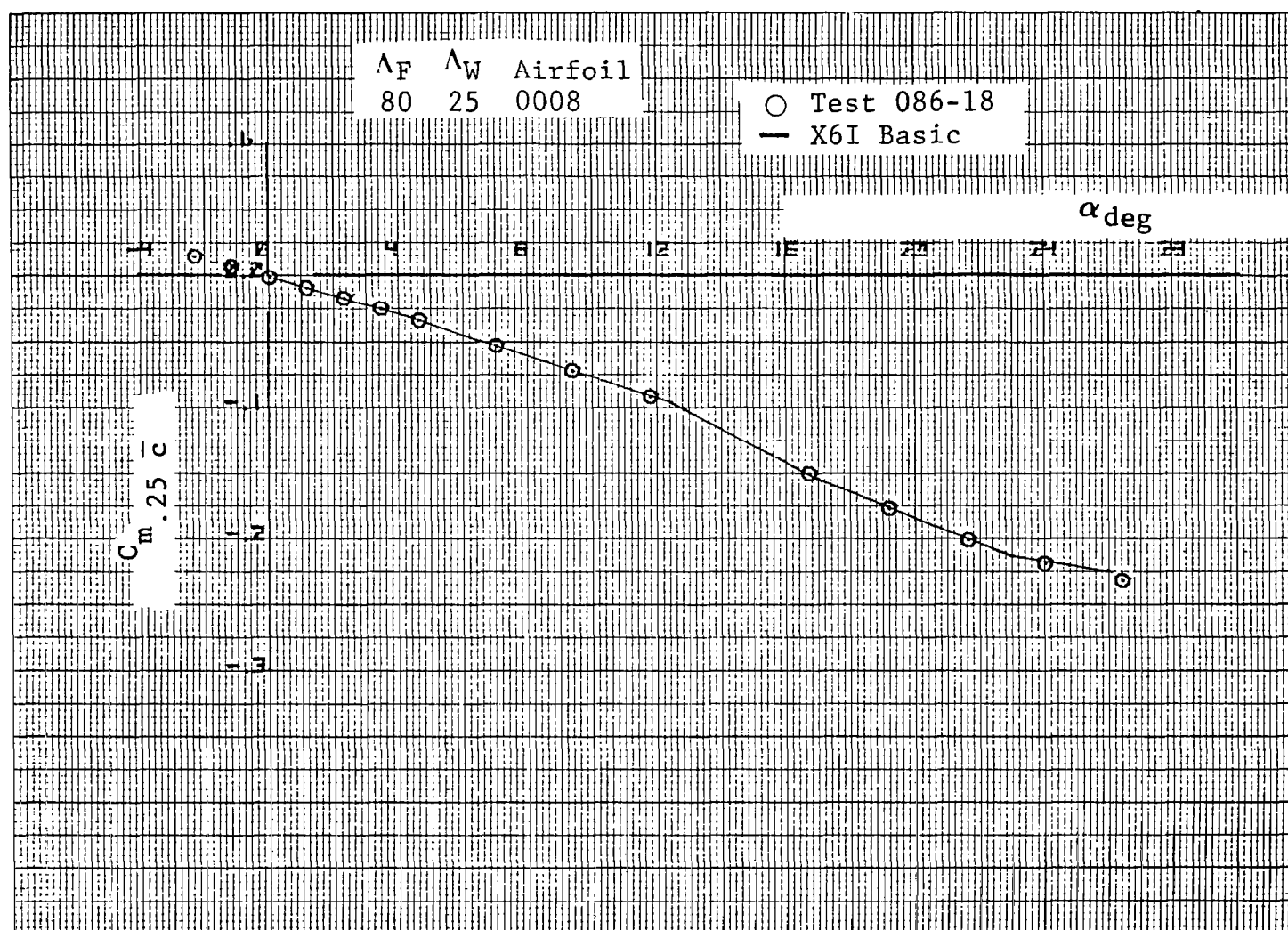(d) Pitching-Moment Variation with Lift

Figure 212. Concluded.

(a) Lift Curve

Figure 213. Comparisons Between Basic SHIPS Prediction and Test
for Basic Wing V

(b)   Drag Polar

Figure 213.   Continued

(c) Pitching-Moment Variation with Angle of Attack

Figure 213. Continued.

(d) Pitching-Moment Variation with Lift

Figure 213. Concluded.
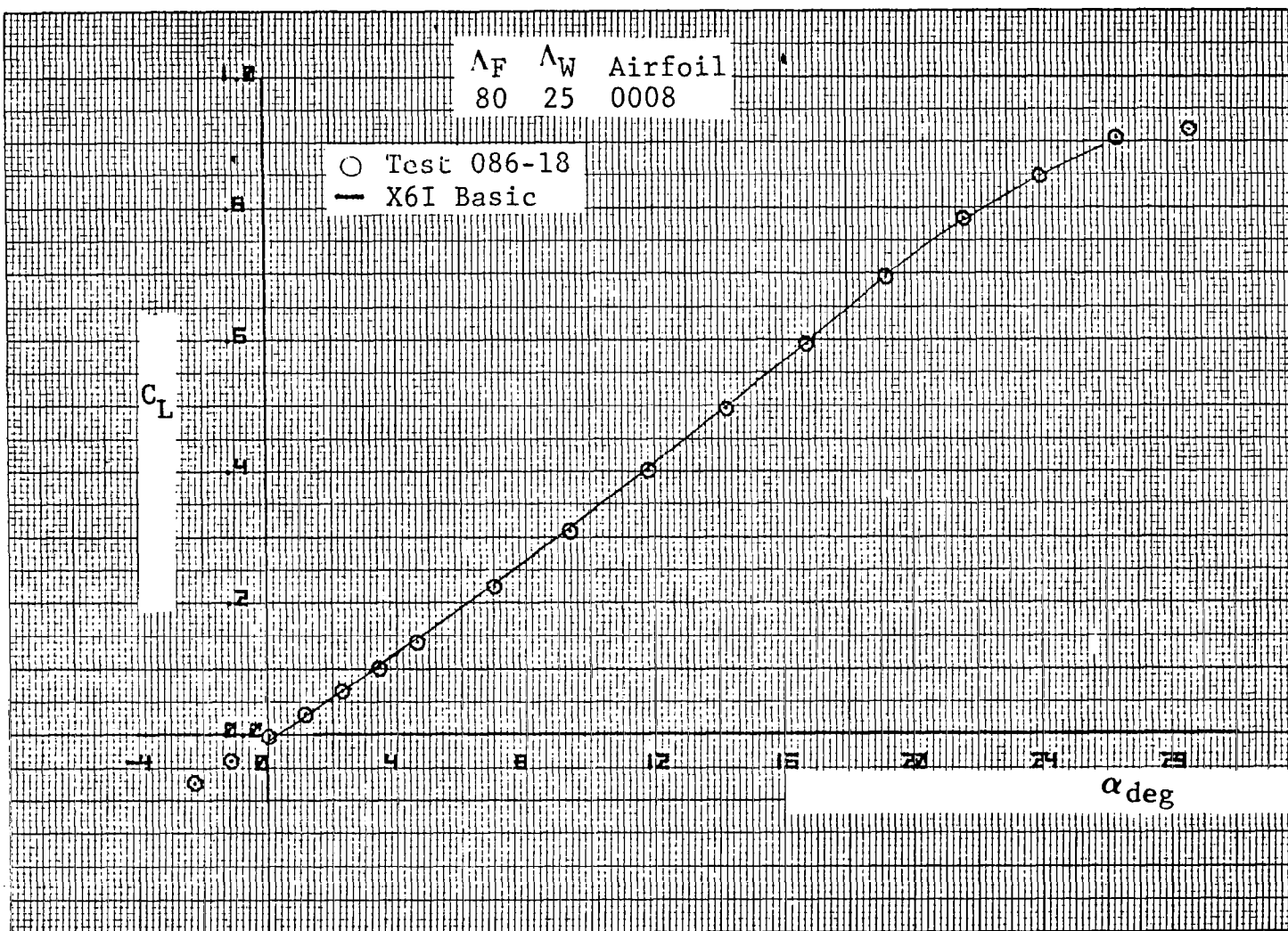
(a) Lift Curve

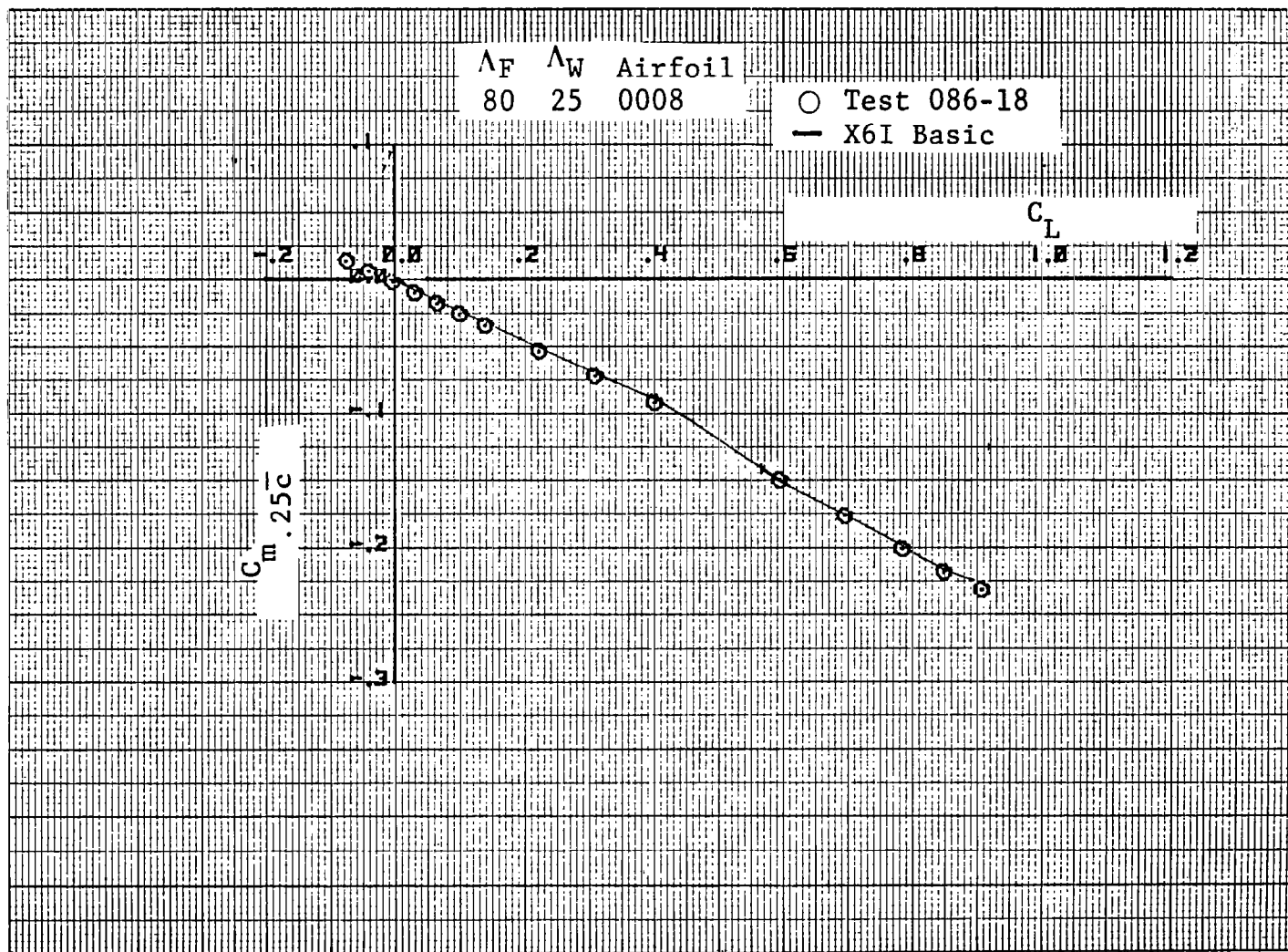Figure 214. Comparisons Between Basic SHIPS Prediction and Test
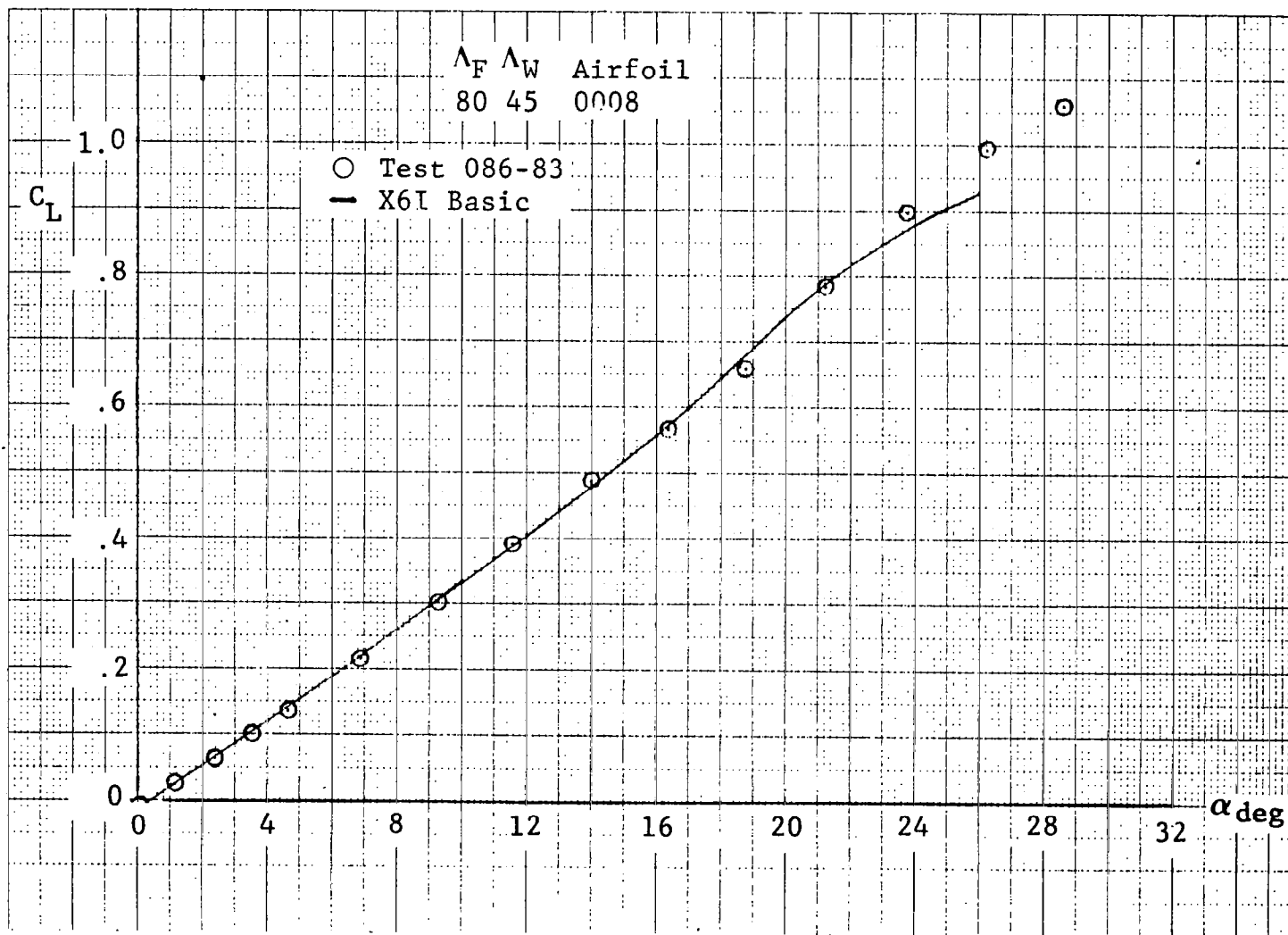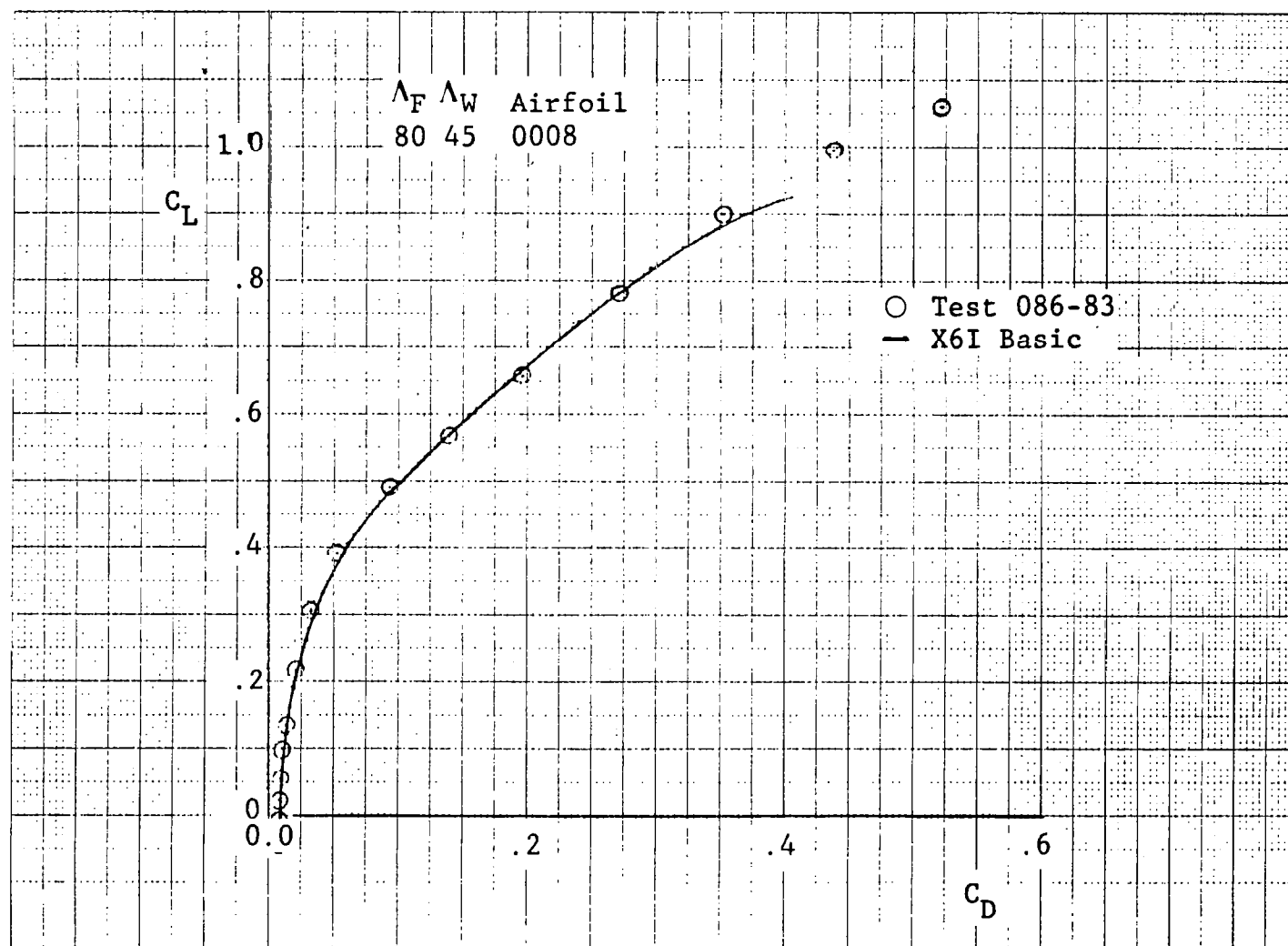Wing I with 80° Fillet

(b) Drag Polar

Figure 214. Continued

342

(c)   Pitching-Moment Variation with Angle of Attack

Figure 214.   Continued.

(d) Pitching-Moment Variation with Lift
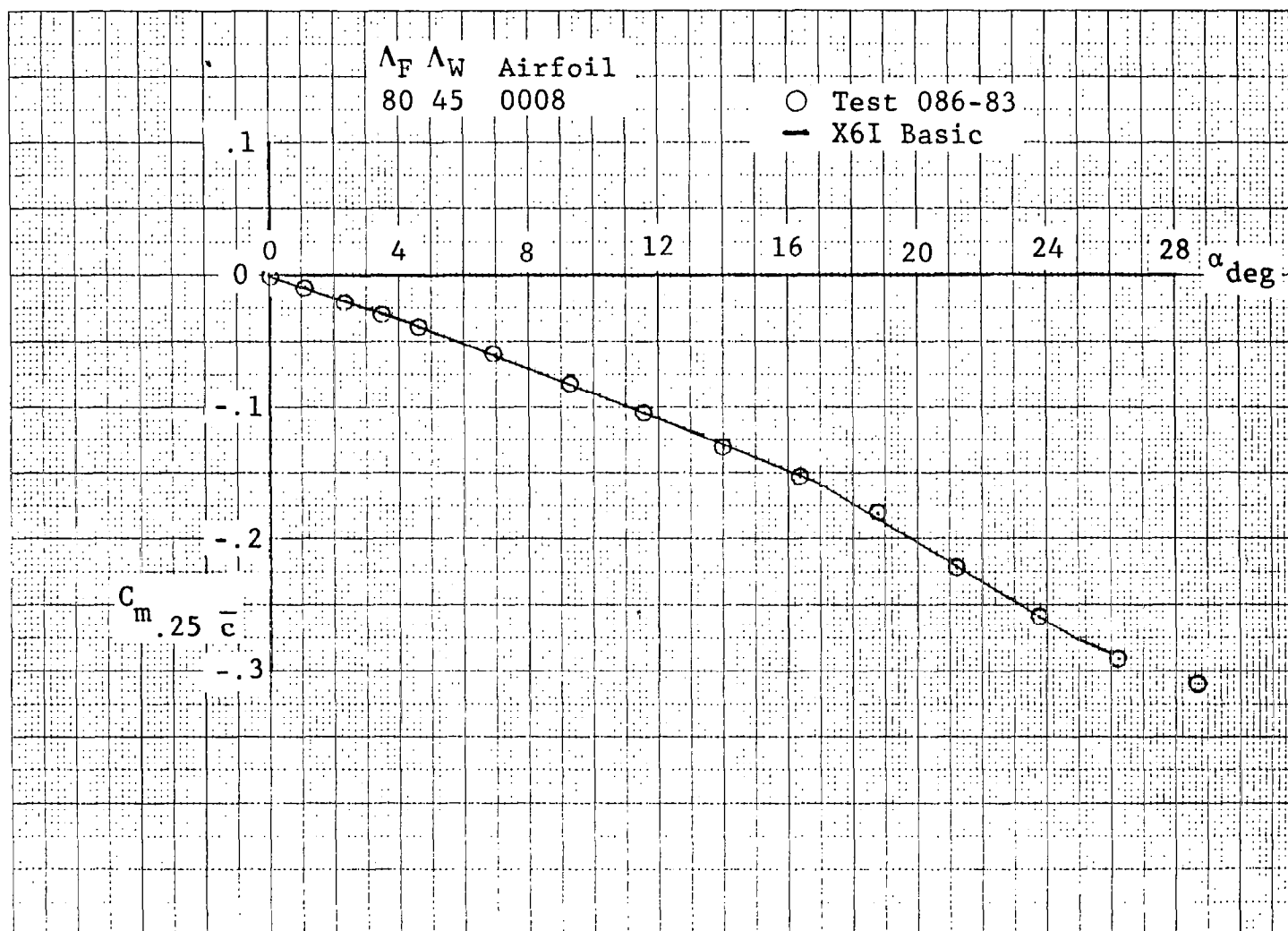
Figure 214.   Concluded
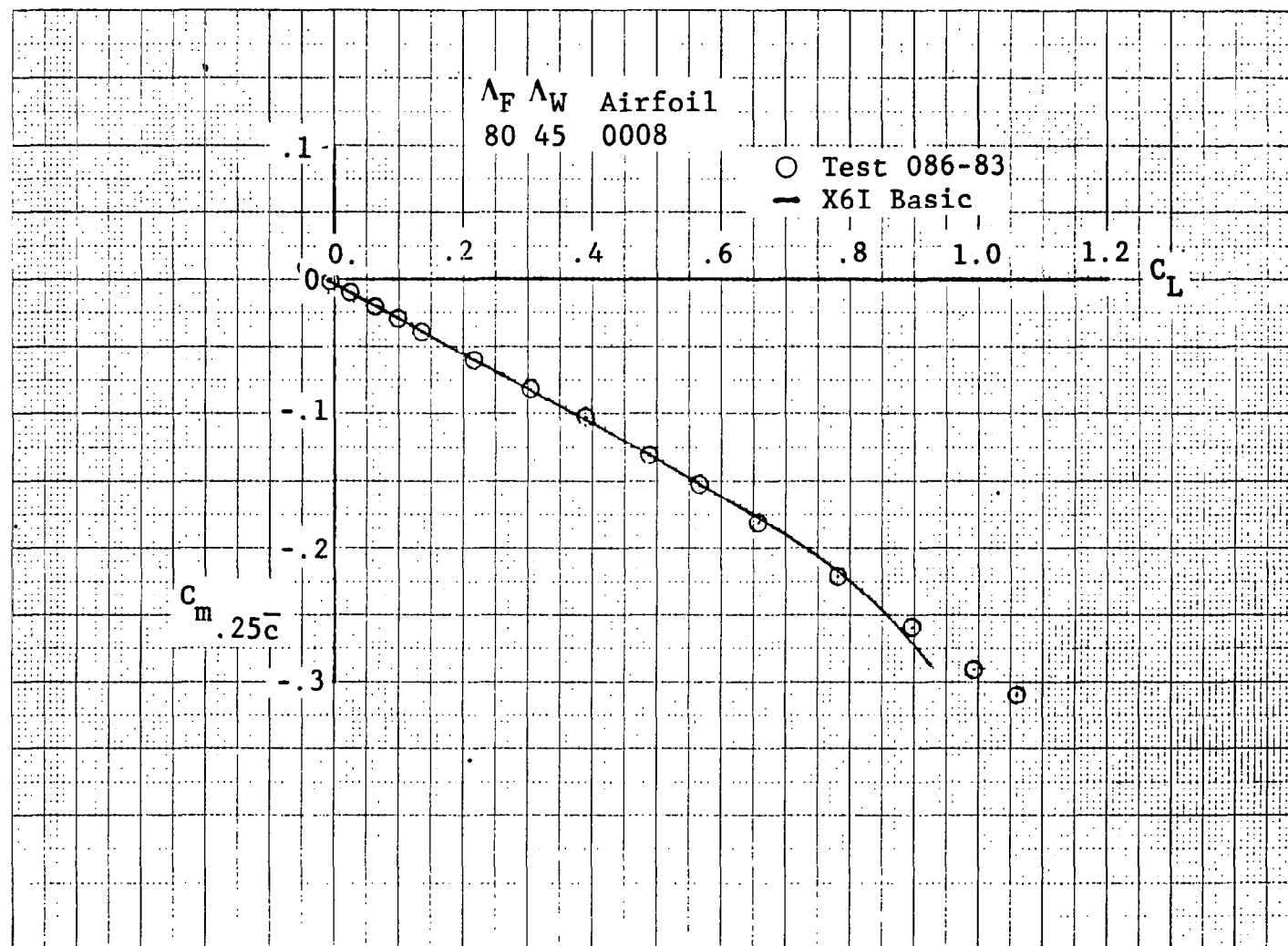
(a) Lift Curve

Figure 215.   Comparisons Between Basic SHIPS Prediction and Test
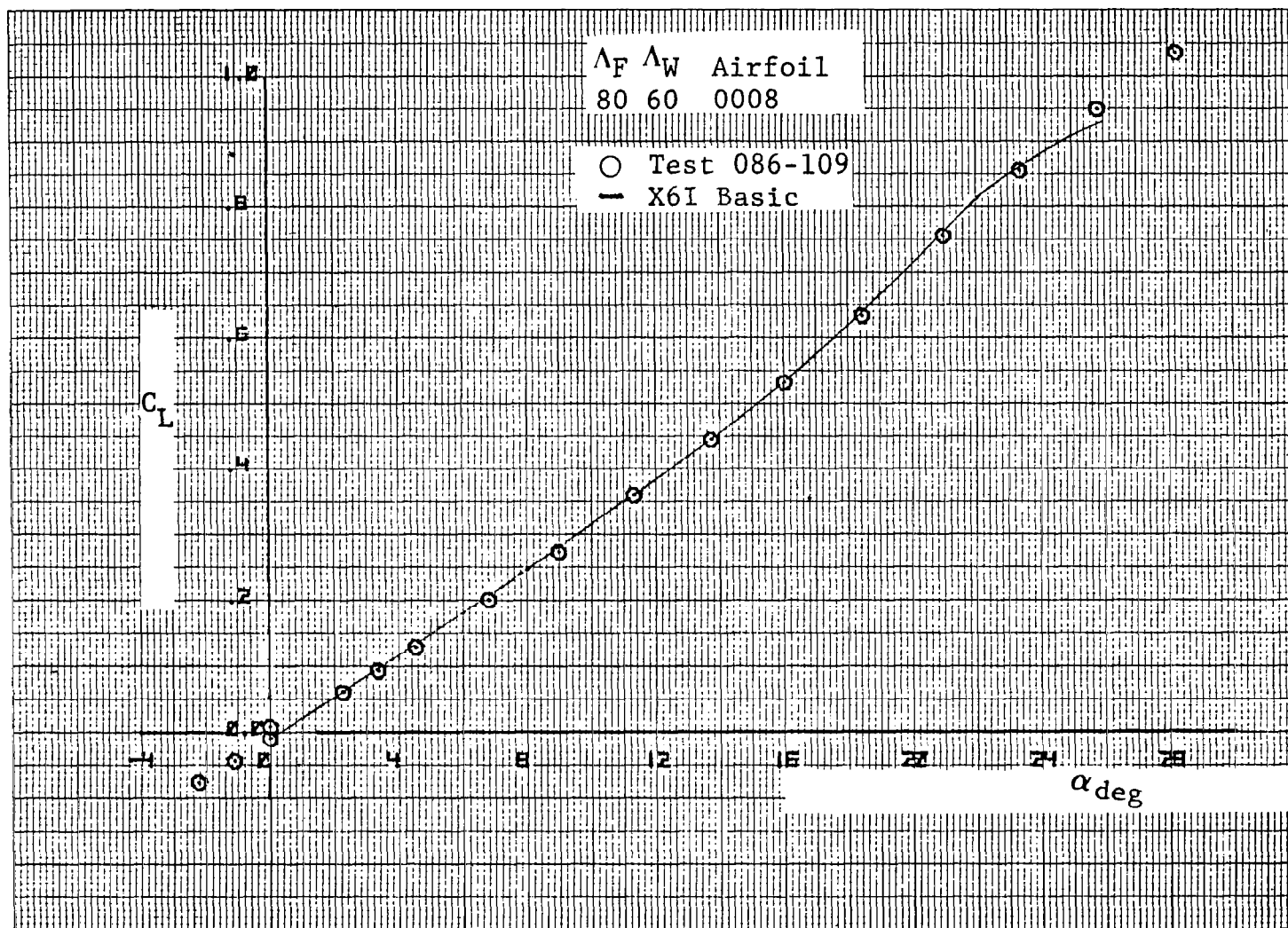Wing III with 80° Fillet

(b) Drag Polar
Figure 215. Continued

(c)   Pitching-Moment Variation with Angle of Attack
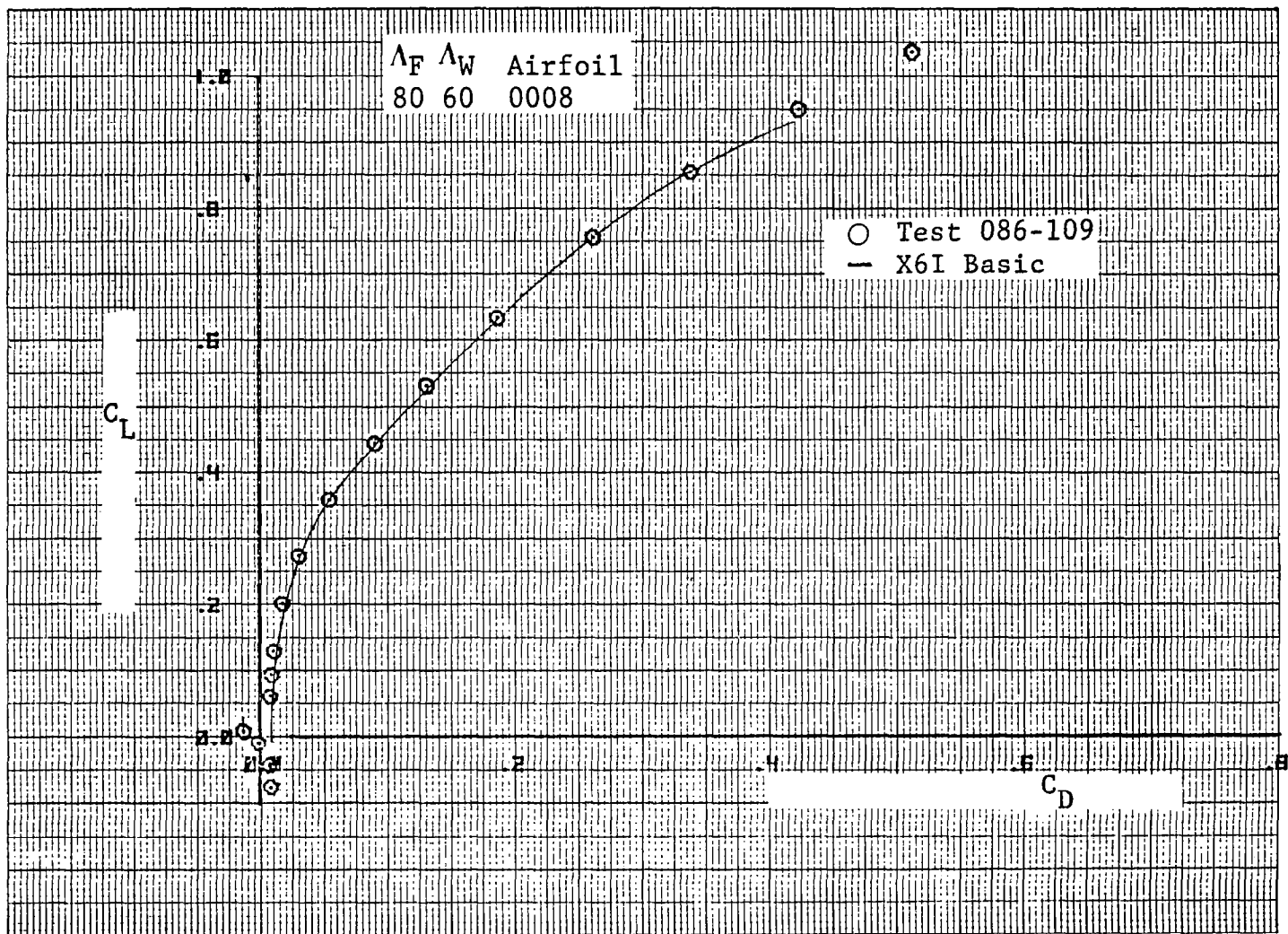
Figure 215.   Continued

(d) Pitching-Moment Variation with Lift
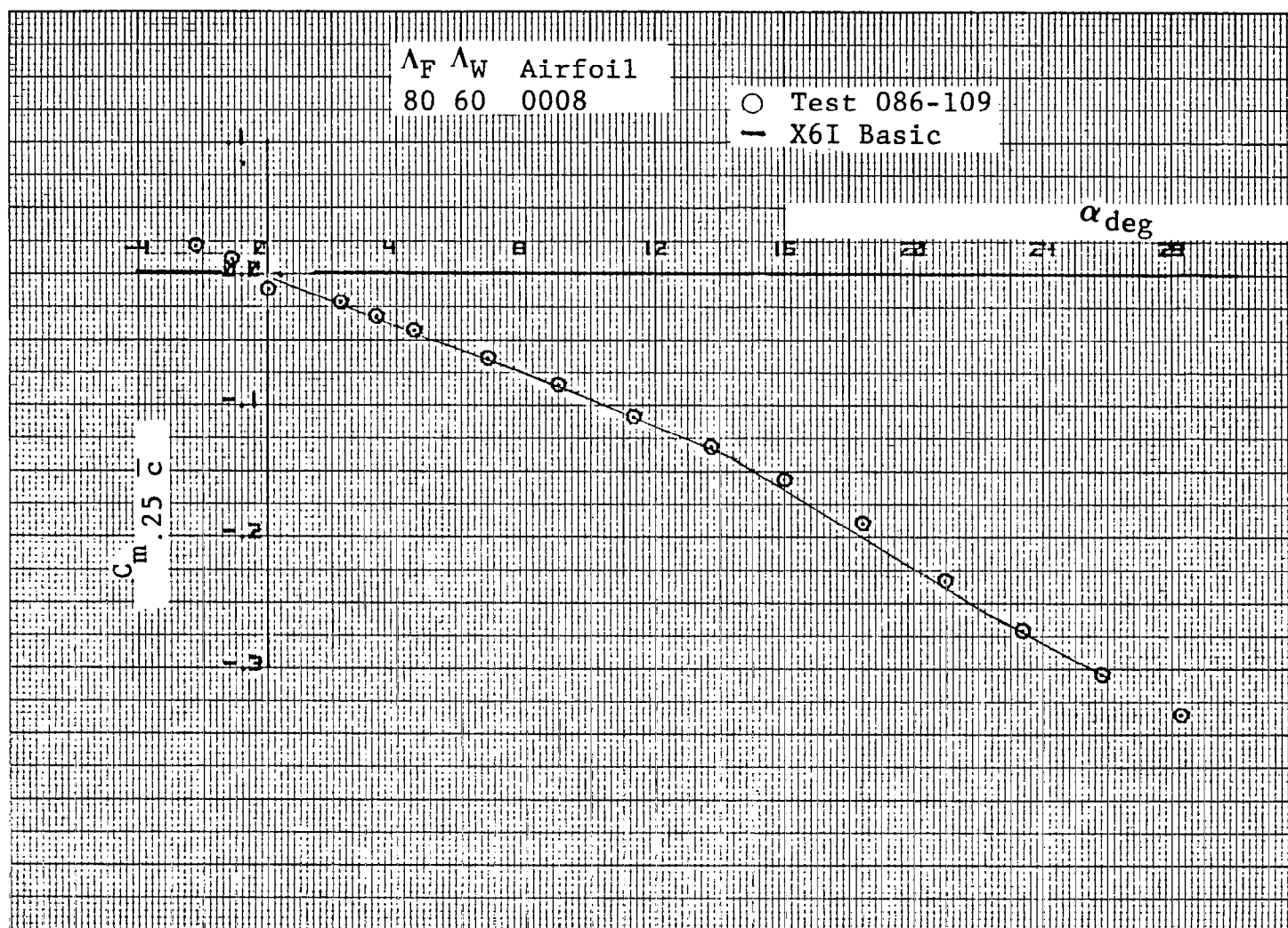Figure 215. Concluded.

(a) Lift Curve

Figure 216. Comparisons Between Basic SHIPS Prediction and Test
for Wing V with 80° Fillet

(b) Drag Polar

Figure 216. Continued

(c) Pitching-Moment Variation with Angle of Attack

Figure 216. Continued

(d) Pitching-Moment Variation with Lift

Figure 216. Concluded.

(a)   Lift Curve

Figure 217.   Comparisons of Basic SHIPS Prediction and Test for Basic Wing I with 35° Fillet

(b) Drag Polar

Figure 217. Continued

(c) Pitching-Moment Variation with Angle of Attack

Figure 217. Continued

(d) Pitching-Moment Variation with Lift

Figure 217. Concluded.

(a) Lift Curve

Figure 218. Comparisons of Basic SHIPS Prediction and Test
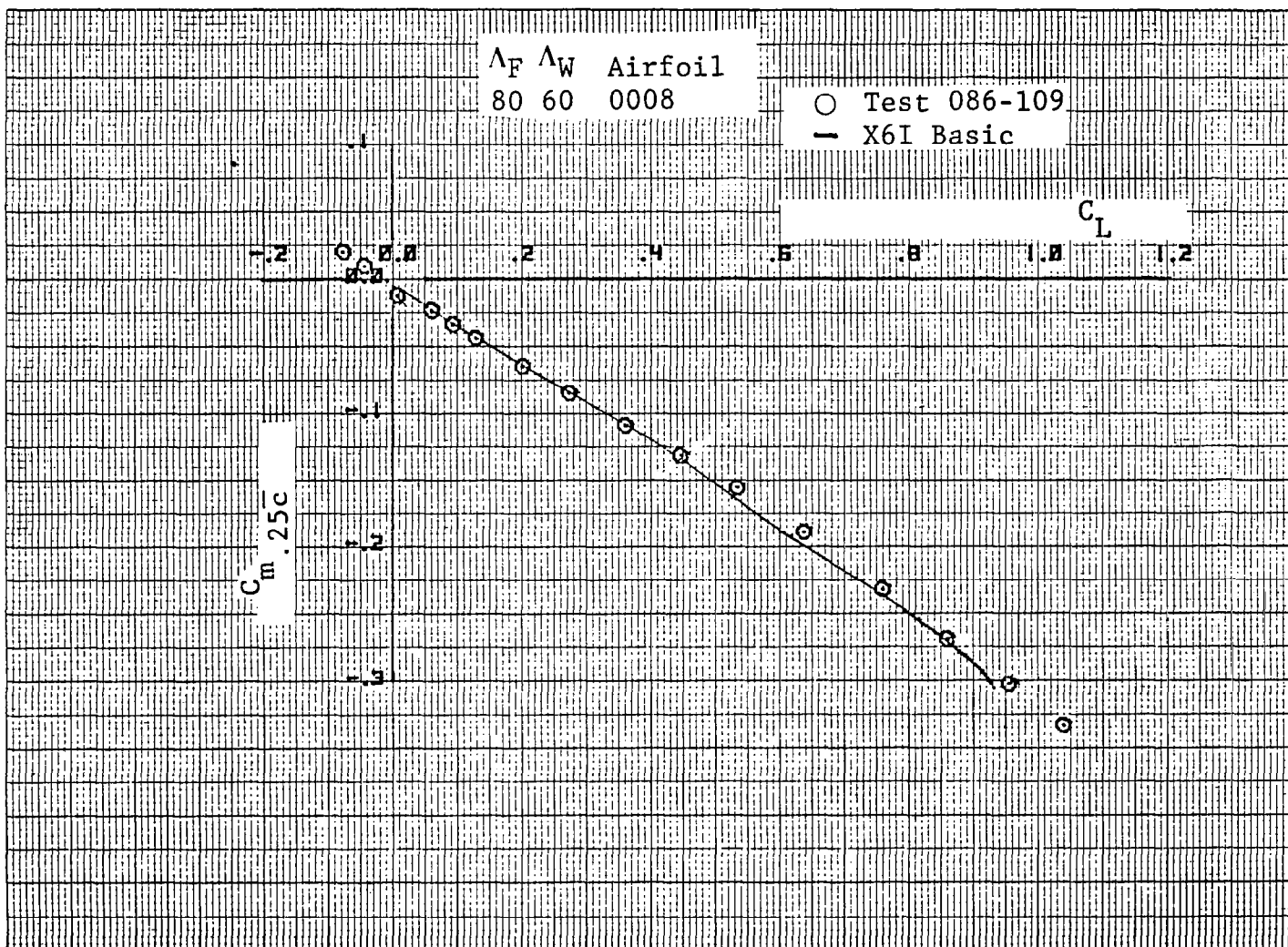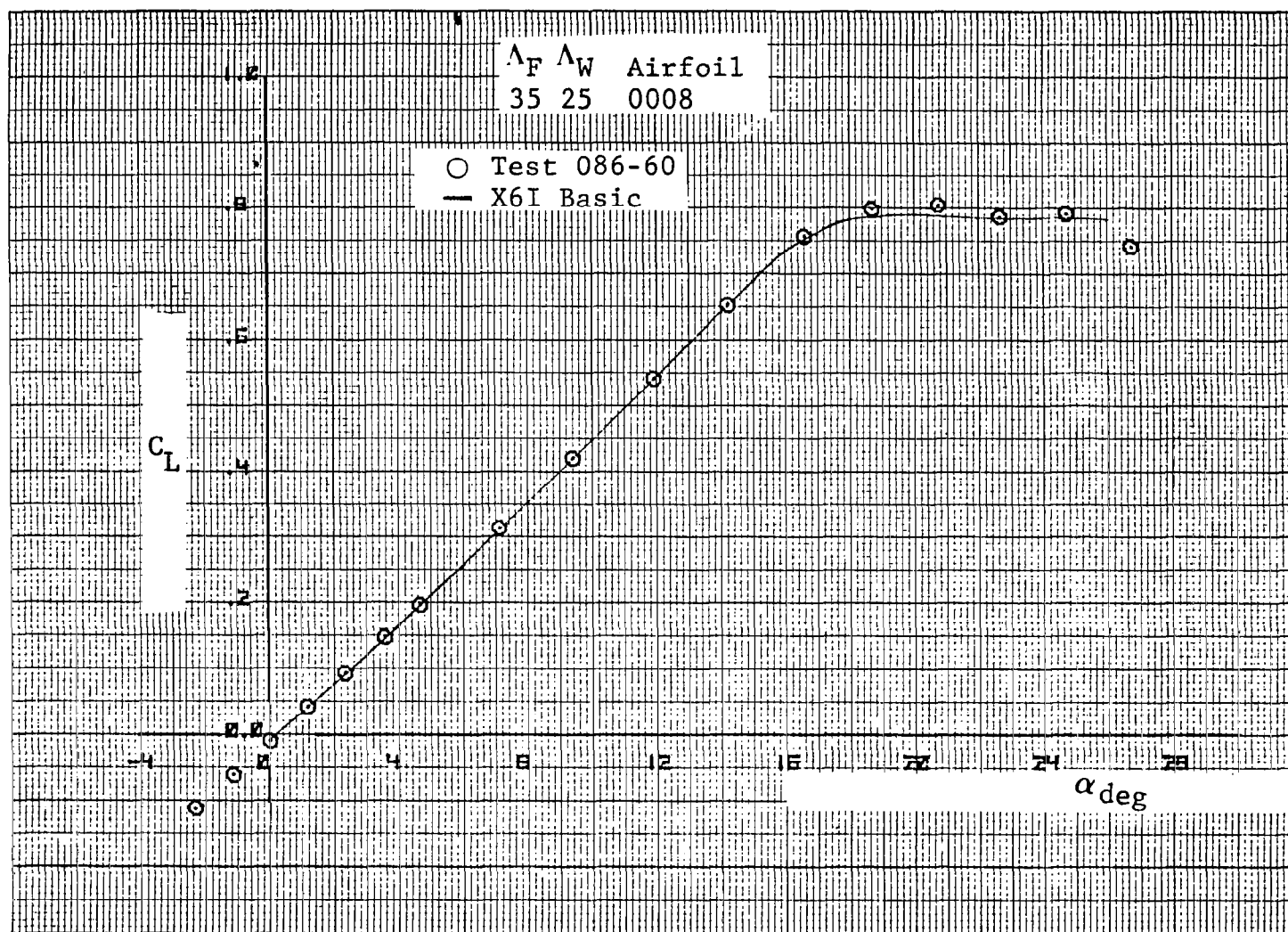for Wing III with 55° Fillet

(b) Drag Polar

Figure 218. Continued

(c)   Pitching-Moment Variation with Angle of Attack

Figure 218.   Continued

(d) Pitching-Moment Variation with Lift

Figure 218. Concluded.

Λ_F	Λ_W	Airfoil
65	60	0008

○ Test 086-117
— X6I Basic
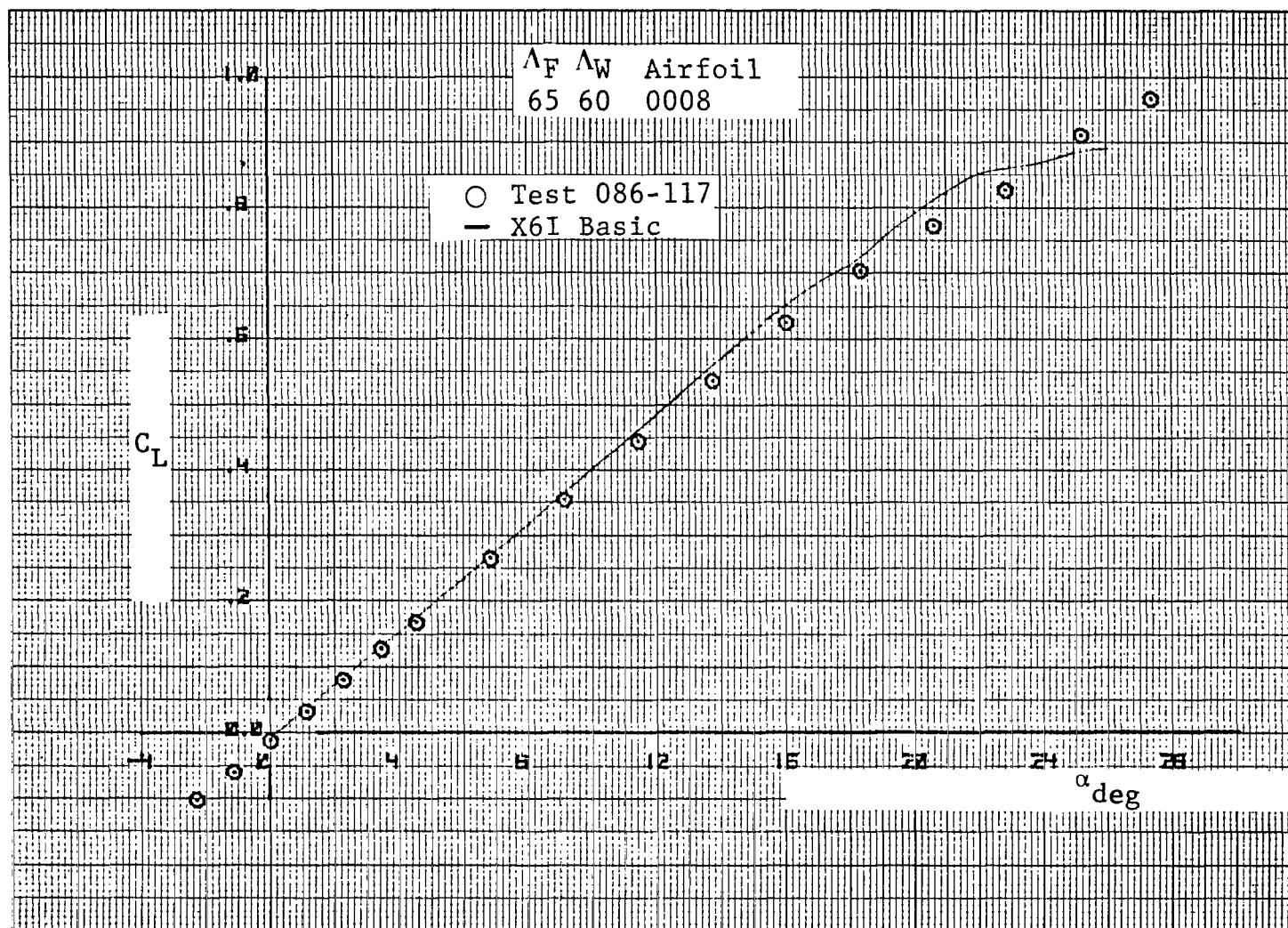
(a) Lift Curve

Figure 219. Comparisons of Basic SHIPS Prediction and Test
for Wing V with 65° Fillet

(b) Drag Polar

Figure 219. Continued

(c) Pitching-Moment Variation with Angle of Attack
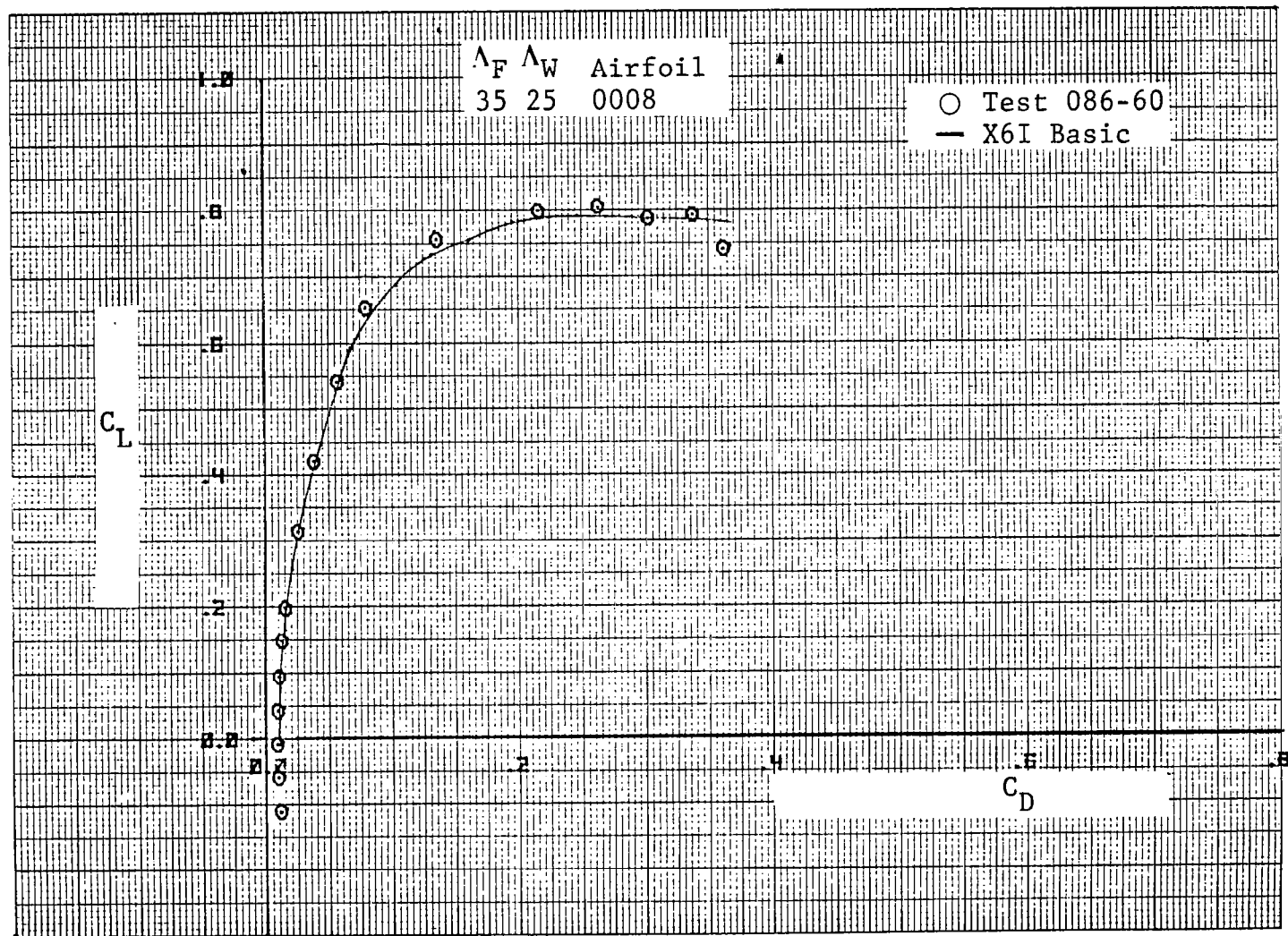
Figure 219. Continued

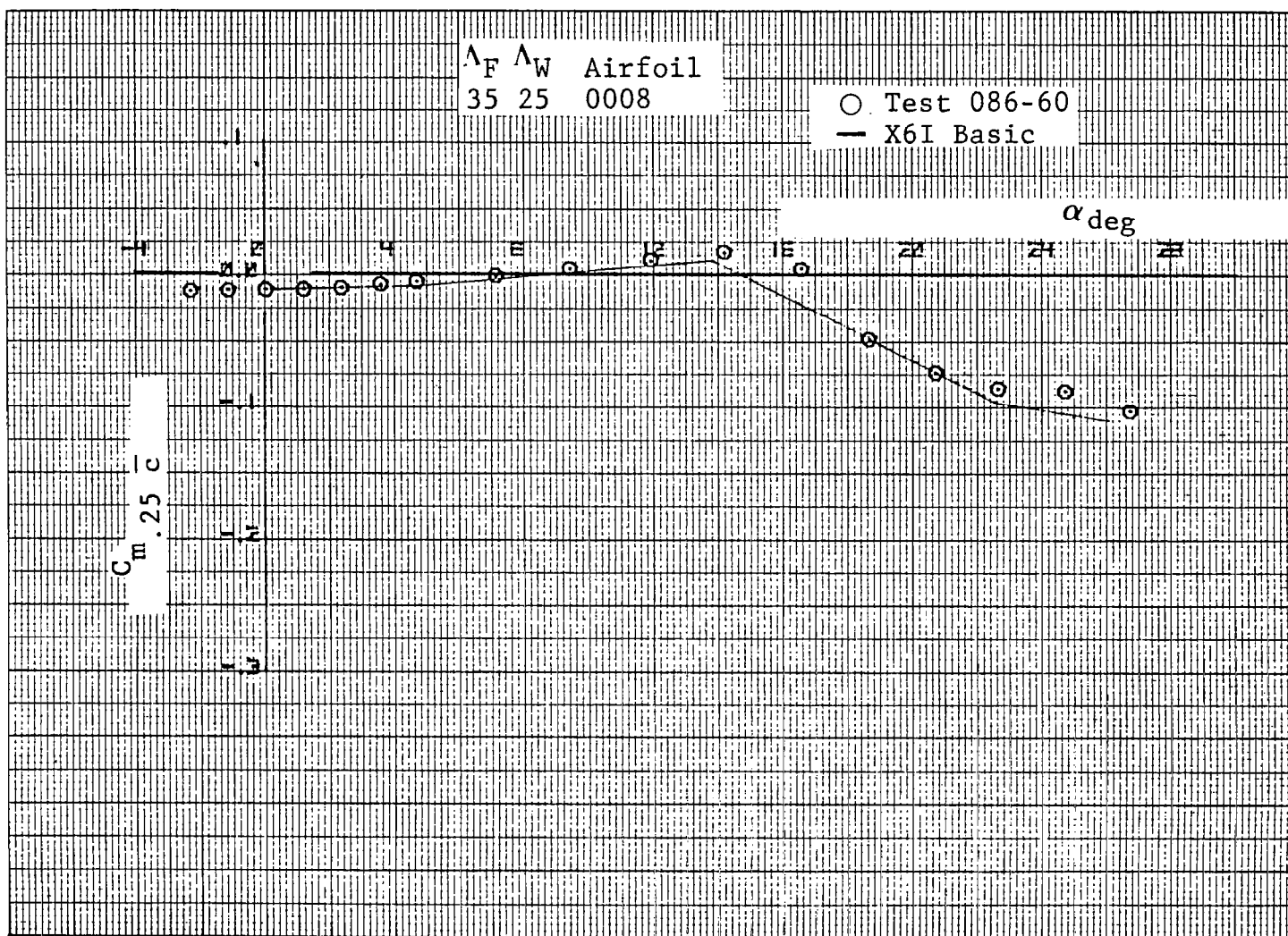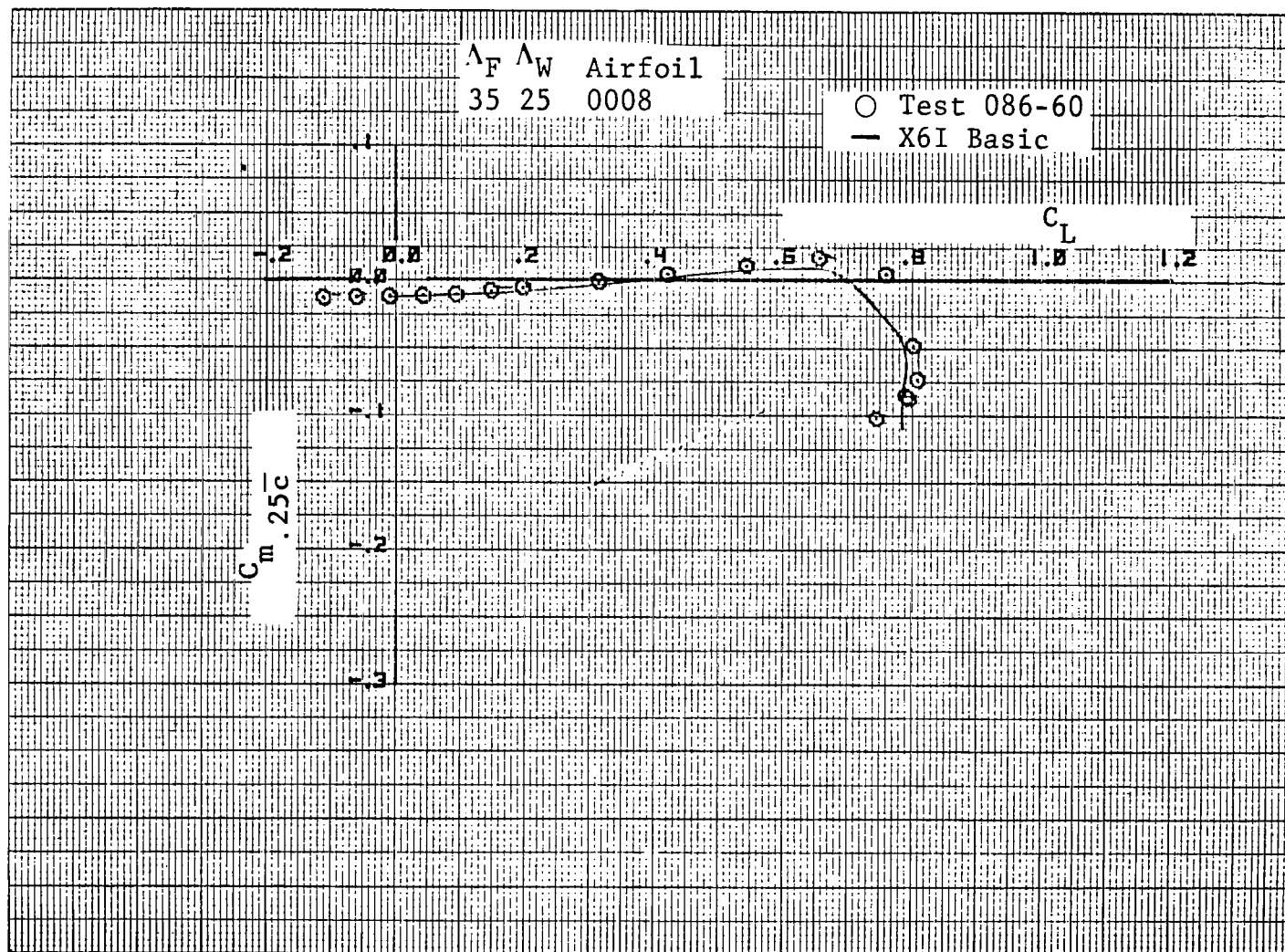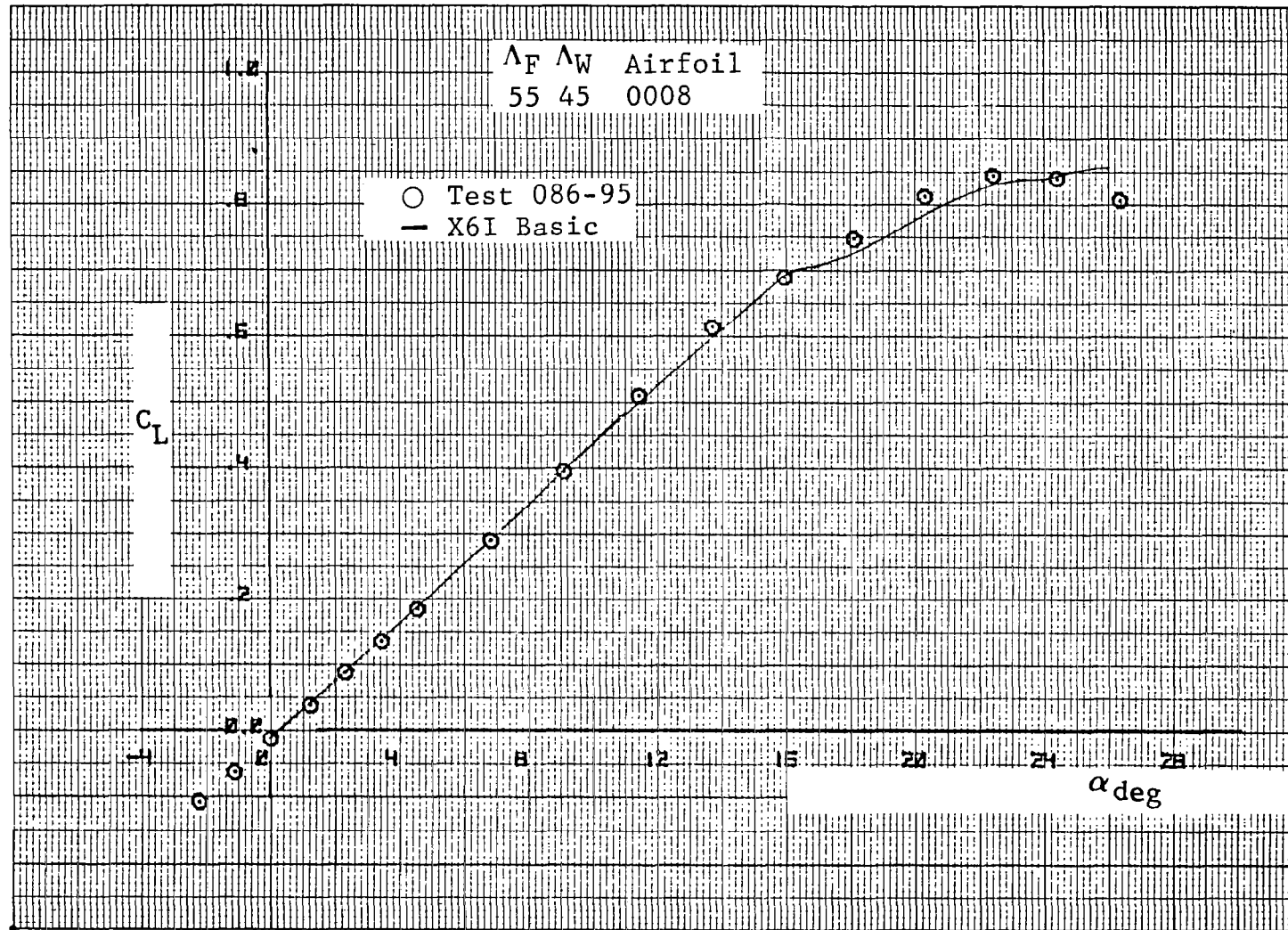(d)   Pitching-Moment Variation with Lift

Figure 219.   Concluded

Λ_F Λ_W Airfoil

□ 75 35 0008 Test 086-68
— 75 40 0008 Prediction X6I Procedure
○ 75 45 0008 Test 086-86

(a) Lift Curve

Figure 220. Comparisons of Basic SHIPS Prediction for
Configuration $\Lambda_{F_o} = 75°$, $\Lambda_{W_o} = 40°$ and Test
Data for $\Lambda_F = 75°$, $\Lambda_W = 35°$ and $45°$

Λ_F Λ_W Airfoil

□ 75 35 0008 Test 086-68
— 75 40 0008 Prediction X6I Procedure
○ 75 45 0008 Test 086-86

(b) Suction-Ratio Variation with Angle of Attack

Figure 220. Continued

(c)   Drag Polars

Figure 220.   Continued
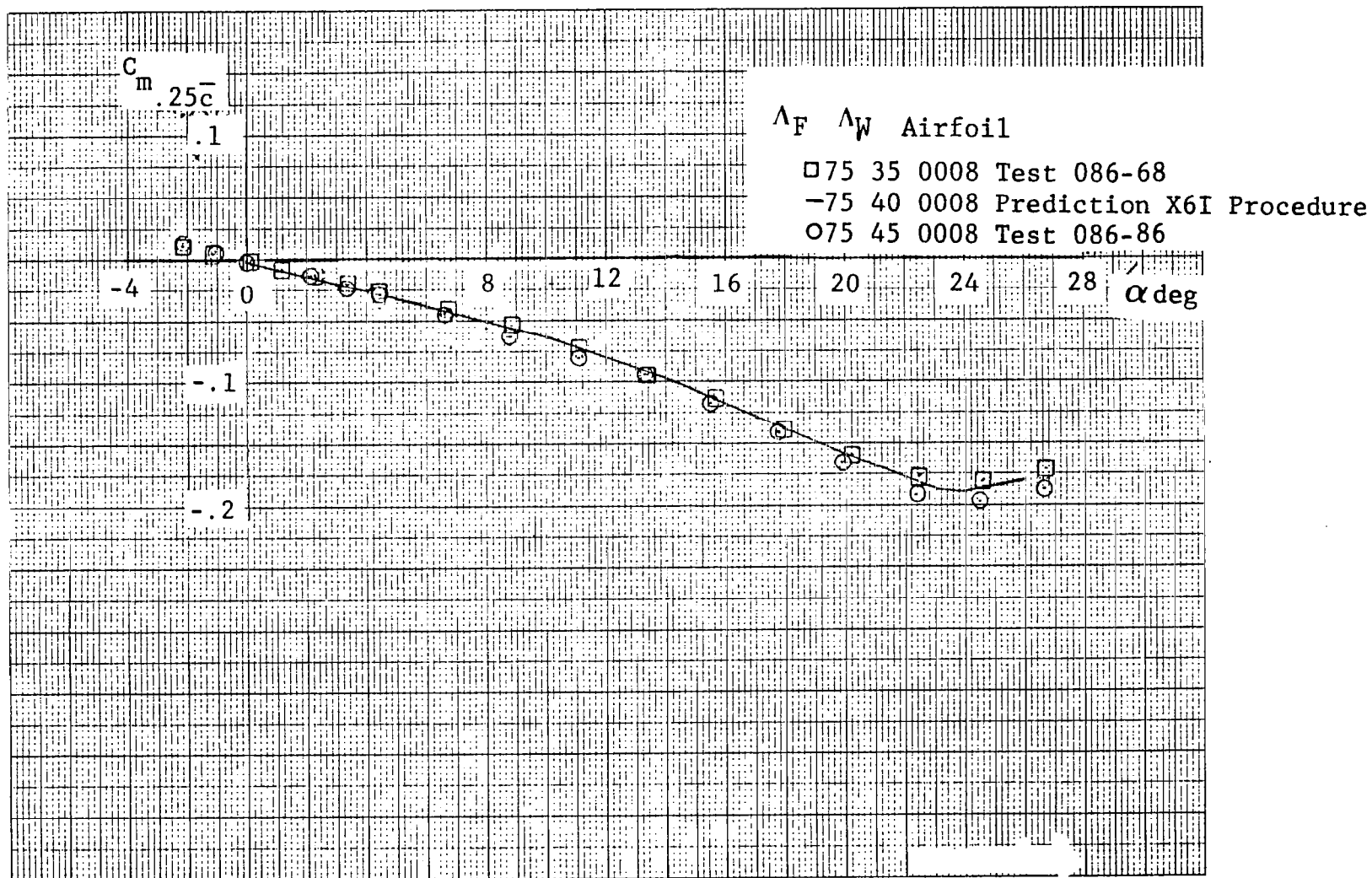
(d)   Pitching-Moment Variation with Angle of Attack
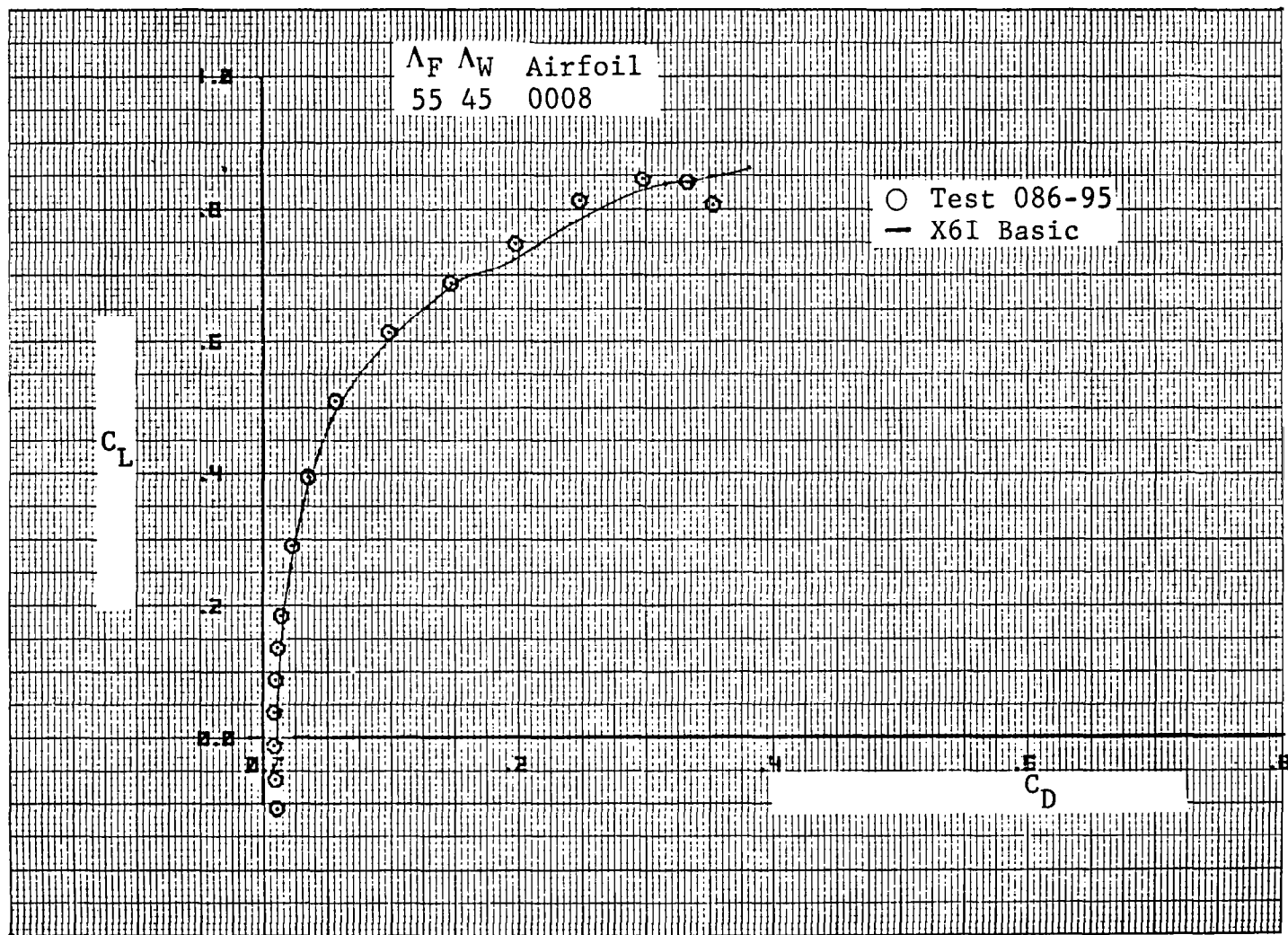
Figure 220.   Continued

368

(e) Pitching-Moment Variations with Lift
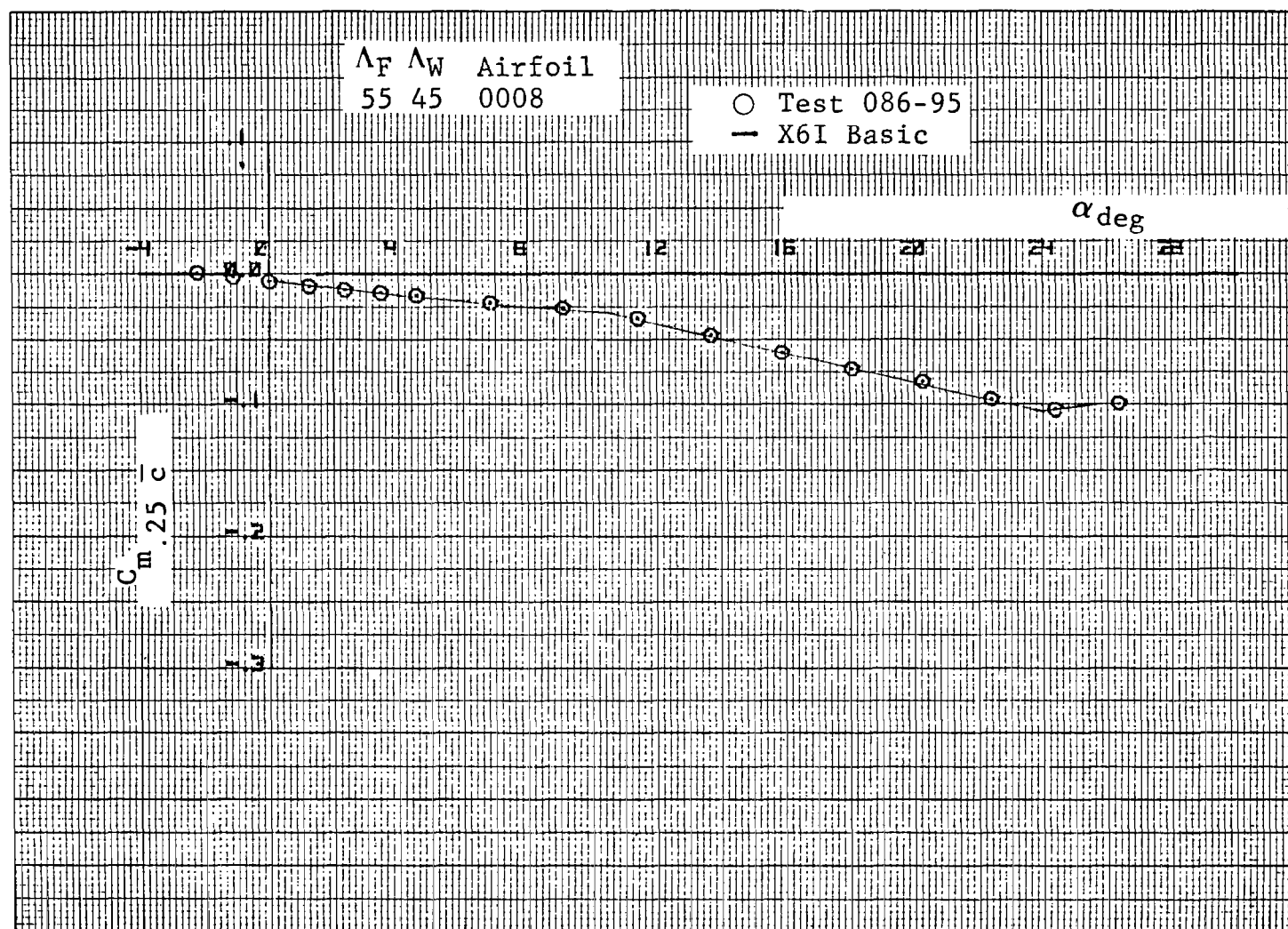
Figure 220. Concluded.

(a)   Lift Curve

Figure 221.   Comparisons of Basic SHIPS Prediction and Test
for Wing I with 60° Fillet

(b) Suction-Ratio Variation with Angle of Attack

Figure 221. Continued

(c)   Drag Polar

Figure 221.   Continued

(d)   Pitching-Moment Variation with Angle of Attack

Figure 221.   Continued

(e) Pitching-Moment Variation with Lift
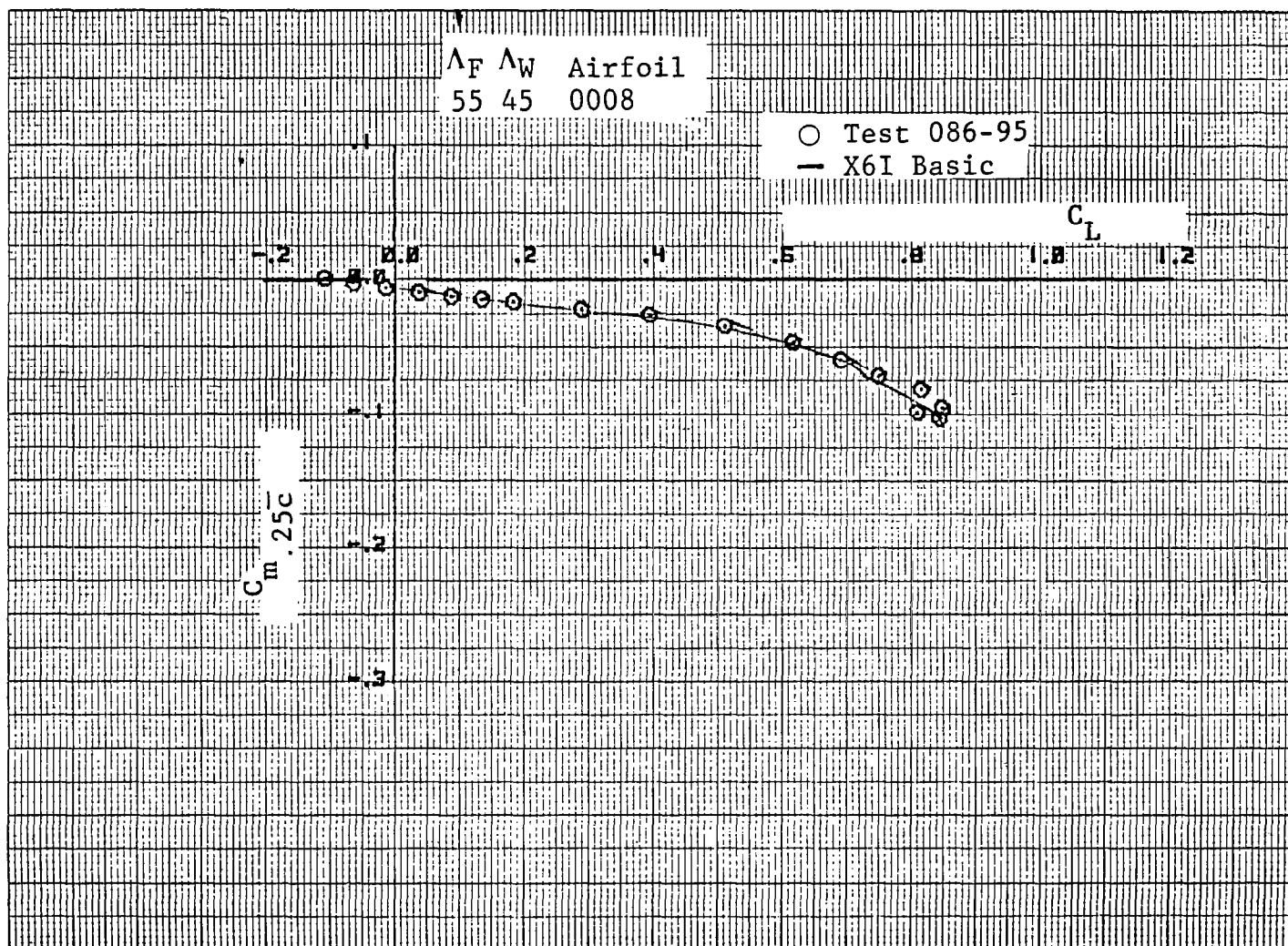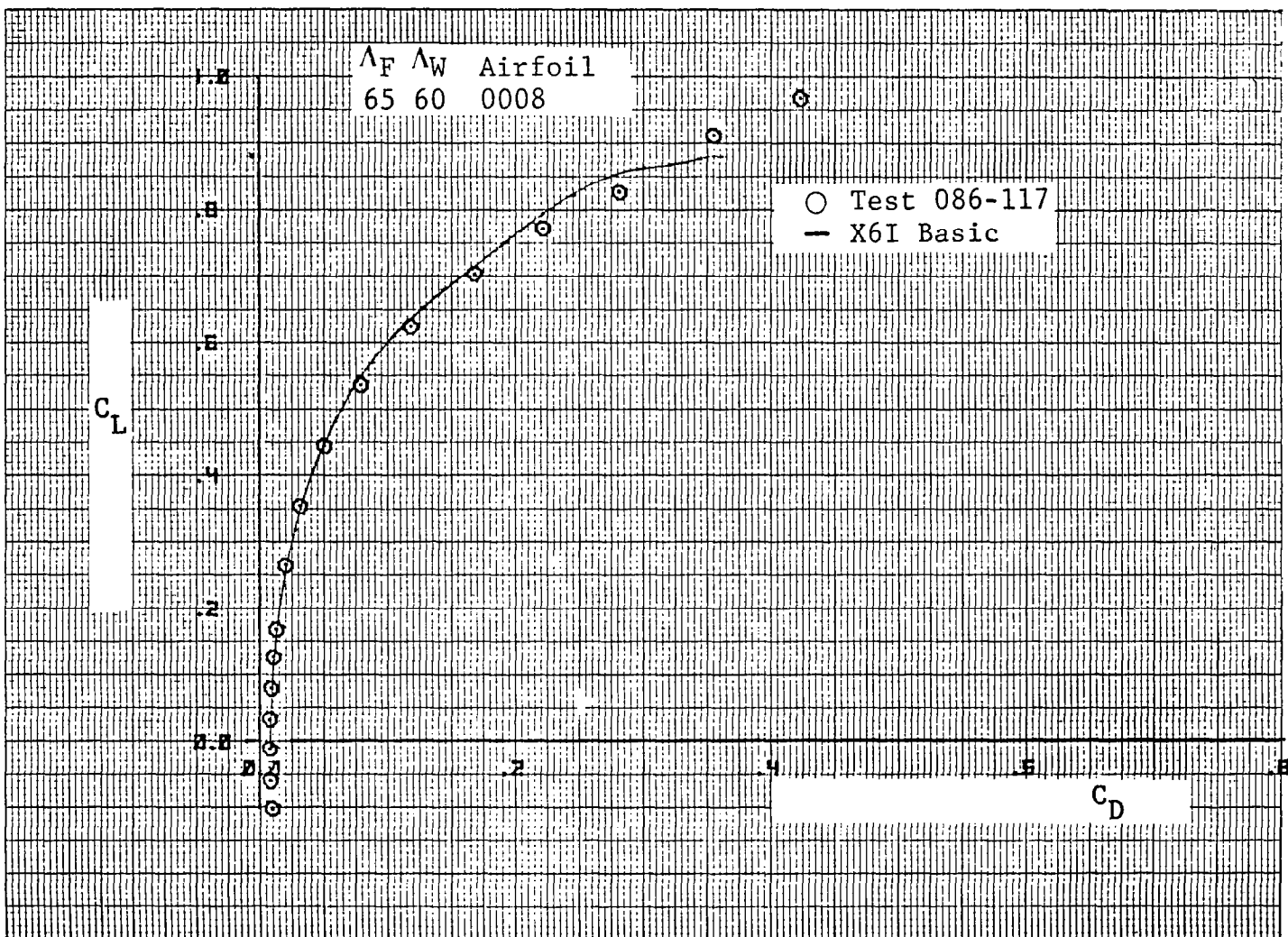
Figure 221. Concluded

(a) Lift Curve

Figure 222.   Comparisons of Basic and Revised SHIPS Predictions
and Test for Wing III with 65° Fillet for Two
Different Test Facilities

(b)   Drag Polar

Figure 222.   Continued

(c) Pitching-Moment Variation with Angle of Attack

Figure 222. Continued

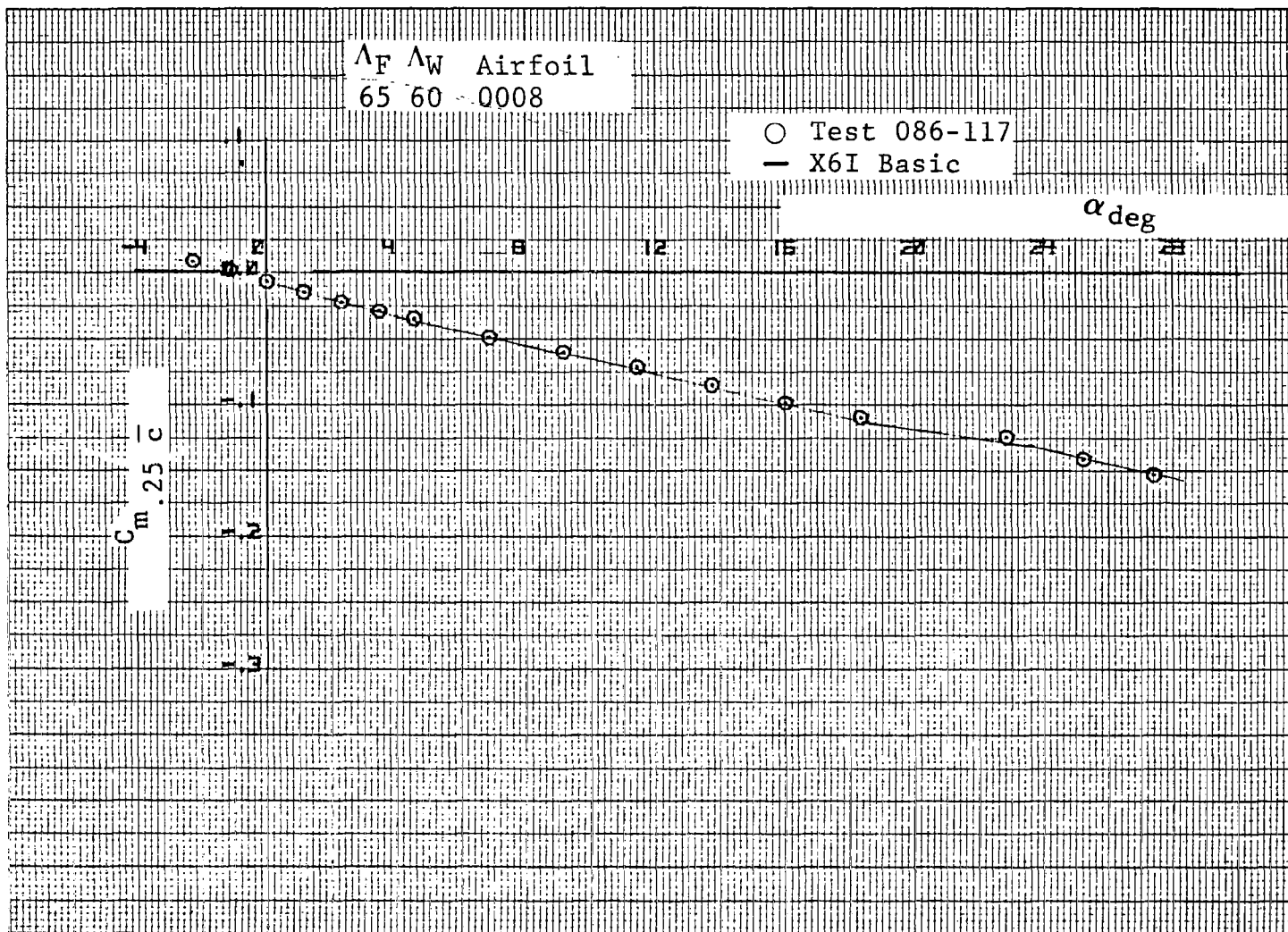(d)   Pitching-Moment Variation with Lift

Figure 222.   Concluded

Λ_F	Λ_W	Airfoil
45	45	0004

○ Test 266-38
— X6I Revised

(a) Lift Curve

Figure 223. Comparisons of Revised SHIPS Prediction and Test
for Wing III with NACA 0004 Airfoil
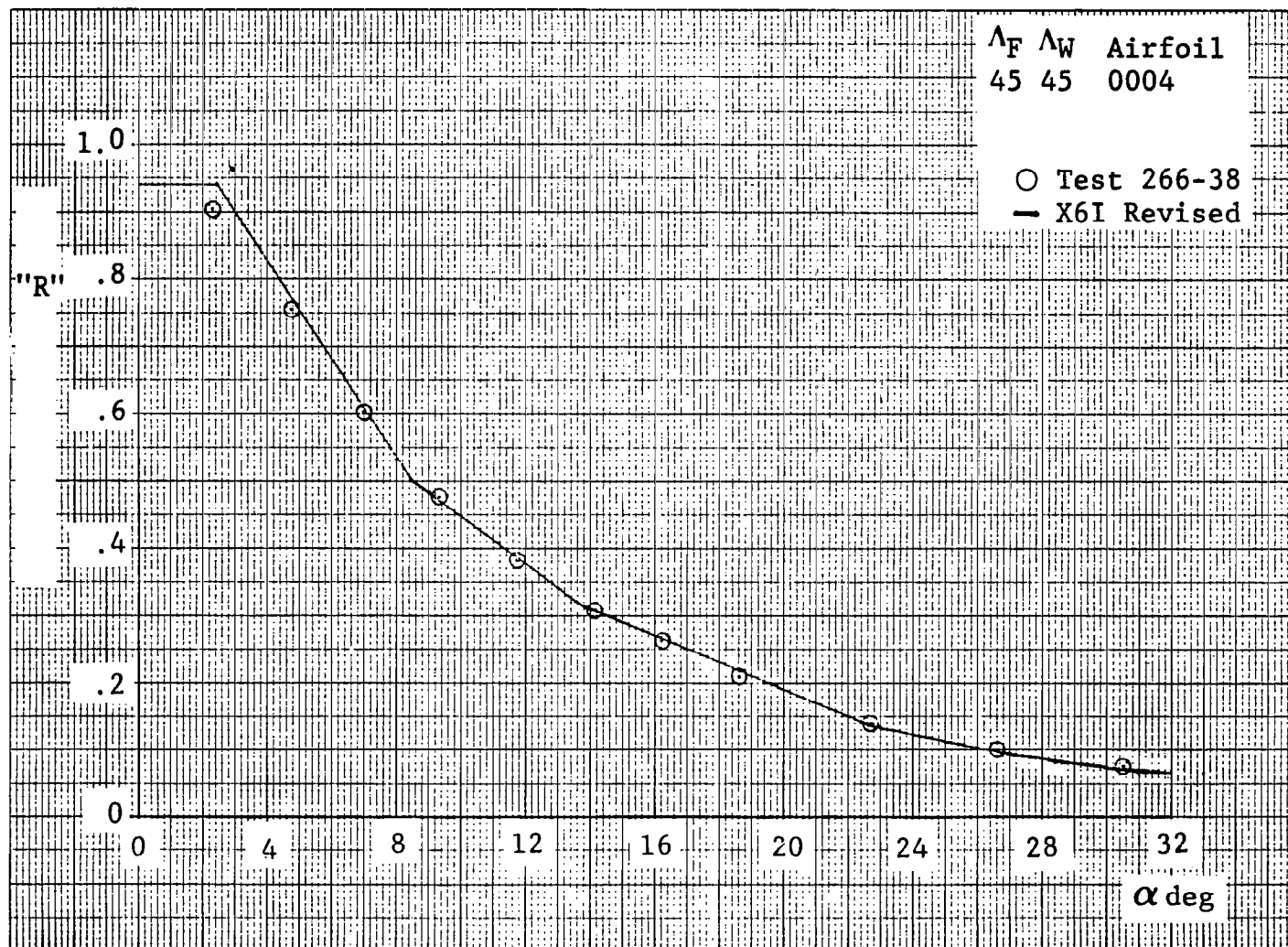
(b)   Suction-Ratio Variation with Angle of Attack
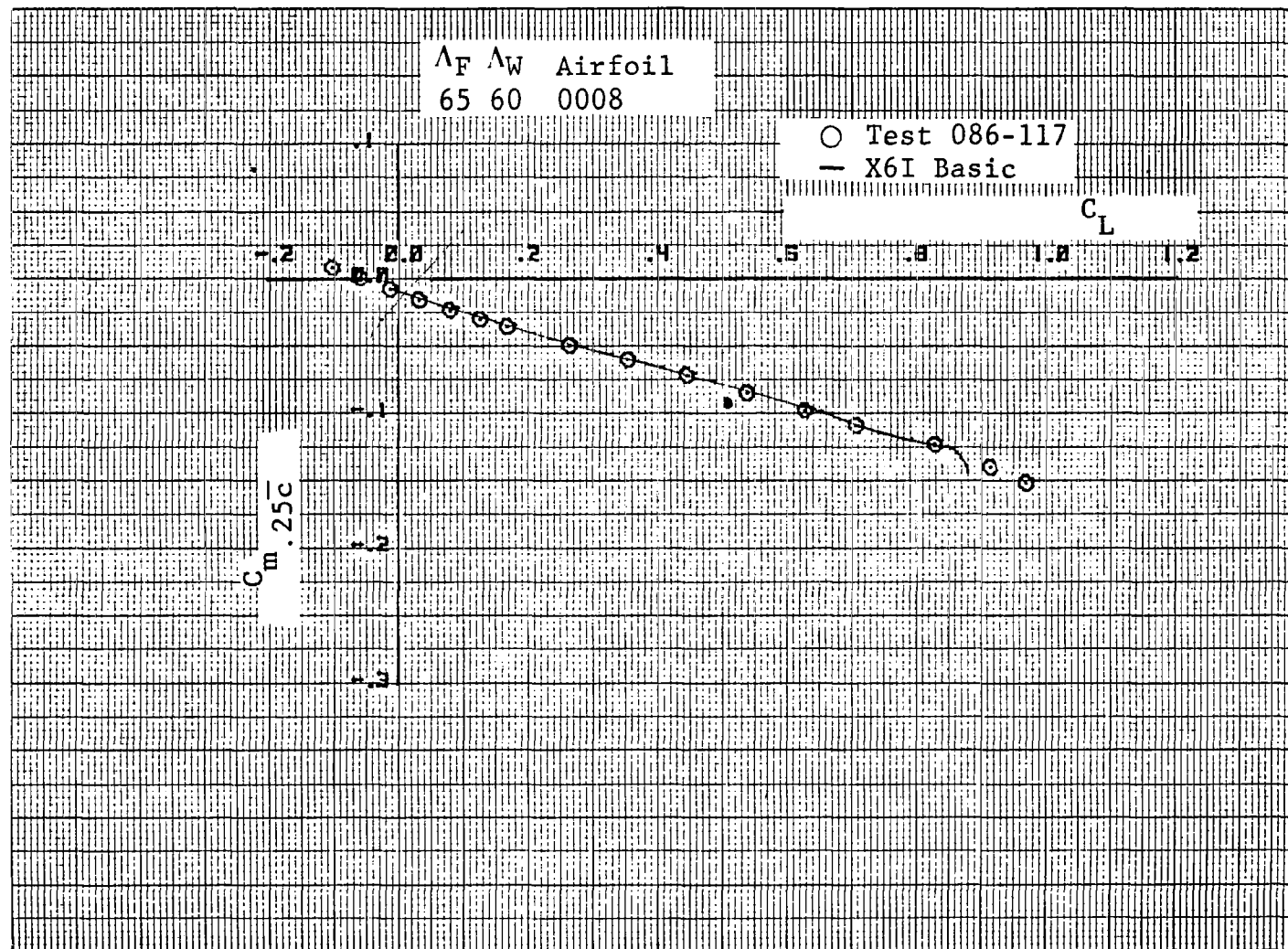Figure 223.   Continued

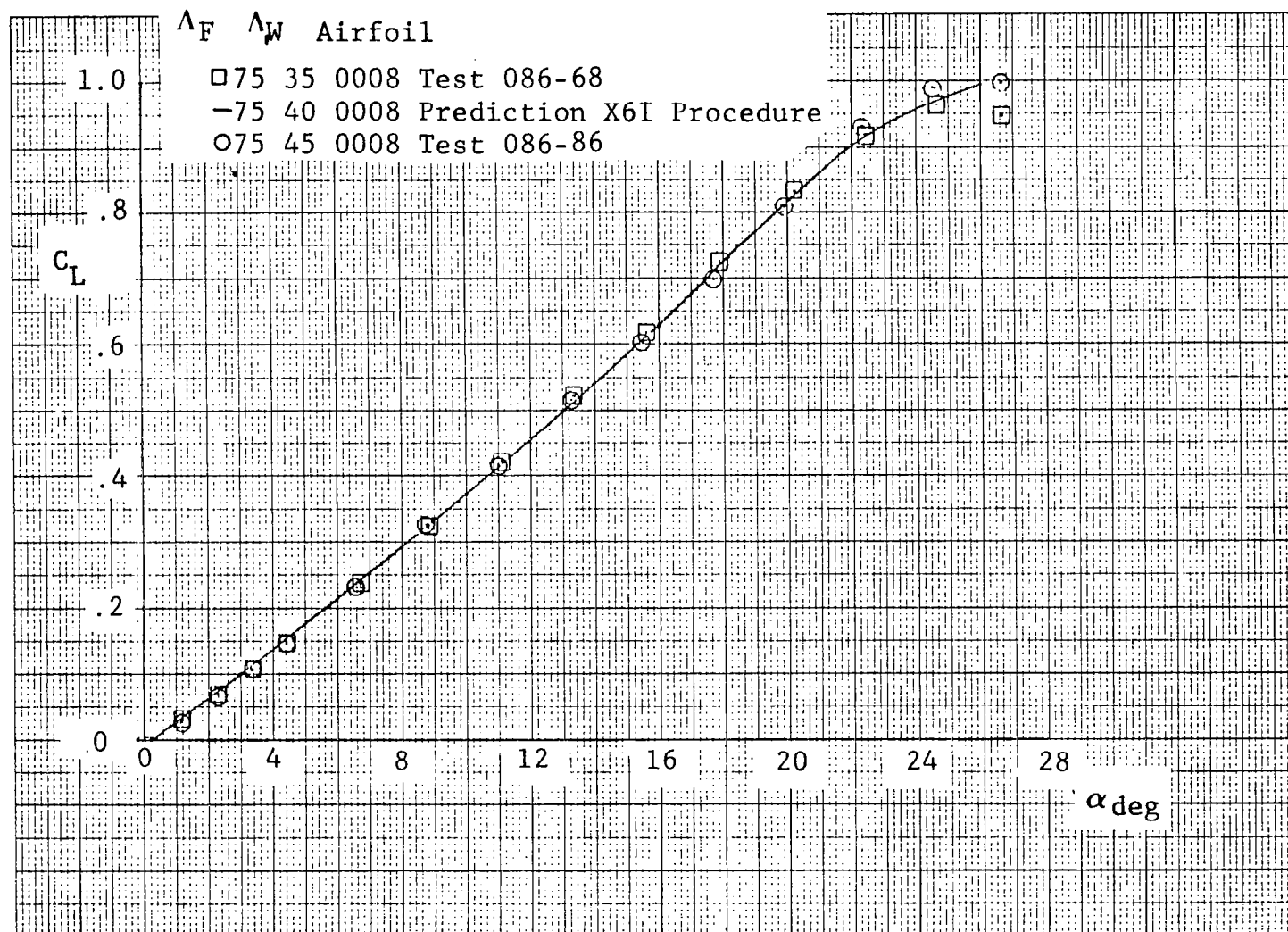(c) Drag Polar

Figure 223. Continued

(d)   Pitching-Moment Variation with Angle of Attack

Figure 223.   Continued
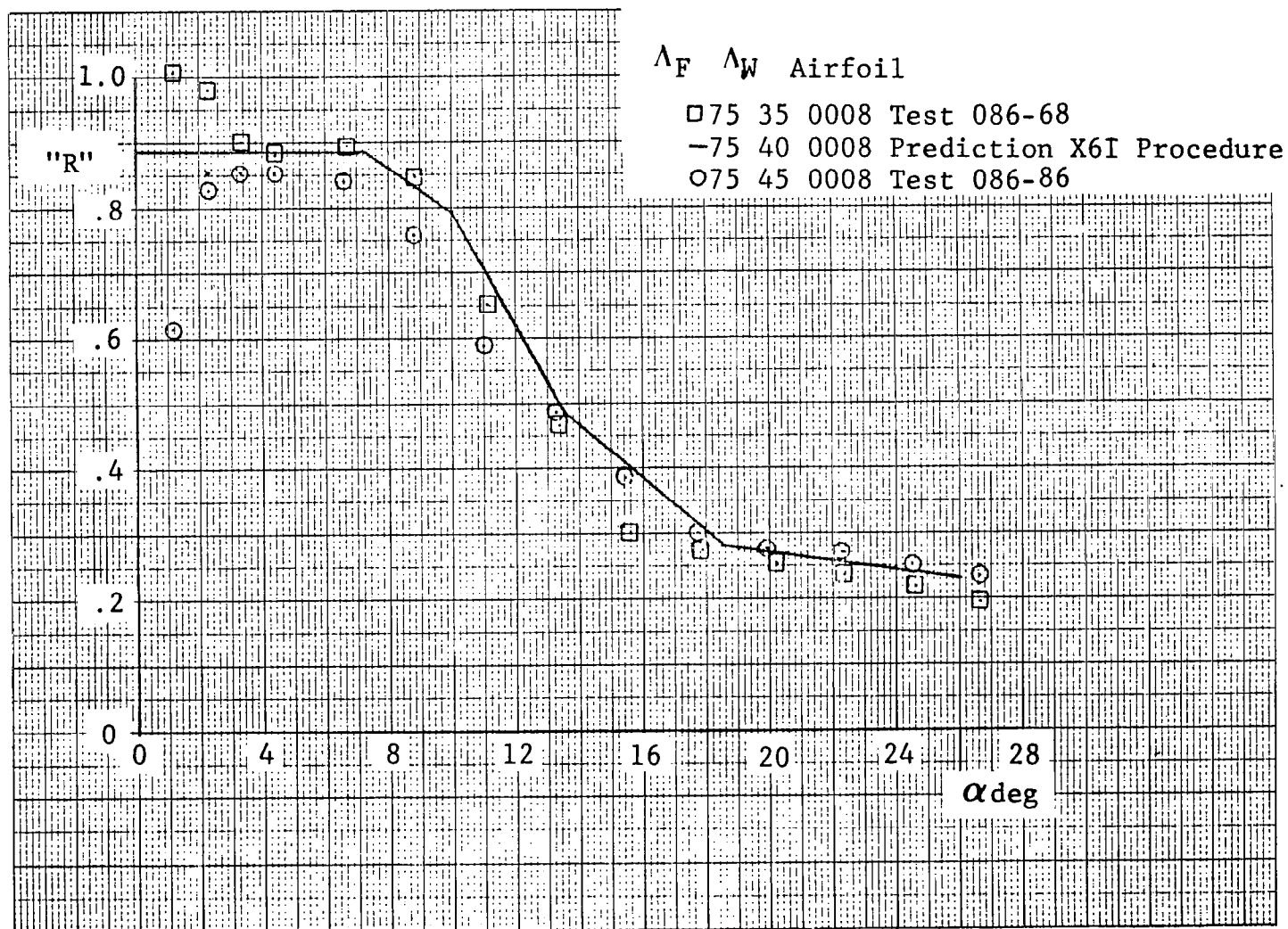
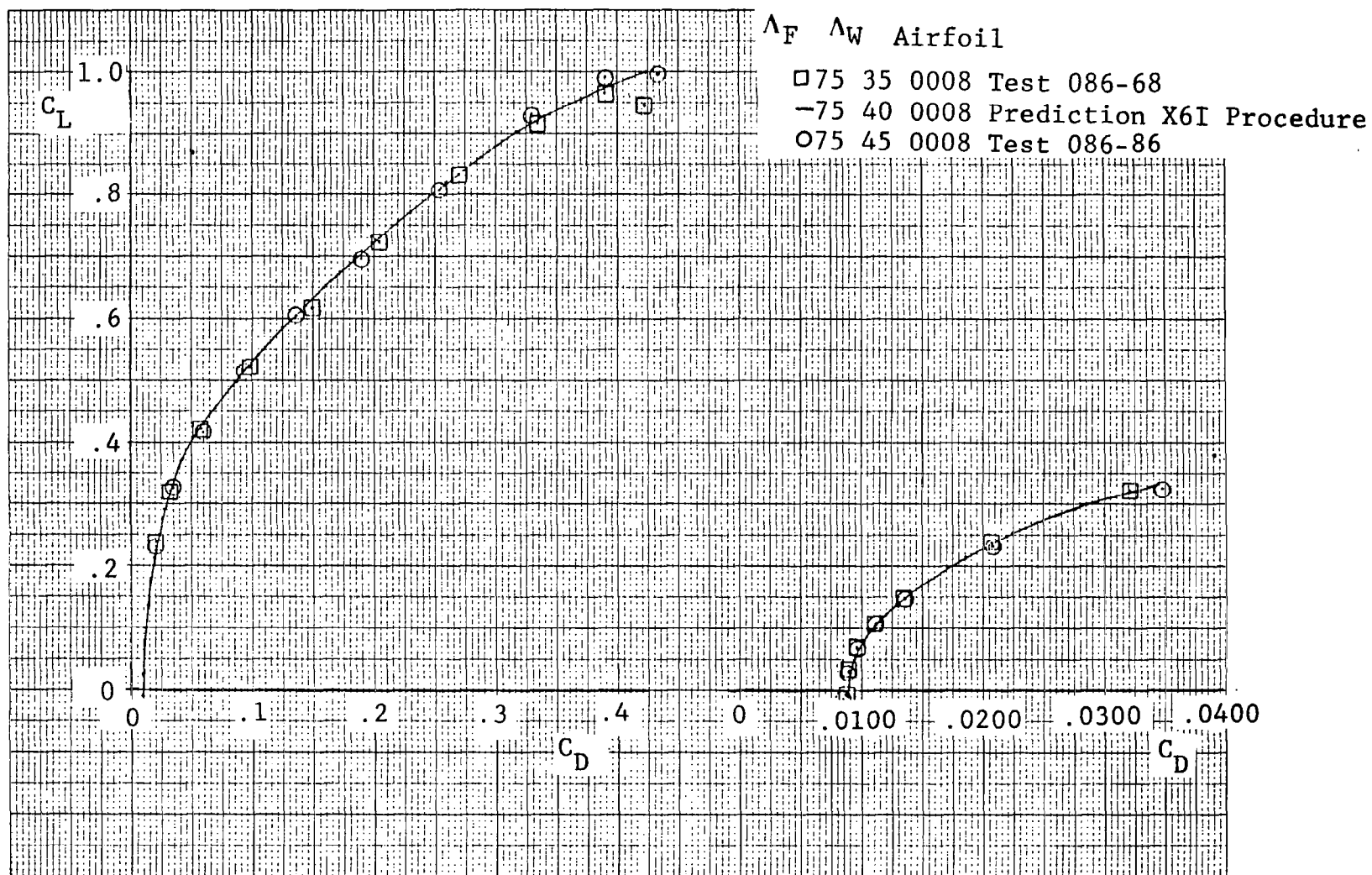(e) Pitching Moment Variation with Lift

Figure 223. Concluded

(a) Lift Curve

Figure 224.   Comparisons of Basic and Revised SHIPS Predictions
and Test for Basic Wing III with NACA 0008 Airfoils for
Two Different Facilities

(b)   Drag Polars

Figure 224.   Continued

(c) Pitching-Moment Variation with Angle of Attack

Figure 224.   Continued

Λ_F	Λ_W	Airfoil
45	45	0008

—— X6I Basic   ○ Test 086-26
-- X6I Revised   □ Test 255-78
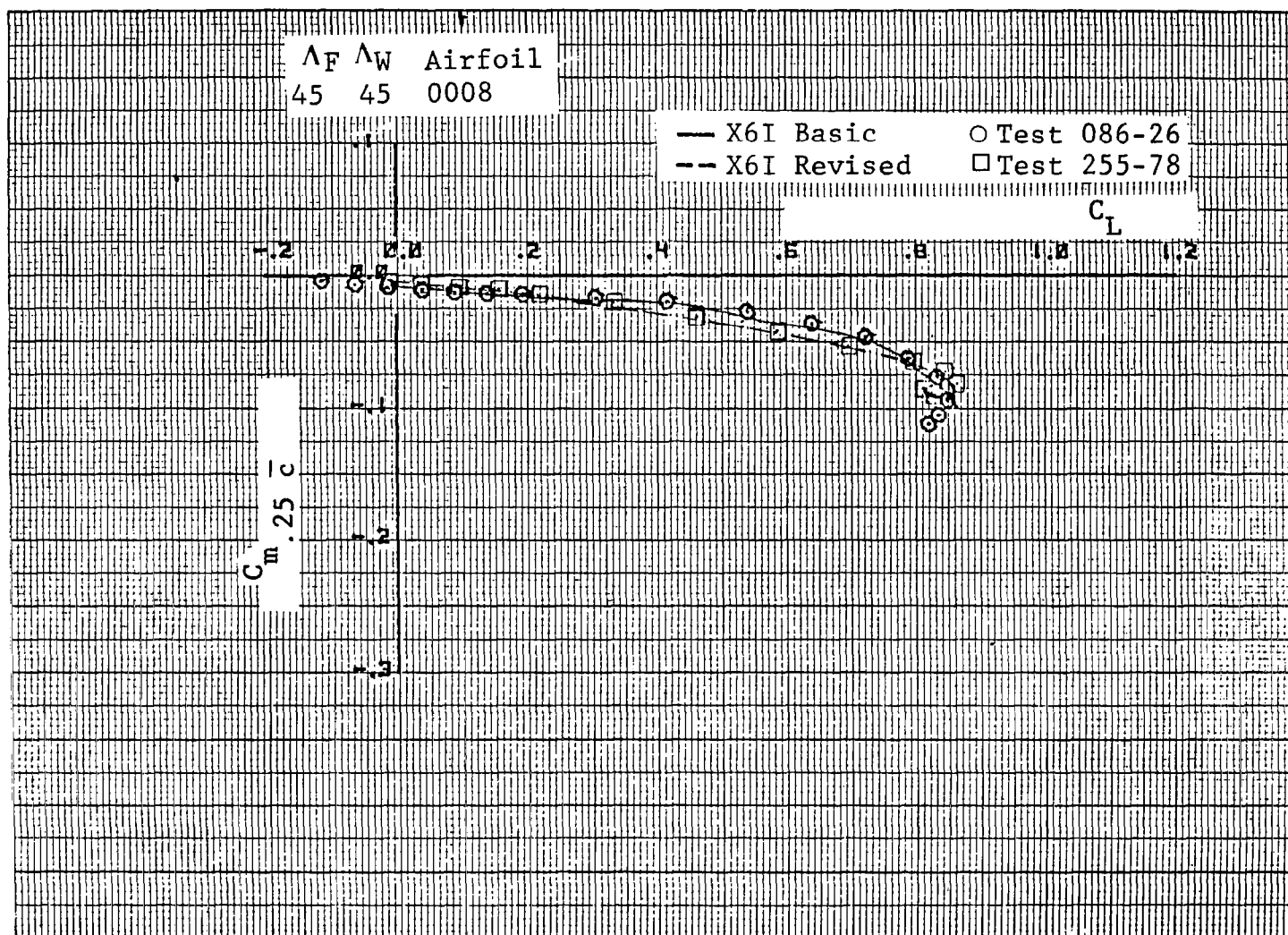
(d) Pitching-Moment Variations with Lift

Figure 224.   Concluded
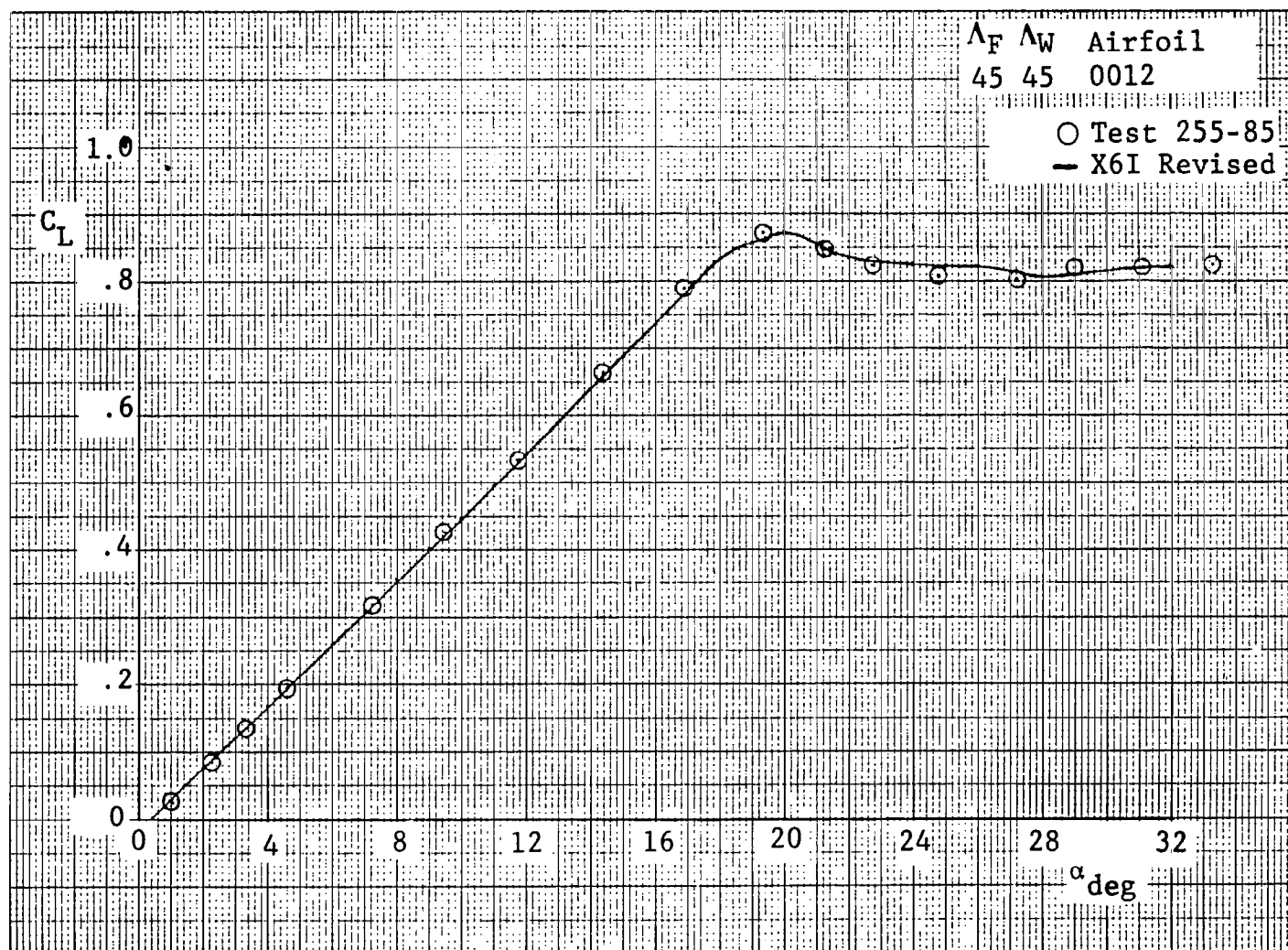
(a) Lift Curve

Figure 225. Comparisons of Revised SHIPS Prediction and Test
for Wing III with NACA 0012 Airfoils
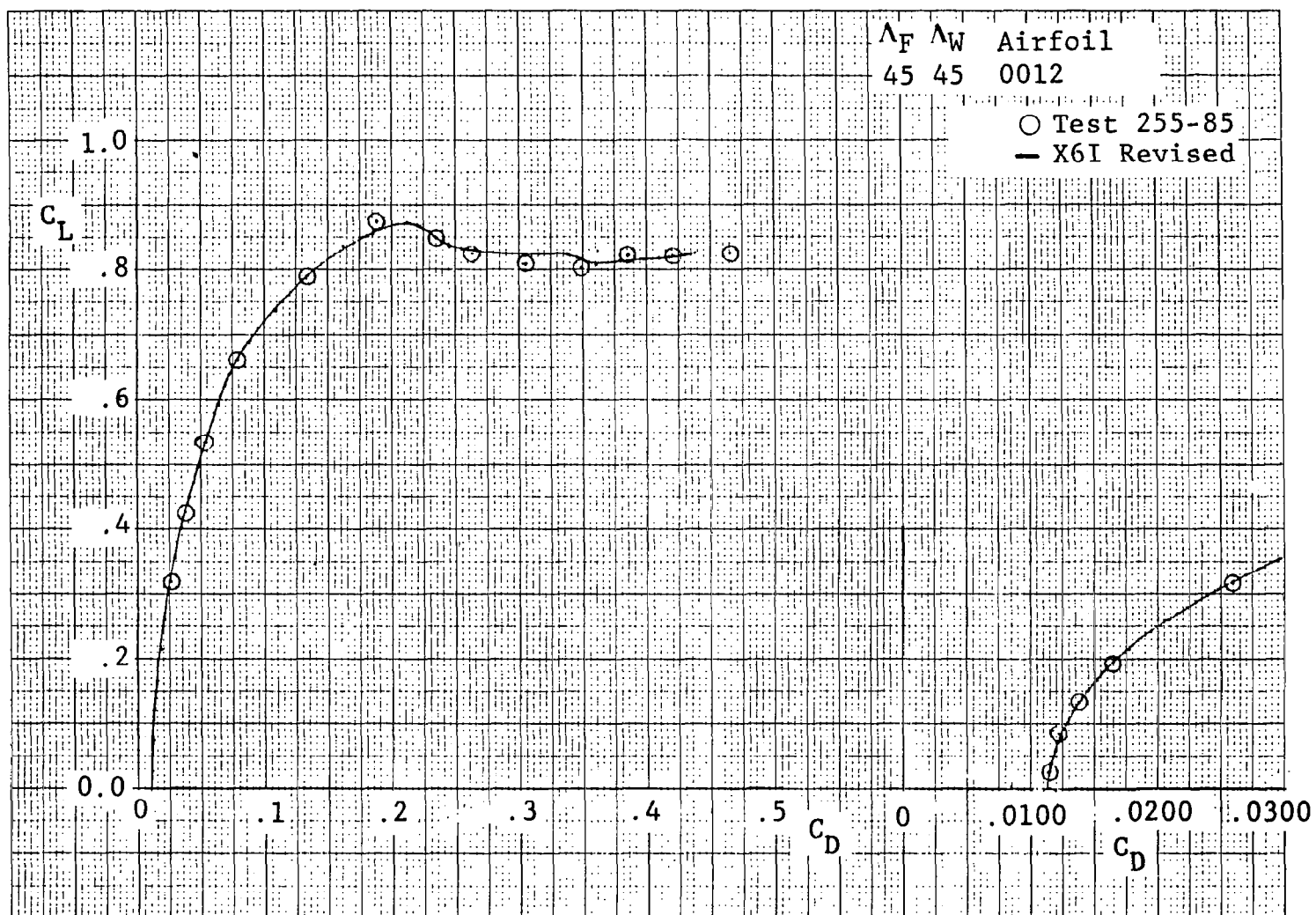
(b) Drag Polar

Figure 225. Continued
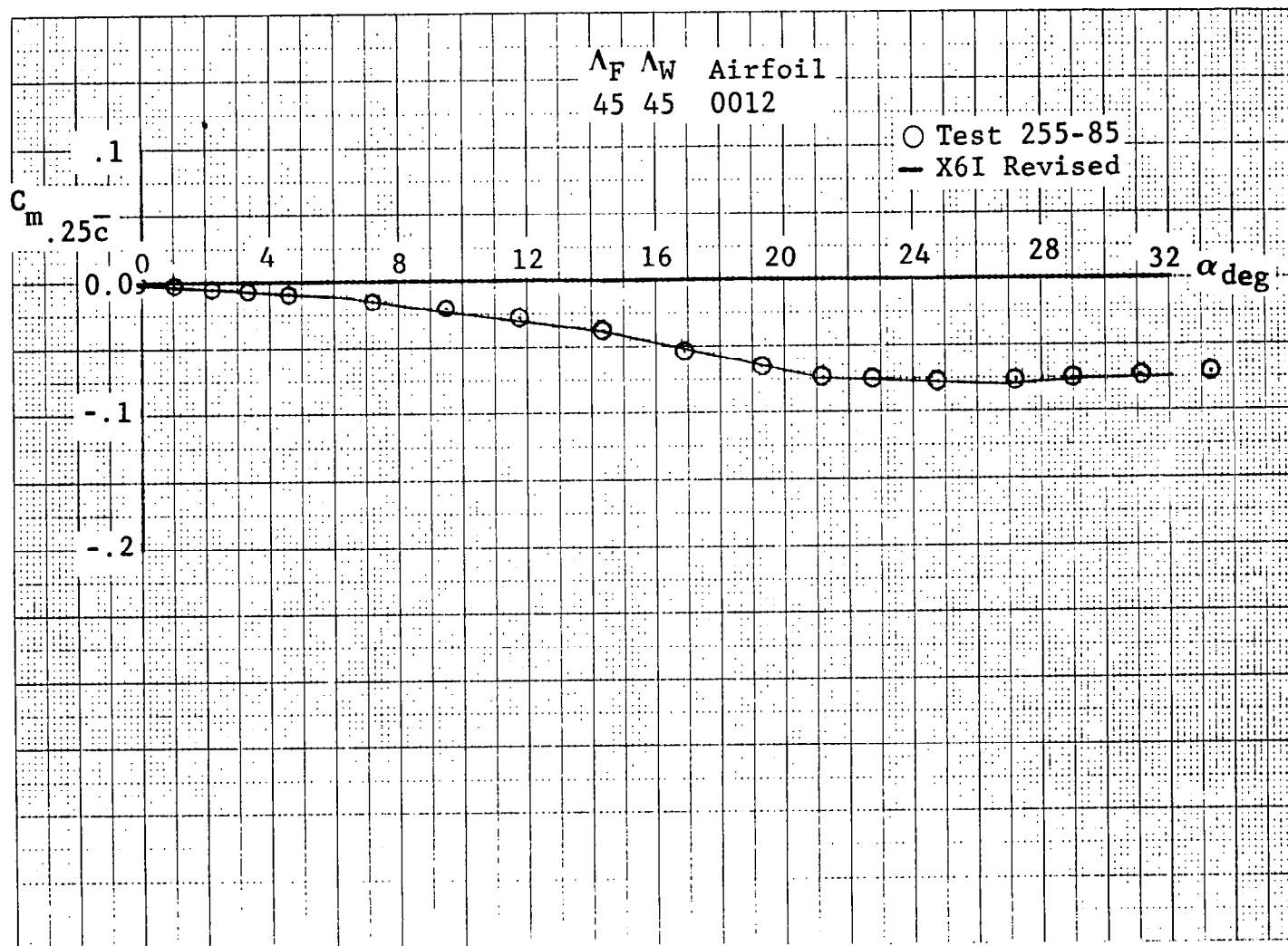
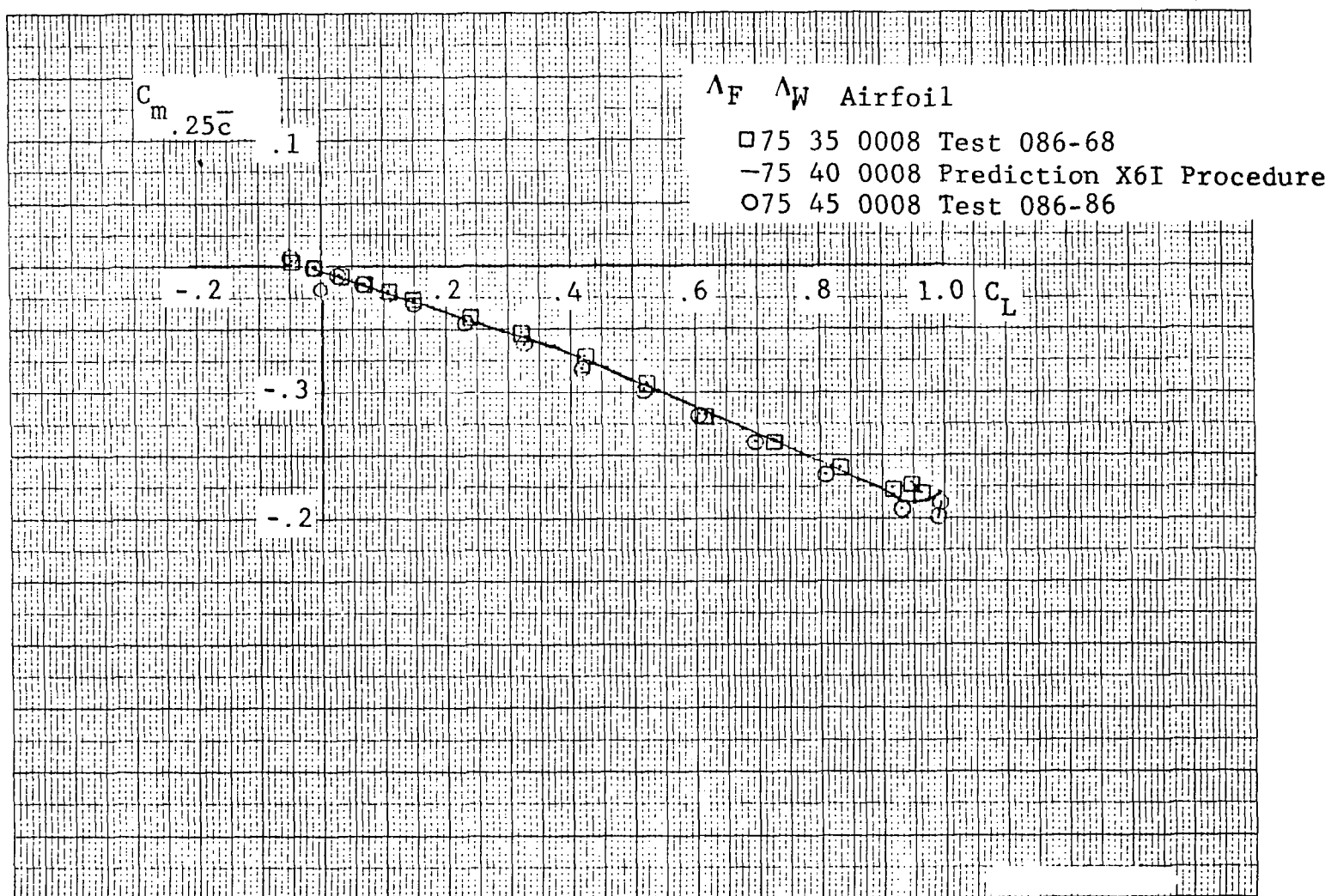(c) Pitching-Moment Variation with Angle of Attack

Figure 225. Continued
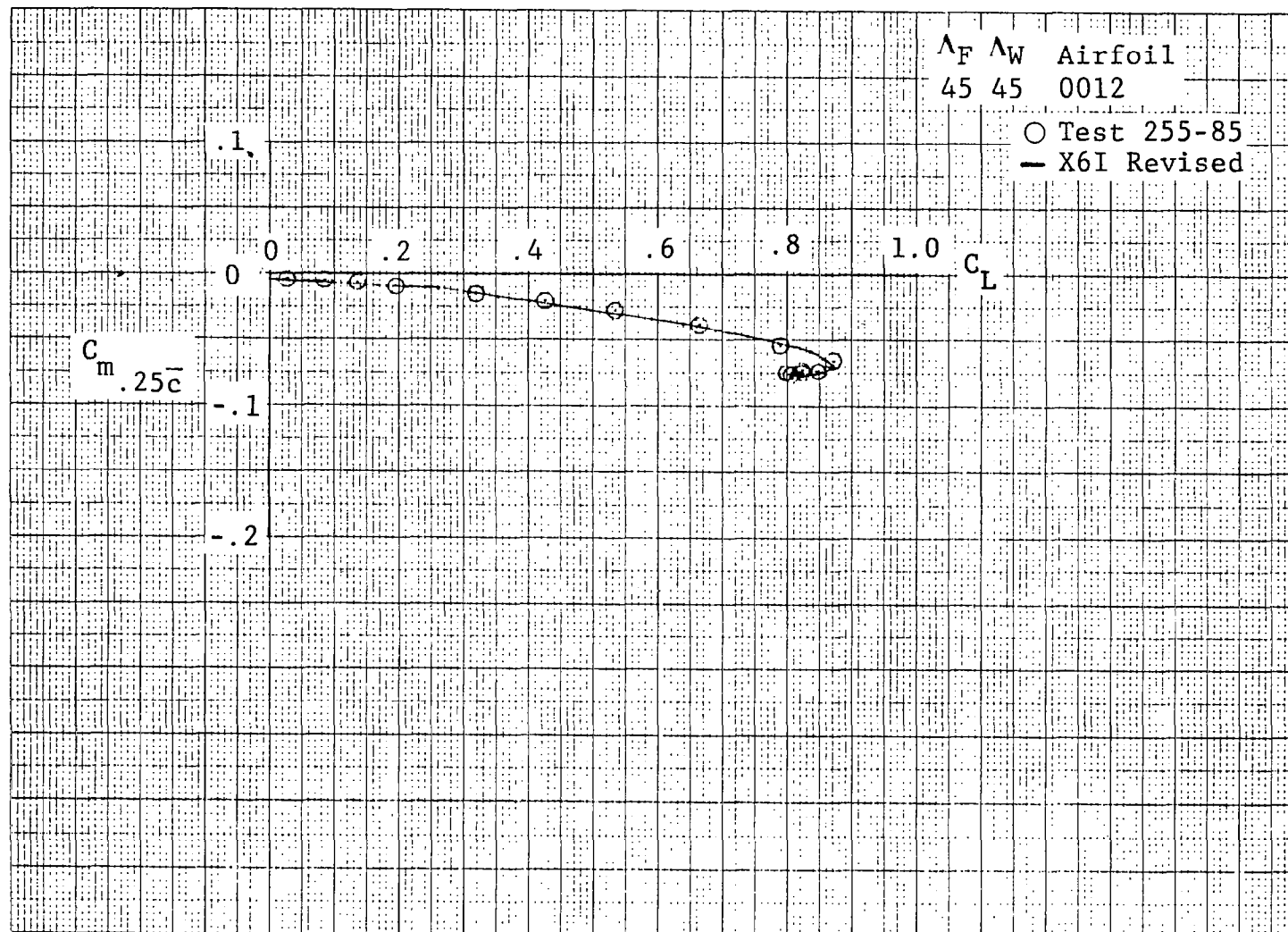
(d) Pitching-Moment Variation with Lift

Figure 225. Concluded
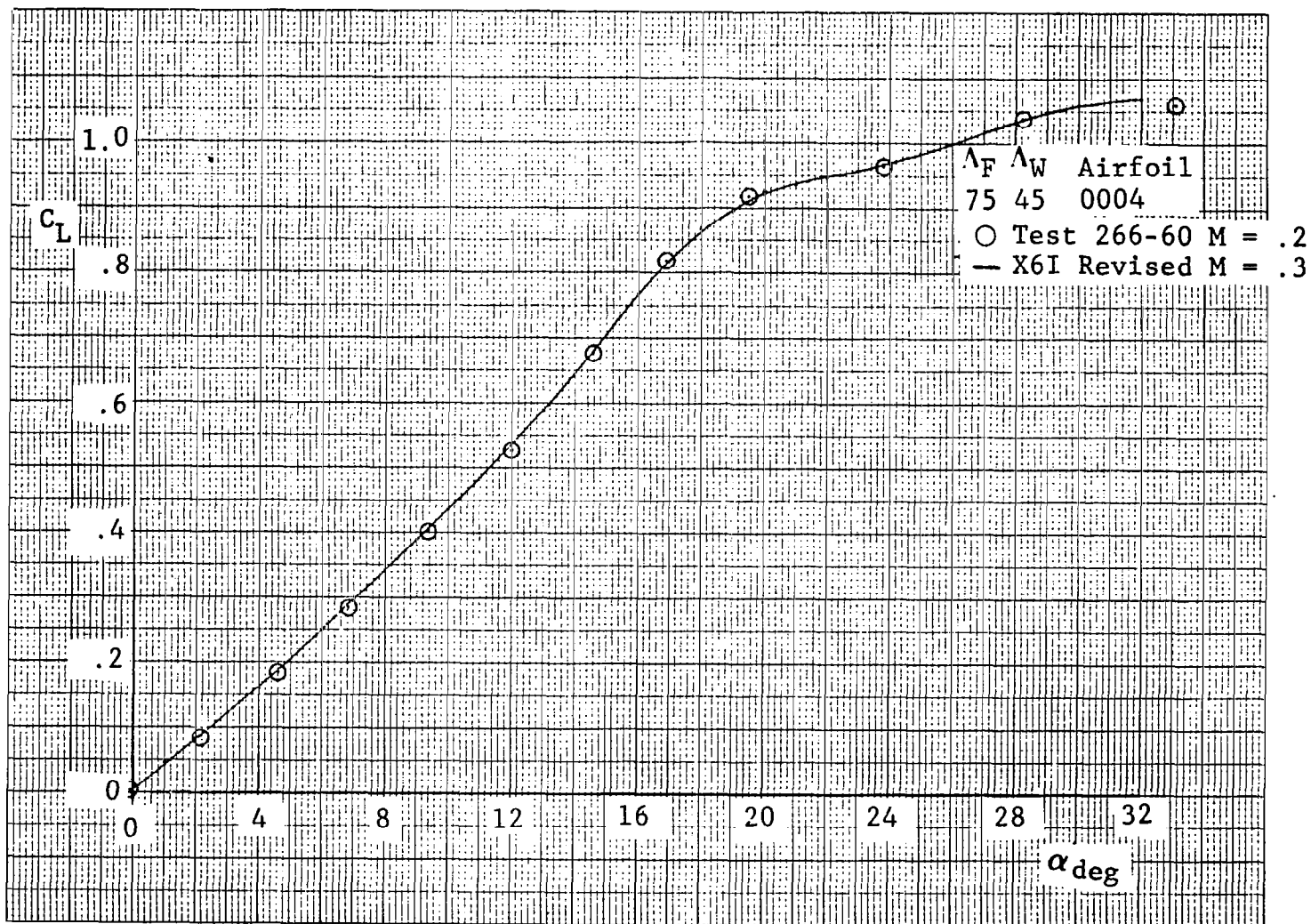
(a) Lift Curve

Figure 226. Comparisons of Revised SHIPS Prediction and Test
for Wing III with 75° Fillet and NACA 0004 Airfoils
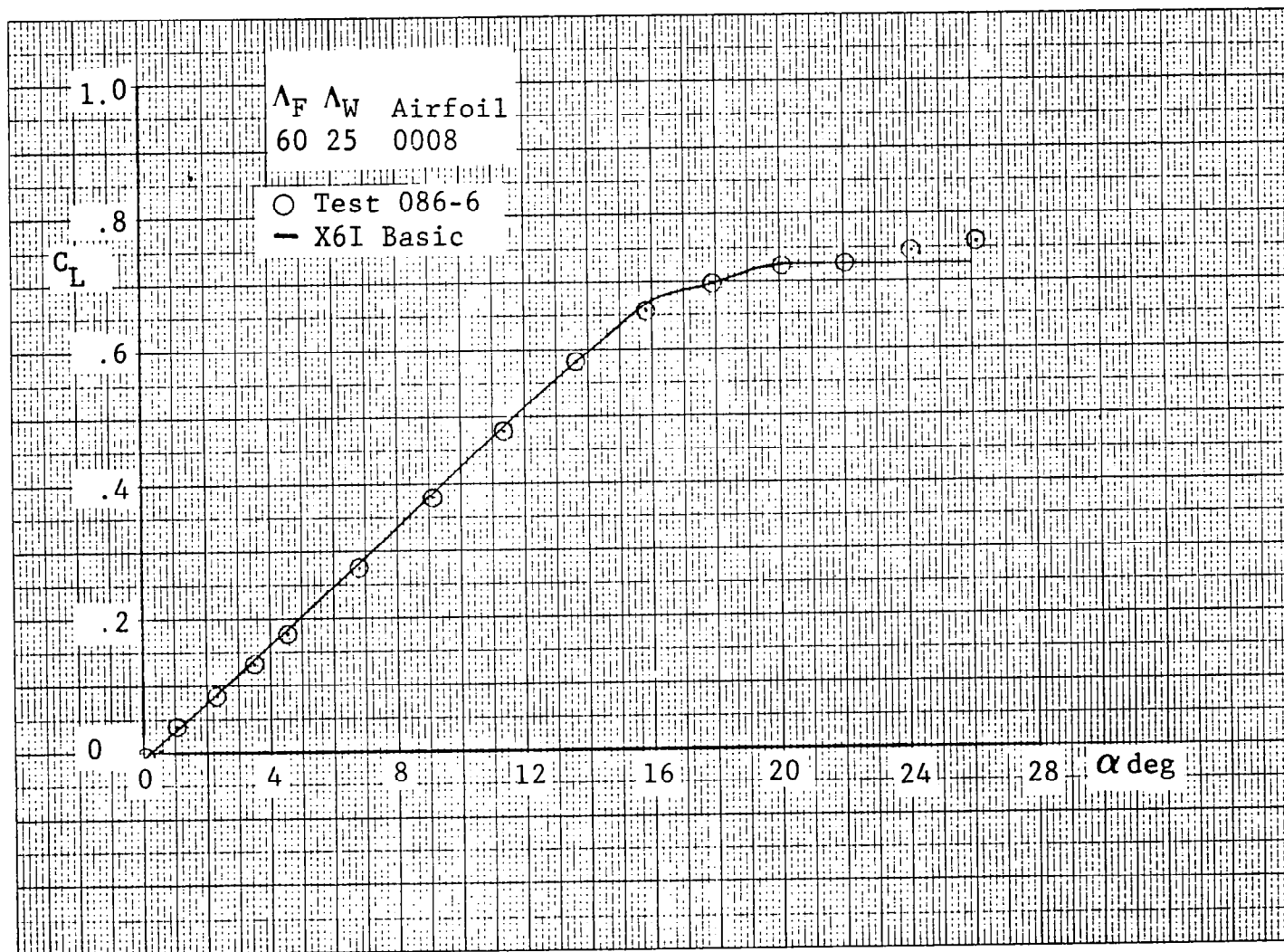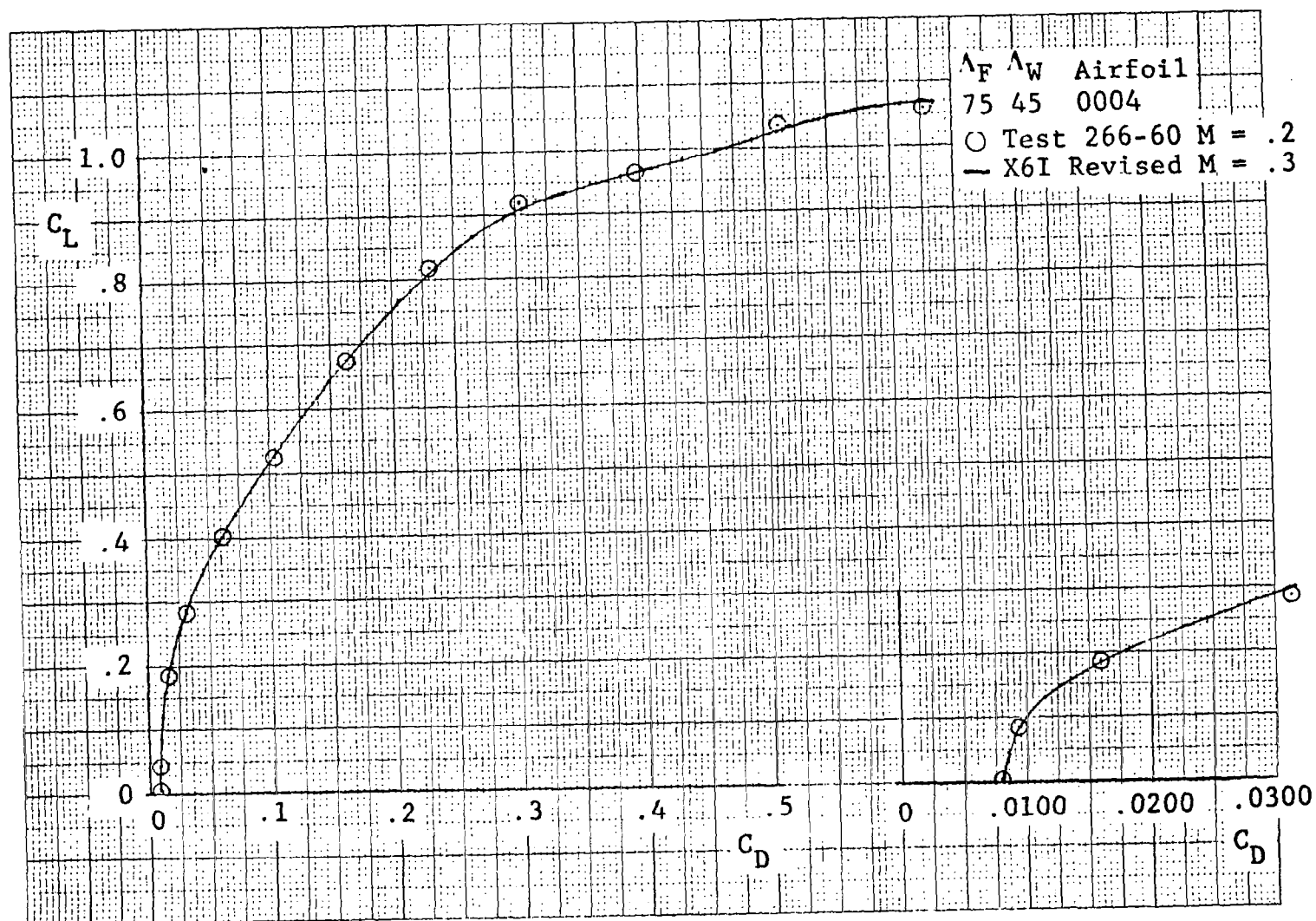
(b) Drag Polar

Figure 226. Continued
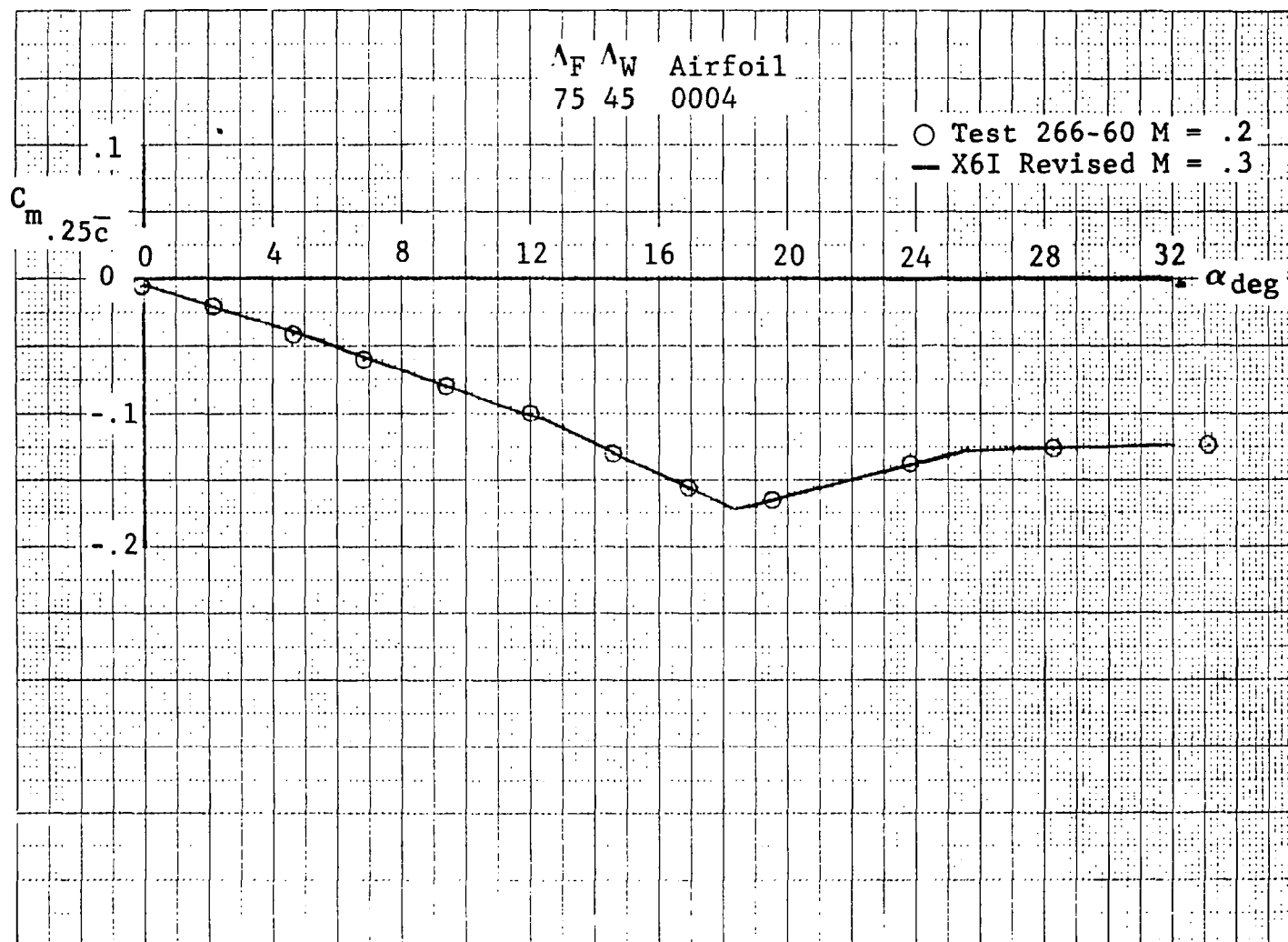
(c)   Pitching-Moment Variation with Angle of Attack.
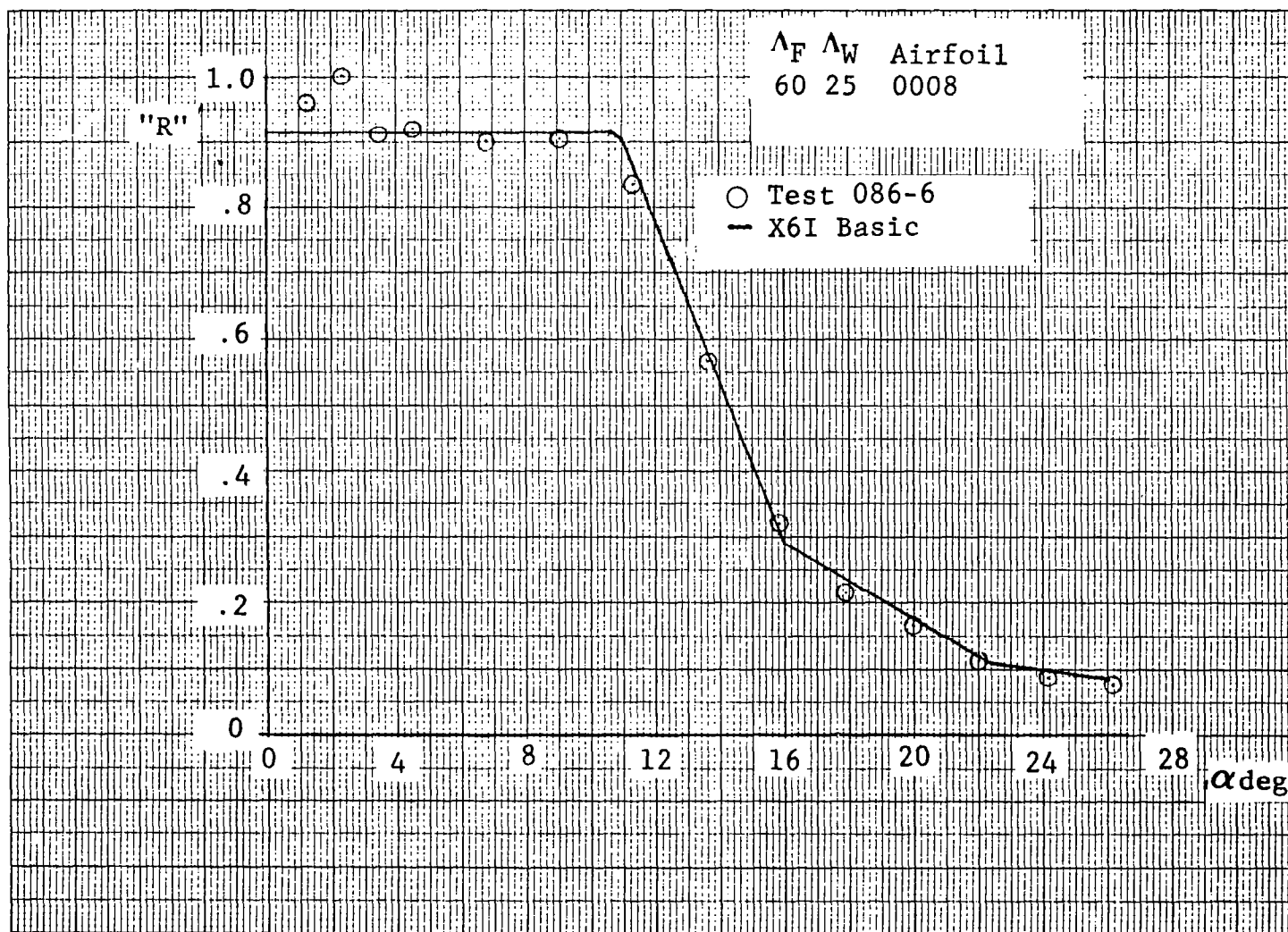
Figure 226.   Continued
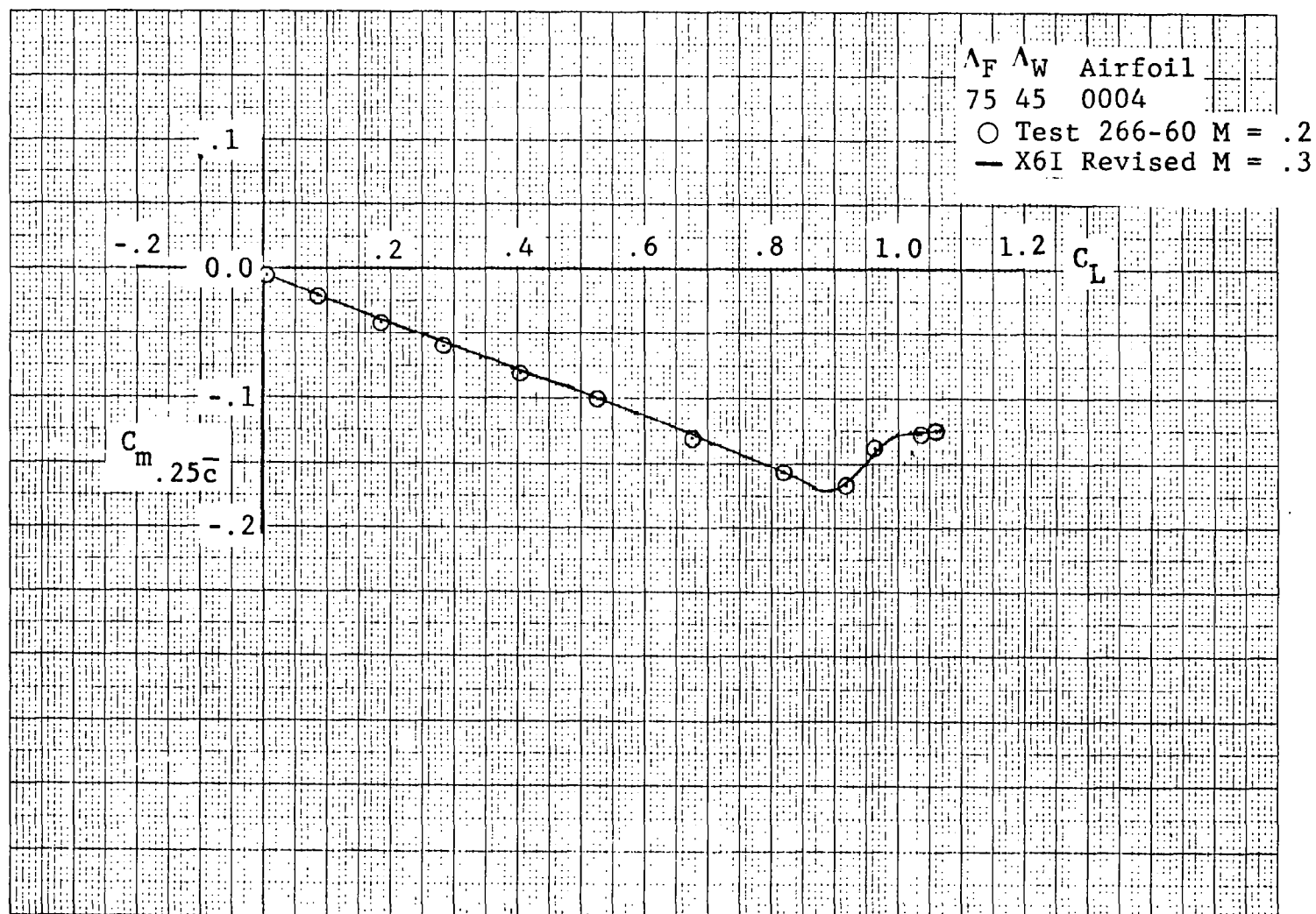
(d) Pitching Moment Variation with lift

Figure 226. Concluded
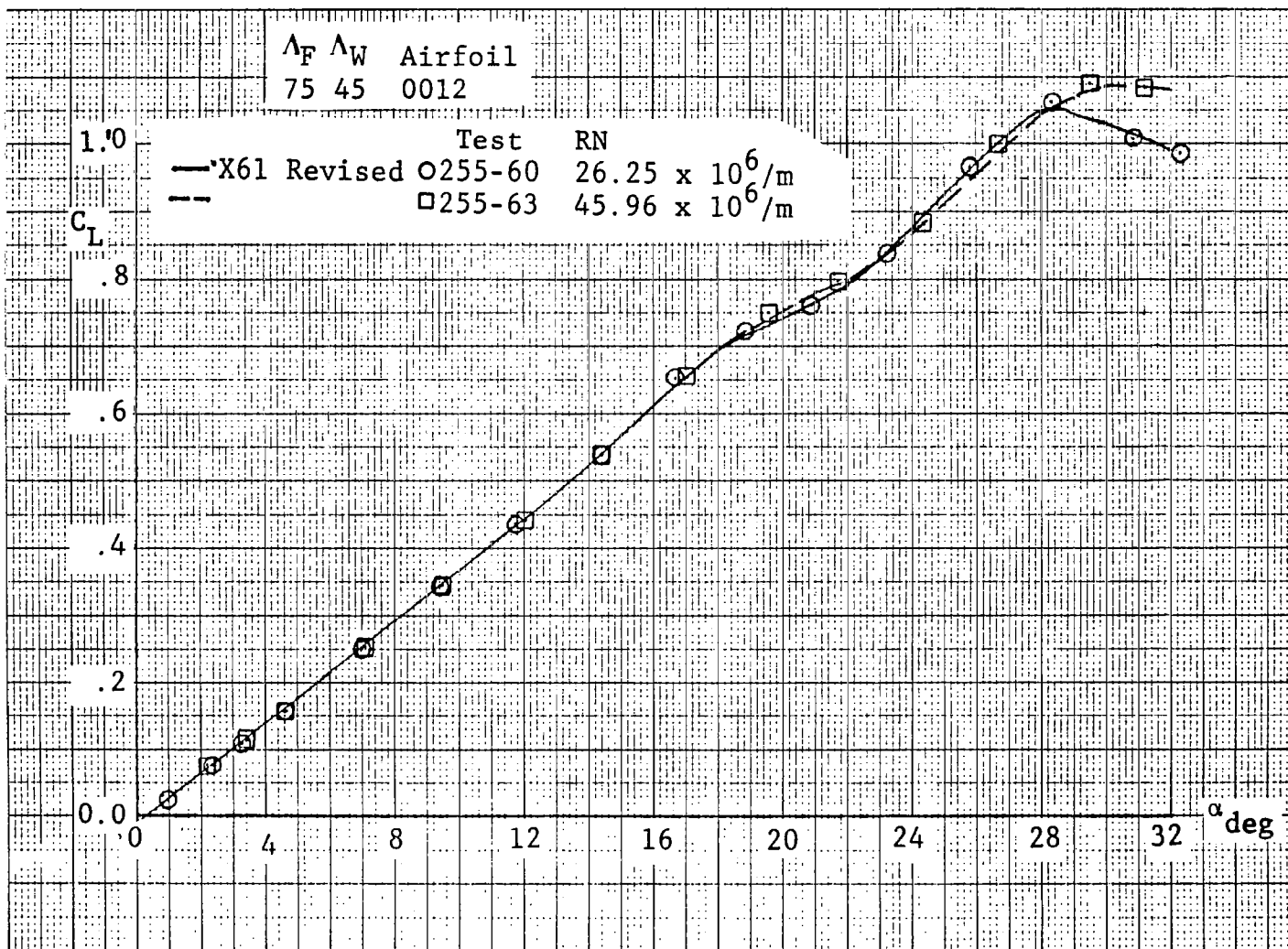
(a) Lift Curve

Figure 227. Comparisons of Revised SHIPS Predictions and Test
for Wing III with 75° Fillet and NACA 0012 Airfoils
Show Effects of Reynolds Number
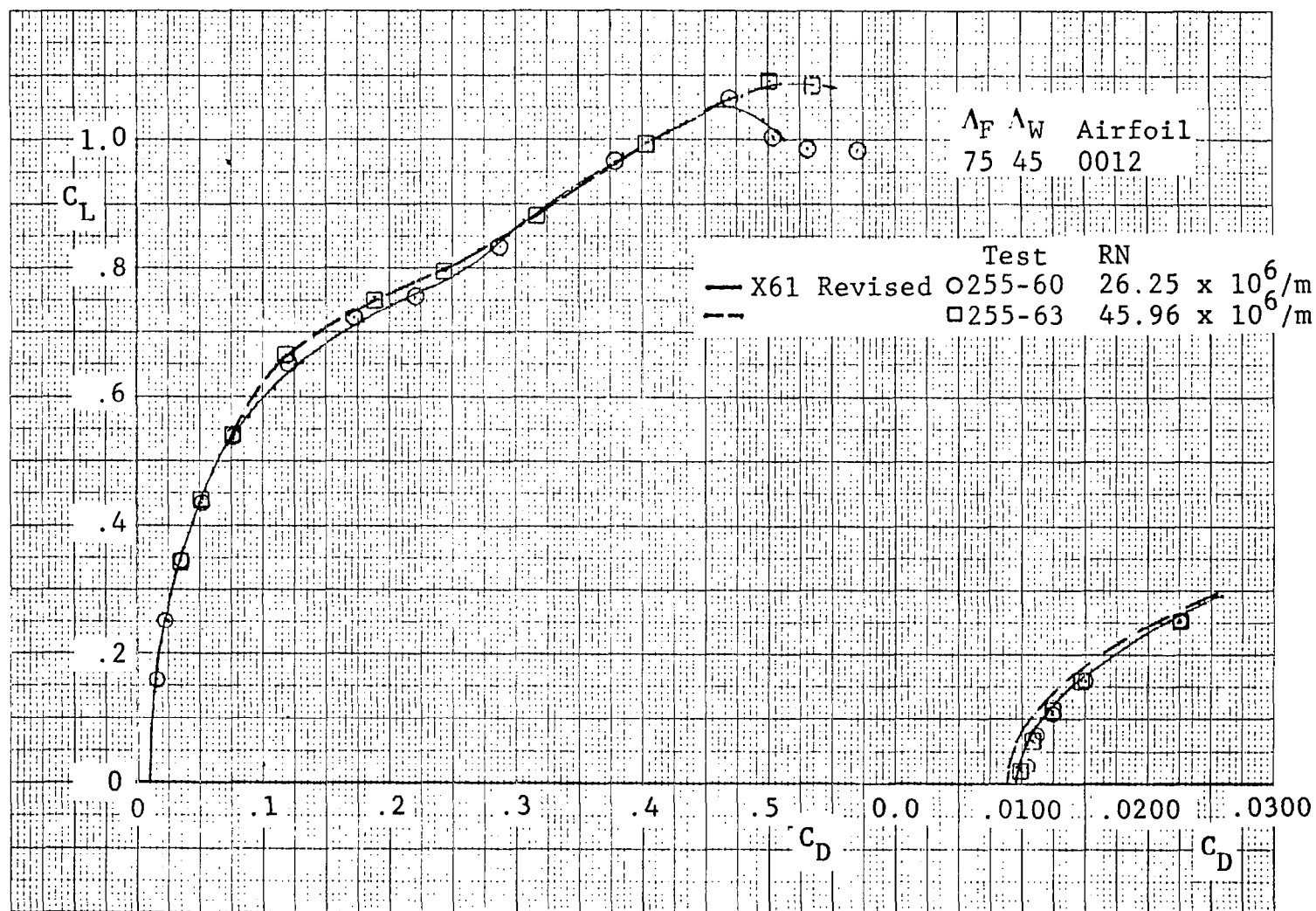
(b) Drag Polar

Figure 227. Continued
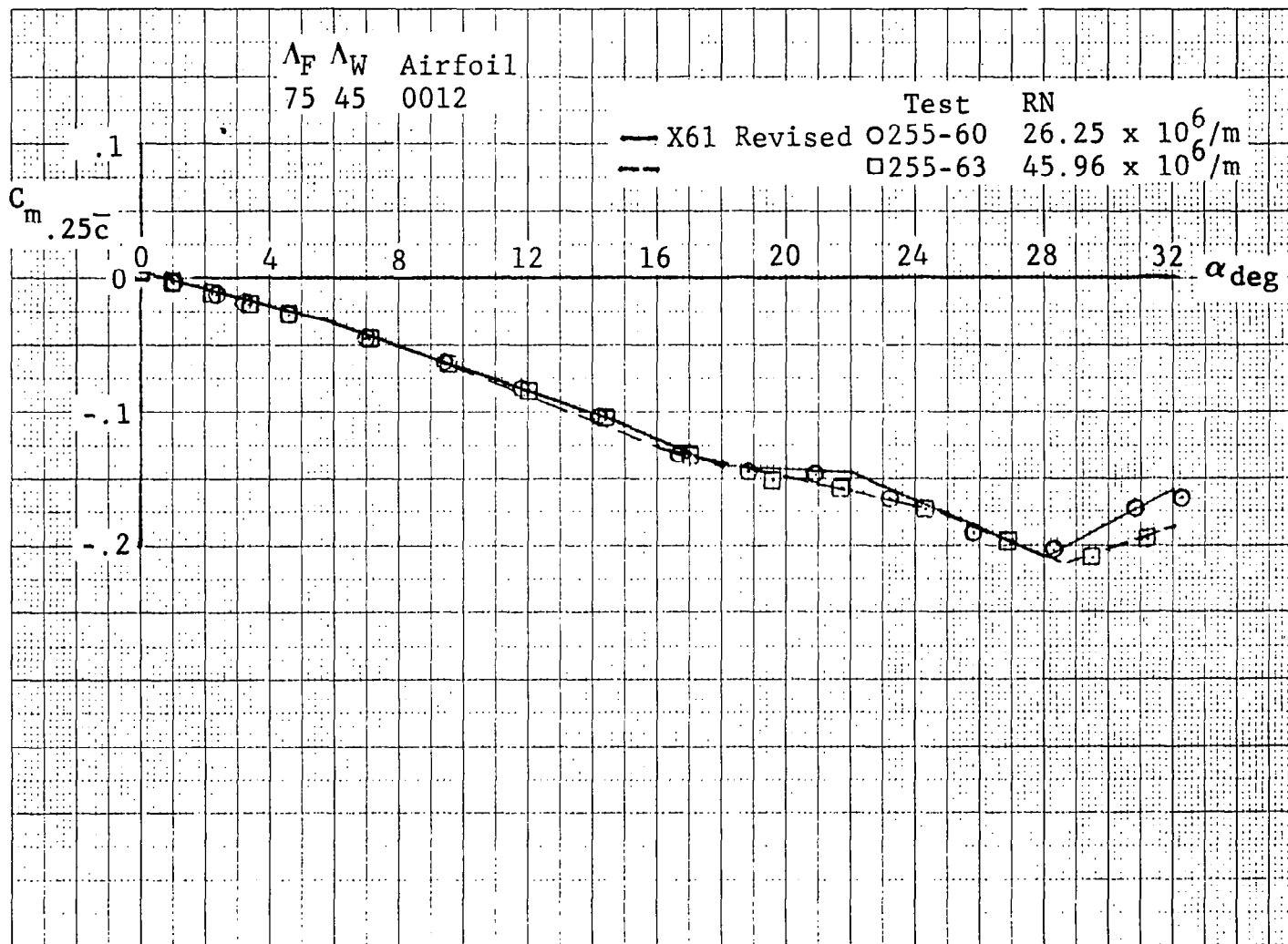
(c) Pitching-Moment Variation with Angle of Attack

Figure 227. Continued
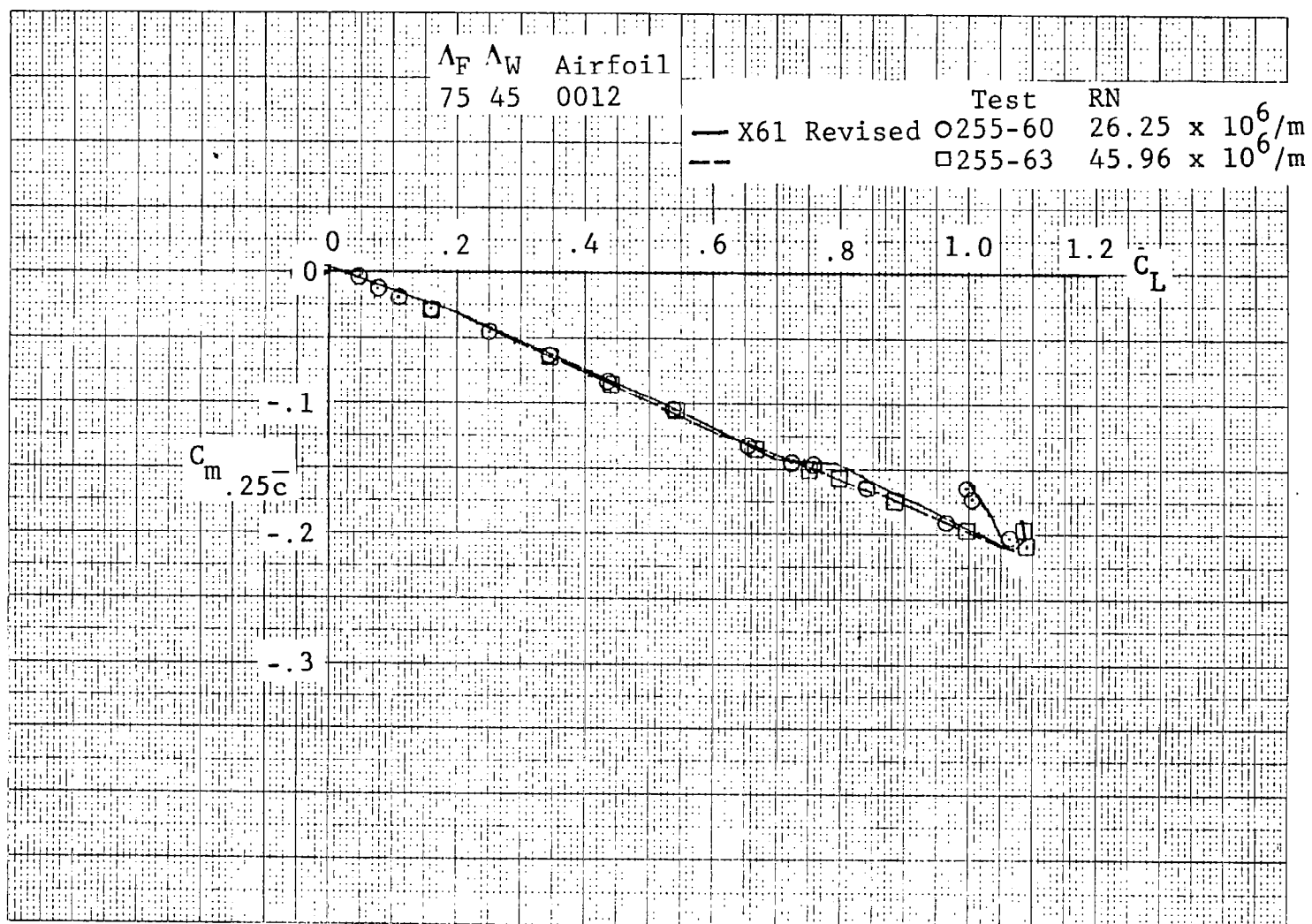
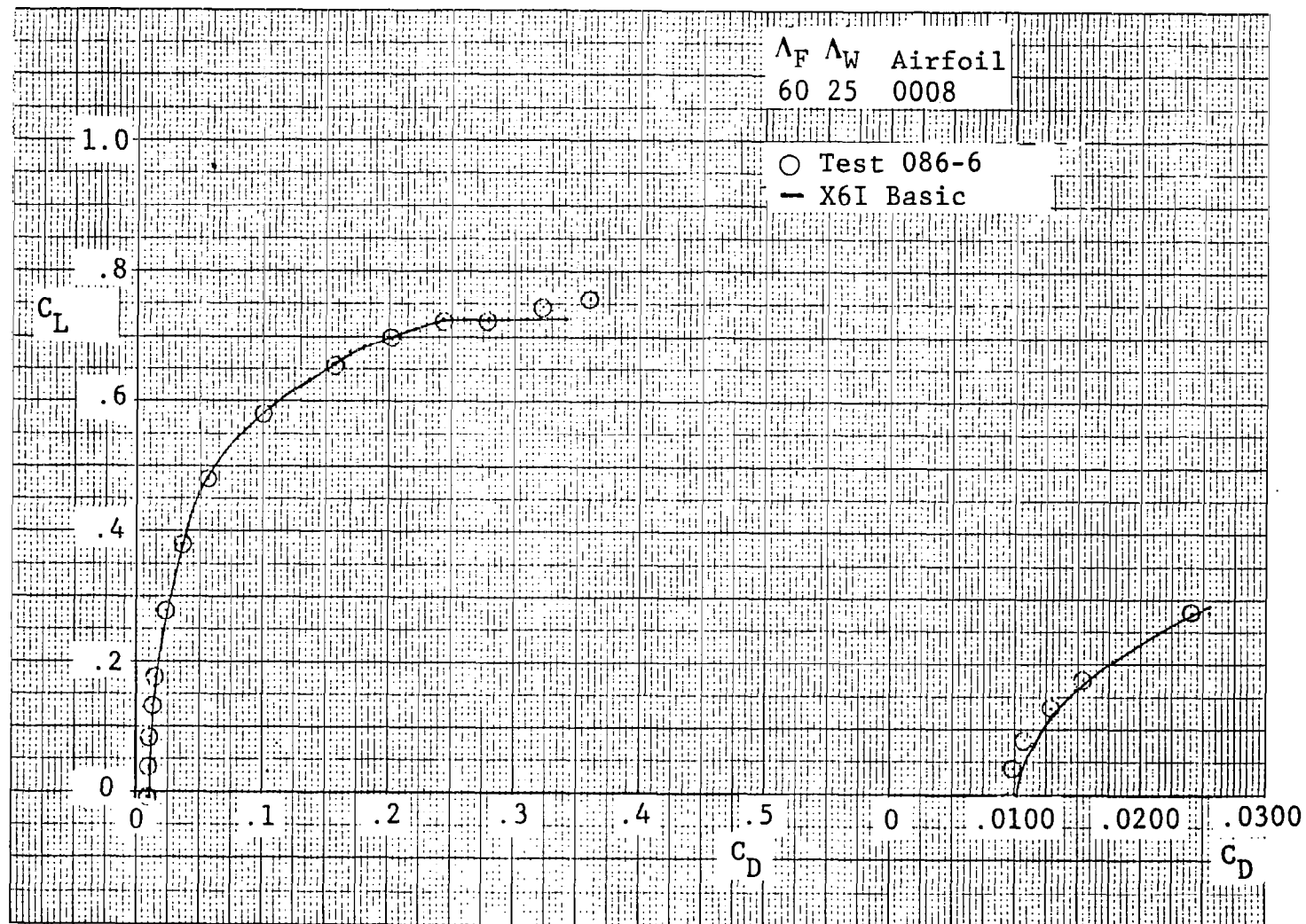(d)   Pitching-Moment Variations with Lift
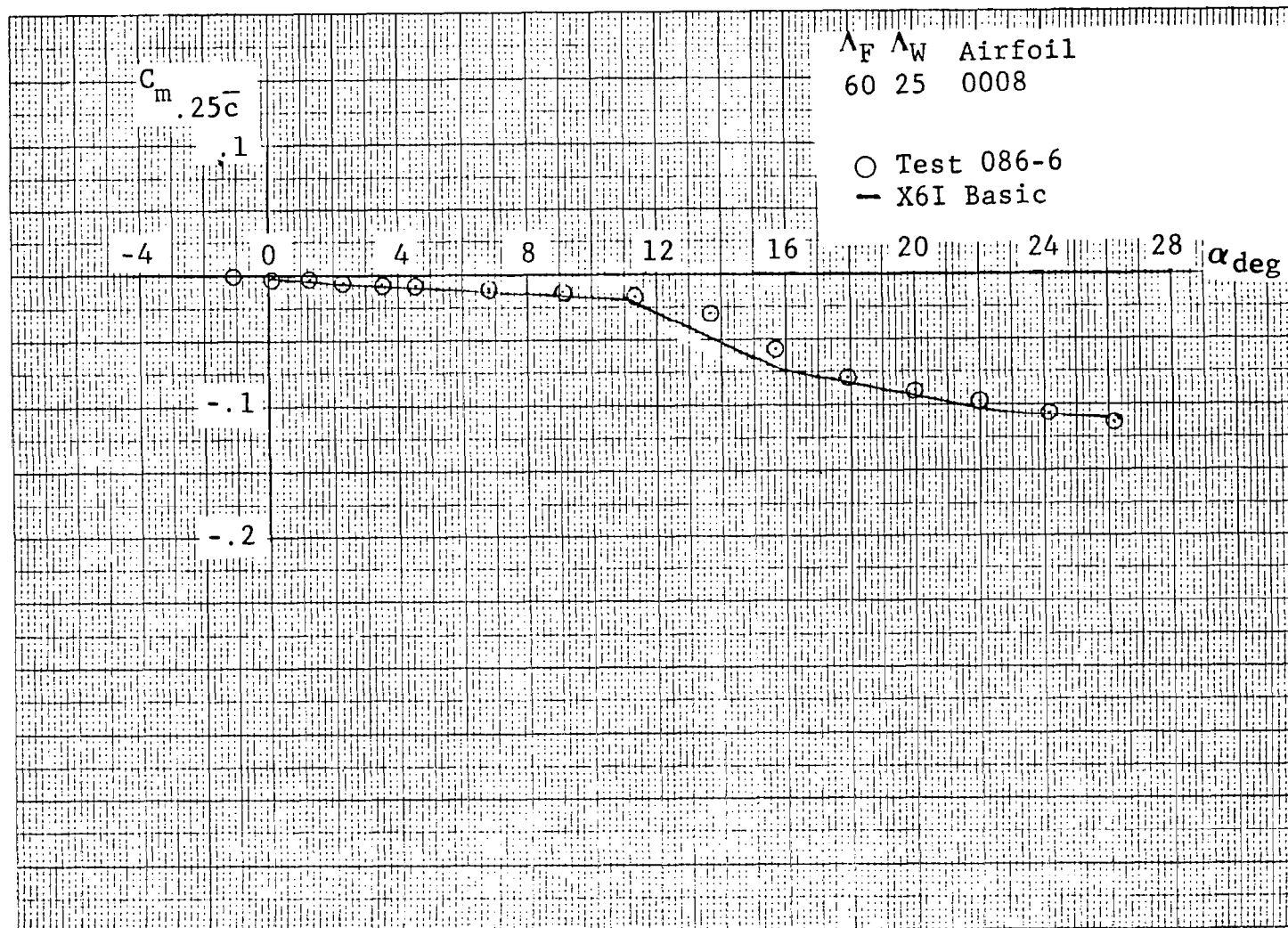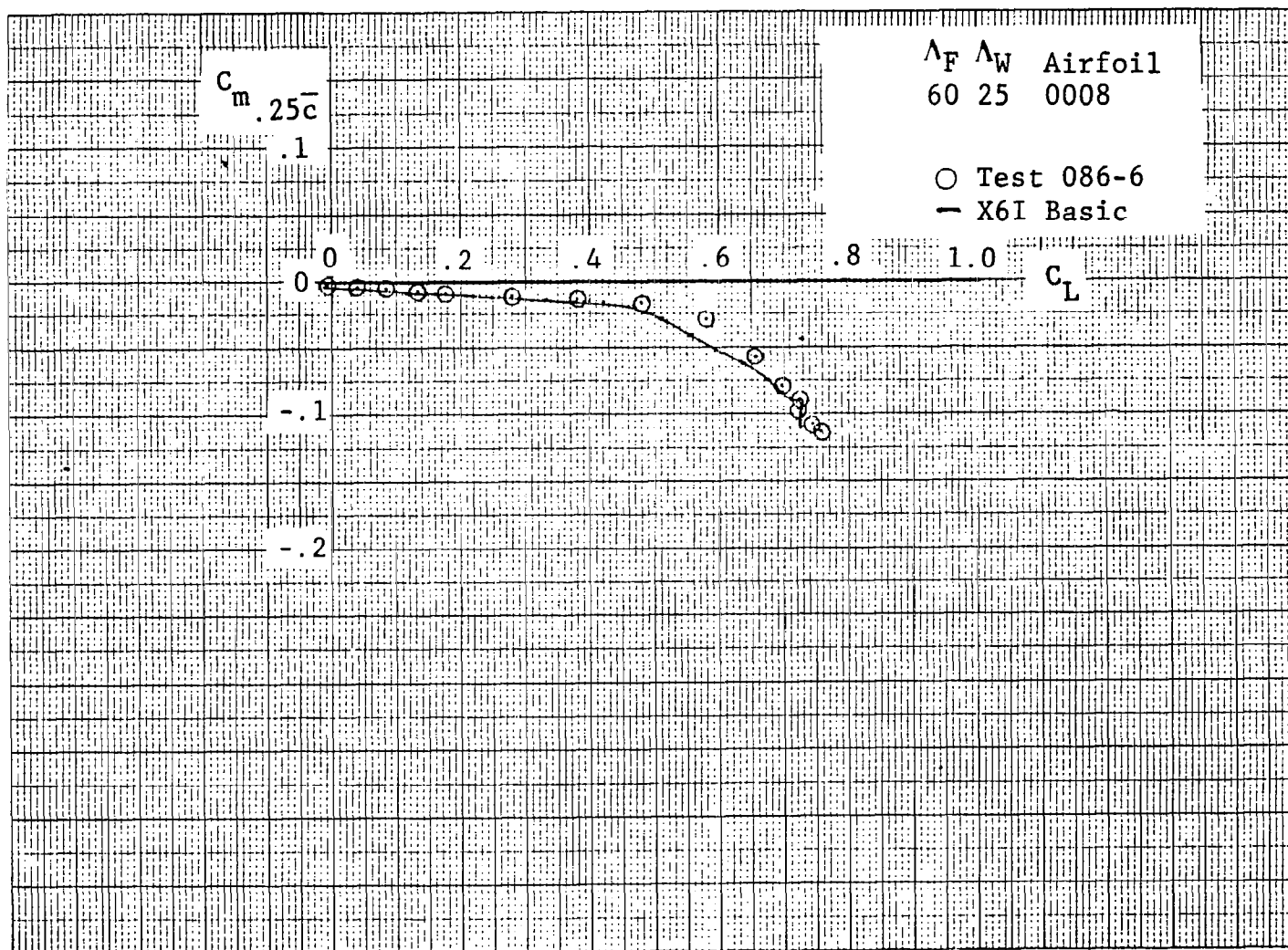
Figure 227.   Concluded
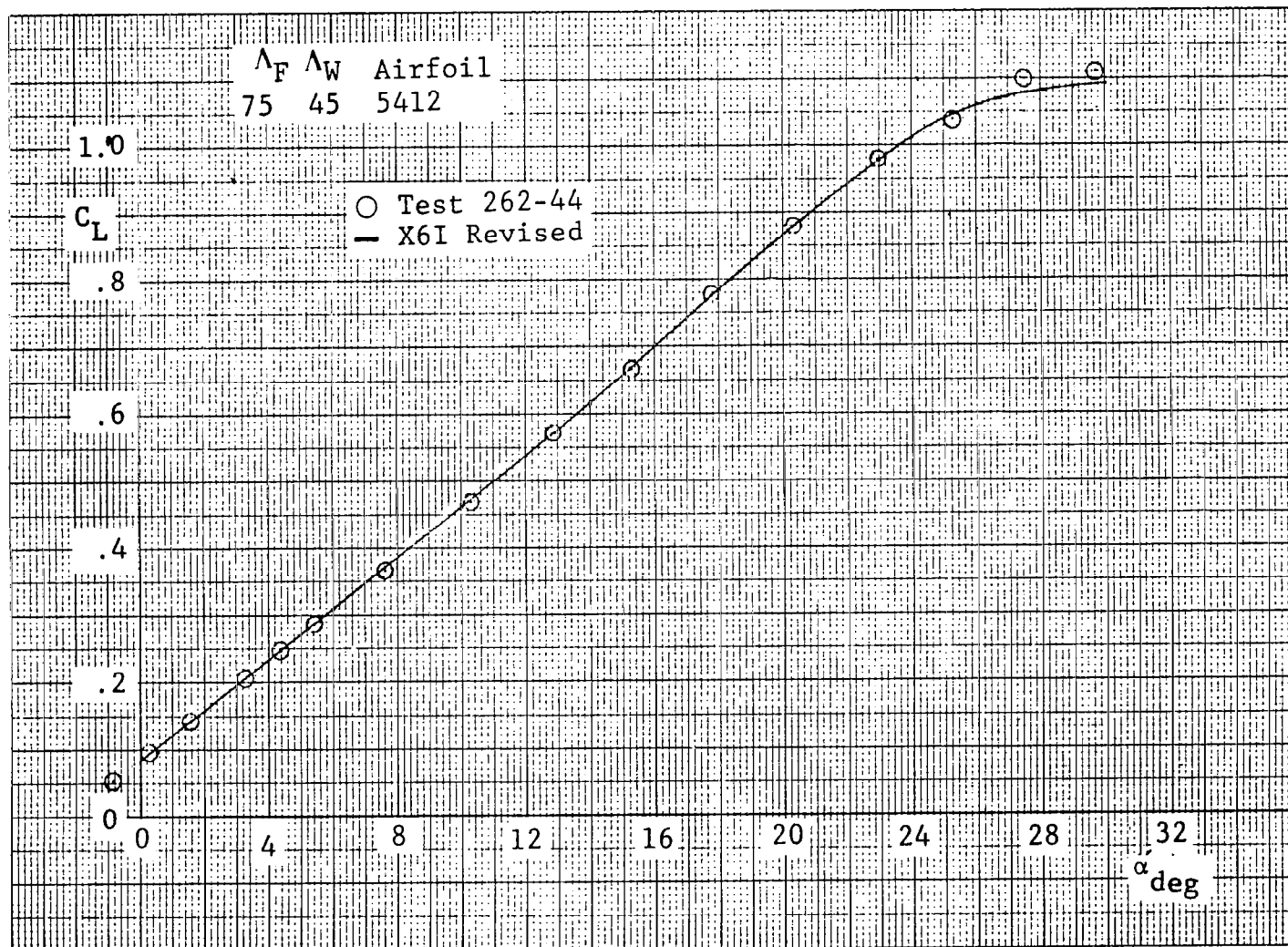
(a) Lift Curve

Figure 228. Comparisons of Revised SHIPS Prediction and Test
for Wing III with 75° Fillet and Cambered NACA
$65_1 412$ Airfoil
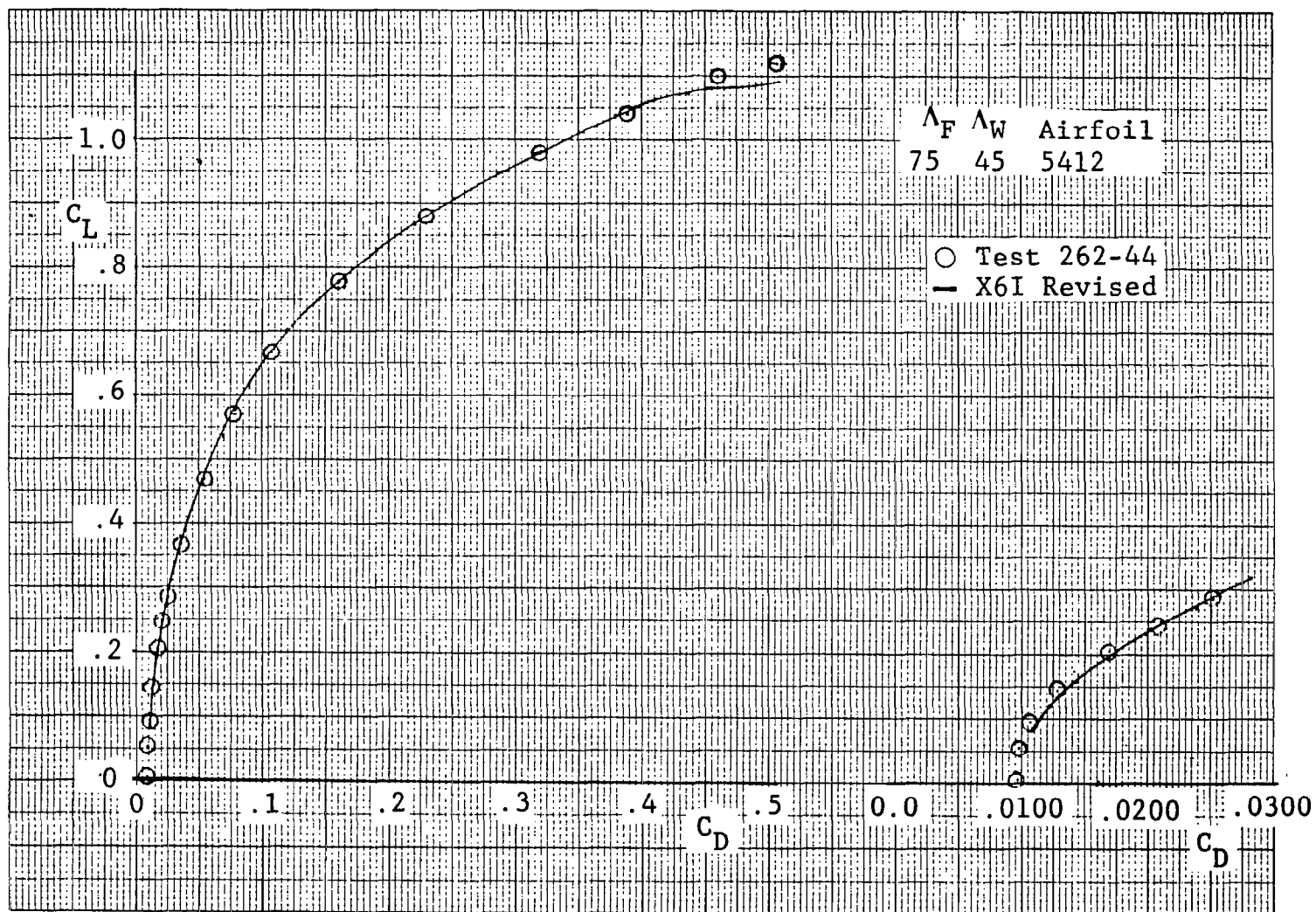
(b) Drag Polar

Figure 228. Continued
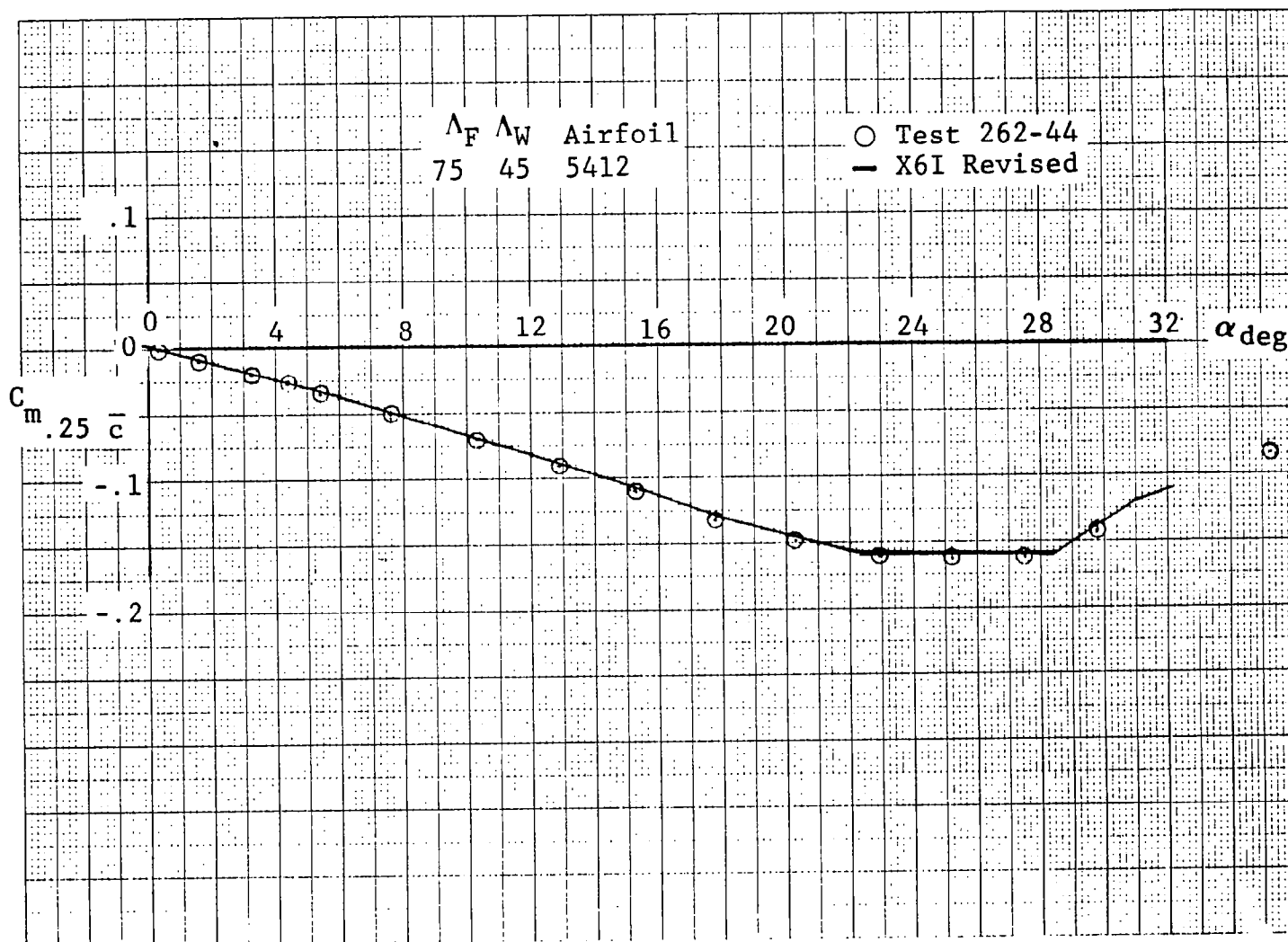
(c) Pitching-Moment Variation with Angle of Attack

Figure 228. Continued

Λ_F Λ_W Airfoil

75 45 5412

○ Test 262-44
— X6I Revised

.1

0.0   .2   .4   .6   .8   1.0   1.2 C_L

0

-.1

C_m .25$\bar{c}$

-.2

-.3
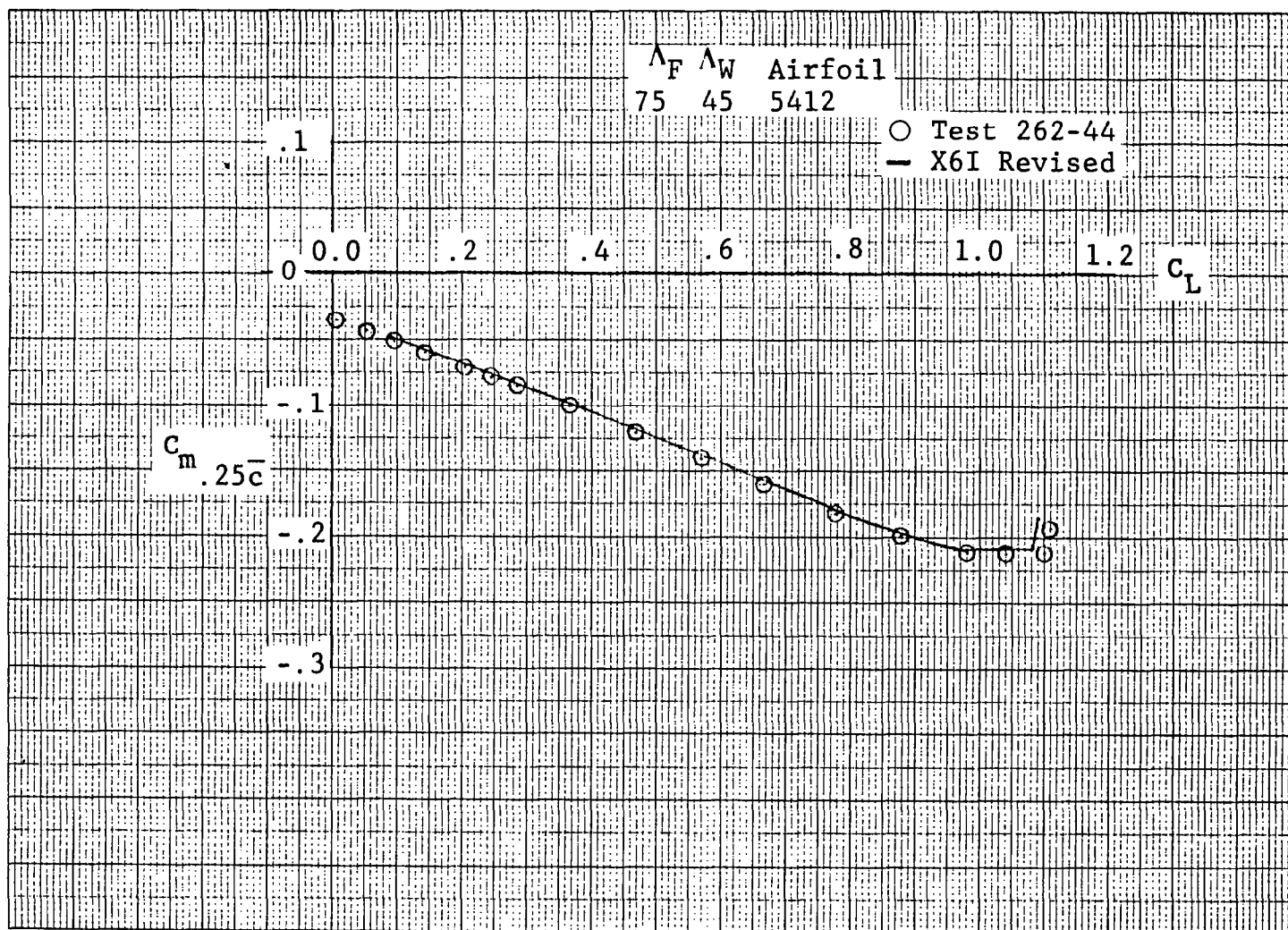
(d)   Pitching-Moment Variation with Lift

Figure 228.   Concluded
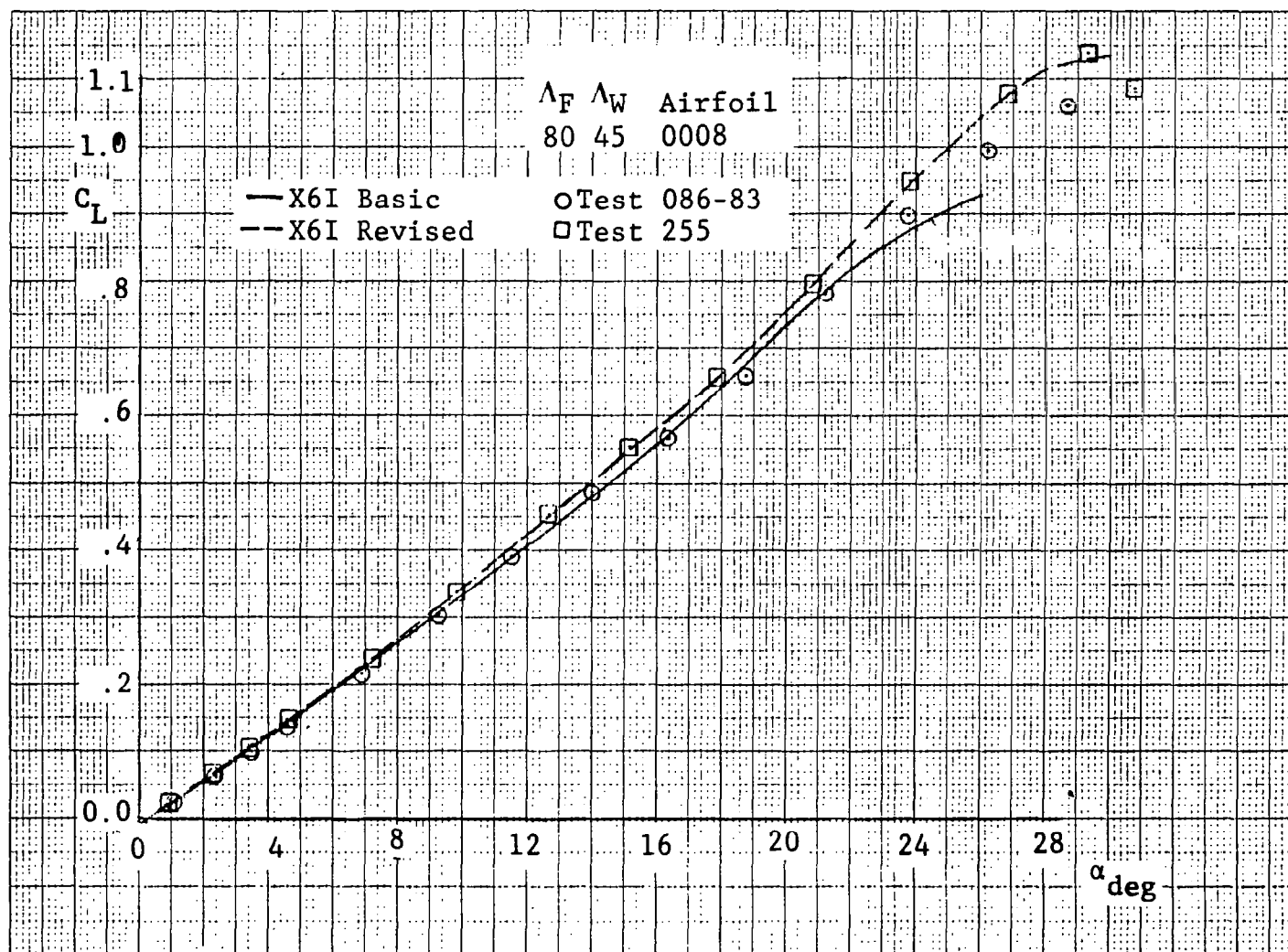
(a) Lift Curve

Figure 229. Comparisons of Basic and REvised SHIPS Predictions and Test for Wing III with 80° Fillet and NACA 0008 Airfoils for Two Different Facilities
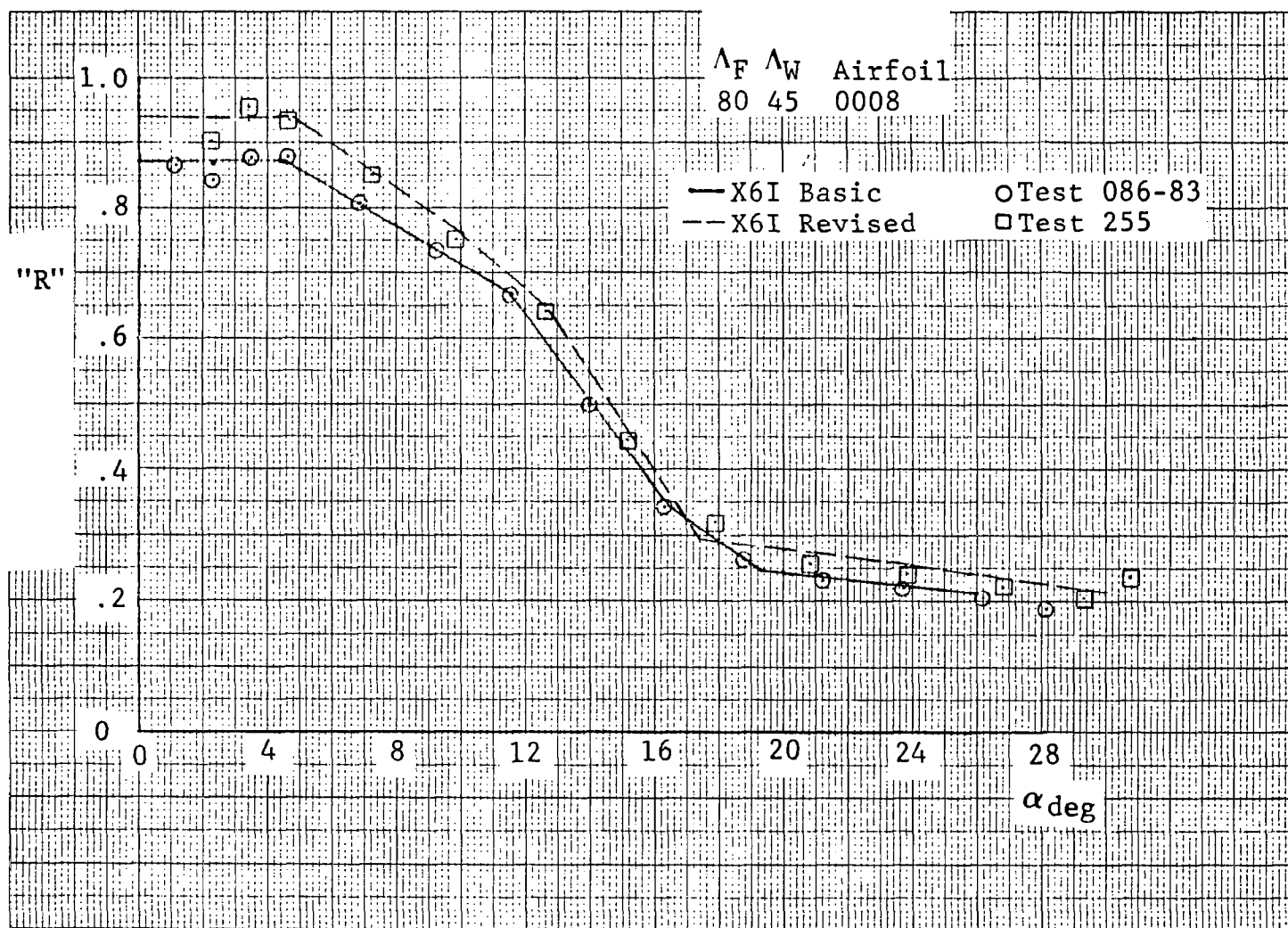
(b)   Suction-Ratio Variations with Angle of Attack

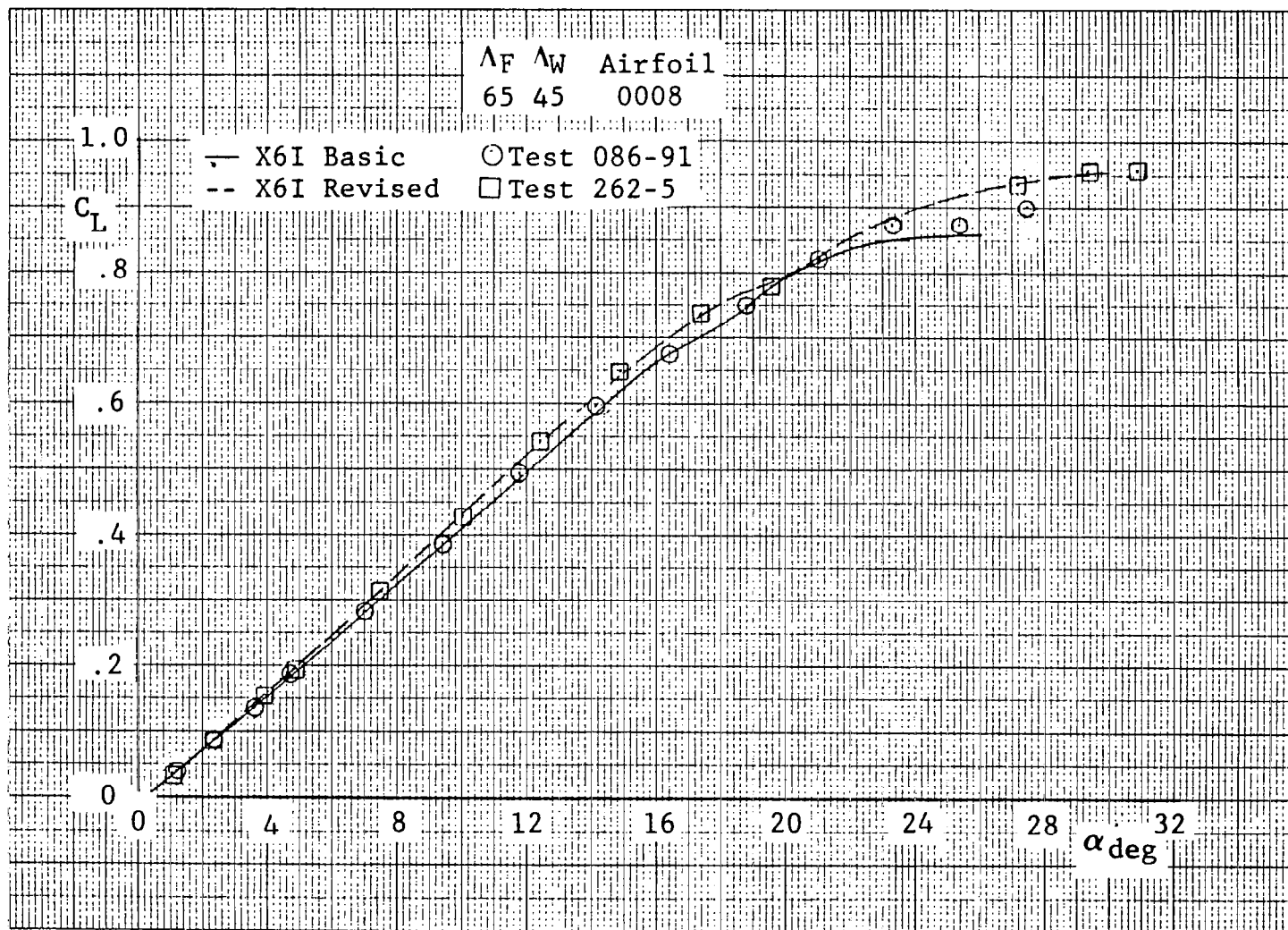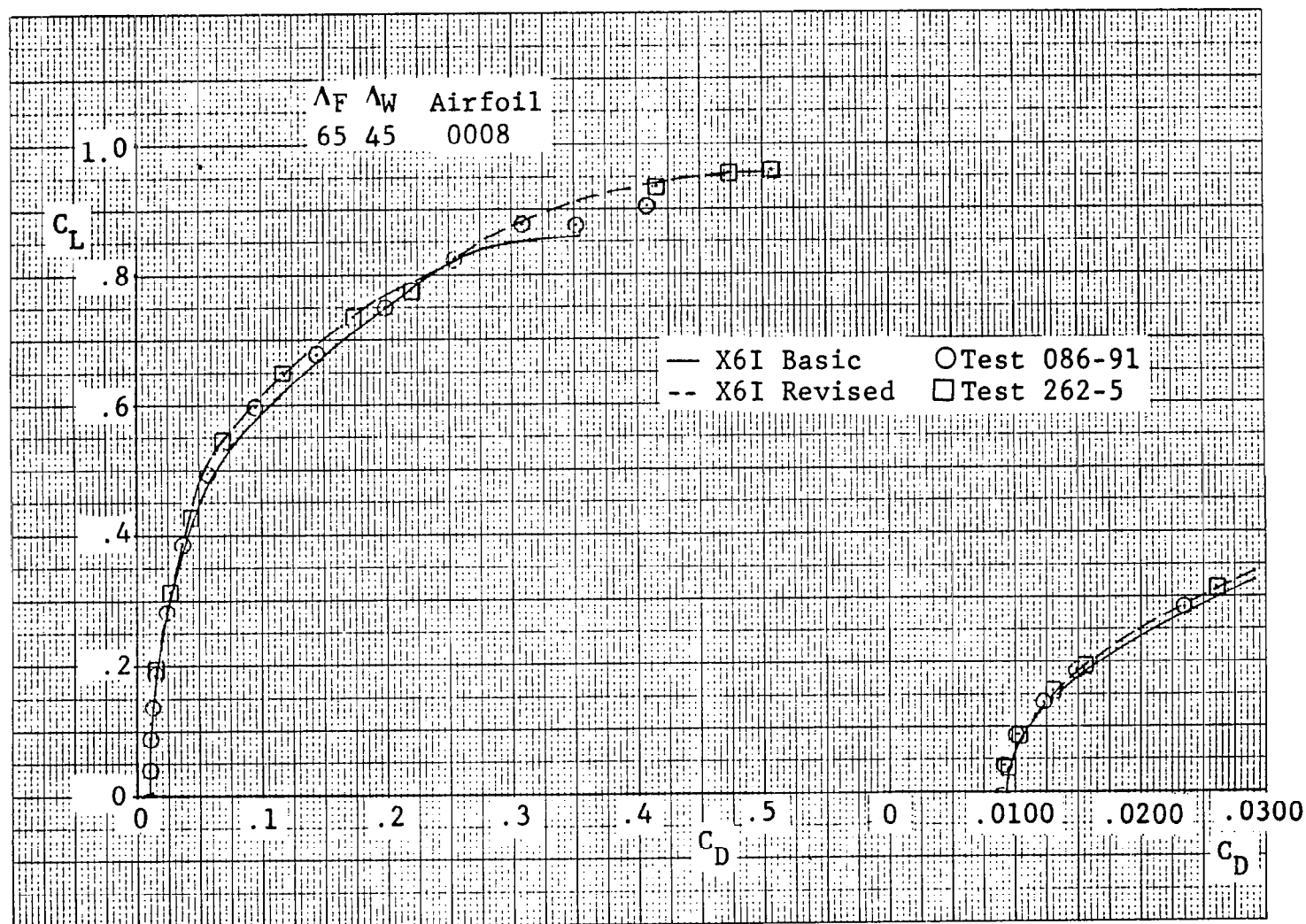Figure 229.   Continued
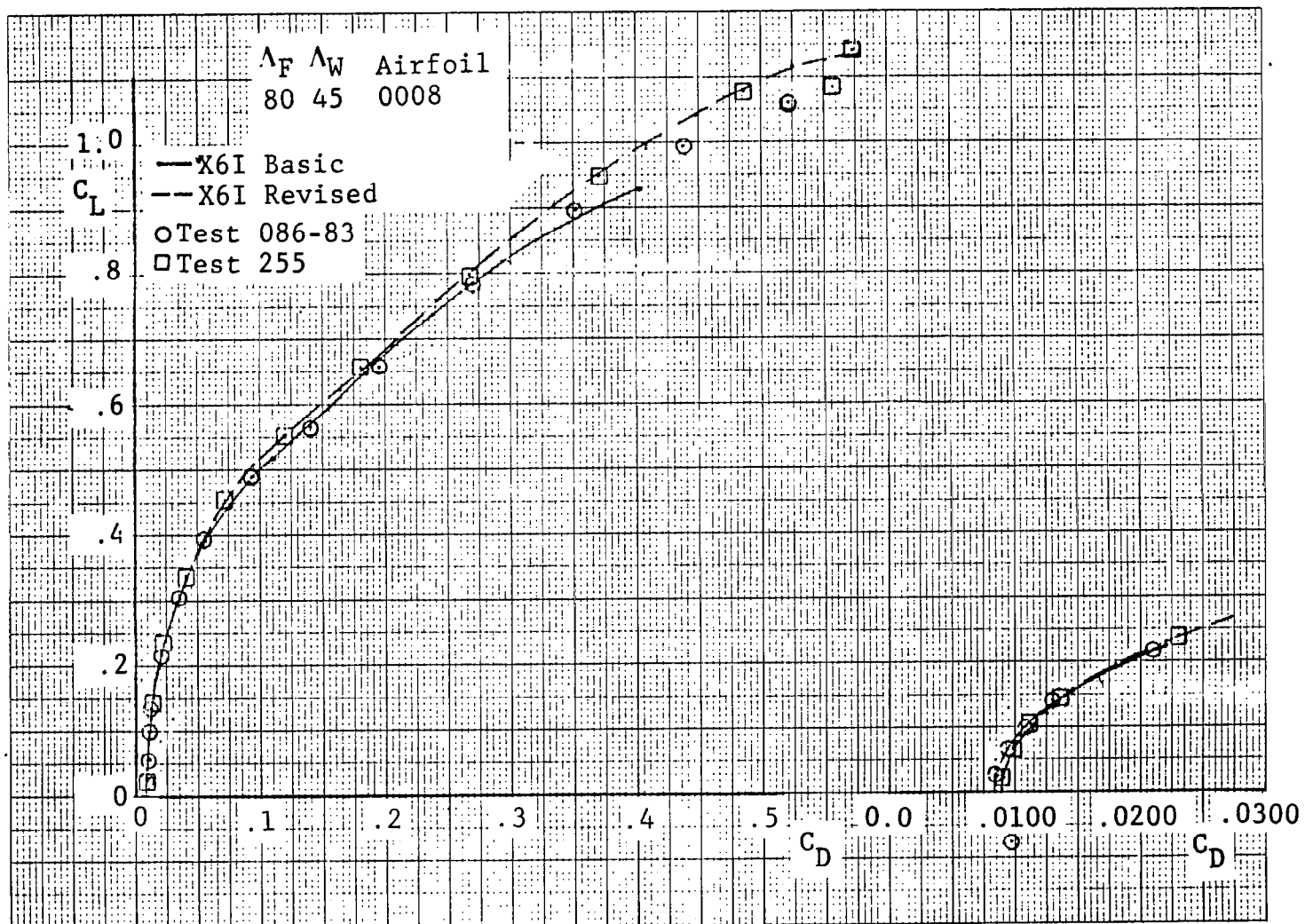
(c) Drag Polar

Figure 229. Continued
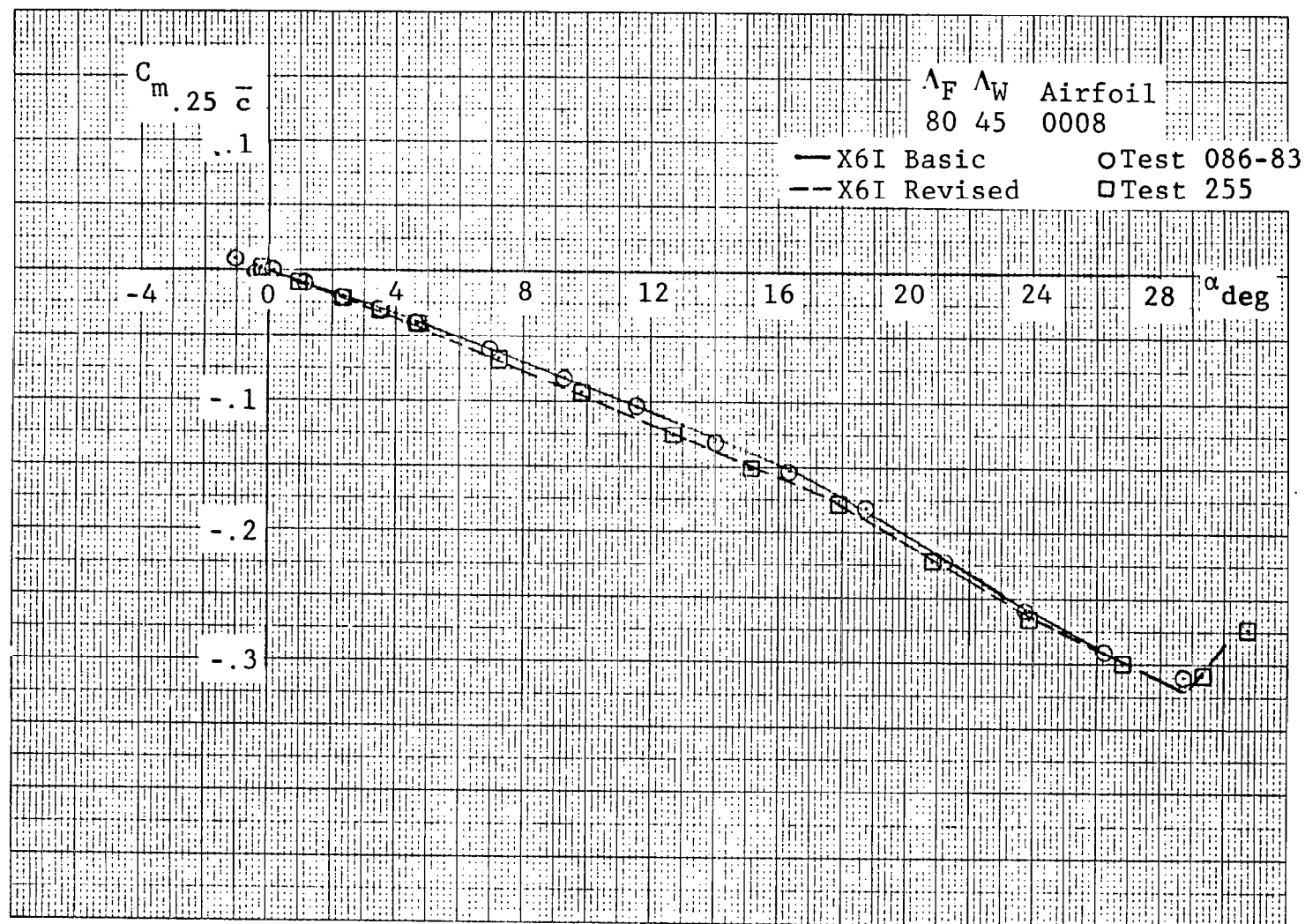
(d)   Pitching-Moment Variations with Angle of Attack

Figure 229.   Continued

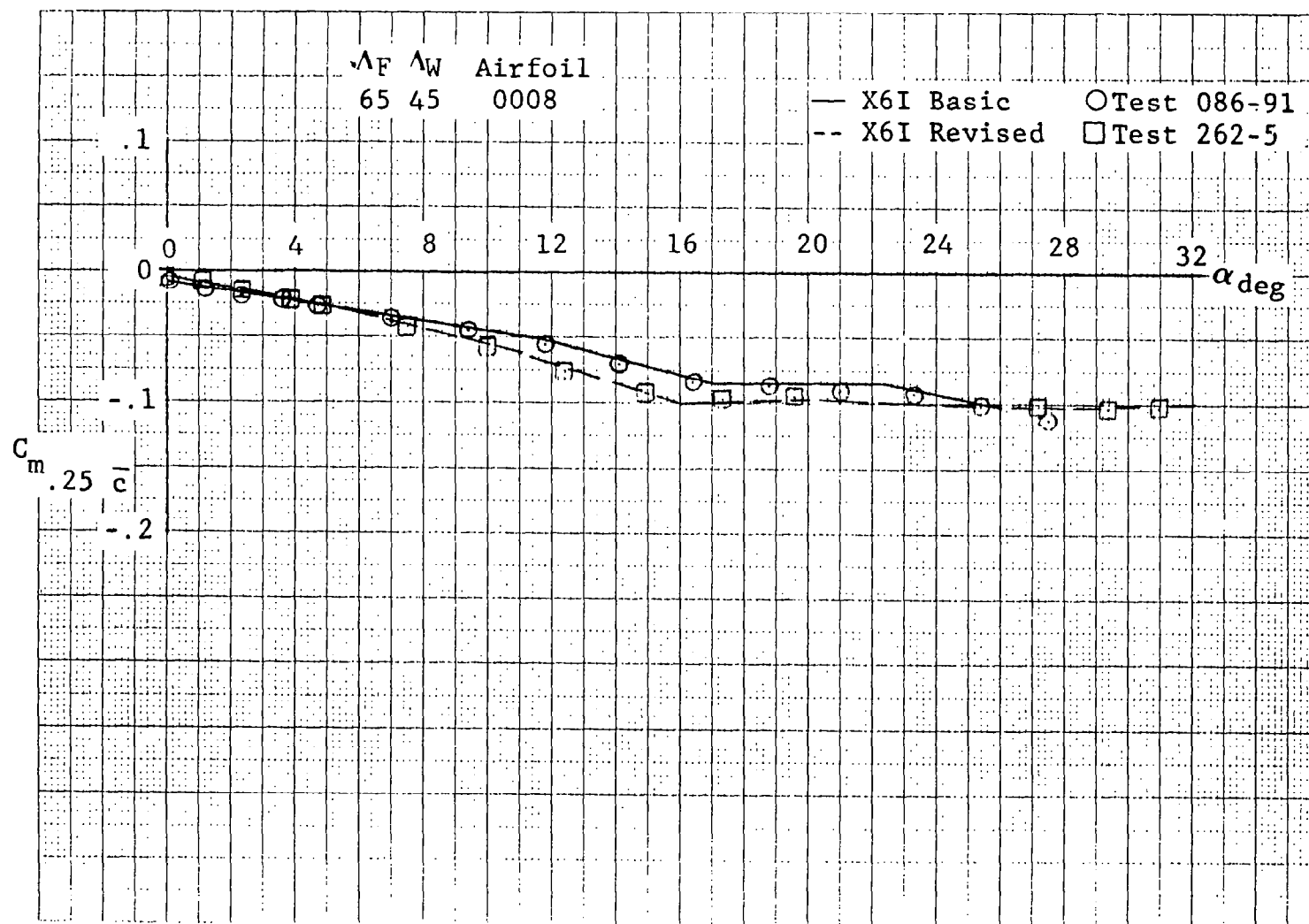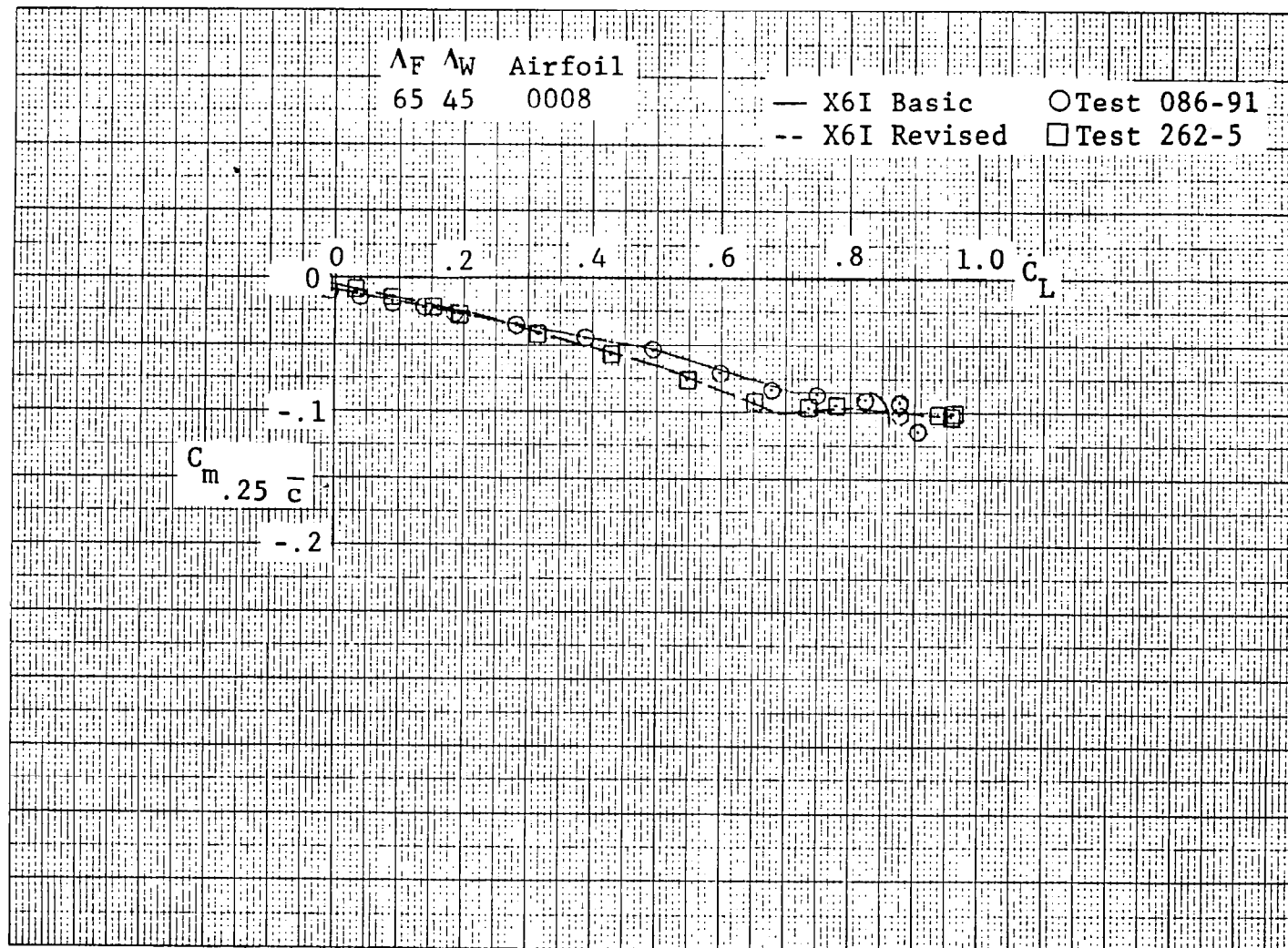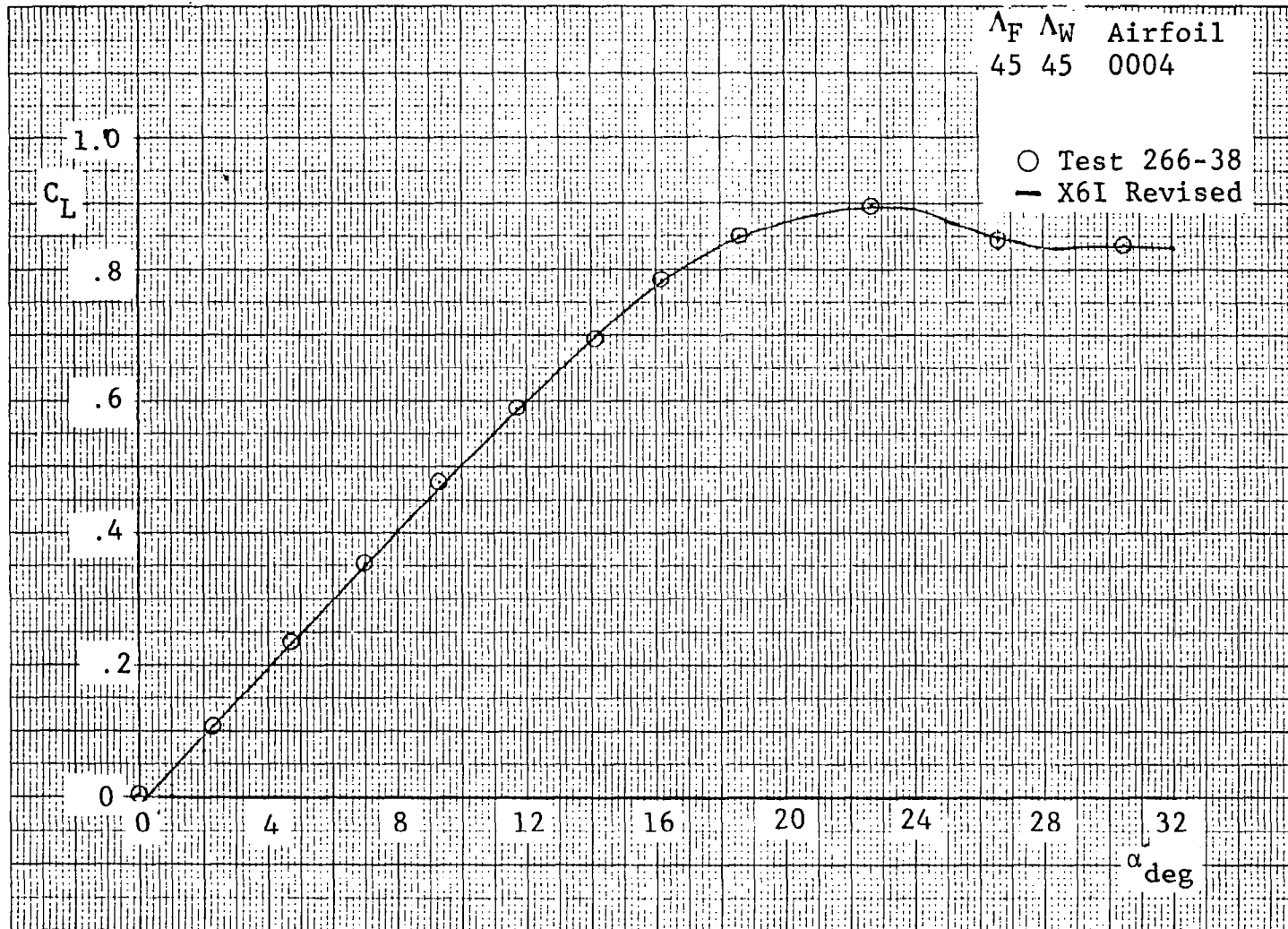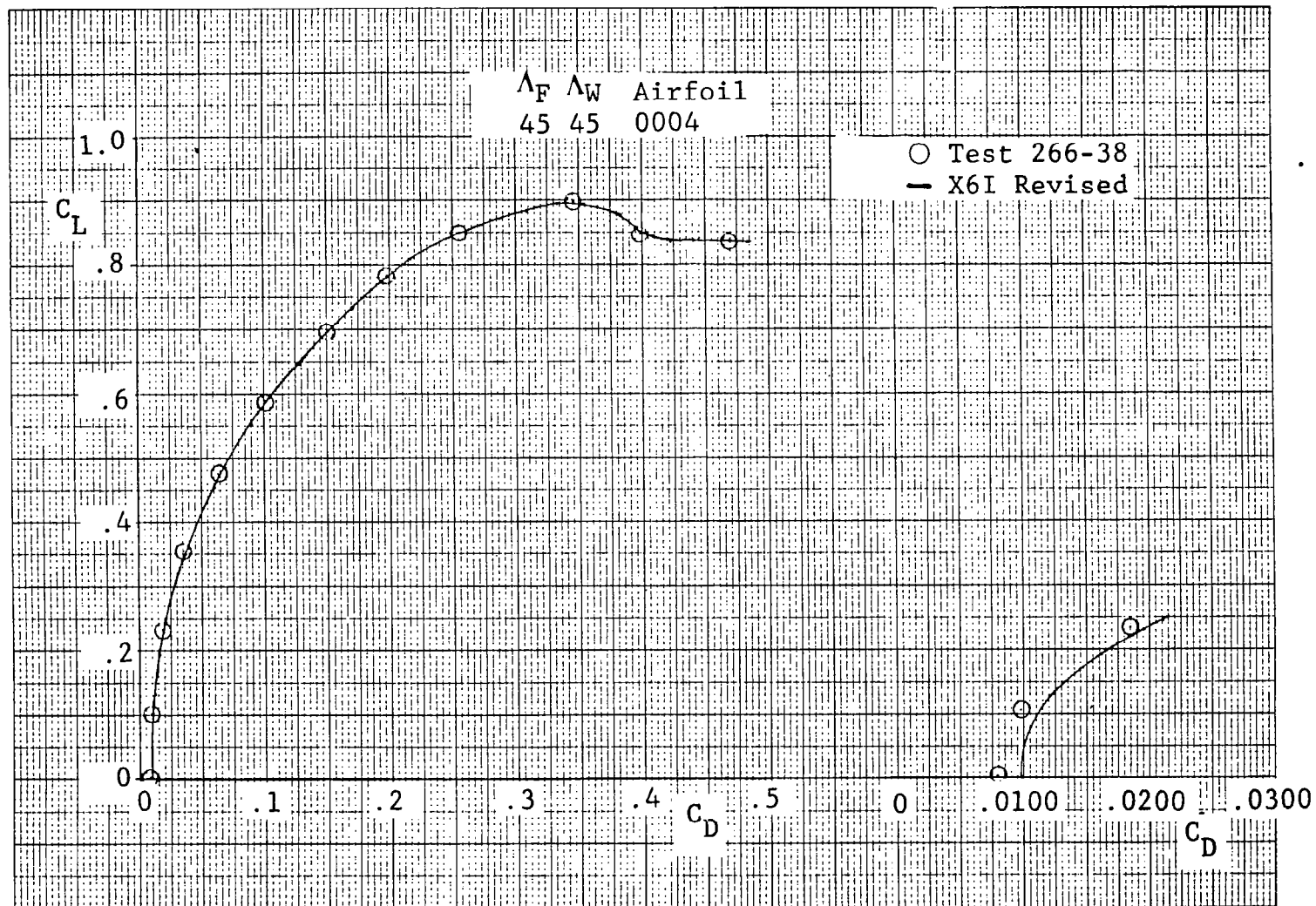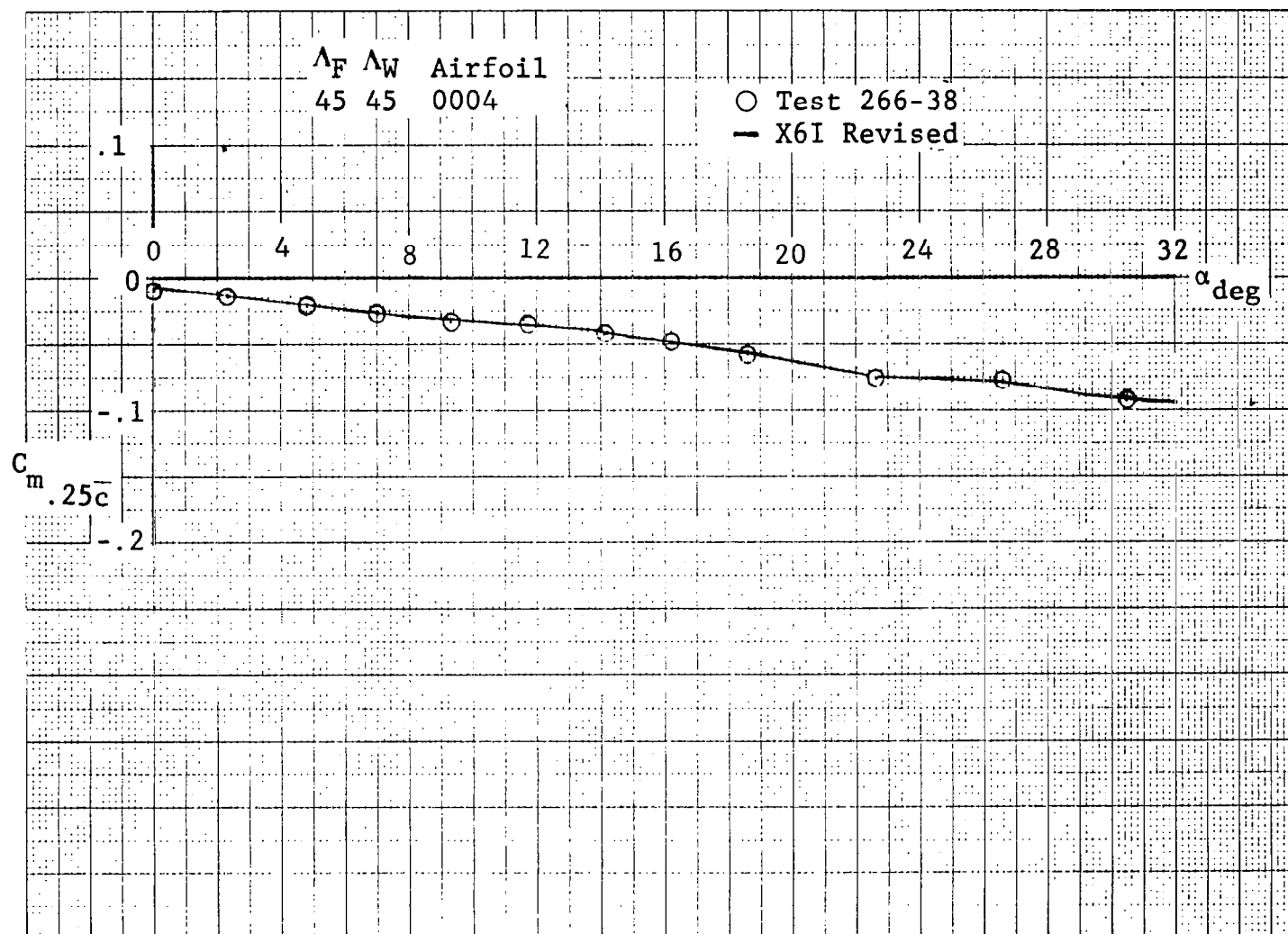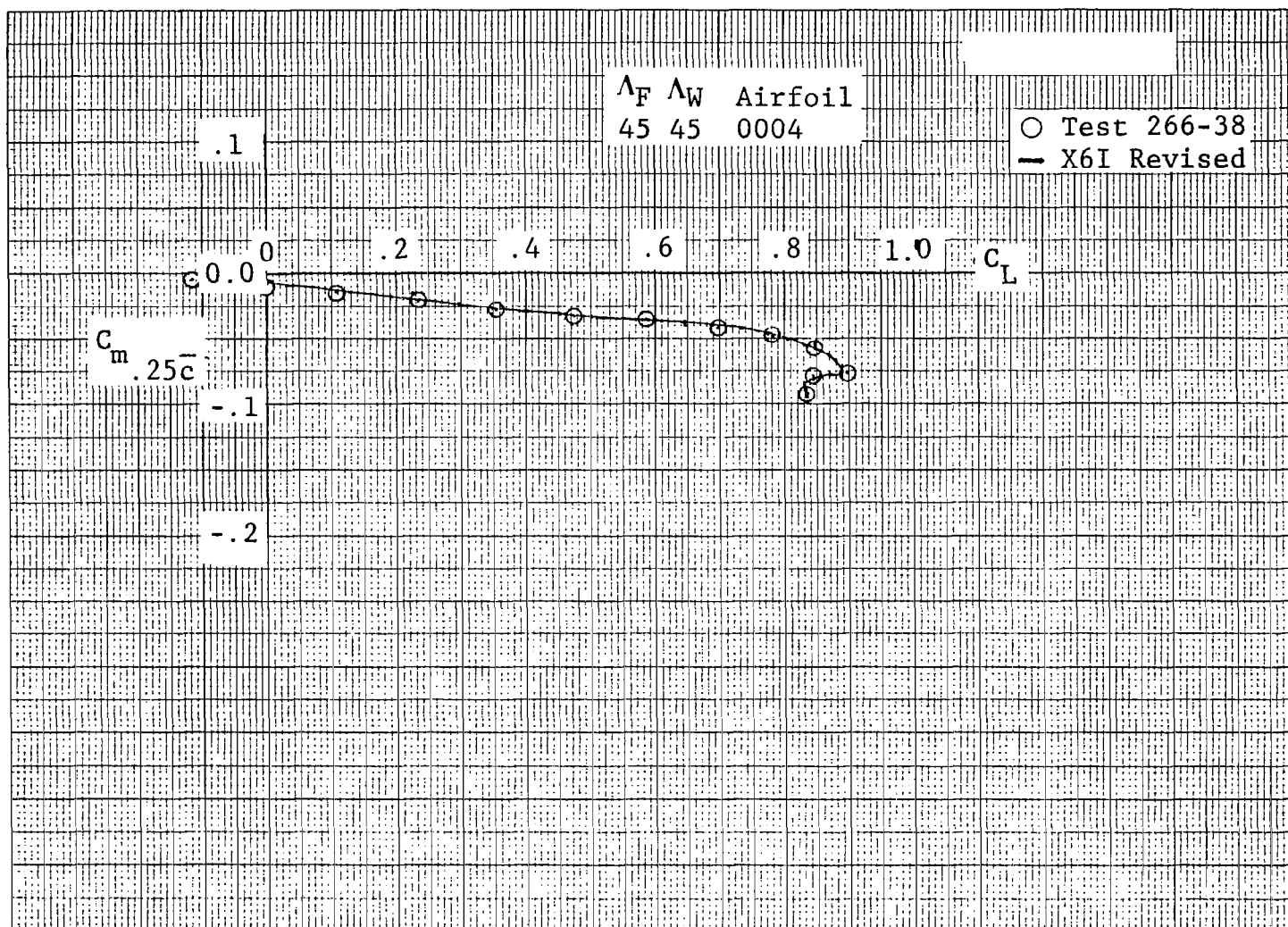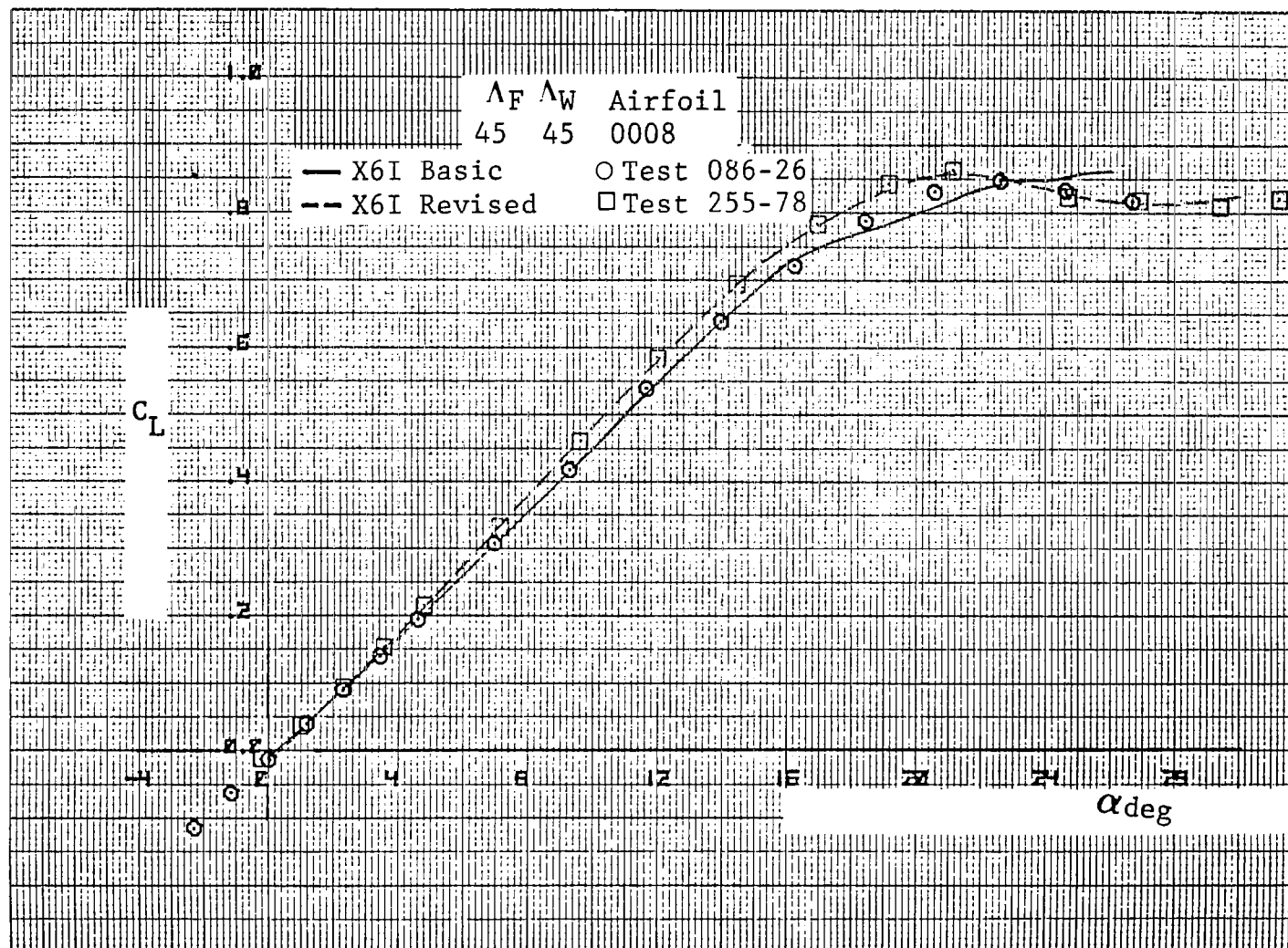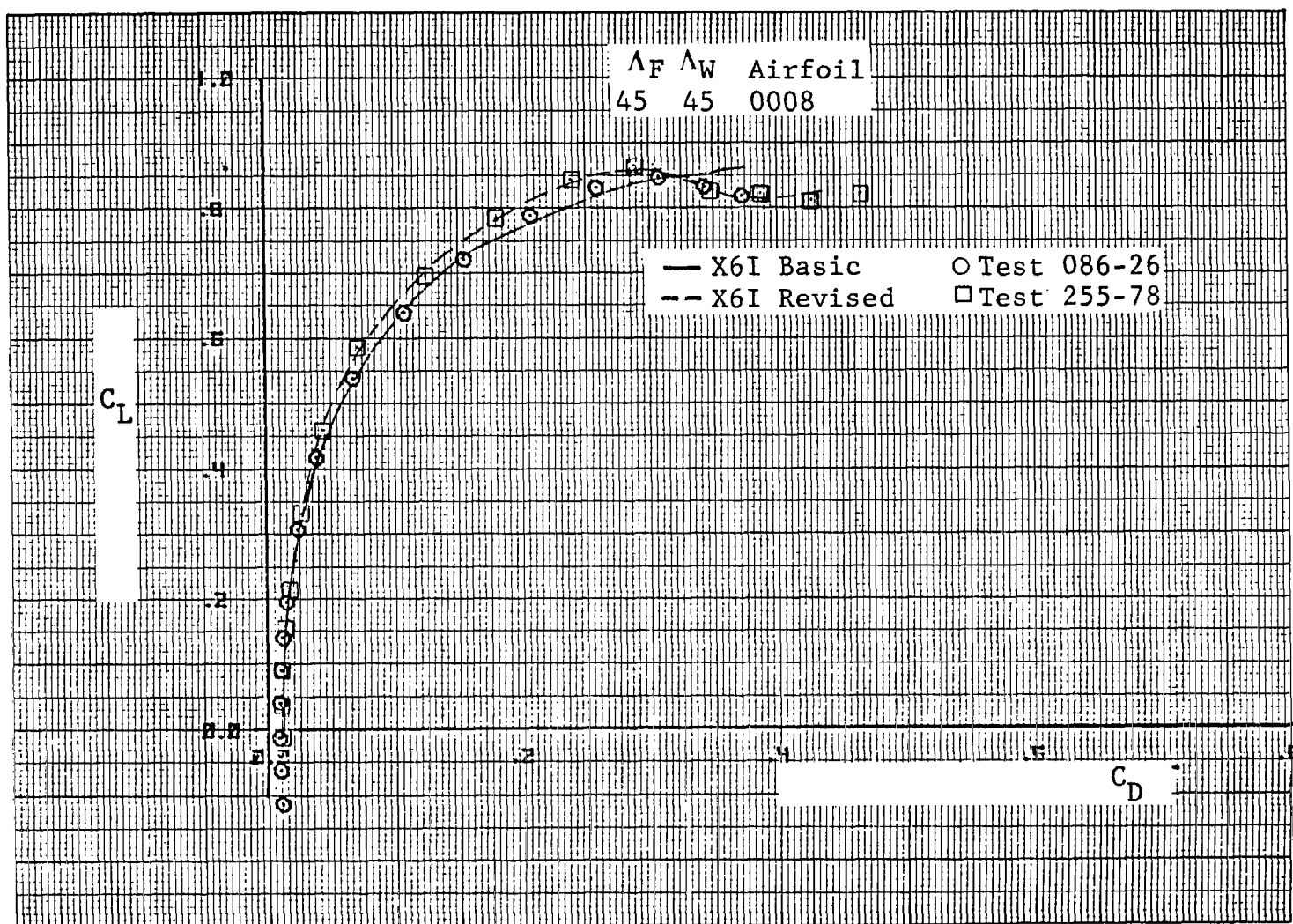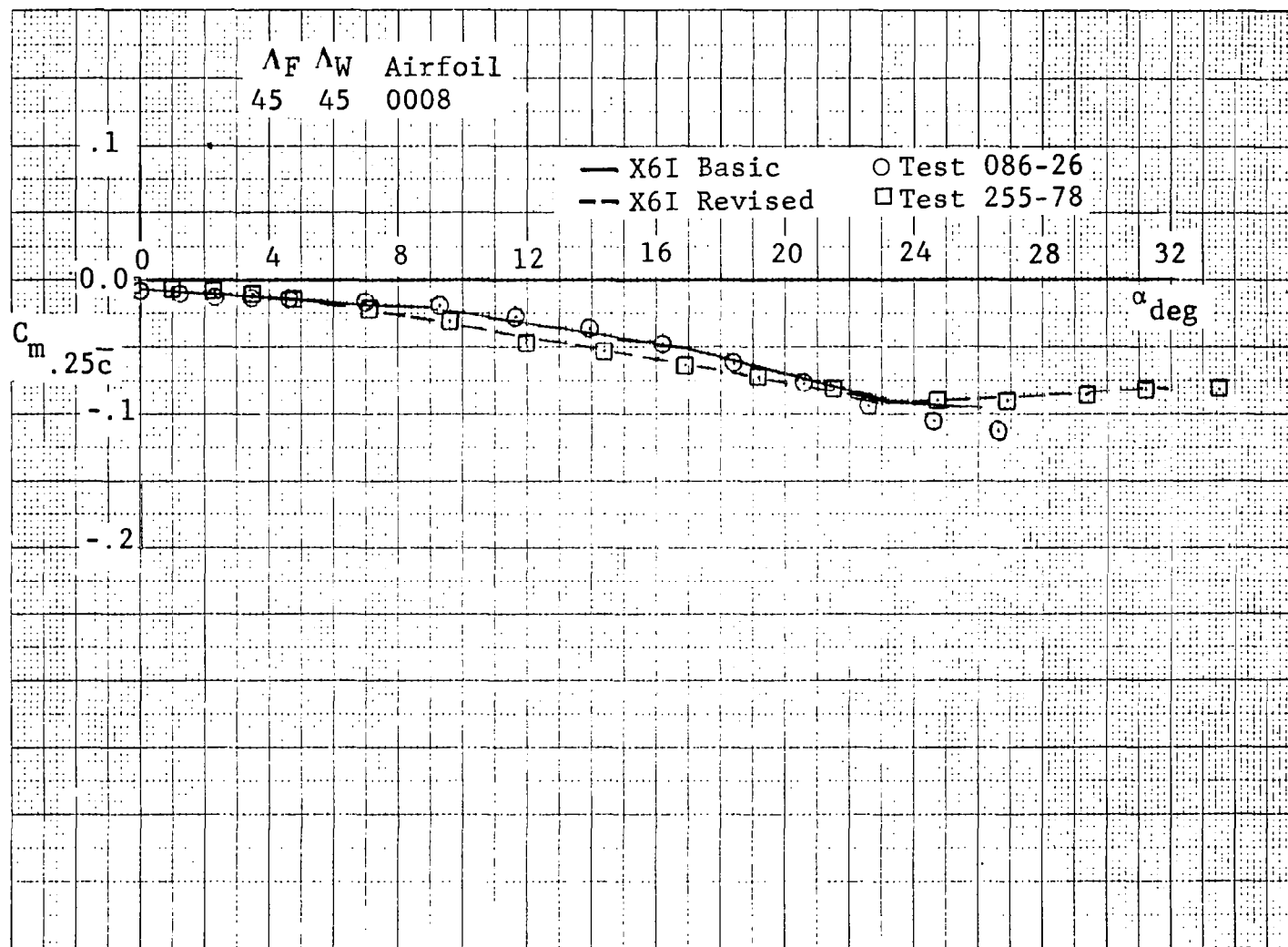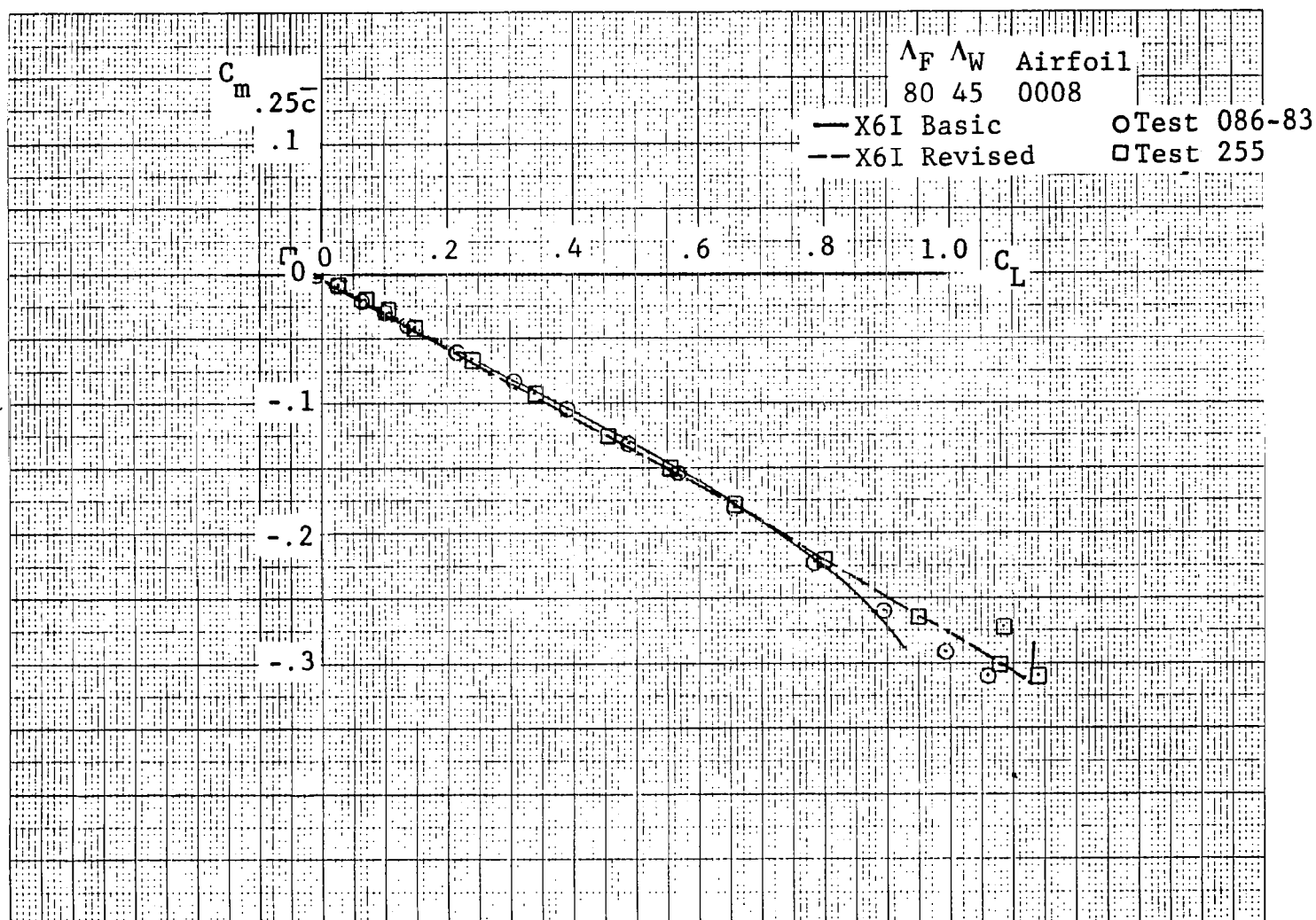(e)   Pitching-Moment Variations with Lift

Figure 229.   Concluded

CONCLUDING REMARKS

The objectives of this investigation were to develop prediction methods for low speed lift, drag, and pitching moment of irregular planform wings and design guidelines appropriate for preliminary design of advanced aerospace vehicles.

At the outset of the investigation it was hoped that quite simple empirical methods could be evolved that would be suitable for solution with nothing more than a hand calculator. As the investigation progressed, it became apparent that the flow fields produced by the component panels of irregular planform wings have complicated interactions that are affected by differences in Reynolds number in different ways depending on the fillet/wing combination and on the airfoil thickness. As a consequence the methods as finally devised are more complex than originally envisioned and require a computer procedure for efficient solution.

The methods provide a significant improvement in capability to accurately predict variations of lift, drag, and pitching-moment with angle of attack for a wide range of irregular planforms, and for a more limited range of planforms can account for effects of airfoil-thickness ratio and Reynolds number.

The investigation also showed that there are differences in test results obtained in different test facilities that introduce inherent uncertainties in the low speed aerodynamic characteristics of any given configuration. The magnitude of the uncertainties can be evaluated for the limited range of irregular planforms by making predictions using both the "Basic" and "Revised" prediction methods.

APPENDIX   A

REYNOLDS NUMBER EFFECT ON LIFT OF SHIPS WINGS

During the investigation described in the main body of this report, a concerted effort was made to derive some simple method to obtain corrections to the lift curves for the effects of Reynolds number. No successful method was found that could adequately describe the effects as a general function of Reynolds number for the complete range of SHIPS planforms.

In order to facilitate extrapolation of test results from a test performed at relatively low Reynolds numbers to flight conditions at low speed, data on the effects of Reynolds number on the lift correlation parameter are presented in this appendix for all configurations having airfoils with thickness ratios of 0.08 or larger. There were no significant effects for the NACA 0004 or thin hexagonal airfoils.

The data are presented in the form of the variation of the incremental value of the lift correlation parameter, $\Delta\left(\dfrac{C_L}{C_{L_\alpha}}\dfrac{A_1}{\eta_B}\right)$, with angle of attack for various values of unit Reynolds number. The baseline for the incremental value is the value of the lift correlation parameter obtained at the standard unit Reynolds number of 26.25 million per meter at each angle of attack for each configuration.

For the reader's convenience the plots are sorted into two major categories:

1. Corrections that were obtained from data for test ARC 12-086. These data should only be applied to predictions made using the "basic" prediction method (Figures 230, 231).

2. Corrections that were obtained from Langley LTPT Tests 255, 262 and 266. These data apply only to predictions made using the "revised" prediction method for the "standard" Reynolds number (Figures 232-235).

The appropriate values of C_{L_α}, A_1 and η_B are listed in Table 19.

TABLE 19   NUMERICAL VALUES OF ELEMENTS IN LIFT CORRELATION PARAMETER

Λ_F	Λ_W									
	25°		35°		45°		53°		60°	
	$C_{L\alpha}$/RAD	A_1	$C_{L\alpha}$/RAD	A_1	$C_{L\alpha}$/RAD	A_1	$C_{L\alpha}$/RAD	A_1	$C_{L\alpha}$/RAD	A_1
80°	1.76586	.36937	1.76374	.37098	1.74586	.37123	1.70925	.37355	1.65654	.37512
75°	2.08310	.45377	2.08631	.45228	2.07674	.45271	2.04603	.45617	2.00300	.46080
70°	2.29286	.50598	2.30071	.50893	2.29871	.50948	2.27424	.51386	2.24118	.51975
65°	2.43851	.54776	2.45071	.55122	2.45518	.55186	2.43673	.55222	2.41261	.56393
60°	2.54296	.58140	2.55923	.58444	2.56920	.58517	2.55642	.59096	2.54004	.59489
55°	2.61996	.60735	2.64002	.61160	2.65469	.61239				
53°							2.67726	.62857		
45°	2.72350	.64957	2.74997	.65443	2.77214	.65534				
35°	2.78881	.68281	2.82083	.68819						
25°	2.83379	.71120								

NOTE: η_B = .41157 for all wings

412

$$\Lambda_W \quad t/c$$
$$-25 \quad .08$$

(a) $\Lambda_F = 25^o$
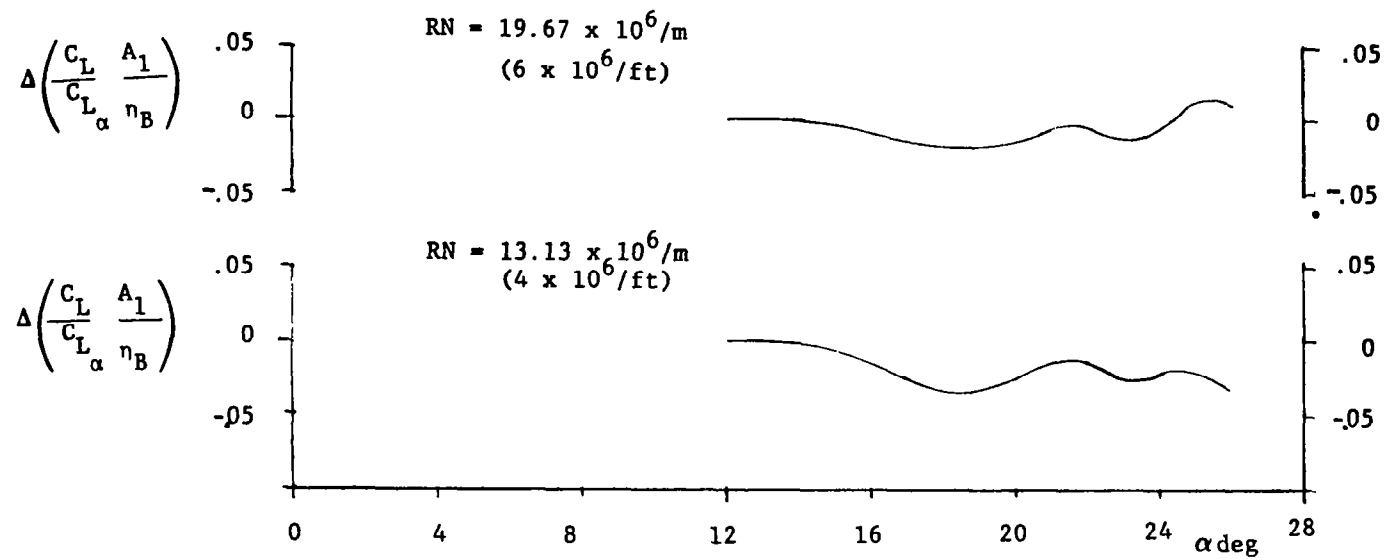
Figure 230.   Incremental Values of Lift Correlation Parameter
at Unit Reynolds Numbers of 13.13 and 19.67 Million
Per Meter From Test ARC 12-086 for SHIPS Planforms
Having Constant Values of Fillet Sweep

$$\Lambda_W \quad t/c$$
$$\text{———} 35 \quad .08$$
$$\text{— —} 25$$

$$\Delta\left(\dfrac{C_L}{C_{L_\alpha}} \dfrac{A_1}{\eta_B}\right)$$

$$RN = 19.67 \times 10^6/m$$
$$(6 \times 10^6/ft)$$

$$\Delta\left(\dfrac{C_L}{C_{L_\alpha}} \dfrac{A_1}{\eta_B}\right)$$

$$RN = 13.13 \times 10^6/m$$
$$(4 \times 10^6/ft)$$

α deg

(b) $\Lambda_F = 35^o$

Figure 230. Continued

$$\Lambda_W \quad t/c$$

——60   .08
–––53
—·—45
—··—35
—···—25

$RN \doteq 19.67 \times 10^6/m$
$(6 \times 10^6/ft)$

$\Delta\left(\dfrac{C_L}{C_{L_\alpha}}\dfrac{A_1}{\eta_B}\right)$

.05
0
-.05

.05
0
-.05

$RN = 13.13 \times 10^6/m$
$(4 \times 10^6/ft)$

$\Delta\left(\dfrac{C_L}{C_{L_\alpha}}\dfrac{A_1}{\eta_B}\right)$

.05
0
-.05

.05
0
-.05

0   4   8   12   16   20   24   28
α deg
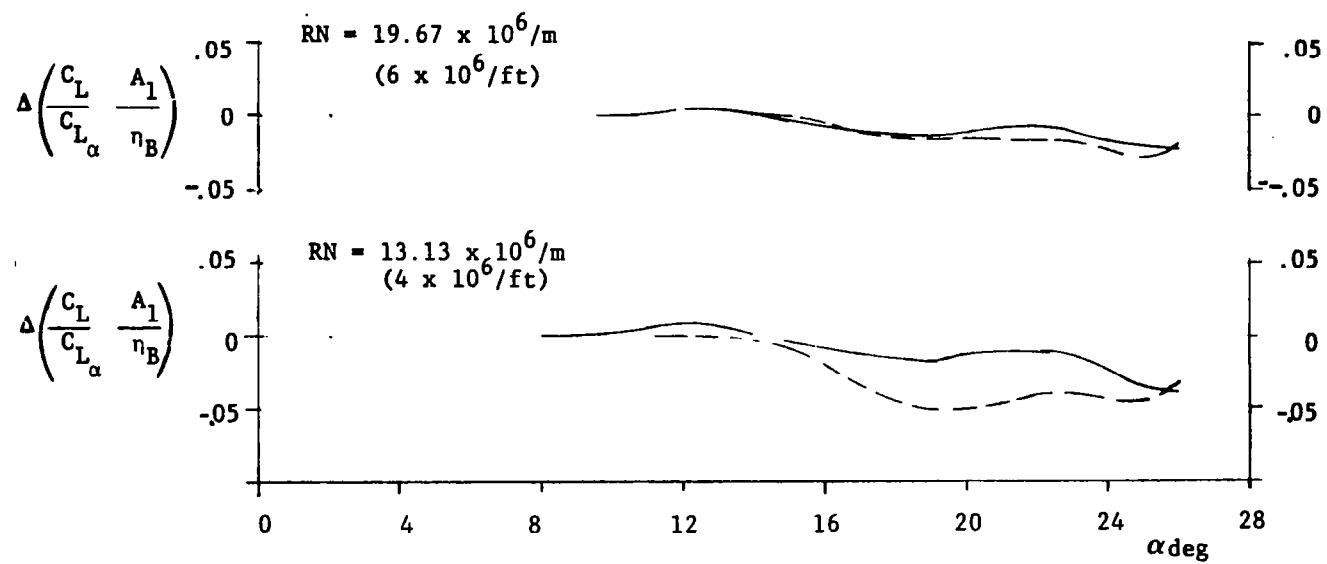
(e) $\Lambda_F = 60^\circ$

Figure 230.   Continued

$$\Lambda_W \quad t/c$$

—————60 .08
———55
——45
——35
——25

$$\Delta\left(\frac{C_L}{C_{L_\alpha}}\frac{A_1}{\eta_B}\right)$$

.05

0

-.05

RN = 19.67 x 10^6/m
(6 x 10^6/ft)

.05

0

-.05

$$\Delta\left(\frac{C_L}{C_{L_\alpha}}\frac{A_1}{\eta_B}\right)$$

.05

0

-.05

RN = 13.13 x 10^6/m
(4 x 10^6/ft)

.05

0

-.05

0   4   8   12   16   20   24   28 α deg

(f) $\Lambda_F = 65^o$

Figure 230. Continued

$$\Lambda_W \quad t/c$$

—— 60 .08
––– 53
— –45
—––35
—·––25

$$\Delta\left(\frac{C_L}{C_{L_\alpha}} \frac{A_1}{n_B}\right)$$

.05

0

-.05

RN = 19.67 x 10^6/m
(6 x 10^6/ft)

.05

0

-.05

$$\Delta\left(\frac{C_L}{C_{L_\alpha}} \frac{A_1}{n_B}\right)$$

.05

0

-.05

RN = 13.13 x 10^6/m
(4 x 10^6/ft)

.05

0

-.05

0   4   8   12   16   20   24   28

αdeg

(g) $\Lambda_F = 70^\circ$

Figure 230. Continued

Λ_W t/c

—— 60   .08
—— —53
—— —45
—— —35
—— —25

$\Delta\left(\dfrac{C_L}{C_{L_\alpha}}\ \dfrac{A_1}{\eta_B}\right)$

.05

0

-.05

RN $= 19.67 \times 10^6$/m
$(6 \times 10^6$/ft)

.05

0

-.05

$\Delta\left(\dfrac{C_L}{C_{L_\alpha}}\ \dfrac{A_1}{\eta_B}\right)$

.05

0

-.05

RN $= 13.13 \times 10^6$/m
$(4 \times 10^6$/ft)

.05

0

-.05

0   4   8   12   16   20   24   28

α deg

(h) $\Lambda_F = 75°$

Figure 230. Continued

Λ_W t/c

————60   .08
— — —55
———45
—— —35
——-—25

$RN = 19.67 \times 10^6/m$
$(6 \times 10^6/ft)$

$\Delta\left(\dfrac{C_L}{C_{L_\alpha}} \dfrac{A_1}{\eta_B}\right)$

$RN = 13.13 \times 10^6/m$
$(4 \times 10^6/ft)$

$\Delta\left(\dfrac{C_L}{C_{L_\alpha}} \dfrac{A_1}{\eta_B}\right)$

α deg

(i) $\Lambda_F = 80^o$

Figure 230.   Concluded

Figure 231. Incremental Values of Lift Correlation Parameter at Unit Reynolds Numbers of 13.13 and 19.67 Million Per Meter from Test ARC 12-086 Showing Effect of Thickness Ratio for Wing I With Various Fillet Sweeps

Λ_F	Λ_W	t/c
—— 60	25	.08
— — 60	25	.12

$$\Delta\left(\frac{C_L}{C_{L_\alpha}}\frac{A_1}{\eta_B}\right)$$

RN = 19.67 x 10^6/m
(6 x 10^6/ft)

$$\Delta\left(\frac{C_L}{C_{L_\alpha}}\frac{A_1}{\eta_B}\right)$$

RN = 13.13 x 10^6/m
(4 x 10^6/ft)

αdeg
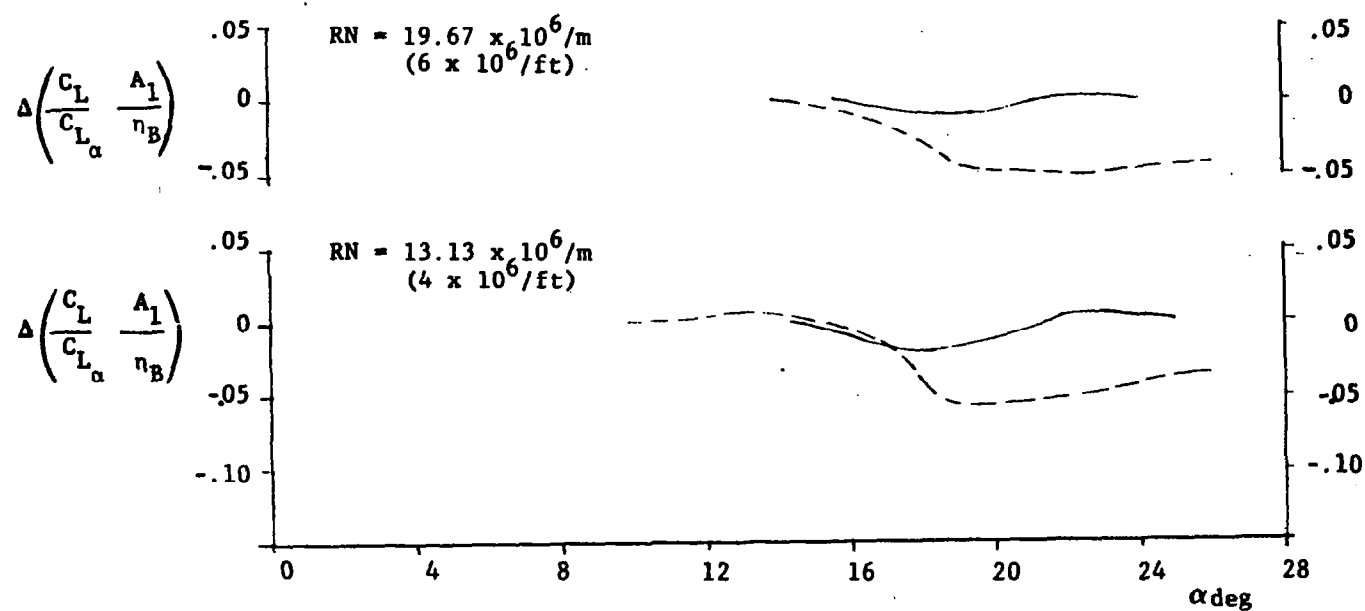
(b) $\Lambda_F = 60°$

Figure 231. Continued

Λ_F	Λ_W	t/c
—— 80	25	.08
—— 80	25	.12

$$\Delta\left(\frac{C_L}{C_{L_\alpha}}\frac{A_1}{\eta_B}\right)$$

RN = 19.67 x 10^6/m
(6 x 10^6/ft)

.05

0

-.05

.05

0

-.05

$$\Delta\left(\frac{C_L}{C_{L_\alpha}}\frac{A_1}{\eta_B}\right)$$

RN = 13.13 x 10^6/m
(4 x 10^6/ft)

.05

0

-.05

-.10

.05

0

-.05

-.10

0   4   8   12   16   20   24 α deg   28
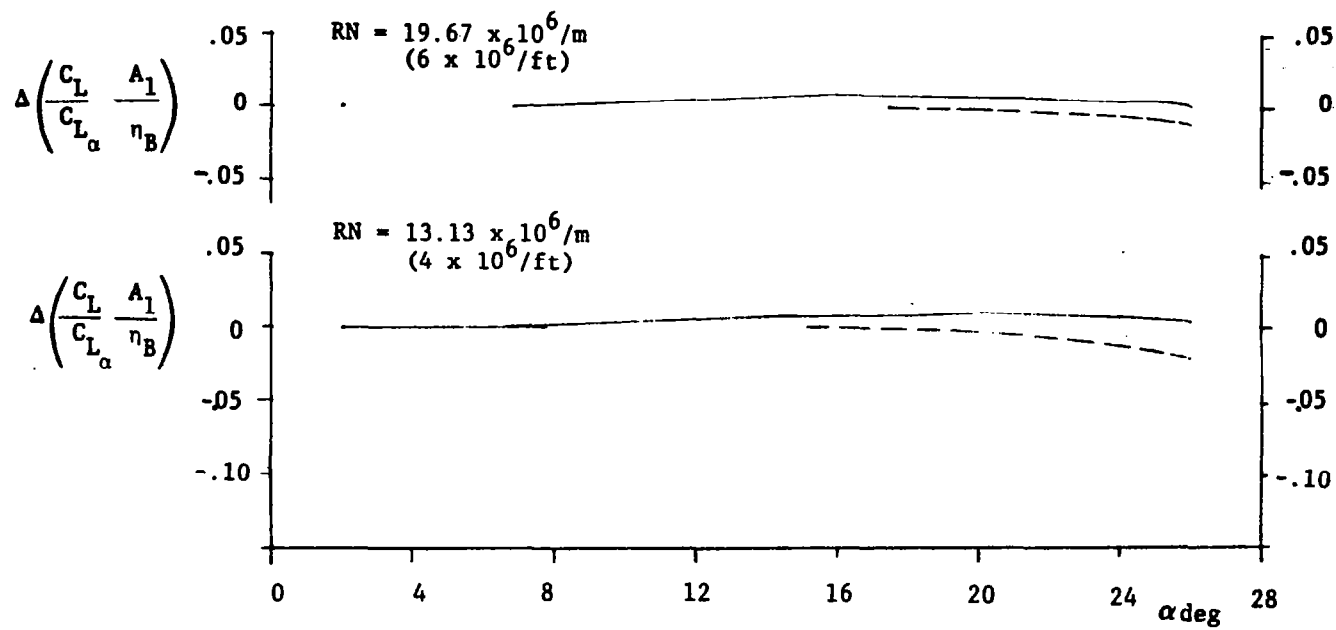
(c) $\Lambda_F = 80°$

Figure 231. Concluded

	Λ_F	Λ_W	t/c
——	45	45	.08
– – –	45	45	.12
—·—	45	45	.15

$$\Delta\left(\frac{C_L}{C_{L_\alpha}}\frac{A_1}{\eta_B}\right)$$

$RN = 19.67 \times 10^6/m$
$(6 \times 10^6/ft)$

$$\Delta\left(\frac{C_L}{C_{L_\alpha}}\frac{A_1}{\eta_B}\right)$$

$RN = 13.13 \times 10^6/m$
$(4 \times 10^6/ft)$

α deg.

(a) $\Lambda_F = 45°$

Figure 232.   Incremental Values of Lift Correlation Parameter
at Unit Reynolds Numbers of 13.13 and 19.67 Million
Per Meter from Various Langley LTPT Tests Showing
Effect of Thickness Ratio for Wing III with Various
Fillet Sweeps

Λ_F	Λ_W	t/c
——65	45	.08
———65	45	.12
—·—65	45	.15

$$\Delta\left(\frac{C_L}{C_{L_\alpha}} \frac{A_1}{\eta_B}\right)$$

$RN = 13.13 \times 10^6/m$
$(4 \times 10^6/ft)$

$$\Delta\left(\frac{C_L}{C_{L_\alpha}} \frac{A_1}{\eta_B}\right)$$

$RN = 19.67 \times 10^6/m$
$(6 \times 10^6/ft)$

α deg

(b) $\Lambda_F = 65^o$

Figure 232. Continued

$$
\begin{array}{ccc}
\Lambda_F & \Lambda_W & t/c \\
\text{——}70 & 45 & .08 \\
\text{——}70 & 45 & .12 \\
\text{——}70 & 45 & .15 \\
\end{array}
$$

$\Delta\left(\dfrac{C_L}{C_{L_\alpha}}\dfrac{A_1}{\eta_B}\right)$ RN = 19.67 x 10^6/m   (6 x 10^6/ft)

$\Delta\left(\dfrac{C_L}{C_{L_\alpha}}\dfrac{A_1}{\eta_B}\right)$ RN = 13.13 x 10^6/m   (4 x 10^6/ft)

α deg

(c) $\Lambda_F = 70^\circ$

Figure 232. Continued

Λ_F	Λ_W	t/c
——75	45	.08
——75	45	.12
——75	45	.15

$\Delta\left(\dfrac{C_L}{C_{L_\alpha}}\dfrac{A_1}{\eta_B}\right)$

.05

0

-.05

RN = 19.67 × 10^6/m
(6 × 10^6/ft)

.05

0

-.05

$\Delta\left(\dfrac{C_L}{C_{L_\alpha}}\dfrac{A_1}{\eta_B}\right)$

.05

0

-.05

RN = 13.13 × 10^6/m
(4 × 10^6/ft)

.05

0

-.05

0   4   8   12   16   20   24   28

αdeg

(d) Λ_F = 75°

Figure 232. Continued

(e) $\Lambda_F = 80^o$

Figure 232. Concluded

$$\Lambda_F \quad \Lambda_W \quad t/c$$
$$\text{———}45 \quad 45 \quad .08$$
$$\text{——}45 \quad 45 \quad .12$$
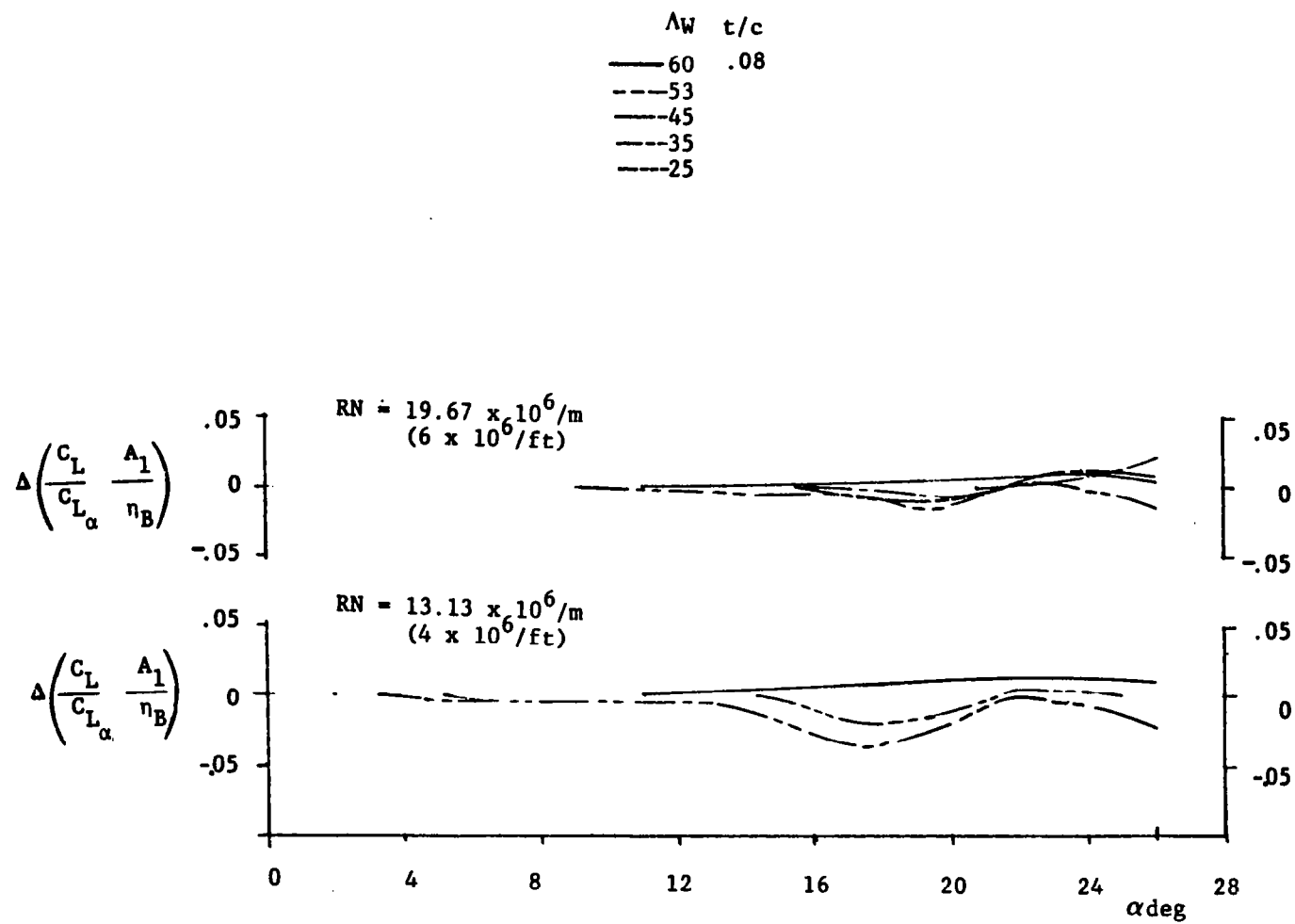$$\text{——}45 \quad 45 \quad .15$$
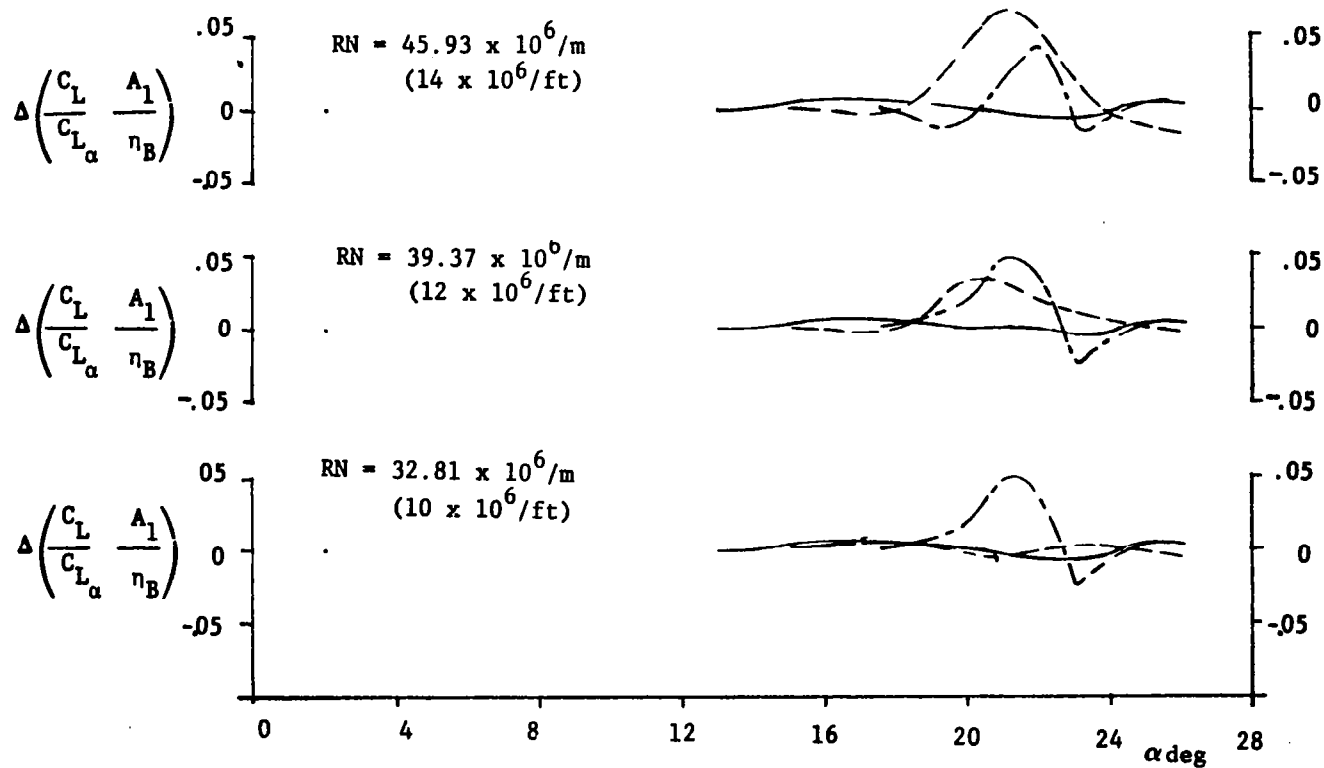
(a) $\Lambda_F = 45°$

Figure 233. Incremental Values of Lift Correlation Parameter at Unit Reynolds Numbers of 32.81, 39.37 and 45.93 Million Per Meter from Various Langley LTPT Tests Showing Effects of Thickness Ratio for Wing III with Various Fillets

Λ_F	Λ_W	t/c
——65	45	.08
---65	45	.12
—-65	45	.15

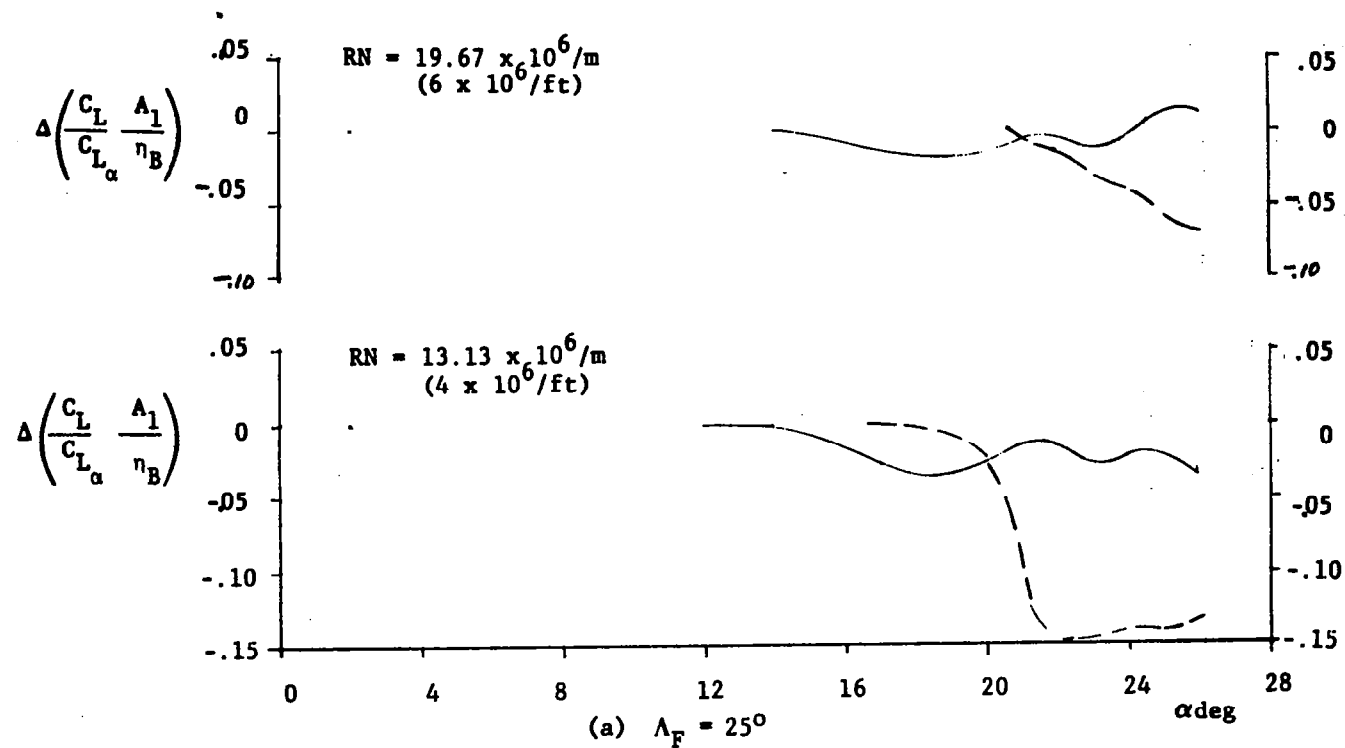$\Delta\left(\dfrac{C_L}{C_{L_\alpha}} \dfrac{A_1}{\eta_B}\right)$

RN = 45.93 x 10^6/m
(14 x 10^6/ft)

$\Delta\left(\dfrac{C_L}{C_{L_\alpha}} \dfrac{A_1}{\eta_B}\right)$

RN = 39.37 x 10^6/m
(12 x 10^6/ft)

$\Delta\left(\dfrac{C_L}{C_{L_\alpha}} \dfrac{A_1}{\eta_B}\right)$

RN = 32.81 x 10^6/m
(10 x 10^6/ft)

α deg

(b) $\Lambda_F = 65^o$

Figure 233.   Continued

(c) $\Lambda_F = 70°$

Figure 233. Continued

$$\Lambda_F \quad \Lambda_W \quad t/c$$
—— 75   45   .08
— — 75   45   .12
—·— 75   45   .15

$RN = 45.93 \times 10^6/m$ $RN = 39.37 \times 10^6/m$ $RN = 32.81 \times 10^6/m$
$(14 \times 10^6/ft)$ $(12 \times 10^6/ft)$ $(10 \times 10^6/ft)$

$$\Delta\left(\frac{C_L}{C_{L_\alpha}} \frac{\Lambda_1}{\eta_B}\right)$$

.05

0

-.05

.05

0

-.05

0   4   8   12   16   20   24 α deg   28
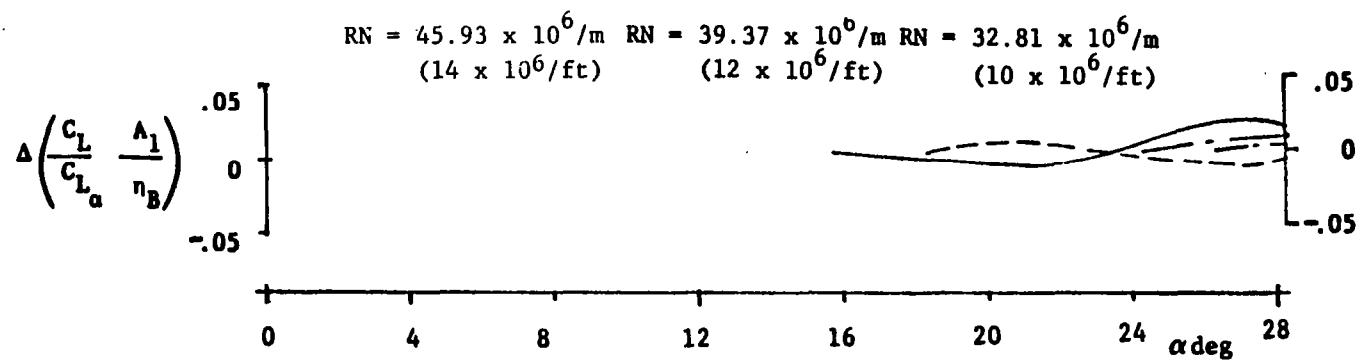
(d) $\Lambda_F = 75°$

Figure 233. Continued
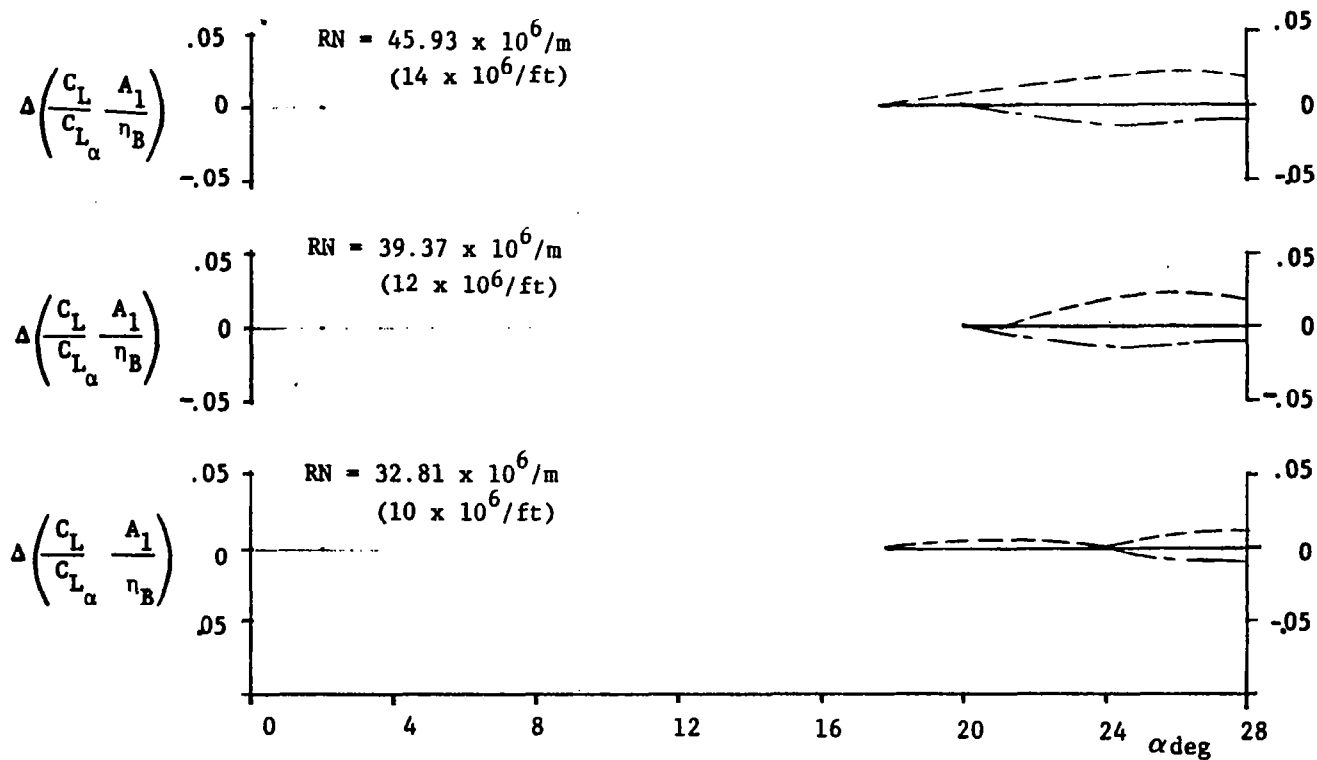
(e) $\Lambda_F = 80°$

Figure 233. Concluded

Λ_F	Λ_W	Airfoil
——70	45	0012
———70	45	5012
——-70	45	5412

$$\Delta\left(\frac{C_L}{C_{L_\alpha}} \quad \frac{A_1}{\eta_B}\right)$$

RN = 19.67 x 10^6/m
(6 x 10^6/ft)

.05
0
-.05

$$\Delta\left(\frac{C_L}{C_{L_\alpha}} \quad \frac{A_1}{\eta_B}\right)$$

RN = 13.13 x 10^6/m
(4 x 10^6/ft)

.05
0
-.05

0   4   8   12   16   20   24   28

α deg

(a) Λ_F = 70°
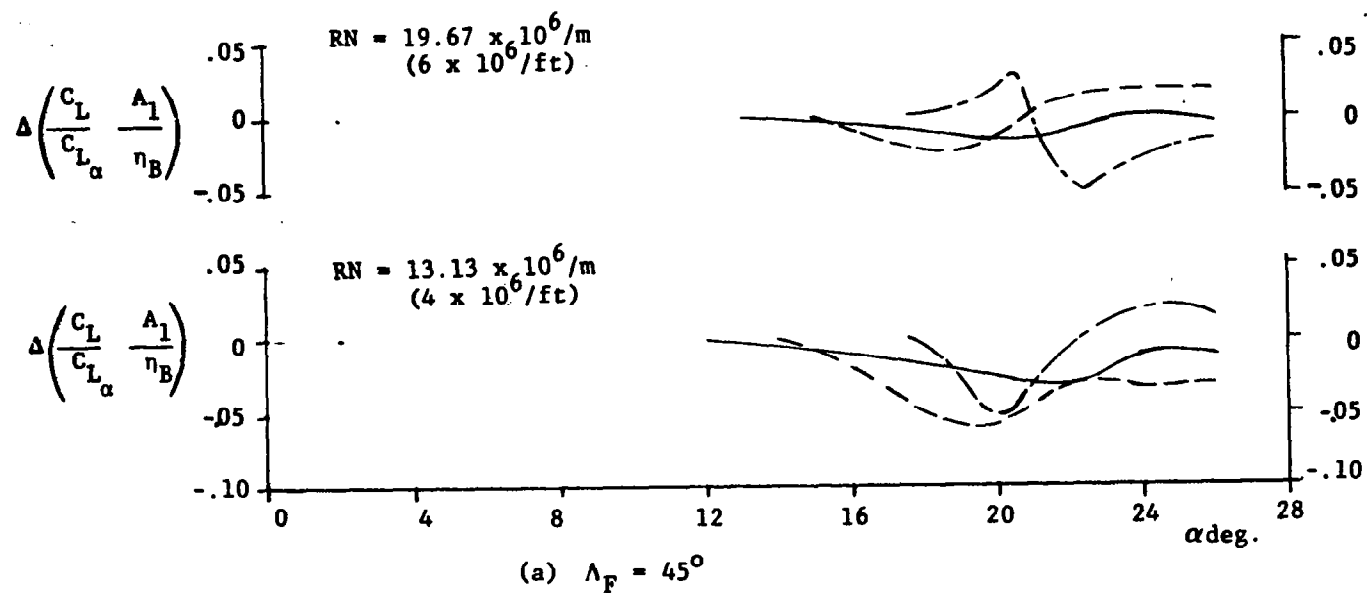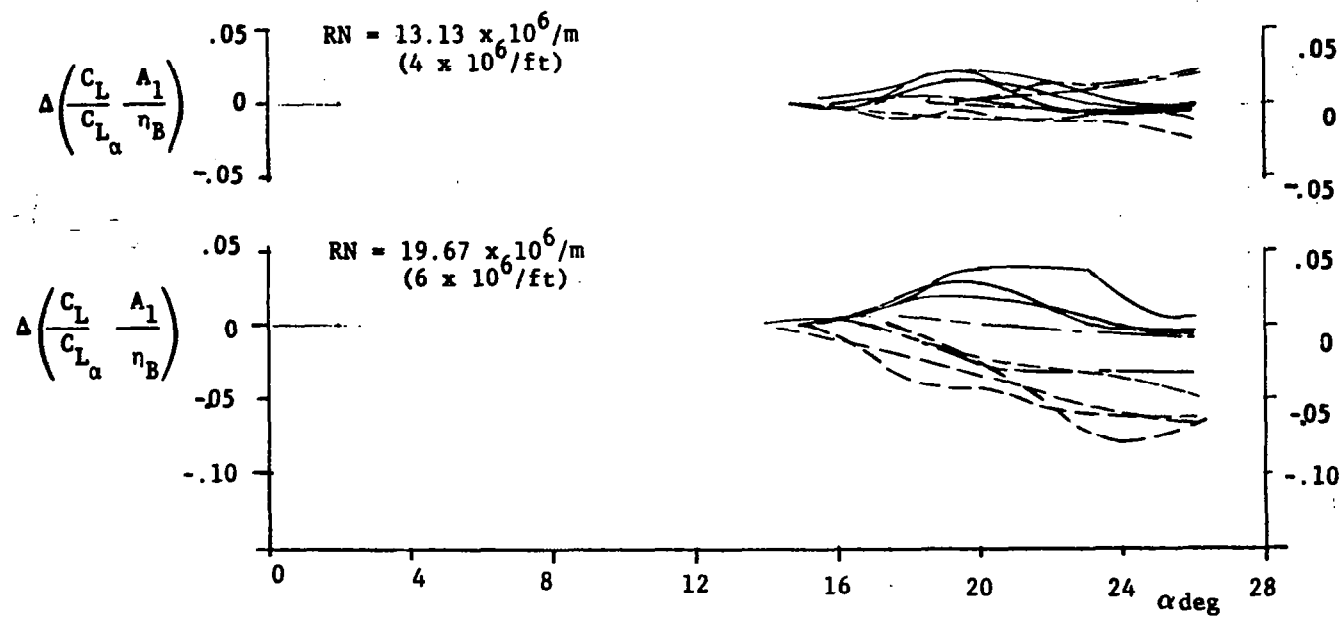
Figure 234. Incremental Values of Lift Correlation Parameter at
Unit Reynolds Numbers of 13.13 and 19.67 Million
Per Meter from Langley LTPT Test 262 Showing Effects
of Airfoil Section and Camber for Wing III with
Various Fillet Sweeps

$$\begin{array}{ccc} \Lambda_F & \Lambda_W & Airfoil \\ 75 & 45 & 0012 \\ 75 & 45 & 5012 \\ 75 & 45 & 5412 \end{array}$$
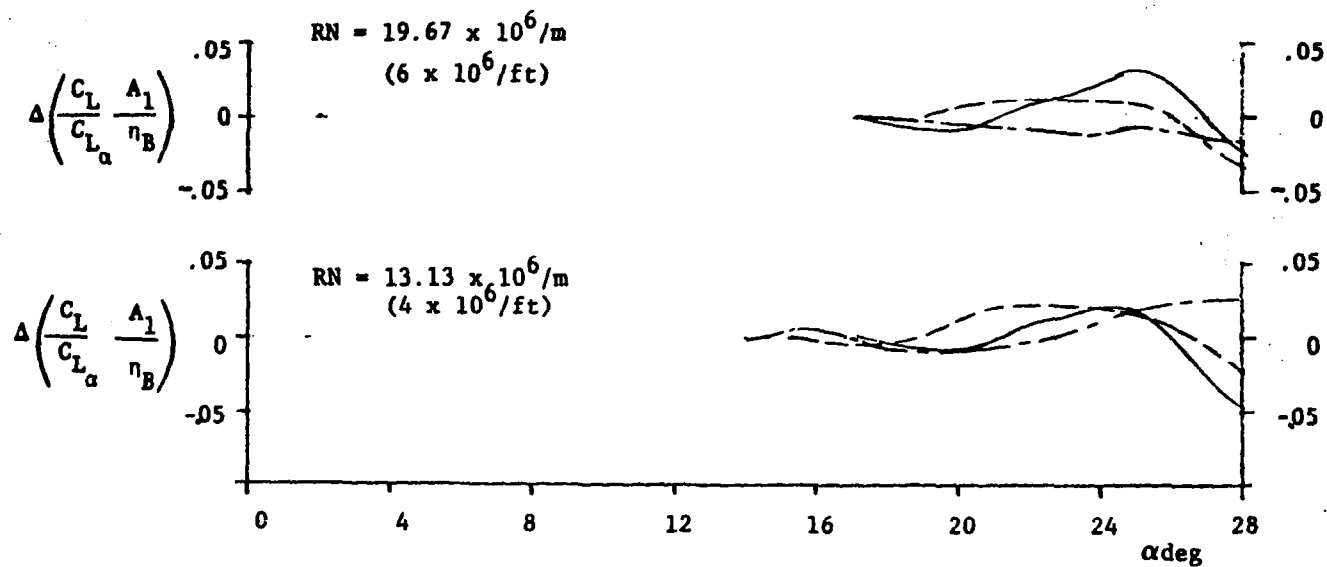
(b) $\Lambda_F = 75^\circ$

Figure 234. Continued

436

Λ_F	Λ_W	Airfoil
——80	45	0012
— —80	45	5012
—·—80	45	5412

$$\Delta\left(\frac{C_L}{C_{L_\alpha}}\frac{A_1}{\eta_B}\right)$$

.05

0

-.05

RN = 19.67 x 10^6/m

(6 x 10^6/ft)

.05

0

-.05

$$\Delta\left(\frac{C_L}{C_{L_\alpha}}\frac{A_1}{\eta_B}\right)$$

.05

0

-.05

RN = 13.13 x 10^6/m

(4 x 10^6/ft)

.05

0

-.05

0 4 8 12 16 20 24 28

α deg

(c) Λ_F = 80°

Figure 234. Concluded

	Λ_F	Λ_W	Airfoil
—————	70	45	0012
— —	70	45	5012
—·—	70	45	5412

$\Delta\left(\dfrac{C_L}{C_{L_\alpha}}\dfrac{A_1}{\eta_B}\right)$

$RN = 45.93 \times 10^6/m$
$(14 \times 10^6/ft)$

.05

0

-.05

.05

0

-.05

$\Delta\left(\dfrac{C_L}{C_{L_\alpha}}\dfrac{A_1}{\eta_B}\right)$

$RN = 39.37 \times 10^6/m$
$(12 \times 10^6/ft)$

.05

0

-.05

.05

0

-.05

$\Delta\left(\dfrac{C_L}{C_{L_\alpha}}\dfrac{A_1}{\eta_B}\right)$

$RN = 32.81 \times 10^6/m$
$(10 \times 10^6/ft)$

.05

0

-.05

.05

0

-.05

0   4   8   12   16   20   24   28

α deg

(a) $\Lambda_F = 70^o$
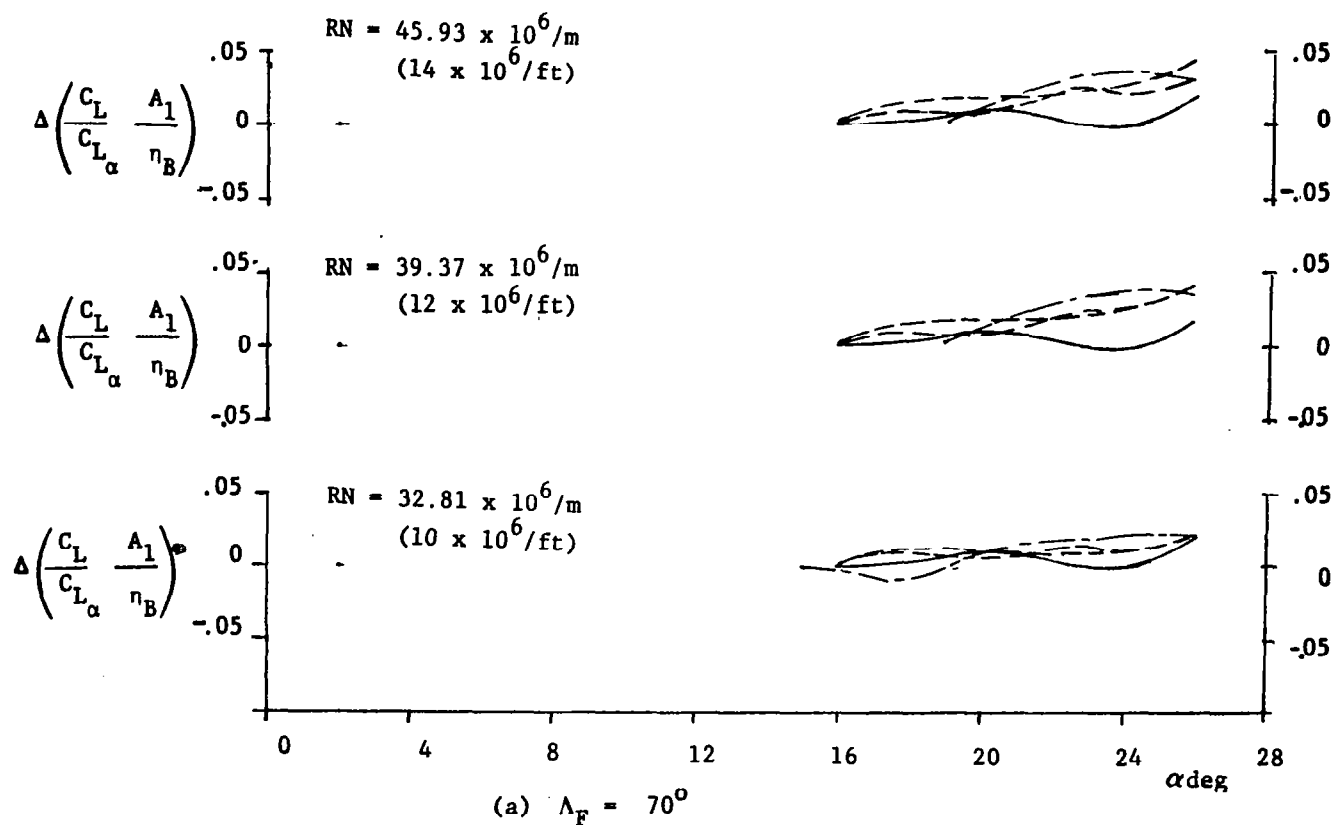
Figure 235. Incremental Values of Lift Correlation Parameter at
Unit Reynolds Numbers of 32.81, 39.37 and 45.93
Million Per Meter from Langley LTPT Test 262 Show-
ing Effects of Airfoil Section and Camber for Wing
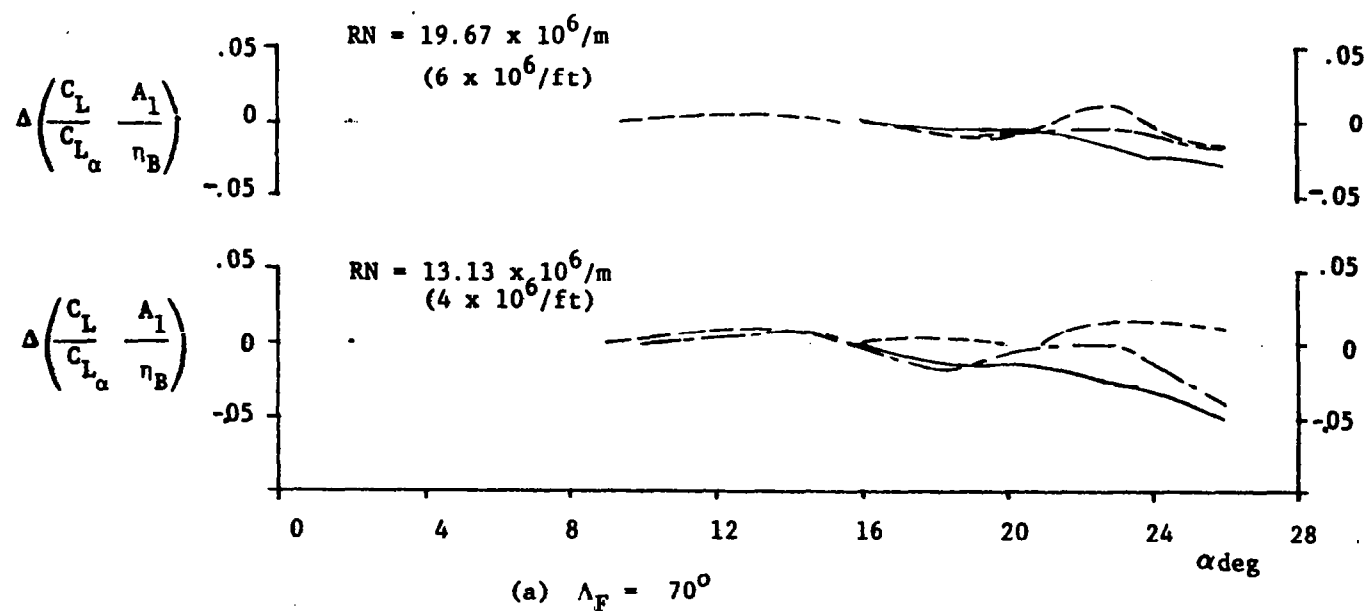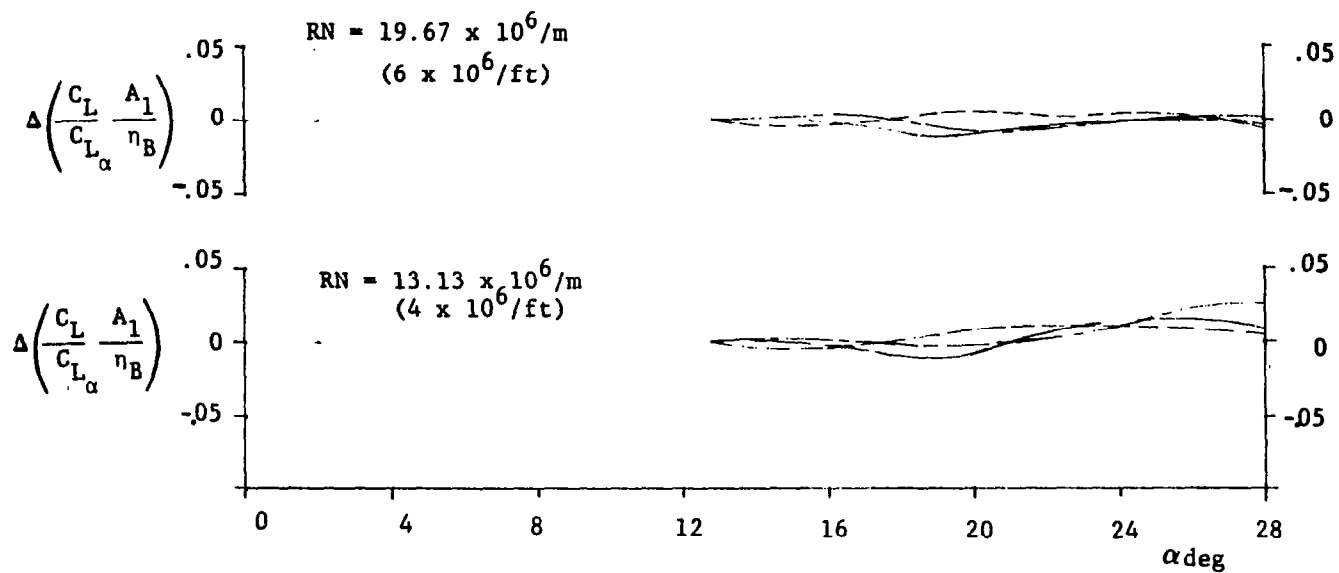III with Various Fillet Sweeps

Λ_F Λ_W Airfoil

	Λ_F	Λ_W	Airfoil
———	75	45	0012
— — —	75	45	5012
—·—	75	45	5412

.05

$\Delta\left(\dfrac{C_L}{C_{L_\alpha}} \dfrac{A_1}{\eta_B}\right)$ 0

-.05

RN = 45.93 × 10^6/m

(14 × 10^6/ft)

.05

0

-.05

$\Delta\left(\dfrac{C_L}{C_{L_\alpha}} \dfrac{A_1}{\eta_B}\right)$ .05   0   -.05

RN = 39.37 × 10^6/m

(12 × 10^6/ft)

.05

0

-.05

$\Delta\left(\dfrac{C_L}{C_{L_\alpha}} \dfrac{A_1}{\eta_B}\right)$ .05   0   -.05

RN = 32.81 × 10^6/m

(10 × 10^6/ft)

.05

0

-.05

0   4   8   12   16   20   24   28 α deg
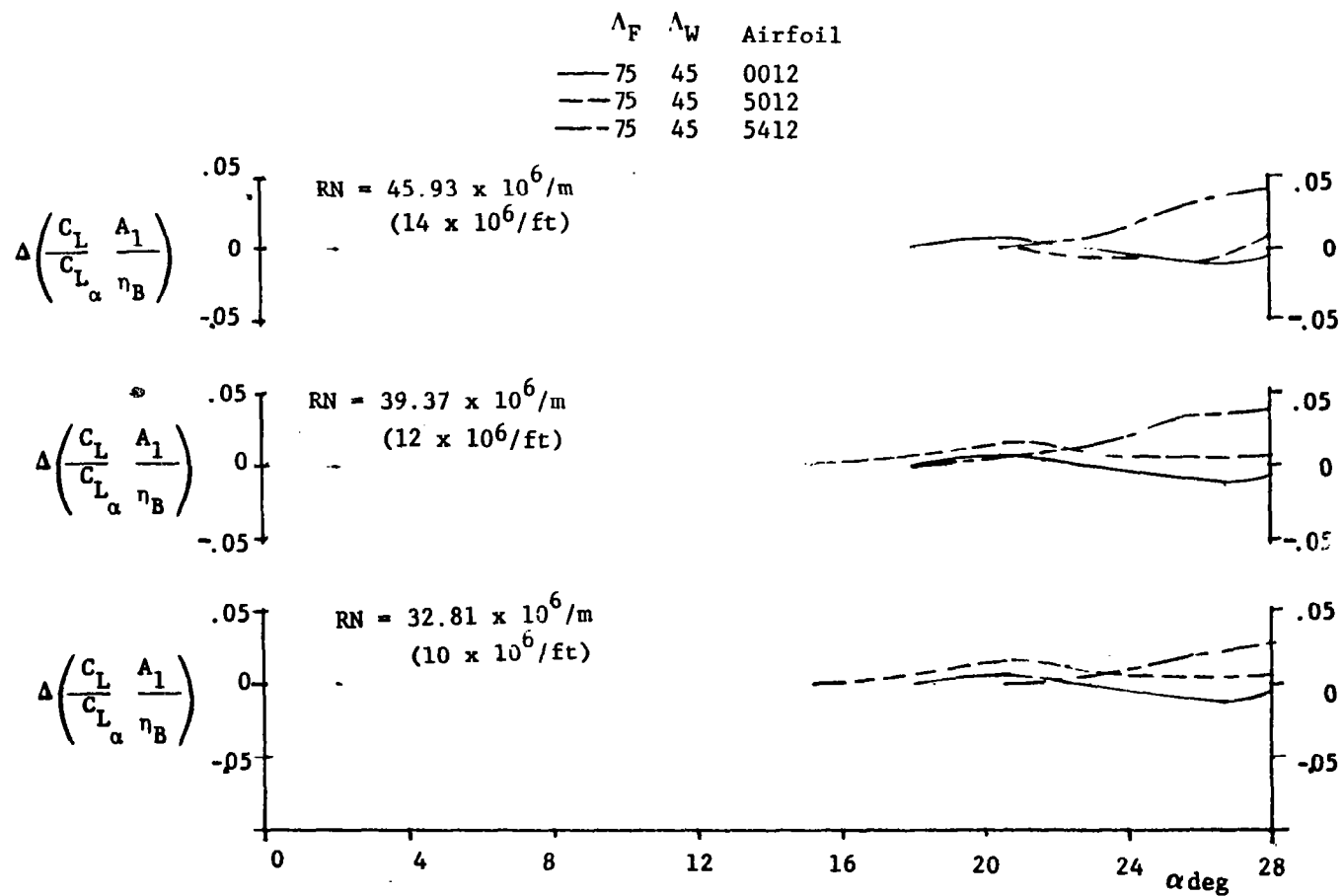
(b) Λ_F = 75°

Figure 235. Continued

(c) $\Lambda_F = 80^\circ$

Figure 235. Concluded

REFERENCES

1. Hopkins, Edward J.; Hicks, Raymond M.; and Carmichael, Ralph L.: Aerodynamic Characteristics of Several Cranked Leading-Edge Wing-Body Combinations at Mach Numbers from 0.4 to 2.94. NASA TN D-4211, 1967.

2. Corsiglia, Victor R.; Koenig, David G.; and Morelli, Joseph P.: Large-Scale Tests of an Airplane Model With a Double Delta Wing, Including Longitudinal and Lateral Characteristics and Ground Effects. NASA TN D-5102, 1969.

3. Stone, David R.; and Spencer, Bernard, Jr.: Aerodynamic and Flow Visualization Studies of Variations in the Geometry of Irregular Planform Wings at a Mach Number of 20.3. NASA TN D-7650, 1974.

4. Kruse, Robert L.; Lovette, George H.; and Spencer, Bernard, Jr.: Reynolds Number Effects on the Aerodynamic Characteristics of Irregular Planform Wings at Mach Number 0.3. NASA TM X-73132, July 1977.

5. Reference deleted. Information referred to is also presented in either Reference 8 or Reference 11.

6. Ericsson, L. E.; and Reding, J. P.; "Nonlinear Slender Wing Aerodynamics." AIAA Paper No. 76-19, 26 January 1976.

7. Benepe, D. B.: Analysis of Nonlinear Lift of Sharp- and Round-Leading-Edge Delta Wings. General Dynamics Fort Worth Division Report ERR-FW-799, 20 December 1968.

8. Schemensky, R. T.: Development of an Empirically Based Computer Program to Predict the Aerodynamic Characteristics of Aircraft, Volume I, Empirical Methods. AFFDL-TR-73-144, Volume I, November 1973.

9.   Mendenhall, M. R.; and Nielson, J. N.: Effect of Symmetrical Vortex Shedding on the Longitudinal Aerodynamic Characteristics of Wing-Body-Tail Combinations. NASA CR-2473, January 1975.

10. Spencer, B., Jr.; and Hammond, A. D.: Low-Speed Longitudinal Aerodynamic Characteristics Associated with a Series of Low-Aspect-Ratio Wings Having Variations in Leading-Edge Contour. NASA TN D-1374, September 1962.

11. USAF Stability and Control DATCOM. Air Force Flight Dynamics Laboratory, October 1960 (Revised August 1968).

12. Spencer, B., Jr.: A Simplified Method for Estimating Subsonic Lift-Curve Slope at Low Angles of Attack for Irregular Planform Wings. NASA TM X-525, 1961.

13. Polhamus, E. C.: A Concept of the Vortex Lift of Sharp-Edge Delta Wings Based on a Leading-Edge-Suction Analogy. NASA TN D-3767, December 1966.

14. Kirby, D. A.: Low-Speed Wind-Tunnel Measurements of the Lift, Drag and Pitching Moment of a Series of Cropped Delta Wings. Aeronautical Research Council (Great Britain) Report R&M 3744, November, 1972.

15. Henderson, W. P.: Studies of Various Factors Affecting Drag Due to Lift at Subsonic Speeds, NASA TN D-3584, September 1966.

16. Braslow, Albert L.; Hicks, Raymond M.; and Harris, Roy V., Jr.: Use of Grit-Type Boundary-Layer-Transition Trips on Wind-Tunnel Models. NASA TN D-3579, 1966. (Also included in NASA SP-124).

17. Chappell, P. D.: "Flow Separation and Stall Characteristics of Plane, Constant-Section Wings in Subcritical Flow." The Aeronautical Journal of the Royal Aeronautical Society, Vol 72, January 1968, pp 82-90.

18. White, F. M.; and Christoph, G. H.: A Simple New Analysis of Compressible Turbulent Two-Dimensional Skin Friction Under Arbitrary Conditions. AFFDL TR-70-133, February 1971.

19. Aerospace Handbook, Second Edition (C. W. Smith, Ed.) General Dynamics' Convair Aerospace Division Report FZA-381-II, October 1972.

20. Hoerner, S. F.: Fluid-Dynamic Drag. Hoerner Fluid Dynamics, Brick Town, N.J., c.1965.

1. Report No. NASA CR-3664	2. Government Accession No.	3. Recipient's Catalog No.
4. Title and Subtitle DEVELOPMENT OF AERODYNAMIC PREDICTION METHODS FOR IRREGULAR PLANFORM WINGS		5. Report Date February 1983
		6. Performing Organization Code
7. Author(s) David B. Benepe, Sr.		8. Performing Organization Report No.
		10. Work Unit No.
9. Performing Organization Name and Address General Dynamics Fort Worth Division P.O. Box 748 Fort Worth, Texas 76101		11. Contract or Grant No. NAS1-15073
		13. Type of Report and Period Covered Contractor Report
12. Sponsoring Agency Name and Address National Aeronautics and Space Administration Washington, DC 20546		14. Sponsoring Agency Code

15. Supplementary Notes

16. Abstract

A set of empirical methods have been developed to predict low-speed lift, drag and pitching-moment variations with angle of attack for a class of low aspect ratio irregular planform wings suitable for application to advanced aerospace vehicles. The data base, an extensive series of wind-tunnel tests accomplished by the Langley Research Center of The National Aeronautics and Space Administration, is summarized. The approaches used to analyze the wind-tunnel data, the evaluation of previously existing methods, data correlation efforts, and the development of the selected methods are presented and discussed. A summary of the methods is also presented to document the equations, computa- tional charts and design guides which have been programmed for digital computer solution. Comparisons of predictions and test data are presented which show that the new methods provide a significant improvement in capability for evaluating the landing characteristics of advanced aerospace vehicles during the preliminary design phase of the configuration development cycle.

17. Key Words (Suggested by Author(s)) Low-speed aerodynamics Lift prediction Drag prediction Pitching-moment prediction Irregular planform wings Aerospace vehicles	18. Distribution Statement Unclassified - Unlimited Subject Category 02

19. Security Classif. (of this report) Unclassified	20. Security Classif. (of this page) Unclassified	21. No. of Pages 480	22. Price A21